

**Lithium, Beryllium and Boron in  
high-K Rhyolites from Lesbos Island,  
Greece**

**Angela Herta Helbling-Marschall**



# **INAUGURAL-DISSERTATION**

zur Erlangung der Doktorwürde der  
Naturwissenschaftlichen-Mathematischen Gesamtfakultät  
der Ruprecht-Karls-Universität  
Heidelberg

vorgelegt von  
Diplom-Geologin Angela Herta Helbling-Marschall  
aus Darmstadt

Tag der mündlichen Prüfung: 23. November 2011



**Thema**

**Lithium, Beryllium and Boron in  
high-K Rhyolites from Lesbos Island,  
Greece**

Gutachter: Prof. Dr. Rainer Altherr  
Prof. Dr. Stephan Klemme



## für Yolanda und für Helena

für eure Geduld und für eure “Last” mit dieser Arbeit;  
nicht zuletzt für eure Ermunterungen:

“Mama, arbeite viel und schön und gut!”

I love deadlines, I love the whooshing noise they make as they go by.  
Douglas Adams (1952-2001)



# Contents

<b>Abstract</b>	<b>iii</b>
<b>Kurzfassung</b>	<b>v</b>
<b>1. Introduction</b>	<b>1</b>
<b>2. Geological setting</b>	<b>5</b>
2.1. The present-day tectonic framework . . . . .	5
2.2. Plate tectonic reconstruction . . . . .	9
2.3. The tectonic setting of the Miocene volcanic rocks . . . . .	16
2.4. The regional volcanic evolution . . . . .	17
2.5. The geological setting of Lesbos Island . . . . .	18
<b>3. The Polychnitos Ignimbrite</b>	<b>29</b>
3.1. Source of the Polychnitos Ignimbrite . . . . .	29
3.2. Vertical profiles - sample locations . . . . .	30
3.3. Profile A - glass and phenocrysts in the vertical profile . . . . .	30
3.4. Profile B - glass and phenocrysts in the vertical profile . . . . .	44
3.5. Additional samples from other locations . . . . .	51
<b>4. Geochemical properties of the volcanic glass</b>	<b>53</b>
4.1. Major and Minor elements . . . . .	53
4.2. Trace elements . . . . .	63
4.3. Melt evolution – discussion of geochemical data . . . . .	74
4.4. Isotope geochemistry . . . . .	84
<b>5. Geochemical properties of the phenocrysts</b>	<b>89</b>
5.1. Geochemical properties of plagioclase and alkali feldspar . . . . .	89
5.2. Strontium isotopic composition of plagioclase . . . . .	92
5.3. Geochemical properties of biotite . . . . .	96
5.4. Geochemical properties of pyroxene . . . . .	97
5.5. Geochemical properties of amphibole . . . . .	98

<b>6. Thermobarometry</b>	<b>99</b>
<b>7. Lithium, Beryllium, and Boron in glass and phenocrysts</b>	<b>105</b>
7.1. Lithium, Beryllium, and Boron concentrations in glass and feldspar	105
7.2. Lithium diffusion	109
7.3. Lithium, Beryllium, and Boron concentrations in biotite	116
7.4. Partition coefficients for Beryllium and Boron	118
7.5. Boron isotopes in the rhyolitic glass	126
<b>8. Conclusions</b>	<b>131</b>
<b>Bibliography</b>	<b>141</b>
<b>Appendix</b>	<b>163</b>
<b>A. Individual sample descriptions</b>	<b>165</b>
A.1. Vertical profiles - sample locations	165
A.2. Sample descriptions – individual samples of profile A	166
A.3. Sample descriptions – individual samples of profile B	189
A.4. Additional samples from other locations	199
<b>B. Element concentration profiles</b>	<b>205</b>
<b>C. Analytical methods</b>	<b>269</b>
C.1. Sample documentation	269
C.2. Electron probe micro-analysis – EPMA	269
C.3. Secondary ion mass spectrometry – SIMS	273
C.4. Laser-ablation ICP-MS	277
C.5. LA-ICP-MS vs. SIMS	278
C.6. Thermal ionisation mass spectrometry – TIMS	280
<b>D. Analytical data</b>	<b>283</b>
D.1. Geochemistry of the glass	283
D.2. Geochemistry of the phenocrysts	291
D.3. Lithium, Beryllium, and Boron in glass and phenocrysts	302
<b>E. Miscellaneous</b>	<b>305</b>

## Abstract

This study investigates the behaviour of Li, Be, and B in volcanic rocks as part of the subduction cycle. The partitioning of Be and B during melt evolution and volcanic processes is examined and the volcanic setting is characterized using petrological, geochemical, and isotopic tools.

The geological setting of Lesbos Island within the Aegean-Anatolian area is part of a complex system of convergence and collision of the Eurasian, African and Arabian plates. Several conflicting models for the tectonic setting of the Miocene volcanism in the Aegean exist, with the quintessential question being, if the volcanic rocks are related to subduction or to crustal extension.

Lesbos Island lies in the northeastern Aegean Sea and consists of thick Miocene volcanic deposits, which overlie a metamorphic basement. The object of this study are two vertical sample profiles (Profile A and Profile B) through the Early Miocene Polychnitos Ignimbrite, an over 100m thick ignimbrite deposit in the centre of the island. The ignimbrite contains large portions of pristine glass and therefore allows the direct observation of the quenched melt. The typical composition of the pristine high-K rhyolitic glass is  $\text{SiO}_2 \approx 69 \text{ wt\%}$ ,  $\text{K}_2\text{O} \approx 7 \text{ wt\%}$ ,  $\text{H}_2\text{O} \approx 4 \text{ wt\%}$ .

The magma source was characterized using the B isotopic composition of the volcanic glass with relatively high  $\delta^{11}\text{B}$  ( $-2.30 \pm 1.28 \text{ ‰}$  to  $-3.22 \pm 1.07 \text{ ‰}$ ), fluid-mobile trace element contents and ratios ( $\text{B} = 101 \text{ }\mu\text{g/g}$ ,  $\text{B/Nb} = 3.90$ ) in comparison to upper continental crust, and results from Sr, Nd, and Pb isotope analyses. The elevated  $\delta^{11}\text{B}$  values demonstrate, that the magma sources for samples from the Profile A and Profile B have been enriched by slab-derived fluids, while crustal material was not assimilated.

Magma chamber  $P$ - $T$  conditions for samples from Profile A were investigated using a combination of six methods, feldspar thermobarometry, accessory mineral saturation thermometry, and  $\text{H}_2\text{O}$  solubility in rhyolitic melts. Pressures in the magma chamber were between 75 MPa and 150 MPa (corresponding magma chamber depth 2.6 km to 5.3 km) and temperatures between 815 °C and 848 °C. Equilibrium between melt and phenocrysts was reached under these conditions. Taking advantage of the high amount of pristine glass, partition coefficients were determined for Be and B between glass, and plagioclase and alkali feldspar ( $D_{\text{Be}} \text{ Pl/glass} = 0.36$  ( $\text{An}_{20}$ );  $D_{\text{Be}} \text{ Pl/glass} = 0.43$  ( $\text{An}_{28}$ );  $D_{\text{B}} \text{ Pl/glass} = 0.009$ ;  $D_{\text{Be}} \text{ Akf/glass} = 0.06$ ;  $D_{\text{B}} \text{ Akf/glass} = 0.005$ ) and establish a well-founded data set for high-silica mag-

matic systems. A positive correlation between the An content of the plagioclase and  $D_{\text{Be}}$  Pl/glass was confirmed.

Using selected trace element contents in the volcanic glass (Sr, Ba, Pb) and simple fractionation models it is shown, that samples from the two vertical profiles did not have a common parent melt and that neither melt evolved from the other by fractional crystallisation and/or crystal assimilation. A separate origin of samples from the two vertical profiles was shown by the significantly different Sr isotopic composition of contained plagioclase phenocrysts (Profile A  $^{87}\text{Sr}/^{86}\text{Sr} = 0.70827(5)$ ; Profile B  $^{87}\text{Sr}/^{86}\text{Sr} = 0.70798(7)$ ). However, both melts have undergone a substantial amount of fractional crystallisation, as expected for rhyolitic melts, and as shown through enrichment of Be ( $5.2 \mu\text{g/g}$ ), Nd ( $46 \mu\text{g/g}$ ), and Nb ( $25 \mu\text{g/g}$ ) of the volcanic glass in comparison to upper continental crust.

The two vertical profiles, Profile A and Profile B, are demonstrated to stem from two separate ignimbrite units within the Polychnitos Ignimbrite, and to have originated from separate volcanic vents, separate volcanic plumbing systems, and ultimately from separate magma source areas within the mantle. The two magmas have evolved separately, yet in a similar way: prior to melting both source areas have been subject to metasomatism from slab fluids, both magmas have undergone a substantial amount of fractional crystallisation without assimilation of ancient crustal material, and both melts have assimilated plagioclase xenocrysts from a co-genetic magma, probably from older volcanics within the same volcanic plumbing system.

Despite substantial petrographic differences throughout both vertical profiles, especially in Profile A, each profile is geochemically homogeneous throughout glass and phenocrysts for all analysed elements, with the exception of lithium. Evidence for significant Li diffusion was detected in glass and minerals, and together with high-temperature devitrification, was used to develop a model combining late degassing (after deposition), Li diffusion and hydrothermal “cooking” of the matrix.

The systematics of lithium, beryllium, and boron were investigated within a well-characterised petrological and geochemical background of mantle signatures, melt evolution, magma chamber conditions and post-depositional processes.

## Kurzfassung

In der vorliegenden Studie wird das Verhalten von Li, Be und B in vulkanischen Gesteinen als Teil des Subduktionszyklusses untersucht. Die Verteilung von Be und B während der Magmenentwicklung und bei vulkanischen Prozessen wird erforscht und die vulkanischen Rahmenbedingungen werden mit Hilfe petrologischer, geochemischer und isotopischer Methoden charakterisiert.

Die geologische Situation von Lesbos innerhalb der Ägäisch-Anatolischen Region ist Teil eines komplexen Systems von Konvergenz und Kollision der eurasischen, afrikanischen und arabischen Platten. Es gibt mehrere sich gegenseitig widersprechende Modelle für die tektonischen Rahmenbedingungen des miozänen Vulkanismus in der Ägäis, deren wesentliche Fragestellung es ist, ob die vulkanischen Gesteine in Beziehung zu Subduktion oder Krustenextension stehen.

Die Insel liegt in der Nord-Ost-Ägäis und besteht aus mächtigen miozänen vulkanischen Ablagerungen, die metamorphem Grundgebirge auflagern. Studienobjekte sind zwei vertikale Probenprofile (Profil A und Profil B) durch den untermiozänen Polychnitos-Ignimbrit, eine über 100 m mächtige Ignimbritablagerung im Zentrum der Insel. Der Ignimbrit enthält große Anteile frischen Glases, das die direkte Untersuchung der abgeschreckten Schmelze erlaubt. Die typische Zusammensetzung des hoch-K Rhyolit-Glases ist  $\text{SiO}_2 \approx 69 \text{ wt\%}$ ,  $\text{K}_2\text{O} \approx 7 \text{ wt\%}$ ,  $\text{H}_2\text{O} \approx 4 \text{ wt\%}$ .

Die Magmenquelle wurde mit Hilfe der B-isotopischen Zusammensetzung des vulkanischen Glases charakterisiert, relativ hohen  $\delta^{11}\text{B}$  Werten ( $-2.30 \pm 1.28 \text{ ‰}$  bis  $-3.22 \pm 1.07 \text{ ‰}$ ), den Gehalten und Verhältnissen fluid-mobiler Spurenelemente ( $\text{B} = 101 \text{ } \mu\text{g/g}$ ,  $\text{B/Nb} = 3.90$ ) im Vergleich zu oberer kontinentaler Kruste und den Ergebnissen aus Sr-, Nd-, and Pb-Isotopen-Untersuchungen. Die erhöhten  $\delta^{11}\text{B}$  Werte zeigen, dass die Magmenquellen der Proben aus Profil A und Profil B durch Fluide aus der subduzierten Platte angereichert und dass kein Krustenmaterial assimiliert wurde.

Die Bedingungen in der Magmenkammer für Proben aus Profil A wurde durch die Kombination aus sechs verschiedenen Methoden, Feldspat-Thermobarometrie, Thermometrie anhand der Sättigung akzessorischer Minerale und der Löslichkeit von  $\text{H}_2\text{O}$  in rhyolitischen Schmelzen begrenzt. In der Magmenkammer herrschten Drücke zwischen 75 MPa und 150 MPa (einer Tiefe der Magmenkammer zwischen 2.6 km und 5.3 km entsprechend) und Temperaturen zwischen  $815^\circ\text{C}$  und  $848^\circ\text{C}$ . Unter diesen Bedingungen wurde Gleichgewicht zwischen Schmelze und

Phänokristen erreicht. Der Vorteil aus dem großen Anteil an vorhandenem frischem Glas wurde genutzt und Verteilungskoeffizienten für Be and B zwischen Glas und Plagioklas und Alkalifeldspat bestimmt ( $D_{\text{Be}} \text{Pl/Glas} = 0.36$  ( $\text{An}_{20}$ );  $D_{\text{Be}} \text{Pl/Glas} = 0.43$  ( $\text{An}_{28}$ );  $D_{\text{B}} \text{Pl/Glas} = 0.009$ ;  $D_{\text{Be}} \text{Akf/Glas} = 0.06$ ;  $D_{\text{B}} \text{Akf/Glas} = 0.005$ ) und begründen einen gut fundierten Datensatz für silikatreiche magmatische Systeme. Eine positive Korrelation zwischen An Gehalt von Plagioklas und  $D_{\text{Be}} \text{Pl/Glas}$  wurde bestätigt.

Mit Hilfe ausgesuchter Spurenelementgehalte im vulkanischen Glas und einfacher Fraktionierungsmodelle kann gezeigt werden, dass Proben der zwei vertikalen Profile keine gemeinsame Stammschmelze haben können und dass keine der beiden Schmelzen aus der anderen durch Kristallfraktionierung und/oder Kristallassimilierung entstanden sein kann. Der getrennte Ursprung der Proben aus den zwei vertikalen Profilen wurde durch die signifikant unterschiedliche Sr-isotopische Zusammensetzung der enthaltenen Plagioklas-Phänokristen gezeigt ( $^{87}\text{Sr}/^{86}\text{Sr}$  0.70827(5) Profil A,  $^{87}\text{Sr}/^{86}\text{Sr}$  0.70798(7) Profil B). Beide Schmelzen durchliefen beachtliche Kristallfraktionierung, wie das für rhyolitische Schmelzen zu erwarten ist, und wie durch die Anreicherung von Be (5.2  $\mu\text{g/g}$ ), Nd (46  $\mu\text{g/g}$ ) und Nb (25  $\mu\text{g/g}$ ) im Vergleich zu oberer kontinentaler Kruste klar wird.

Die zwei vertikalen Profile, Profil A and Profie B, stammen nachweislich aus zwei getrennten Ignimbriteinheiten innerhalb des Polychnitos-Ignimbrits, und entstammen unterschiedlichen Eruptionssorten, unterschiedlichen Magmafördersystemen, und letztlich unterschiedlichen Magmenquellen im Erdmantel. Die zwei Magmen haben sich getrennt voneinander entwickelt, jedoch in ganz ähnlicher Art und Weise: vor der Schmelzbildung wurden beide Quellregionen durch Fluide aus der subduzierten Platte metasomatisch überprägt, beide Magmen wurden deutlich durch Kristallfraktionierung differenziert, ohne Assimilation von altem Krustenmaterial, und beide Magmen assimilierten Plagioklas-Xenokristen eines kogenetischen Magmas, wahrscheinlich älterer Vulkanite aus dem selben Fördersystem.

Trotz deutlicher petrographischer Unterschiede innerhalb der beiden vertikalen Probenprofile, besonders in Profil A, sind Glas und Phänokristen in beiden Profilen geochemisch homogen bezüglich aller analysierten Elemente, mit der Ausnahme von Lithium. In Glas und Mineralen wurden Belege für gravierende Lithiumdiffusion entdeckt und zusammen mit Hinweisen auf Hochtemperatur-Devitrifikation benutzt um ein Modell zu entwickeln, dass eine späte Entgasung (nach der Ablagerung), Li-Diffusion und hydrothermales "Kochen" der Matrix kombiniert.

Die Lithium-, Beryllium- und Bor-Systematik wurde vor einem gut definierten petrologisch-geochemischen Hintergrund von Mantelsignaturen, Magmenentwicklung, Magmenkammerbedingungen und Post-Ablagerungs-Prozessen untersucht.

## 1. Introduction

**Lesbos Island, Greece** With a surface area of  $\approx 1630\text{km}^2$  Lesbos is the third largest Greek island. It lies in the northeastern Aegean Sea and is separated from the west coast of Anatolia by a narrow strip of water (7 to 10km wide). The island consists of thick deposits of Miocene volcanic rocks, which cover about two thirds of the surface area and, together with Neogene sediments, rest upon a Palaeozoic metamorphic basement. The study presented here concerns the Early Miocene ignimbrite sequence in the centre of the island, referred to as the Polychnitos Ignimbrite, with a total thickness of over 100m and an exposed surface area today of  $\approx 190\text{km}^2$  (PE-PIPER, 1980a).

The Anatolia–Aegean area is part of a complex system of convergence and collision involving the Eurasian, African, and Arabian plates (e.g. BOZKURT, 2001). A number of smaller orogenic belts, including Turkey and Greece, constitute the Eastern Mediterranean Orogen, which furthermore is part of the Alpine–Himalayan orogenic belt, that formed when Tethys was destroyed (DERCOURT *et al.*, 1986, 1993; ŞENGÖR, 1989; ROSENBAUM & LISTER, 2002). There are several conflicting models for the tectonic setting of the Miocene volcanic rocks in the north-eastern Aegean and Western Anatolia, which revolve around the question, if the volcanic rocks are subduction-related (e.g. FYTIKAS *et al.*, 1984) or related to crustal extension (e.g. SEYİTOĞLU & SCOTT, 1992a,b; DINTER, 1998). Past models have also involved subduction *and* extension in differing time frames (e.g. YILMAZ *et al.*, 2001), crustal thickening (YILMAZ, 1990) or an a-typical back-arc setting with a stagnant slab (AGOSTINI *et al.*, 2010).

**High-K Rhyolites** Igneous rocks high in potassium are generated either by crustal melting or differentiation of mantle melts or a combination of the two. It has been shown experimentally and through analyses of natural migmatitic rocks, that high-K granitic and rhyolitic melts can be generated entirely from crustal melting, without the contribution of a mantle component, namely by biotite dehydration melting of immature sediments (metagreywacke) at lower crustal pressures (PATIÑO DOUCE & BEARD, 1996; PATIÑO DOUCE, 1997; PATIÑO DOUCE & MCCATHY, 1998; OTAMENDI & PATIÑO DOUCE, 2001).

Examples of late Miocene crust-derived, so-called S-type granites exist as small bodies in the southern Aegean, on the islands of Tinos, Paros, Naxos, and Ikaria

(ALTHERR *et al.*, 1982, 1988; MEZGER *et al.*, 1985; SKARPELIS *et al.*, 1992; PEEPER *et al.*, 1997).

On the other hand, examples of high-K basaltic andesites and shoshonites in Western Anatolia were shown to have been generated predominantly by melting in the mantle (INNOCENTI *et al.*, 2005; TONARINI *et al.*, 2005). Note however, these rocks are less differentiated than rhyolites.

**Lithium, Beryllium, and Boron** Boron and Boron isotopes are ideal tracers for subduction zone processes (ISHIKAWA & NAKAMURA, 1994; LEEMAN & SISSON, 2002; TURNER *et al.*, 2007), because the lower continental crust is depleted in B and isotopically light, while slab fluids are B-rich and isotopically heavy. The advantage of B isotopes over other isotope systems is the capability to distinguish between (1) crustal contamination, i.e. contamination in the magma chamber from crustal wall rocks or during magma ascent in the crust and (2) slab signals, i.e. contamination of the magma source by melt or fluid derived from subducted sediments, altered oceanic crust, or serpentinite (TONARINI *et al.*, 2005).

Lithium is traditionally studied together with B, and was believed to be a tracer for fluid-processes (e.g. review by TOMASCAK, 2004), just like B. However, this perception has been strongly modified, after the extremely fast diffusion properties and kinetic isotope fractionation of lithium were identified by RICHTER *et al.* (2003) and later workers (LUNDSTROM *et al.*, 2005; COOGAN *et al.*, 2005; TENG *et al.*, 2006; JEFFCOATE *et al.*, 2007; PARKINSON *et al.*, 2007; GALLAGHER & ELLIOTT, 2009). It was suggested by RICHTER *et al.* (2003) to use Li disequilibria to detect rapid processes, active only shortly before magma solidification (i.e. shortly before eruption or after deposition). Today Li is being established as a geospeedometer and tracer for late volcanic processes such as cooling and degassing (BERLO *et al.*, 2004; COOGAN *et al.*, 2005; KURITANI & NAKAMURA, 2006; KENT *et al.*, 2007; JEFFCOATE *et al.*, 2007; GALLAGHER & ELLIOTT, 2009).

Beryllium is not fluid mobile, or at least much less so than B, but it is also incompatible during fractional crystallisation. Therefore the B/Be ratio is an important tracer for fluid influx corrected for fractional crystallisation (RYAN & LANGMUIR, 1993).

**Study framework** The light elements Li, Be and B have been studied in the petrology group at the Institut für Geowissenschaften (Universität Heidelberg) for more than a decade in different geological settings. The crucial instrument for the investigation of Li, Be, and B element concentrations and isotopes is the secondary ion mass spectrometer (SIMS) at the Institut für Geowissenschaften, operated by

---

Thomas Ludwig. The SIMS enables precise in-situ analysis of element concentration between  $\approx 1 \text{ ng/g}$  and several tens of weight percent (concentration differences of a factor of  $10^8$ ). The accuracy for B isotope analysis is better than 2‰ (LUDWIG *et al.*, 2011).

The investigations at Heidelberg started with the examination of Li partitioning in mantle rocks (SEITZ & WOODLAND, 2000; OLKER, 2001; PAQUIN & ALTHERR, 2002) and eclogites (WOODLAND *et al.*, 2002). Subsequently concentrations of all three elements were investigated in mantle rocks (PAQUIN *et al.*, 2004; KALIWODA, 2004; KALIWODA *et al.*, 2004, 2008), and rocks from the continental crust, such as amphibolites (HEPP *et al.*, 2004). Other studies investigated Li, Be, and B in serpentinite mounts (PABST, 2009) or in granites from Greenland (KALIWODA *et al.*, 2011); several more studies have been published.

In early 2000 a larger project on the subduction cycle of Li, Be, and B on the example of the Aegean region was initiated by Angelika Kalt and Rainer Altherr and financially supported by the Deutsche Forschungsgemeinschaft (DFG). Within this larger framework, a number of studies were conducted on Li, Be, and B, among these in granites (HILLERS *et al.*, 2009; HEZEL *et al.*, 2011), high-pressure metamorphic rocks (e.g. MARSCHALL, 2005; MARSCHALL *et al.*, 2006a,b), metapelites (STEPPAN, 2003), serpentinites (PELLETIER *et al.*, 2008), lavas from Nea Kameni (Santorini) and Nisyros (CABATO, 2007; SONNTAG, 2007), pumice from Santorini (PANIENKA, 2011) and this study, the high-K rhyolitic ignimbrite from Lesbos Island. Analytical work for this thesis was predominantly carried out between 2000 and 2005 at the Institut für Geowissenschaften, Universität Heidelberg.

**Polychnitos Ignimbrite** Two vertical sample profiles through the extensive pyroclastic density flow deposit are objects of this study; the Polychnitos Ignimbrite contains large portions of pristine glass, which allows the direct observation of the quenched melt. The magma chamber conditions and therefore equilibrium environment between melt and minerals are investigated using a combination of thermobarometric methods.

Partition coefficients for Be and B between phenocrysts and glass (melt) for mafic systems have been published previously (RYAN, 1989; DUNN & SEN, 1994; BINDEMAN *et al.*, 1998; EVENSEN *et al.*, 1999; BINDEMAN & DAVIS, 2000; EVENSEN, 2001), however data for differentiated systems are scarce (EVENSEN, 2001; EVENSEN & LONDON, 2002). Partition coefficients are obtained for rhyolitic melts in this study taking advantage of the high amount of pristine glass in the Polychnitos Ignimbrite.

The structure of a vertical sample profile through the ignimbrite deposit (Pro-

file A) changes dramatically within the profile height of 40m from an unwelded, grey to white coloured ash tuff at the bottom to a densely welded, black, glassy rock at the top.

An investigation of the exact geochemistry (major, minor, and trace element composition), isotopic composition, and the water content of glass and minerals reveals that changes throughout the ignimbrite deposit are purely of physical nature and are not caused by chemical differences. The geochemical and isotopic fingerprint is compared locally (to other volcanic rocks on Lesbos Island) and regionally (to volcanic rocks from W Anatolia) to provide insight into the magma source and into the melt evolution.

This study gains further insight into the systematics of Li, Be, and B in the subduction cycle. The partitioning of the three elements during melt evolution and volcanic processes is investigated and the volcanic setting is characterized using petrological, geochemical, and isotopic tools.

## 2. Geological setting

### 2.1. The present-day tectonic framework

The Eastern Mediterranean Orogen is part of the Alpine–Himalayan orogenic belt, that formed when Tethys was destroyed, by suturing of Gondwana-derived fragments to Eurasian crust (DERCOURT *et al.*, 1986, 1993; ŞENGÖR, 1989; ROSENBAUM & LISTER, 2002). It consists of a number of smaller orogenic belts, including those of Greece and Turkey (Fig. 2.1). The Hellenide Orogen links the orogenic belt of the Balkan Peninsula to Turkey (PE-PIPER & PIPER, 2001), while the Turkish Orogen connects the Mediterranean Orogen to the Asiatic Tethyan System (ŞENGÖR & YILMAZ, 1981; BOZKURT, 2001).

KETİN (1966) introduced a fourfold Alpine subdivision of Turkey from N to S: Pontides, Anatolides, Taurides, and Border Folds (Fig. 2.1). ŞENGÖR & YILMAZ (1981) divided KETİN's (1966) Pontides into two parts, the Rhodope-Pontide fragment and the Sakarya continent (Fig. 2.1), which are separated by the E-trending Intra-Pontide suture.

The Anatolia–Aegean area is part of a complex system of convergence and collision involving the Eurasian, African, and Arabian plates (e.g. BOZKURT, 2001). The present-day tectonics of the eastern Mediterranean region are controlled by the following major elements: the North Anatolian Fault (NAF), the East Anatolian Fault (EAF), the Dead Sea Fault (DSF) and the Aegean–Cyprean Arc (Figs. 2.1 & 2.2).

The North Anatolian Fault and the East Anatolian Fault are two intra-continental strike-slip faults along which the Anatolian plate escapes westwards at a rate of  $\approx 20$  mm/a (WESTAWAY, 1994; STRAUB & KAHLE, 1995; PFISTER *et al.*, 1998; KAHLE *et al.*, 1998) from the collision of the Arabian Plate with the Eurasian Plate (ŞENGÖR & YILMAZ, 1981; ŞENGÖR *et al.*, 1985). The extrusion of Anatolia to the W is accompanied by anticlockwise rotation and translation (MCKENZIE, 1970; DEWEY & ŞENGÖR, 1979; ROTSTEIN, 1984; WESTAWAY, 1994). Where the NAF and EAF meet, E of Karlıova in north-eastern Turkey, they form a continental triple junction. The North Anatolian Fault (NAF) is a dextral fault zone of  $\approx 1500$  km length, that runs in a broad arc shape approximately E–W from eastern Turkey to eastern Greece. It is principally a single zone a few hundred metres to 40 km wide and along most of its length composed of a few shorter subparallel fault strands. Just

## 2. Geological setting

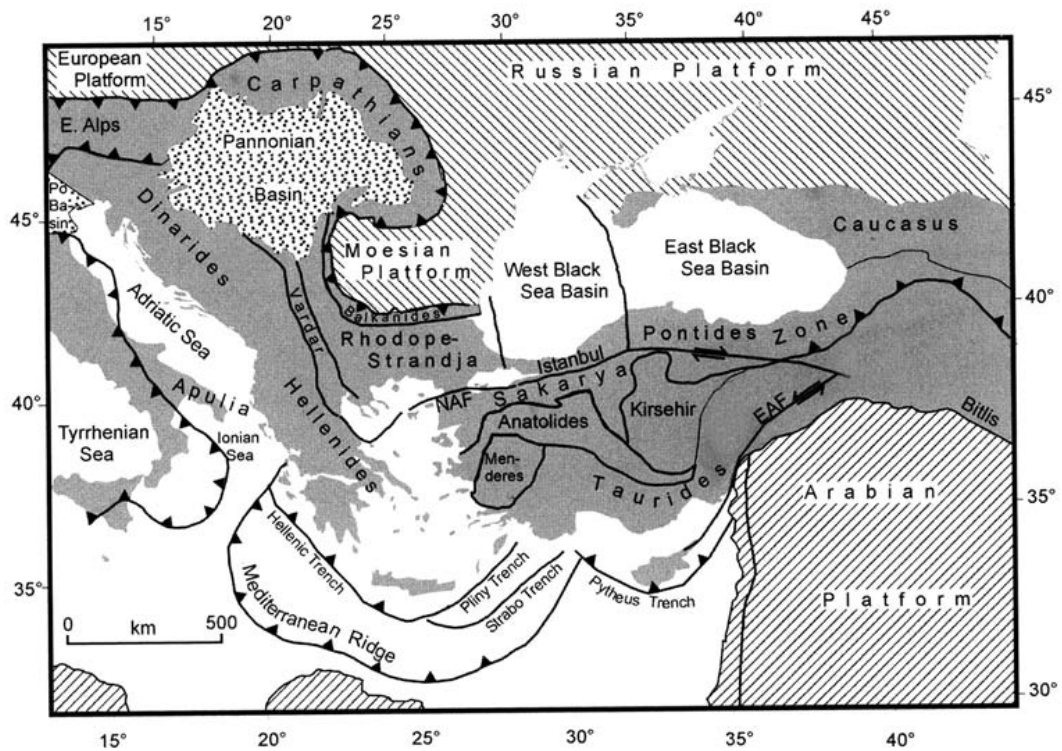


**Fig. 2.1.** The components of the eastern Mediterranean orogen in their regional context. EAF = East Anatolian Fault, NAF = North Anatolian Fault. (PE-PIPER & PIPER, 2002)

E of the Sea of Marmara at Dokurcun the NAF splits into two major strands, the northern strand, which contains the most active section of the NAF, and the southern strand, respectively. The NAF forms part of the plate boundary between the Anatolian and Eurasian plates (AMBRASEYS, 1970; MCKENZIE, 1972; DEWEY, 1976; ŞENGÖR *et al.*, 1985; KIRATZI, 1993).

The East Anatolian Fault (EAF) is a  $\approx 550$  km long, approximately NE-trending, sinistral fault zone, that runs from Karlıova to Kahramanmaraş. At both ends the EAF forms triple junctions, at Karlıova (K in Fig. 2.2) with the NAF and at Kahramanmaraş with the Dead Sea Fault (DSF in Fig. 2.2). It consists of a series of parallel faults, which are subparallel or oblique to the general trend (ŞENGÖR *et al.*, 1985; HEMPTON, 1985; DEWEY *et al.*, 1986; TAYMAZ *et al.*, 1991; LYBÉRIS *et al.*, 1992; WESTAWAY, 1994). The EAF forms part of the plate boundaries between the Anatolian and Eurasian plates and between the African and Arabian plates and it is considered a conjugate structure to the NAF (BOZKURT, 2001).

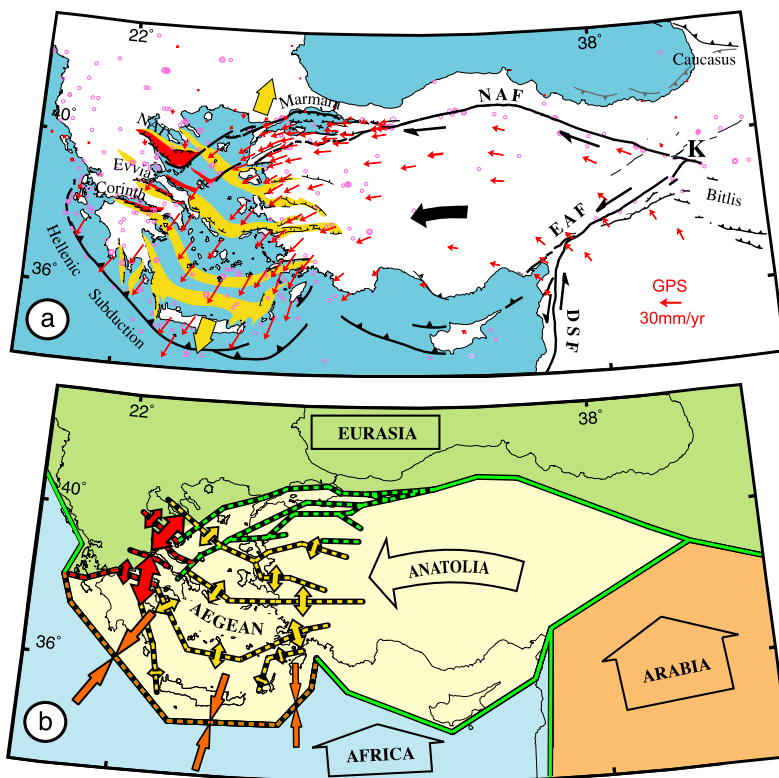


**Fig. 2.2.** Tectonic setting of continental extrusions in the eastern Mediterranean and simplified boundary conditions.

Ⓐ The Anatolian–Aegean region escapes westward from the Bitlis–Caucasus collision zone between Arabia and Eurasia, as shown by GPS velocity vectors (red arrows, referenced to a fixed Eurasia, from MCCLUSKY *et al.*, 2000).<sup>86</sup> The extruded region is bounded to the north by the North Anatolian Fault (NAF), to the East by the East Anatolian Fault (EAF) and to the Southwest by the Hellenic subduction zone. In the west the NAF interacts with the back-arc Aegean extension associated with the Hellenic subduction. Yellow features indicate Aegean sutures that have been active in the last 15Ma and diverging yellow arrows indicate overall direction of extensions. The structures in red have accelerated extension rates as an effect of the NAF propagating into the region (ARMIJO *et al.*, 1996). NAT = North Aegean Trough, DSF = Dead Sea Fault, K = Karlova Triple Junction, pink circles = earthquakes with  $M \geq 6$  between 1970 and 2001. Central Anatolia and the central Aegean Sea have no significant seismicity.

Ⓑ Simplified geometry of structures used to model the GPS velocities. Motion at distant boundaries (green) combines Anatolia/Eurasia motion given by MCCLUSKY *et al.* (2000) with Eurasia/Africa/Arabia motion from SELLA *et al.* (2003). Motion from hatched structures is as determined by FLERIT *et al.* (2003). The Aegean region is allowed to undergo extension (yellow structures with extension direction indicated by yellow double arrows). The red structures and arrows indicate features where extension is allowed to be increased by the NAF's western end. The orange structures model the closure due to subduction with convergence direction indicated by arrows. Direction and size of arrows are schematic and not to scale. (FLERIT *et al.*, 2004)

## 2. Geological setting

---

The Dead Sea Fault (DSF) is a sinistral intra-plate strike-slip fault zone, ~ 1000km long, N–S trending and runs along the E coast of the Mediterranean. It separates the African Plate from the Arabian Plate (e.g. ŞENGÖR & YILMAZ, 1981; GARFUNKEL, 1991; ROTSTEIN & KAFKA, 1982; DEWEY *et al.*, 1986; AKSU *et al.*, 1992), taking up the differential movement of these plates (the Arabian plate is moving faster to the N than the African Plate) (BARKA & REILINGER, 1997; DEMETS *et al.*, 1994).

The Aegean–Cyprean Arc denotes the location, where the present subduction of the African Plate underneath the Aegean–Anatolian Plate takes place in a N–NE direction (e.g. PAPAACHOS & COMNINAKIS, 1971; MCKENZIE, 1978; FYTIKAS *et al.*, 1984; MEULENKAMP *et al.*, 1988; SPAKMAN *et al.*, 1988; MART & WOODSIDE, 1994). The nature and structure of the Aegean Arc varies: in the W, at the Ionian trench, the convergence between the Aegean lithosphere and the Ionian basin is taken up, while in the E it acts more like a transform fault (MCKENZIE, 1978; LE PICHON & ANGELIER, 1979; LE PICHON *et al.*, 1979). The nature and structure of the Cyprean Arc, is a matter of ongoing debate. It is proposed by WOODSIDE (1976, 1977); NUR & BEN-AVRAHAM (1978); DEWEY & ŞENGÖR (1979); ŞENGÖR (1979a); BEN-AVRAHAM *et al.* (1988); VIDAL *et al.* (2000) that W of Cyprus eastern Mediterranean oceanic crust is subducted to the NE. S of Cyprus the subduction to the N is affected by the collision with the Eratosthenes Seamount (DEWEY & ŞENGÖR, 1979; ROTSTEIN & KAFKA, 1982; GLOVER & ROBERTSON, 1998). While E of Cyprus supposedly no subduction, but strike-slip movement takes place (MCKENZIE, 1972, 1976; MORELLI, 1978; HARSCH *et al.*, 1981; SWARBRICK, 1993; KEMPLER & GARFUNKEL, 1994; MART, 1994; PAYNE & ROBERTSON, 1995).

In the hanging plate, N of the subduction zone, one of the most rapidly extending areas of continental crust on Earth is found (e.g. TAYMAZ *et al.*, 1991; PE-PIPER & PIPER, 2001; BOZKURT, 2001): the Aegean Extensional Province, including western Anatolia and parts of Greece, Macedonia, Bulgaria, and Albania (BOZKURT, 2001). There are different models for the extension (BOZKURT, 2001; AGOSTINI *et al.*, 2010):

1. *Tectonic escape model*: the westward extrusion of the Anatolian block along its boundaries since the late Serravallian (Middle Miocene) (see Fig. 2.2) (e.g. MCKENZIE, 1972; DEWEY & ŞENGÖR, 1979; ŞENGÖR, 1979b, 1987; GÖRÜR *et al.*, 1995; MCCLUSKY *et al.*, 2000).
2. *Back-arc spreading model*: back-arc extension caused by the S–SW migration of the Aegean Trench (MCKENZIE, 1978; LE PICHON & ANGELIER, 1979;

HORVÁTH & BERCKHEMER, 1982; MEULENKAMP *et al.*, 1988). However, age suggestions for the initiation of the subduction roll-back process range between 5 Ma and 60 Ma (e. g. MCKENZIE, 1978; LE PICHON & ANGELIER, 1979, 1981; MEULENKAMP *et al.*, 1988; KISSEL & LAJ, 1988).

3. *Orogenic collapse model*: extension induced by spreading of over-thickened crust in the latest Oligocene/Early Miocene, after the most recent collision across Neotethys in the Palaeocene (e. g. SEYİTOĞLU & SCOTT, 1991, 1992a).
4. *Two-stage model*: orogenic collapse (first stage) in the Miocene/Early Pliocene followed by westward escape of the Anatolian block (second stage) in the Plio-Quaternary (KOÇYIĞIT *et al.*, 1999) or orogenic collapse combined with slab retreat (e. g. GAUTIER *et al.*, 1999; JOLIVET, 2001).
5. *Differential advancement of upper plates*: a simple model where extension is associated by the differential movement of the Greek and Anatolian microplates over a heterogeneous African plate was suggested by DOGLIONI *et al.* (2002) and described in detail in the light of the most recent geodynamic and geochemical evidence by AGOSTINI *et al.* (2010).

## 2.2. Plate tectonic reconstruction

The whole section “Plate tectonic reconstruction” follows largely publications by STAMPFLI (2000) and STAMPFLI & BOREL (2002). Their work is based on a new plate tectonic model, integrating geodynamic constraints, such as dynamic plate boundaries, plate buoyancy, ocean spreading rates and major tectonic and magmatic events.

The Tethys is the ocean that separated the late Palaeozoic supercontinents Gondwana and Laurasia after the break-up of Pangaea. However, it did not consist of a single tectonic plate, but rather of a number of variably-sized continental fragments (BOZKURT *et al.*, 2000). It is still a matter of debate which Tethys existed at what time. However, there is a general agreement about the following (STAMPFLI, 2000):

- a mainly Palaeozoic ocean north of the Cimmerian continent(s): the Palaeotethys,
- a younger Late Palaeozoic to Mesozoic ocean located south of the Cimmerian continent(s): the Neotethys,

## 2. Geological setting

---

- and a Middle Jurassic ocean: the Alpine Tethys (FAVRE & STAMPFLI, 1992; STAMPFLI & MARCHANT, 1997).

The large, multi-branched, collisional orogen, that formed by closure of Palaeotethys, extends today from the E Carpathians and the N Dobruja to the Asiatic shores and is called *Cimmerides*. The orogenic products from the closure of the Neotethyan oceans are called *Alpides* (ŞENGÖR *et al.*, 1984).

### 2.2.1. Palaeotethys (STAMPFLI, 2000; STAMPFLI & BOREL, 2002):

Between the Neoproterozoic and the Silurian several stages of opening of back-arc basins, both successful and aborted, can be identified, leading first to the genesis of the Rheic Ocean, then of Palaeotethys. After southward subduction of the Rheic ocean and subsequently of its mid-ocean ridge underneath Gondwana, slab roll-back triggered the opening of Palaeotethys. The opening was associated with the detachment of the ribbon-like Hun superterrane from Gondwana's northern margin (Fig. 2.3; STAMPFLI, 1996; VON RAUMER *et al.*, 1998).

Subsidence of Palaeotethys (Early Ordovician to Early Silurian times, from Australia to India) as well as closure (Moscovian to Early Triassic times, from Morocco to Greece) along a certainly very oblique convergence zone, was diachronous. The diachronous closure is discussed in STAMPFLI *et al.* (1991) and STAMPFLI (1996), where the authors insist on the likely development of back-arc oceans within the Permo-Triassic Eurasian margin.

### 2.2.2. Variscan and Eocimmerian events (STAMPFLI, 2000; STAMPFLI & BOREL, 2002):

The Variscan domain extends spatially over the whole Alpine area and even further into the Dinarides and Hellenides, northern Turkey and the Caucasus, as well as temporally. With time and deformations becoming younger, the Variscan possibly grades southwards and eastwards into Eocimmerian (Triassic) deformations (STAMPFLI, 2000).

The Variscan orogeny in the Aegean region was a major accretion of terranes mainly in Devonian times and did not result from continent-continent collision. While the major Variscan deformation did indeed result from collision and the subduction of the Palaeotethys mid-ocean ridge in the Early Carboniferous (STAMPFLI & BOREL, 2002).

The Eocimmerian events mark the final closure of Palaeotethys, as indicated by mélanges and remnants of fore-arc basins in the Dinarides, Hellenides and Taurides (Dinaro-Hellenide region) (STAMPFLI, 2000). Due to the presence of oceanic

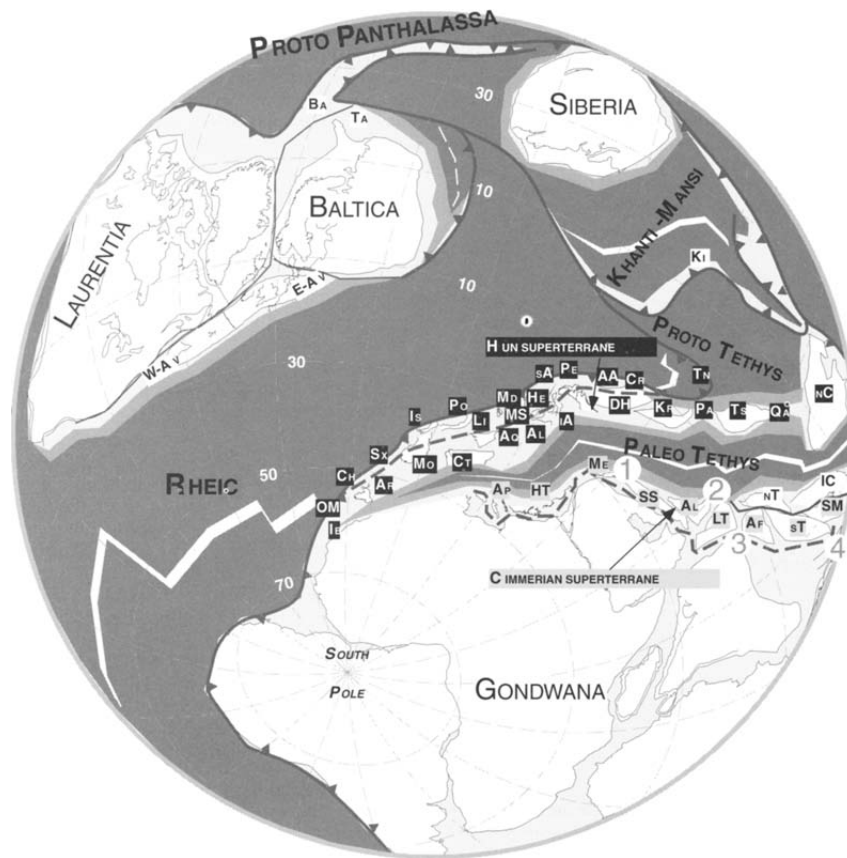


**Fig. 2.3.** Early Silurian reconstruction, 435 Ma. The opening of Palaeotethys separated the Hun superterrane from Gondwana. The opening was associated with diachronous back-arc spreading and slab roll-back of the Rheic ocean.

*Hun Cordillera terranes:* Early Palaeozoic active margin of the Hun composite terrane from west to east: OM, Ossa-Morena; Ch, Channel terrane; Sx, Saxo-Thuringian; Is, Istanbul; Po, Pontides; Li, Ligerian; Md, Moldanubian; MS, Moravo-Silesicum; He, Helvetic; sA, south Alpine; Pe, Penninic; AA, Austro-Alpine; Cr, Carpathian; Tn, north Tarim.

*Hun Gondwana terranes:* blocks forming the northern margin of Palaeotethys, from west to east: Ib, Iberic; Ar, Armorica; Mo, Moesia; Ct, Cantabria; Aq, Aquitaine; A1, Alboran; Ia, intra-Alpine (Adria, Carnic, Austro-Carpathian); DH, Dinaric-Hellenic; Kr, Karakum-Turan; Pa, Pamirs; Ts, south Tarim; Qa, Qantang.

*The Cimmerian terrane:* blocks forming the southern margin of Palaeotethys that were detached during the Late Permian opening of Neotethys, from west to east: Ap, Apulia *sensu stricto*; HT, Hellenides–western Taurides externides; Me, Menderes-Taurus; Ss, Sanandaj-Sirjan; AL, Alborz; Lt, Lut-Central Iran; Af, central Afghanistan; sT, south Tibet; SM, Sibumasu.

*Anamian blocks:* defining the future northern and southern branch of Palaeotethys: nT, north Tibet; IC, Indochina and Borneo; sC, south China. (STAMPFLI, 2000)

plateaus and Mariana-type back-arc basins the collision of the Cimmerian terranes with the continental margin of Eurasia is more complex in northern Turkey and Iran (e.g. OKAY, 2000). The Eocimmerian deformational domain is found south of a relatively undeformed Variscan domain, while the Cimmerian deformation is accompanied by Triassic flysch, mélanges and volcanics and collisional-type intrusive events marking the closure of Palaeotethys or the marginal oceans.

In the Dinaro-Hellenide domain Pelagonia (Late Carboniferous arc) collided directly with the Gondwana margin (STAMPFLI *et al.*, 1998), while the Karakaya domain in northern Turkey (ŞENGÖR *et al.*, 1980; OKAY *et al.*, 1994) is a complex Cimmerian deformation zone. This deformation zone shows the closure of Palaeotethys between an oceanic plateau, the Nilüfer formation, and the Gondwana margin, then the subsequent closure of the Karakaya back-arc and its northward thrusting on the Variscan Sakarya margin of Eurasia (OKAY, 2000).

The Karakaya suture is known to extend through Lesbos and the island's basement is part of the Sakarya zone of NW Anatolia (PE-PIPER & PIPER, 2002).

### **2.2.3. The marginal oceans** (STAMPFLI, 2000; STAMPFLI & BOREL, 2002):

The N-ward subduction of Palaeotethys triggered the opening of back-arc oceans along the Eurasian margin (Fig. 2.4). From area to area the history of these back-arc basins is different. Karakaya, Agh-Darband, and Küre marginal basins were closed during the Cimmerian collisional events, while others, namely Meliata, Maliac, and Pindos, remained open. The delayed subduction of the latter induced the opening of younger back-arc oceans, like Vardar and Black Sea.

Hence, Karakaya and Küre back-arc sequences are *not* remnants of Palaeotethys *sensu strictu*, but represent a Mariana-type marginal ocean developing south of the Sakarya margin.

The Pontides comprise three zones, which show Laurasian affinity, namely the Strandja, İstanbul, and Sakarya zone (Fig. 2.1). Late Triassic deformation and regional metamorphism in Turkey is predominantly found in the Sakarya zone. The Sakarya zone is a 1500km long, elongated, continental fragment, distinct from neighbouring zones. The Karakaya complex is a Carboniferous-Triassic subduction-accretion-collision complex in the Sakarya zone (OKAY, 2000).

### **2.2.4. Neotethys** (STAMPFLI, 2000; STAMPFLI & BOREL, 2002):

The diachronous opening (Late Carboniferous to late Early Permian) of Neotethys, which took place from East of Australia and advanced to the Eastern Mediterranean and Ionian Sea, separated another ribbon-like terrane from Gondwana, namely the

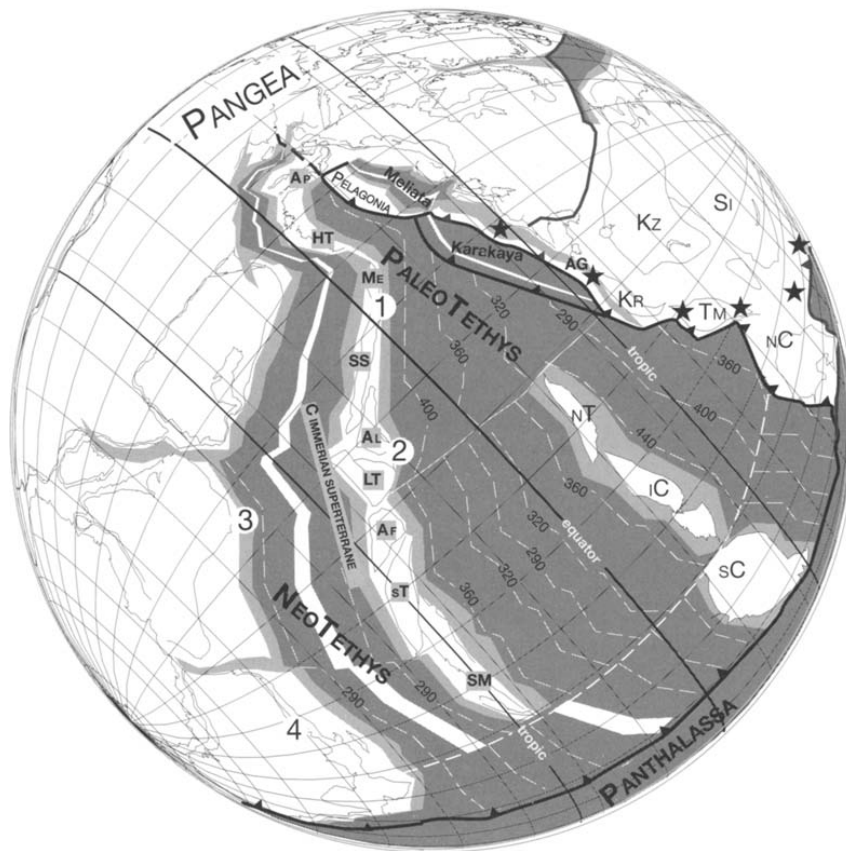


**Fig. 2.4.** Permian–Triassic boundary reconstruction, 248 Ma. The slab-roll-back of the whole Palaeotethys induced the opening of back-arc oceans in the active Eurasian margin [Meliata, Karakaya (Ka) und Agh-Darband (Ag)] and the strong slab-pull force is opening the Neotethys Ocean. This opening is separating the Cimmerian Superterrane from Gondwana. See Fig. 2.3 for legend. (Numbers 1–4 show positions of subsidence curves published in the original paper.) (STAMPFLI, 2000)

Cimmerian superterrane (Fig. 2.4, STAMPFLI & BOREL, 2002). The opening of Neotethys is also connected with the final closure of Palaeotethys in the Middle Triassic.

While the geodynamic evolution of the Neotethys is relatively well constrained, the relationship with the East Mediterranean basin is still under debate. STAMPFLI (1989) proposed that the East Mediterranean domain corresponded to an oceanic basin since the Late Palaeozoic and subsequent plate tectonic reconstructions show the eastern Mediterranean as part of the Neotethyan oceanic system (STAMPFLI

*et al.*, 1991, 2001; STAMPFLI & PILLEVUIT, 1993).

The onset of magmatism along its Iranian margin is evidence for the subduction of Neotethys. The strong slap-pull that was created contributed to the break-up of Pangaea and the opening of the Jurassic ocean in Early Jurassic time. However, Neotethys replaced Palaeotethys while Pangaea was stable. Major changes in the plate tectonic situation in Late Jurassic to Early Cretaceous are associated with the diachronous subduction of the Neotethys active ridge along the Eurasian N margin.

The Tethyside system is directly related to a N-ward subduction of Neotethys and the associated back-arc basins (Semail and Spontang). The Neotethys slab was subducted in its entity, while leaving hardly any ophiolitic traces. (All Neotethys ophiolites are derived from Cretaceous back-arc basins.) The present tectonic regime follows the closure of Neotethys.

### **2.2.5. Alpine Tethys** (STAMPFLI, 2000; STAMPFLI & BOREL, 2002):

The Alpine Tethys opened along a rift at the northern margin of the Meliata ocean, separating the future Austro-Carpathian domain from Europe (Fig. 2.5). It was linked to the Eurasian back-arc oceans and via a transform ocean to the Central Atlantic.

The Vardar ocean opened when the Meliata ocean subducted underneath the young oceanic crust of Neotethys and had replaced the Meliata ocean altogether by the Jurassic. The Vardar Ocean obducted southward onto the Pelagonian margin, then subducted N-ward under Moesia, opening the Black Sea. The Black Sea represents the third generation of back-arc opening in the region.

The Alpine orogenic system *sensu stricto* (Alps, Carpathians, Balkan) is directly related to the evolution of Maliac-Maliata/Vardar and their southward subduction. It moved from the Austro-Carpathians to the Alpine Tethys and extended W-ward to the western Alps in Late Cretaceous time.

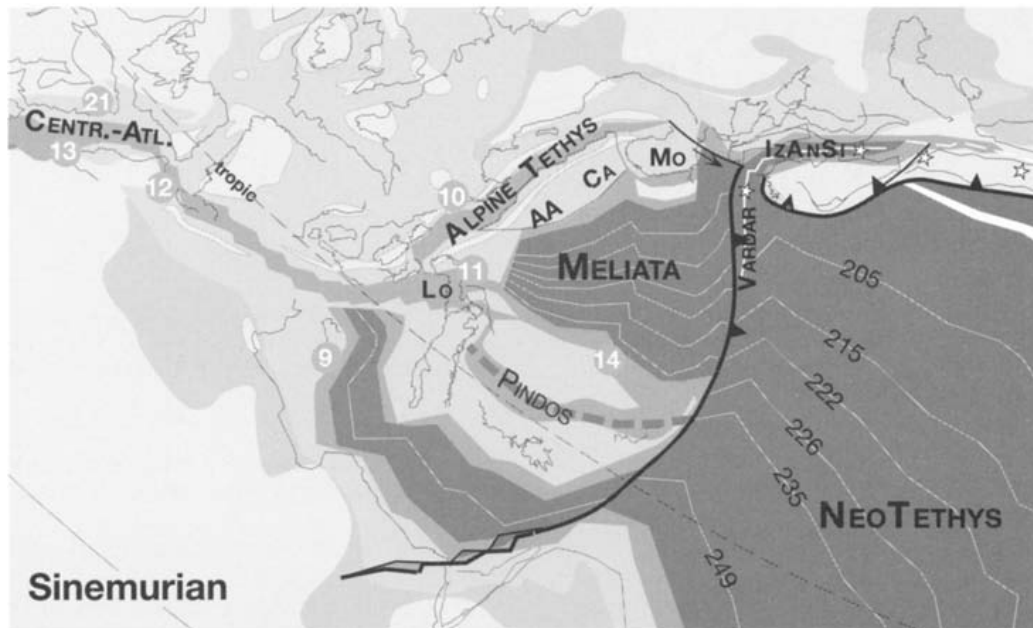


**Fig. 2.5.** Sinemurian reconstruction of the western Tethyan area, ~193 Ma. AA, Austo-Alpine; CA Inner Carpathian; IzAnSi, İzmir-Ankara Ocean; Mo, Moesia; Lo, Lombard basin; ☆, Magmatic arc activity. Palaeogeography modified after ZIEGLER (1988). (Numbers 9–21 show positions of subsidence curves published in the original paper.) (STAMPFLI, 2000)

### 2.3. The tectonic setting of the Miocene volcanic rocks

There are several conflicting models for the tectonic setting of the Miocene volcanic rocks in the north-eastern Aegean and western Anatolia. The models have to contain mechanisms to account for an abrupt and diachronous termination of igneous activity: Thrace (26 Ma), Samothraki (18.5 Ma), Límnos (18 Ma), Lesbos (16.5 Ma) (PE-PIPER & PIPER, 2002).

1. FYTIKAS *et al.* (1984) interpret the volcanic rocks as related to subduction of the Eastern Mediterranean ocean floor N-ward beneath Eurasia with back-arc extension and subduction roll-back, resulting in a southward migration of the active volcanic arc. (See also PE-PIPER & PIPER, 1989)
2. YILMAZ (1989, 1990) and GÜLEÇ (1991) explain the volcanism in western Anatolia with multiple episodes of magmatism in different tectonic settings through time. YILMAZ (1989), YILMAZ (1990), ALTUNKAYNAK & YILMAZ (1998), ALTUNKAYNAK & YILMAZ (1999), GENÇ (1998), ALDANMAZ *et al.* (2000) and YILMAZ *et al.* (2001) see a shift in the tectonic regime from N–S compression during the late Oligocene to early Miocene to N–S extension from the late Miocene onwards.
3. YILMAZ (1990) correlates the volcanic rocks with crustal thickening, resulting from collision and therefore underthrusting.
4. SEYİTOĞLU & SCOTT (1992a,b) interpret the volcanic rocks as being synchronous with local extension. In their model the compressional regime ceased earlier and extensional conditions prevail at least since early Miocene/latest Oligocene.
5. DINTER (1998) correlates the volcanism with early Miocene extension in the Symvolon shear zone and Thasos detachment. In this model the magma supply ends when extension is taken up on the Strymon valley detachment in the Middle Miocene to early Pliocene.
6. AGOSTINI *et al.* (2010) interpret the Aegean rift and setting for the volcanism as an atypical back-arc setting, not related to slab roll-back, steepening and asthenospheric replacement. In his model the volcanic rocks are products from partial melting of the same mantle domain (indicating a small non-convective mantle wedge) and progressive slab dehydration until complete dehydration (implying a stagnant slab). Differential movement between the Greek and Anatolian microplates is responsible for diachronous evolution and

eventually leads to the development of tear zones or slab windows, allowing sub-slab upwelling. This accounts for the generation of slab-related and slab-unrelated magmatism.

## 2.4. The regional volcanic evolution

Based on the volcanological data available it becomes clear, that the evolution of the Eastern Aegean islands is similar to that in Western Anatolia (FYTIKAS *et al.*, 1979) (Fig. 2.6). High-K calc-alkaline to shoshonitic volcanics of Oligocene to Middle Miocene age are followed by a few scattered alkali basalt products, ranging in age from Upper Miocene to Quaternary (BORSI *et al.*, 1972; BESENECKER & PICHLER, 1974; ROBERT, 1976; FYTIKAS *et al.*, 1976).

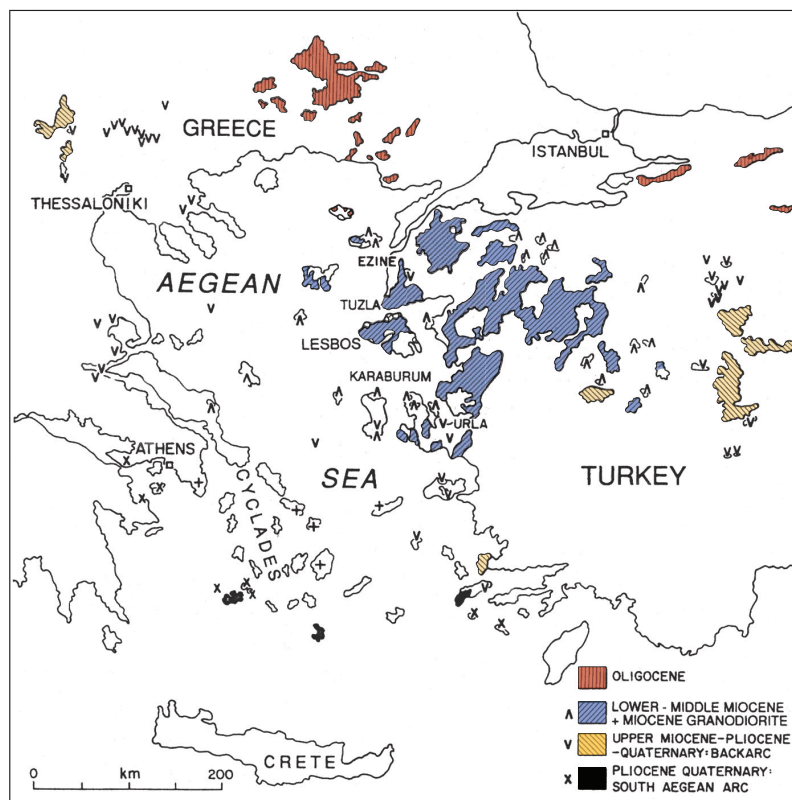


**Fig. 2.6.** General map of Aegean Sea and adjacent areas of Greece and Turkey, showing Cenozoic volcanic rocks associated with those on Lesbos Island. (PE-PIPER & PIPER, 1993)

## 2. Geological setting

---

The Oligo-Miocene volcanism can be distinguished in two groups according to their geographic position (VILMINOT & ROBERT, 1974):

1. The volcanism of the north-eastern Aegean (Samothraki, Gökçeada [also known as Imbros or İmroz], Límnos, Agios Efstratios, Lesbos, and Chios islands) and of Anatolia (Ezine, Bergama, Karaburun and İzmir) is completely restricted to the Turkish palaeoplate. The composition of the eruption products is dominated by intermediate rocks with an alkaline trend, occasionally clearly potassic, which are accompanied by some basic rocks and once in a while abundant rhyolites (PARASKEVOPOULOS, 1956).
2. The volcanism of the Dodecanese (Samos, Patmos, Kalymnos, Kos islands) and the Bodrum peninsula which roughly forms a line in N–S direction (PARASKEVOPOULOS, 1956) comprises abundant intermediate and acidic rocks, as well as alkaline rocks, which sometimes are extremely potassic, like common on Patmos Island (ROBERT, 1973; ROBERT *et al.*, 1992).

In the whole of Western Anatolia the rhyolitic magmas were erupted as ignimbrites in the same time interval between 21 Ma and 17 Ma (AYDAR, 1998). The explosive volcanic activity follows the NE–SW striking fissures, in the main direction of the Miocene basins (AYDAR, 1998). In some places (Serbo-Macedonian massif, Western Anatolia, Aegean area) extrusive activity was accompanied by granodioritic and dioritic intrusions (SMITH & MOORES, 1974; ALTHERR *et al.*, 1976, 1982; MEZGER *et al.*, 1985; ALTHERR *et al.*, 1988; HENJES-KUNST *et al.*, 1988; ALTHERR & SIEBEL, 2002).

### 2.5. The geological setting of Lesbos Island

Lesbos Island lies in the NE of the Aegean Sea and is the third largest Greek island after Crete and Euboea. It has a surface area of  $\sim 1630\text{ km}^2$ . The east coast of Lesbos is separated from the west coast of Anatolia by the 7 – 10 km wide Mytilene strait.

The eastern Aegean islands (Lesbos and Chios islands with the neighbouring Psara and Oinoussai islands north of the crystalline belt and the Dodecanese south of the belt) just offshore the Anatolian coast have a close geological relationship to the Anatolian mainland. The geological structure of the Greek mainland Hellenides can be applied only limited to these islands (DÜRR *et al.*, 1986).

The rocks on Lesbos Island were first described and analysed by VON HAUER (1873). Further early work was carried out by DE LAUNAY (1890, 1891, 1897,

1898), including a first geological map (DE LAUNAY, 1890), and PHILLIPPSON (1910). Modern geological research started with work by GEORGALAS (1949) and PRAGER (1966).

Lesbos Island belongs to the Sakarya microcontinental block, which formed during the Early Mesozoic along the Karakaya suture zone by amalgamation of several continental fragments. The relationship of the Sakarya block towards the north-eastern adjacent Rhodope block is uncertain. However, both blocks lay along the northern margin of the ocean of the Vardar–İzmir–Ankara zone, an important Mesozoic (Neotethyan) ocean (PE-PIPER *et al.*, 2001).

HECHT (1972–1975) created a geological map of Lesbos in the scale of 1 : 50 000 (Fig. 2.7). The island comprises thick layers of Miocene volcanic rocks, which together with Neogene sediments, rest upon a Palaeozoic metamorphic basement.

### 2.5.1. The metamorphic basement: ophiolite and sub-ophiolitic mélange

The Lesbos ophiolite consists of ultramafic rocks, principally harzburgite and lherzolite with minor dunite (MIGIROS *et al.*, 2000). It overlies a regional mélange of supra-subduction MORB lavas, seamount fragments, and deep-water continental margin sediments (KATSIKATSOS *et al.*, 1982). The tectonostratigraphy consists of a well developed amphibolitic sole of amphibolite and amphibolitic schist and a thick sub-ophiolitic mélange, with harzburgite tectonically overlying lava sequences. It is similar to ophiolites of the western ophiolite belt of Greece and differs from the ones in the eastern ophiolitic belt (PE-PIPER *et al.*, 2001). K-Ar ages of the amphibolitic schists range from  $153 \pm 5$  Ma to  $158 \pm 5$  Ma (HATZIPANAGIOTOU & PE-PIPER, 1995). The Lesbos ophiolite is younger than the ophiolites from the Western Ophiolite Belt and it is probably also younger than the ones from the Eastern Ophiolite Belt (PE-PIPER *et al.*, 2001). The well developed sub-ophiolitic mélange with seamount fragments indicate that a large amount of subduction has taken place. Genetically, the Lesbos ophiolite is not linked to either the Western or the Eastern Ophiolite Belt. It was probably derived from oceanic crust from between the Sakarya and Rhodope microcontinents (PE-PIPER *et al.*, 2001).

### 2.5.2. Late Palaeozoic-Triassic metamorphic basement

A series of different units of marbles and phyllites, marbles and schists, and schists and marbles. Most of them contain fossils (Megalodonts, Crinoidea, Foraminifera, and Brachiopods). The metamorphic grade is up to greenschist facies. A thickness is determined only for Permo-Carboniferous marbles and schist and is more than 400 m.

### 2.5.3. Volcanic rocks

The general succession of volcanic rocks (Table 2.1) was established by HECHT (1972–1975) and modified by PE-PIPER (1980a) and PE-PIPER & PIPER (1993). The volcanic rocks are found in a series of stratovolcanoes, which extent SW–NE across the centre of the island (PE-PIPER, 1980b). The phase of intensive volcanic activity lasted for about 1 Ma from 18.4 – 17.3 Ma with only minor earlier (21.5 Ma) and later (16.5 Ma) volcanism (PE-PIPER & PIPER, 1993).

### 2.5.4. Lower Lava Unit and Eressos Formation

While HECHT (1972–1975) basically included all highly altered volcanic rocks in the Lower Lava Unit, PE-PIPER (1980a) assigned only rocks to it underlying the Skoutaros Unit and Acid Volcanics, which are approximately synchronous with each other. Almost all rocks mapped as Lower Lava Unit by HECHT (1972–1975) are normally magnetised. Exceptions are rocks near Stipsi and Anemotia, which are both normally and reversely magnetised (PE-PIPER, 1980a).

Both HECHT (1972–1975) and PE-PIPER (1980a) had considered rocks associated with the Sigri Pyroclastics in the Agra region to belong to the Lower Lava Unit. According to PE-PIPER & PIPER (1993) most of the rocks seem to be either lavas of the Skoutaros Formation or intrusions of uncertain relationship to the surrounding rocks on the basis of field relations and petrography. HECHT (1972–1975) included andesites, with only poor outcrops in Parakila, in the Lower Lava Unit. However these andesites resemble geochemically and petrographically rocks of the Skoutaros (PE-PIPER & PIPER, 1993). Additionally thin lavas underlying the Acid Volcanic Unit in the North of the island were correlated petrologically with the Skoutaros Unit (PE-PIPER & PIPER, 1993).

Within the Lower Lava Unit PE-PIPER (1980b) distinguishes the Eressos Formation consisting of coarse grained porphyritic andesite with hornblende and biotite phenocrysts, interbedded with agglomerates and volcanoclastic rocks. North of Eressos rocks of the Eressos Formation have been tilted to the near vertical, either by caldera collapse (PE-PIPER, 1980a) or extensional faulting (PE-PIPER & PIPER, 1993).

PE-PIPER & PIPER (1993) decided to keep the name *Lower Lava Unit* only as an informal term for two areas of normally magnetised altered volcanics: 1. for a rhyodacite, underlying Sigri Pyroclastics, immediately NE of Agra; 2. for altered rocks, including basalt, underlying the Sykaminea Formation N of Petra.

2.5. The geological setting of Lesbos Island

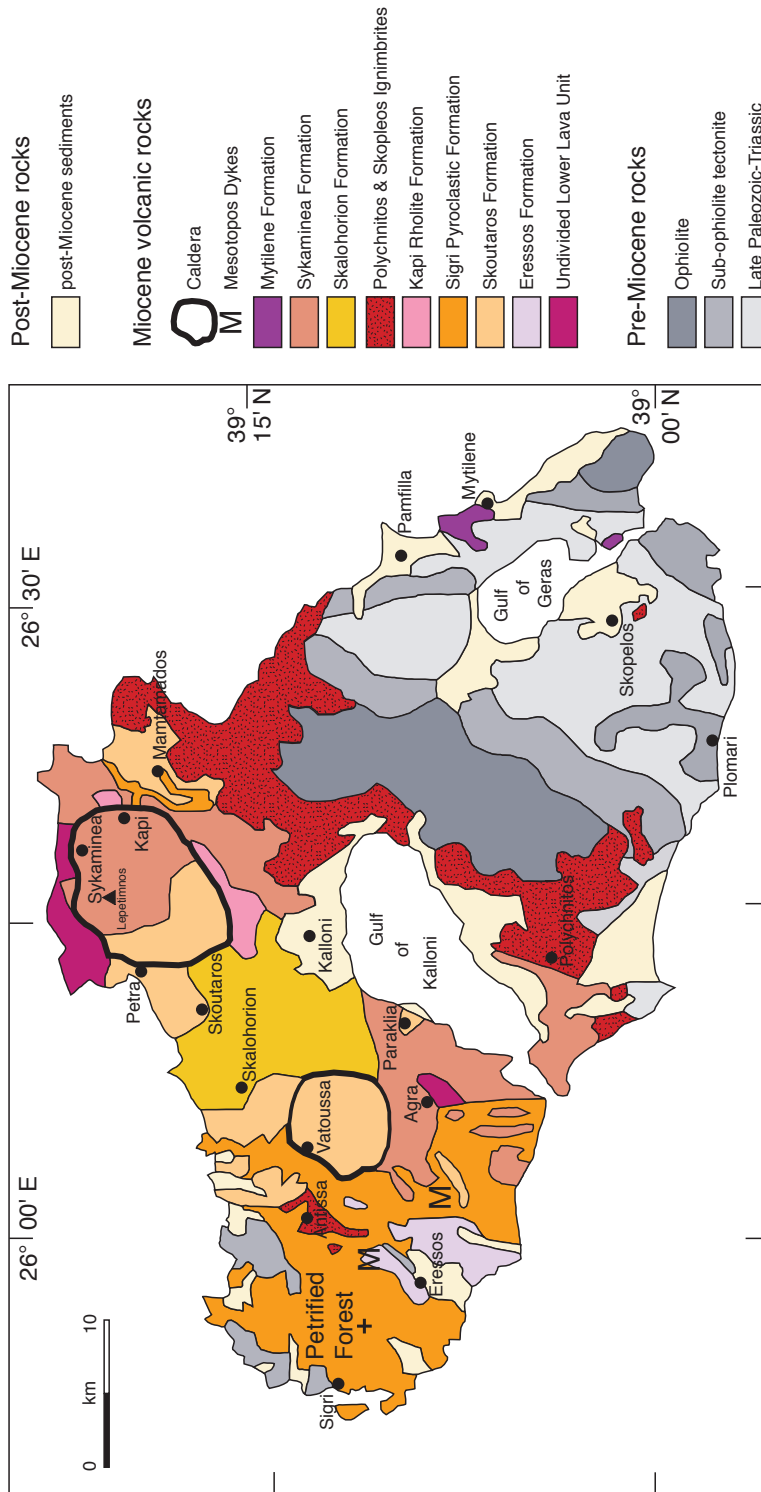


Fig. 2.7. Geological map of the island of Lesbos after HECHT (1972–1975), modified by PE-PIPER & PIPER (1993)

**Table 2.1.** Summary of stratigraphic nomenclature, age, and rock types for the Miocene volcanic rocks of Lesbos Island modified from PE-PIPER & PIPER (1993)

	Stratigraphic nomenclature		Age		Type section (thickness)	Characteristic lithologies (mostly flows, minor intru- sions, unless otherwise noted)
	PE-PIPER (1980a,b) based on HECHT (1972–1975)	PE-PIPER & PIPER (1993)	Magnetic epoch	Radiometric dates (K-Ar)		
Late Volcanics		(Pontian Marls)				
		Mesotopos Dykes	16 (N, mid)	$16.5 \pm 0.5 \text{ Bt}^2$	Mesotopos (dykes)	andesite (Am, Bt, Cpx)
	Mytilene Lava Unit	Mytilene Formation	16 (N, mid)	$16.8 \pm 0.9 \text{ WR}^4$	N of Mytilene (10m)	basalt, andesite (Ol, Px), minor felsic pyroclastics
		(Pontian Marls)				
Early Volcanics Upper Lava Unit		Sykaminea Unit <sup>1</sup>	16 (R)	$17.3 \pm 0.5 \text{ Bt}^3$ $17.4 \pm 1.0 \text{ WR}^4$	Sykaminea (several hundred m)	andesite and dacite (Am, Bt), minor felsic pyro- clastics, minor basalt, and basalt andesite (Px, Bt)
		Skalohorion Formation	16 (R, base)		Skalohorion (above Skoutaros Fm. type section (200m)	basalt, andesite, and dacite (Fs megacrysts, Px, Am)
Acid Volcanic Unit		Polychmitos Ignimbrite	17 (N)	$17.2 \pm 0.5 \text{ Bt}^2$	SE of Mandamados (100m)	rhyolite ignimbrite
		<i>Skopelos Ignimbrite</i>	?		<i>Skopelos</i> (10m)	<i>rhyolite ignimbrite – unknown stratigraphic relationship</i>
		Kapi Rhyolites	17 (N)		E of Kapi (30m)	dacite and rhyolite domes and flows
		Sigri Pyroclastics	17 (N)		Antissa-Sigri road (300m)	Felsic pyroclastics, dacite and rhyolite tephra
Early Volcanics Upper Lava Unit		Skoutaros Unit <sup>1</sup>	17 (N)	$18.4 \pm 0.5 \text{ WR}^2$	N of Vatoussa (100m)	basalt, andesite (Ol, Px), minor dacite (Am) at top
		Lower Lava Unit	?			altered volcanic rock
		Eressos Formation	19 (N)	$21.6 \pm 1.5 \text{ Am}^4$	Eressos (100m)	andesite (Am, Bt)

<sup>1</sup>Part of the Upper Lava Unit by HECHT (1972–1975); radiometric ages determined using biotite, amphibole and whole rock are marked Bt, Am, WR respectively; <sup>2</sup>BORSI *et al.* (1972), ages corrected to the STEIGER & JÄGER (1977) decay constant by PE-PIPER & PIPER (1993); <sup>3</sup>Ar-Ar date PE-PIPER (1980a); <sup>4</sup>PE-PIPER & PIPER (1993)

### 2.5.5. Skoutaros Formation

The Skoutaros Formation is the lower part of the Upper Lava Unit of HECHT (1972–1975). PE-PIPER (1980a) distinguished within this unit the lower, normally magnetised *Skoutaros Formation*, and the upper, reversely magnetised, and lithologically distinct *Sykaminea Formation*.

The rocks of the Skoutaros Formation consist of andesite and basalt lava flows without hydrous mineral phases, dated  $17.2 \pm 0.5 \text{ Ma}^1$  (BORSI *et al.*, 1972), approximately synchronous with the Sigri Pyroclastics and Polychnitos Ignimbrite (PE-PIPER, 1980a). The type locality, a thick section through the eroded wall of Vatoussa caldera, reveals  $\sim 100 \text{ m}$  of Skoutaros lava. However, the base is concealed. The series consists mainly of lava flows, 2–20 m thick, with weathered tops and some interbedded agglomerate (large mafic clasts in a finer grained felsic matrix). The upper part of the section include some andesites and dacites that contain amphibole and biotite (PE-PIPER & PIPER, 1993). Upwards the section passes into the Skalohorion Formation.

### 2.5.6. Acid Volcanic Unit

The Acid Volcanic Unit consists of a series of felsic rocks underlying the Sykaminea Formation (PE-PIPER, 1980a). The only radiometric date, K-Ar on biotite of the Polychnitos Ignimbrite, gave an age of  $17.0 \pm 0.5 \text{ Ma}^1$  (BORSI *et al.*, 1972).

**Sigri Pyroclastic Formation** The Sigri Pyroclastic Formation comprises unwelded agglomerate and air-fall tuff, which is  $> 300 \text{ m}$  thick near Vatoussa Caldera. To the W and the E, the deposit is more fine-grained and thinner. Near Agra and Vatoussa, the formation is thin and interbeds with the Skoutaros Formation (PE-PIPER & PIPER, 1993). The Sigri Pyroclastics overlie the Lower Lava Unit (Eressos Fm?) in both, the western part of the island (in the Eressos area) and near Mandamados, and are overlain by Polychnitos Ignimbrite (PE-PIPER, 1980a). The Sigri Pyroclastic Formation encloses the renowned Lesbos Petrified Forest.

**Polychnitos Ignimbrite** The research described here concentrates on samples from this pyroclastic density flow deposit. A more detailed description of the deposit, of sample locations and descriptions follows in chapter 3, page 29.

Historically the term ignimbrite was used for strongly welded deposits only, today ignimbrites are defined as pumiceous, ash-rich deposits of pyroclastic density

---

<sup>1</sup>Age corrected to the STEIGER & JÄGER (1977) decay constant by PE-PIPER & PIPER (1993)

currents, irrespective of their degree of welding. The term is applied to welded and unwelded deposits alike. The Polychnitos Ignimbrite is an ignimbrite in both the historic and the modern sense.

The complete ignimbrite sequence in the centre of the Island is referred to as the Polychnitos Ignimbrite (PE-PIPER, 1980a). It covers today  $\approx 190 \text{ km}^2$  on Lesbos Island and the total thickness is at least 100 m. PE-PIPER (1980a) distinguishes several ignimbrite sheets: The lowest ignimbrite sheet is 40 – 60 m thick. It is glassy at the basal 2 – 5 m, followed upwards by a thick, coarse lithic ignimbrite. The amount of glass decreases upwards as well as the amount and size of lithic clasts. At the top the sheet changes into a highly welded crystalline tuff. PE-PIPER (1980a) reports at least three similar higher ignimbrite sheets in the area of Nea Kidoniai and Mandamados and one higher sheet in the Polychnitos area. Locally fine thin ignimbrite sheets can be found interbedded with the pyroclastics below the Polychnitos Ignimbrite (PE-PIPER, 1980a). PE-PIPER (1980a) recognises two separate areas with ignimbrite deposits, which may be correlative:

1. W of Antissa, an ignimbrite deposit 40 m thick, together with Sigri Pyroclastics, lithologically similar to the Polychnitos Ignimbrite. It is overlain by at least one thin dacite of Lower Lava Unit lithology. It may be correlative to the Polychnitos Ignimbrite (PE-PIPER & PIPER, 1993).
2. E of Antissa, a small ignimbrite, overlain by Upper Lava Unit rocks. It may be correlative to the Polychnitos Ignimbrite or younger (PE-PIPER, 1980a; PE-PIPER & PIPER, 1993).

More recently, the volcano-sedimentary stratigraphy of Polychnitos Ignimbrite has been studied in a PhD thesis at the University of Patras, Greece (LAMERA, 2004), but has unfortunately not been published and is not available for reference. A number of more or less extensive conference abstracts exists by the same authors (LAMERA *et al.*, 2001, 2004a,b; ST. SEYMOUR *et al.*, 2004), however, they do not provide sufficient documentation for the conclusions drawn. Yet, their contents are of such a significance to this study, that they are summarised below despite their poor documentation.

According to LAMERA *et al.* (2001, 2004a,b) the Polychnitos Ignimbrite can be divided into eight cooling units (Table 2.2) of which only four are derived from vents on Lesbos Island and can therefore be termed autochthonous. These are namely the Purple Unit, and the Megafamma Units I, II, and III. LAMERA *et al.* (2004b) state, that the Purple Unit was derived from Kalloni Gulf Caldera, while the three Megafamma Units were derived from Stipsi Caldera (as established by KOULI & ST. SEYMOUR, 2006). The underlying White Unit, Grey Unit, Pink Unit and the overlying

**Table 2.2.** Representative column displaying the volcano-stratigraphy for the Polychnitos Ignimbrite with the eight cooling units with their respective sources and the underlying units as proposed by LAMERA *et al.* (2004b); ST. SEYMOUR *et al.* (2004); KOULI & ST. SEYMOUR (2006).

Stratigraphic nomenclatur	Origin and Source Area		
Polychnitos Ignimbrite	Quarry Unit	allochthonous	Bergama-İzmir area
	Megafiamma Unit III	autochthonous	Stipsi Caldera
	Megafiamma Unit II	autochthonous	Stipsi Caldera
	Megafiamma Unit I	autochthonous	Stipsi Caldera
	Purple Unit	autochthonous	Kalloni Gulf Caldera
	Pink Unit	allochthonous	Ayvacık area, Biga Peninsula
	Grey Unit	allochthonous	Asia Minor
	White Unit	allochthonous	Asia Minor
Breccia Unit			
Lower Lavas			
Metamorphic Basement			

Quarry Unit are allochthonous with vents located in Asia Minor (LAMERA *et al.*, 2004a,b; ST. SEYMOUR *et al.*, 2004). The Breccia Unit used to be considered part of the Polychnitos Ignimbrite, but a separate laharic origin has been argued for by LAMERA *et al.* (2004a).

**Skopelos Ignimbrite** (PE-PIPER, 1980a) This deposit is the third found in an area separate from the other ignimbrite deposits. It consists of ignimbrite and tuff, 10 – 20m thick. In contrast to the other two separate deposits E and W of Antissa, the lithology is distinct from the Polychnitos Ignimbrite. The deposit is shard-rich and schist clasts are common. The age and relationship to other volcanic rocks of the island of the Skopelos Ignimbrite is unknown.

**Kapi Rhyolite Formation** (PE-PIPER & PIPER, 1993) The Kapi Rhyolite Formation consists of domes and flows of dacite and flow-banded rhyolite, sometimes together with felsic pyroclastics. Field relations indicate variable ages, synchronous with the Skoutaros and Skalohorion Formations. The type locality E of Kapi shows flow-banded rhyolite and vitrophyric lava interbedding with tuffs. The tuffs locally contain large blocks of obsidian. Regional mapping shows that the Kapi Rhyolite Formation overlies the main Sigri Pyroclastics, which is interbedded with lava from the Skoutaros Formation and underlies the Sykaminea Formation at the Lepetimnos Volcanic Centre.

### 2.5.7. Sykaminea and Skalohorion Formations

The Sykaminea Formation is the upper part of the Upper Lava Unit of HECHT (1972–1975) (see also chapter 2.5.5). It overlies the Skoutaros Formation and consists of reversely magnetised intermediate lavas, minor pyroclastics, minor basalts and minor basalt andesite, which form large stratovolcanoes in N and central Lesbos (PE-PIPER, 1980a).

In central Lesbos a reversely magnetised intermediate lava is found between the Skoutaros and the Sykaminea Formation (PE-PIPER, 1980a). This lava, featuring feldspar megacrysts commonly in association with mafic xenoliths, was defined by PE-PIPER (1980a) and termed the *Skalohorion Formation*.

### 2.5.8. Mytilene Formation

This formation consists of local, normally magnetised basalt flows, which interbed with felsic pyroclastic rocks, in the area NW of Mytilene (PE-PIPER & PIPER, 1993). An age of  $16.8 \pm 0.9$  Ma (PE-PIPER & PIPER, 1993) indicates, that these basalts are chronologically part of the main volcanic sequence of Lesbos Island. They might be slightly younger than the main sequence, however they are geochemically distinct from late basalts in western Anatolia in the Urla and Ezine area, dated at 9.7 – 11.9 Ma (BORSI *et al.*, 1972).

Reversely magnetised basalt in the area of Polychnitos has previously also been part of the same formation (the former Mytilene Unit) (HECHT, 1972–1975; PE-PIPER, 1980a). PRAGER (1966) reported basalt to overlie Pontian marls E of Polychnitos, an observation that could not be repeated by PE-PIPER & PIPER (1993) and proved inconsistent with a more recently gained radiometric age of  $17.4 \pm 1.0$  Ma (PE-PIPER & PIPER, 1993). This basalt is therefore correlated with the main Sykaminea Formation, interpreted as the final phase of this formation and subsequently included into it (PE-PIPER & PIPER, 1993).

### 2.5.9. Mesotopos Dykes

Generally most lavas on Lesbos Island are cut by dykes with a similar lithology and age. In some areas also younger dykes are recognised. For example N of Eressos Sigri Pyroclastics are cut by amphibole-bearing dacite dykes. The dykes are therefore younger than the Eressos Formation and resemble petrographically the amphibole-biotite-bearing lavas near the top of the Skoutaros Formation (PE-PIPER & PIPER, 1993). Some dykes in the Eressos–Agra region have a different lithology: additionally to amphibole and biotite, they contain phenocrysts of pyroxene. These dykes are termed the *Mesotopos Dykes* (PE-PIPER & PIPER, 1993). BORSI *et al.* (1972) dated a sample described as “dyke from Eressos area”. The age of  $16.5 \pm 0.5 \text{ Ma}^1$  (BORSI *et al.*, 1972) is too young for either the Eressos or the Skoutaros Formations and could therefore be adopted for the Mesotopos Dykes (PE-PIPER & PIPER, 1993).

### 2.5.10. Post-Miocene sediments

HECHT (1972–1975) The post-Miocene sediments consist of Neogene (latest Miocene–basal Pliocene) marls, tuffites, and freshwater limestones, Pleistocene fluvial sands, clays and conglomerates, and Holocene slope wash, sliding scree, talus, conglomerates (with gravels of serpentine, limestone, basalt or phyllites), and alluvial plains of clays, sands, gravels, coastal sands, fluvial deposits.

There seems to be no sign, that the post-Miocene sediments were ever in contact with seawater, except HECHT (1972–1975) describes the chiefly marly freshwater limestones on the Plomari–Mytilene sheet of the geological map, to contain oligohaline deposits with marls and sandstones, which contain several shell beds. There are also some coastal sands within the Holocene alluvial plains.

### 2.5.11. Calderas

Six calderas have been localised and characterised by KOULI & ST. SEYMOUR (2006) using remote sensing techniques in combination with fieldwork (Fig. 2.8). Four of the calderas (Mesotopos, Agra, Antissa and Skalohorion caldera) had not been known formerly. Vatoussa caldera had first been marked on a geological map, proposed as volcanic centre and suspected to be a caldera by PE-PIPER (1980a). The existence of Stipsi caldera was first reported by PE-PIPER (1998), eventually its geometry was defined by VAMOUKAKIS *et al.* (2001). KOULI & ST. SEYMOUR (2006) established the structure as a major caldera.

---

<sup>1</sup>Age corrected to the STEIGER & JÄGER (1977) decay constant by PE-PIPER & PIPER (1993)

## 2. Geological setting

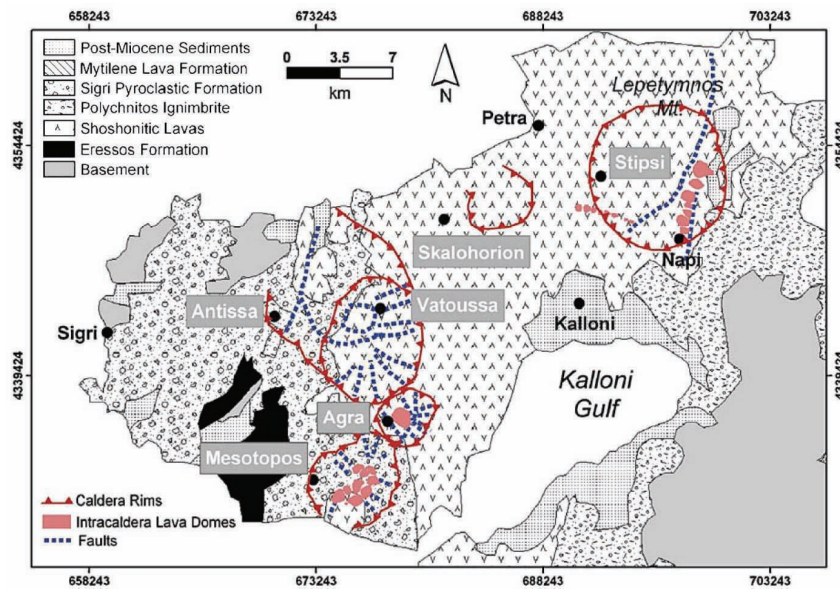


**Fig. 2.8.** The structural features of the six calderas of the Lesbos volcanic field within their geological context from (KOULI & ST. SEYMOUR, 2006).

### 2.5.12. Present-day tectonic setting of Lesbos Island

Lesbos Island is tectonically active. It has three main fault systems  $40^{\circ}$  N –  $40^{\circ}$  W,  $30^{\circ}$  N –  $0^{\circ}$  E, and E – W. The island has four geothermal fields of different size, water temperatures and water chemistry (PAPASTAMAKIS, 1972; KELEPERTSIS & ESSON, 1987) and a high seismic activity (VOULGARIS *et al.*, 2004). Earthquake foci are shallow ( $h \leq 50$  km) and concentrated in three zones with different magnitude ranges between  $\leq 5.5$  and 7.0. Lesbos Island

### **3. Polychnitos Ignimbrite – the ignimbrite deposit and profile descriptions**

#### **3.1. Source of the Polychnitos Ignimbrite**

As mentioned before in section 2.5.6 on page 23, the volcano-sedimentary stratigraphy of the Polychnitos Ignimbrite has been studied in an unpublished PhD thesis (LAMERA, 2004), which is not available for reference. The proposed stratigraphic column, distinguishing eight cooling units and a separate lahar (Table 2.2 on page 25), as well as additional work carried out to identify the cooling units' sources, has so far only been reported in conference abstracts (LAMERA *et al.*, 2001, 2004a,b; ST. SEYMOUR *et al.*, 2004). Naturally these conference abstracts, even though quite extensive, do not provide sufficient documentation for their results. However, their contents is of such importance for this study, that they will be summarized below, despite their poor documentation.

According to LAMERA *et al.* (2001, 2004a,b); ST. SEYMOUR *et al.* (2004) only four of the eight cooling units of the Polychnitos Ignimbrite (Purple Unit and Megafiamma Units I, II, III) are derived from vents on Lesbos Island and are therefore autochthonous. While the Purple Unit was derived from Kalloni Gulf Caldera (LAMERA *et al.*, 2004b), the three Megafiamma Units were derived from Stipsi Caldera, which was established by KOULI & ST. SEYMOUR (2006). Using remote sensing and a digital elevation model of Lesbos Island, KOULI & ST. SEYMOUR (2006) have identified a number of lineaments at the central part of the Polychnitos ignimbrite, which they interpret as flow lines of the upper part of the ash flow (different cooling units and source regions are not mentioned). KOULI & ST. SEYMOUR (2006) propose the undivided ignimbrite's origin from Stipsi caldera.

The remaining four suggested cooling units, the White Unit, Grey Unit, the Pink Unit and the Quarry Unit are considered allochthonous with vents located in Asia Minor (LAMERA *et al.*, 2004b,a; ST. SEYMOUR *et al.*, 2004). According to major elements, 40 trace elements, and REE profiles ST. SEYMOUR *et al.* (2004) consider the Pink Unit to be identical to a Miocene ignimbrite sheet outcropping near Ayvalık at the proximal coast of Asia Minor, with the source being in the Ayvacık area on the Biga Peninsula. The Quarry Unit's origin is proposed to lie in the Bergama-İzmir region.

PE-PIPER (1980a), using oriented thin sections to determine tephra orientation and therefore flow directions, comes to the following results. All ignimbrite samples with a significant lineation level (95%) plotted show a broadly radial flow pattern away from the centre of the island. In the NE part of Lesbos, where cooling units were established and more closely spaced correlative samples are available, PE-PIPER (1980a) comes to a more detailed interpretation of the orientation data. The bottom cooling units show a flow direction to the S or the SE (unit A) and to the S and the SSE (unit B). PE-PIPER (1980a) suggests a source N of Mandamados for these two lower cooling units. The source suggested for the Pink Unit by LAMERA *et al.* (2004b,a) and ST. SEYMOUR *et al.* (2004) Ayvacık is situated N of Mandamados and if the "lower units" by PE-PIPER (1980a) are equivalent to the Pink Unit, their results are in agreement. A single analysis from unit C shows a flow direction to the E, while higher cooling units in the area between Mandamados and Nea Kidoniai have flow directions to the NE and PE-PIPER (1980a) therefore proposes their source to be at the Vatoussa Centre, which PE-PIPER (1980a) identifies as a possible caldera.

### **3.2. Vertical profiles - sample locations**

Most of the samples used in this study are from two vertical profiles through the Polychnitos Ignimbrite. The first profile (Profile A) was taken at a cape at the NE side of Kalloni Gulf (Fig. 3.1), close to the village Kofinas and consists of 11 samples taken over a vertical length of 40m. The second profile through the ignimbrite (Profile B), with four samples, was taken over a vertical length of 7 m (from a total of 30m of vertical outcrop, at the N side of Tavros mountain (374m above sea-level) W of Nees Kidonies (Fig. 3.1). Additional samples of volcanic glass were taken from fiamme at road cuts from two different roads NE of the Gulf of Kalloni. Without having conclusive clues it is difficult to put the samples of this study into correlation to the eight cooling units proposed by LAMERA *et al.* (2004b). However, it seems possible, that the vertical profiles studied here are part of the three Megafiamma Units.

### **3.3. Profile A - glass and phenocrysts in the vertical profile**

Profile A was taken close to the village Kofinas at a cape at the NE side of Kalloni Gulf, between Ancient Pyra, an archaeological site and Aghia Nikolao, a chapel (Figs. 3.1 & 3.2). The individual samples of Profile A are described in the appendix

### 3.3. Profile A - glass and phenocrysts in the vertical profile

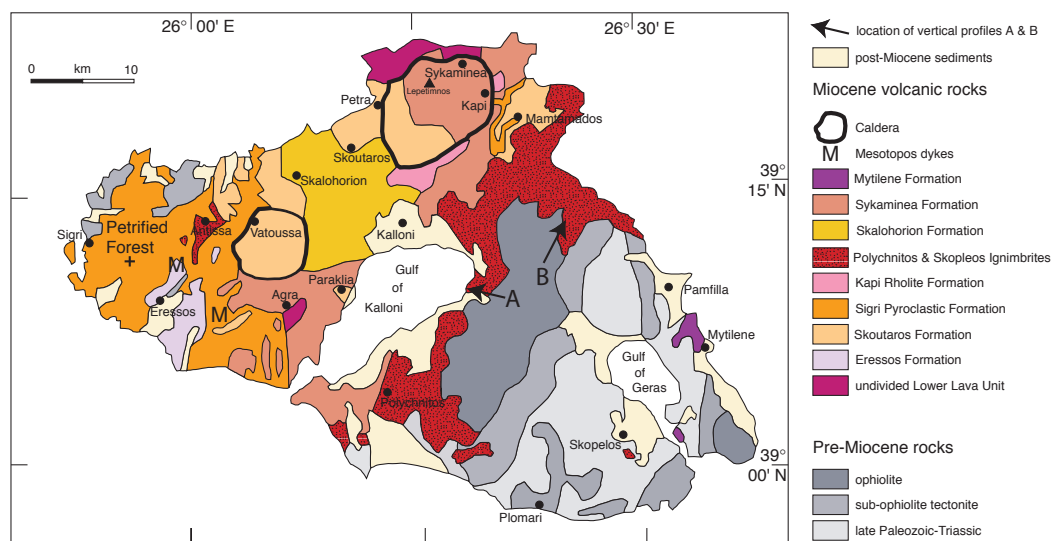


**Fig. 3.1.** Map showing the location of the two vertical profiles A (cape near Kofinas) and B (N side of Tavros mountain).

in section A.2 on page 166. The following description is a summary of the characteristics for all 11 samples throughout the 40m of vertical profile.

#### 3.3.1. Petrography

The structure of the ignimbrite throughout Vertical Profile A changes from an unwelded, grey to white coloured ash tuff at the bottom to a densely welded, black, glassy rock at the top (40m). In the top sample (LE-66) the matrix is difficult to distinguish from the fiamme, because they are both similarly black and glassy. The grade of welding increases more or less constantly from bottom to top, apparent in the overall density of the rocks as well as a transition from the contained pumice into fiamme and further an upward increasing compaction of the fiamme. The overall colour changes with increased density from bottom to top slowly from grey to white, then to grey (within 24m), after that more quickly to pink (between 24 and 32 m, Fig. 3.4), and finally to red and to black (within the top 8m). All these structural features are more or less horizontal throughout the outcrop. All samples contain a small proportion (< 1 vol%) of macroscopically visible feldspar and biotite. A representative column is displayed in Fig. 3.3.

### 3. The Polychnitos Ignimbrite

---



**Fig. 3.2.** “Cape Kofinas”; sample location for Profile A, a cape at the NE side of Kalloni Gulf, near the village Kofinas, between Ancient Pyra, an archaeological site, and Aghia Nikolao, a chapel. (a) “Cape Kofinas”, seen from the SE shore of the Gulf of Kalloni, (b) “Cape Kofinas” in the background, in the foreground the Polychnitos Ignimbrite can be seen overlying the metamorphic basement, note the typical structure for an ignimbrite deposit, the bottom mantles the substrata, the top is horizontal.

### 3.3. Profile A - glass and phenocrysts in the vertical profile

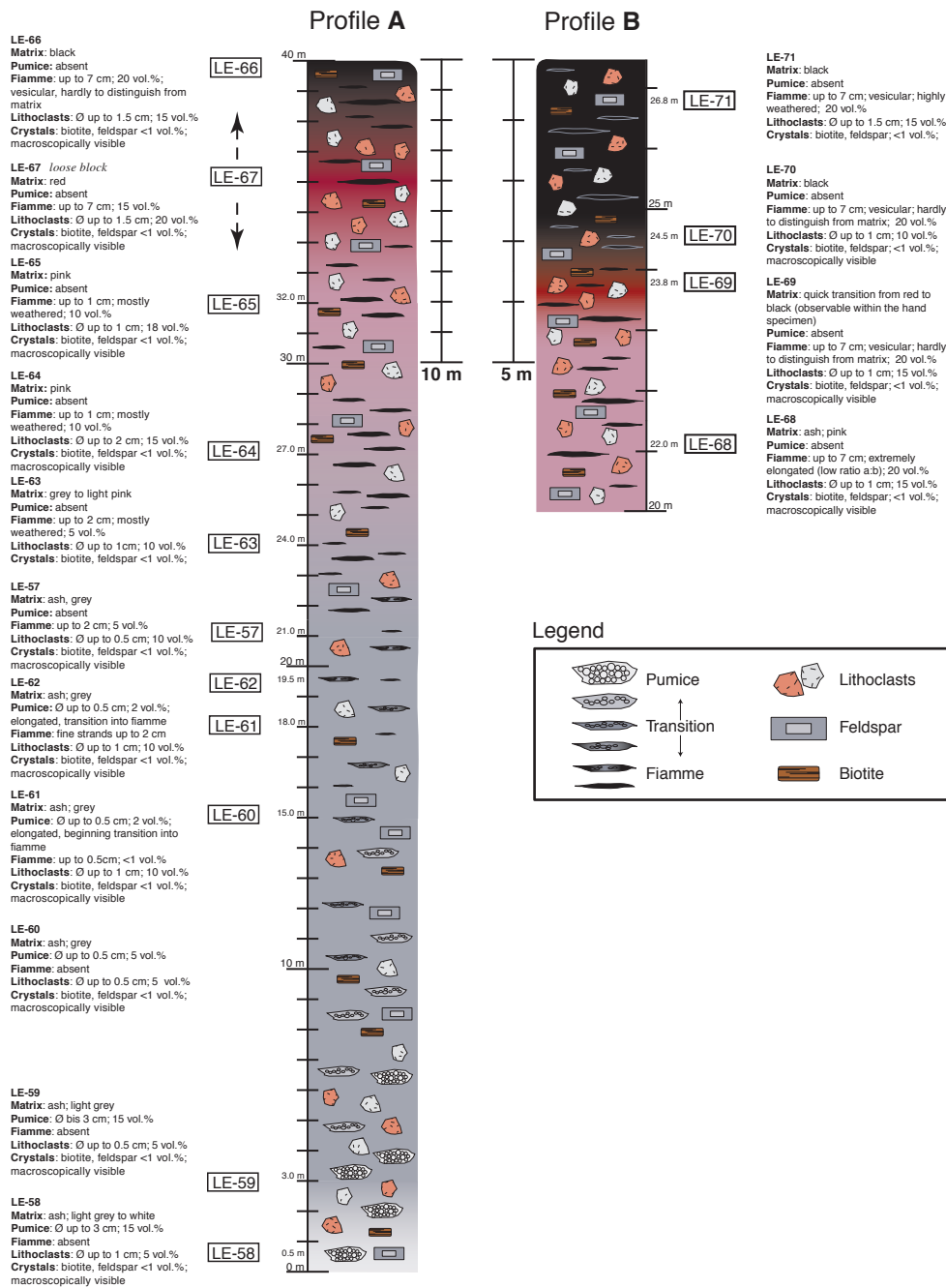


**Fig. 3.3.** Schematic sketch of the two vertical profiles A (cape near Kofinas) and B (N side of Tavros mountain).

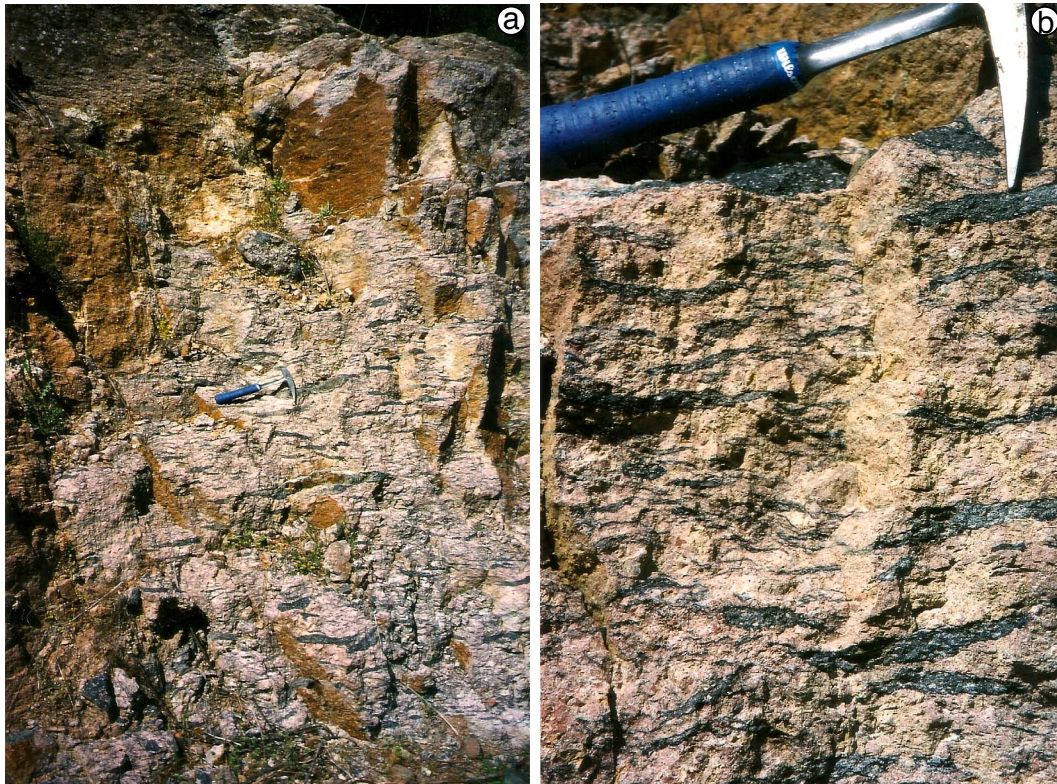


**Fig. 3.4.** Example photos of Vertical Profile A. (a) The near-top of Profile A, note the numerous very flat fiamme, and pink matrix colour; hammer for scale, this is the sample location of LE-65, (b) Close-up view of near-top of Profile A, description under a).

### 3.3.2. Lithoclasts, Pumice and Fiamme

The amount and size of lithoclasts increases from bottom to the top of the profile, from 5 vol% to 18 – 20 vol% and from 0.5 – 1 cm to 1.5 – 2 cm. Pumice is present only in the bottom 5 samples, while fiamme exist in the top 8 samples, with two samples in the middle (LE-61 and LE-62) containing both. The transition from pumice to fiamme is displayed clearly, with the amount and size of pumice *decreasing* upward (15 – 2 vol% and 3 – 0.5 cm) and the amount and horizontal elongation of fiamme *increasing* upward (< 1 – 20 vol% and 0.5 – 7 cm).

### 3.3.3. Matrix

In the vertical profile A the matrix of the ignimbrite samples shows a number of changes, when comparing the individual samples (Fig. 3.5). At the bottom of the profile (LE-58), the matrix shows individual cusped and platy glass shards with clearly defined rims, mostly around a few  $\mu\text{m}$  to a few tenths of  $\mu\text{m}$  with some substantially larger shards (Fig. 3.5 a). Moving further up the profile (LE-59), the matrix remains unchanged, while the larger glass shards display small filled and un-filled vesicles. These vesicles appear in all platy and cusped glass shards in the next overlying sample (LE-60, Fig. 3.5 b).

From sample LE-61 upwards, the matrix seems denser than below, as if slightly compacted (Fig. 3.5 c). The slightly vesicular glass shards show signs of deformation (LE-61 and LE-62): the glass shards appear slightly bent and are less discretely defined and more rounded than in the samples below. Some shards in the matrix of sample LE-62 are not only vesicular, but also show partly frizzy rims.

In the next sample in the profile (LE-57) the individual glass shards show incipient devitrification. The shards have craggy rims and selvages of microcrystals (Fig. 3.5d). However, parts of the matrix consist of areas of dense pristine glass with perlitic rings; the portion of pristine glass is still high in this sample.

Further upwards to sample LE-63, the outlines of the individual platy and cusped shards is still visible, but they have a fuzzy texture, including cavities, showing complete devitrification (Fig. 3.5 e). Analytical sums for devitrified glass in this succession is  $> 99.6\%$ , while for pristine glass sums are  $96.1\%$  on average. The described characteristics for individual glass shards in sample LE-63 are also displayed in sample LE-64, however the fuzziness is larger (Fig. 3.5 f). Therefore devitrification in this sample seems more advanced, which is supported by the fact, that the matrix of this sample additionally contains some spherulites, which are a product of devitrification in natural glass.

Moving further upward in the vertical profile A to sample LE-65 the matrix has the same fuzzy texture with cavities within the outlines of the former glass shards and includes spherulites as in the two samples below. This sample contains additionally a “blob” of  $\text{SiO}_2$  within the matrix, which is interpreted as secondary phase. (Fig. 3.5 g)

The outline of the former glass shards is barely visible in sample LE-67. The shards have a fuzzy texture, including cavities and “blobs” which are possibly  $\text{SiO}_2$  (Fig. 3.5 h). Despite the advanced devitrification of the matrix in sample LE-67, pristine glass was found in the centre of a large fiamma (Fig. 3.5 i). The glass is corroded at the rims of the fiamma and visually more and more pristine towards the centre.

### 3. The Polychnitos Ignimbrite

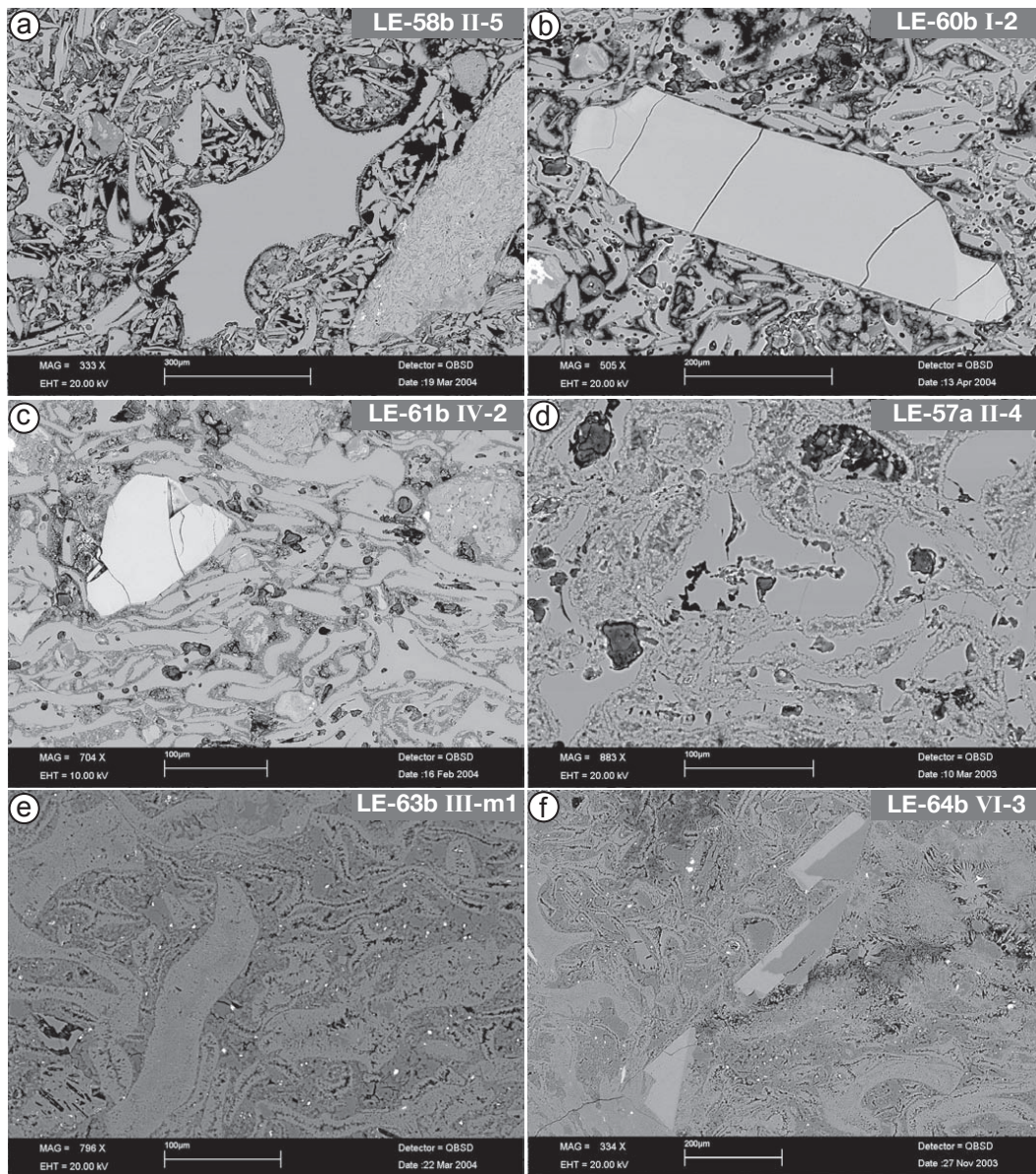


**Fig. 3.5.** Changes in glass texture in the matrix of samples in Profile A. (a) Cusped and platy glass shards in the matrix of sample LE-58 (b) Cusped and platy glass shards with small vesicles in the matrix of sample LE-60 (c) Slightly deformed, platy and cusped, partly vesicular glass in the matrix of sample LE-61 (d) Platy and cusped glass shards (some with craggy rims) with selvages of microcrystals in sample LE-57, this shows beginning devitrification. *Continued next page.*

### 3.3. Profile A - glass and phenocrysts in the vertical profile

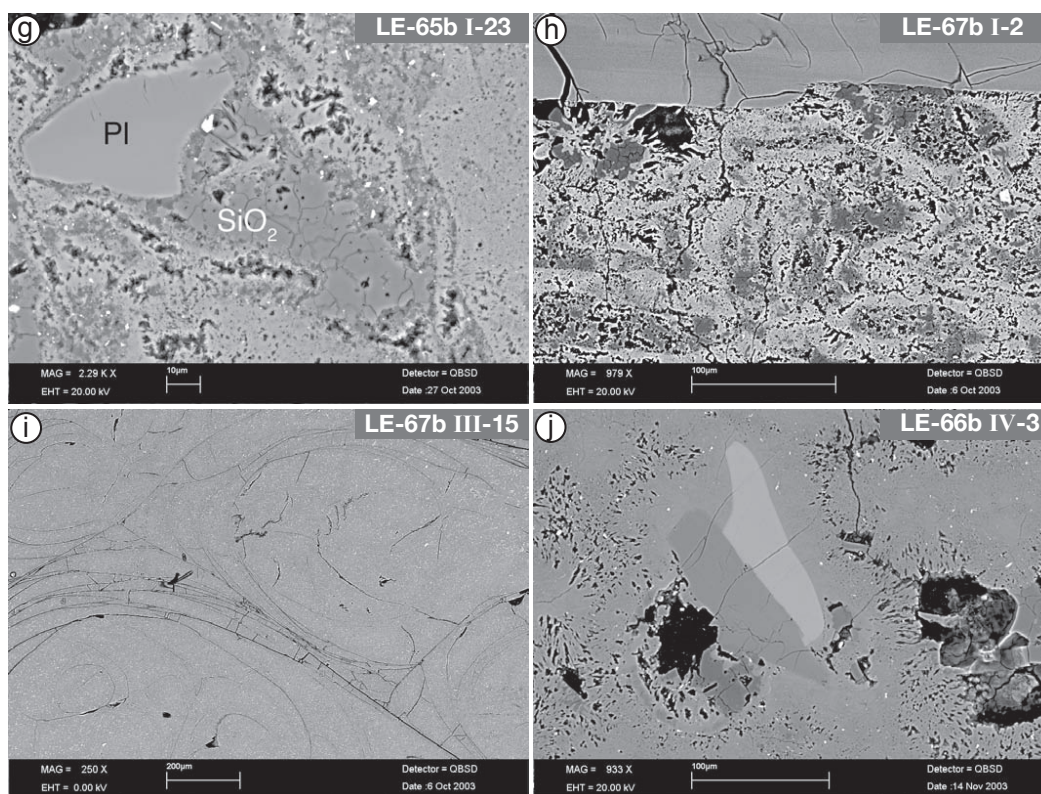


**Fig. 3.5. (continued)** Change in glass texture in the matrix and fiamme of samples in Profile A. (e) Devitrified matrix in sample LE-63, outlines of the individual platy and cusped shards are still visible, however they have a fuzzy texture, including cavities. (f) Devitrified matrix in sample LE-64, outlines of the individual platy and cusped shards are still visible, but they have a fuzzy texture, including cavities, in the right hand upper corner visible are some spherulites (g) Devitrified matrix in sample LE-65, outlines of the individual platy and cusped shards are still visible, but they have a fuzzy texture, including cavities. In the central part of the BSE image a “blob” of  $\text{SiO}_2$  can be seen. (h) Devitrified matrix in sample LE-67. The outlines of the individual platy and cusped shards are barely visible, they have a fuzzy texture, including cavities. At the left hand side of the BSE, just underneath the PI crystal in the top part image a “blob” (possibly of  $\text{SiO}_2$ ) can be seen. (i) Pristine glass in the central part of a large fiamme in sample LE-67. The glass contains perlitic rings and crystallites. (j) Devitrified glass in sample LE-66 with spherulites, matrix and fiamme have a fuzzy texture, including cavities. The outline of former glass shards are not visible any more. The sample contains some “blobs” similar to sample LE-65, and sample LE-67. Some few small spherulites can also be found in the matrix.

The matrix in sample LE-66 at the top of the vertical profile shows a fuzzy texture, the outlines of the former glass shards are not visible any more. Smaller spherulites can be found as well as “blobs” similar to those in sample LE-65 and LE-67 (Fig. 3.5 j).

**Spherulites** are a characteristic product of high-temperature devitrification in natural glass (MCPHIE *et al.*, 1993). They form radiating arrays of crystal fibres, with each fibre having a slightly different crystallographic orientation from the adjacent crystals. In former silicic glassy rocks spherulites consist of alkali feldspar and/or quartz (or cristobalite), in former mafic glassy rocks they consist of plagioclase and/or pyroxene (MCPHIE *et al.*, 1993).

The morphology of spherulites in rhyolitic glasses varies according to the temperature of their formation (LOFGREN, 1971), they are not spherical throughout their growth history (LOFGREN, 1971, 1974). Spherulites formed at high temperature (700°C) consist of open clusters of widely spaced crystal fibres. At low temperatures (< 400°C), spherulites comprise bundles of radiating fibres; bow-tie shaped sheafs of fibre characterise intermediate temperatures of formation (400°C to 650°C). In addition, the width of crystal fibres increases with increasing formation temperatures.

The internal crystal fibre structure can be recrystallised to a quartz-feldspar mosaic as a result of later alteration, metamorphism or deformation. Spherulites typically have diameters of 0.1 cm to 2 cm, but may be much larger (e.g. 10 cm to 20 cm in welded ignimbrite (STEVEN & LIPMAN, 1976).

The spherulites found in the top half of Profile A in sample LE-63, LE-64, LE-65, LE-67, and LE-66, and also in Profile B in sample LE-69, are fan or bow-tie shaped, sometimes forming elongated trains, suggesting an intermediate formation temperatures (400°C to 650°C).

#### 3.3.4. Phenocrysts

All samples contain plagioclase (Pl), alkali feldspar (Akf), and biotite (Bt). Most samples also contain Fe-Ti oxide, and individual samples contain apatite (Ap), zircon (Zrn), orthopyroxene (Opx), or SiO<sub>2</sub>-phase as phenocrysts.

**Plagioclase** is the main phase in all samples, accounting for 32% to 70% of all documented phenocrysts. The relative amount of feldspar is roughly constant, so that Pl and Akf show an opposite trend: a high relative amount of Pl correlates with a low relative amount of Akf, while a lower relative amount of Pl correlates with higher relative amounts of Akf.

### 3.3. Profile A - glass and phenocrysts in the vertical profile

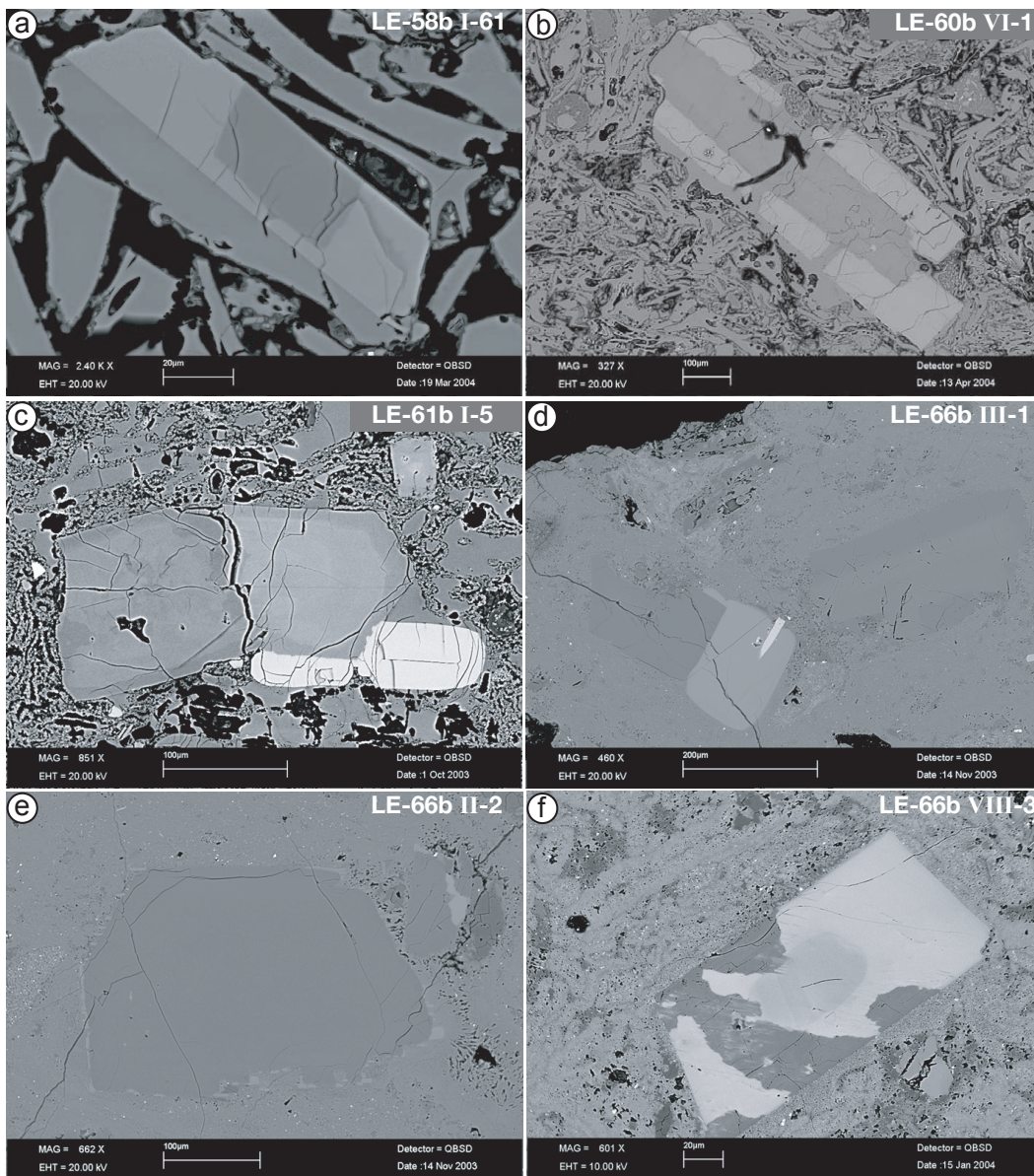


**Fig. 3.6.** Relationship and characteristics of Pl and Akf in Profile A. (a) Small euhedral Pl core with extensive euhedral Akf overgrowth and a wide glass selvage (b) Subhedral Pl with extensive Akf overgrowth (long laths around most of the Pl's rim and a glass selvage (c) Zoned subhedral and slightly fragmented Pl with satellitic Akf overgrowth and some glass selvage (d) Subhedral and slightly fragmented Pl with definite and sharp grain boundary and satellitic, rounded Akf overgrowth showing incipient resolution (e) Subhedral Pl with a narrow selvage of small Akf crystals (overgrowth) (f) Euhedral and zoned Akf, replaced in patches by Pl

### 3. The Polychnitos Ignimbrite

---

Fig. 3.6 shows a range of characteristic Pl crystals. The phenocrysts vary substantially in their sizes, from  $435 \times 260 \mu\text{m}$  to  $840 \times 430 \mu\text{m}$  on average, while Pl phenocrysts up to  $1500 \times 1000 \mu\text{m}$  occur. No trend concerning Pl sizes could be established.

Throughout most of the profile the phenocrysts are subhedral. However, subtle differences exist: at the top and bottom of the profile phenocrysts in most samples are subhedral to anhedral, while in the middle of profile A, phenocrysts tend to be more anhedral to euhedral.

Zonation in Pl phenocrysts are common. At the bottom of the profile (sample LE-58 to LE-62) usually 25% of the phenocrysts are zoned, further up 14 – 44% Pl are zoned. Zoned Pl are usually subhedral.

There are clear trends concerning Akf overgrowth and glass selvages around Pl phenocrysts. From bottom to top of the profile the amount of Pl phenocrysts with Akf overgrowth decreases almost steadily from 100% to 10%, just as well as the overgrowth decreases from thick Akf selvages (Fig. 3.6 a & b) to satellitic overgrowth (Fig. 3.6 c & d) and tiny crystals (Fig. 3.6 e) and from fully- or mostly-encasing to only partly-encasing.

There is, however, one crystal at the top of the profile, where the relationship between Akf and Pl is reversed: In sample LE-66 one formerly euhedral Akf phenocryst was found, which is in patches replaced by Pl (Fig. 3.6 f).

The thickness and the amount of crystals displaying a glass selvage decreases as well from bottom to top from 100% to 25%, while the Pl in the top two samples (LE-67, LE-66) do not have any glass selvages at all.

**Alkali feldspar** is a main phase in all samples of Profile A, comprising between 14% and 34% of all phenocrysts documented. There is always less Akf than Pl (except for sample LE-63, which contains just as much Akf as Pl (both 32%), and there is usually more Akf than Bt (except in sample LE-59 which contains *less* documented Akf than Bt, and in sample LE-64, with documented Akf and Bt both at 19%).

Akf phenocrysts tend to be euhedral to subhedral in the middle of the profile and more rounded at the bottom, while they are more anhedral to subhedral at the top of Profile A. The amount of Akf phenocrysts containing a small, old Pl core (Fig. 3.7 a) is between 75% and 0%: the relative amount is low at the bottom of the vertical profile (LE-58, LE-59), then reaches a maximum in sample LE-60. Above this sample the amount of Akf with Pl core decreases towards the top of the profile, to sample LE-65. But the amount is higher again in the two samples at the top (LE-67, LE-66).

### 3.3. Profile A - glass and phenocrysts in the vertical profile

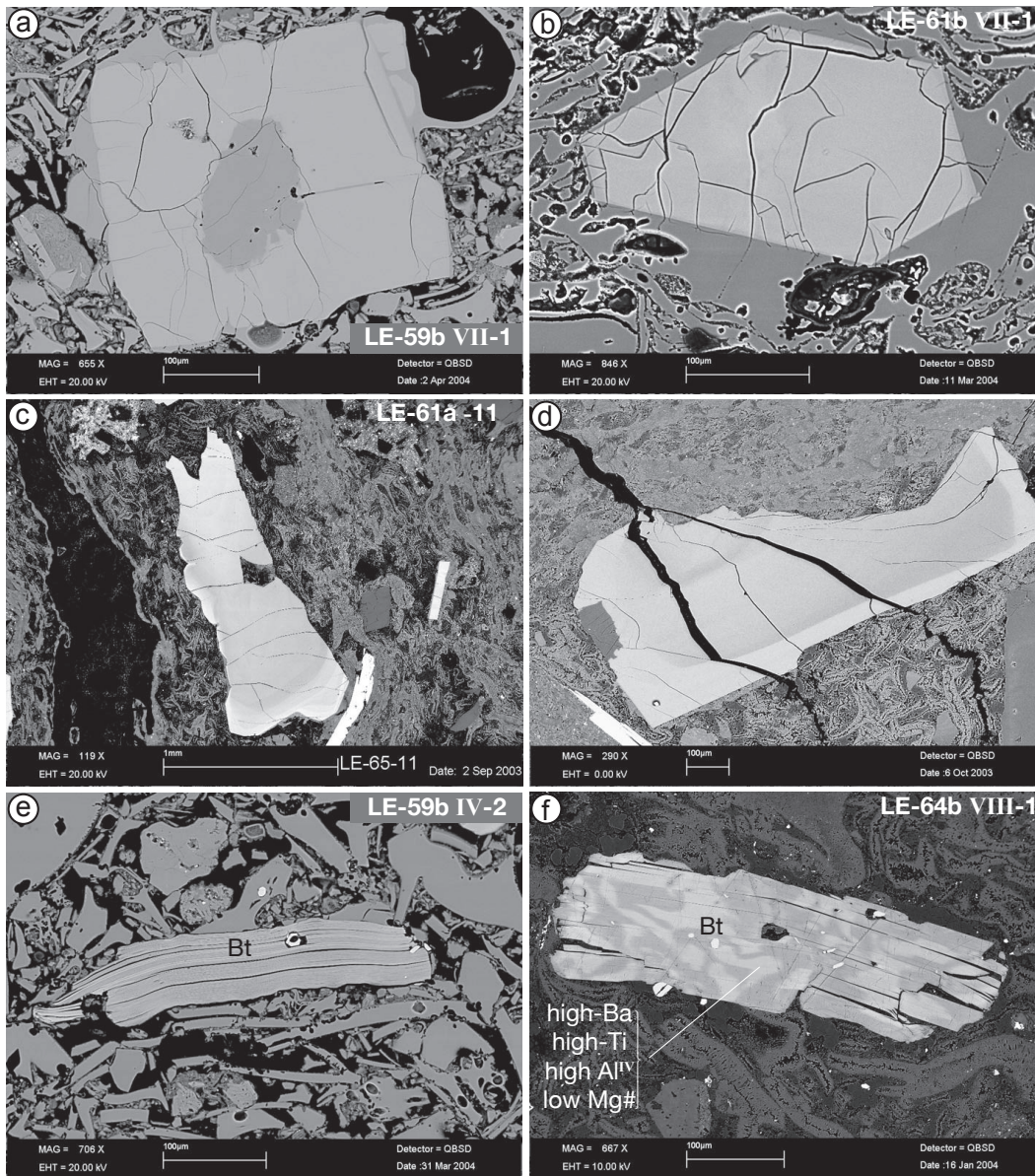


**Fig. 3.7.** Characteristics of Akf and Bt phenocrysts in Profile A. (a) Akf phenocryst with an irregularly rounded, i. e. corroded, rim and a typical small Pl core (b) Euhedral Akf phenocryst with an extensive glass selvage (c) Anhedral Akf phenocryst with a strong zonation pattern, the remnants of a former glass selvage are visible (d) Fragmented, formerly euhedral Akf phenocrysts with strong zonation pattern (e) Bt, banded and slightly bent (f) Bt with irregular, patchy zonations; light coloured patches have high-Ba, high-Ti, high Al<sup>IV</sup> abundances, and low Mg#

### 3. The Polychnitos Ignimbrite

---

Zonation occurs in 0 – 80% of Akf phenocrysts in Profile A. At the bottom of the profile (LE-58 to LE-62) zonations are less common at 0 – 10%, with the exception of sample LE-59, in which 33% of the Akf phenocrysts show zonations. In the top half of the profile (LE-57 to LE-66) zonation in Akf phenocrysts is more common, ranging from 33% to 80%.

The thickness of the glass selvage and the amount of Akf phenocrysts displaying a glass selvage decreases – as described before for Pl – from bottom to top in Profile A more or less steadily from 100% to 10%. Fig. 3.7 a–d shows a range of characteristic Akf phenocrysts found in Profile A.

**Biotite** is a main component in the samples of Profile A, however, relative amounts are lower than for Pl and Akf phenocrysts. Bt comprises usually between 21% and 14% of all documented phenocrysts, but drops to only 2% in the top-most sample of the profile. While Bt phenocrysts at the bottom of the profile tend to be euhedral, fragmented, partly dissolved (Fig. 3.7 c), and sometimes zoned, towards the top they tend to become subhedral, fragmented and corroded, sometimes rounded and containing holes. Towards the top Bt phenocrysts also tend to have inclusions of Ap and Zrn and instead of regular zonations they show in BSE images irregular patches of light colour (Fig. 3.7 d). These patches show high-Ba, high-Ti, high Al<sup>IV</sup> abundances, and have low Mg#. Bt phenocrysts do not have glass selvages.

**Fe-Ti oxide** The three samples at the bottom of Profile A (LE-58, LE-59, LE-60) include no Fe-Ti oxides, but all other samples contain 2 – 15% (1 – 4 grains). Nearly all of the minerals are rounded, show exsolution lamellae, and have inclusions of Ap and Zrn, which can reach a substantial size. The Fe-Ti oxides occur in clusters of 2 – 5 grains or as single minerals, and are usually between 150 × 100 μm and ∅400 μm. Fig. 3.8 a shows an example for an isolated Fe-Ti oxide.

**Apatite and Zircon** are quite common as inclusions in Bt, Fe-Ti oxide and Cpx, but also occur in Pl. One Ap and one Zrn grain each is documented which are not an inclusions, but isolated phenocrysts. Sample LE-63 contains an isolated, euhedral, relatively large (100 × 70 μm), phenocryst of Ap (Fig. 3.8 b) and an isolated, relatively large (150 × 25 μm), euhedral, prismatic phenocryst of Zrn (Fig. 3.8 c & d).

**Orthopyroxene and Clinopyroxene** Sample LE-67 contains the only recorded Opx phenocryst in Profile A. The Opx is subhedral, 300 × 250 μm, corroded, and

### 3.3. Profile A - glass and phenocrysts in the vertical profile

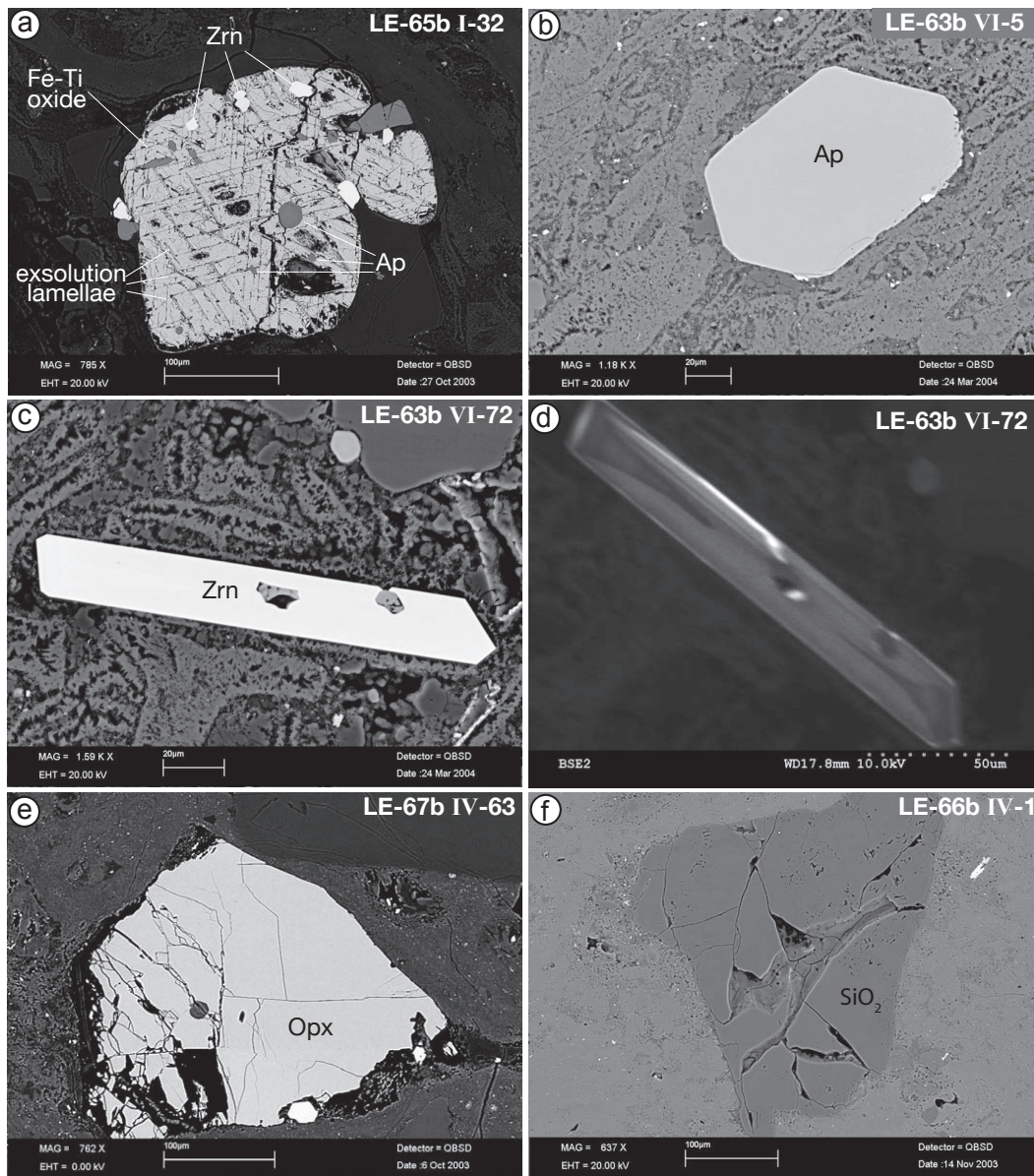


**Fig. 3.8.** Characteristics of additional minerals (Fe-Ti oxide, SiO<sub>2</sub>-phase, Ap, Zrn) in Profile A. (a) Typical Fe-Ti oxide: round, with clearly visible inclusions (Ap and Zrn) and exsolution lamellae. (b) Euhedral phenocryst of Ap (c) and (d) Euhedral, prismatic phenocryst of Zrn as BSE image and CL image, respectively (e) The only Opx found in Profile B, a subhedral, fractured phenocryst (f) SiO<sub>2</sub>-phase, anhedral, with large cracks and cavities, and a corroded rim. Considered a xenocryst.

fractured (Fig. 3.8 d). It is thought to be a xenocryst, possibly from the underlying Skoutaros Formation, for which Opx has been described.

No Cpx was found in any sampl in Profile A, in contrast to Profile B, where three out of four samples contain a few Cpx phenocrysts.

**SiO<sub>2</sub>-phase** Additional to the “blobs” of SiO<sub>2</sub> recorded in the matrix, one large grain of a SiO<sub>2</sub>-phase was documented in sample LE-66 (Fig. 3.8 e). It is anhedral, 320 × 220 μm, with large cracks and cavities, and a corroded rim. It is considered a xenocryst.

#### **3.4. Profile B - glass and phenocrysts in the vertical profile**

Profile B consists of four samples and was taken at the N side of Tavros mountain (374 m above sea-level), in the valley between Tavros mountain and Mesovouni flank. The location is close to the chapel Aghia Haralambos, W of the village Nees Kidonies and NNW of the villages Komi and Pigi. (See Fig. 3.1 on page 31) The individual samples of Profile B are described in the appendix in section A.3 on page 189. The following description is a summary of the characteristics for all four samples within the 7 m of the vertical profile as a whole.

##### **3.4.1. Petrography**

Vertical Profile B is throughout the whole sample range densely welded and glassy, and shows no significant changes. Only the colour changes in the bottom two samples from pink (22m) to red and black (within 15 cm in sample LE-69, 23.8 m), and remains black in the top two samples. In the top samples (LE-70 and LE-71) the matrix is difficult to distinguish from the fiamme, because they are both similarly black and glassy. All samples contain a small proportion (< 1 vol%) of macroscopically visible feldspar and biotite. A representative column is displayed in Fig. 3.3, some photos of the outcrop can be found in Fig. 3.9.

##### **3.4.2. Lithoclasts, Pumice, and Fiamme**

Lithoclasts and fiamme, do not show any significant changes throughout the vertical profile. Pumice is absent in all samples of Profile B. The size of lithoclasts increases slightly towards the top of the profile, from 1.0 – 1.5 cm, while the amount is more or less stable at 15 vol% (only exception LE-70, 10 vol%). The amount and horizontal elongation of fiamme is stable at < 20 vol% and 7 cm throughout the profile,



**Fig. 3.9.** Example photos of Vertical Profile B. (a) Bottom of Profile B, note the quick change of matrix colour; hammer for scale, this is the sample location of LE-65, (b) The near-top of Profile B, note the numerous fiamme, thin part of Profile B with grey matrix colour (below coin, sample location LE-70), sudden change upwards to black matrix.

while they change in their characteristics from dense (LE-68) to vesicular (LE-69, LE-70) and finally highly weathered (LE-71) from bottom to top.

### 3.4.3. Matrix

In vertical profile B, despite its vertical extent of only 6.8 m – like seen before in Profile A – the matrix undergoes a number of changes from bottom to top. At the bottom of the profile, in sample LE-68 the matrix shows partial devitrification. Parts of the matrix show a fuzzy texture, including cavities with the outlines of the former glass shards barely visible. In these parts “blobs” of  $\text{SiO}_2$  are occasionally found.

However, the matrix also contains pieces of pristine glass as “islands”. These islands have irregular rims with a fuzzy texture, but are suitable for analysis. They

show to be within the average of analytical sums for pristine glass, which is 96.6% in this succession, while devitrified glass has average analytical sums 100.4%. The sample contains additional pristine glass in the centres of two large fiamme. This glass also shows schlieren and strings of crystallites Fig. 3.10a).

Moving further upwards in the profile to sample LE-69 the matrix is completely devitrified. The “islands” of pristine glass are gone and the matrix does not only show the typical fuzzy texture, but also dark “blobs” like the SiO<sub>2</sub>-phases found in sample LE-68 and in Profile A. The matrix of this sample also contains faint spherulites of fan or bow-tie shapes (Fig. 3.10b).

The next sample LE-70, however, does not show further advanced devitrification. On the contrary, the glass in this sample is – except for a few fuzzy patches– pristine, with schlieren and strings of crystallites and is most suitable for analysis. It is possible though, that this glass is not part of the matrix, but of a fiamme, as it is not possible to distinguish between the two in this sample (Fig. 3.10c).

The top sample in this short succession, LE-71, shows complete devitrification. The texture of the matrix is fuzzy and outlines of former glass shards are not visible. However, no spherulites or “blobs” of SiO<sub>2</sub> were found. The sample contains a highly vesicular fiamme, which is also devitrified (Fig. 3.10d).

Hence, Profile B shows – with exception of sample LE-70 – progressive devitrification from bottom to top in the matrix and eventually also the fiamme.

#### 3.4.4. Phenocrysts

All samples of Profile B contain plagioclase (Pl), biotite (Bt) and clinopyroxene (Cpx). Only some samples have alkali feldspar (Akf), Fe-Ti oxide, SiO<sub>2</sub>, BaSO<sub>4</sub> and orthopyroxene (Opx). In contrast to Profile A, in Profile B 5 – 10% of the phenocrysts are clusters or clots of two or more minerals of the same or of different types. Typically these clots are Pl with Pl, Pl with Bt, or Cpx with Cpx.

**Plagioclase** is the dominant phase in all samples of Profile B with 64 – 73% of all documented phenocrysts. The phenocrysts are subhedral to anhedral and approximately of the same size range throughout the profile, i.e. between 200 × 200 μm and up to 3.3 × 1.5 mm, on average 750 × 500 μm (Fig. 3.11a). About 25 – 30% of the Pl phenocrysts are zoned; zoned crystals are mostly subhedral, only four zoned anhedral phenocrysts have been documented (Fig. 3.11b).

Akf overgrowth is extremely rare, it is documented only for one Pl phenocryst (sample LE-71, b IV-13) and consists of tiny Akf crystals around a small portion of the rim. Glass selvages are likewise rare, documented only once (LE-68, b VII-5), where only a small portion of the rim shows a narrow, but pristine glass selvage.

### 3.4. Profile B - glass and phenocrysts in the vertical profile

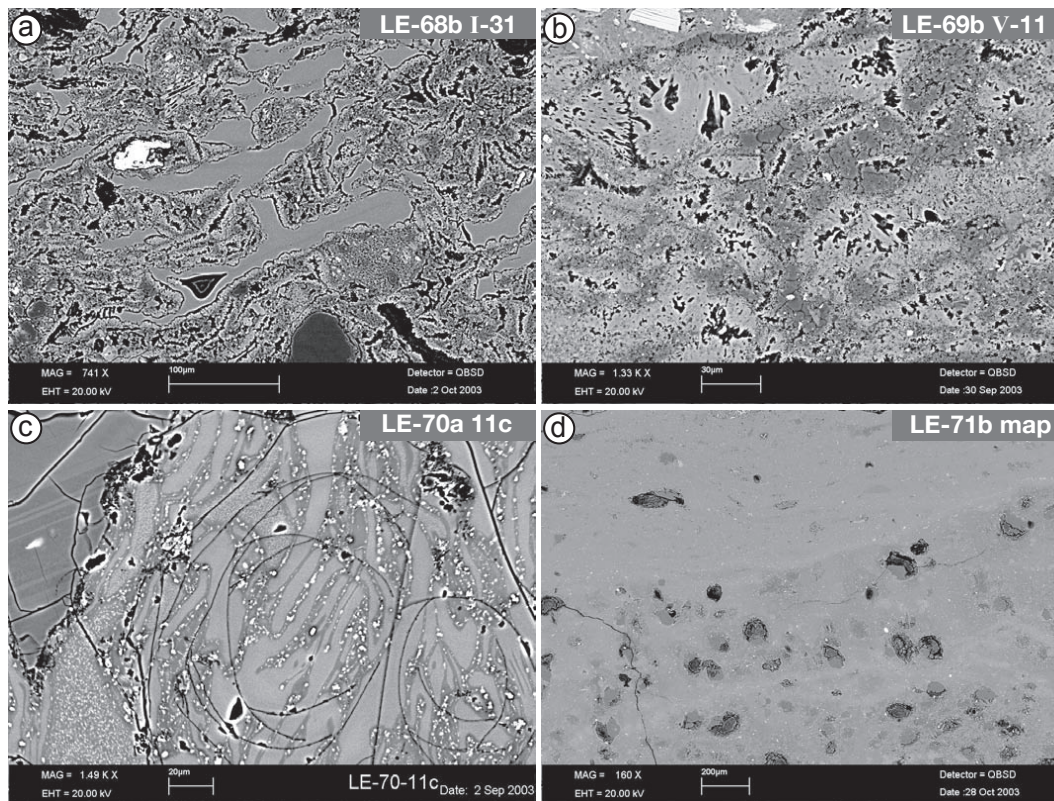


**Fig. 3.10.** Change in glass texture in the matrix and fiamme in the vertical profile B. (a) The matrix of sample LE-68 has a fuzzy texture including cavities, with the outlines of former shards barely visible. However, pieces of pristine glass are frequently found as “islands” within the matrix. The pristine shards are surrounded by the fuzzy texture and often have very irregular rims. (b) The texture of the matrix in sample LE-69 is fuzzy, the outlines of former shards are barely visible. The glass in the matrix of this sample is devitrified and not suitable for analysis. (c) The glass in sample LE-70 shows schlieren, perlite rings and inclusions of crystallites arranged along the schlieren. It is not possible to distinguish between matrix and fiamme in this sample. The analytical sums are close to the average for pristine glass in Profile B. (d) The texture in the matrix of sample LE-71 is fuzzy, outlines of former shards can not be observed. However, spherulites or SiO<sub>2</sub> “blobs” are also missing. The glass of this sample shows devitrification.

### 3. The Polychnitos Ignimbrite

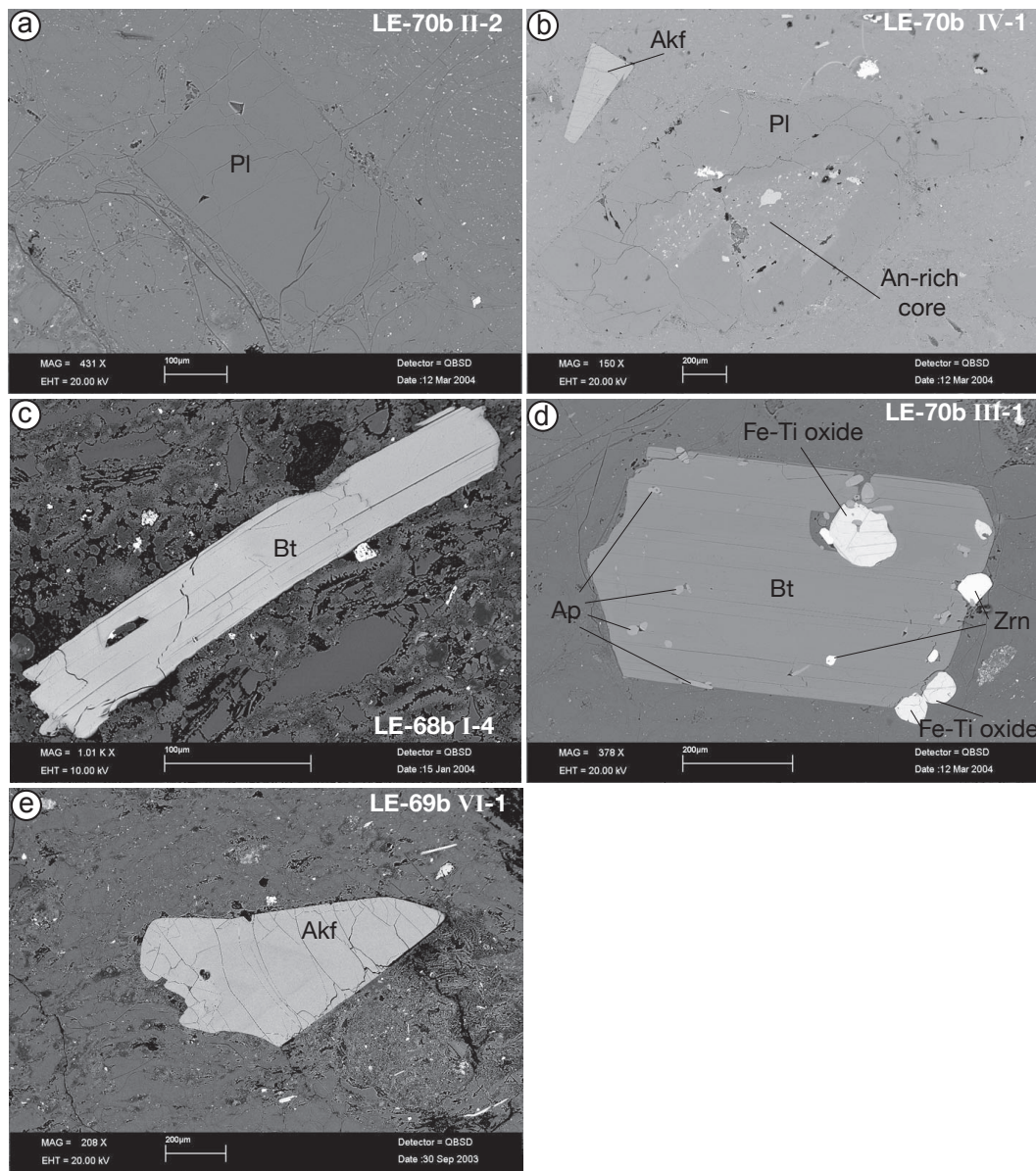


**Fig. 3.11.** Characteristic Pl, Bt, and Akf phenocrysts from Profile B. (a) Subhedral Pl with sharp rim, without zonation or inclusion (b) Subhedral Pl with An-rich core with inclusions and one of the few Akf phenocryst in Profile B, which is small, euhedral, unzoned. (c) Euhedral Bt without inclusions or zonation (d) Subhedral Bt with inclusions of Ap, Zrn, and Fe-Ti oxides (e) Anhedral, zoned Akf fragment

**Biotite** is contained in all four samples in relative amounts of 16 – 27% of all documented phenocrysts. The phenocrysts are mostly subhedral (two thirds to three quarters) and are on average  $480 \times 150 \mu\text{m}$ . A large number (between a third and two thirds) has inclusions, usually of Ap and Zrn, but also Fe-Ti oxides. Glass selvages are extremely rare, documented only once for Bt (LE-68, b III-83b) (Fig. 3.11 c & d).

**Alkali feldspar** As a major difference to Profile A, Akf is not a main phase in Profile B, but only an accessory mineral. Each thin section in Profile B contains only one or two Akf phenocrysts. They vary greatly in their sizes and characteristics. The size ranges from relatively small in samples LE-68 ( $170 \times 90 \mu\text{m}$ ) at the bottom and LE-71 at the top of the profile ( $190 \times 180 \mu\text{m}$ ) to medium size in sample LE-70 ( $350 \times 200 \mu\text{m}$ ) and large in LE-69 ( $900 \times 350 \mu\text{m}$ ).

Akf phenocrysts are euhedral, subhedral and anhedral, some rounded, one with an old small Pl core, some with zonation, some with inclusions, and some fractured (Fig. 3.11 b & e).

**Orthopyroxene and Clinopyroxene** One crystal of Opx was found in Profile B, in sample LE-68b (Fig. 3.12 a). The crystal is very corroded, like the only other Opx found in Profile A, in sample LE-67b, which suggests both of them to be xenocrysts, picked up from an older unit. Opx has been described in the underlying Skoutaros Formation.

While there was no Cpx found in any samples in Profile A, Cpx comprises 2 – 4% of all phenocrysts documented in the three top samples in Profile B (LE-69, LE-70, LE-71). They all vary greatly in their characteristics. The Cpx phenocrysts range in size from relatively small ( $650 \times 500 \mu\text{m}$ ) to large ( $2.0 \times 0.3 \text{ mm}$ ), they are subhedral to anhedral, all partly rounded, they occur in clusters or as isolated grains, and may or may not contain inclusions (Fig. 3.12 b & c).

**Fe-Ti oxide** Only the bottom sample (LE-68) and the top sample (LE-71) of Profile B contains documented Fe-Ti oxides. They vary greatly in their characteristics: subhedral to euhedral and anhedral, rounded to irregularly shaped, with and without inclusions, however all have exsolution lamellae. Their sizes are between  $120 \times 120 \mu\text{m}$  and  $500 \times 350 \mu\text{m}$  (Fig. 3.12 d).

**SiO<sub>2</sub> phase** Additionally to the “blobs” of SiO<sub>2</sub> in the matrix, there is one large anhedral grain of a SiO<sub>2</sub> phase documented in sample LE-68, measuring

### 3. The Polychinitos Ignimbrite

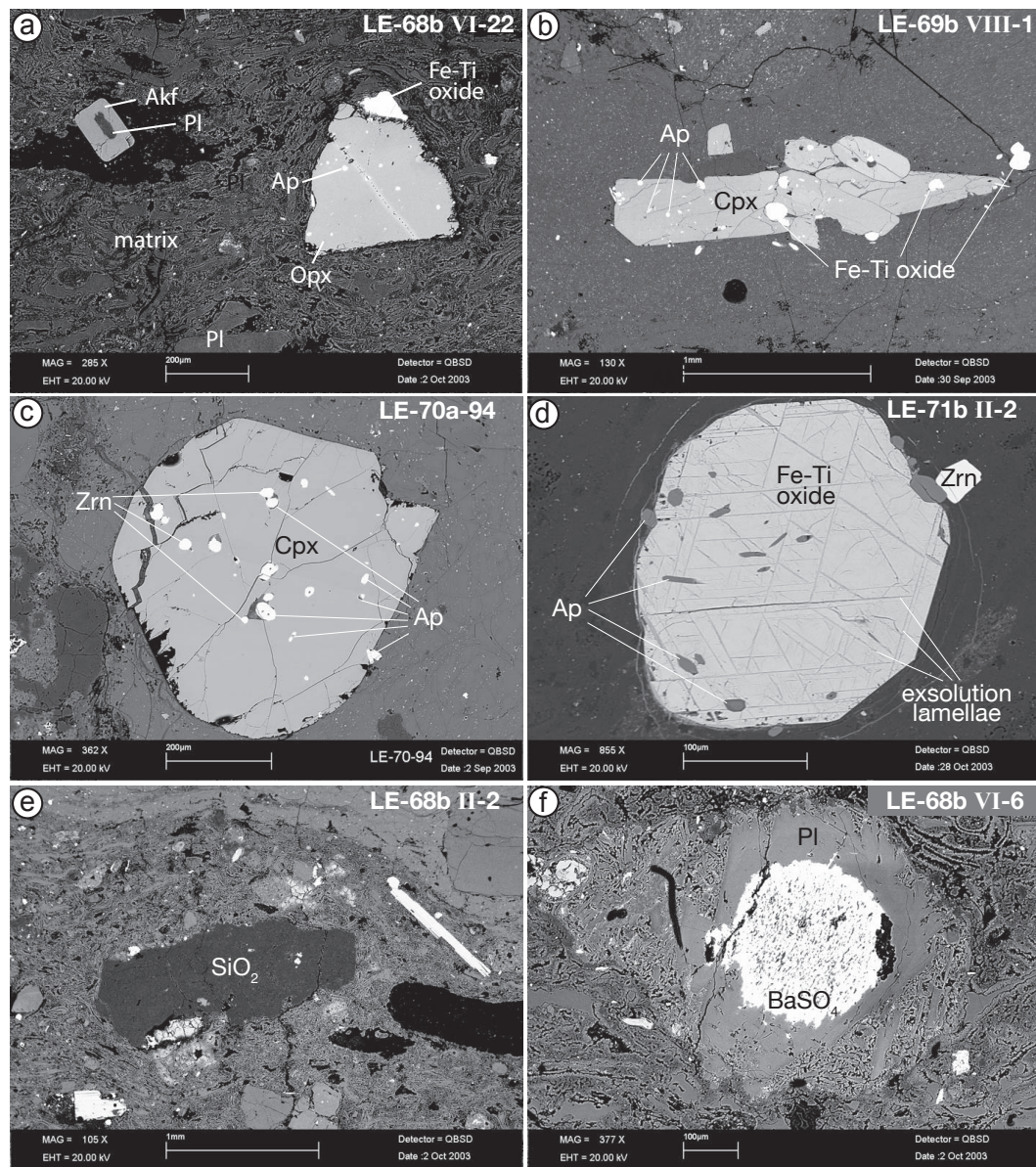


**Fig. 3.12.** (a) Anhedrous Opx phenocryst with Ap inclusions, showing beginning dissolution, also shown a very untypical Fe-Ti oxide (anhedral, without inclusions and exsolution lamellae) and an euhedral Akf phenocryst with a small Pl core (b) Several Cpx crystals with inclusions of Ap and Fe-Ti oxide in a cluster (c) Subhedral, isolated, Cpx phenocrysts with inclusions of Ap and Zrn, partly rounded with some portions of the rim retaining the crystal shape (d) Subhedral Fe-Ti oxide with inclusions of Ap and Zrn satellite, partly rounded, with part of the rim retaining the definite crystal shape (e) Anhedrous SiO<sub>2</sub>-phase, considered a xenocryst (f) Round BaSO<sub>4</sub>-phase as inclusion in an anhedrous Pl with a corroded rim

1750 × 500 μm. It is interpreted as xenocryst, as it shows all signs of corrosion and dissolution (Fig. 3.12 e).

**BaSO<sub>4</sub> phase** There is also a BaSO<sub>4</sub> phase as large inclusion in a Pl crystal documented in sample LE-68. The Pl is anhedral, zoned, 500 × 400 μm, with a corroded rim, while the BaSO<sub>4</sub> is circular (∅300 μm) with a sieve texture and an irregular rim. This is probably a xenocryst, with the BaSO<sub>4</sub>-phase and especially the encasing Pl showing signs of corrosion and dissolution (Fig. 3.12 f).

### 3.5. Additional samples from other locations

Additional samples of volcanic glass were taken from fiamme at road cuts from two different roads NE of the Gulf of Kalloni. These sample contain 95 – 97 % (modal percentage) glass. Phenocrysts of Akf, Pl, and Bt are always contained in differing proportions, while Cpx, Fe-Ti oxide, Am, and Zrn are found only in some samples. The samples are described individually in the appendix in section A.4 on page 199.



## 4. Geochemical properties of the volcanic glass

### 4.1. Major and Minor elements

The volcanic glass in all samples is relatively homogeneous with respect to all major and minor elements. The chemical composition does not change between different pristine glass phases (matrix or fiamme or glass selvages attached to phenocrysts), nor locally within the glass. Element concentration maps for different elements and different samples (different glass textures) were obtained using a Leo 440 scanning electron microscope (SEM, Institut für Geowissenschaften, Universität Heidelberg).

The first sample (LE-62 b, Fig. 4.1), which consists of a dense glass fiamme without perlitic rings, schlieren or micro-crystallites, shows no significant variation in any of the elements mapped (Na, Mg, Si, K, Fe). The elements merely show the difference between glass and interstitial cavities.

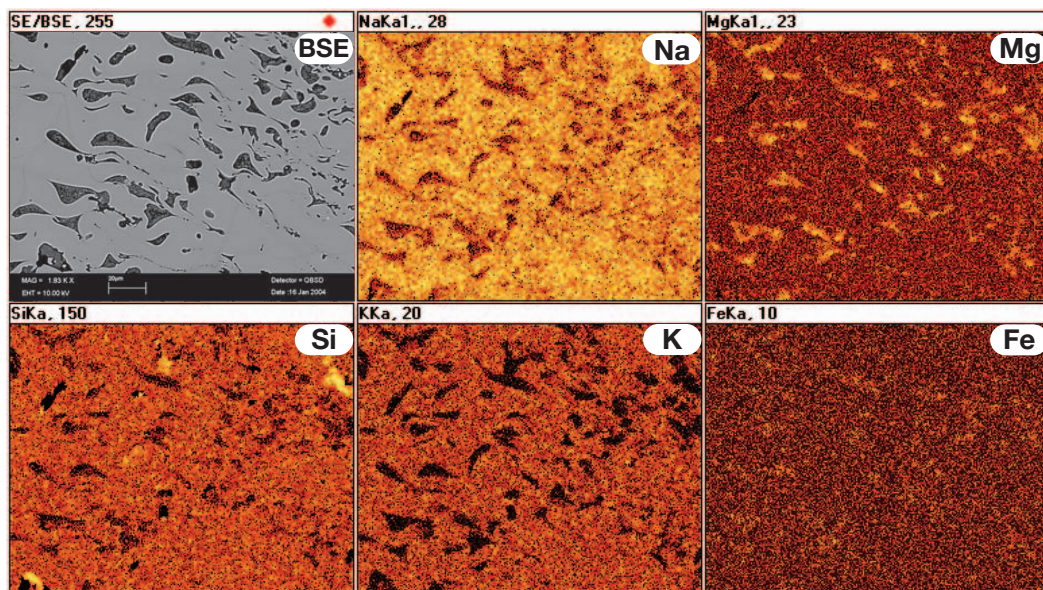


**Fig. 4.1.** Element concentration maps (Na, Mg, Si, K, Fe) in the fiamme of sample LE-62 b (IV map) and BSE image for orientation. Low element concentrations are shown in red, high concentrations in yellow. The scale bar at the bottom of the BSE image indicates a length of 20 µm and is also valid for the concentration maps.

#### 4. Geochemical properties of the volcanic glass

However, small differences in element distributions can be observed in the next sample (LE-68 b, Fig. 4.2), consisting of glass of a fiamme, which has perlitic rings and minor cracks, schlieren and micro-crystallites. Along the perlitic rings the concentration of Na (and to a much smaller extend of K) are lower, than in the rest of the glass. This effect is confined to the immediate vicinity of the perlitic rings and is therefore secondary. For in-situ analysis data points on or close to perlitic rings were avoided.

The concentration of Fe varies along the schlieren in the glass. Schlieren, which are lighter in the BSE image, have a slightly higher concentration of Fe. To an even smaller extend this effect is also shown in the concentrations of Ca and Mg. High Fe concentrations show the sites of small Fe-Ti oxides.

The element map of the devitrified matrix of sample LE-65 shows that the former textures are preserved in the distribution of some element concentrations. While the outlines of the platy and cusped glass shards are still visible in the BSE image, the texture is fuzzy and has cavities. (Analytic totals are on average 99.7%, while for pristine glass they are on average 96.1%).

Element concentrations in the former shards show higher Al, higher K, lower

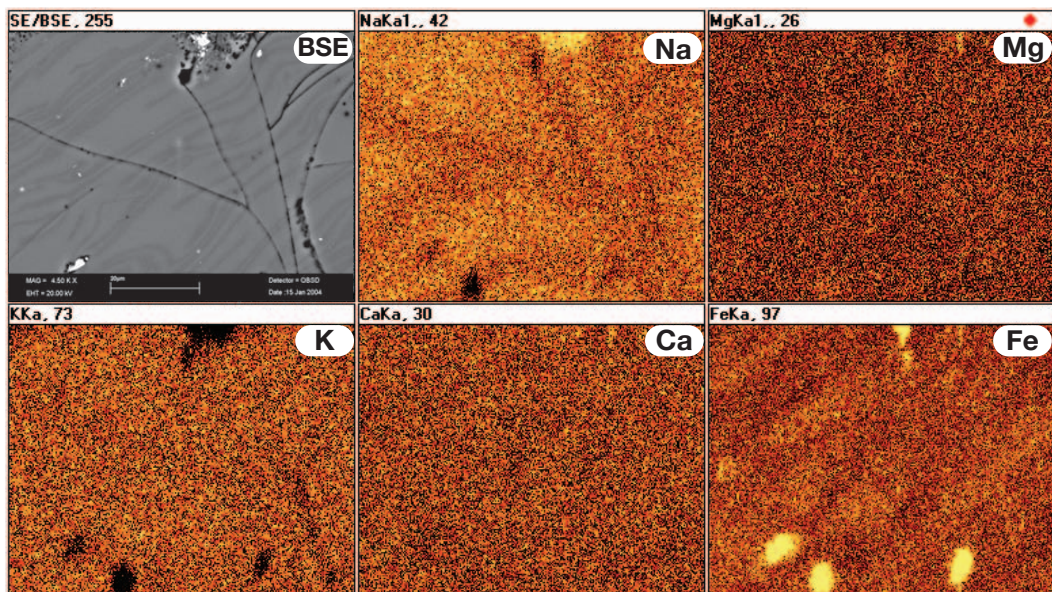


**Fig. 4.2.** Element concentration maps (Na, Mg, K, Ca, Fe) in the fiamme of sample LE-68 b (II-31 map) and BSE image for orientation. Low element concentrations are shown in red, high concentrations in yellow. The scale bar at the bottom of the BSE image indicates a length of 20 µm and is also valid for the concentration maps.

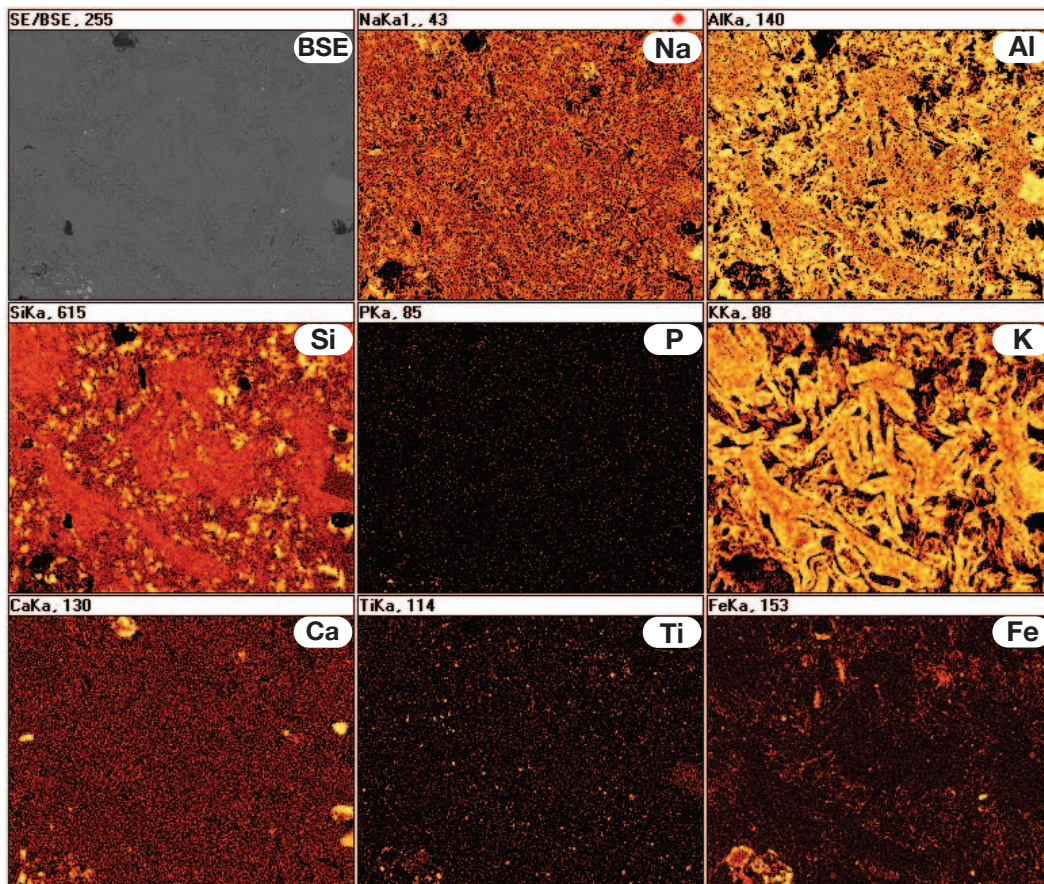


**Fig. 4.3.** Element concentration maps (Na, Al, Si, P, K, Ca, Ti, Fe) in the devitrified matrix of sample LE-65 b I and BSE image for orientation. Low element concentrations are shown in red, high concentrations in yellow. Please note, that elements show different mobility during the devitrification process. It seems that Al, K, Si, and to a lower extent Fe have a low mobility and therefore preserve the former texture in different degrees. While Na, P, and Ca show no significant pattern and seem to have had a high mobility during devitrification. The individual pictures are  $\approx 250 \mu\text{m}$

Si, and slightly lower Fe, while Na, P and Ca show no significant distribution patterns (Note however, that P, and Ca concentrations in the glass are very low). The elements show different mobility during the devitrification process. It seems that especially K has a very low mobility and preserves the former texture of the pristine glass to a high degree. The existence of numerous small Fe-Ti oxides, visible in the BSE image, shows up clearly in the distribution map for Ti.

#### 4.1.1. Classification diagrams

Chemical compositions of minerals and glass (16 chemical elements) were determined using a Cameca® SX 51 electron microprobe at the Institut für Geowissenschaften, Universität Heidelberg. Details concerning the analytic setup are found in the appendix in section C.2 on page 269.

Using the nomenclature of the IUGS (International Union of Geological Sciences) of Total Alkali vs. Silica (TAS,  $\text{Na}_2\text{O} + \text{K}_2\text{O}$  vs.  $\text{SiO}_2$ ) by LE BAS *et al.* (1986) and the classification based on  $\text{K}_2\text{O}$  vs.  $\text{SiO}_2$  by EWART (1982), the volcanic glasses studied here are of high-K rhyolitic composition (Fig. 4.4 and Fig. 4.5). According to the dividing line of MIYASHIRO (1978) (Fig. 4.4) the glass compositions are alkalic.

In the TAS diagram (Fig. 4.4) the data plot clearly in the rhyolite field. In the  $\text{K}_2\text{O}$  vs.  $\text{SiO}_2$  diagram (Fig. 4.5) analyses fall into the upper part of the high-K rhyolite field. In both diagrams samples show a negative correlation between  $\text{Na}_2\text{O} + \text{K}_2\text{O}$  and  $\text{K}_2\text{O}$ , respectively, vs.  $\text{SiO}_2$ .

The samples from the two vertical profiles A and B plot in two different groups, with samples from Profile A being higher in  $\text{SiO}_2$  and lower in  $\text{Na}_2\text{O} + \text{K}_2\text{O}$  and  $\text{K}_2\text{O}$  than samples from profile B, respectively. For comparison data from Pl rims and Akf rims (in equilibria with the glass) from both profiles are also plotted into the two diagrams. Compositions are slightly different for Pl rims in the two vertical profiles, while the compositions for Akf rims are indistinguishable.

According to the main chemical components in the TAS diagram (Fig. 4.4) and in the  $\text{K}_2\text{O}$  vs.  $\text{SiO}_2$  diagram (Fig. 4.5) there are two possible fractionation trends in order to evolve either melt A (melt with a composition of the glass in Profile A) into melt B (melt with a composition of glass in Profile B) or in the opposite direction from melt B into melt A.

Melt A could have evolved into melt B by Pl fractionation and Akf assimilation. Or melt B could have evolved into melt A by Akf fractionation and Pl assimilation. Alternatively a common parent melt could have developed along separate fractionation trends into melt A and melt B respectively. The possible fractionation trends are discussed further at the end of this chapter in section 4.3 on page 74.

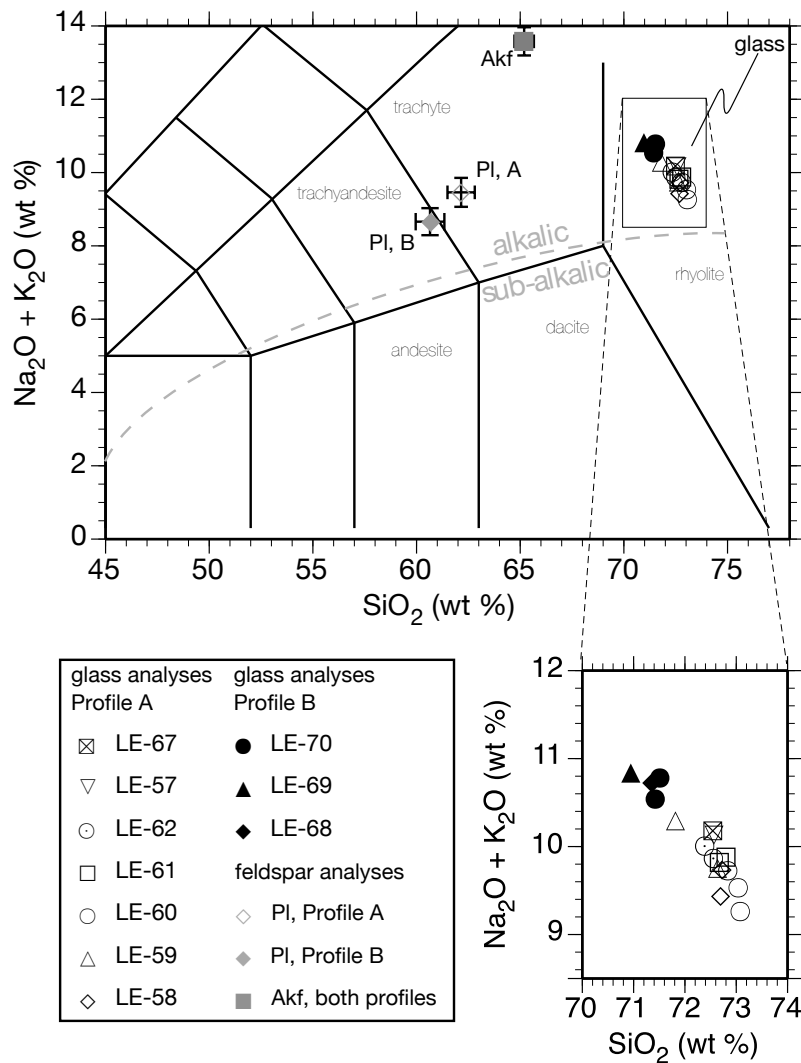


**Fig. 4.4.** Glass analyses (recalculated to 100% without  $\text{H}_2\text{O}$ ) from the two vertical profiles A and B. For comparison PI and Akf average data from the two vertical profiles are also plotted in the diagram; error bars show  $2\sigma$  standard deviation. Classification based on LE BAS *et al.* (1986), dividing line alkalic vs. sub-alkalic by MIYASHIRO (1978).

#### 4. Geochemical properties of the volcanic glass

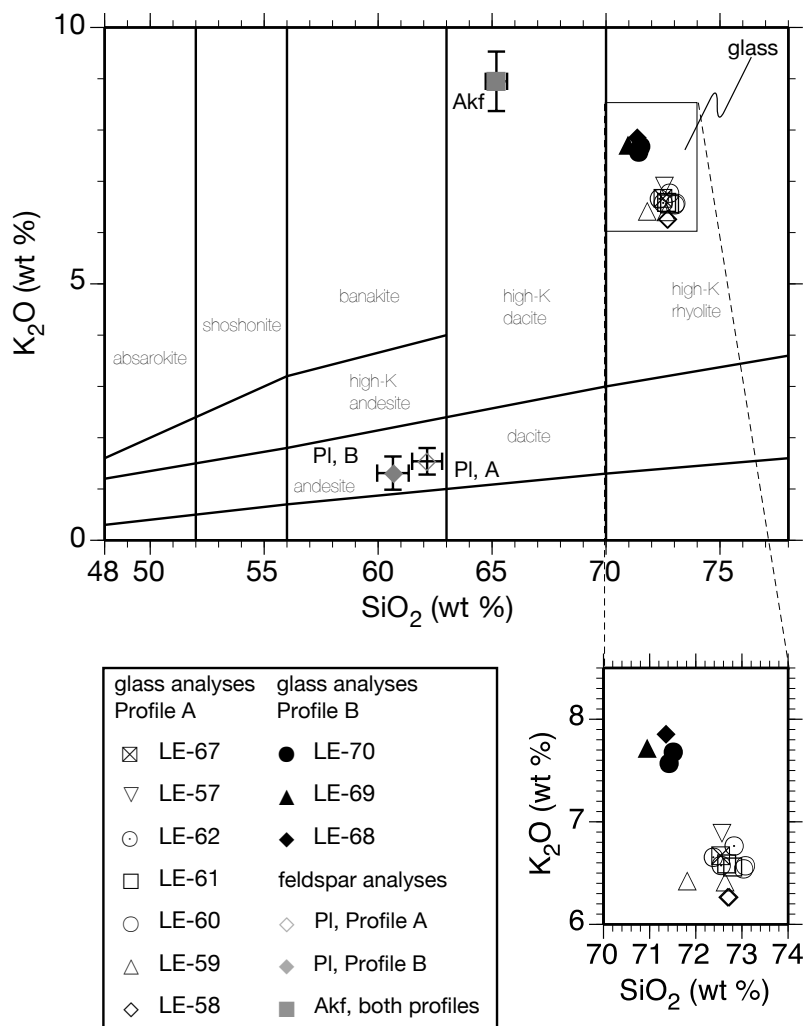


**Fig. 4.5.** Glass analyses (recalculated to 100% without H<sub>2</sub>O) from the two vertical profiles A and B. For comparison average data of PI and Akf from the two vertical profiles are also plotted in the diagram; error bars show 2σ standard deviation. Classification EWART (1982)

According to the Alumina Saturation Index (ASI) (Fig. 4.6 a) the glass compositions are peraluminous with values between 1.04 and 1.20 (after SHAND, 1951). Samples from Profile A and B plot again as two different groups. However, differences are not very strong.

Data from this study show generally a good agreement with literature data for rhyolites from Lesbos and Western Anatolia (Fig. 4.6 b) and for volcanic rocks from

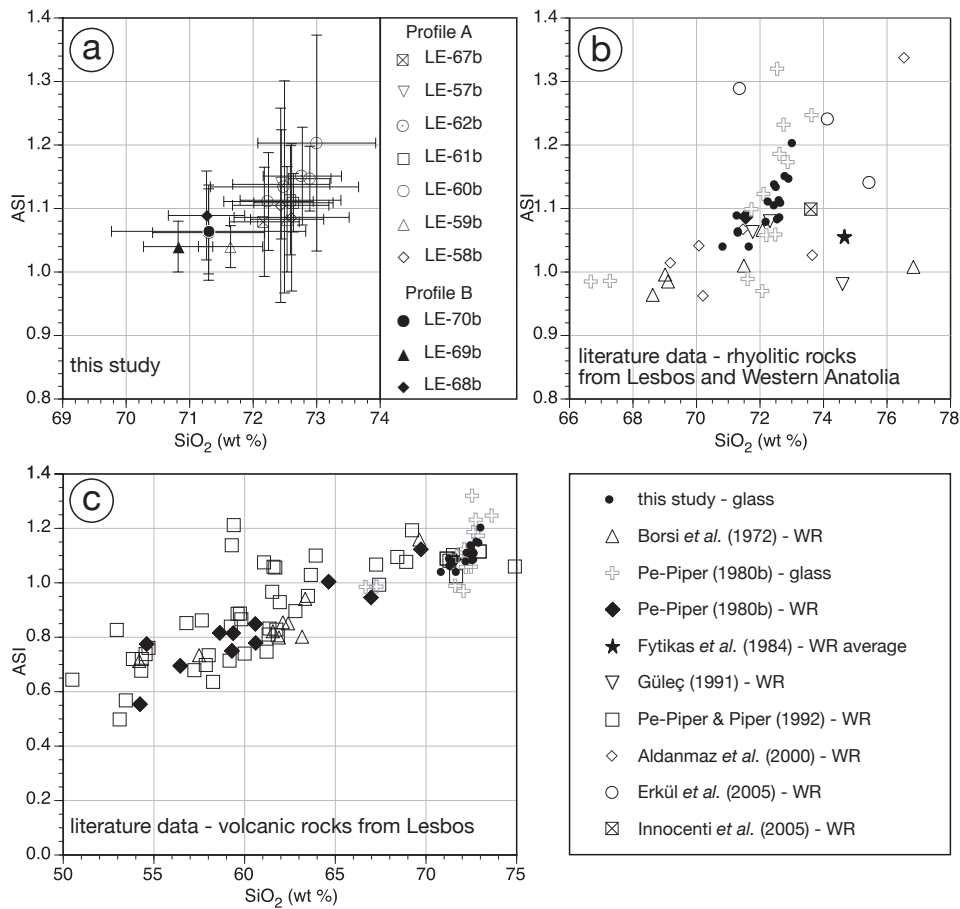


**Fig. 4.6.** Alumina Saturation Index (ASI) plotted against SiO<sub>2</sub> contents: (a) This study, error bars show  $2\sigma$  standard deviation (b) Literature data for rhyolites from Lesbos and Western Anatolia (c) Range of volcanic rocks from Lesbos Island

Lesbos Island (Fig. 4.6 c) with SiO<sub>2</sub> contents ranging from 50 vol% to 75 vol%. All data plotted creates a generally linear trend.

PE-PIPER (1980b) presents electron microprobe data for individual glass shards (Fig. 4.6 c); the quality of the data cannot be expected to be very high, due to restrictions of the analytical technique pre-1980. Therefore the scatter of these data points in the plot is unfortunate, but not surprising.

The chemical composition of the volcanic glass is not only reasonably homogeneous within each sample, but also changes very little throughout each of the vertical profiles (Figs. 4.7 & 4.8).

#### 4. Geochemical properties of the volcanic glass

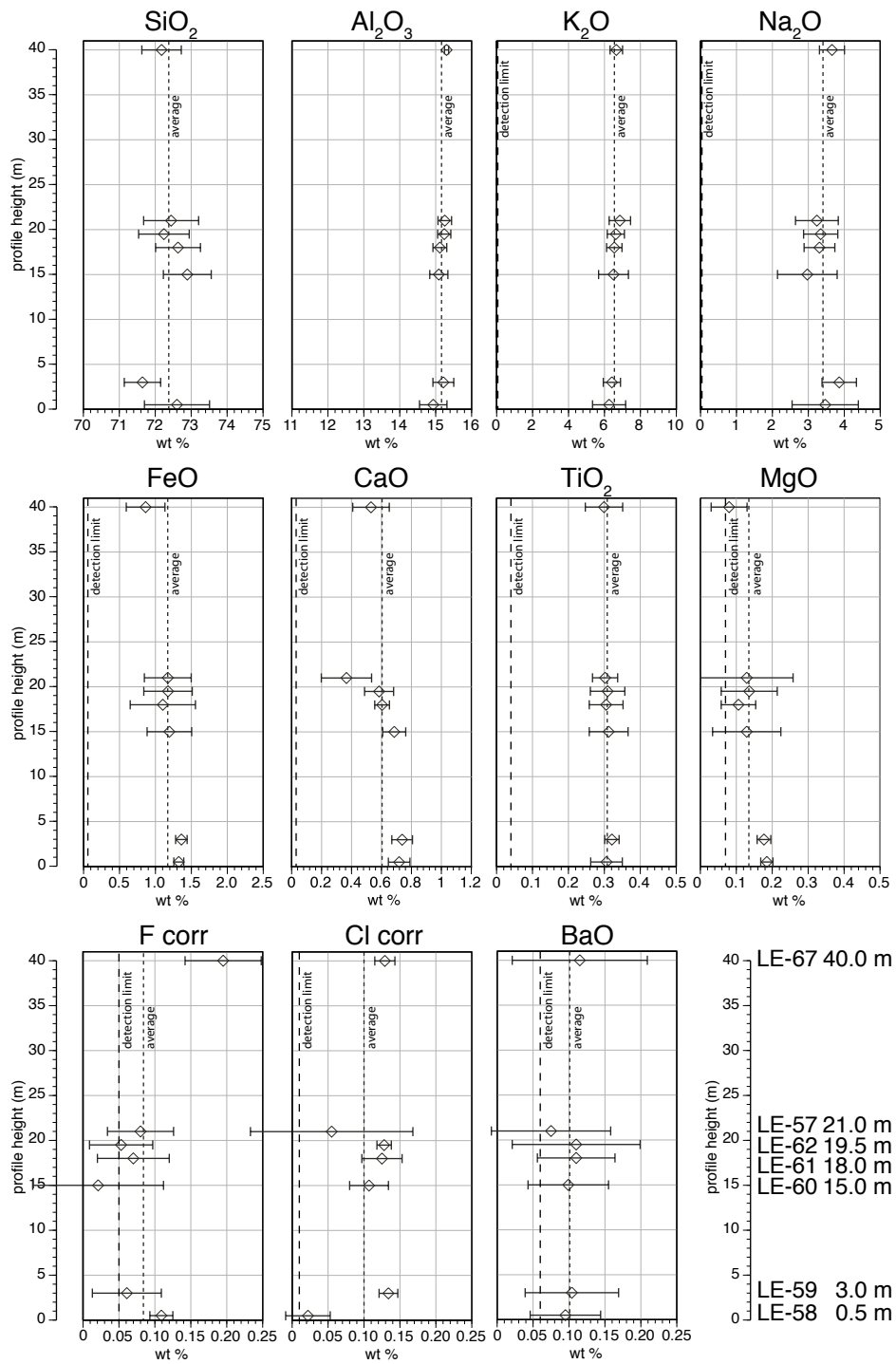


**Fig. 4.7.** (previous page) Major, minor and trace elements contents in the samples of vertical profile A, determined using electron probe micro-analysis and plotted versus profile height (m). All concentrations were re-calculated for water-free samples, error bars are  $2\sigma$  standard deviation. Major elements (Si, Al, Na, K) and minor elements (Fe, Ca, Ti, Mg) are well above the detection limit, while of the trace elements (F, Cl, Ba), F and Ba values are close to the detection limit.

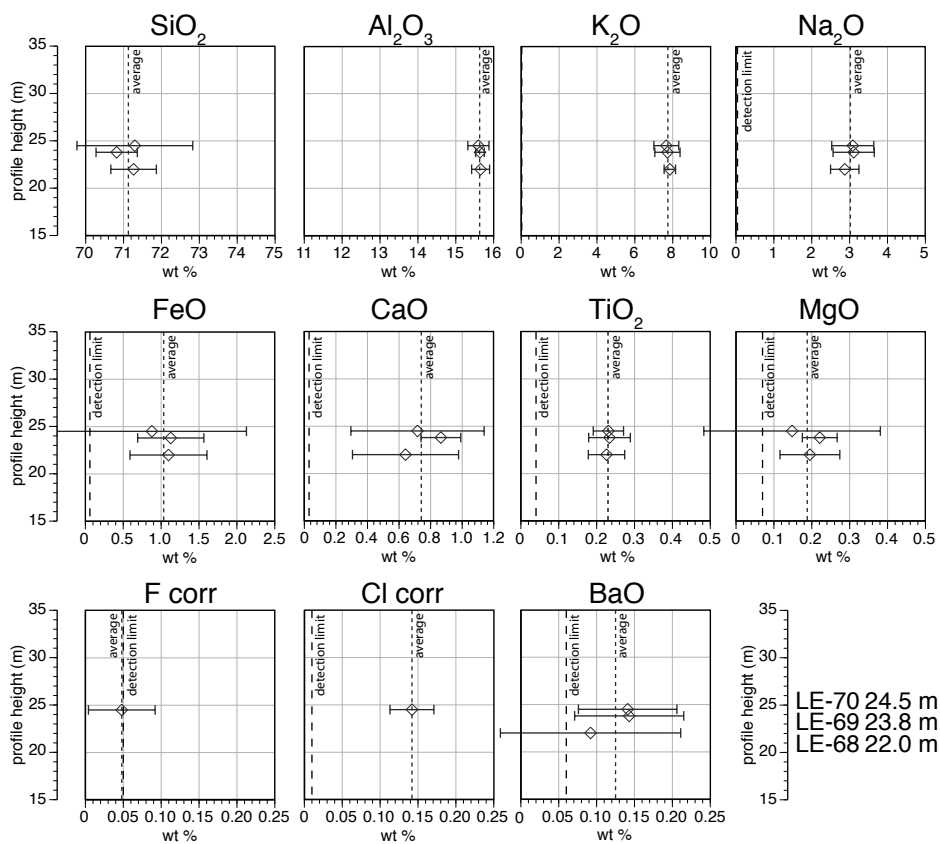


**Fig. 4.8.** Major, minor and trace elements contents in the samples of vertical profile A, determined using electron probe micro-analysis and plotted versus profile height (m). All concentrations were re-calculated for water-free samples, error bars are  $2\sigma$  standard deviation. Major elements (Si, Al, Na, K) and minor elements (Fe, Ca, Ti, Mg) are well above the detection limit, while of the trace elements (F, Cl, Ba), F values in Profile B are at the detection limit and can not be taken seriously. Ba values are also close to the detection limit.

#### 4.1.2. H<sub>2</sub>O content

In-situ concentrations of Hydrogen in glass (polished thin sections) were determined by ion microprobe at the Institut für Geowissenschaften, Universität Heidelberg. <sup>1</sup>H/<sup>30</sup>Si count ratios were converted into H<sub>2</sub>O concentrations. Details about the analytical setup can be found in the appendix in section C.3.3 on page 276.

H<sub>2</sub>O-content is not correlated to SiO<sub>2</sub>-content (Fig. 4.9). SiO<sub>2</sub> values have not been recalculated to 100% without H<sub>2</sub>O. Most samples from Profile A (LE-58, LE-59, LE-61, LE-62, LE-67) and all samples from Profile B (LE-68, LE-69, LE-70) show approximately the same H<sub>2</sub>O values, with an average of 4.01 wt% ( $2\sigma = 0.40$  wt%), while LE-60 and LE-57 show slightly higher values of 4.63 wt% and 5.20 wt%. This, however is unrelated to SiO<sub>2</sub>-content.

When adding the average sum of each glass sample from EMP analysis with the corresponding average H<sub>2</sub>O-content, total sums are between 99.04 wt% and 101.36 wt%, with an average total of 100.45 wt% ( $2\sigma = 1.30$  wt%). Due to a large deviation of the standard materials available (see C.3.3) these values have an accuracy of  $\pm 25\%$ , so that the values could range between 2.9 wt% and 5.4 wt%. These results suggests, that H<sub>2</sub>O is the predominant volatile component of the volcanic glasses studied here and that the H<sub>2</sub>O concentration is around 4%.

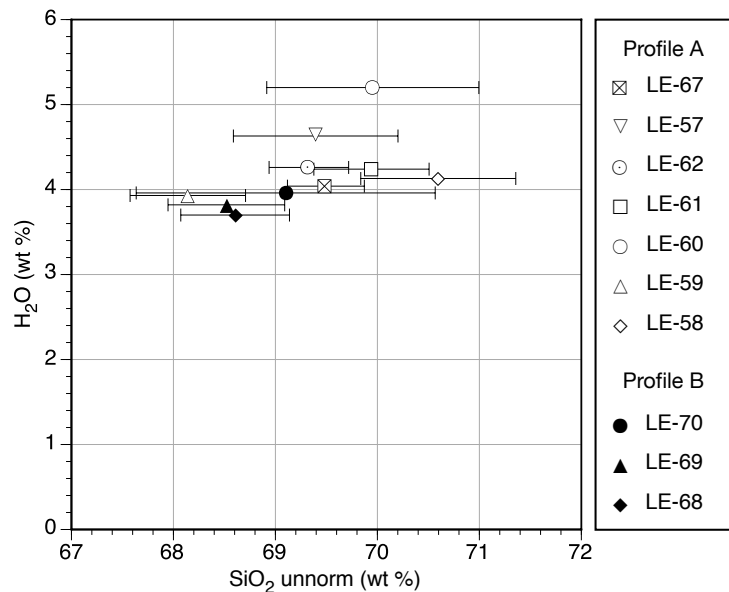


**Fig. 4.9.** H<sub>2</sub>O content versus SiO<sub>2</sub> content (SiO<sub>2</sub> contents have not been recalculated to 100% without H<sub>2</sub>O). Error bars represent standard deviation of the mean ( $2\sigma$ ), for H<sub>2</sub>O they are smaller than the symbols.

## 4.2. Trace elements

Trace element concentrations in volcanic glass have been determined using LA-ICP-MS at the Institut für Geowissenschaften, Universität Frankfurt in cooperation with Yann Lahaye, details concerning the analytical setup can be found in the appendix in section C.4.1 on page 277.

For the REE (Rare Earth Elements) pattern (Fig. 4.10) all values have been normalized to C1 chondritic values (BOYNTON, 1985). All samples show the same relatively flat pattern expressed by the two following chondrite-normalised element ratios:  $(La/Yb)_{cn} = 18.3 \cdots 22.8$  and  $(La/Sm)_{cn} = 5.8 \cdots 6.8$  and a negative Eu anomaly  $(Eu/Eu^*)_{cn} = 0.33 \cdots 0.39$ . Average  $(Eu/Eu^*)_{cn} = 0.36 \pm 0.04$  ( $2\sigma$  s.d.).

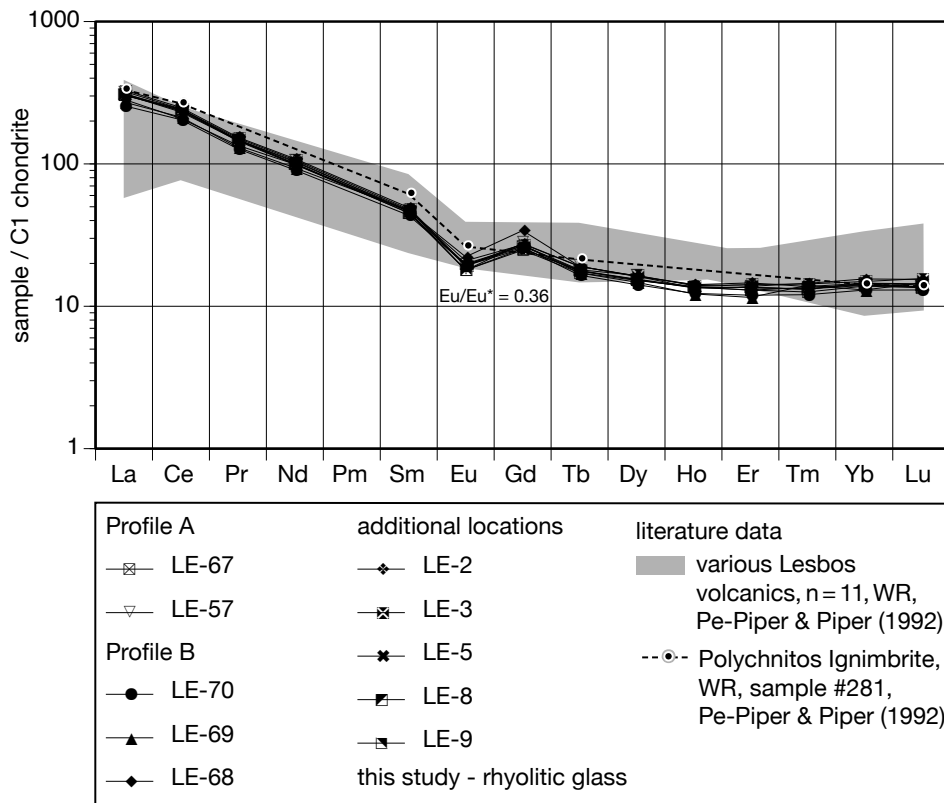


**Fig. 4.10.** REE pattern in rhyolitic glass from selected samples in Profile A and Profile B, and from additional samples in other locations in comparison to whole rock (WR) literature data (11 analyses). Polychnitos Ignimbrite sample #281 is from the Polychnitos area, at the SW edge of the deposit. All concentrations have been normalised to C1 chondritic values (BOYNTON, 1985). Average  $(Eu/Eu^*)_{cn} = 0.36$ ;  $2\sigma = 0.04$

#### 4. Geochemical properties of the volcanic glass

Values show good agreement with whole rock (WR) literature data for Lesbos Island. The WR data for the Polychnitos Ignimbrite (PE-PIPER & PIPER, 1992) shows virtually no difference to the values obtained for the glass in this study. The overall trend for various Lesbos volcanics (11 analyses, PE-PIPER & PIPER, 1992) shows a higher variation and is slightly flatter (i.e. lower values for the light REE and higher values for the heavy REE).

The REE pattern for various rhyolites (WR) from Western Anatolia (Fig. 4.11) shows little variation and very little difference to the pattern from this study. Most samples from Western Anatolia show the same principal shape, slightly shifted to higher or lower values. Only two samples show a slightly different pattern. Overall variation is larger for light REE than for heavy REE.

The largest differences between the individual samples exist in the Eu anomalies. The sample from INNOCENTI *et al.* (2005) shows the largest Eu anomaly, with  $(Eu/Eu^*)_{cn} = 0.1$ . The other literature data shows a range of values,  $(Eu/Eu^*)_{cn} = 0.39 \dots 0.49$  for data from ERKÜL *et al.*, 2005 and  $(Eu/Eu^*)_{cn} = 0.36 \dots 0.53$  for data from ALDANMAZ *et al.*, 2000. These samples are therefore to the same extend

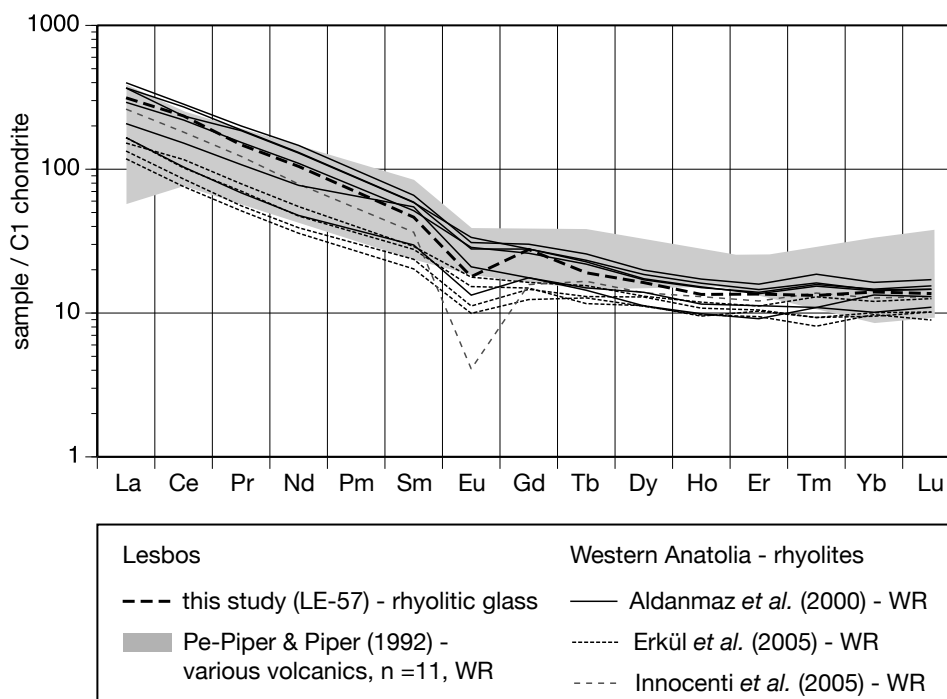


**Fig. 4.11.** REE pattern for various rhyolites (WR) from Western Anatolia in comparison to Lesbos volcanics. All concentrations have been normalised to C1 chondritic values (BOYNTON, 1985)

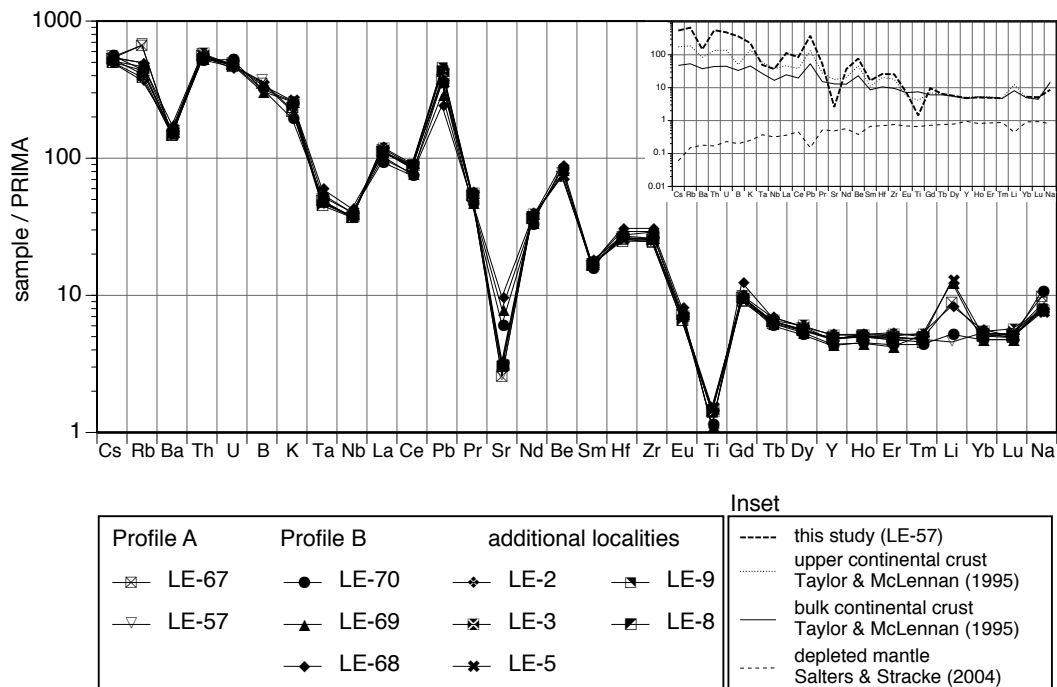


**Fig. 4.12.** Compatibility diagram of selected samples from Profile A and Profile B, and additional samples from other locations. Values are averages from repeated measurements (between 5 and 10 per sample) and have been normalised to primitive mantle values (PRIMA, MCDONOUGH & SUN, 1995). Values for Li, Be, and B were determined by SIMS and values for K, Ti, and Na by EPMA. The average Li values shown are only very roughly representative of the Li contents in the sample due to the large inhomogeneities within all samples.

Eu depleted as samples from this study at one end of the range and less depleted, with a smaller anomaly, and a larger Eu/Eu\* ratio at the other end of the range.

Looking at a compatibility plot (Fig. 4.12) of trace elements arranged with increasing compatibility from left to right, and all values normalised to primitive mantle (PRIMA, MCDONOUGH & SUN, 1995), values obtained as averages from repeated measurements in volcanic glass in Profile A and Profile B, as well as from additional samples from other locations, show no notable deviation from each other, except in Li.

Lithium does not only vary greatly between individual samples, but also within each sample. The average Li values shown in the compatibility diagram (Fig. 4.12) are only very roughly representative of the Li contents in the sample due to the large inhomogeneity. For repeated measurements of the same sample values vary between 8.4  $\mu\text{g/g}$  and 34.4  $\mu\text{g/g}$  (LA-ICP-MS data for sample LE-69). These vari-

ations are not limited to LA-ICP-MS analyses, they occur also for SIMS (even to a larger extent, due to higher number of measurements, see section 7.1, page 105). A systematic pattern for this inhomogeneity, i.e. as effect around phenocrysts or due to different glass textures (fiamme vs. matrix, schlieren, perlitic rings), could not be established during this study.

Beryllium shows a positive anomaly, typical for continental crust (TAYLOR & MCLENNAN, 1995), while boron fits smoothly into the compatibility diagram.

If the volcanic glass represents the residual melt the following negative anomalies can be explained by crystallisation of phenocrysts from the original melt: Sr and Eu due to crystallisation of Pl, Ba, and to a much slighter extend Rb due to crystallisation of Akf, and finally Ti due to crystallisation of Fe-Ti oxides.

The other anomalies, positive as well as negative, depict the typical pattern for continental crust and/or island arc volcanic rocks: Zr and Hf positive anomaly (Zr/Hf = 37), Nb-Ta trough (negative anomaly, Nb/Ta = 14), Be positive anomaly, and Pb positive anomaly (TAYLOR & MCLENNAN, 1995). The ratios for Zr/Hf and Nb/Ta in this study are very close to estimates for continental crust (Nb/Ta in upper continental crust (UCC) =  $12.5 \pm 1.8$  and Nb/Ta in bulk continental crust (BCC) =  $12 \dots 13$ , BARTH *et al.*, 2000) and bulk silicate Earth (BSE) (Zr/Hf = 34.4 and Nb/Ta =  $14.0 \pm 0.3$ , MÜNKER *et al.*, 2003).

**Trace element ratios** for selected elements (Table 4.1 & Fig. 4.13) have been plotted and compared to literature data. For element concentrations in upper continental crust (UCC) two of the most recent trace element data sets have been chosen (RUDNICK, 2005; TAYLOR & MCLENNAN, 2009), which are largely in agreement with each other. The only notable difference concerns the Be concentration, which is also reflected in different Be/Nd ratios. The implications from the element ratios will be discussed separately for the two literature sources, RUDNICK (2005) and TAYLOR & MCLENNAN (2009).

Indication for fractional crystallisation and/or partial melting are shown to different extents by Be, Nd, and Nb, elements which are considered not to be fluid-mobile. Compared to UCC values of RUDNICK (2005) the Be/Nd ratio shows 1.5-fold enrichment. The Be concentrations are also higher than average continental crust by a factor of 2.5, suggesting a higher degree of differentiation than average continental crust. (As appropriate for rhyolitic volcanics; a higher differentiation of the samples is supported by a number of geochemical characteristics, such as the high concentration of SiO<sub>2</sub>). Nd shows a 1.7-fold enrichment in comparison to UCC (RUDNICK, 2005), while Nb is enriched by a factor of 2.1.

**Table 4.1.** Summary of selected trace element concentrations and their respective ratios for literature data and the rhyolitic volcanic glass from Lesbos Island of this study

	Be ( $\mu\text{g/g}$ )	Nd ( $\mu\text{g/g}$ )	Be/Nd	B ( $\mu\text{g/g}$ )	Nb ( $\mu\text{g/g}$ )	B/Nb
rhyolitic glass, average <sup>1</sup>	5.2	46	0.12	101	25	3.90
rhyolitic glass, min. value <sup>1</sup>	4.8	41	0.10	92	24	3.41
rhyolitic glass, max. value <sup>1</sup>	5.5	50	0.13	109	28	4.36
Upper Continental Crust (UCC) <sup>2</sup>	2.1	27	0.08	17	12	1.42
Upper Continental Crust (UCC) <sup>3</sup>	3.0	26	0.12	15	12	1.25
enrichment factor, UCC <sup>2</sup> into glass	2.5	1.7	1.5	5.9	2.1	2.8
enrichment factor, UCC <sup>3</sup> into glass	1.7	1.8	1.0	6.7	2.1	3.1

<sup>1</sup>this study<sup>2</sup>RUDNICK (2005)<sup>3</sup>TAYLOR & MCLENNAN (2009) (updated from TAYLOR & MCLENNAN, 1995)

These values agree with each other to a large extent, suggesting an enrichment of highly incompatible elements between 1.7- and 2.5-fold in comparison to UCC (RUDNICK, 2005) by fractional differentiation. This could have been caused by  $\approx 40\text{--}60\%$  fractional crystallisation.

The Be/Nd ratio for the samples studied here is the same as suggested by TAYLOR & MCLENNAN (2009) for UCC. Concentrations of Be and Nd are higher than UCC (TAYLOR & MCLENNAN, 2009). However the factor of enrichment is nearly the same for both elements, so that the Be/Nd ratio remains the same as for UCC. In comparison to UCC (TAYLOR & MCLENNAN, 2009) Be concentrations, are higher than average continental crust by a factor of 1.7, Nd by a factor of 1.8 (to nearly the very same extent as Be), while Nb is enrichment by a factor of 2.1.

Based on TAYLOR & MCLENNAN (2009), UCC enrichment (factor 1.7 to 1.8) indicates  $\approx 40\%$  fractional crystallisation. Nb enrichment is slightly higher (factor 2.1), as can be expected from its higher incompatibility. Using the two different data sets (RUDNICK, 2005; TAYLOR & MCLENNAN, 2009) the same principal processes are shown, differing only in details: Be, Nd, Nb are between 2.5- and 1.7-fold more enriched than UCC (RUDNICK, 2005; TAYLOR & MCLENNAN, 2009), indicating fractional crystallisation with a high degree of crystallisation (between  $\approx 40\%$  and  $\approx 60\%$ ).

Please note, that generally felsic systems are Be richer than mafic systems. Continental crust has a higher B/Nd, because in higher differentiated systems Be is more

compatible than Nd. The assumption, that Be and Nd have the same compatibility is only true during partial melting in the mantle.

Metasomatism is indicated by fluid-mobile elements, such as B and by the B/Nb ratio. Boron is enriched by a factor of 5.9 relative to UCC of RUDNICK (2005), the B/Nb ratio by 2.8. This enrichment can be subdivided into one component by fractional crystallisation (indicated by 2.1-fold enrichment of Nb in respect to UCC of RUDNICK, 2005) and a second component by fluid metasomatism (indicated in the B/Nb ratio, enriched by factor 2.8 in respect to UCC of RUDNICK, 2005). The total enrichment of 5.9 is the product of these two components.

The same principles apply, when using the slightly different values for UCC from TAYLOR & MCLENNAN (2009). Boron is enriched by a factor of 6.7 relative to UCC (TAYLOR & MCLENNAN, 2009), the B/Nb ratio by 3.1. This total enrichment can be subdivided into one component by fractional crystallisation (indicated by 2.1-fold enrichment of Nb relative to UCC of TAYLOR & MCLENNAN, 2009) and a second component by fluid metasomatism (indicated in the B/Nb ratio, enriched by factor 3.1 relative to UCC, TAYLOR & MCLENNAN, 2009). The total enrichment of 6.7 is the product of these two components.

When combining the results from the two data sets (RUDNICK, 2005; TAYLOR & MCLENNAN, 2009), the component by fractional crystallisation results in an enrichment by a factor 2.5 to 1.7, indicating a high degree of crystallisation between  $\approx 40\%$  and  $\approx 60\%$ , the second component by fluid metasomatism results in an enrichment factor between 2.4 and 3.9.

Li concentrations and Li/Yb ratios show typical crustal values (RUDNICK, 2005; TAYLOR & MCLENNAN, 2009). It is possible that the lack of increased Lithium abundances and Li/Yb ratios, which would be expected from metasomatism (shown by B and B/Nb) was caused by a late degassing process. This process could also account for the very inhomogeneous distribution of Li in the glass on thin section scale. However, this large inhomogeneity also makes it very difficult to reach any conclusive results from Li data.

A distinction between Profile A and Profile B has not been made; however trace element concentrations are very similar, except for a slight difference in B content. The difference in B concentrations between Profile A and Profile B would have only slightly changed some of the enrichment factors, but would have lead to the very same conclusions. The magma source for melts from both vertical profiles must have been subject to fluid metasomatism, as indicated by the large B enrichment.

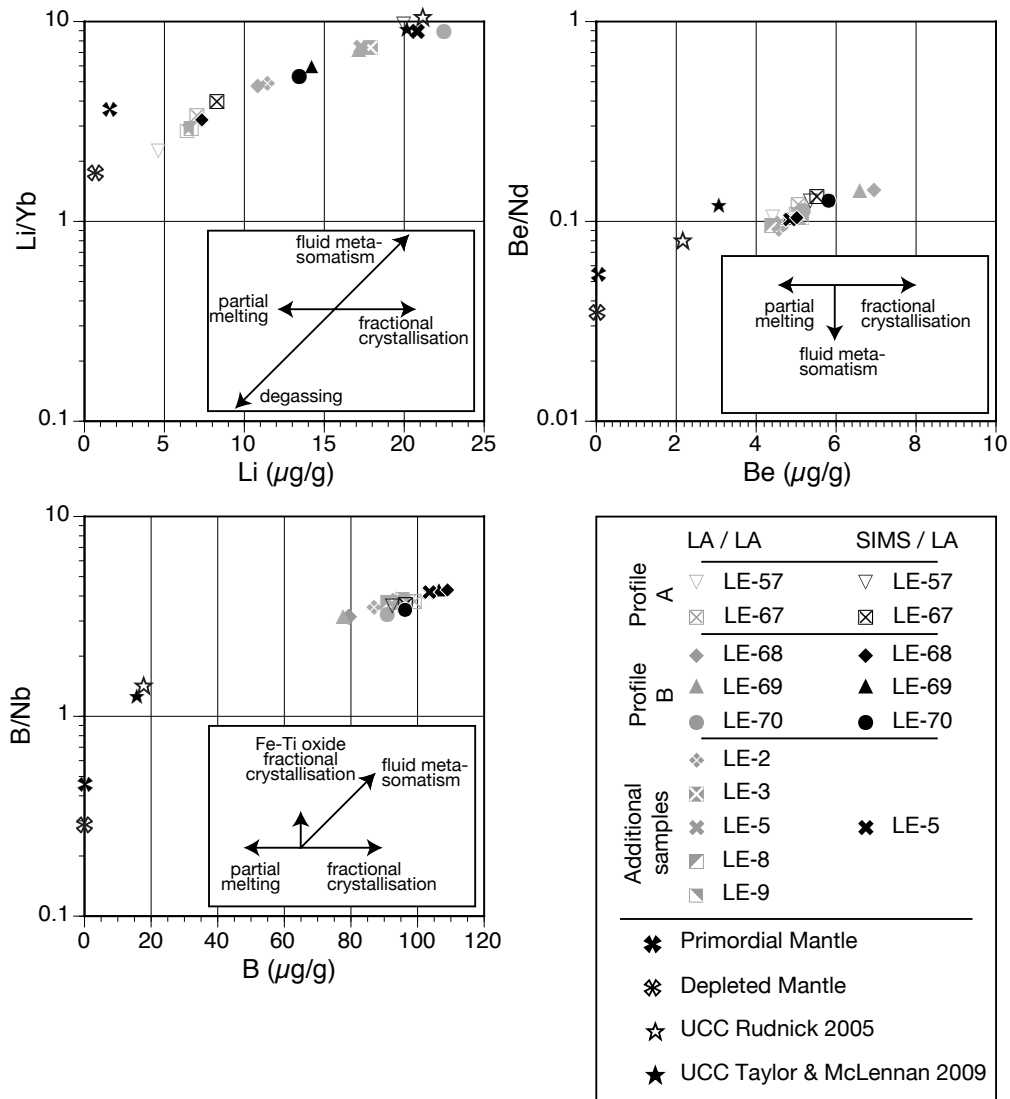


**Fig. 4.13.** REE ratios for selected elements in the volcanic glass. Data points with grey symbols are based entirely on LA-ICP-MS (LA) data, while for black symbols values for Li, Be, and B were determined from SIMS measurements and values for Nb, Nd, and Yb were determined using LA-ICP-MS. Values for Primordial mantle (PRIMA) by MCDONOUGH & SUN (1995), Depleted Mantle by SALTERS & STRACKE (2004), Upper Continental Crust (UCC) by RUDNICK (2005) and TAYLOR & MCLENNAN (2009) (updated from TAYLOR & MCLENNAN, 1995).

#### 4. Geochemical properties of the volcanic glass

A comparison to whole rock data for various Lesbos volcanics from PE-PIPER & PIPER (1992) in a compatibility diagram (Fig. 4.14), shows a good agreement to data from this study. Differences in values between more evolved melts (Polychnitos Ignimbrite) and more primitive melts (various other Lesbos volcanics) are more pronounced in more fractionated elements, namely Pb, Sr, Ti. Differences in WR data in comparison to values determined from volcanic glass are small and only occur in the elements, which are compatible in the phenocrysts, namely Ba, Sr, and Ti. Further differences between WR and glass data would only be expected if crystallisation rates had been much higher.

Data from this study agree very well with WR literature data from various rhyolites from Western Anatolia (ALDANMAZ *et al.*, 2000; ERKÜL *et al.*, 2005; INNOCENTI *et al.*, 2005) as shown in another compatibility diagram (Fig. 4.15). All data shows the same general shape with the same positive and negative anomalies.

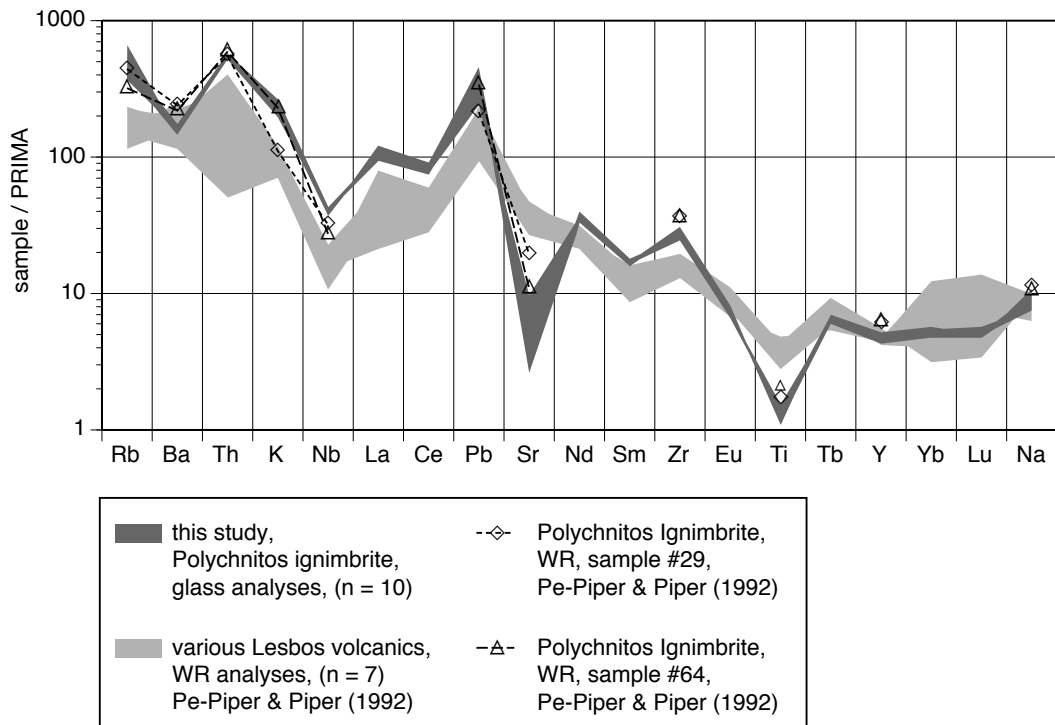


**Fig. 4.14.** Compatibility diagram of selected samples (10 samples) from Profile A and Profile B, from other locations, and WR literature data (7 samples) from PE-PIPER & PIPER (1992). Values from this study are averages from repeated measurements (between 5 and 10 per sample). All data has been normalised to primitive mantle values (PRIMA, MCDONOUGH & SUN, 1995).

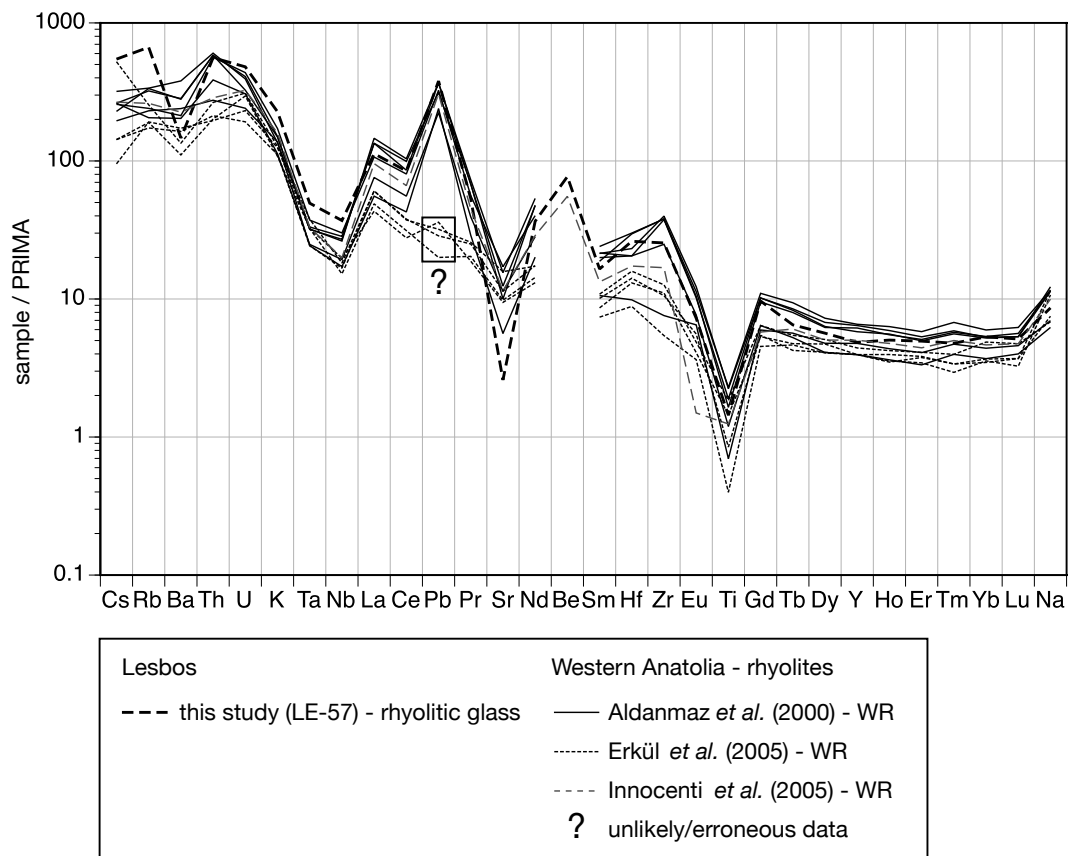


**Fig. 4.15.** Compatibility diagram for various rhyolites (WR) from Western Anatolia in comparison to data from this study (glass, sample LE-57). All concentrations have been normalised to primitive mantle values (PRIMA, MCDONOUGH & SUN, 1995). Pb data from ERKÜL *et al.* (2005) marked with a question mark is extremely unlikely and probably due to an error.

Unfortunately, there is only one literature data point for Be, for which, however, the agreement is very strong with data from this study.

The literature data show the same anomalies typical for continental crust and/or island arc volcanic rocks, namely Zr and Hf positive anomaly, Nb-Ta trough (negative anomaly), Be positive anomaly, and Pb positive anomaly. However, data from ERKÜL *et al.* (2005) most peculiarly fails to show a Pb anomaly. It is most probable, that this is due to an analytical or computing error.

The negative anomalies found in this study, which are explained to stem from crystallisation of phenocrysts from a less fractionated melt, are also evident in the WR literature data: Sr and Eu due to crystallisation of plagioclase, Ba, and to a

#### 4. Geochemical properties of the volcanic glass

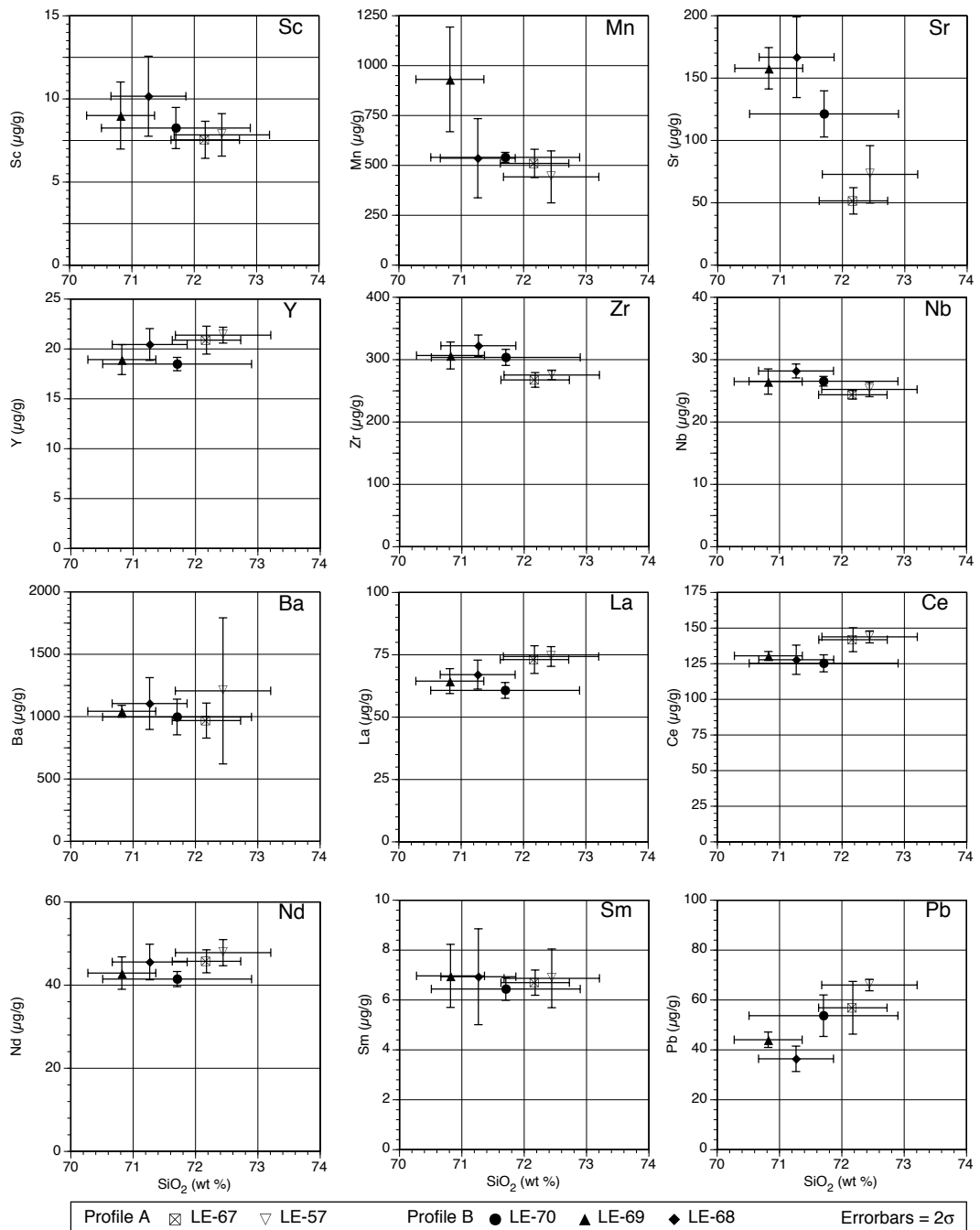


**Fig. 4.16.** Selected average trace element contents in glass from samples from Profile A and Profile B versus  $\text{SiO}_2$ .  $\text{SiO}_2$  contents have been re-calculated to 100% for water-free samples; error bars are  $2\sigma$  standard deviation. The plots of all other elements analysed are found in the appendix, Fig. D.1 on pages 287–289.

much slighter extend Rb due to crystallisation of alkali feldspar, and finally Ti due to crystallisation of Fe-Ti oxides and biotite. As before, differences between WR data and data from volcanic glass would only be expected if crystallisation rates had been much higher.

When plotting trace element values versus  $\text{SiO}_2$  contents most elements show little or no correlation among the sample set (selected elements, marked with bold letters in the text, are shown in Fig. 4.16. Plots of all trace elements analysed are shown in the appendix, Fig. D.1 on pages 287–289).

The LREE (**La**, **Ce**, **Pr**, **Nd**, but not **Sm**) show very slight correlations with  $\text{SiO}_2$  and samples from Profile A and from Profile B plot as two separate groups. HREE, **Sc**, **Y**, and **Sm** show no correlation at all.

The HFSE (**Nb**, **Ta**, and **Hf**) show also no correlation, while **Zr** shows a very slight negative trend. None of the other elements (**Ba**, **V**, **Rb**, **Ca**, **Cs**, **Th**) shows any correlation. An apparent correlation of **Mn** with  $\text{SiO}_2$  is dependent on one high-Mn/low- $\text{SiO}_2$  value, while the other four values show no correlation at all.

Two elements, however, show very strong correlations: a negative correlation between **Sr** values and  $\text{SiO}_2$  and a positive correlation between **Pb** values and  $\text{SiO}_2$ .

Using partition coefficients for Sr, Pb and Ba between Akf and Pl and rhyolitic melt by BACHMANN *et al.* (2005) simple fractionation models for a hypothetical melt evolution from melt B to melt A have been developed (Fig. 4.17) and will be discussed. These models require that melt B would have developed into melt A by *Pl fractionation*. However, this is the contradictory to the fractionation trends developed earlier from the TAS and  $\text{K}_2\text{O}$  vs.  $\text{SiO}_2$  diagrams (Fig. 4.18 a, based on

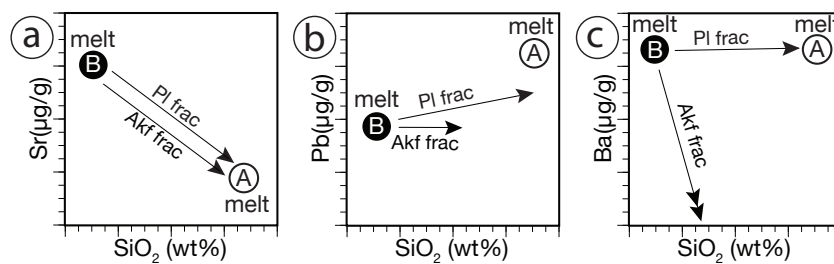


**Fig. 4.17.** Schematic diagrams for Pl and Akf fractionation trends for Sr, Pb, and Ba plotted versus  $\text{SiO}_2$ , using partition coefficients from BACHMANN *et al.* (2005). Arrows depicting fractionation trends correspond to  $\approx 20\%$  fractional crystallisation, except for Akf fractionation in ©, where arrow corresponds only to  $\approx 10\%$  fractional crystallisation of Akf.

Figs 4.4 & 4.5 and section 4.1.1 on page 56), where melt B could evolve into melt A by *Akf* fractionation and Pl assimilation. A detailed discussion of possible fractionation trends follows in the next section.

### 4.3. Melt evolution – discussion of geochemical data

In section 4.1.1 on page 56 hypothetical fractionation trends for melt evolution of melt A and melt B were developed, based on the relationship between the glass compositions and the compositions of Pl and Akf rims in the TAS diagram and  $K_2O$  vs.  $SiO_2$  diagram (Figs 4.4 & 4.5, pages 57 & 58). These melt evolution scenarios (Fig. 4.18, paragraphs 1. a, b & c), linking melt A genetically with melt B by Pl and Akf fractionation/assimilation will be discussed in detail. Later additional melt evolution hypotheses incorporation also Bt fractionation/assimilation will also be discussed (paragraphs 2. a & b, 3. a & b).

The amount of Pl and Akf fractionation or assimilation required has been calculated using the  $K_2O$  and  $SiO_2$  composition of the melts and of the Pl and Akf crystal rims. In the following, the hypotheses that one melt has evolved from the other or that the two melts have evolved separately from the same parent melt, will be tested.

The three different hypothetical melt evolution scenarios, involving only Pl and Akf fractionation/assimilation, are the following:

1. a) The simplest case: melt A could have evolved into melt B by Akf assimilation (50%) or in the opposite direction melt B could have evolved into melt A by Akf fractionation (50%) (Fig. 4.18 a). In this case there is no contribution of Pl fractionation/assimilation or from any other mineral phase.
1. b) Melt A could have evolved into melt B by Akf assimilation (28.8%) and Pl fractionation (7.8%) via a transition melt (melt T; Fig. 4.18 a). In the opposite direction melt B could have evolved into melt A by Pl assimilation and Akf fractionation via melt T (Fig. 4.18 a).
1. c) Alternatively the two melts could have evolved from a common parental melt (melt P) along separate fractionation paths (Fig. 4.18 b). Melt A could have evolved from its parent melt P by Akf fractionation (28.8%), while melt B would have evolved from the same melt P by Pl fractionation (7.8%).

In fact there are significantly less Akf phenocrysts in samples from Profile B than in samples from Profile A. While Akf is very rare in Profile B, it is a common phenocryst in Profile A (see section 3.3.4 on page 40 and section 3.4.4 on page 49 about alkali feldspar in Profile A and in Profile B, respectively).

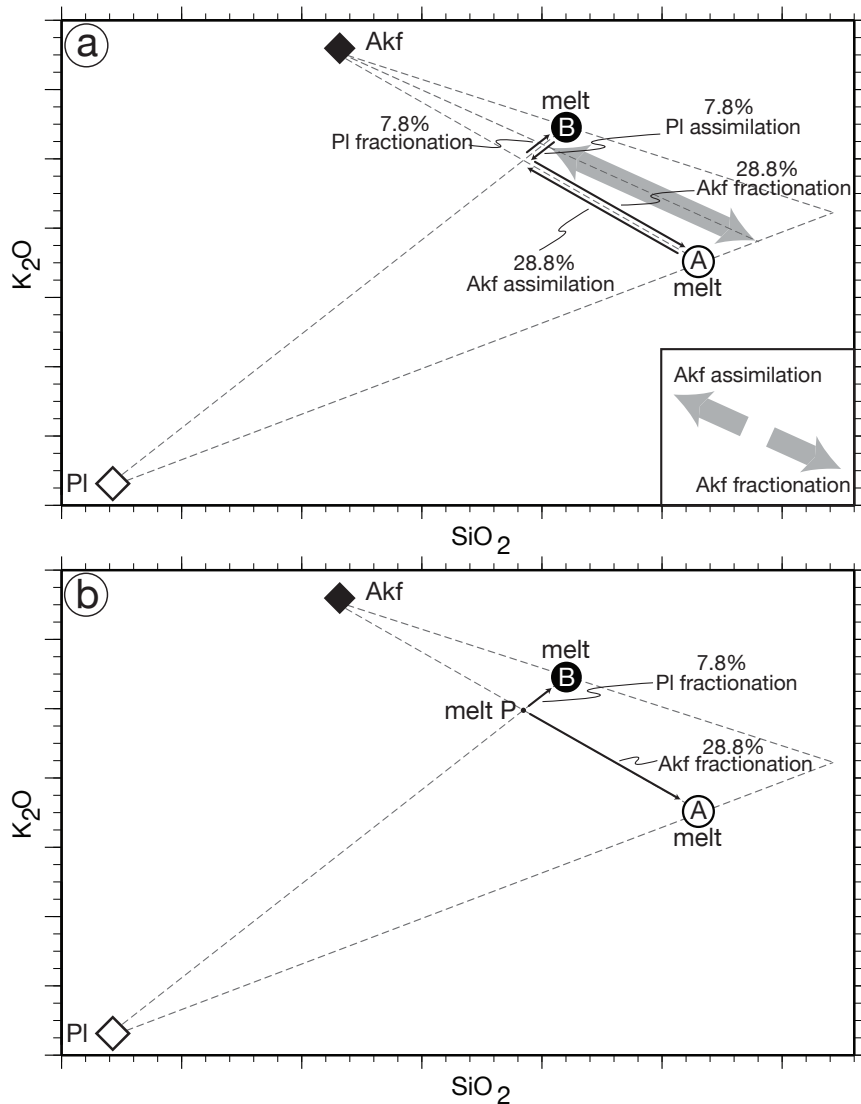


**Fig. 4.18.** Schematic diagram of the relationship between melt compositions from Profile A and Profile B and PI and Akf phenocryst rim compositions in the K<sub>2</sub>O vs. SiO<sub>2</sub> diagram. Possible fractional crystallisation paths and fractionation amounts have been included: a melt evolution from melt A directly into melt B, or vice versa from melt B into melt A. b evolution of a parental melt P along separate fractionation paths into melt B and melt A.

The amount of crystal fractionation required was calculated from K<sub>2</sub>O contents of melts and PI and Akf rims. The fat grey arrow displays Akf fractionation or Akf assimilation, respectively, according to the simplest model under 1. a), direct evolution of melt A into melt B or vice versa by Akf assimilation or fractionation, without contribution of PI fractionation or PI assimilation.

BACHMANN *et al.* (2005) calculated partition coefficients for Sr, Pb and Ba between Akf and Pl and high-silica rhyolitic glass obtained from samples of the crystal rich Fish Canyon Tuff. These partition coefficients have been used to create simple models for crystal fractionation (Fig. 4.19) in the high-silica rhyolitic glass from Polychnitos Ignimbrite. Values by BACHMANN *et al.* (2005) are largely in agreement with other literature data (BLUNDY & WOOD, 1991; ICENHOWER & LONDON, 1996; REN *et al.*, 2003; REN, 2004; BÉDARD, 2006). Though individual numbers do vary from each other, it is generally accepted that Sr is highly compatible in Akf and Pl, Ba is highly compatible in Akf, while Pb is slightly compatible in Akf and slightly incompatible in Pl. There is a slight disagreement about Pb in Pl, which is seen as either slightly compatible or slightly incompatible with partition coefficients varying from 1.2 (BLUNDY & WOOD, 1991) to 0.8 (REN *et al.*, 2003) and to 0.61 (BACHMANN *et al.*, 2005). This disagreement is negligible in the models presented here; Pb contents would change only very insignificantly, due to the gentle slopes for Pl fractionation/assimilation for all three values.

The models have been created using trace elements plotted against K<sub>2</sub>O instead of SiO<sub>2</sub>, because the K<sub>2</sub>O contents is only influenced by fractionation or assimilation of Akf, Pl or Bt, while the SiO<sub>2</sub> contents could theoretically be effected by a large number of different phases (Qtz, Akf, Pl, Bt, Cpx, Opx, etc.).

1. a) The direct evolution from melt A to melt B by Akf assimilation only or from melt B to melt A by Akf fractionation only, can be ruled out based on the fractionation curves for Sr, Pb and, Ba (Fig. 4.19 a, b & c). For all six fractionation/assimilation models an extremely high and unrealistic amount of 50% of fractionation or assimilation would be required in order to change the K<sub>2</sub>O contents to the correct target value (the K<sub>2</sub>O contents of melt A to melt B or vice versa). At the same time these fractionation/assimilation models would produce values of Pb and especially of Sr and Ba that mismatch those of the samples. Akf assimilation causes Sr and especially Ba contents (Sr > 250 µg/g; Ba > 950 µg/g) much higher than found in melt B while Akf fractionation would lead to Sr and Ba depletion. Therefore, this melt evolution scenario, direct evolution from melt A to melt B or vice versa, can be ruled out.
1. b) The second melt evolution scenario, evolution from melt A to melt B via a transitional melt (melt T) by a combination of Akf assimilation and Pl fractionation or in the opposite direction from melt B to melt A via a melt T by a combination of Pl assimilation and Akf fractionation, can also be ruled out according to the corresponding trace element fractionation curves (4.19 d, e

### 4.3. Melt evolution – discussion of geochemical data

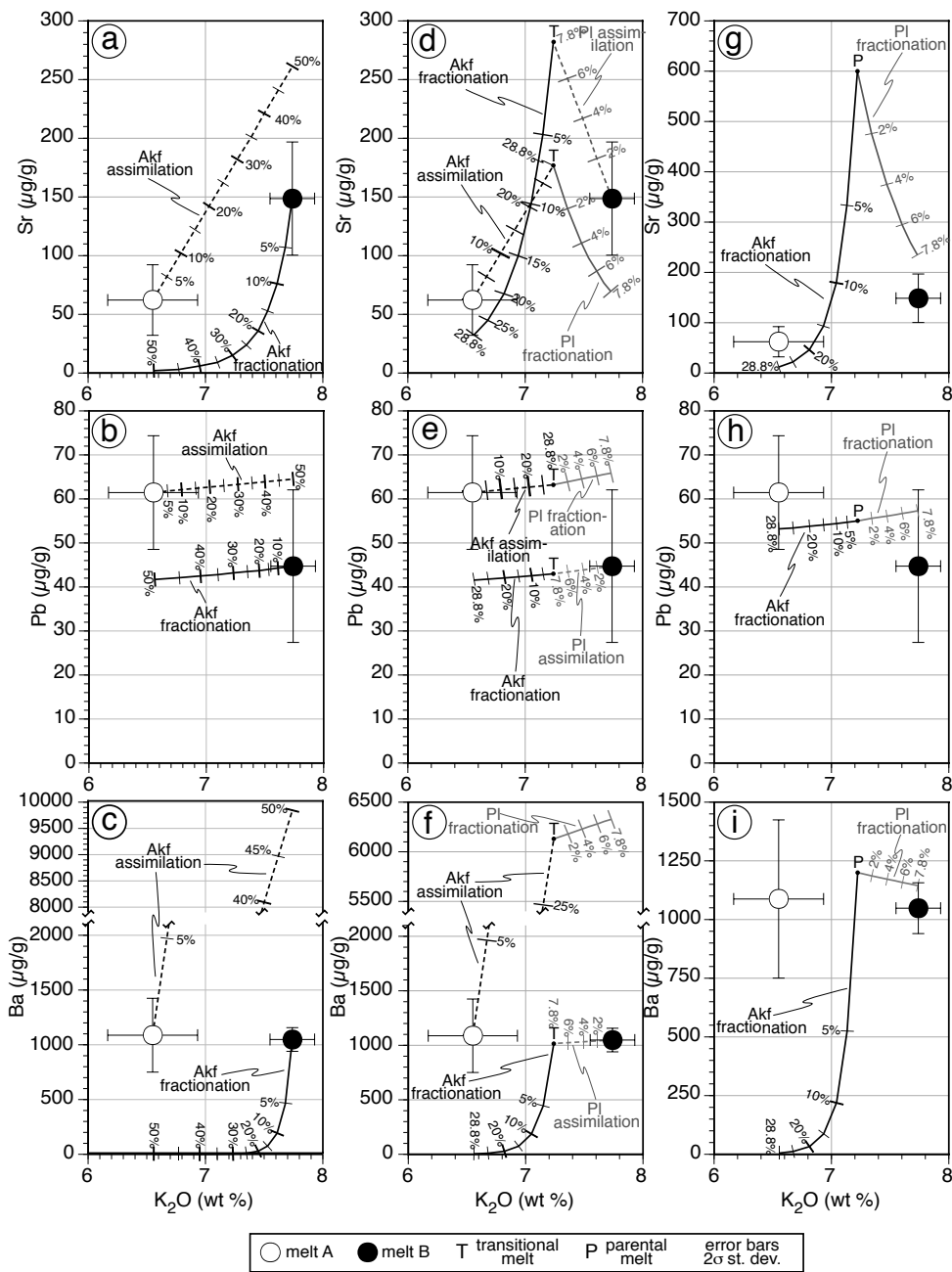


**Fig. 4.19.** Fractionation curves for Sr, Pb, and Ba vs.  $K_2O$  based on partition coefficients by BACHMANN *et al.* (2005). The position of transitional melt (melt T) and parental melt (melt P) has been determined using major elements (TAS diagram and  $K_2O$  vs.  $SiO_2$  diagram), the composition of melt P and is variable for contents of Sr, Pb and Ba and has been subjectively chosen.

#### 4. Geochemical properties of the volcanic glass

---

& f). While one could argue about the viability of trends in Sr and Pb plots (4.19 d & e), it is very clear in the Ba plot (4.19 f) that Akf assimilation and Pl fractionation (in order to evolve melt A to melt B) would create Ba contents much too high ( $> 6300 \mu\text{g/g}$ ). Pl assimilation and Akf fractionation (in order to evolve melt B into melt A) would strongly deplete Ba contents, however Ba contents in samples of melt A is  $\approx 1000 \mu\text{g/g}$ , approximately the same as in samples of melt B.

1. c) Testing the third hypothesis, a separate development of melt A and melt B from a common parent melt P seems generally credible for the Sr fractionation model (Fig. 4.19 g), while a rhyolitic parent melt with such a high Sr content ( $\approx 600 \mu\text{g/g}$ ) seems unlikely. For the Pb fractionation curve (Fig. 4.19 h) the hypothesis seems feasible as well. The trend of Pl and Akf fractionation curves in the Pb plot have the wrong slope, but do end up within the error bars of the melt contents. Yet, the hypothesis clearly has to be abandoned when looking at the Ba fractionation model (Fig. 4.19 i). Since already the smallest fractionation of Akf would dramatically lower Ba contents, the required fractionation of 28.8% Akf would produce an evolved melt depleted in Ba. At the same time, Pl fractionation would decrease Ba contents from parent to evolved melt only slightly. However, both glasses, melt A and melt B, contain Ba in the same quantity.

None of the hypotheses above is tested positive, therefore melt evolution of one melt from the other or of both melts from a common parent melt by a combination of Akf and Pl fractionation/assimilation is not possible.

For a complete picture, however, it is necessary to add Bt as mineral phase to the potential fractionation/assimilation paths. Biotite is the third main phenocryst in the samples, it has nearly the same  $\text{K}_2\text{O}$  content as Akf (9.5 wt %  $\text{K}_2\text{O}$  in Bt; 10.0 wt %  $\text{K}_2\text{O}$  in Akf), but considerably less  $\text{SiO}_2$  (37.5 wt %  $\text{SiO}_2$  in Bt).

The relationship between glass compositions and Pl, Akf and Bt mineral rim compositions in the  $\text{K}_2\text{O}$  vs.  $\text{SiO}_2$ -diagram is displayed in Fig. 4.20 for melt evolution from melt B to melt A. According to the discussion above involving Pl and Akf fractionation/assimilation only, these scenarios could be reversed to fit evolution from melt A into melt B or the evolution from common parent melts  $\text{P}_1$ ,  $\text{P}_2$ , or  $\text{P}_3$  in combination with transitional melts. These possibilities are not displayed in Fig. 4.20, but they will be discussed.

The hypotheses involving Pl and Akf fractionation/assimilation were all discussed and abandoned above in 1. a, b & c.

4.3. Melt evolution – discussion of geochemical data

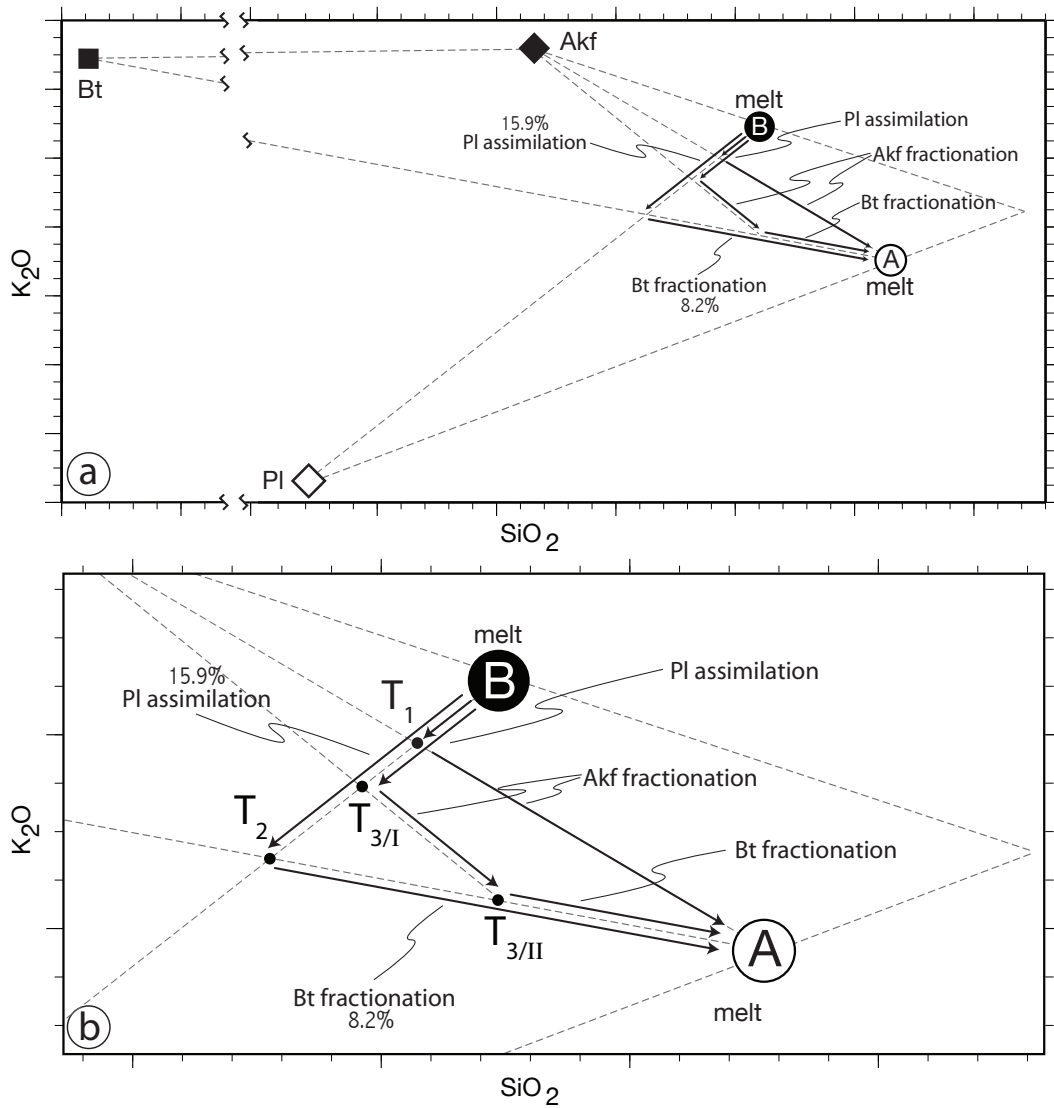


**Fig. 4.20.** Schematic diagram of the relationship between melt compositions from Profile A and Profile B and three different phenocrysts: Pl, Akf and Bt, represented as phenocryst rim compositions in the K<sub>2</sub>O vs. SiO<sub>2</sub> diagram. Diagram (b) shows a close-up view of diagram (a). Possible fractional crystallisation paths and fractionation amounts have been included: melt evolution from melt B into melt A via different transitional melts T<sub>1</sub>, T<sub>2</sub>, and T<sub>3/I</sub> and T<sub>3/II</sub>. The amount of crystal fractionation required was calculated from K<sub>2</sub>O contents of melts and crystal rim compositions of Pl, Akf and Bt, respectively.

#### 4. Geochemical properties of the volcanic glass

---

2. a) Melt A could have evolved into melt B by Pl fractionation and Bt assimilation via a transitional melt  $T_2$ , or in the opposite direction melt B could have evolved into melt A by Pl assimilation and Bt fractionation via a melt  $T_2$ .
2. b) Melt A and melt B could have evolved from a common parent melt  $P_2$  by Bt fractionation (melt A) and Pl fractionation (melt B).

This second set of hypotheses will be tested and abandoned below.

3. a) Melt A could have evolved into melt B by Pl fractionation, Bt assimilation, and Akf assimilation via two transitional melts  $T_{3/I}$  and  $T_{3/II}$ , or in the opposite direction melt B could have evolved into melt A by Pl assimilation, Akf fractionation, and Bt fractionation via  $T_{3/I}$  and  $T_{3/II}$ .
3. b) Melt A and melt B could have evolved from a common parent melt  $P_3$  in combination with a transitional melt  $T_3$ .

This last set of hypotheses will be discussed later.

In the third set of hypotheses Pl, Akf, and Bt fractionation/assimilation paths cover a whole area of possible paths with varying contributions of each mineral. The first two fractionation scenarios involving only two minerals, Pl and Akf (and no Bt) or Pl and Bt (and no Akf) constitute the end-members of the possible array of paths in the third case.

Again partition coefficients for Sr and Ba, this time between Bt and Pl and rhyolitic melt by BACHMANN *et al.* (2005) have been used to create simple models for crystal fractionation (Fig. 4.21).

Testing the second set of hypotheses, melt evolution scenarios involving only Bt and Pl:

2. a) Evolution from melt A to melt B via a transitional melt (melt  $T_2$ ) by a combination of Bt assimilation and Pl fractionation or in the opposite direction from melt B to melt A via melt  $T_2$  by a combination of Pl assimilation and Bt fractionation, can be ruled out according to the corresponding fractionation curves (4.21 a & b). While the model seems valid when looking at the Ba fractionation curve, the hypothesis has to be abandoned, when looking at Sr fractionation. Pl assimilation and Bt fractionation (in order to evolve melt B into melt A) would create Sr contents much higher than observed, while Bt assimilation and Pl fractionation (in order to evolve melt A to melt B) would deplete Sr contents to values much lower than observed.

### 4.3. Melt evolution – discussion of geochemical data

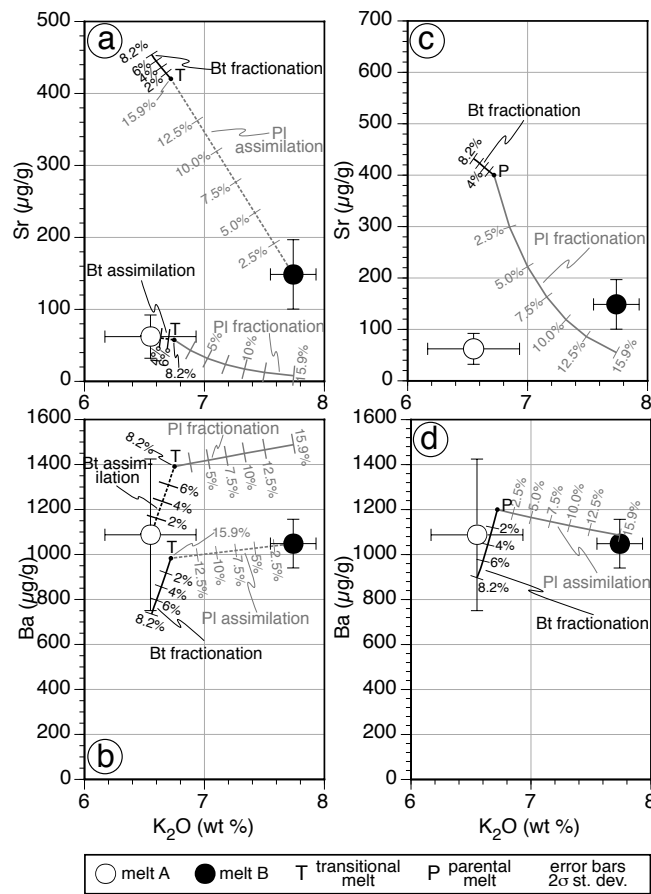


**Fig. 4.21.** Fractionation curves for Sr and Ba vs.  $K_2O$  based on partition coefficients by BACHMANN *et al.* (2005). The position of transitional melt (melt T) and parental melt (melt P) has been determined using major elements (TAS diagram and  $K_2O$  vs.  $SiO_2$  diagram), the composition of melt P and is variable for contents of Sr and Ba and has been chosen subjectively.

2. b) A separate development of melt A and melt B from a common parent melt  $P_2$  according to the hypotheses is convincing for the Ba fractionation model (Fig. 4.21 d). However, when looking at the Sr model (4.21 c), the hypotheses has to be abandoned. A parent melt with a high initial Sr content would be needed, still by Bt fractionation a melt with an even higher Sr contents would be created, while PI fractionation would severely deplete Sr contents. This is in contradiction to the Sr contents found in melt A and melt B, which are not that different.

Melt evolution from one melt into the other or of both melt from a common parent

melt by Pl and Bt fractionation/assimilation is not possible, after the second set of hypotheses was tested negative.

Fractionation and assimilation of Akf and Bt develop into the same direction in the TAS diagram (Fig. 4.20). Both, Akf and Bt fractionation evolve the melt to higher SiO<sub>2</sub> and lower K<sub>2</sub>O contents. In the opposite direction, Akf and Bt assimilation evolve the melt to lower SiO<sub>2</sub> and higher K<sub>2</sub>O contents. These two fractionation paths can replace each other, but they cannot replace Pl fractionation or Pl assimilation (evolution to higher SiO<sub>2</sub> and higher K<sub>2</sub>O or lower SiO<sub>2</sub> and lower K<sub>2</sub>O, respectively). So far we have been looking at the two end-members of this fractionation scenario. In the following we will test and abandon the third set of hypotheses, a combination of Akf and Bt fractionation/assimilation in addition to Pl fractionation/assimilation.

3. a) Testing the hypothesis of melt evolution of one melt into the other by Akf and Bt assimilation and Pl fractionation (evolving melt A into melt B) or by Akf and Bt fractionation and Pl assimilation (evolving melt B into melt A):

In order to have Ba contents of the model melts match Ba contents of the melts found, Akf fractionation (to evolve melt B into melt A) or Akf assimilation (to evolve melt A into melt B) must have been insignificant, because even the smallest amount of Akf fractionation or Akf assimilation would have a high impact on Ba contents, depleting or enriching Ba amounts dramatically (e.g. Fig. 4.19 f). However, both melts, melt A and melt B, contain approximately the same amount of Ba.

If Akf contribution was indeed insignificant and the melt evolution largely dependent on Bt fractionation/assimilation, the fractional evolution of melt A into melt B or vice versa can be ruled out due to the mismatch in Sr contents of model melts and melts found as described before (see paragraph 2. a on page 80; Fig. 4.21 a).

In order to have Sr contents of the model melts match Sr contents of the melts found, the fractionation models are largely dependent on Akf fractionation or Akf assimilation. Because only Akf fractionation could balance out the large effect of Pl assimilation or vice versa, only Akf assimilation could balance out the large effect of Pl fractionation on the Sr contents (Fig. 4.19 d). Therefore Bt fractionation (to evolve melt B into melt A) or Bt assimilation (to evolve melt A into melt B) must have been negligible. Though not quantitatively substantial, yet Bt fractionation would increase the effect of Pl assimilation (Fig. 4.21 a) on the Sr contents, while Akf fractionation would counterbalance the effect (Fig. 4.19 g). (Vice versa Bt assimilation would increase the

effect of Pl fractionation on the Sr contents, while Akf assimilation would counterbalance the effect.)

If the fractional melt evolution was indeed largely dependent on Akf fractionation/assimilation and therefore Bt contribution fairly insignificant, the fractional evolution of melt A into melt B or vice versa can be ruled out due to a mismatch in Ba contents between model melts and the melts found caused by Akf fractionation/assimilation (see paragraph 1.b on page 76; Fig. 4.19 f).

Following all this, melt evolution from melt A to melt B or vice versa from melt B to melt A by Pl, Akf *and* Bt fractionation and assimilation can also be ruled out.

3. b) Testing, if melt A and melt B could have evolved from a common parent melt P in combination with a transitional melt T:

There are a number of different combinations of Pl, Akf, and Bt fractionation and assimilation possible, depending on where the parent melt would plot (according to the composition). But these combinations would not change Ba or Sr contents of the evolved melts to a large extent.

The effect of Bt fractionation or Bt assimilation on the Sr contents is much smaller than that of Akf fractionation or Akf assimilation (e.g. Figs. 4.21 a & 4.19 d). Yet, fractionation and assimilation of Akf and Bt affect Sr contents in opposite directions. Akf fractionation and Bt *assimilation* deplete Sr contents, while Akf assimilation and Bt *fractionation* increase Sr contents.

Therefore a combination of Akf, Bt, and Pl fractionation would produce a good model fit for Sr. Bt fractionation would help to balance the effect of Akf fractionation against that of Pl fractionation and create two evolved melts with roughly equal amounts of Sr (Figs. 4.19 g & 4.21 c).

Akf and Bt fractionation affect Ba contents in the same direction (they both deplete Ba contents), while Akf and Bt assimilation increase Ba contents (Figs. 4.19 f & 4.21 b). However, Bt fractionation or Bt assimilation has a very gentle effect, while the effect of Akf fractionation or Akf assimilation on the Ba contents is very strong.

Therefore, even the smallest contribution of Akf fractionation (or Akf assimilation) would have an extreme effect on Ba contents and would produce derivative melts with a huge difference in Ba abundances. This cannot be balanced out in any way by Bt fractionation, to match the contribution from Pl fractionation. In order to have Ba contents of the model melts match Ba contents of the melts found, Akf fractionation (to evolve a parent melt P into

melt A) or Akf assimilation (to evolve melt P into melt B) must have been insignificant.

If Akf contribution was indeed insignificant and the melt evolution largely dependent on Bt fractionation/assimilation the fractional evolution of the two melts from a common parents melt can be ruled out due to the mismatch in Sr contents as discussed before (see paragraph 2. b on page 80; Fig. 4.21 c).

Consequently melt evolution of melt A and melt B from a common parent melt by a combination of Akf, Bt and Pl fractionation has to be ruled out as well. Therefore, also the last set of hypotheses has to be abandoned.

To recapitulate all three sets of hypothesis and their results: melt A and melt B neither have evolved from a common parent melt nor has one melt evolved from the other melt by different combinations of plagioclase fractionation / assimilation, alkali feldspar fractionation / assimilation and biotite fractionation / assimilation. An alternative fractionation trend would be to evolve melt B into melt A by Akf fractionation and minor quartz (Qtz) fractionation. However, Qtz phenocrysts were not found in any of the samples.

More evidence for the separate origin of melt A and melt B can be found in the Sr isotope composition of the Pl phenocrysts (page 93).

#### **4.4. Isotope geochemistry**

Separates of volcanic glass, hand-picked from two samples, which were chosen for their high glass content, were analysed using TIMS for Sr, Nd, and Pb isotopes. Detailed information on sample preparation and analytical setup can be found on page 280 in section C.6 in the appendix. Analytic results are illustrated in Figs. 4.22 & 4.23.

The two samples show the same Nd isotopic composition, while they differ slightly in their Sr isotopic composition. In the  $\epsilon_{Nd}$  vs.  $^{87}Sr/^{86}Sr$  diagram Fig. 4.22a data plots in “quadrant IV” (FAURE, 1986), with values for  $\epsilon_{Nd}$  lower than CHUR (chondritic uniform reservoir, DEPAOLO & WASSERBURG, 1976a,b; DEPAOLO, 1988) and values for  $^{87}Sr/^{86}Sr$  higher than UR (undifferentiated reservoir, DEPAOLO, 1988). The data plot in a field where continental basalt and continental crust overlap. There are two possible explanations for this: (1) contamination in the magma chamber from crustal wall rocks or during magma ascent in the crust or (2) contamination of the magma source by melt or fluid from continental sediments.

These two scenarios can not be distinguished by the Nd and Sr isotopic composition. However, boron isotopes analysed in the volcanic glass, presented in section

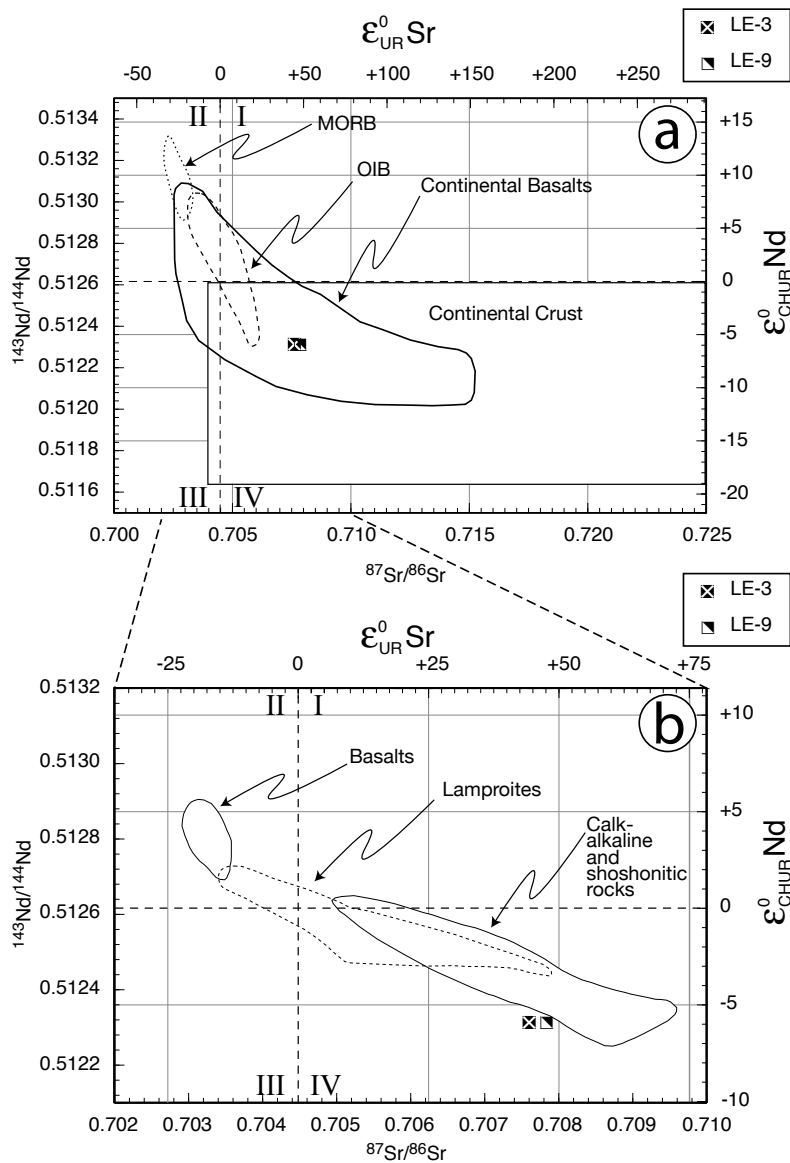


**Fig. 4.22.**  $\epsilon_{\text{Nd}}$  vs.  $^{87}\text{Sr}/^{86}\text{Sr}$  for volcanic glass from additional locations in comparison to (a) MORB, OIB, continental basalt, and continental crust (after FAURE, 1986) and in comparison to (b) Tertiary and Quaternary volcanic rocks from Western Anatolia, after INNOCENTI *et al.* (2005), including data from INNOCENTI *et al.* (2005); ALICI *et al.* (2002); ALDANMAZ *et al.* (2000); ROBERT *et al.* (1992); GÜLEÇ (1991). Quadrants I, II, III, IV from FAURE (1986). CHUR (chondritic uniform reservoir, DEPAOLO & WASSERBURG, 1976a,b; DEPAOLO, 1988) and UR (undifferentiated reservoir, DEPAOLO, 1988).

7.5 on page 126 show evidence of a metasomatic event.

When compared to a collection of literature data for Tertiary and Quaternary volcanic rocks from Western Anatolia (Fig. 4.22 b, INNOCENTI *et al.*, 2005), data from this study is in good agreement with the literature data and plots close to values for calc-alkaline and shoshonitic rocks. Data from this study (LE-3 and LE-9,  $^{143}\text{Nd}/^{144}\text{Nd} = 0.51231$ ) also agrees well with additional literature data for  $\epsilon_{\text{Nd}}$  from Lesbos (PE-PIPER *et al.*, 1998, LL410, Sykaminea high-K,  $^{143}\text{Nd}/^{144}\text{Nd} = 0.51237$ ).

Pb isotopic data (Fig. 4.23 a & b) for the same two samples from additional locations show high  $^{207}\text{Pb}/^{204}\text{Pb}$  and relatively low  $^{206}\text{Pb}/^{204}\text{Pb}$ . While sample LE-3 is in good agreement with various other Lesbos volcanics from PE-PIPER & PIPER (1992), sample LE-9 displays higher values for  $^{208}\text{Pb}/^{204}\text{Pb}$  and  $^{207}\text{Pb}/^{204}\text{Pb}$ . Values for  $^{206}\text{Pb}/^{204}\text{Pb}$  in LE-9 are slightly raised in comparison to LE-3, however both are in the same range as the literature data. Sample #513 (rhyolite, “Acid Volcanics”, Sigri Pyroclastics) from PE-PIPER & PIPER (1992) was chosen for comparison because of the highest similarity to the samples from this study.

Samples from this study and sample #513 (PE-PIPER & PIPER, 1992) follow roughly in a linear trend in a plot Pb contents vs.  $\text{SiO}_2$  (Fig. 4.23 c). Samples with higher  $\text{SiO}_2$  contents also have higher Pb contents. The difference between the two samples of this study (LE-3 and LE-9) in  $^{207}\text{Pb}/^{204}\text{Pb}$  and  $^{208}\text{Pb}/^{204}\text{Pb}$  can not be explained by their bulk Pb concentrations and/or fractionation grade, which are quite similar.

As before for Sr and Nd, in order to achieve the Pb isotope signature found in the Lesbos volcanics, two processes are possible: (1) contamination in the magma chamber from crustal wall rocks or during magma ascent in the crust or (2) contamination of the magma source by melt or fluid from continental sediments.

With the help of boron isotopes analysed in the volcanic glass, presented in section 7.5 on page 126, a metasomatic event can be demonstrated and crustal contamination rejected as cause for the crustal signatures evident in the radiogenic isotopes. However, no conclusive answer can be reached on the age of the metasomatic event, using B isotopes.

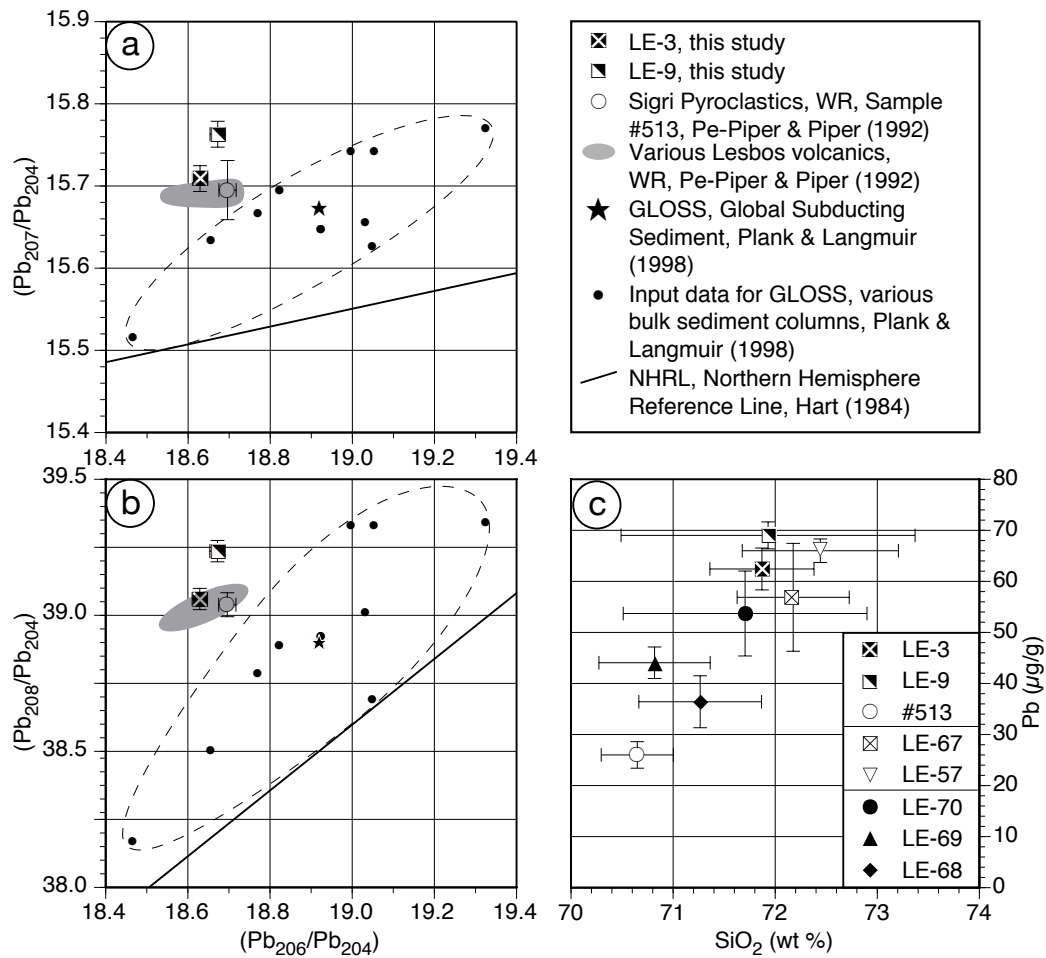


**Fig. 4.23.** (a) and (b) Pb isotope diagrams for volcanic glass from this study (additional locations) in comparison to whole rock data for Sigrí pyroclastics and various other Lesbos volcanics from PE-PIPER & PIPER (1992) and GLOSS (Global Subducting Sediment) from PLANK & LANGMUIR (1998). Also shown is input data for GLOSS, which are averages from various bulk sediment columns subducted at trenches worldwide. Error bars reflect analytical precision (better than 5%) for this study, error limits at  $1\sigma$  level for PE-PIPER & PIPER (1992) identified by repeat determination. (c) Pb concentrations vs.  $\text{SiO}_2$  for the same samples (LE-3, LE-9, #513) plus data from Profile A (LE-57, LE-67) and Profile B (LE-68, LE-69, LE-70). Error bars for samples from this study show standard deviation of the mean at  $2\sigma$  level, data points are averages from repeated measurements. Error bars for sample #513 (PE-PIPER & PIPER, 1992) reflect analytical precision (better than  $\pm 10\%$ ) for Pb as reported in PE-PIPER (1994) and estimated precision of XRF analysis of  $\approx 0.5\%$  for  $\text{SiO}_2$ .



## 5. Geochemical properties of the phenocrysts

### 5.1. Geochemical properties of plagioclase and alkali feldspar

Plagioclase and alkali feldspar occur in every sample of Profile A as the main phenocrysts. Plagioclase also occurs as the main phenocryst in every sample in Profile B, alkali feldspar, however, is only found in very small amounts in Profile B.

Chemical compositions of plagioclase and alkali feldspar were determined using a Cameca® SX 51 electron microprobe at the Institut für Geowissenschaften, Universität Heidelberg. Details about the analytical setup can be found in the appendix on page 269 in section C.2.

Average rim compositions for Pl and Akf in each sample are plotted in Fig. 5.1. The average rim compositions are homogeneous throughout each vertical profile for

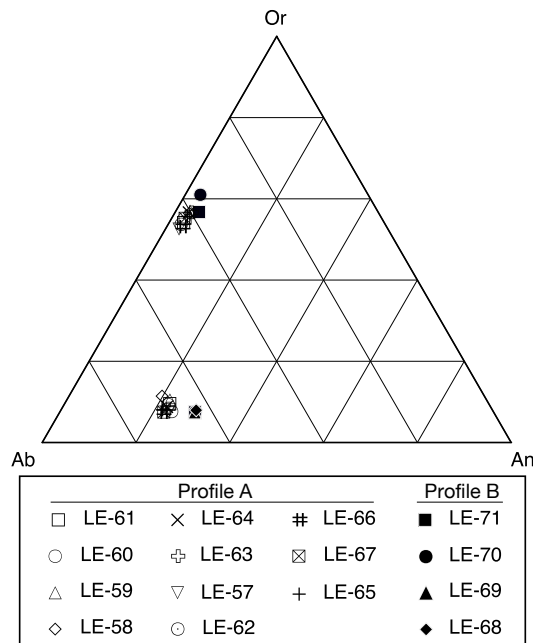


**Fig. 5.1.** Plagioclase and alkali feldspar average rim compositions for each sample in Profile A and Profile B in the Ab-Or-An-system.

## 5. Geochemical properties of the phenocrysts

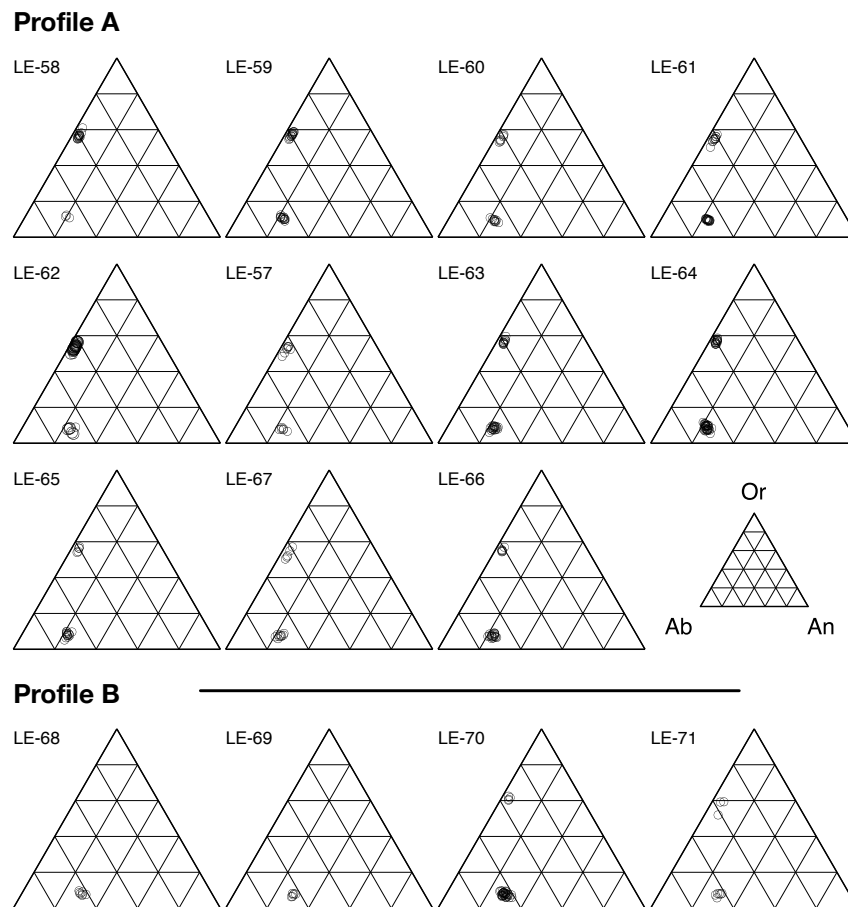


**Fig. 5.2.** All data points for plagioclase and alkali feldspar rim compositions for samples in Profile A and in Profile B in the Ab-Or-An-system. Rim compositions for Pl are  $Or_{5-12}An_{19-27}Ab_{64-73}$  in Profile A and  $Or_{6-10}An_{25-34}Ab_{60-66}$  in Profile B. Rim compositions are  $Or_{47-61}An_{2-5}Ab_{36-49}$  for Akf in Profile A and  $Or_{52-62}An_{3-6}Ab_{35-42}$  in Profile B.

Pl, a bit less so for Akf. There is a small, but clear difference in Pl rim compositions between the two vertical Profiles.

The individual data points for Pl and Akf rim compositions are relatively homogeneous (Fig. 5.2). Taking all data points for rim compositions into account, rim compositions for Pl are  $Or_{5-12}An_{19-27}Ab_{64-73}$  in Profile A and  $Or_{6-10}An_{25-34}Ab_{60-66}$  in Profile B. Rim compositions are  $Or_{47-61}An_{2-5}Ab_{36-49}$  for Akf in Profile A and  $Or_{52-62}An_{3-6}Ab_{35-42}$  in Profile B.

When looking at Pl and Akf internal analyses (all analyses, except for mineral rims), in comparison to the rim compositions, a wider range of compositions occurs

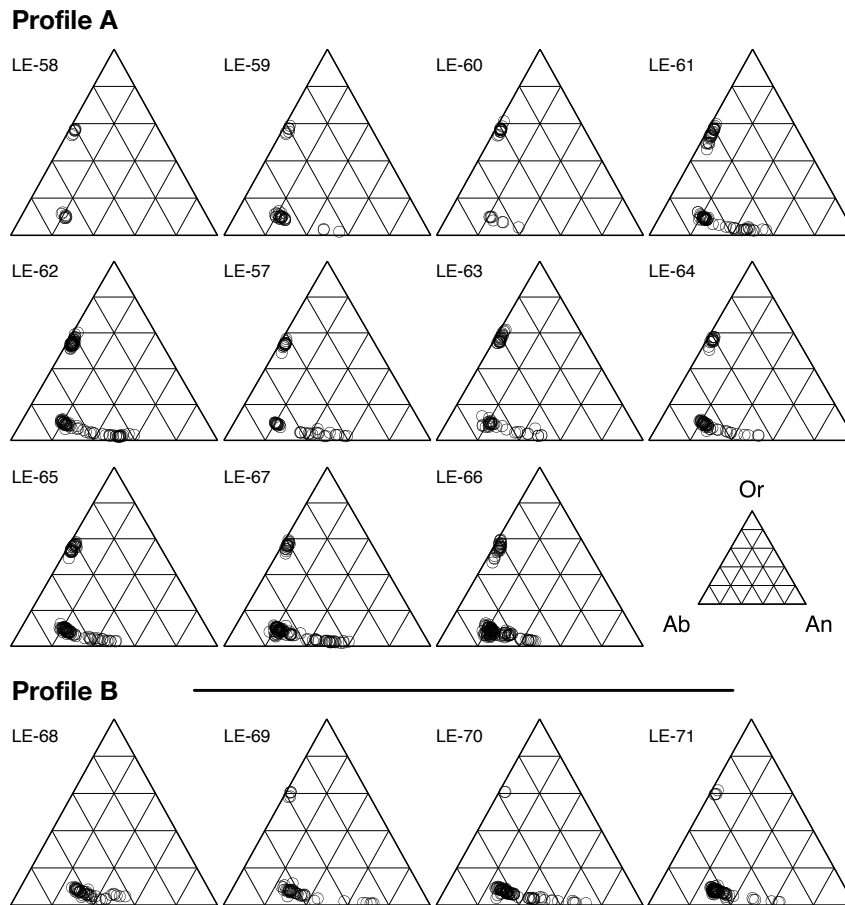


**Fig. 5.3.** All plagioclase and alkali feldspar internal compositions (all analyses, except for mineral rims) in Profile A and in Profile B in the Ab-Or-An-system. Internal compositions for Pl in Profile A are  $Or_{2-13}An_{16-59}Ab_{38-74}$  and in Profile B  $Or_{1-12}An_{23-72}Ab_{27-69}$ . Internal compositions for Akf are  $Or_{46-62}An_{1-5}Ab_{35-49}$  in Profile A and  $Or_{58-62}An_{2-3}Ab_{35-39}$  in Profile B.

(Fig. 5.3). Most compositions range to higher An and Or contents, respectively, but compositions with lower An and Or than the rim compositions exist.

Internal compositions for Pl in Profile A are  $Or_{2-13}An_{16-59}Ab_{38-74}$  and in Profile B  $Or_{1-12}An_{23-72}Ab_{27-69}$ . The internal compositions for Akf in Profile A are  $Or_{46-62}An_{1-5}Ab_{35-49}$  and in Profile B  $Or_{58-62}An_{2-3}Ab_{35-39}$ .

Plagioclase and alkali feldspar both contain high amounts of Strontium and Barium. In Pl there is up to  $6950 \mu\text{g/g}$  Ba (0.78 wt% BaO) and up to  $4630 \mu\text{g/g}$  Sr (0.55 wt% SrO). In Akf there is up to  $28700 \mu\text{g/g}$  Ba (3.20 wt% BaO) and up to  $2621 \mu\text{g/g}$  Sr (0.31 wt% SrO).

Average contents of Sr in Akf rims is higher in Profile B (2090  $\mu\text{g/g}$  Sr; 0.25 wt% SrO) than in Profile A (980  $\mu\text{g/g}$  Sr; 0.12 wt% SrO). The same is true for average contents in Pl rims in Profile B (2500  $\mu\text{g/g}$  Sr; 0.30 wt% SrO) and Profile A (1215  $\mu\text{g/g}$  Sr; 0.14 wt% SrO). Average contents of Ba are not significantly different in Profile A and Profile B.

In chemical profiles across all Pl phenocrysts, Sr shows a trend parallel to Ca, and Ba shows a trend parallel to K. In Akf, however, Ba shows chemical profiles across phenocrysts, that are unrelated to any of the main components. Yet, there is one Pl phenocryst (LE-61 b VIII-11), which also shows a Ba profile that is unrelated to any main component.

### 5.2. Strontium isotopic composition of plagioclase

Strontium isotopes were analysed in-situ by LA-ICP-MS in selected plagioclase crystals (Fig. 5.4). The work was carried out in cooperation with Yann Lahaye at the Institut für Geowissenschaften at the Universität Frankfurt am Main. Details of the analytical setup can be found in section C.4 on page 277.

Strontium isotopes were determined for 33 points in 13 different plagioclase crystals from six different samples from the two vertical profiles (Fig. 5.5). Crystals were chosen for their large size and obvious An zonations (for An contents see bottom of Fig. 5.4).

Core and rim Sr isotopic compositions in the individual crystals are not significantly different. However, there is a significant difference between the average  $^{87}\text{Sr}/^{86}\text{Sr}$  of all analysed spots of Profile A and of Profile B. In Profile A the average  $^{87}\text{Sr}/^{86}\text{Sr}$  of all analysed spots is  $0.70827 \pm 5.3 \cdot 10^{-5}$  ( $2\sigma$  relative standard deviation of the mean), in Profile B the average  $^{87}\text{Sr}/^{86}\text{Sr}$  is  $0.70798 \pm 7.2 \cdot 10^{-5}$  ( $2\sigma$  relative standard deviation of the mean). Each profile is chemically homogeneous as well as isotopically, while the chemical compositions and isotopic compositions differ between samples from the two vertical profiles.

Due to the indistinct Sr isotopic composition of the individual cores and rims and among samples from each vertical profile, a late contamination of the melt in the magma chamber or during magma ascent seems highly unlikely. Contamination from the Variscan basement, from the Late Palaeozoic–Triassic basement, or from young basalt injections would have introduced very different Sr isotopic compositions.

As described above, some Pl cores have anorthite contents very different to the rims and some of them show resolved margins, therefore they must be assimilated.

## 5.2. Strontium isotopic composition of plagioclase

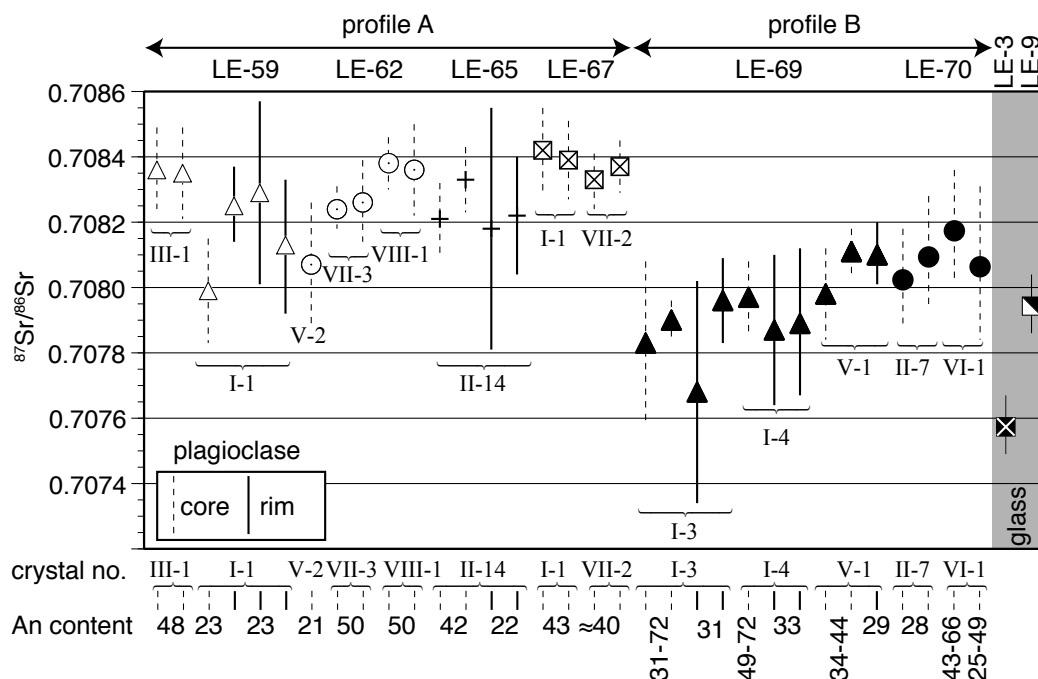


**Fig. 5.4.** Strontium isotope data for plagioclase from Profile A and Profile B, determined by LA-ICP-MS. Below Anorthite contents are indicated for each crystal and rim and core analytical spots. In the grey area TIMS data for two glass samples (LE-3, LE-9) from additional locations are plotted for comparison. Error bars for plagioclase data show range of data within an analytic cycle of  $n = 5$  measurements, for glass data error bars reflect reported uncertainties. The analytical data can be found in Table D.9 on page 297.

However, since all analysed assimilated Pl cores show the same Sr isotopic signature as the rims, cores and rims have to be co-genetic.

The Lesbos volcanic system has been active for around 3.5 Ma prior to the eruption of the Polychnitos ignimbrite. The oldest volcanic rock unit is the Eressos formation at 21.6 ± 1.5 Ma (PE-PIPER & PIPER, 1993) while the Polychnitos Ignimbrite is dated at 17.2 ± 0.5 Ma (BORSI *et al.*, 1972) (see the volcanic stratigraphy, Table 2.1, on page 22). One can therefore speak of an established volcanic system, where contamination from non-volcanic rocks can be less and less expected, while contamination and interaction with older volcanic rocks in the system is increasingly likely. The plagioclase cores therefore most probably stem from older volcanic rocks from within the same magmatic system.

The isotopic difference between Profile A and Profile B underpins the difference

between the two vertical profiles, which has been discussed before based on the chemical compositions of glass and phenocrysts. It is further proof, that the two melts could not have evolved from each other or from a common source, as this would be evident in the Sr isotopic signatures of the plagioclase crystals; i.e. fractional crystallisation could not have produced different Sr isotopic compositions in melt A and in melt B. Furthermore, as discussed above, the assimilation of material – other than from co-genetic volcanics – must be ruled out, as this would have produced differences in Sr isotopic compositions between Pl rims and cores.

Therefore the two vertical profiles must have had different sources and must have derived their different Sr isotopic signature from their respective sources in the lower crust or the lithospheric mantle. Moreover the two vertical profiles must have originated from distinct magma chambers or different sections of one magma plumbing system. While each vertical profile probably has been contaminated by older volcanic rocks in their magma chambers, this must have happened in separate locations.

LAMERA *et al.* (2001, 2004a,b) postulate eight cooling units for the Polychnitos Ignimbrite with at least five different eruption centres (see Table 2.2 on page 25). Unfortunately, it is not possible to correlate Profile A and B with these postulated cooling units, due to a lack of published documentation and especially petrographic and petrologic descriptions by LAMERA *et al.* (2001, 2004a,b). Nevertheless, this confirms the existence of different cooling units, from different eruptions centres and different magma sources within the Polychnitos Ignimbrite as proposed for the ignimbrite units corresponding to the two vertical profiles. Yet, it is important to note, that even though the samples from Profile A and from Profile B are distinctively different, they are alike in their characteristics; they are similar, but not the same.

(E.g. the location of the two vertical profiles lies about 10km linear distance apart within the Polychnitos Ignimbrite on Lesbos Island. The samples from the Profile B are petrographically similar to the samples in the upper part of Profile A; they are densely welded, flamme-rich pyroclastic rocks, with phenocrysts of plagioclase, alkali feldspar and biotite. The contents of major and trace elements in phenocrysts and glass in samples from both vertical profiles is similar.)

## 5.2. Strontium isotopic composition of plagioclase

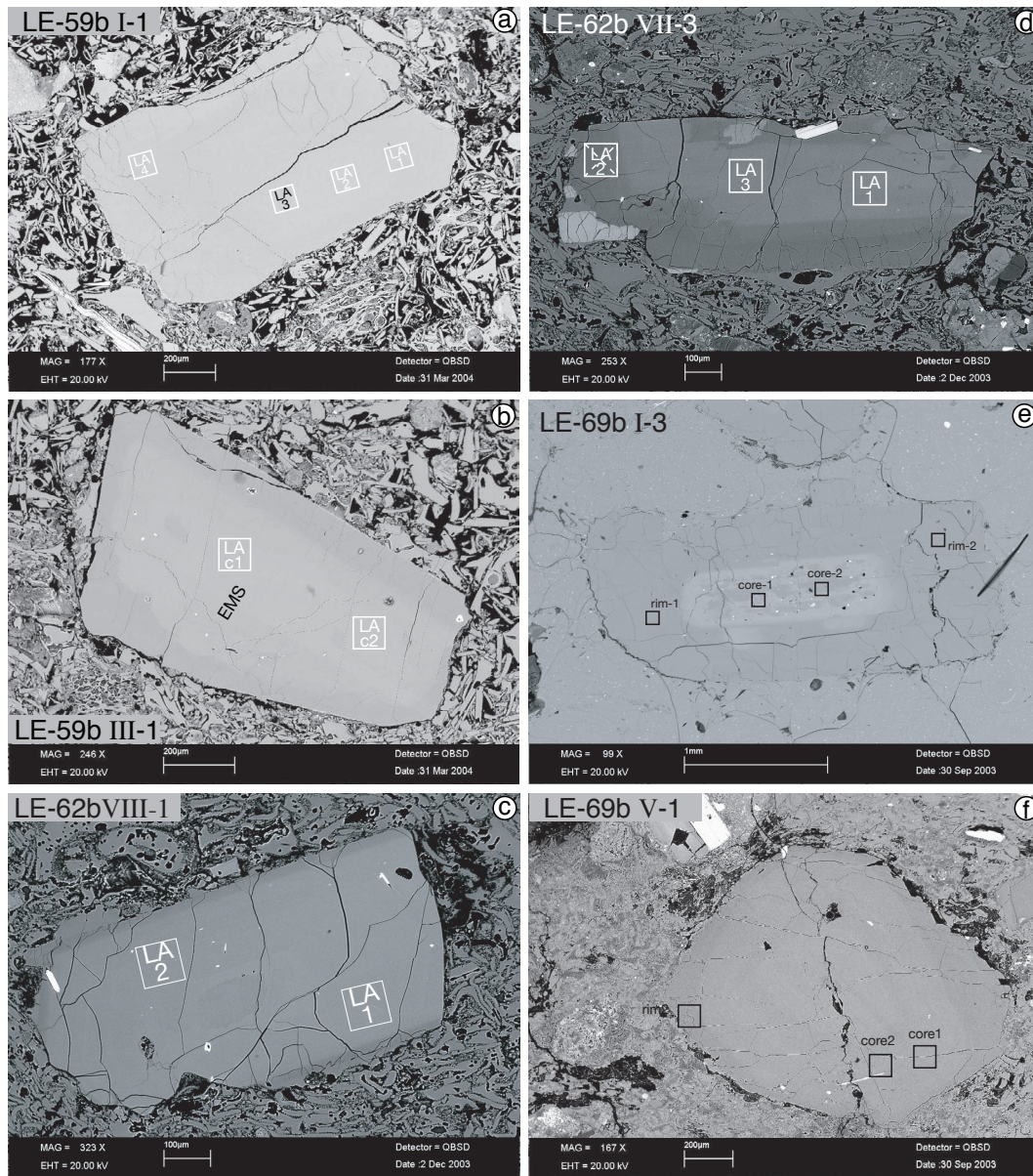


**Fig. 5.5.** BSE images of six of 13 selected plagioclase crystals in which strontium isotopes were analysed in-situ by LA-ICP-MS, squares mark the location and number of analysis point.

### 5.3. Geochemical properties of biotite

The biotites in samples from Profile A and Profile B are defined as micas in between annite–phlogopite–siderophyllite–eastonite. In Fig. 5.6 analyses from biotites in Profile A show a higher variation, than those from Profile B. Biotites from Profile A are also more Ti-rich than from Profile B, as shown in the two plots Ti vs. Ba (Fig. 5.6 a) and  $Al^{IV}$  vs. Ti (Fig. 5.6 d).

Biotites from samples with altered, devitrified glass seem to be also altered, since their variation in the diagrams is substantially larger than for biotites from samples with unaltered glass.

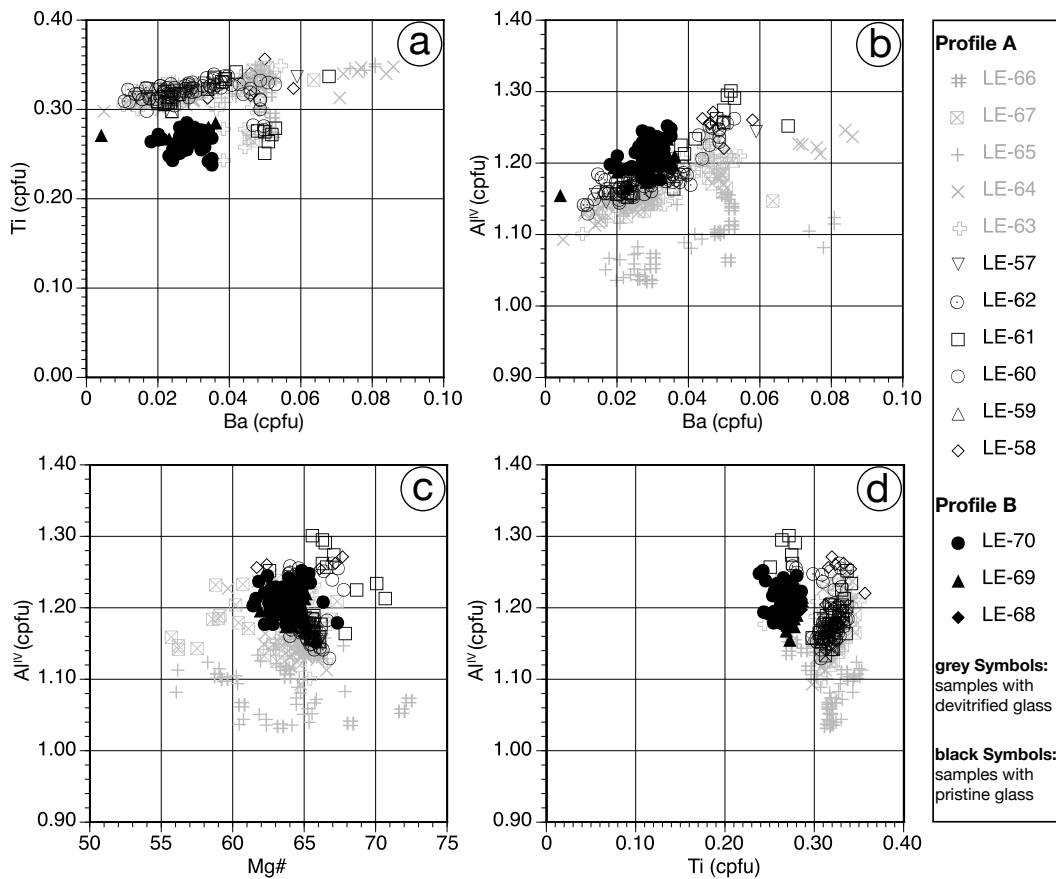


**Fig. 5.6.** Biotite analyses for samples of Profile A and of Profile B presented in four different plots: (a) Ti vs. Ba, (b)  $Al^{IV}$  vs. Ba, (c)  $Al^{IV}$  vs. Mg#, and (d)  $Al^{IV}$  vs. Ti. There is no data for biotite in LE-71, even though the samples does contain biotite phenocrysts.

## 5.4. Geochemical properties of pyroxene

Pyroxene was found in one sample from Profile A (LE-67), in all samples from Profile B (although only analysed in LE-69 and LE-70) and one sample from an additional location (LE-5). The analysed minerals are all Ca-Mg-Fe-pyroxenes (with minor amounts of Al and Ti) and therefore plotted in the quadrilateral system (Fig. 5.7). For across grain mineral profiles, only the extreme data is plotted, while from manual acquisition all data is included.

One orthopyroxene from LE-67 is an enstatite ( $\text{En}_{66}$ ), while the pyroxenes from all other samples are diopsides, with some data points qualifying as augite. The analyses differ very little, with most analyses clustering closely together. Some analyses, however, from the core of one Cpx grain (LE-70 11e) have a slightly lower  $\text{Fe}^{2+}$ -content and form a separate cluster. The rim composition of that grain has the same compositions as the rest of the analysed pyroxenes.

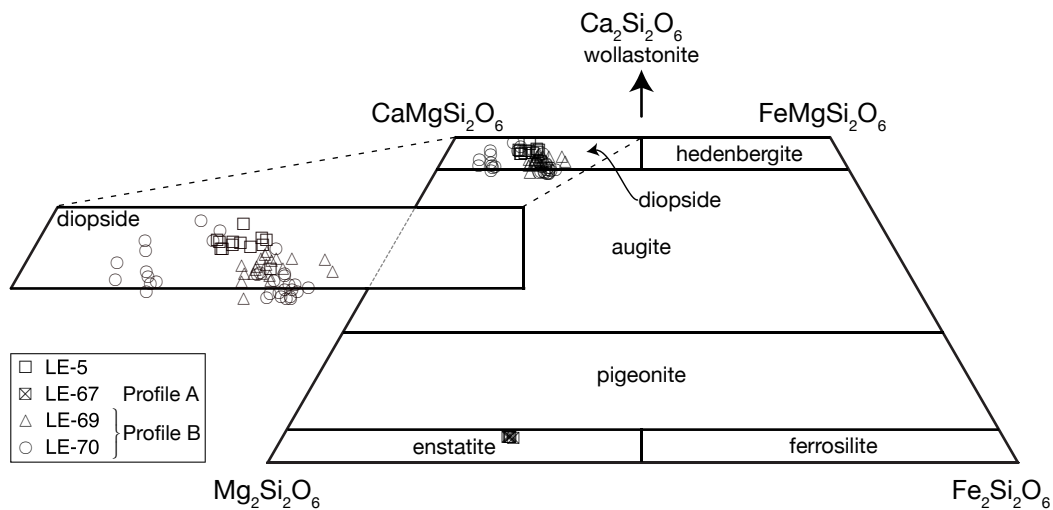


**Fig. 5.7.** Ca-Mg-Fe-pyroxene analyses from samples from Profile A (LE-67) and Profile B (LE-69, LE-70) and one from one additional location (LE-5). For samples from Profile B open symbols were chosen (not solid black, like usual) for more transparency. The quadrilateral system for Ca-Mg-Fe clinopyroxenes and orthopyroxenes, range and accepted names from MORIMOTO (1989).

### 5.5. Geochemical properties of amphibole

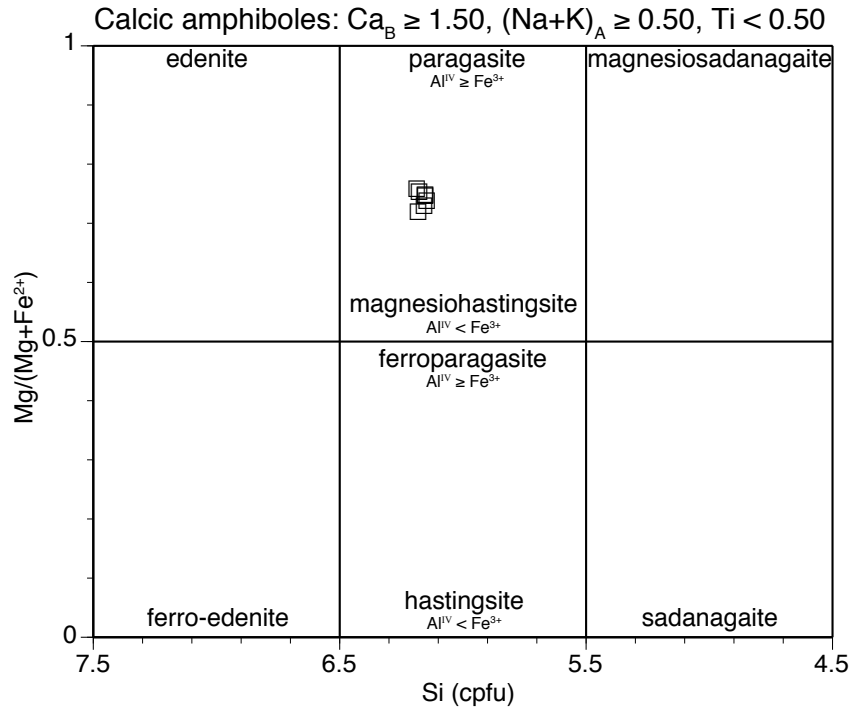


**Fig. 5.8.** Analyses for the only known amphibole in this study, from sample LE-5 from an additional location, represented in the plot  $Mg/(Mg + Fe^{2+})$  vs.  $SiO_2$ . With  $Al^{IV} < Fe^{3+}$  the amphibole is identified as magnesiohastingsite. Nomenclature from LEAKE (1978) and LEAKE *et al.* (1997).

According to the nomenclature by LEAKE (1978) and LEAKE *et al.* (1997) the one amphibole found in LE-5 from an additional location falls into the category of calcic amphibole ( $Ca_B \geq 1.50$ ,  $(Na + K)_A \geq 0.50$ , and  $Ti < 0.50$ ). The subsequent plot  $Mg/(Mg + Fe^{2+})$  vs.  $SiO_2$  (Fig. 5.8) identifies it as magnesiohastingsite with  $Al^{IV} < Fe^{3+}$ .

## 6. Thermobarometry

Pressure and temperature conditions for samples from this study have been investigated using a number of different methods:

- two-feldspar thermometer and barometer with statistical variation analysis (BENISEK *et al.*, 2004)
- plagioclase-liquid thermometer and barometer (PUTIRKA, 2008)
- alkali feldspar-liquid thermometer (PUTIRKA, 2008)
- zircon saturation thermometer (WATSON & HARRISON, 1983)
- apatite saturation thermometer (HARRISON & WATSON, 1984)
- H<sub>2</sub>O solubility (HOLTZ *et al.*, 1995; LIU *et al.*, 2005)

The results are displayed in Fig. 6.1, conditions and applications will be discussed in the following paragraphs.

For the input into the feldspar thermometers and barometers two euhedral phenocrysts from one sample (LE-62) were chosen, a plagioclase and an alkali feldspar phenocryst each with flat element profiles for Na, Ca, K, and Ba (Fig. 6.2); these were plagioclase profile LE-62b V-2a and alkali feldspar profile LE-62b IV-2a. The average element compositions along the profiles were calculated for both minerals. Some data points at the utmost rims were discarded prior to averaging, because they showed slight changes in compositions, also these rims might have not crystallised in the magma chamber, but during ascent under different pressure and temperature conditions. All feldspar thermometers and barometers showed to be very sensitive to very small compositional changes, therefore using average data will help to calculate more reliable results.

For the two-feldspar thermometer of BENISEK *et al.* (2004) the first author provided an Excel file with the mixing parameters. The newer solid solution model by the same authors (BENISEK *et al.*, 2010) failed to work for the low pressures in volcanic systems (tested for data from Fish Canyon Tuff from BENISEK *et al.*, 2004). The input data (albite (Ab), anorthite (An), orthoclase (Or) and celsian (Cls)

## 6. Thermobarometry

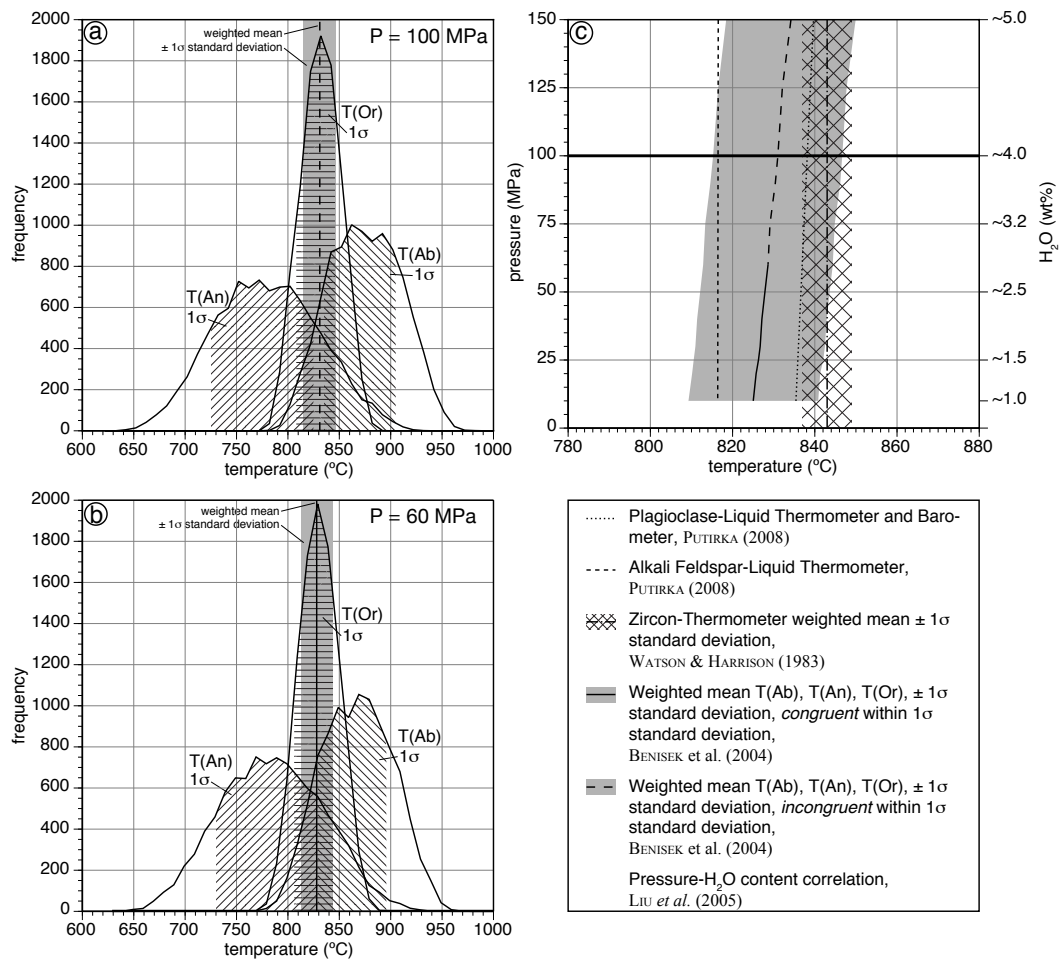


**Fig. 6.1.** Results from various thermo- and barometers (a) temperature-frequency curves for P = 100 MPa, 1 $\sigma$  fields are *incongruent*, two-feldspar thermometer and barometer with statistical variation analysis (BENISEK *et al.*, 2004), (b) temperature-frequency curves for P = 60 MPa, 1 $\sigma$  fields are *congruent*, two-feldspar thermometer and barometer with statistical variation analysis (BENISEK *et al.*, 2004), (c) combined results from various thermobarometric methods (BENISEK *et al.*, 2004; WATSON & HARRISON, 1983; LIU *et al.*, 2005; PUTIRKA, 2008).

---

contents for plagioclase and alkali feldspar) were randomly varied for each parameter within the boundaries of their individual uncertainties ( $1\sigma$  standard deviation (mean) for each average) and randomly paired until 10 000 pairs were created. For each pair, temperatures were calculated based on pressure, Ab, An and Or components, and subsequently plotted by frequency, thus creating three temperature curves, T(Ab), T(An) and T(Or) (Fig. 6.1a & b). For these three temperature curves the congruent area, in which the  $1\sigma$  standard deviation for all three curves would overlap, was determined and the weighted mean from the three mean values  $\pm 1\sigma$  of each temperature curve calculated. The temperature curves are congruent within  $1\sigma$  standard deviation for pressures from 0MPa to 60MPa, weighted mean temperature for 60MPa is  $829 \pm 16^\circ\text{C}$ . However, due to the high amount of  $\text{H}_2\text{O}$  in the volcanic glass pressures must have been around 100MPa; between 75MPa and 150MPa (HOLTZ *et al.*, 1995; LIU *et al.*, 2005).

In-situ concentrations of hydrogen were determined by ion microprobe at the Universität Heidelberg and converted into  $\text{H}_2\text{O}$  concentrations (see section 4.1.2 on page 62). For sample LE-62  $\text{H}_2\text{O}$  concentration is  $\approx 4.3$  wt%, for all seven samples with pristine glass from Profile A, also due to a reduced accuracy of the analytical results (see section C.3.3 on page 276 in the appendix)  $\text{H}_2\text{O}$  concentrations are in the range between 3.3 wt% and 5.4 wt%.

At 100MPa the two-feldspar thermometer of BENISEK *et al.* (2004) yields a temperature of  $831 \pm 16^\circ\text{C}$ , however curves are incongruent within  $1\sigma$ , if only by a very small amount. The weighted mean temperature difference between pressures from 60MPa to 100MPa only changes by  $2^\circ\text{C}$ , well within the  $1\sigma$  standard deviation of  $\pm 16^\circ\text{C}$ .

As input for the plagioclase-liquid thermometer and barometer (PUTIRKA, 2008) and the alkali feldspar-liquid thermometer (PUTIRKA, 2008) the average data from the two element profiles LE-62b V-2a (Pl) and LE-62b IV-2a (Akf) were used again in combination with the average glass composition and the  $\text{H}_2\text{O}$  content for sample LE-62. The plagioclase-liquid thermometer and barometer (PUTIRKA, 2008) yields as optimal pressure-temperature combination of 30MPa and  $836^\circ\text{C}$ , but shows only a slight pressure dependence. For pressures between 10MPa and 270MPa temperatures vary from  $835^\circ\text{C}$  to  $843^\circ\text{C}$ . At 100MPa the plagioclase-liquid thermometer yields  $838^\circ\text{C}$ . The alkali feldspar-liquid thermometer (PUTIRKA, 2008) yields  $816^\circ\text{C}$ .

The whole vertical profile is supposedly from one ignimbrite layer, from a single cooling unit. The glass has shown to be homogeneous throughout the profile in all major, minor and trace elements. Also the chemical composition of the plagioclase and alkali phenocrysts does not change throughout the vertical profile. Therefore, temperatures are expected to have been the same throughout the whole vertical pro-

## 6. Thermobarometry

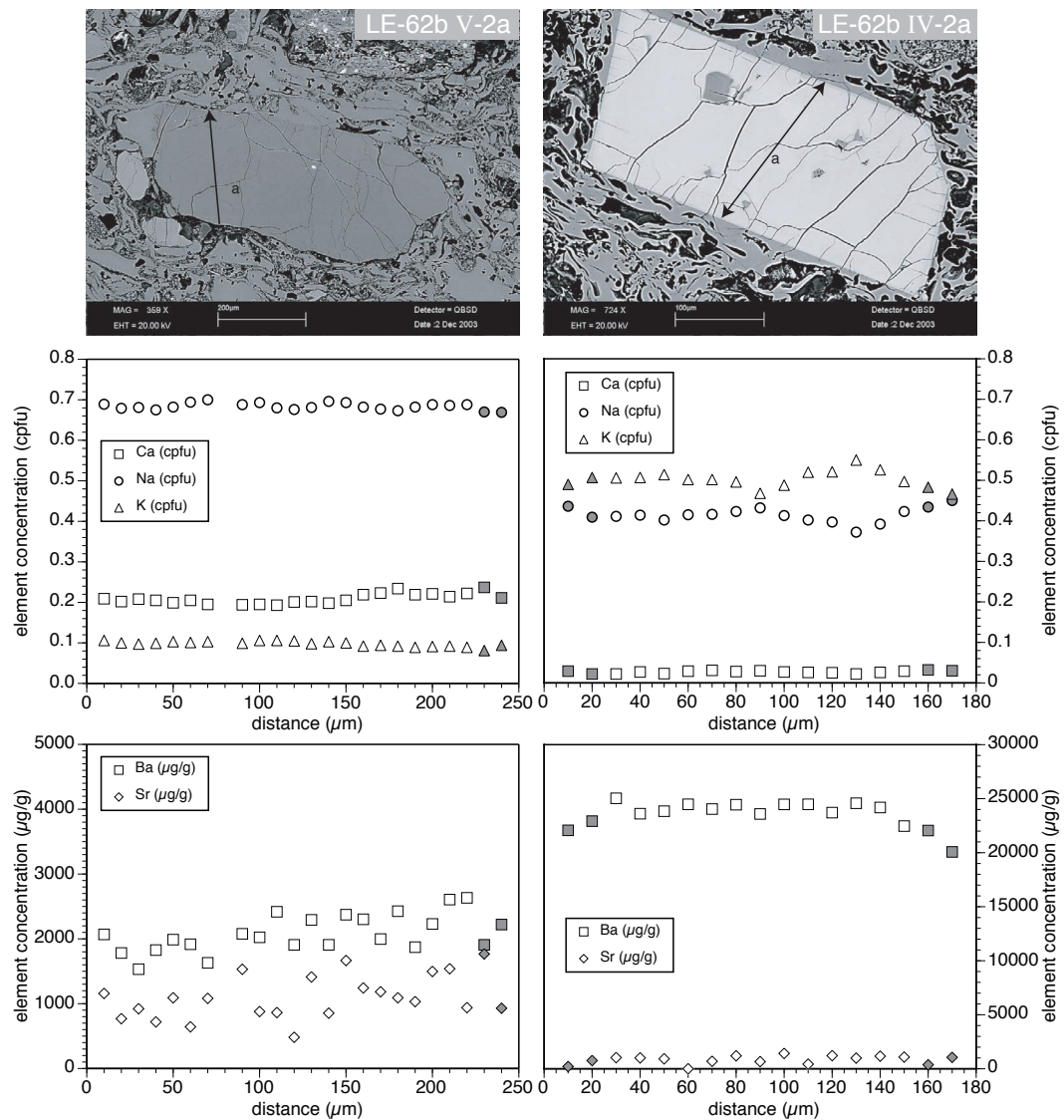


**Fig. 6.2.** Phenocrysts chosen as input for various thermobarometric methods. BSE picture and element profiles for the plagioclase LE-62b V-2a and an alkali feldspar LE-62b IV-2a each from sample LE-62. Data points with grey fillings were not included in the calculation of the average compositions.

---

file before eruption. Differences in cooling rates might have occurred after deposition.

The samples in Profile A contain zircon and apatite phenocrysts (see Fig. 3.8 on page 43 in the sample description). Therefore the zircon saturation thermometer (WATSON & HARRISON, 1983) and the apatite saturation thermometer (HARRISON & WATSON, 1984) could be applied. The zircon saturation thermometer was calculated for samples LE-57 and LE-67 from Profile A, for which the Zr content in the glass has been analysed by LA-ICP-MS at the Universität Frankfurt (details of the analytical setup can be found on page 277, analyses are found on pages 285–286). Zirconium in LE-62 was not analysed, but as explained above, all samples throughout the whole vertical profile are expected to have experienced the same temperature conditions before eruption.

The arithmetic mean for temperatures from the zircon saturation thermometer (WATSON & HARRISON, 1983) is  $839 \pm 6^\circ\text{C}$  ( $1\sigma$  standard deviation). Also sample LE-57 is from 21.0m in Profile A, in the middle of the profile, and LE-67 is from  $\approx 36$ m, close to the top of the vertical profile (LE-62 is from just below LE-57, at 19.5m). The temperatures for both samples deviates only by  $4^\circ\text{C}$  which is indistinguishable within error. For samples from Profile B the zircon saturation thermometer yields  $845 \pm 6^\circ\text{C}$  ( $1\sigma$  standard deviation), this is within  $1\sigma$  the same as the temperature for samples from Profile A.

Unfortunately,  $\text{P}_2\text{O}_5$  analysed in the glass of all samples by electron microprobe was below the detection limit of 0.13 wt%, therefore with the help of the apatite saturation thermometer (HARRISON & WATSON, 1984), it can only be said, that the temperatures must have been below  $955 \pm 4^\circ\text{C}$  ( $1\sigma$  standard deviation).

Combining all results from the six methods (Fig. 6.1), it is possible to restrict the pressure-temperature range for samples from Profile A between 75MPa and 150MPa and between  $815^\circ\text{C}$  and  $848^\circ\text{C}$ . Based on a rock density of  $2850\text{kg}/\text{km}^3$  (continental crust) the pressure corresponds to a depth of the magma chamber between 2.6km and 5.3km at lithostatic conditions.



## **7. Lithium, Beryllium, and Boron in glass and phenocrysts**

### **7.1. Lithium, Beryllium, and Boron concentrations in glass, plagioclase and alkali feldspar**

Lithium, beryllium, and boron concentrations were analysed in glass and minerals by secondary ion mass spectrometry (SIMS) at the Institut für Geowissenschaften, Universität Heidelberg. Details of the analytical setup can be found in section C.3.1 on page 273 in the appendix.

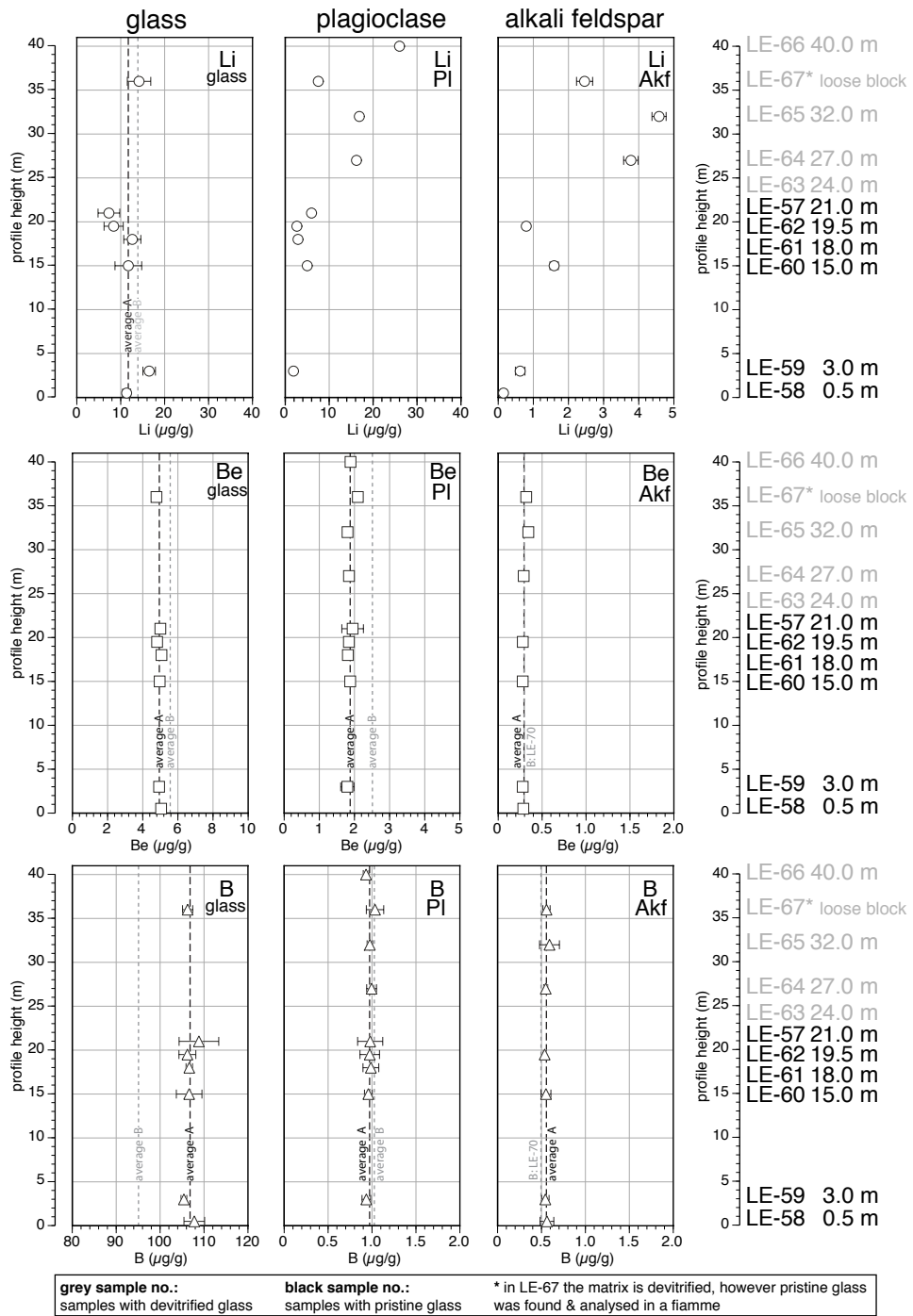
Concentrations of Be and B are very much constant throughout each vertical profile in glass and in mineral rims of plagioclase and alkali feldspar phenocrysts (Figs.7.1 & 7.2). The average Be contents is approximately the same in both vertical profiles in a particular phase (glass, Pl rims, Akf rims). The average B contents in glass is higher in Profile A than in Profile B by  $11.7 \mu\text{g/g}$ , that is a factor of  $\approx 1.1$ . The average contents of B are approximately the same in both profiles in each mineral phase (Pl rims, Akf rims).

However, Li varies greatly within the glass of each sample (as mentioned before for laser-ablation analysis in section 4.2 on page 65), therefore the calculated average contents are only very roughly representative of the true Li concentrations. Lithium concentrations in one sample vary by a factor of up to 5.6 (sample LE-69) and lie for all samples together between a minimum of  $3.0 \mu\text{g/g}$  (sample LE-62) and a maximum of  $37.1 \mu\text{g/g}$  (sample LE-69, total variation by factor of 10.9).

An underlying systematic pattern (e.g. around phenocrysts, or due to different glass textures like pumice, fiamme, matrix, schlieren, perlitic rings) for these large Li variation in the volcanic glass could not be detected during this study. Given the approximate nature of the Li average concentrations the Li contents in the volcanic glass seems to be roughly the same in both vertical profiles and throughout them ( $\approx 10 \dots 20 \mu\text{g/g}$ ).

Lithium concentration differences in Pl and Akf rims will be discussed later in section 7.2 on page 109.

7. Lithium, Beryllium, and Boron in glass and phenocrysts



7.1. Lithium, Beryllium, and Boron concentrations in glass and feldspar

**Fig. 7.1.** (previous page) Lithium, beryllium, and boron contents in rhyolitic glass, plagioclase rims and alkali feldspar rims of Profile A. Samples with grey legend text are samples with devitrified glass. Averages are simple arithmetic means, error bars show  $2\sigma$  standard error. The data can be found in Table D.14 on page 303 in the appendix.

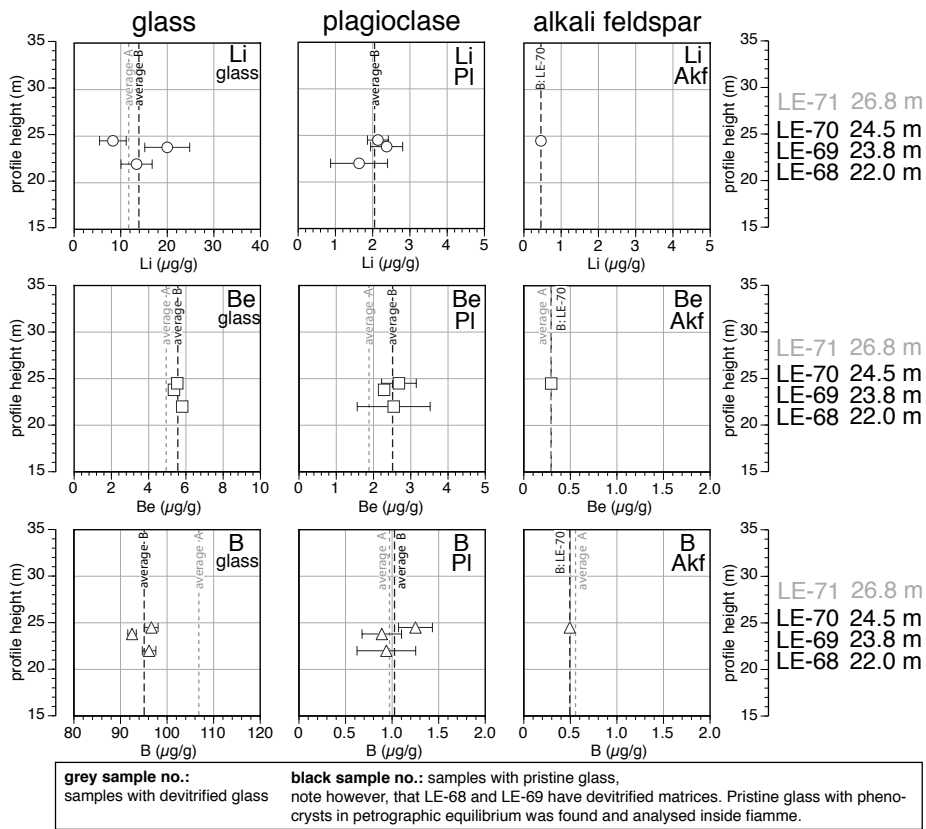


**Fig. 7.2.** Lithium, beryllium, and boron contents in rhyolitic glass, plagioclase rims and alkali feldspar rims of Profile B. Sample LE-71 has devitrified glass and was not analysed. Sample LE-68 and LE-69 have devitrified glass in their matrices, however pristine glass and phenocrysts in petrographic equilibrium with this glass was found and analysed inside large fiamme. Averages are simple arithmetic means, error bars show  $2\sigma$  standard error. The data can be found in Table D.14 on page 303 in the appendix.

7. Lithium, Beryllium, and Boron in glass and phenocrysts

When light element contents (Li, Be, B) in glass are plotted against SiO<sub>2</sub> contents (Fig. 7.3), samples from Profile A and from Profile B plot only in the B vs. SiO<sub>2</sub> plot as two groups and show a positive correlation to SiO<sub>2</sub>. Hence, the higher the SiO<sub>2</sub> contents of the glass, the higher the B contents. Contents of Li and Be seem unrelated to the SiO<sub>2</sub> contents of the glass.

Trace element ratios and effects of fractional crystallisation and fluid metasomatism were discussed before on pages 66–68 in chapter 4.2.

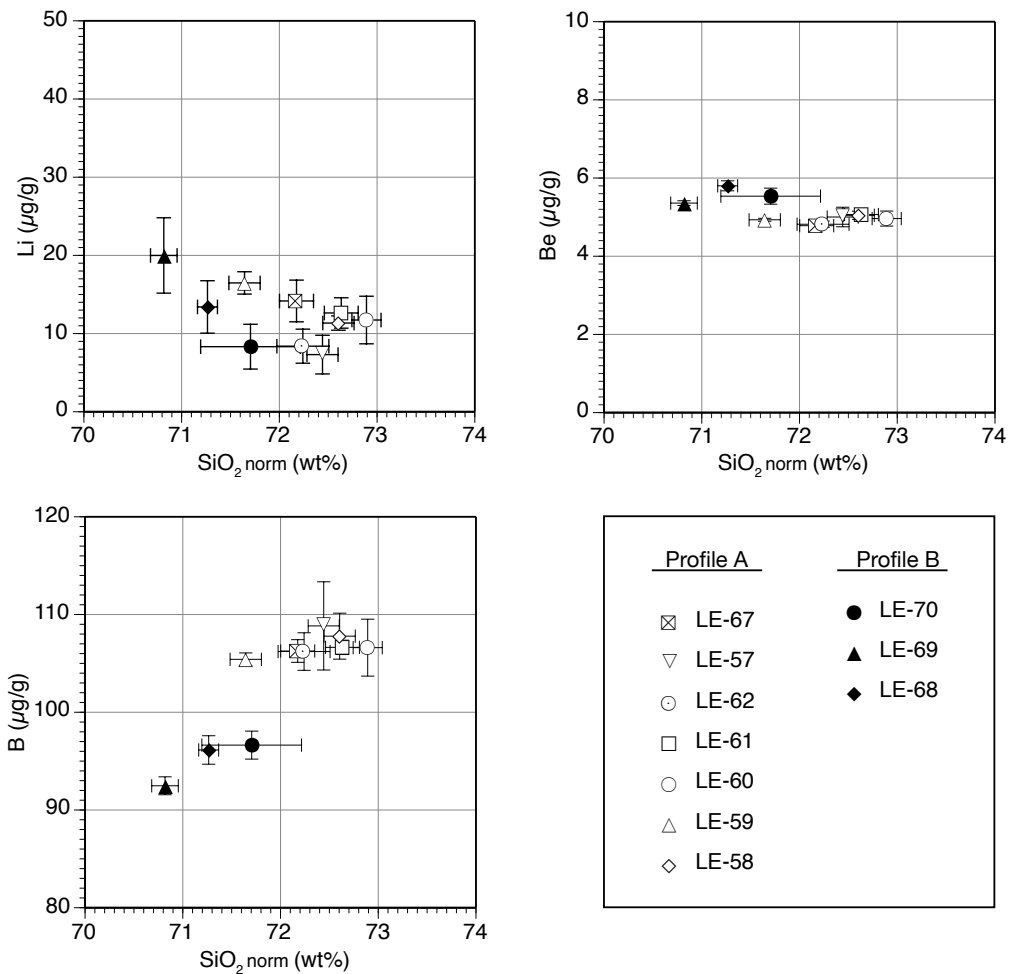


**Fig. 7.3.** Lithium, beryllium, and boron contents versus SiO<sub>2</sub> in rhyolitic glass in samples of Profile A and Profile B. Averages are arithmetic means, error bars show 2σ standard errors.

## 7.2. Lithium diffusion

Lithium concentrations in Pl and Akf rims from samples with devitrified glass matrices at the top of Profile A are substantially higher than in minerals from samples with unaltered, pristine glass at the bottom of the profile (see Fig. 7.1). While Be and B concentrations in glass, Pl and Akf show no differences throughout each of the vertical profiles.

The Li concentrations differences in the mineral rims are caused by different Li diffusion behaviour in phenocrysts at the bottom of Profile A and towards the top. See Fig. 7.4 for Li, Be, and B concentration profiles in Pl phenocrysts from sample LE-59 (Profile A, 3.0 m) and from sample LE-65 (Profile A, 32.0 m). The Pl crystals in both samples are similar in size and rim composition (though the Pl in LE-65 shows a core-rim variation of the main elements, Fig. B.1, page 206), and both have a central crack approximately orthogonal to the profile direction. (For main element concentration profiles in LE-59b I-1 see Fig. B.1 on page 206 and in LE-65b II-14 see Fig. B.30 on page 235.)

Both Pl phenocrysts have a Li contents maximum of  $\approx 20 \mu\text{g/g}$ , but while LE-65b II-14 shows a flat plateau, undisturbed by the central crack and unrelated to the main element variation, with only a very small decrease in Li concentration at the rim (to  $17 \mu\text{g/g}$ ), Li concentrations in LE-59b I-1 show a dramatic diffusion profile, with a drop in concentrations to  $2.5 \mu\text{g/g}$  and  $1 \mu\text{g/g}$  at the rims and to  $3.5 \mu\text{g/g}$  and  $4.0 \mu\text{g/g}$  at the central crack. So, while the Pl in LE-65 shows only a small amount of diffusive loss of Li, the Pl in LE-59 is dramatically depleted in Li at the rim and at the central crack.

The cracks in the Pl crystals must have appeared after the pyroclastic flow was deposited, otherwise the two Pl parts would have separated during transport. Diffusive loss of Li at the central crack in sample LE-59 can have only started then and at about the same time as diffusive loss at the rim, since the diffusion profile is near symmetrical towards the mineral rim and towards the crack.

Alkali feldspar (e.g. sample LE-59b VI-1, Fig. 7.5, for main element profiles see Fig. B.7 page 212) also shows diffusive loss of Li, however due to the low concentration of Li in Akf, the effect is less significant. Again the concentrations for Be and B are constant throughout the profile and all three light elements concentrations (Li, Be, B) are unrelated to the dramatic step-wise Ba zonation ( $\approx 20000 \mu\text{g/g}$  at the former crystal core,  $\approx 18000 \mu\text{g/g}$  in the intermediate zone,  $\approx 10000 \mu\text{g/g}$  at the rim).

Element profiles across large glass fragments (“glass shards”) also show evidence of Li diffusive loss (e.g. sample LE-59b I-1, Fig. 7.5), again concentrations for Be, and B are constant across the element profile. (For main element profiles

see Fig. B.2, page 207; for another example see Fig. B.6, page 211).

Plagioclase rims at the bottom of Profile A are especially depleted in Li, however also crystal centres, Akf phenocrysts, glass fragments and Pl at the top of Profile A and in Profile B certainly are expected to have lower Li concentrations than initially during crystal growth in the magma chamber.

In all presented samples Be and B concentration are constant along the whole length of the four element concentration profiles (Figs. 7.4 & 7.5). The same is true for most analysed element concentration profiles, deviations from that rule are connected to phenocrysts with strong zonation in the main elements; Be and B are usually constant in mineral rims. However Be and B rim concentrations throughout the whole vertical profile A are expected to reflect initial values during mineral growth and in equilibrium between minerals and melt.

The diffusive loss of Li from Pl and Akf phenocrysts and large glass shards could be caused by late degassing of the pyroclastic flow deposit after its deposition.

Alkalis are known to be largely mobilised during exsolution of a H<sub>2</sub>O-rich vapour phase in magmatic systems (SAKUYAMA & KUSHIRO, 1979) and Li seems to be especially susceptible to vapour transport, before eruption at shallow depth (BERLO *et al.*, 2004; KENT *et al.*, 2007) or after eruption and deposition (KURITANI & NAKAMURA, 2006).

Substantial Li diffusion is known to take place within days or even hours, it is one of the fasted elements to diffuse in silicates (JAMBON & SEMET, 1978; GILETTI & SHANAHAN, 1997; RICHTER *et al.*, 2003), markedly faster than K, Pb, and Cs in Ab and Or glass (JAMBON & SEMET, 1978), it is many orders of magnitude higher than for most other cations in clinopyroxene (COOGAN *et al.*, 2005), and it is faster than Na or other alkalis in albite and anorthite crystals (GILETTI & SHANAHAN, 1997). Lithium has also a low activation energy, diffusion in feldspars could be measured down to temperatures as low as 200 °C (GILETTI & SHANAHAN, 1997). Furthermore, diffusion of <sup>6</sup>Li at 500 °C in albite glass is approximately 100 times faster than in crystalline albite (GILETTI & SHANAHAN, 1997).

So, while Li diffusion is faster than that of Cs (JAMBON & SEMET, 1978) in glass, diffusion of Be and B is slower than Cs in haplogranitic melt by two orders of magnitude and in the same range as diffusion of heavy REE (MUNGALL *et al.*, 1999).

Unfortunately, Li, Be, and B diffusion behaviour has not been determined under the same conditions for all three elements. However, diffusion coefficients for Be and B have been determined by MUNGALL *et al.* (1999) in haplogranitic melt (HPG8) at 1573 °C. Both are in the same order of magnitude with  $D = 3.72 \cdot 10^{-12} \text{ m}^2/\text{s}$  for Be and  $D = 1.82 \cdot 10^{-12} \text{ m}^2/\text{s}$  for B. Diffusion coefficients

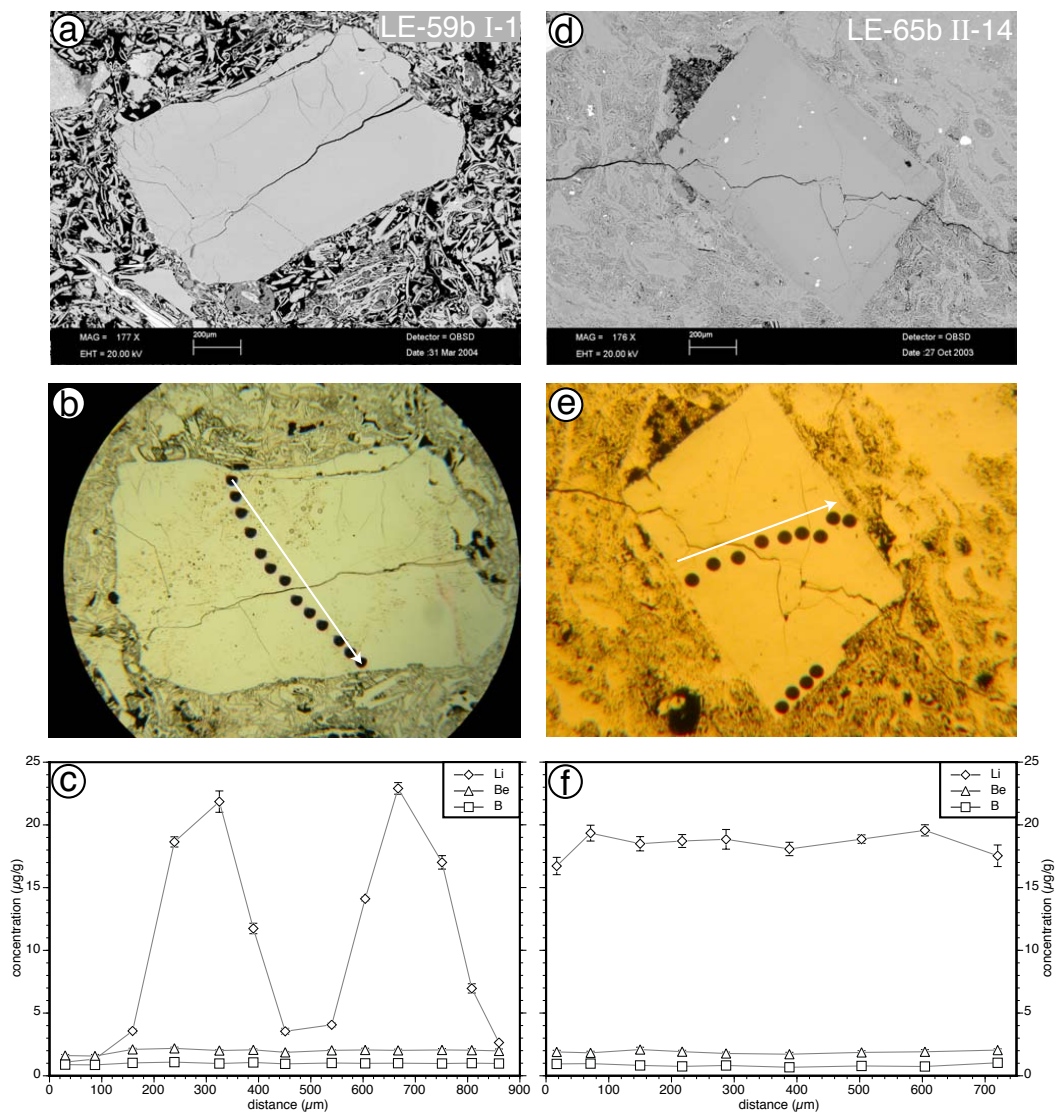


**Fig. 7.4.** Lithium, beryllium, and boron concentrations in plagioclase phenocrysts in sample LE-59 (Profile A, 3.0m), and LE-65 (Profile A, 32.0m). (a) BSE image, LE-59b I-1 (b) Reflected light image of gold coated sample after SIMS analysis, analytical spots appear black on gold coating, LE-59b I-1, (c) element profile for Li, Be, and B across LE-59b I-1, (d) BSE image, LE-65b II-14, (e) Reflected light image of gold coated sample after SIMS analysis, analytical spots appear black on gold coating, LE-65b II-14, (f) element profile for Li, Be, and B across LE-65b II-14. (For main element concentration profiles in LE-59b I-1 see Fig. B.1 on page 206 and in LE-65b II-14 see Fig. B.30 on page 235.)

## 7. Lithium, Beryllium, and Boron in glass and phenocrysts

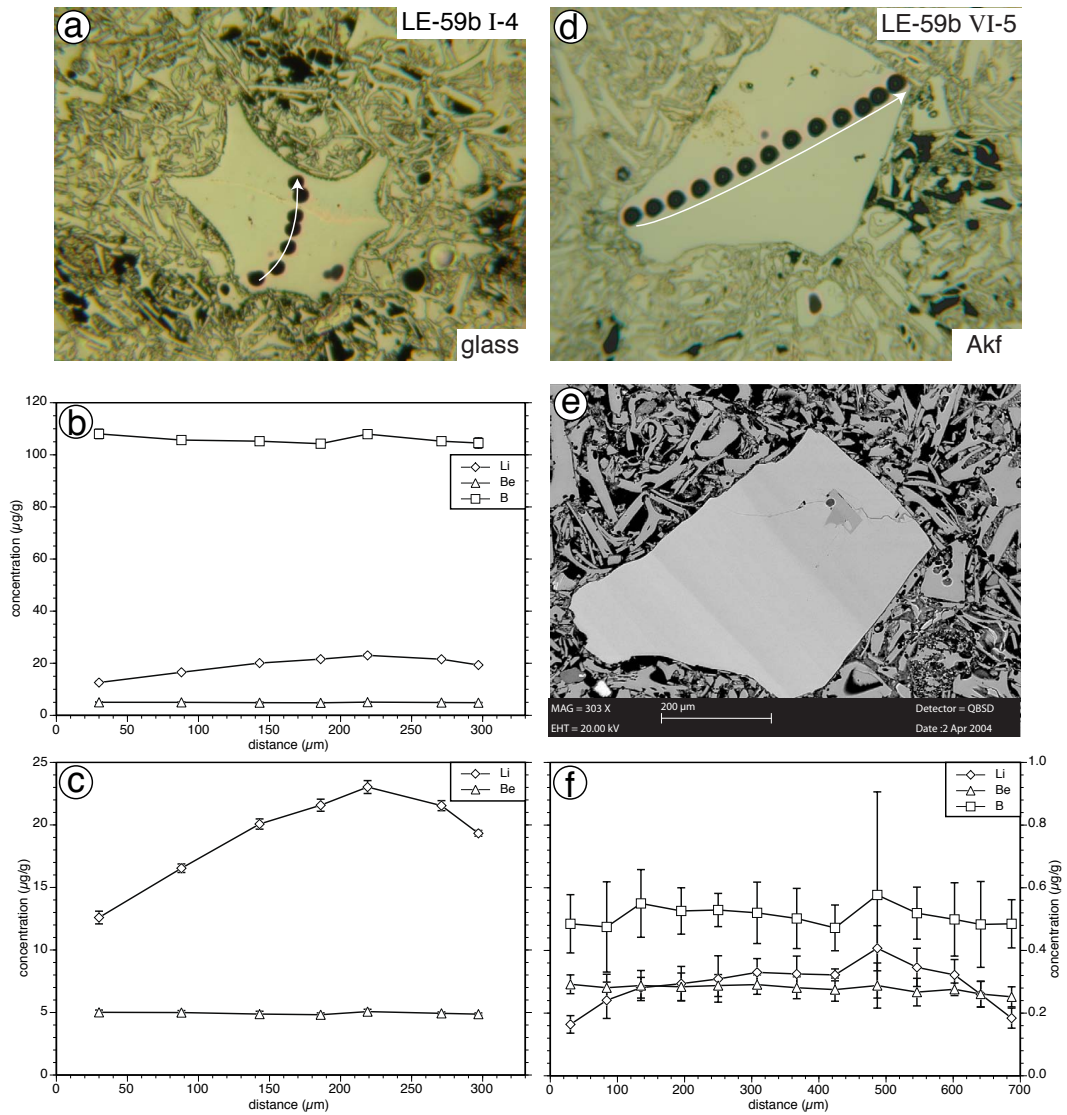


**Fig. 7.5.** Lithium, beryllium, and boron concentrations in glass and alkali feldspar phenocrysts fragment in sample LE-59 (Profile A, 3.0m). (a) Reflected light image of gold coated sample after SIMS analysis, analytical spots appear black on gold coating, glass fragment, LE-59b I-4, (b) & (c) element profile for Li, Be, and B across LE-59b I-4, (d) Reflected light image of gold coated sample after SIMS analysis, analytical spots appear black on gold coating, alkali feldspar LE-59 VI-5, (e) BSE image, LE-59 VI-5, note three zones of step-wise Ba zonation (see Fig. B.7 on page 212 for Na, K, Ca, Ba, and Sr profiles in this phenocryst), (f) element profile for Li, Be, and B across LE-59b VI-5.

for Li and B have been determined in different rhyolite melts (in review paper by ZHANG *et al.*, 2010, rhyolite 5 and rhyolite 14, respectively). BAKER (1992) determined  $D = 7.63 \cdot 10^{-15} \text{ m}^2/\text{s}$  for B at 1573 °C. The diffusion coefficient determined by JAMBON & SEMET (1978) for Li at lower temperatures (1128 °C) is with  $D = 1.7 \cdot 10^{-10} \text{ m}^2/\text{s}$  more than 4 orders of magnitude faster. Even at temperatures as low as 570 °C Li diffusion is with  $D = 9 \cdot 10^{-15} \text{ m}^2/\text{s}$  still faster than B diffusion at 1573 °C. So, the same diffusional transport that is achieved within one day for lithium, is expected to take around 55 years for beryllium and boron.

Based on the observation described so far a model will be developed; the key observations are summarised below:

- Li is strongly susceptible to vapour transport and is largely mobilised during exsolution of a H<sub>2</sub>O-rich vapour phase from silicate melts (BERLO *et al.*, 2004; KURITANI & NAKAMURA, 2006; KENT *et al.*, 2007).
- Li diffusion is very fast in comparison to most elements and much faster than diffusion of Be and B in minerals (GILETTI & SHANAHAN, 1997; COOGAN *et al.*, 2005), glass (JAMBON & SEMET, 1978), and melts (MUNGALL *et al.*, 1999; RICHTER *et al.*, 2003).
- Li diffusion in glass of albite composition is much faster (factor  $\approx 100$ ) than in crystalline albite (GILETTI & SHANAHAN, 1997).
- In samples from this study Li was lost diffusively from glass, as detected in large glass fragments (Fig. 7.5).
- In samples from this study Li is distributed heterogeneously and apparently unsystematically within glass matrices. Lithium concentrations vary between 3.0 µg/g and 37.1 µg/g (see this chapter section 7.1 on p. 105).
- In samples from this study Li was lost from Pl and Akf phenocrysts, especially pronounced in Pl at the bottom of Profile A (Figs. 7.4 & 7.5).
- In this study, samples from the top of Profile A (LE-63, LE-64, LE-65, LE-67, and LE-66) have devitrified glass matrices; however pristine glass can be found in fiamme. The samples with devitrified glass matrices show very obvious red and pink alteration colours, which are prominent in the field and in hand specimens.

The model will be explained subsequently, a schematic sketch can be found in Fig. 7.6. Profile A is thought to be representative of a complete flow and cooling unit (Fig. 7.6 b). Shown in the column are matrix colours, corresponding to field observations and sample descriptions, as displayed in the schematic sketch and sample description of Profile A (Fig. 3.3 on p. 33). Red and pink matrix colours are symptomatic for samples with devitrified glass matrices, these colours clearly stand out in the field and in hand specimens and mark hydrothermal alteration.

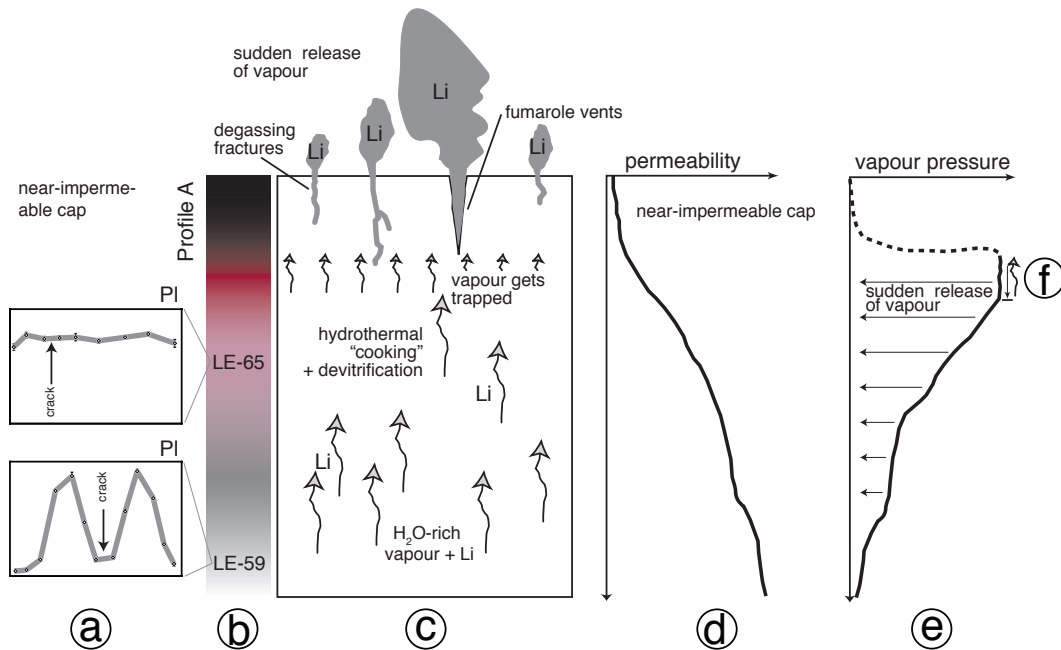


**Fig. 7.6.** Model for degassing and Li loss from the pyroclastic cooling unit after deposition. (a) Li diffusion profiles for PI phenocrysts from LE-59 and LE-65. (b) Representative column for Profile A. Displayed are matrix colours, corresponding to field observations and sample descriptions, as shown in the schematic sketch of Profile A in Fig. 3.3 on p. 33. (c) Degassing model, featuring loss of a H<sub>2</sub>O-rich vapour phase with high amounts of lithium; vapour phase accumulated near the top due to decreasing permeability and caused hydrothermal “cooking” of the matrix and devitrification of glass. The vapour got trapped below the highly-welded near-impermeable cap at the top, until it released along cooling fractures, or along degassing fractures and fumarole vents, opened up by increased vapour pressure. (d) Inferred model permeability. High permeability at the bottom decreases towards the top due to increased degree of welding with highly-welded near-impermeable cap at the top. (e) Inferred model vapour pressure. The vapour pressure increases from bottom to top, due to decreasing permeability and steady degassing. Vapour got trapped below the near-impermeable cap, accumulated and eventually pressure started to increase from the accumulation zone downwards (see (f)). The sudden release of vapour through cooling fractures, degassing fractures and/or fumarole vents lead to a decline of vapour pressure through the entire vertical profile.

It is expected that entrained gas and vapour from pore spaces and between particles escaped (as an ignimbrite is a gravity-driven gas-pyroclast mix, e.g. FREUNDT *et al.*, 2000) after the deposition of the cooling unit. Additionally, a H<sub>2</sub>O-rich vapour phase could have been exsolved from the glass (Fig. 7.6 c; note the high amount of H<sub>2</sub>O still contained in glass today; 3.7 wt% to 5.2 wt%). The vapour phase will have contained a high amount of Li, as Li would have been available in relatively high quantities (still up to a maximum of 37.1 µg/g in glass today) and is strongly susceptible to vapour transport (BERLO *et al.*, 2004; KENT *et al.*, 2007; KURITANI & NAKAMURA, 2006), i.e. Li will strongly partition into the vapour phase from glass and minerals.

The diffusive loss of Li from the glass and minerals along degassing paths caused Li disequilibria. Hence, Li diffusion will have subsequently taken place, as detected in large glass fragments (Fig. 7.5), causing a heterogeneous and in thin section apparently chaotic Li distribution, additionally Li diffusion within minerals and from minerals into the glass will have occurred (Fig. 7.6 a, see also Fig. 7.4).

In the lower part of the profile, which has a high inferred permeability, due to the unwelded glass matrix, the vapour ascended relatively easily (Fig. 7.6 d) and incorporated large amounts of Li from glass and minerals. As the vapour phase ascended higher in the profile the inferred permeability decreases, due to a higher degree of welding, and eventually vapour will have started to accumulate. The higher the vapour ascended, the more Li will have already been dissolved and the less Li would partition into it. The accumulated vapour climbed as a front through the ignimbrite profile and eventually got trapped below the near-impermeable cap (Fig. 7.6 e).

The vapour pressure increased steadily throughout the profile from bottom to the top (Fig. 7.6 e). As more gas collected and got trapped below the top cap, the vapour pressure started reversing downward and built up to a constant value from the top to the bottom (f in Fig. 7.6). But before this pressure build-up got to the bottom, the vapour escaped and the vapour pressure dropped. The vapour was released through cooling fractures, which will eventually have developed or the build-up of vapour pressure will have caused fractures and fumarole vents to open up (Fig. 7.6 c). In both cases the vapour was released relatively sudden. This prompted a rapid decline of vapour pressure through the entire vertical profile (Fig. 7.6 e).

At the bottom of the profile in sample LE-59 the diffusive loss of Li is much more pronounced than in the middle of the profile in sample LE-65 (Fig. 7.6 a). As explained before, in the lower part of the profile the vapour could ascent relatively easily, causing a constant flow. Also the vapour was able to incorporate large amounts of Li (strong partitioning into the vapour phase from glass and minerals). The higher the vapour ascended in the profile, the more Li it would have already

absorbed, and the Li disequilibrium between vapour on the one side and glass and minerals on the other side had got smaller; the vapour would not be fully Li saturated but it would have been closer to saturation than at the bottom. The smaller the Li disequilibrium was, which is the principal motor of partitioning, the smaller were the amounts of Li incorporated into the vapour. At the same time vapour exsolution from the glass higher up in the profile was slower than at the bottom, due to the upward increasing vapour pressure. The prevalent vapour pressures and differences in the amounts of Li incorporation throughout the profile (lower vapour pressures at the bottom with large amounts of Li partitioning into the vapour and steadily higher pressures towards the top with less and less Li partitioning into the vapour) is preserved in the difference in Li diffusion behaviour in plagioclase phenocrysts from LE-59 (3 m) and LE-65 (32 m; Fig. 7.6 a).

As the vapour accumulated, it caused hydrothermal “cooking” of the matrix and devitrification of glass components. The devitrification level today of the matrices increases continuously towards the top (LE-63 at 24m is less devitrified than LE-66 at 40m profile height; see profile description in section 3.3.3 on p. 35). The “cooking” lasted only a limited amount of time, since pristine glass is preserved in the internal parts of larger fiamme in all devitrified samples of Profile A, except in the topmost one (LE-66).

The top of Profile A shows regular fissures, fractures, and clefts. The origin for these (cooling fractures, degassing structures, or weathering) was not explored during field work. The existence of degassing structures at an unspecified location within the ignimbrite has been reported by LAMERA *et al.* (2001). Therefore, the model adequately combines all observations as described in the key observations.

### 7.3. Lithium, Beryllium, and Boron concentrations in biotite

The Li, Be, and B contents in Bt could not be described in any systematic way in this study. Biotite is a complex mineral, its three-dimensional grain-shape is difficult to determine in thin section and its geometry is strongly anisotropic. Therefore a discrimination between rim and core data is not sensible in Bt. Zonation and diffusion in biotite is strongly anisotropic and imperceptible mechanic delamination of sheets opens diffusion pathways and adds further to anisotropy. The patchy Ba-zonation pattern described for Bt towards the top of Profile A (section 3.3.4 on page 42) is a sign for the heterogeneity of some of the Bt crystals in this study.

Most chemical characteristics in Bt have been plotted against Li, Be, and B for the data points which are in a high spacial agreement between EMP and SIMS analysis (Fig. 7.7). All parameters seem entirely uncorrelated to Li, Be, and B contents.

### 7.3. Lithium, Beryllium, and Boron concentrations in biotite

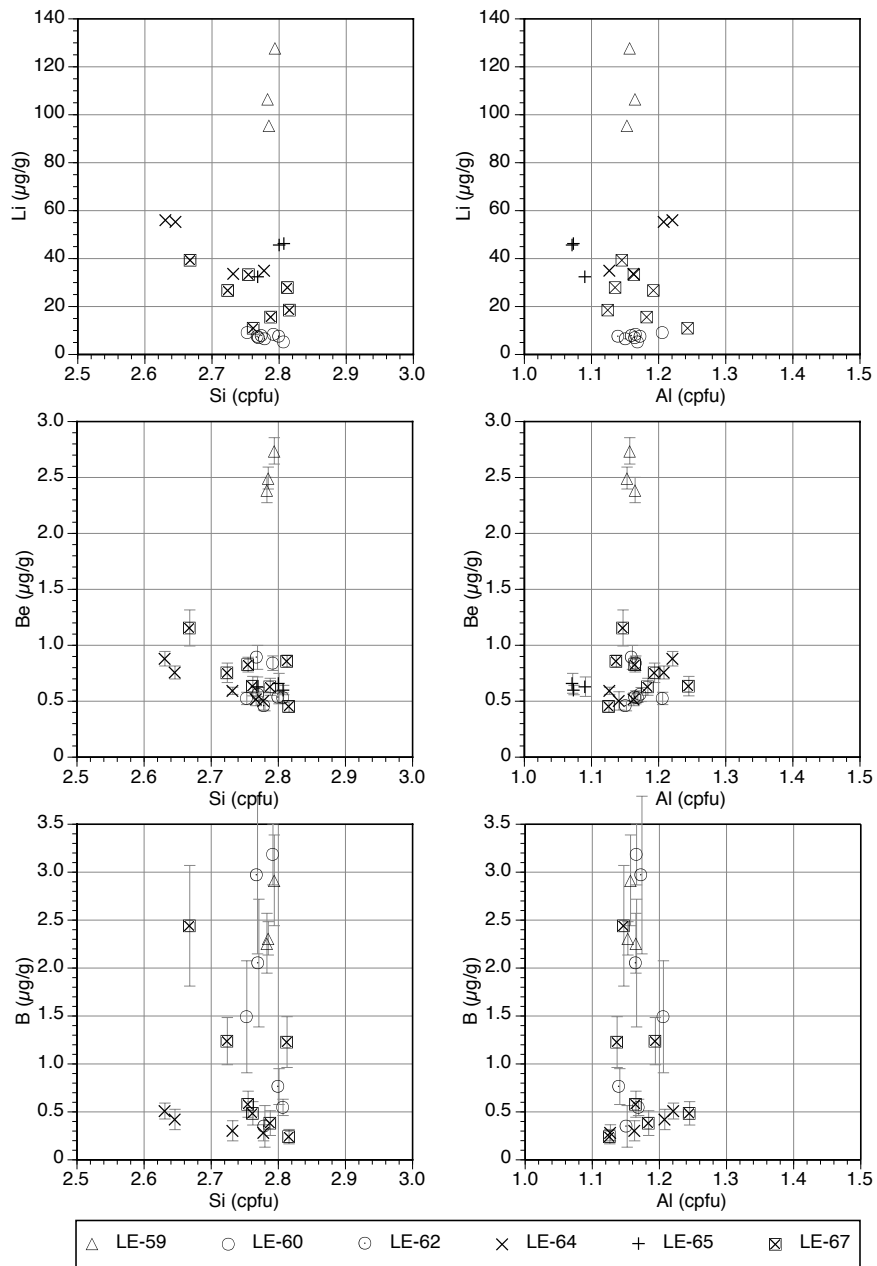


**Fig. 7.7.** Light elements contents (Li, Be, B) versus Si (cpfu) and Al (cpfu) in biotite from Profile A. Error bars are given only for Li, Be, and B contents and show  $2\sigma$  standard deviation (mean).

#### 7.4. Partition coefficients for Beryllium and Boron

Phenocrysts in this study repeatedly have glass selvages (Fig. 7.8 b, c & e; glass that is directly attached to the phenocryst, like a thick coating), so that glass and phenocrysts show petrographic equilibrium. Where available, all glass phases (glass selvages, matrix, and pumice or fiamme) were analysed and compared; they show the same composition in each sample. Hence data from all different glass phases, as long as it was pristine, was assumed to be in equilibrium with the phenocrysts. In some samples (LE-67, LE-68, LE-69) the matrices were devitrified, however pristine glass was found and analysed in fiamme. In LE-68 and LE-69 Pl phenocrysts in petrographic equilibrium with the fiamme were analysed (e.g. Fig. 7.8 f), while that was not the case in LE-67.

Partition coefficients were calculated for Be and B using average glass and average mineral rim data for a number of samples in Profile A and in Profile B, including LE-68 and LE-69, for which good quality data of pristine glass and Pl and Akf rims could be obtained; results are displayed in Fig. 7.9.

Partition coefficients for Li were not calculated due to the high variation of Li in the volcanic glass, described before in section 4.2 on p. 65 and in this chapter in section 7.1 on p. 105 and due to diffusive loss in Pl and Akf phenocryst, as discussed before in the previous section on (p. 109). Lithium equilibrium between minerals and glass was not retained.

Partition coefficients for Be and B are constant throughout each vertical profile (Fig. 7.9) and the standard error is small for most samples. Partition coefficients for Be and B between Akf and glass ( $D_{\text{Be Akf/glass}}$ ;  $D_{\text{B Akf/glass}}$ ) have very similar values in Profile A and in Profile B, while values for Be partition coefficients between Pl and glass ( $D_{\text{Be Pl/glass}}$ ) vary significantly from Profile A to Profile B. Values for B partition coefficients between Pl and glass ( $D_{\text{B Pl/glass}}$ ) vary slightly, but not significantly, from Profile A to Profile B. A relationship between  $D_{\text{Be Pl/glass}}$ ,  $D_{\text{B Pl/glass}}$  and the anorthite (An) contents of the plagioclase and/or temperature dependency will be discussed later.

Partition coefficients from this study are compared to literature data in Fig. 7.10, comprising all available data as to date from a large range of rock types, natural rocks and experimental data. For  $D_{\text{Be Pl/glass}}$  (Fig. 7.10 a) literature data range from 0.1 to 1.99 (both values EVENSEN & LONDON, 2002). Data from EVENSEN & LONDON (2002); EVENSEN *et al.* (1999); BINDEMAN & DAVIS (2000) and DUNN & SEN (1994) show both, incompatible and some compatible values. Data from PANIENKA (2011) and CABATO (2007), both from high-Si natural volcanic rocks lie at close range to data from this study, as well as data from RYAN (1989) from experimental data based on natural basalts.

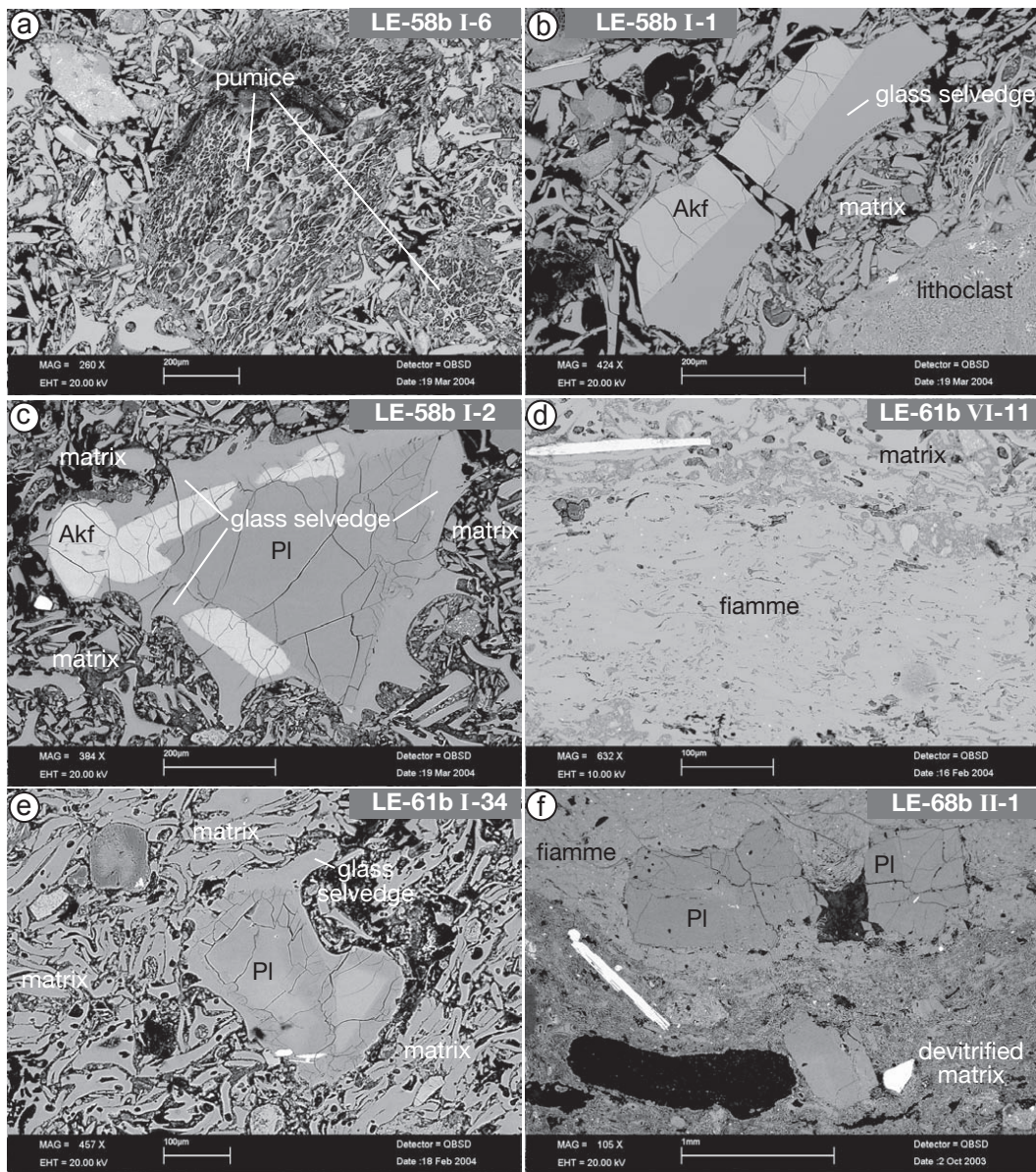


**Fig. 7.8.** Different glass phases in samples LE-58 and LE-61 (a) pumice, phenocrysts and matrix in LE-58 (b) Akf with glass selvage in petrographic equilibrium in LE-58 (c) Pl with Akf selvages and glass selvage in petrographic equilibrium and matrix in LE-58; all glass phases in sample LE-58, pumice, matrix and glass selvages have the same composition (d) fiamme and matrix in LE-61 (e) Pl with glass selvage in petrographic equilibrium and matrix in LE-61; all glass phases in sample LE-61, fiamme, matrix and glass selvages have the same composition (f) fiamme and Pl phenocrysts in petrographic equilibrium in LE-68, the matrix is devitrified; Pl in the matrix was not analysed in this sample, only Pl in the fiamme.

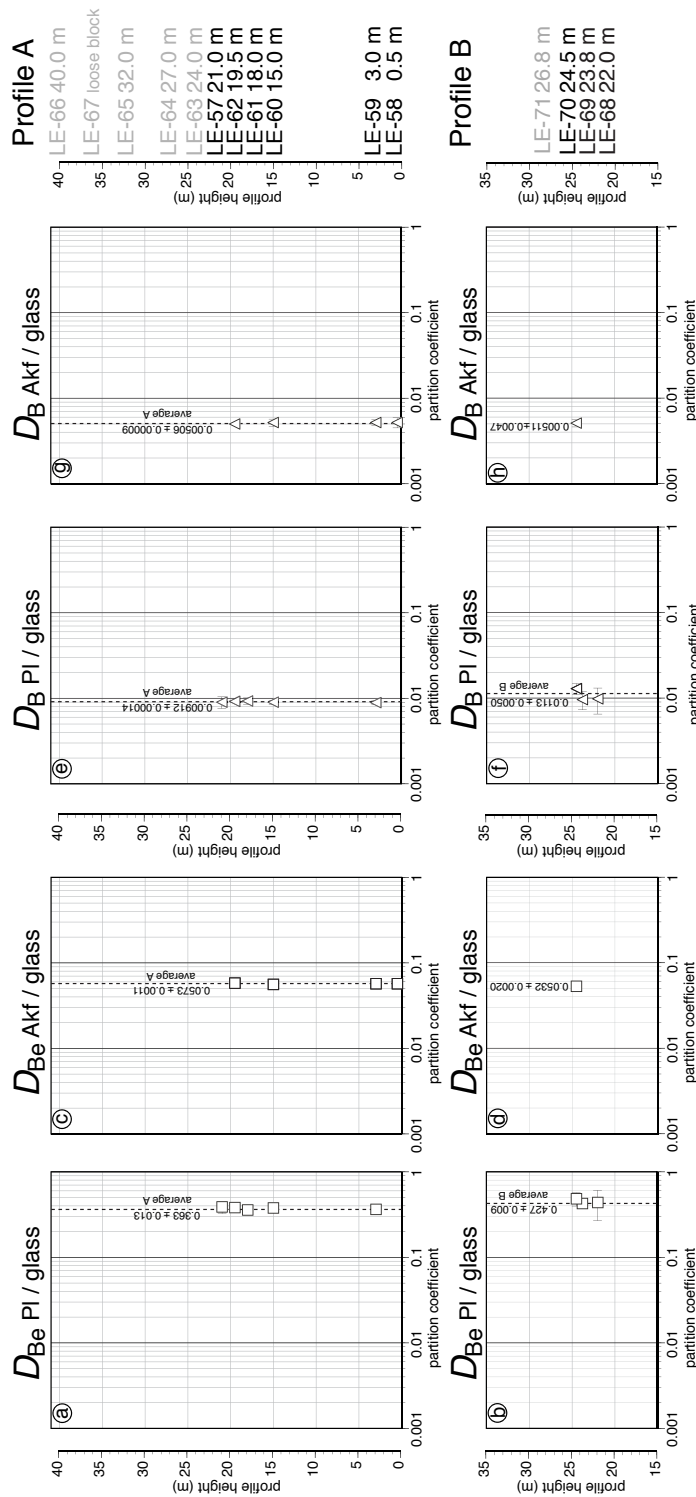


**Fig. 7.9.** Partition coefficients for PI and Akf in glass for Be, and B. Partition coefficients were calculated from average data for each sample and plotted against the profile height (m). Average partition coefficients are weighted means, errors are  $2\sigma$  standard errors. Partition coefficients have not been calculated for samples with devitrified glass, respective sample numbers are grey in the legend on the right. The data can be found in Table D.13 on page 302 in the appendix.

7.4. Partition coefficients for Beryllium and Boron

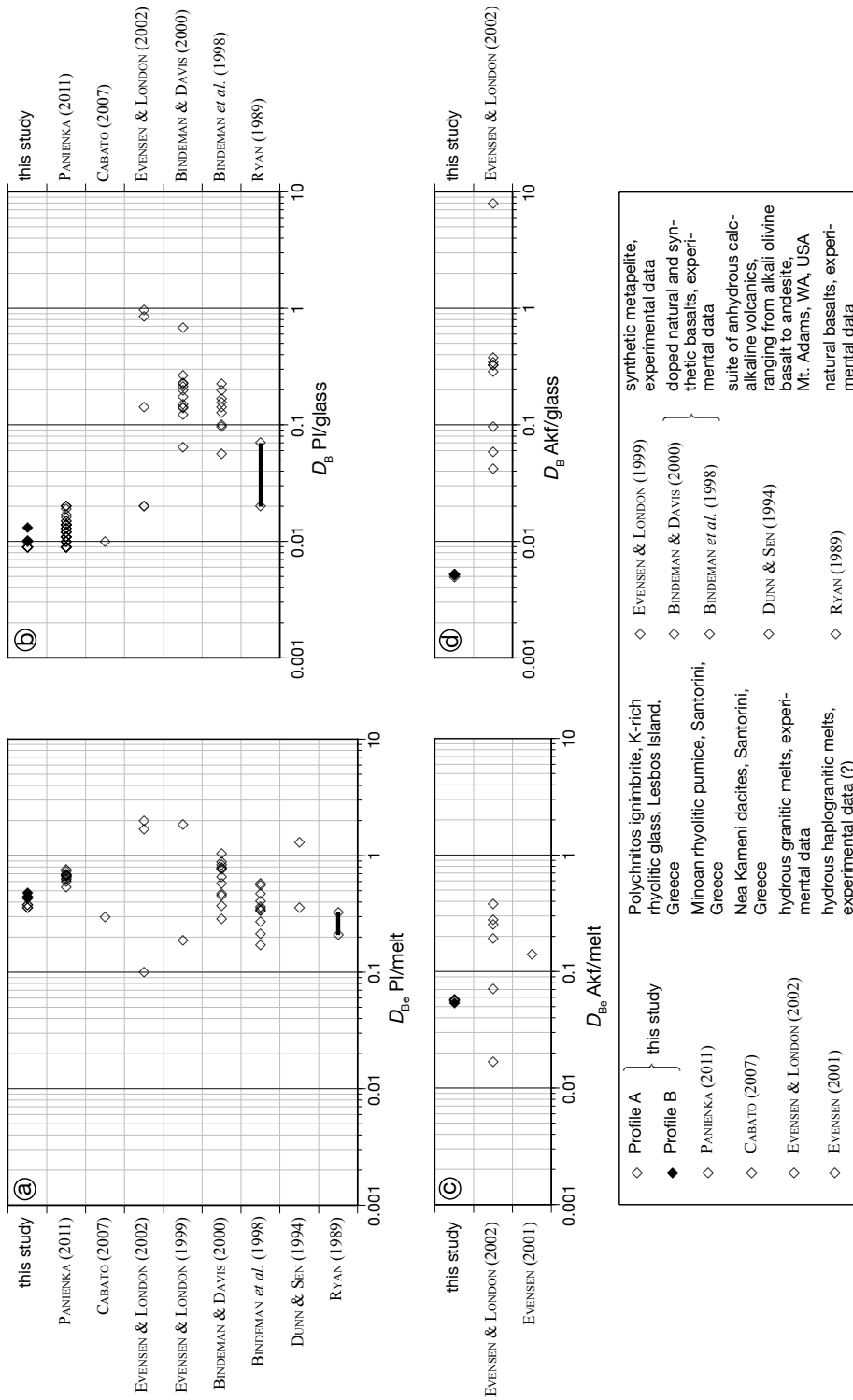


**Fig. 7.10.** Partition coefficients for Be, and B for PI/glass and Akf/glass (averages for each sample) from this study compared to literature data.

For  $D_{Be}$  Akf/glass only two other studies exist (EVENSEN & LONDON, 2002; EVENSEN, 2001), which again, show a much larger spread of data than this study, with values considerably lower and much higher (up to a whole order of magnitude).

For  $D_B$  Pl/glass and  $D_B$  Akf/glass EVENSEN & LONDON (2002); BINDEMAN & DAVIS (2000); BINDEMAN *et al.* (1998); RYAN (1989) show values up to three orders of magnitude higher than data from PANIENKA (2011), CABATO (2007) and data from this study.

All literature data and data from this study have been determined by secondary ion mass spectrometry. Analysis of trace elements and especially B at low concentration levels ( $< 5 \mu\text{g/g}$ ) has been proven prone to contamination. As described in the chapter “Analytical Methods” in section C.3.1 on page 273 in the appendix, a series of measures as described and tested for effectiveness in MARSCHALL & LUDWIG (2004) were taken at the Institut für Geowissenschaften, Universität Heidelberg to avoid contamination. Data from this study, from CABATO (2007), and PANIENKA (2011) were all analysed at the Institut für Geowissenschaften, Universität Heidelberg and have taken the steps necessary to avoid contamination. These three studies (this study; CABATO, 2007; PANIENKA, 2011) also incidentally show the lowest values  $D_B$  Pl/glass, so that the much higher values from older publications (RYAN, 1989; BINDEMAN *et al.*, 1998; BINDEMAN & DAVIS, 2000; EVENSEN & LONDON, 2002) could have possibly been caused by contamination. Other factors (An content, i.e. plagioclase composition, and temperature), which might have caused this large spread of values for  $D_B$  Pl/glass and  $D_B$  Akf/glass will be discussed later.

In previous studies (BINDEMAN *et al.*, 1998) a relationship between  $D_{Be}$  Pl/glass,  $D_B$  Pl/glass and the anorthite contents of Pl has been suggested. Therefore the partition coefficient from this study have all been plotted against the anorthite (An) content of Pl and the orthoclase (Or) content of Akf, respectively (Fig. 7.11).

For  $D_{Be}$  Pl/glass (Fig. 7.11 a & b), even for the small range of An contents covered by this study, a positive correlation between the partition coefficient and the An contents of the Pl can be seen. For  $D_B$  Pl/glass a slight positive correlation with An contents relies on one high value from LE-70, therefore this trend is doubtful for the dataset from this study. There is no correlation for partition coefficients  $D_{Be}$  Akf/glass and  $D_B$  Akf/glass (Fig. 7.11 c & d) with the Or content of Akf. A slight negative correlation between Or contents and  $D_{Be}$  Akf/glass could be suspected (Fig. 7.11 c), however the data range in this study is too small to be more definite about this.

Subsequently, the data from this study was compared to data from BINDEMAN *et al.* (1998) and other literature data in the same type of plots:  $D_{Be}$  Pl/glass and

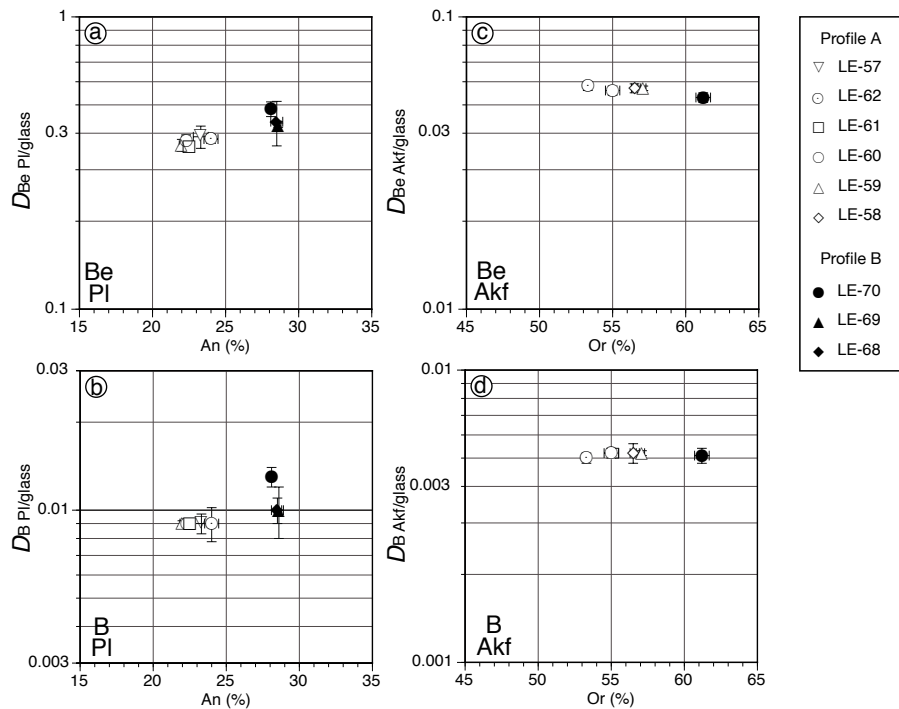


**Fig. 7.11.** Average partition coefficients for Be and B for PI/glass and Akf/glass plotted against average anorthite (An) and orthoclase (Or) contents of PI and Akf, respectively. Averages are arithmetic means, errors are  $2\sigma$  standard errors.

$D_{B}^{PI/glass}$  vs. An and  $D_{Be}^{Akf/glass}$  and  $D_{B}^{Akf/glass}$  vs. Or (Fig. 7.12). This could also potentially answer the question, if the difference between this study and literature data is caused by compositional differences or analytical issues.

For  $D_{Be}^{PI/glass}$  vs. An (Fig. 7.12 a) data from PANIENKA (2011) would fit a linear positive trend from this study very well, however, all other data do not fit in a systematic way. Unfortunately CABATO (2007) has been very vague about the An contents in her study, so the data point is only a rough approximation. The linear trend from BINDEMAN *et al.* (1998) does not fit any other data set, including that of BINDEMAN & DAVIS (2000), despite both studies using the same run-products and covering the same temperature range (1426 K to 1572 K).

For  $D_{B}^{PI/glass}$  vs. An (Fig. 7.12 b) data from PANIENKA (2011) and CABATO (2007) are in good agreement with this study. Despite the fact that the linear negative trend from BINDEMAN *et al.* (1998) seems to fit data from BINDEMAN & DAVIS (2000) all other literature data (BINDEMAN *et al.*, 1998; BINDEMAN & DAVIS, 2000; EVENSEN & LONDON, 2002) are one to two orders of magni-

7. Lithium, Beryllium, and Boron in glass and phenocrysts

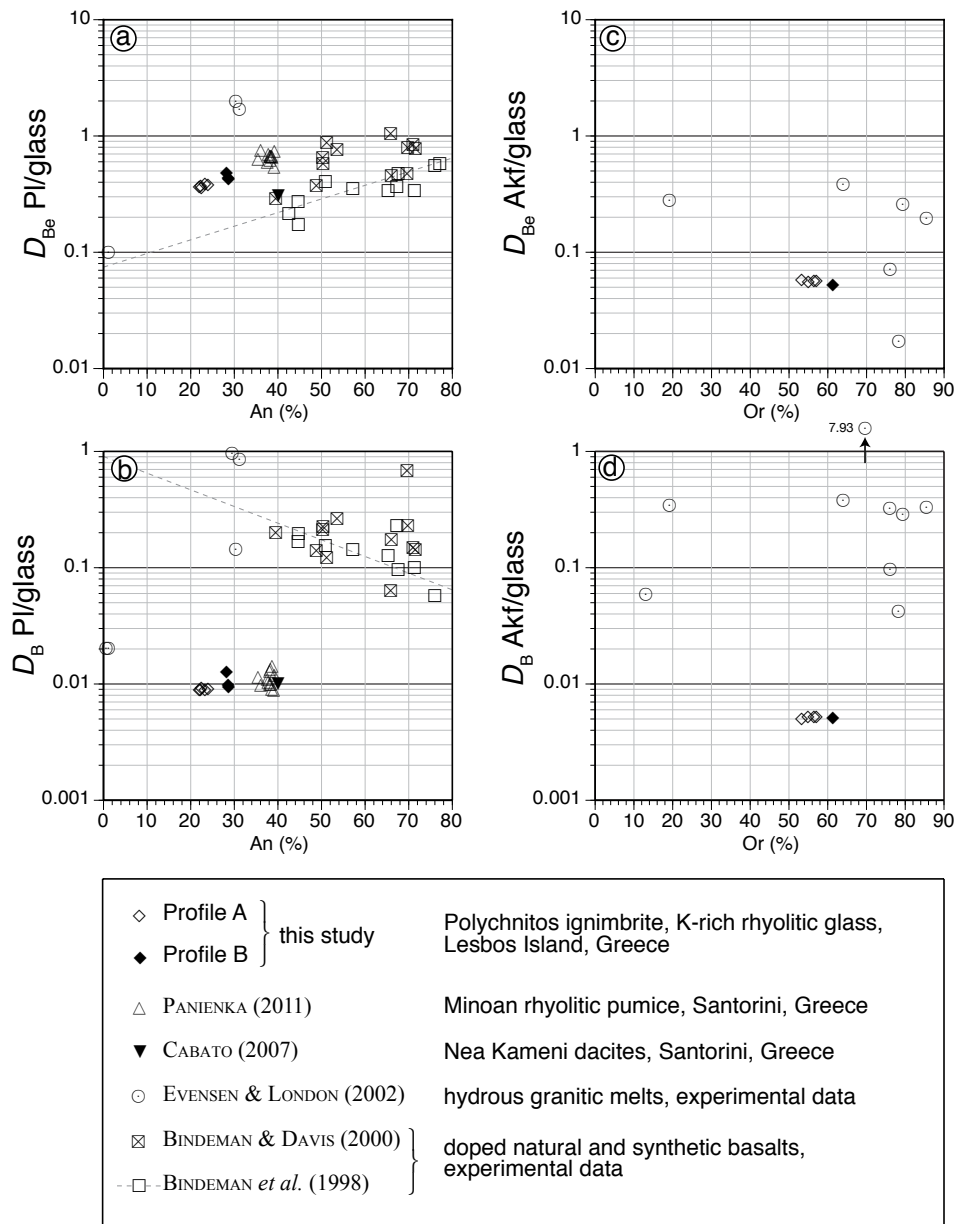


**Fig. 7.12.** Partition coefficients for Be and B for PI/glass and Akf/glass plotted against An and Or contents of PI and Akf, respectively, for this study in comparison to literature data. Broken lines are regression lines from BINDEMAN *et al.* (1998).

tude higher than data from the Universität Heidelberg (this study; CABATO, 2007; PANIENKA, 2011). Compositional differences (An contents) clearly cannot explain this difference, and neither can temperature differences. Experimental data from BINDEMAN & DAVIS (2000) and BINDEMAN *et al.* (1998) cover a high temperature range (1153 °C to 1299 °C), but experimental data from EVENSEN & LONDON (2002), with temperatures from 675 °C to 850 °C are in the same range as the temperature determined for data for this study ( $831 \pm 16$  °C,  $1\sigma$  standard deviation, see chapter 6 on page 99). Nevertheless, the pressure in experiments from EVENSEN & LONDON (2002) is at  $200 \pm 10$  MPa higher than the pressure determined for this study (75 MPa to 150 MPa).

It is likely that analytical problems with detecting B at low levels, as described before (page 122) play the major role in the much higher values for  $D_B$  Pl/glass in BINDEMAN *et al.* (1998); BINDEMAN & DAVIS (2000) and EVENSEN & LONDON (2002).

For  $D_{Be}$  Akf/glass vs. Or and  $D_B$  Akf/glass vs. Or (Fig. 7.12 c & d) the only available data for comparison from EVENSEN & LONDON (2002) does not plot in any systematic way. For  $D_B$  Akf/glass vs. Or the major source for the large difference of data from EVENSEN & LONDON (2002) to data from this study probably is once more the analytical problem with detecting B at low concentration levels.

The partition coefficients determined in this study (Table 7.1) for natural rocks from a well-confined geochemical background and from defined magma chamber conditions, constitute a reliable dataset for rhyolitic systems. They are based on data acquired following a well-grounded analytical protocol and can be used with confidence in other rhyolitic systems.

For  $D_{Be}$  Akf/glass and  $D_B$  Akf/glass data from this study are the only values from a natural system.

**Table 7.1.** Partition coefficients determined in this study for samples from Profile A and Profile B from the high-K rhyolitic Polychnitos Ignimbrite on Lesbos Island, Greece.

$D_{Be}$ Pl/glass	$D_{Be}$ Akf/glass	$D_B$ Pl/glass	$D_B$ Akf/glass
0.36 (An <sub>20</sub> )	0.06	0.009	0.005
0.43 (An <sub>28</sub> )			

### 7.5. Boron isotopes in the rhyolitic glass

The Boron isotopic composition of the volcanic glass has been determined, using a modified secondary ion mass spectrometer at the Institut für Geowissenschaften, Universität Heidelberg. Details about the analytical setup are found in section C.3.2 on page 274. Samples were chosen for their high initial glass content. Glass portions were prepared by separating large pieces of glass from selected samples, mounting in epoxy, and polishing. Results are displayed in Fig. 7.13.

The samples from Profile A and from Profile B do not show significantly different  $\delta^{11}\text{B}$  values, neither between their average data, nor between individual samples. However, the two glass pieces (I and II) of sample LE-9 from an additional location show significantly different values. While  $\delta^{11}\text{B}$  values from piece I are in agreement with the  $\delta^{11}\text{B}$  values from profile A and B,  $\delta^{11}\text{B}$  values for piece II are significantly higher than values of the vertical profiles and also higher than  $\delta^{11}\text{B}$  values for piece I. No explanation for this discrepancy has been found in the course of this study.

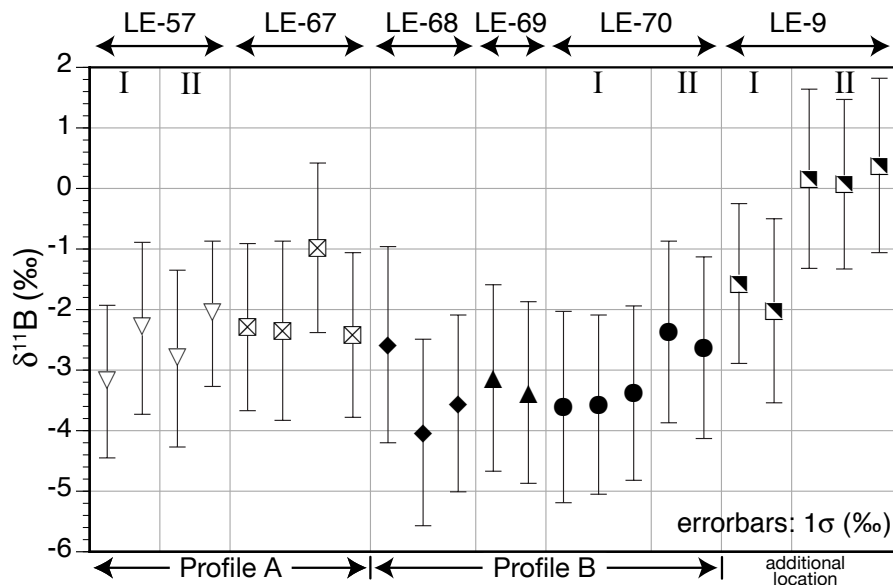


**Fig. 7.13.** Boron isotopic compositions of the rhyolitic glass in samples of Profile A and Profile B and a sample from an additional location. Roman numerals refer to different glass pieces of one samples, where more than one is available. Error bars are  $1\sigma$  standard error.

The Boron isotopic composition of the rhyolitic glass is relatively heavy with  $\delta^{11}\text{B}$  values of  $-2.30 \pm 1.28\text{‰}$  ( $1\sigma$ ) on average for samples from Profile A and  $\delta^{11}\text{B}$  of  $-3.22 \pm 1.07\text{‰}$  ( $1\sigma$ ) on average for samples from Profile B. These values are indistinguishable within error.

The advantage of B isotopes over Sr, Nd, or Pb isotopes is the capability to distinguish between (1) crustal contamination, i.e. contamination in the magma chamber from crustal wall rocks or during magma ascent in the crust or (2) slab signals, i.e. contamination of the magma source by melt or fluid from continental sediments (TONARINI *et al.*, 2005). These two scenarios are difficult to distinguish with Sr, Nd, or Pb isotopic signatures.

The  $\delta^{11}\text{B}$  value for mantle and MORB is under discussion, a large range of values has been published ( $\delta^{11}\text{B}$   $-10.5\text{‰}$  to  $+0.2\text{‰}$ , SPIVACK & EDMOND, 1987; ISHIKAWA & NAKAMURA, 1992; CHAUSSIDON & JAMBON, 1994; CHAUSSIDON & MARTY, 1995; RYAN *et al.*, 1996; MORIGUTI & NAKAMURA, 1998; LE ROUX *et al.*, 2004). Due to the low abundance of B in mantle rocks and primitive volcanics B isotope analyses are highly challenging. For a compilation of  $\delta^{11}\text{B}$  data see Table 7.2. A lab comparison study by GONFIANTINI *et al.* (2003) showed disastrous discrepancies between results from different labs, with differences of  $> 5\text{‰}$  for all investigated materials.

The function of  $\delta^{11}\text{B}$  as a tracer crucially depends on a reliable value for the unmodified mantle until that is established every interpretation will be somewhat questionable. Values from LE ROUX *et al.* (2004) were chosen in this study, as the most recent and analytically reliable, they are however based on only a small number of four MORB samples.

Continental crust ( $\delta^{11}\text{B}$   $-10 \pm 3\text{‰}$ , CHAUSSIDON & ALBARÈDE, 1992; KASEMANN *et al.*, 2000; MARSCHALL & LUDWIG, 2006) is isotopically lighter than mantle ( $\delta^{11}\text{B}$   $-7.7$  to  $-6.9\text{‰}$ , LE ROUX *et al.*, 2004), while altered oceanic crust is isotopically heavy through interaction with heavy sea water ( $\delta^{11}\text{B}$   $+39.61 \pm 0.04\text{‰}$ , FOSTER *et al.*, 2010) (Fig. 7.14). Melts generated from altered oceanic crust, island arc volcanic rocks (IAB) and continental arc volcanic rocks (CAB), are therefore generally isotopically heavier than mantle.

Hence, the magma source for the volcanic rocks from this study with their relatively heavy  $\delta^{11}\text{B}$  ( $-2.30 \pm 1.28\text{‰}$  to  $-3.22 \pm 1.07\text{‰}$ ) is corresponding to metasomatic enrichment by slab-derived fluids, but not to assimilation of material from the continental crust (Fig. 7.14). This is in agreement with earlier conclusion based on trace element ratios, Sr, Nd, and Pb isotopic composition and the high-K character of the glass. This is also in agreement with the interpretation of  $\delta^{11}\text{B}$  values for basaltic andesites of approximately the same age (21 to 15 Ma) from W Anatolia

## 7. Lithium, Beryllium, and Boron in glass and phenocrysts

**Table 7.2.** Compilation of literature data on B isotopic composition from different reservoirs.

Material	$\delta^{11}\text{B}_{\text{SRM951}} (\text{‰})$	Reference
Mantle/MORB	$-10.5 \dots +0.2$	Pre-2000: SPIVACK & EDMOND (1987); ISHIKAWA & NAKAMURA (1992); CHAUSSIDON & JAMBON (1994); CHAUSSIDON & MARTY (1995); RYAN <i>et al.</i> (1996); MORIGUTI & NAKAMURA (1998)
	$-7.7 \dots -6.9$	LE ROUX <i>et al.</i> (2004)
W Anatolian mantle; post-subduction	$-2$	TONARINI <i>et al.</i> (2005)
Continental Crust	$-10 \pm 3$	CHAUSSIDON & ALBARÈDE (1992); KASEMANN <i>et al.</i> (2000); MARSCHALL & LUDWIG (2006)
Modern seawater	$+39.61 \pm 0.04$	FOSTER <i>et al.</i> (2010)
Island arc volcanic rocks (IAB)		
Lesser Antilles	$-5.3 \dots +1.8$	SMITH <i>et al.</i> (1997)
Lesser Antilles	$+5.6 \dots +12.9$	GURENKO <i>et al.</i> (2005)
Kuriles	$-3.8 \dots +5.9$	ISHIKAWA & TERA (1997)
Tonga/Kermadec	$-11.6 \dots +37.6$	CLIFT <i>et al.</i> (2001)
Izu	$+4.6 \dots +12.0$	NAKAMURA <i>et al.</i> (1992); ISHIKAWA & NAKAMURA (1994); STRAUB & LAYNE (2002)
NE Japan	$-4.7 \dots +3.4$	MORIGUTI <i>et al.</i> (2004)
Halmahera arc	$-2.3 \dots +3.6$	PALMER (1991)
Aeolian Islands	$-6.1 \dots +2.3$	TONARINI <i>et al.</i> (2001)
South Sandwich Islands	$+12 \dots +18$	TONARINI <i>et al.</i> (2004b, 2011)
Continental arc volcanic rocks		
W Anatolia	$-15.0 \dots -0.1$	TONARINI <i>et al.</i> (2005)
Phlegrean Volc. District	$-10.6 \dots -2.8$	TONARINI <i>et al.</i> (2004a)
Phlegrean Volc. District	$-9.8 \dots -7.9$	TONARINI <i>et al.</i> (2009)
Central Andes	$-9.7 \dots +4.2$	SCHMITT <i>et al.</i> (2002); ROSNER <i>et al.</i> (2003)
Ecuadorian Andes	$-17.9 \dots +3.5$	LE VOYER <i>et al.</i> (2008)
El Salvadore	$-2.7 \dots +6.3$	TONARINI <i>et al.</i> (2007)
Washington Cascades	$-9.1 \dots -0.4$	LEEMAN <i>et al.</i> (2004)
Kamchatka	$-3.7 \dots +5.6$	ISHIKAWA <i>et al.</i> (2001)
Italy, Silicate rocks	$-9.6 \dots -5.6$	D'ORAZIO <i>et al.</i> (2007)
Italy, Cabonatites	$-5.9 \pm 0.5$	D'ORAZIO <i>et al.</i> (2007)

See also PALMER & SWIHART (2002) for a review on Boron isotope geochemistry.

( $\delta^{11}\text{B} -7.3 \text{‰}$  to  $-0.15 \text{‰}$ , TONARINI *et al.*, 2005).

When the average Boron isotope value is plotted against the average B contents of each sample (Fig. 7.15) samples from Profile A and from Profile B plot as two distinct groups. The two parameters are positively correlated so that samples with higher B contents have also higher  $\delta^{11}\text{B}$  values. This is in agreement with the influx of slab fluids containing B with a heavy  $\delta^{11}\text{B}$  signature ( $\delta^{11}\text{B} -5 \text{‰}$  to  $+20 \text{‰}$ , ROSNER *et al.*, 2003; MARSCHALL *et al.*, 2007).

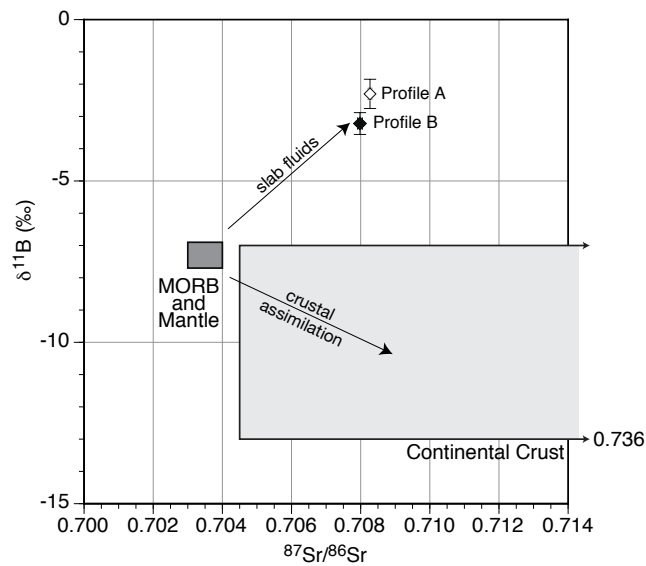


**Fig. 7.14.** Average boron isotopic compositions versus average boron content in rhyolitic glass in samples of Profile A and Profile B. Averages are arithmetic means, error bars are  $2\sigma$  standard error.  $^{87}\text{Sr}/^{86}\text{Sr}$  values for MORB/mantle and continental crust are from FAURE (1986),  $\delta^{11}\text{B}$  values for MORB/mantle from LE ROUX *et al.* (2004),  $\delta^{11}\text{B}$  values for continental crust from CHAUSSIDON & ALBARÈDE (1992); KASEMANN *et al.* (2000); MARSCHALL & LUDWIG (2006).

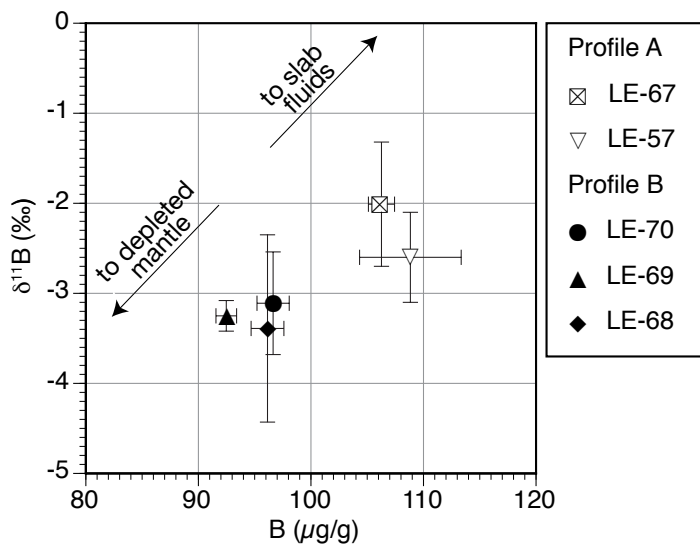


**Fig. 7.15.** Average boron isotopic compositions versus average boron content in rhyolitic glass in samples of Profile A and Profile B. Averages are arithmetic means, error bars are  $2\sigma$  standard error.



## 8. Conclusions

This study investigated the lithium, beryllium and boron systematics, i.e. concentrations, mineral profiles, and isotope ratios in samples from two vertical profiles and additional locations from a unit mapped as Polychnitos Ignimbrite on Lesbos Island, Greece. The Polychnitos Ignimbrite is an excellent study object, for its high contents of well-preserved glass and homogeneous geochemical make-up.

Mantle signatures, magma chamber conditions, melt evolution and post-depositional processes were investigated and provide a well-defined petrological, geochemical and isotopic background.

**The ignimbrite deposit / ignimbrite units** Samples from two different vertical profiles through the Polychnitos Ignimbrite show characteristic differences, that are irreconcilable with being part of the same ignimbrite unit. The two vertical profiles cannot be part of the same flow unit and they cannot even have originated from the same magma chamber. Therefore it is distinguished between Profile A and Profile B as representing two separate units of the Polychnitos Ignimbrite. (At the same time samples from the two vertical profiles closely resemble each other in glass and mineral composition and share some general petrographic characteristics)

The volcano-sedimentary stratigraphy of the Polychnitos Ignimbrite has been studied in an unpublished PhD thesis (LAMERA, 2004) at the University of Patras, Greece, which was not available for reference (chapter 2.5.6, p. 23; chapter 3.1, p. 29). Results from the thesis have so far only been reported in conference abstracts (LAMERA *et al.*, 2001, 2004a,b; ST. SEYMOUR *et al.*, 2004), which naturally lack sufficient documentation. Therefore, it was not possible to correlate the two vertical profiles from this study with eight cooling units proposed for the Polychnitos Ignimbrite by LAMERA *et al.* (2001, 2004a,b) and (ST. SEYMOUR *et al.*, 2004), which would have been beneficial. Please note, that all of these references were difficult to discover in the first place.

Yet, the location where all eight proposed cooling units outcrop superimposed on each other is described in LAMERA *et al.* (2001). A sample profile through all eight cooling units could provide an interesting future project, tracing differences and similarities for ignimbrite units from at least five proposed source vents (LAMERA *et al.*, 2001, 2004a,b; ST. SEYMOUR *et al.*, 2004).

Most of the eight cooling units are proposed to have separate source vents, some on Lesbos Island (Stipsi Caldera and Gulf Caldera) and some on the Turkish mainland (Bergama-İzmir area, Ayvacık area, Biga Peninsula, unspecified: Asia Minor; LAMERA *et al.*, 2001, 2004a,b; ST. SEYMOUR *et al.*, 2004). Despite the missing correlation of Profile A and Profile B with LAMERA *et al.*'s eight cooling units, this confirms the existence of individual units within the Polychnitos Ignimbrite with separate source vents (LAMERA *et al.*, 2001, 2004a,b; ST. SEYMOUR *et al.*, 2004) and probably magma plumbing systems, magma chambers, *et cetera*, as established in this study for ignimbrite units corresponding to Profile A and Profile B.

**Deposition and Cooling** Profile A changes over the profile height of 40m from an unwelded, grey to white coloured, ash tuff with pumice at the bottom into a densely welded, black, glassy ignimbrite deposit with fiamme at the top (chapter 3.3, p. 30).

Profile B is shorter, with a profile height of only 7 m. Throughout the whole sample range Profile B is densely welded and glassy, with fiamme and shows macroscopically no significant changes, despite a dramatic matrix colour change from pink to red and to black (chapter 3.4, p. 44).

Glass and phenocrysts in both ignimbrite units are considered to be in petrographic equilibrium, because glass selvages frequently attached to euhedral phenocrysts show the same chemical composition as glass in matrices and fiamme (chapter 4, p. 53; Fig. 7.8, p. 119).

Despite the physical changes throughout both of the vertical profiles, each profile is geochemically homogeneous, in pristine glass and mineral rim compositions, in main, minor and trace elements (chapter 4, p. 53), with the exception of lithium (chapter 7.2, p. 109).

Substantial Li diffusion was detected in minerals (plagioclase and alkali feldspar) and glass (large unwelded fragments) from Profile A, with differences between samples at the bottom and at the top of the profile (Figs. 7.4 & 7.5). The model developed in this study proposes considerable degassing of a Li-rich H<sub>2</sub>O vapour phase after the ignimbrite's deposition. The model suitably combines a number of observations (chapter 7.2, p. 113). The devitrification of the glass, which can be observed in both vertical profiles to increase towards each top, was caused by the Li-rich H<sub>2</sub>O vapour phase by hydrothermal "cooking".

Therefore the devitrification must have occurred immediately after deposition, it is not of a more recent date (e.g. weathering), and the devitrification took place under hot conditions. This is supported by findings from spherulites, which are

---

characteristic products of high-temperature devitrification and were documented in the matrices of samples from both profiles (chapter 3.3.3, p. 38, chapter 3.4.3, p. 46). The distinctive fan or bow-tie shape of the spherulites indicate devitrification temperatures of 400 – 650 °C (LOFGREN, 1971).

As a future project the temperature of the devitrification could be more precisely identified with an investigation of the devitrification products, for example with a TEM study, and used to pinpoint conditions for Li diffusion in glass and phenocrysts, and Li partitioning into the vapour phase.

Potassium has been shown to preserve the textures of pristine glass fragments after devitrification. This is evident in element distribution maps of a devitrified glass matrix (Fig. 4.3, p. 55). And while plagioclase and alkali feldspar seem unaffected by the hydrothermal “cooking” causing devitrification in the glass, biotite shows first signs of alterations. Biotite in samples with devitrified glass show a much larger chemical variation than biotite from samples with pristine glass (chapter 5.3, p. 96). Additionally in samples towards the top of Profile A it is much more common to find biotite with patchy zonation patterns, indicating secondary alteration (chapter 3.3.4, p. 42).

**Magma chamber** Conditions for samples from Profile A in the magma chamber were constrained to pressures between 75 MPa and 150 MPa, corresponding to a magma chamber depth between 2.6 km and 5.3 km at lithostatic conditions, and temperatures between 815 °C and 848 °C with the combination of different thermobarometric methods (chapter 6, p. 99).

Equilibrium between melt and phenocrysts was attained under these magma chamber conditions and partition coefficients between melt (glass) and plagioclase and alkali feldspar for Be and B were determined. Partition coefficients ( $D_{\text{Be Pl/glass}}$ ,  $D_{\text{B Pl/glass}}$ ,  $D_{\text{Be Akf/glass}}$ ,  $D_{\text{B Akf/glass}}$ ; chapter 7.4, p. 118) for natural rhyolitic rocks establish a well-founded data set. A positive correlation between  $D_{\text{Be Pl/glass}}$  and the An content of the plagioclase, which has been suggested previously (BINDEMAN *et al.*, 1998) was confirmed (Fig. 7.11 a, p. 123).

Cores and rims of plagioclase with substantially different An contents (cores An<sub>59–72</sub>; rims An<sub>19–25</sub>) were shown to be derived from a co-genetic magma using Sr isotopic analysis of selected plagioclase crystals (chapter 5.2, p. 92). The cores most likely stem from older volcanic rocks within the same magmatic system. This is independently valid for samples from Profile A and from Profile B. For samples from both vertical profiles Sr isotopic compositions of rim and cores are the same within error. However, the Sr isotopic compositions differ significantly between samples from the two vertical profiles. This is evidence for a separate origin of

samples from the two locations and will be referred to again below. A late contamination in the magma chamber or during magma ascent, from the basement or from young basalt injections seem highly unlikely for samples from both profiles in the face of the homogeneous Sr isotopic compositions of the plagioclase phenocrysts. Such a contamination event would have most probably introduced plagioclase or melt with a different Sr isotopic composition.

**Melt evolution** Samples from Profile A and Profile B do not share a common parent magma, and melt from Profile A has not evolved from melt from Profile B or vice versa. This was shown with trace element contents (Sr, Ba, Pb) in glass and minerals, and simple fractionation models (chapter 4.3, p. 74). The hypothesis of melt evolution by fractional crystallisation as suggested by the relationship of plagioclase and alkali feldspars in main element composition (chapter 4.1.1, p. 56), had to be abandoned.

Further proof against a common parent magma or evolution of one melt from the other are the different Sr isotopic compositions of plagioclase from Profile A and Profile B; i.e. fractional crystallisation could not have produced or explained the different Sr isotopic compositions in the corresponding melt A and melt B (chapter 5.2, p. 92).

A selection of trace element concentration and ratios (Be, B, Nd, Nb, Be/Nd, B/Nb) were compared to literature data for concentrations in upper continental crust (UCC; RUDNICK, 2005; TAYLOR & MCLENNAN, 2009) and indicate a 1.7- and 2.5-fold enrichment of the elements Be, Nd, and Nb, which are considered not to be fluid mobile. This enrichment could have been caused by a high degree of  $\approx 40\text{--}60\%$  fractional crystallisation, which is appropriate for rhyolitic volcanics. A higher differentiation of the samples is supported by a number of geochemical characteristics, such as the high concentration of  $\text{SiO}_2$  (chapter 4.2, p. 66). Trace element concentrations in Profile A and Profile B are very similar, except for a slight difference in B content.

Fluid-mobile elements, such as enrichment of B and the B/Nb ratio indicate fluid-metasomatic overprint of the magma source.

**Magma source** Boron, considered a highly fluid-mobile element, is enriched relative to UCC (RUDNICK, 2005; TAYLOR & MCLENNAN, 2009), as is the B/Nb ratio. This enrichment can be subdivided into one component by fractional crystallisation (see above) and a second component by fluid metasomatism (indicated in the B/Nb ratio, enriched by factor 2.8 to 3.1 with respect to UCC; RUDNICK, 2005; TAYLOR & MCLENNAN, 2009) (chapter 4.2, p. 66).

---

The calculated enrichment factors are given for an average B concentration of Profile A and Profile B (101  $\mu\text{g/g}$ ). The difference in B concentration between glass from the two profiles (Profile A: 107  $\mu\text{g/g}$ ; Profile B: 95  $\mu\text{g/g}$ ) would have only slightly changed B and B/Nb enrichment factors and would have led to the very same conclusions. The magma source for melts from both vertical profiles must have been subject to fluid metasomatism, as indicated by the large B enrichment.

Based on Nd, Sr and Pb isotopic composition of the glass, the magma or its source could have been subject to either (1) crustal contamination, i.e. contamination in the magma chamber from crustal wall rocks or during magma ascent in the crust or (2) slab signals, i.e. contamination of the magma source by melt or fluid derived from subducted continental sediments (chapter 4.4, p. 84). These two scenarios are difficult to distinguish in these isotope systems, however a distinction is possible with B isotopes (TONARINI *et al.*, 2005).

The magma source for the volcanic rocks from this study with their relatively heavy  $\delta^{11}\text{B}$  ( $-2.30 \pm 1.28\text{‰}$  to  $-3.22 \pm 1.07\text{‰}$ ) is corresponding to metasomatic enrichment by slab-derived fluids, but not to assimilation of material from the continental crust (chapter 7.5, p. 7.5). This is in agreement with the interpretation of  $\delta^{11}\text{B}$  values for basaltic andesites of approximately the same age (21 to 15 Ma) from W Anatolia ( $\delta^{11}\text{B}$   $-7.3\text{‰}$  to  $-0.15\text{‰}$ , TONARINI *et al.*, 2005).

This is also consistent with the geochemical character of the glass, enriched in the fluid mobile elements Cs, Rb, U, B, and K, also a sign for a mantle source enriched in fluids and therefore fluid mobile elements (chapter 4.2, p. 63; Fig. 4.12, p. 65).

The two vertical profiles through the Polychnitos Ignimbrite, Profile A and Profile B, belong to two separate ignimbrite units. The magma source area in the mantle of both profiles (both ignimbrite units) has been subject to metasomatism from slab fluids, prior to melting. The magma has been subject a considerable amount of fractional crystallisation, and has not been altered by assimilation of continental crust, neither during magma ascent, nor in the magma chamber. Both melts have assimilated plagioclase xenocrysts (evident from high-An cores) from a co-genetic magma, most probably from older volcanics from within the same volcanic plumbing system.

However, this must have happened independently for the two melts, they must ultimately originate from separate mantle regions, with a different Sr isotopic composition.



## Acknowledgements

**Heidelberg** First of all I would like to thank Prof. Dr. Rainer Altherr for being my supervisor for this project. I appreciate his hands-off approach to supervision, providing me with the opportunity to maintain an acceptable work-live balance with my family, while finishing this project over the course of many years to the level of quality very nearly to my satisfaction. (Apparently nobody is ever *fully* satisfied with his or her work) Yet, Rainer Altherr would always provide guidance when needed, initially at the department, but eventually over the distances of 1 000 km and more recently 6 000 km. Especially memorable is my full introduction to Greece, with food, people, customs, greek language and last but not least the pretty and pretty interesting rocks of Lesbos Island and the Polychnitos Ignimbrite. My love for Greece was founded there and then.

Thomas Ludwig is mentioned here firstly as the master of the SIMS, who made parts of this project possible in the first place and lastly as the one, who gave this book its physical form twice, providing the L<sup>A</sup>T<sub>E</sub>X-template and printing advice. In between these two major tasks he has been indispensable providing computer counselling, mathematical, physical, analytical, linguistic advice, and tea, coffee and cake.

Hans-Peter Meyer has with great skill adjusted microprobe analysis of the glass samples to the utmost quality, he has always helped with analytical questions and provided all mineral formula calculation programmes. Ilona Fin und Oliver Wien- and produced quality samples in all shapes and sizes, often marvelled at from Heidelberg “outsiders”.

Financial support was granted over the course of 18 months by a stipend from the women’s representative (Frauenbeauftragte) of the Universität Heidelberg to assist the recommencement of this study after my first daughter Helena’s birth. This support is greatly acknowledged.

**Bristol** The Department of Earth Sciences at the University of Bristol is immensely thanked for the four years of providing me with a much-needed work space, despite their constantly overcrowded department. Moreover, I was granted access to the library and computing facilities including all services, I could mingle in a lively scientific environment and share the burden of writing-up.

---

**Tübingen, Frankfurt, and Salzburg** Wolfgang Siebel at the Universität Tübingen performed TIMS analysis of Sr, Nd, and Pb and Yann Lahaye at the Universität Frankfurt operated LA-ICP-MS for trace elements and Sr Isotopes; both provided ample background information on analytical issues. Artur Benisek at the Universität Salzburg provided me with an Excel-Sheet for thermobarometric calculations and advice on the issue. A warm thanks to all three.

**Friends and Family** I greatly thank my mother, Herta Helbling, for all her assistance, be it to travel numerous times to Bristol, to provide us with greatly needed childcare and household support, and company, be it sending parcels with all we could wish for, or just finding the right words on the telephone. Her support alone made it possible, that I could make any progress during Horst's 2.5 month trip to Antarctica and his other absences. Thank you so much from all of us.

A great thanks to all participants of the successful Bristol-London-Exchange programme, especially to my write-up partner Katharina for her excellent idea and fantastic work-ethic.

Thanks to all, who have taken care of and entertained Helena and Yolanda, so that I could do science. Thank you Winnie Marschall "Winnie-Oma", Erich, Eva und Vera Marschall, Nastia Bezyazykova, Emily Lowe, Herta und Cordula Helbling, our wonderful Bristol childminder Jennie Andersen, the lovely staff at the extended day care programme of the St. Werburgh's Nursery, and our new friends on Cape Cod, Jill, Tor and Kalea, Patricia, Lola and Aisha, Martha, Julie, Petra, Tess and Nola, and the formidable multi-tasking WHOI secretary-"auntie" Suellen.

My lovely daughters Helena and Yolanda, to whom this thesis is dedicated for their life-long affiliation with this study, I thank you for your motivation and for your understanding, when it was so difficult for you to understand.

Last, but not least I wish to recognize the manifold functions my dear partner Horst had to carry out during the decade-long project. He accompanied me on my second tour to Lesbos Island and hugely assisted field-work, intellectually and physically. He has been my sustainer, motivator, co-supervisor, and 24/7 proof-reader; he has been demanding, soothing, supporting and boosting confidence. Danke, Mann!





## Bibliography

- Achterbergh E, Ryan CG, Jackson SE, Griffin WL (2001) Data reduction software for LA-ICP-MS. In: Sylvester P (ed.) *Laser-Ablation-ICPMS in the Earth Sciences, Principles and Application*, vol. 29 of *Short Course Series*, 239–243, Mineralogical Association of Canada
- Agostini S, Doglioni C, Innocenti F, Manetti P, Tonarini S (2010) On the geodynamics of the Aegean rift. *Tectonophysics* 488: 7–21, doi:10.1016/j.tecto.2009.07.025
- Aksu AE, Calon TJ, Piper DJW, Turgut A, Izdar E (1992) Architecture of late orogenic Quaternary basins in northeastern Mediterranean Sea. *Tectonophysics* 210: 191–213, doi:10.1016/0040-1951(92)90322-W
- Aldanmaz E, Pearce JA, Thirlwall MF, Mitchell JG (2000) Petrogenetic evolution of late Cenozoic, post-collision volcanism in western Anatolia, Turkey. *Journal of Volcanology and Geothermal Research* 102: 67–95, doi:10.1016/S0377-0273(00)00182-7
- Alici P, Temel A, Gourgaud A (2002) Pb-Nd-Sr isotope and trace element geochemistry of Quaternary extension-related alkaline volcanism: a case study of Kula region (western Anatolia, Turkey). *Journal of Volcanology and Geothermal Research* 115: 487–510, doi:10.1016/S0377-0273(01)00328-6
- Altherr R, Henjes-Kunst F, Matthews A, Friedrichsen H, Hansen BT (1988) O-Sr isotopic variations in Miocene granitoids from the Aegean: evidence for an origin by combined assimilation and fractional crystallization. *Contributions to Mineralogy and Petrology* 100: 528–541, doi:10.1007/BF00371381
- Altherr R, Keller J, Kott K (1976) Der jungtertiäre Monzonit von Kos und sein Kontakthof (Ägäis, Griechenland). *Bulletin Société Géologique de France* 18: 403–412
- Altherr R, Kreuzer H, Wendt I, Lenz H, Wagner G, Keller J, Harre W, Hoehndorf A (1982) A late Oligocene/early Miocene high temperature belt in the Attic-Cycladic crystalline complex (SE Pelagonian, Greece). *Geologisches Jahrbuch, Reihe E: Geophysik* 23: 97–164
- Altherr R, Siebel W (2002) I-type plutonism in a continental back-arc setting: Miocene granitoids and monzonites from the central Aegean Sea, Greece. *Contributions to Mineralogy and Petrology* 143: 397–415, doi:10.1007/s00410-002-0352-y
- Altunkaynak Ş, Yılmaz Y (1998) The Mount Kozak magmatic complex, Western Anatolia. *Journal of Volcanology and Geothermal Research* 85: 211–231, doi:10.1016/S0377-0273(98)00056-0
- Altunkaynak S, Yılmaz Y (1999) The Kozak Pluton and its emplacement. *Geological Journal* 34: 257–274

- Ambraseys NN (1970) Some Characteristic features of the Anatolian Fault Zone. *Tectonophysics* 9: 143–165
- Armijo R, Meyer B, King G, Rigo A, Papanastassiou D (1996) Quarternary evolution of the Corinth rift and its implications for the Late Cenozoic evolution of the Aegean. *Geophysical Journal International* 126: 11–53
- Aydar E (1998) Early Miocene to Quarternary evolution of volcanism and the basin formation in western Anatolia: a review. *Journal of Volcanology and Geothermal Research* 85: 69–82, doi:10.1016/S0377-0273(98)00050-X
- Bachmann O, Dungan MA, Bussy F (2005) Insights into shallow magmatic processes in large silicic magma bodies: the trace element record in the Fish Canyon magma body, Colorado. *Contributions to Mineralogy and Petrology* 149: 338–349, doi:10.1007/s00410-005-0653-z
- Baker DR (1992) Tracer diffusion of network formers and multicomponent diffusion in dacitic and rhyolitic melts. *Geochimica et Cosmochimica Acta* 56: 617–631, doi:10.1016/0016-7037(92)90086-X
- Barka AA, Reilinger R (1997) Active tectonics of the Eastern Mediterranean region: deduced from GPS, neotectonic and seismicity data. *Annali di Geofisica* 40: 587–610
- Barth MG, McDonough WF, Rudnick RL (2000) Tracking the budget of Nb and Ta in the continental crust. *Chemical Geology* 165: 197 – 213, doi:10.1016/S0009-2541(99)00173-4
- Le Bas MJ, Le Maitre RW, Streckeisen A, Zanettin B (1986) A chemical classification of volcanic rocks based on the total alkali – silica diagram. *Journal of Petrology* 27: 745–750
- Bédard JH (2006) Trace element partitioning in plagioclase feldspar. *Geochimica et Cosmochimica Acta* 70: 3717–3742, doi:10.1016/j.gca.2006.05.003
- Ben-Avraham Z, Kempler D, Ginzburg A (1988) Plate convergence in the Cyprean Arc. *Tectonophysics* 146: 231–240
- Benisek A, Dachs E, Kroll H (2010) A ternary feldspar-mixing model based on calorimetric data: development and application. *Contributions to Mineralogy and Petrology* 160: 327–337, doi:10.1007/s00410-009-0480-8
- Benisek A, Kroll H, L C (2004) New developments in two-feldspar thermometry. *American Mineralogist* 89: 1496–1504
- Benninghoven A, Rüdener FG, Werner HW (1987) *Secondary Ion Mass Spectrometry*. John Wiley & Sons, New York, Chichester, Brisbane, Toronto, Singapore
- Berlo K, Blundy J, Turner S, Cashman K, Hawkesworth CJ, Black S (2004) Geochemical precursors to volcanic activity at Mount. St. Helens, USA. *Nature* 306: 1167–1169
- Besenecker H, Pichler H (1974) Die jungen Vulkanite der Insel Chios (östliche Ägäis, Griechenland). *Geologisches Jahrbuch* 9: 41–65

- Bindeman IN, Davis AM (2000) Trace element partitioning between plagioclase and melt: investigation of dopant influence on partition behavior. *Geochimica et Cosmochimica Acta* 64: 2863–2878, doi:10.1016/S0016-7037(00)00389-6
- Bindeman IN, Davis AM, Drake MJ (1998) Ion microprobe study of plagioclase-basalt partition experiments at natural concentration levels of trace elements. *Geochimica et Cosmochimica Acta* 62: 1175–1193, doi:10.1016/S0016-7037(98)00047-7
- Blundy JD, Wood BJ (1991) Crystal-chemical controls on the partitioning of Sr and Ba between plagioclase feldspar, silicate melts, and hydrothermal solutions. *Geochimica et Cosmochimica Acta* 55: 193 – 209, doi:10.1016/0016-7037(91)90411-W
- Borsi S, Ferrara G, Innocenti F, Mazzuoli R (1972) Geochronology and petrology of recent volcanics in the Eastern Aegean Sea (West Anatolia and Lesvos Island). *Bulletin of Volcanology* 3: 473–496, doi:10.1007/BF02597122
- Boynton WV (1985) Developments in Geochemistry. In: *Rare Earth Element Geochemistry*, vol. 115, Elsevier
- Bozkurt E (2001) Neotectonics of Turkey – a synthesis. *Geodinamica Acta* 14: 3–30
- Bozkurt E, Winchester JA, Piper JDA (2000) Introduction. In: Bozkurt E, Winchester JA, Piper JDA (eds.) *Tectonic and Magmatism in Turkey and the Surrounding Area*, vol. 173 of *Geological Society Special Publication*, vii–xvii, The Geological Society
- Cabato MEJA (2007) *Abundances of Lithium, Beryllium and Boron in Phenocrysts from Santorini Volcano (Greece): Implications on Magma Genesis and Eruption Mechanisms*. Dr. rer. nat. thesis, Universität Heidelberg, Heidelberg, Germany
- Catanzaro F, Champion C, Garner E, Marinenko G, Sappenfield K, Shields W (1970) Boric acid: isotopic and assay standard reference materials. *National Bureau of Standards (US) Special Publications* 260: 1–70
- Chaussidon M, Albarède F (1992) Secular boron isotope variations in the continental crust: an ion microprobe study. *Earth and Planetary Science Letters* 108: 229–241, doi:10.1016/0012-821X(92)90025-Q
- Chaussidon M, Jambon A (1994) Boron content and isotopic composition of oceanic basalts: Geochemical and cosmochemical implications. *Earth and Planetary Science Letters* 121: 277–291, doi:10.1016/0012-821X(94)90073-6
- Chaussidon M, Marty B (1995) Primitive boron isotope composition of the mantle. *Science* 269: 383–386
- Clift PD, Rose EF, Shimizu N, Layne GD, Draut AE, Regelous M (2001) Tracing the evolving flux from the subducting plate in the Tonga-Kermadec arc system using boron in volcanic glass. *Geochimica et Cosmochimica Acta* 65: 3347–3364, doi:10.1016/S0016-7037(01)00670-6
- Coogan LA, Kasemann SA, Chakraborty S (2005) Rates of hydrothermal cooling of new oceanic upper crust derived from lithium-geospeedometry. *Earth and Planetary Science Letters* 240: 415 – 424, doi:10.1016/j.epsl.2005.09.020
- DePaolo DJ (1988) *Neodymium Isotope Geochemistry*. Springer Verlag, Berlin, Stuttgart

- DePaolo DJ, Wasserburg GJ (1976a) Inferences about Magma Sources and Mantle Structure from Variations of  $^{143}\text{Nd}/^{144}\text{Nd}$ . *Geophysical Research Letters* 3: 743–746, doi:10.1029/GL003i012p00743
- DePaolo DJ, Wasserburg GJ (1976b) Nd isotope variations and petrogenetic models. *Geophysical Research Letters* 3: 249–252, doi:10.1029/GL003i012p00743
- Dercourt J, Ricou L-E, Vrielynck B (eds.) (1993) *Atlas Tethys Palaeoenvironmental Maps*. Gauthier-Villars, Paris
- Dercourt J, Zonenshain LP, Ricou L-E, Kazmin VG, Le Pichon X, Knipper AL, Grandjacquet C, Sbertshikov IM, Geysant J, Lepvrier C, Pechersky DH, Boulin J, Sibuet J-C, Savostin LA, Sorokhtin O, Westphal M, Bazhenov ML, Lauer JP, Biju-Duval B (1986) Geological evolution of the Tethys belt from the Atlantic to the Pamirs since the Lias. *Tectonophysics* 123: 241–315
- Dewey JF, Hempton MR, Kidd WSF, Şaroğlu F, Şengör AMC (1986) Shortening of continental lithosphere: the neotectonics of Eastern Anatolia – a young collision zone. *Geological Society, London, Special Publications* 19: 3–36, doi:10.1144/GSL.SP.1986.019.01.01
- Dewey JF, Şengör AMC (1979) Aegean and surrounding regions: complex multiplate and continuum tectonics in convergent zone. *Bulletin of the Geological Society of America* 90: 84–92
- Dewey JW (1976) Seismicity of Northern Anatolia. *Bulletin of the Seismological Society of America* 66: 843–868
- Dinter DA (1998) Late Cenozoic extension of the Alpine collisional orogen, northeastern Greece: Origin of the north Aegean basin. *Geological Society of America Bulletin* 110: 1208–1230
- Doglioni C, Agostini S, Crespi M, Innocenti F, Manetti P, Riguzzi F, Savasci Y (2002) On the extension in western Anatolia and the Aegean sea. *Journal of the Virtual Explorer* 8, doi:10.3809/jvirtex.2002.00049
- D’Orazio M, Innocenti F, Tonarini S, Doglioni C (2007) Carbonatites in a subduction system: The Pleistocene alvikites from Mt. Vulture (southern Italy). *Lithos* 98: 313–334, doi:10.1016/j.lithos.2007.05.004
- Patiño Douce AE (1997) Generation of metaluminous A-type granites by low-pressure melting of calc-alkaline granitoids. *Geology* 25: 743–745
- Patiño Douce AE, Beard JS (1996) Effects of  $P$ ,  $f(\text{O}_2)$  and Mg/Fe ratio on dehydration melting of model metagreywackes. *Journal of Petrology* 37: 999–1024
- Patiño Douce AE, McCathy TC (1998) Melting of crustal rocks during continental collision and subduction. In: Hacker B, Liou J (eds.) *When Continents Collide: Geodynamics and Geochemistry of Ultrahigh-Pressure Rocks*, chap. 2, 27–55, Kluwer Academic Publishers
- Dunn T, Sen C (1994) Mineral/matrix partition coefficients for orthopyroxene, plagioclase, and olivine in basaltic to andesitic systems: A combined analytical and experimental

- study. *Geochimica et Cosmochimica Acta* 58: 717–733, doi:10.1016/0016-7037(94)90501-0
- Dürr S, Jakobshagen V, Wallbrecher E (1986) Ostägäische Inseln. In: Jakobshagen V (ed.) *Geologie von Griechenland*, vol. 19 of *Beiträge zur regionalen Geologie der Erde*, chap. 2.6, 169–187, Gebrüder Borntraeger, Berlin, Stuttgart
- Dyar MD, Wiedenbeck M, Robertson D, Cross LR, Delaney JS, Ferguson K, A FC, Grew ES, Guidotti CV, Hervig RL, Hughes JM, Husler J, Leeman W, McGuire AV, Rhede D, Rothe H, Paul RL, Richards I, Yates M (2001) Reference minerals for the microanalysis of light elements. *Geostandards Newsletter: the Journal of Geostandards and Geoanalysis* 25: 441–463, doi:10.1111/j.1751-908X.2001.tb00616.x
- Erkül F, Helvacı C, Sözbilir H (2005) Evidence for two episodes of volcanism in the Bigadiç borate basin and tectonic implications for western Turkey. *Geological Journal* 40: 545–570, doi:10.1002/gj.1026
- Evensen JM (2001) *The geochemical budget of beryllium in silicic melts, and superliquidus, subliquidus, and starting state effects on the kinetics of crystallization in hydros haplogranite melts*. Ph.D. thesis, University Oklahoma, Norman, OK, USA
- Evensen JM, London D (1999) Beryllium reservoirs and sources for granitic melt: The significance of cordierite. In: *1999 GSA Annual Meeting, Denver, Colorado, Abstract with Program*, vol. 31, 305
- Evensen JM, London D (2002) Experimental silicate mineral/melt partition coefficients for beryllium and the crustal Be cycle from migmatite to pegmatite. *Geochimica et Cosmochimica Acta* 66: 2239–2265, doi:10.1016/S0016-7037(02)00889-X
- Evensen JM, London D, Wendlandt RF (1999) Solubility and stability of beryl in granitic melts. *American Mineralogist* 84: 733–745
- Ewart (1982) The mineralogy and petrology of Tertiary–Recent orogenic volcanic rocks: with special reference to the andesitic-basaltic compositional range. In: Thorpe RS (ed.) *Andesites*, 25–87, John Wiley & Sons
- Faure G (1986) *Principles of Isotope Geology*. John Wiley & Sons, New York, Chichester, Brisbane, Toronto, Singapore, 2nd edn.
- Favre P, Stampfli G (1992) From rifting to passive margin: the examples of the Red Sea, Central Atlantic and Alpine Tethys. *Tectonophysics* 215: 69–97, doi:10.1016/0040-1951(92)90075-H, geodynamic of Rifting, Volume III. Thematic Discussions
- Flerit F, Armijo R, King G, Meyer B (2004) The mechanical interaction between the propagating North Anatolian Fault and the back-arc extension in the Aegean. *Earth and Planetary Science Letters* 224: 347–362
- Flerit F, Armijo R, King GCP, Meyer B, Barka A (2003) Slip partitioning in the Sea of Marmara pull-apart determined from GPS velocities vectors. *Geophysical Journal International* 154: 1–7

- Foster GL, Pogge von Strandmann PAE, Rae JWB (2010) Boron and magnesium isotopic composition of seawater. *Geochemistry Geophysics Geosystems (G3)* 11, doi:10.1029/2010GC003201
- Freundt A, Wilson CNJ, Carey SN (2000) Ignimbrites and block-and-ash flow deposits. In: Sigurdsson H, Houghton B, McNutt S, Rymer H, Stix J (eds.) *Encyclopedia of Volcanoes*, 581–599, Academic Press, San Diego
- Fytikas M, Giuliani O, Innocenti F, Manetti P, Mazzuoli R, Peccerillo A, Villari L (1979) Neogene volcanism of the Northern and Central Aegean region. *Annales Géologiques des Pays Hélieniques* 30: 106–129
- Fytikas M, Giuliani O, Innocenti F, Marinelli G, Mazzuoli R (1976) Geochronological data on recent magmatism of the Aegean Sea. *Tectonophysics* 31: T29–T34
- Fytikas M, Innocenti F, Manetti P, Mazzuoli R, Peccerillo A, Villari L (1984) Tertiary to Quarternary evolution of volcanism in the Aegean region. *Geological Society, London, Special Publications* 17: 687–699, doi:10.1144/GSL.SP.1984.017.01.55
- Gallagher K, Elliott T (2009) Fractionation of lithium isotopes in magmatic systems as a natural consequence of cooling. *Earth and Planetary Science Letters* 278: 286–296, doi:10.1016/j.epsl.2008.12.009
- Garfunkel Z (1991) Internal structure of the Dead Sea Leaky Transform (Rift) in relation to plate kinematics. *Tectonophysics* 80: 81–108
- Gautier P, Brun JP, Moriceau R, Sokoutis D, Martinod J, Jolivet L (1999) Timing, kinematics and cause of Aegean extension: a scenario based on a comparison with simple analogue experiments. *Tectonophysics* 315: 31–72, doi:10.1016/S0040-1951(99)00281-4
- Genç ŞC (1998) Evolution of the Bayramiş magmatic complex, northwestern Anatolia. *Journal of Volcanology and Geothermal Research* 85: 233–249, doi:10.1016/S0377-0273(98)00057-2
- Georgalas GC (1949) Contribution à la connaissance des roches eruptives d'île de Mételin. *Bulletin Volcanologique* 9: 31–63
- Giletti BJ, Shanahan TM (1997) Alkali diffusion in plagioclase feldspar. *Chemical Geology* 139: 3 – 20, doi:10.1016/S0009-2541(97)00026-0
- Glover C, Robertson AHF (1998) Neotectonic intersection of the Aegean and Cyprus tectonic arcs: extensional and strike-slip faulting in the Isparta Angle, SW Turkey. *Tectonophysics* 298: 103–132
- Gonfiantini R, Tonarini S, Gröning M, Adorni-Braccesi A, Al-Ammar AS, Astner M, Bächler S, Barnes RM, Bassett RL, Cocherie A, Deyhle A, Dini A, Ferrara G, Gaillardet J, Grimm J, Guerrot C, Krähenbühl U, Layne G, Lemarchand D, Meixner A, Northington DJ, Pennisi M, Reitznerová E, Rodushkin I, Sugiura N, Surberg R, Tonn S, Wiedenbeck M, Wunderli S, Xiao Y, Zack T (2003) Intercomparison of Boron Isotope and Concentration Measurements. Part II: Evaluation of Results. *Geostandards Newsletter: The Journal of Geostandards and Geoanalysis* 27: 41–57, doi:10.1111/j.1751-908X.2003.tb00711.x

- Görür N, Şengör AMC, Sakin M, Tüysüz O, Akkök R, Yiğitbaş E, Oktay FY, Barka A, Sarınca N, Ecevitoglu B, Demirbağ E, Ersoy Ş, Algan O, Güneysu C, Akyol A (1995) Rift deformation in the Gökova region, southwest Anatolia: implications for the opening of the Aegean Sea. *Geological Magazine* 132: 637–650
- Güleç N (1991) Crust-Mantel interaction in Western Turkey: implications from Sr and Nd isotope geochemistry. *Geological Magazine* 128: 417–435
- Gurenko AA, Trumbull RB, Thomas R, Lindsay JM (2005) A melt inclusion record of volatiles, trace elements and Li-B isotope variations in a single magma system from the Plat Pays Volcanic Complex, Dominica, Lesser Antilles. *Journal of Petrology* 46: 2495–2526, doi:10.1093/petrology/egi063
- Harrison TM, Watson EB (1984) The behavior of apatite during crustal anatexis: Equilibrium and kinetic considerations. *Geochimica et Cosmochimica Acta* 48: 1467 – 1477, doi:10.1016/0016-7037(84)90403-4
- Harsch W, Küpfer T, Rast B, Sägger R (1981) Seismotectonic considerations on the nature of the Turkish-African plate boundary. *Geologische Rundschau* 70: 368–384
- Hart SR (1984) A large-scale isotope anomaly in the Southern Hemisphere mantle. *Nature* 309
- Hatzipanagiotou K, Pe-Piper G (1995) Ophiolitic and sub-ophiolitic metamorphic rocks from the Vatera area, southern Lesbos (Greece): geochemistry and geochronology. *Ophioliti* 20: 17–29
- von Hauer F (1873) Analysen von Felsarten von Mytilini. *Verhandlungen der geologischen Reichsanstalt* 1883: 218–222
- Hecht J (1972–1975) Geological Map of Lesbos, 1:50 000. Plomari-Mytilini, Ayia Paraskevi, Mithimna, Polychnitos and Eressos sheets.
- Hempton MR (1985) Structure and deformation history of the Bitlis suture near Lake Hazar, southeastern Turkey. *Geological Society of America Bulletin* 96: 233–243
- Henjes-Kunst F, Altherr R, Kreuzer H, Hansen BT (1988) Disturbed U—Th—Pb systematics of young zircons and uranorhites: The case of the Miocene Aegean Granitoids (Greece). *Chemical Geology: Isotope Geoscience section* 73: 125 – 145, doi:10.1016/0168-9622(88)90011-5
- Hepp S, Altherr R, Kalt A, Ludwig T (2004) Li, Be and B in amphibolites from the Schwarzwald (Germany). *Supplement issue to Geochimica et Cosmochimica Acta* 68: A41
- Hezel DC, Kalt A, Marschall HR, Ludwig T, Meyer H-P (2011) Major-element and Li, Be compositional evolution of tourmaline in an S-Type granite-pegmatite system and its country rocks: an example from Ikaria, Aegean Sea, Greece. *The Canadian Mineralogist* 49: 321–340
- Hillers M, Altherr R, Ludwig T, Meyer H-P, Marschall HR, Kasztovszky Zs, Gméling K (2009) Lithium, beryllium and boron in I-type granitoids from the Aegean Sea, Greece. *Contributions to Mineralogy and Petrology* submitted

- Holtz F, Behrens H, Dingwell DB, Johannes W (1995) H<sub>2</sub>O solubility in haplogranitic melts: Compositional, pressure, and temperature dependence. *American Mineralogist* 80: 94–108
- Horváth F, Berckhemer H (1982) Mediterranean Geodynamics. In: Berckhemer H, Hsü K (eds.) *Alpine Mediterranean Geodynamics*, vol. 7, 131–173, American Geophysical Union
- Icenhower J, London D (1996) Experimental partitioning of Rb, Cs, Sr, and Ba between alkali feldspar and peraluminous melt. *American Mineralogist* 81: 719–734
- Innocenti F, Agostini S, Di Vincenzo G, Doglioni C, Manetti P, Savaşçin MY, Tonarini S (2005) Neogene and Quaternary volcanism in Western Anatolia: Magma sources and geodynamic evolution. *Marine Geology* 221: 397–421, doi:10.1016/j.margeo.2005.03.016
- Ishikawa T, Nakamura E (1992) Boron isotope geochemistry of the oceanic crust from DSDP/ODP Hole 504B. *Geochimica et Cosmochimica Acta* 56: 1633–1639, doi:10.1016/0016-7037(92)90230-G
- Ishikawa T, Nakamura E (1994) Origin of the slab component in arc lavas from across-arc variation of B and Pb isotopes. *Nature* 370: 205–208, doi:10.1038/370205a0
- Ishikawa T, Tera F (1997) Source, composition and distribution of the fluid in the Kurile mantle wedge: Constraints from across-arc variations of B/Nb and B isotopes. *Earth and Planetary Science Letters* 152: 123–138, doi:10.1016/S0012-821X(97)00144-1
- Ishikawa T, Tera F, Nakazawa T (2001) Boron isotope and trace element systematics of the three volcanic zones in the Kamchatka arc. *Geochimica et Cosmochimica Acta* 65: 4523–4537, doi:10.1016/S0016-7037(01)00765-7
- Jambon A, Semet MP (1978) Lithium diffusion in silicate glasses of albite, orthoclase, and obsidian composition: An ion-microprobe determination. *Earth and Planetary Science Letters* 37: 445 – 450, doi:10.1016/0012-821X(78)90060-2
- Jeffcoate A, Elliott T, Kasemann S, Ionov D, Cooper K, Brooker R (2007) Li isotope fractionation in peridotites and mafic melts. *Geochimica et Cosmochimica Acta* 71: 202–218, doi:10.1016/j.gca.2006.06.1611
- Jolivet L (2001) A comparison of geodetic and finite strain pattern in the Aegean, geodynamic implications. *Earth and Planetary Science Letters* 187: 95–104
- Kahle H-G, Straub C, Reilinger, McClusky S, King R, Hurst K, Veis G, Kastens K, Cross P (1998) The strain estimates in the Eastern Mediterranean region, estimated by repeated GPS measurements. *Tectonophysics* 294: 237–252
- Kaliwoda M (2004) *Petrologie und Li-, Be- und B-Systematik von Mantelxenolithen aus dem Harrat Uwayrid (Saudi Arabien)*. Dr. rer. nat. thesis, Universität Heidelberg, Germany
- Kaliwoda M, Altherr R, Ludwig T (2004) Metasomatic phenomena and Li-Be-B characteristics of mantle xenoliths from Harrat Uwayrid, Saudi Arabia. *Supplement issue to Geochimica et Cosmochimica Acta* 68: A53

- Kaliwoda M, Ludwig T, Altherr R (2008) A new SIMS study of Li, Be, B and  $\delta^7\text{Li}$  in mantle xenoliths from Harrat Uwayrid (Saudi Arabia). *Lithos* 106: 261–279
- Kaliwoda M, Marschall HR, Marks MAW, Ludwig T, Altherr R, Markl G (2011) Boron and boron isotope systematics in the peralkaline Ilímaussaq intrusion (South Greenland) and its granitic country rocks: a record of magmatic and hydrothermal processes. *Lithos* 125: 51–64
- Kasemann S, Erzinger J, Franz G (2000) Boron recycling in the continental crust of the central Andes from the Palaeozoic to Mesozoic, NW Argentina. *Contributions to Mineralogy and Petrology* 140: 328–343, doi:10.1007/s004100000189
- Katsikatsos G, Mataragas D, Migiros G, Triantaphyllis E (1982) Geological study of Lesvos Island. IGME internal report Athens
- Kelepertsis AE, Esson J (1987) Major- and trace-element mobility in altered volcanic rocks near Stypsi, Lesbos, Greece and genesis of a kaolin deposit. *Applied Clay Sciences* 2: 11–28
- Kempler D, Garfunkel Z (1994) Structures and kinematics in the northeastern Mediterranean: A study of an irregular plate boundary. *Tectonophysics* 234: 19–32
- Kent AJ, Blundy J, Cashman KV, Cooper KM, Donnelly C, Pallister JS, Reagan M, Rowe MC, Thornber CR (2007) Vapor transfer prior to the October 2004 eruption of Mount St. Helens, Washington. *Geology* 35: 213–234, doi:10.1130/G22809A.1
- Ketin İ (1966) Tectonic units of Anatolia (Asia Minor). *Bulletin of the Mineral Research and Exploration Institute of Turkey* 66: 23–34
- Kiratzi AA (1993) A study on the active crustal deformation of the North and East Anatolian fault zones. *Tectonophysics* 225: 191–203
- Kissel C, Laj C (1988) The Tertiary geodynamical evolution of the Aegean arc: a paleomagnetic reconstruction. *Tectonophysics* 146: 183–201
- Koçyiğit A, Yusufğlu H, Bozkurt E (1999) Evidence from the Gediz Graben for episodic two-stage extension in western Turkey. *Journal of the Geological Society (London)* 159: 605–616
- Kouli M, St. Seymour K (2006) Contribution of remote sensing techniques to the identification and characterization of Miocene calderas, Lesvos Island, Aegean Sea, Hellas. *Geomorphology* 77: 1–16, doi:10.1016/j.geomorph.2005.12.006
- Kuritani T, Nakamura E (2006) Elemental fractionation in lavas during post-eruptive degassing: Evidence from trachytic lavas, Rishiri Volcano, Japan. *Journal of Volcanology and Geothermal Research* 149: 124 – 138, doi:10.1016/j.jvolgeores.2005.06.008
- Lamera S (2004) *The Geochemistry and Volcanic Stratigraphy of the Polychnitos Ignimbrite Sheet, Lesvos, Hellas*. unpublished PhD thesis, University of Patras, Patras, Greece
- Lamera S, Seymour KS, Vamvourakis C, Kouli M, Paraskevas E, Pe-Piper G (2001) The Polychnitos Ignimbrite of Lesvos Island. In: *Proceedings of the 9th International Congress, Athens, September 2001*, vol. 34, 917–921

- Lamera S, St. Seymour K, Kouli M, Vamvoukakis K (2004a) The stratigraphy, geochemistry and sources of the Polychnitos Ignimbrite, Lesvos Island, Hellas. In: *32nd IGC - Florence*
- Lamera S, Tzortzi J, Zelilidis A, St. Seymour K, Kouli M, Vamvoukakis C (2004b) A Lahar-like deposit at the sole of the Polychnitos Ignimbrite, Lesvos volcanic field Northern Aegean, Hellas. In: *Proceeding of the 7th Pan-Hellenic Geographical Congress of the Hellenic Geographical Society in Mytilini, Greece*, E1H116, 1–7, Hellenic Geographical Society
- de Launay L (1890) La géologie de l'île de Mételin. *Comptes Rendus Hebdomadaires de Séances de l'Académie des Sciences* 110: 158–161
- de Launay L (1891) Descriptions géologique des îles de Mételin et de Thasos. *Nouvelles archives des missions scientifiques et littéraires* 127–170
- de Launay L (1897) Sur la géologie des îles des Mételin, ou Lesbos, et de Lemnos dans la mer Egée. *Comptes Rendus Hebdomadaires de Séances de l'Académie des Sciences* 125
- de Launay L (1898) Etude géologique sur la mer Égée. La géologie des îles de Mételin (Lesbos), Lemnos et Thasos. *Annales des mines, mémoires* 13: 157–292
- Leake BE (1978) Nomenclature of amphiboles. *American Mineralogist* 63: 1023–1052
- Leake BE, Woolley AR, Arps CE, Birch WD, Gilbert MC, Grice JD, Hawthorne FC, Kato A, Kisch HJ, Krivovichev VG, Linthout K, Laird J, Mandarino JA, Maresch WV, Nickel EH, Rock NM, Schumacher JC, Smith DC, Stephenson NC, Ungaretti L, Whittaker EJ, Youzhi G (1997) Nomenclature of amphiboles: Report of the Subcommittee on Amphiboles of the International Mineralogical Association, Commission on New Minerals and Mineral Names. *The Canadian Mineralogist* 35: 219–246
- Leeman WP, Sisson VB (2002) Boron: Mineralogy, Petrology and Geochemistry. In: Grew ES, Anovitz ML (eds.) *Geochemistry of boron and its implications for crustal and mantle processes*, vol. 33, 645–708, Mineralogical Society of America, Washington DC, 2nd edn.
- Leeman WP, Tonarini S, Chan LH, Borg LE (2004) Boron and lithium isotopic variations in a hot subduction zone—the southern Washington Cascades. *Chemical Geology* 212: 101–124, doi:10.1016/j.chemgeo.2004.08.010
- Liu Y, Zhang Y, Behrens H (2005) Solubility of H<sub>2</sub>O in rhyolitic melts at low pressures and a new empirical model for mixed H<sub>2</sub>O-CO<sub>2</sub> solubility in rhyolitic melts. *Journal of Volcanology and Geothermal Research* 143: 219 – 235, doi:10.1016/j.jvolgeores.2004.09.019, volcanic Eruption Mechanisms - Insights from intercomparison of models of conduit processes
- Lofgren G (1971) Spherulitic textures in glassy and crystalline rocks. *Journal of Geophysical Research* 76: 5635–5648
- Lofgren G (1974) An experimental study of plagioclase crystal morphology: isothermal crystallisation. *American Journal of Science* 274: 243–273

- Ludwig T, Marschall HR, Pogge von Strandmann PAE, Shabaga BM, Fayek M, Hawthorne FC (2011) A secondary ion mass spectrometry (SIMS) re-evaluation of B and Li isotopic compositions of Cu-bearing elbaite from three global localities. *Mineralogical Magazine* (in press)
- Ludwig T, Stalder R (2007) A new method to eliminate the influence of in situ contamination in SIMS analysis of hydrogen. *Journal of Analytical Atomic Spectrometry* 22: 1415–1419, doi:10.1039/b705848a
- Lundstrom CC, Chaussidon M, Hsui AT, Kelemen P, Zimmerman M (2005) Observations of Li isotopic variations in the Trinity Ophiolite: Evidence for isotopic fractionation by diffusion during mantle melting. *Geochimica et Cosmochimica Acta* 69: 735–751, doi:10.1016/j.gca.2004.08.004
- Lybérís N, Yürür T, Chorowicz J, Kaspoğlu E, Gündoğdu N (1992) The East Anatolian Fault: an oblique collisional belt. *Tectonophysics* 204: 1–156
- Marschall H (2005) *Lithium, Beryllium and Boron in High-Pressure Metamorphic Rocks from Syros (Greece)*. Dr. rer. nat. thesis, Universität Heidelberg, Heidelberg, Germany
- Marschall H, Ludwig T (2004) The low-boron contest: minimising surface contamination and analysing boron concentrations at the ng/g-level by secondary ion mass spectrometry. *Mineralogy and Petrology* 81: 265–278, doi:10.1007/s00710-004-0037-5
- Marschall HR, Altherr R, Ludwig T, Kalt A, Gméling K, Kasztovszky Zs (2006a) Partitioning and budget of Li, Be and B in high-pressure metamorphic rocks. *Geochimica et Cosmochimica Acta* 70: 4750–4769
- Marschall HR, Altherr R, Rüpke L (2007) Squeezing out the slab – modelling the release of Li, Be and B during progressive high-pressure metamorphism. *Chemical Geology* 239: 323–335, doi:10.1016/j.chemgeo.2006.08.008
- Marschall HR, Ludwig T (2006) Re-examination of the boron isotopic composition of tourmaline from the Lavicky granite, Czech Republic, by secondary ion mass spectrometry: back to normal. Critical comment on “Chemical and boron isotopic compositions of tourmaline from the Lavicky leucogranite, Czech Republic” by S.-Y. Jiang et al., *Geochemical Journal*, 37, 545–556, 2003. *Geochemical Journal* 40: 631–638
- Marschall HR, Ludwig T, Altherr R, Kalt A, Tonarini S (2006b) Syros metasomatic tourmaline: evidence for very high- $\delta^{11}\text{Be}$  fluids in subduction zones. *J Petrology* 47: 1915–1942, doi:10.1093/petrology/egl031
- Mart Y (1994) Ptolemaïs basin: The tectonic origin of a Senonian marine basin underneath the southeastern Mediterranean Sea. *Tectonophysics* 234: 5–17
- Mart Y, Woodside J (1994) Preface: Tectonics of the Eastern Mediterranean. *Tectonophysics* 234: 1–3
- McClusky S, Balassanian S, Barka A, Demir C, Ergintav S, Georgiev I, Gurkan O, Hamburger M, Hurst K, Kahle H, Kastens K, Kekelidze G, King R, Kotzev V, Lenk

## Bibliography

---

- O, Mahmoud S, Mishin A, Nadariya M, Ouzounis A, Paradissis D, Peter Y, Prilepin M, Reilinger R, Sanli I, Seeger H, Tealeb A, Toksöz MN, Veis G (2000) Global Positioning System constraints on plate kinematics and dynamics in the eastern Mediterranean and Caucasus. *Journal of Geophysical Research* 105: 5695–5719
- McDonough WF, Sun S-s (1995) The composition of the Earth. *Chemical Geology* 120: 223–253
- McKenzie D (1976) The East Anatolian Fault: A major structure in Eastern Turkey. *Earth and Planetary Science Letters* 29: 189–193
- McKenzie D (1978) Active tectonics of the Alpine-Himalayan belt: the Aegean Sea and surrounding regions. *The Geophysical Journal of the Royal Astronomical Society* 55: 217–254
- McKenzie DP (1970) Plate tectonics of the Mediterranean region. *Nature* 226: 239–243
- McKenzie DP (1972) Active Tectonics of the Mediterranean region. *The Geophysical Journal of the Royal Astronomical Society* 30: 109–182
- McPhie J, Doyle M, Allen R (1993) *Volcanic Textures: a guide to the interpretation of textures in volcanic rocks*. Centre for Ore Deposit and Exploration Studies, University of Tasmania
- DeMets C, Gordon RG, Argus DF, Stein S (1994) Effect of recent revisions to the geomagnetic reversal time scale on estimates of current plate motions. *Geophysical Research Letters* 21: 2191–2194
- Meulenkamp JE, Wortel MJR, van Wamel WA, Spakman W, Hoogerduyn Strating E (1988) On the Hellenic subduction zone and the geodynamic evolution of Crete since the late Middle Miocene. *Tectonophysics* 146: 203–215
- Mezger K, Altherr R, Okrusch M, Henjes-Kunst F, Kreuzer H (1985) Genesis of acid/basic rock associations: a case study – The Kallithea intrusive complex, Samos, Greece. *Contributions to Mineralogy and Petrology* 90: 353–366, doi:10.1007/BF00384714
- Migiros G, Hatzipanagiotou K, Gartzos E, Serelis K, Tsikouras B (2000) Petrogenetic evolution of ultramafic rocks from Lesvos Island (NE Aegean, Greece). *Chemie der Erde* 60: 27–46
- Miyashiro A (1978) Nature of alkalic volcanic rock series. *Contributions to Mineralogy and Petrology* 66: 91–104, doi:10.1007/BF00376089
- Morelli C (1978) Eastern Mediterranean: Geophysical results and implications. *Tectonophysics* 46: 333–346
- Moriguti T, Nakamura E (1998) Across-arc variation of Li isotopes in lavas and implications for crust/mantle recycling at subduction zones. *Earth and Planetary Science Letters* 163: 167 – 174, doi:10.1016/S0012-821X(98)00184-8
- Moriguti T, Shibata T, Nakamura E (2004) Lithium, boron and lead isotope and trace element systematics of Quaternary basaltic volcanic rocks in northeastern Japan: mineralogical controls on slab-derived fluid composition. *Chemical Geology* 212: 81–100, doi:10.1016/j.chemgeo.2004.08.005
- Morimoto N (1989) Nomenclature of pyroxenes. *Canadian Mineralogist* 27: 143–156

- Mungall J, Dingwell D, Chaussidon M (1999) Chemical diffusivities of 18 trace elements in granitoid melts. *Geochimica et Cosmochimica Acta* 63: 2599 – 2610, doi:10.1016/S0016-7037(99)00209-4
- Münker C, Pfänder JA, Weyer S, Büchl A, Kleine T, Mezger K (2003) Evolution of planetary cores and the Earth-Moon system from Nb/Ta systematics. *Science* 301: 84–87
- Nakamura E, Ishikawa T, Birck J-L, Allègre CJ (1992) Precise boron isotopic analysis of natural rock samples using a boron-mannitol complex. *Chemical Geology: Isotope Geoscience section* 94: 193–204, doi:10.1016/0168-9622(92)90012-Y
- Nur A, Ben-Avraham Z (1978) The Eastern Mediterranean and the Levant: tectonics of continental collision. *Tectonophysics* 46: 297–311
- Okay AI (2000) Was the Late Triassic orogeny in Turkey caused by the collision of an oceanic plateau? In: Bozkurt E, Winchester JA, Piper JDA (eds.) *Tectonics and Magmatism in Turkey and the Surrounding Area*, vol. 173 of *Special Publications*, 25–41, Geological Society
- Okay AI, Şengör AMC, Görür N (1994) Kinematic history of the opening of the Black Sea and its effect on the surrounding regions. *Geology* 22: 267–270
- Olker B (2001) *Entwicklung und Anwendung eines Computerprogramms zur numerischen Modellierung von Diffusionsprofilen in Mineralkörnern*. Dr. rer. nat. thesis, Universität Heidelberg, Heidelberg, Germany
- Otamendi JE, Patiño Douce AE (2001) Partial melting of aluminous metagreywackes in the Northern Sierra Comechingones, Central Argentina. *Journal of Petrology* 42: 1751–1772
- Ottolini L, Bottazzi P, Vannucci R (1993) Quantification of lithium, beryllium, and boron in silicates by secondary-ion mass spectrometry using conventional energy filtering. *Analytical Chemistry* 65: 1960–1968, doi:10.1021/ac00063a007
- Pabst S (2009) *Investigation of blueschist and serpentinized harzburgite from the Mariana forearc: Insights into the mechanisms of element mobilization in subduction zones and storage of fluid-mobile elements in the mantle wedge*. Dr. rer. nat. thesis, Universität Heidelberg, Heidelberg, Germany
- Palmer MR (1991) Boron-isotope systematics of Halmahera arc (Indonesia) lavas: Evidence for involvement of the subducted slab. *Geology* 19: 215–217, doi:10.1130/0091-7613(1991)019<0215:BISOHA>2.3.CO;2
- Palmer MR, Swihart GH (2002) Boron isotope geochemistry: an overview. In: Grew ES, Anovitz LM (eds.) *Boron mineralogy, petrology, and geochemistry*, vol. 33 of *Reviews in Mineralogy*, 709–744, Mineralogical Society of America, Washington, DC, 2nd edn.
- Panienka S (2011) *The Evolution of the Pre-Eruptive Minoan Volcanic Plumbing System*. Dr. rer. nat. thesis in preparation, Universität Heidelberg, Heidelberg, Germany
- Papastamakis A (1972) Hot Springs of Polichnitos, Lesbos Island. IGME (in Greek)

- Papazachos BC, Comninakis PE (1971) Geophysical and tectonic features of the Aegean Arc. *Journal of Geophysical Research* 76: 8517–8533
- Paquin J, Altherr R (2002) Subduction-related lithium metasomatism during exhumation of the Alpe Arami ultrahigh-pressure garnet peridotite (Central Alps, Switzerland). *Contributions to Mineralogy and Petrology* 143: 623–640
- Paquin J, Altherr R, Ludwig T (2004) Li-Be-B systematics in the ultrahigh-pressure garnet peridotite from Alpe Arami (Central Swiss Alps): implications for slab-to-mantle wedge transfer. *Earth and Planetary Science Letters* 218: 507–519, doi:10.1016/S0012-821X(03)00677-0
- Paraskevopoulos GM (1956) über den Chemismus und die provinzialischen Verhältnisse der tertiären und quartären Ergußgesteine des ägäischen Raumes und der benachbarten Gebiete. *Tschermaks Mineralogische und Petrographische Mitteilungen* 6: 13–72
- Parkinson IJ, Hammond SJ, James RH, Rogers NW (2007) High-temperature lithium isotope fractionation: Insights from lithium isotope diffusion in magmatic systems. *Earth and Planetary Science Letters* 257: 609–621, doi:10.1016/j.epsl.2007.03.023
- Payne AS, Robertson AHF (1995) Neogene supra-subduction zone extension in the Polis graben system, west Cyprus. *Journal of the Geological Society* 152: 613–628
- Pe-Piper G (1980a) The Cenozoic volcanic sequence of Lesbos, Greece. *Zeitschrift der Deutschen Geologischen Gesellschaft* 131: 889–901
- Pe-Piper G (1980b) Geochemistry of Miocene shoshonites, Lesbos, Greece. *Contributions to Mineralogy and Petrology* 72: 387–396
- Pe-Piper G (1994) Lead isotopic composition of Neogene volcanic rocks from the Aegean extensional region. *Chemical Geology* 118: 27–41, doi:10.1016/0009-2541(94)90168-6
- Pe-Piper G (1998) The nature of Triassic extension-related magmatism in Greece: evidence from Nd and Pb isotope geochemistry. *Geological Magazine* 135: 331–348, doi:10.1017/S0016756898008735
- Pe-Piper G, Christofides G, Eleftheriadis G (1998) Lead and neodymium isotopic composition of Tertiary igneous rocks of northern Greece and their regional significance. *Acta Vulcanologica* 10: 255–263
- Pe-Piper G, Kotopouli CN, Piper DJW (1997) Granitoid rocks of Naxos, Greece: regional geology and petrology. *Geological Journal* 32: 153–171
- Pe-Piper G, Piper DJ (1989) Spatial and temporal variation in Late Cenozoic back-arc volcanic rocks, Aegean Sea region. *Tectonophysics* 169: 113 – 134, doi:10.1016/0040-1951(89)90186-8
- Pe-Piper G, Piper DJW (1992) Geochemical variations with time in the Cenozoic high-K volcanic rocks of the island of Lesbos, Greece; significance for shoshonite petrogenesis. *Journal of Volcanology and Geothermal Research* 53: 371–387

- Pe-Piper G, Piper DJW (1993) Revised stratigraphy of the Miocene volcanic rocks of Lesbos, Greece. *Neues Jahrbuch für Geologie und Paläontologie / Monatshefte* 1993: 97–110
- Pe-Piper G, Piper DJW (2001) Late Cenozoic, post-collisional Aegean igneous rocks: Nd, Pb and Sr isotopic constraints on petrogenetic and tectonic models. *Geological Magazine* 138: 653–668, doi:10.1017/S0016756801005957
- Pe-Piper G, Piper DJW (2002) *The igneous rocks of Greece*, vol. 30 of *Beiträge zur regionalen Geologie der Erde*. Gebrüder Borntraeger, Berlin, Stuttgart
- Pe-Piper G, Piper DJW, Matarangas D, Varti-Matarangas M (2001) The sub-ophiolitic melange of the island of Lesbos, Greece. *Neues Jahrbuch für Mineralogie, Monatshefte* 2001: 241–260
- Pearce NJ, Perkins WT, Westgate JA, Gorton MP, Jackson SE, Neal CR, Chenery SP (1997) A compilation of new and published major and trace element data for NIST SRM 610 and NIST SRM 612 glass reference Materials. *Geostandards Newsletter: the Journal of Geostandards and Geoanalysis* 21: 115–144, doi:10.1111/j.1751-908X.1997.tb00538.x
- Pelletier L, Vils F, Kalt A, Gméling K (2008) Li, B and Be contents of harzburgites from the Dramala Complex (Pindos Ophiolite, Greece): Evidence for a MOR-type Mantle in a Supra-subduction Zone Environment. *Journal of Petrology* doi:10.1093/petrology/egn057
- Pfister M, Rybach L, Simsek S (1998) Geothermal reconnaissance of the Marmara Sea region (NW Turkey): surface heat flow density in an area of active continental extension. *Tectonophysics* 291: 77–89
- Phillipson A (1910) Reisen und Forschungen im westlichen Kleinasien I. *Petermann's Mitteilungen, Ergänzungsheft* 167
- Le Pichon X, Angelier J (1979) The Hellenic arc and trench system: a key to the neotectonic evolution of the Eastern Mediterranean. *Tectonophysics* 60: 1–42
- Le Pichon X, Angelier J (1981) The Aegean Sea. *Philosophical transactions of the Royal Society, Series A* 300: 357–372
- Le Pichon X, Angelier J, Aubouin J, Lybérís N, Monti S, Renard V, Got H, Hsü K, Marty Y, Mascle J, Mathews D, Mitropoulos P, Tsofliés P, Chronies G (1979) From subduction to transform motion: a seabeam survey of the Aegean trench system. *Earth and Planetary Science Letters* 44: 441–450
- Plank T, Langmuir CH (1998) The chemical composition of subducting sediment and its consequences for the crust and mantle. *Chemical Geology* 145: 325–394, doi:10.1016/S0009-2541(97)00150-2
- Pouchou JL, Pichoir F (1984) A new model for quantitative analyses. I. Application to the analysis of homogeneous samples. *La Recherche Aérospatiale* 3: 13–38
- Pouchou JL, Pichoir F (1985) 'PAP' ( $\phi$ - $\rho$ -Z) correction procedure for improved quantitative microanalysis. In: Armstrong JT (ed.) *Microbeam Analysis*, 104–106, San Francisco Press

- Prager M (1966) Présentation d'une esquisse géologique des terrains volcaniques d'île de Lesbos (Grèce). *Annales Géologiques des Pays Hélieniques* 16: 512–527
- Putirka KD (2008) Thermometers and Barometers for Volcanic Systems. *Reviews in Mineralogy and Geochemistry* 69: 61–120
- Rainer A (2009) *Correct Spelling for Earth Scientists (Original title: Formen sind kein leerer Wahn)*. Irrelevant Contents Publishers, Heidelberg, Karlsruhe, Germany
- Rankenburg K, Lassiter JC, Brey G (2004) Origin of megacrysts in volcanic rocks of the Cameroon volcanic chain – constraints on magma genesis and crustal contamination. *Contributions to Mineralogy and Petrology* 147: 129–144, doi:10.1007/s00410-003-0534-2
- von Raumer JF, Stampfli GM, Mosar J (1998) From Gondwana to Pangea - an Alpine point of view. *Terra Nostra: Schriften der Alfred-Wegener-Stiftung* 98: 154–156
- Ren M (2004) Partitioning of Sr, Ba, Rb, Y, and LREE between alkali feldspar and peraluminous silicic magma. *American Mineralogist* 89: 1290–1303
- Ren M, Parker DF, White JC (2003) Partitioning of Sr, Ba, Rb, Y, and LREE between plagioclase and peraluminous silicic magma. *American Mineralogist* 88: 1091–1103
- Richter FM, Davis AM, DePaolo DJ, Watson EB (2003) Isotope fractionation by chemical diffusion between molten basalt and rhyolite. *Geochimica et Cosmochimica Acta* 67: 3905 – 3923, doi:10.1016/S0016-7037(03)00174-1
- Robert U (1973) *Le roches volcaniques de l'île Patmos (Dodecanèse, Grèce)*. Thèse 3<sup>ème</sup> cycle, unpublished, Paris
- Robert U (1976) Donnée nouvelles sur le volcanisme du Sud-Est de la Mer Egée: existence d'un episode à caractère alcalin. In: *International congress on thermal waters, geothermal energy and vulcanism of the Mediterranean area, Proceedings*, vol. 3 of *Vulcanism*, 211–224, National Technical University Athens, Greece
- Robert U, Foden J, Varne R (1992) The Dodecanese Province, SE Aegean: a model for tectonic control on potassic magmatism. *Lithos* 28: 241–260, doi:10.1016/0024-4937(92)90009-N
- Rosenbaum G, Lister GS (2002) Reconstruction of the evolution of the Alpine-Himalayan orogen – an introduction. *Journal of the Virtual Explorer* 8: 1–2
- Rosner M, Erzinger J, Franz G, Trumbull RB (2003) Slab-derived boron isotope signatures in arc volcanic rocks from the Central Andes and evidence for boron isotope fractionation during progressive slab dehydration. *Geochemistry Geophysics Geosystems (G3)* 4, doi:10.1029/2002GC000438
- Rosner M, Wiedenbeck M, Ludwig T (2008) Composition-induced variations in SIMS instrumental mass fractionation during boron isotope ratio measurements of silicate glasses. *Geostandards and Geoanalytical Research* 32: 27–38, doi:10.1111/j.1751-908X.2008.00875.x
- Rotstein Y (1984) Counterclockwise rotation of the Anatolian block. *Tectonophysics* 108: 71–91

- Rotstein Y, Kafka LA (1982) Seismotectonics of the southern boundary of Anatolia, eastern Mediterranean region: subduction, collision and arc jumping. *Journal of Geophysical Research*, B 87: 7694–7706
- le Roux P, Shirey S, Benton L, Hauri E, Mock T (2004) In situ, multiple-multiplier, laser ablation ICP-MS measurement of boron isotopic composition ( $\delta^{11}\text{B}$ ) at the nanogram level. *Chemical Geology* 203: 123–138, doi:10.1016/j.chemgeo.2003.09.006
- Rudnick RL (2005) The Composition of the Continental Crust. In: Rudnick RL (ed.) *The Crust*, vol. 3 of *Treatise on Geochemistry*, Elsevier Amsterdam, International
- Ryan JG (1989) *The systematics of lithium, beryllium, and boron in young volcanic rocks*. PhD thesis, Columbia University, New York, USA
- Ryan JG, Langmuir CH (1993) The systematics of boron abundances in young volcanic rocks. *Geochimica et Cosmochimica Acta* 57: 1489–1498
- Ryan JG, Leeman WP, Morris JD, Langmuir CH (1996) The boron systematics of intraplate lavas: Implications for crust and mantle evolution. *Geochimica et Cosmochimica Acta* 60: 415–422, doi:10.1016/0016-7037(95)00402-5
- Sakuyama M, Kushiro I (1979) Vesiculation of hydrous andesitic melt and transport of alkalis by separated vapor phase. *Contributions to Mineralogy and Petrology* 71: 61–66, doi:10.1007/BF00371881
- Salters VJM, Stracke A (2004) Composition of the depleted mantle. *Geochemistry Geophysics Geosystems (G3)* 5: 1–27, doi:10.1029/2003GC000597
- Schmitt AK, Kasemann S, Meixner A, Rhede D (2002) Boron in central Andean ignimbrites: implications for crustal boron cycles in an active continental margin. *Chemical Geology* 183: 333–347, doi:10.1016/S0009-2541(01)00382-5
- Seitz H-M, Woodland AB (2000) The distribution of lithium in peridotitic and pyroxenitic mantle lithologies – an indicator of magmatic and metasomatic processes. *Chemical Geology* 166: 47–64
- Sella GF, Dixon TH, Mao A (2003) REVEL: A model for recent plate velocities from space geodesy. *Journal of Geophysical Research, solid Earth* 107, doi:10.1029/2000JB000033
- Şengör AMC (1979a) Mid-Mesozoic closure of Permo-Triassic Tethys and its implications. *Nature* 279, doi:10.1038/279590a0
- Şengör AMC (1979b) The North Anatolian transform fault: its age, offset and tectonic significance. *Journal of the Geological Society (London)* 136: 269–282
- Şengör AMC (1987) Cross-faults and differential stretching of hanging walls in regions of low-angle normal faulting: examples from western Turkey. *Geological Society, London, Special Publications* 28: 575–589, doi:10.1144/GSL.SP.1987.028.01.38
- Şengör AMC (1989) The Tethyside orogenic system: an introduction. In: Şengör AMC (ed.) *Tectonic evolution of the Tethyan region*, NATO ASI series: Series C ; 259, 1–22, Kluwer Academic Publishers, Dordrecht

- Şengör AMC, Görür N, Şaroğlu F (1985) Strike-slip faulting and related basin formation in zones of tectonic escape: Turkey as a case study. In: Biddle KT, Christie-Blick N (eds.) *Strike-slip Faulting and Basin Formation*, vol. 37 of *Special publication*, 227–264, Society of Economic Paleontologists and Mineralogists
- Şengör AMC, Yılmaz Y (1981) Tethyan evolution of Turkey: a plate tectonic approach. *Tectonophysics* 75: 181–241
- Şengör AMC, Yılmaz Y, Ketin İ (1980) Remnants of a pre–Late Jurassic ocean in northern Turkey: Fragments of Permian-Triassic Paleo-Tethys? *Geological Society of America Bulletin* 91: 599–609, doi:10.1130/0016-7606(1980)91<599:ROAPJO>2.0.CO;2
- Şengör AMC, Yılmaz Y, Sungurlu O (1984) Tectonics of the Mediterranean Cimmerides: nature and evolution of the western termination of Paleo-Tethys. In: Dixon JE, Robertson AHF (eds.) *The Geological Evolution of the Eastern Mediterranean*, vol. 17, 77–112, Geological Society of London, London
- Seyitoğlu G, Scott B (1991) Late Cenozoic crustal extension and basin formation in West Turkey. *Geological Magazine* 128: 155–166
- Seyitoğlu G, Scott BC (1992a) The age of the Büyük Menderes Graben (west Turkey) and its tectonic implications. *Geological Magazine* 129: 239–242
- Seyitoğlu G, Scott BC (1992b) Late Cenozoic volcanic evolution of NE Aegean Region. *Journal of Volcanology and Geothermal Research* 54: 157–176
- Shand SJ (1951) *Eruptive rocks: their genesis, composition, classification, and their relation to ore-deposits, with a chapter on meteorites*. Wiley & Sons, 4th edn.
- Shaw DM, Higgins MD, Truscott MG, Middleton TA (1988) Boron contamination in polished thin sections of meteorites: Implications for other trace-element studies by alpha-track image or ion microprobe. *American Mineralogist* 73: 894–900
- Skarpelis N, Kyriakopoulos K, Villa IM (1992) Occurrence and  $^{40}\text{Ar}/^{39}\text{Ar}$  dating of a granite in Thera (Santorini, Greece). *Geologische Rundschau* 81: 729–735
- Smith AG, Moores EM III (1974) Hellenides. *Geological Society, London, Special Publications* 4: 159–185, doi:10.1144/GSL.SP.2005.004.01.09
- Smith HJ, Leeman WP, Davidson J, Spivack AJ (1997) The B isotopic composition of arc lavas from Martinique, Lesser Antilles. *Earth and Planetary Science Letters* 146: 303–314, doi:10.1016/S0012-821X(96)00209-9
- Sonntag I (2007) *Die Verteilung von Litium, Beryllium und Bor in Phänokristallen von kalkalkalischen Gesteinen am Beispiel der Insel Nisyros (Ägäis)*. Dr. rer. nat. thesis, Universität Heidelberg, Heidelberg, Germany
- Spakman W, Wortel MJR, Vlaar NJ (1988) Subduction zone: a tomographic image and its geodynamic implications. *Geophysical Research Letters* 15: 60–63
- Spivack A, Edmond J (1987) Boron isotope exchange between seawater and the oceanic crust. *Geochimica et Cosmochimica Acta* 51: 1033–1043, doi:10.1016/0016-7037(87)90198-0

- St. Seymour K, Lamera S, Neriman S, Kouli M, Vamvoukakis K (2004) Vent-related ignimbrites of Eastern Lesvos and proximal Asia Minor: The case for Polychnitos ignimbrite and Sarimsak Stone. In: *32nd IGC - Florence*
- Stampfli G (1989) *Late Palaeozoic evolution of the eastern Mediterranean region*. ICGP 276 Palaeozoic geodynamic domains and their alpidic evolution in the Tethys, Lausanne, Switzerland, Short Course I-II
- Stampfli G (1996) The Intra-Alpine terrain: a Palaeotethyan remnant in the Alpine Variscides. *Eclogae Geologicae Helvetiae* 89: 13–42
- Stampfli G, Marchant RH (1997) Geodynamic evolution of the Tethyan margins of the Western Alps. In: Pfeiffner OA, Lehner P, Heitzman PZ, Mueller S, Steck A (eds.) *Deep structures of the Swiss Alps – results from NRP 20*, 223–239, Birkhäuser AG
- Stampfli G, Marcoux J, Baud A (1991) Tethyan margins in space and time. *Palaeogeography, Palaeoclimatology, Palaeoecology* 87: 373–409
- Stampfli G, Mosar J, Favre P, Pillecuit A, Vannay J (2001) Permo-Mesozoic evolution of the western Tethys realm: the Neo-Tethys East Mediterranean Basin connection. In: Ziegler P, Cavazza W, Robertson A, CrasquinSoleau S (eds.) *Peri-Tethys Memoir 6: Peri-Tethyan Rift/Wrench Basins and Passive Margins*, vol. 186 of *Memoirs du Museum National D'Histoire National*, 51–108, Publications Scientifiques du Museum, 57 rue Cuvier, 75005 Paris, France, Workshop on International Geological Correlation Program, Matera, Italy, Sep 01-05, 1999
- Stampfli GM (2000) Tethyan oceans. In: Bozkurt E, Winchester JA, Piper JDA (eds.) *Tectonic and Magmatism in Turkey and the Surrounding Area*, vol. 173 of *Geological Society Special Publication*, 1–23, The Geological Society
- Stampfli GM, Borel GD (2002) A plate tectonic model for the Paleozoic and Mesozoic constrained by dynamic plate boundaries and restored synthetic oceanic isochrons. *Earth and Planetary Science Letters* 196: 17 – 33, doi:10.1016/S0012-821X(01)00588-X
- Stampfli GM, Mosar J, De Bono A, Vavassis I (1998) Late Palaeozoic, Early Mesozoic plate tectonics of the western Tethys. In: *Proceedings of the 8th International Congress, Patra, September 2001 of the 8th Pan-Hellenic Geographical Congress of the Hellenic Geographical Society in Mytilini, Greece*, vol. 32, 113–120, Geological Society of Greece
- Stampfli GM, Pillecuit A (1993) An alternative Permo-Triassic reconstruction of the kinematics of the Tethyan realm. In: Dercourt J, Ricou L-E, Vrielynck B (eds.) *Atlas Tethys Palaeoenvironmental Maps, Explanatory Notes*, 55–62, Gauthier-Villars
- Steiger RH, Jäger E (1977) Subcommission on geochronology: Convention on the use of decay constants in geo- and cosmochronology. *Earth and Planetary Science Letters* 36: 359–362
- Steppan N (2003) *Li, Be und B in Mineralen metapelitischer Gesteine: Fallstudien auf der Insel Ikaria, im künischen Gebirge und den Schweizer Alpen*. Dr. rer. nat. thesis, Universität Heidelberg, Heidelberg, Germany

## Bibliography

---

- Steven T, Lipman P (1976) Calderas of the San Juan volcanic field, southwestern Colorado. *United States Geological Survey Professional Paper* 958: 1–35
- Straub C, Kahle H-G (1995) Active crustal deformation in the Marmara Sea region, NW Anatolia, inferred from GPS measurements. *Geophysical Research Letters* 22: 2533–2536, doi:0094-8534/95/95GL-02219
- Straub SM, Layne GD (2002) The systematics of boron isotopes in Izu arc front volcanic rocks. *Earth and Planetary Science Letters* 198: 25–39, doi:10.1016/S0012-821X(02)00517-4
- Swarbrick RE (1993) Sinistral strike-slip and transpressional tectonics in an ancient oceanic setting: the Mamonia Complex, southwest Cyprus. *Journal of the Geological Society* 150: 381–392
- Taylor SR, McLennan S (2009) *Planetary Crusts - Their Composition, Origin and Evolution*, vol. 10 of *Cambridge Planetary Science*. Cambridge University Press
- Taylor SR, McLennan SM (1995) The geochemical evolution of the continental crust. *Reviews in Geophysics* 33: 241–265
- Taymaz T, Jackson J, McKenzie D (1991) Active tectonics of the north and central Aegean Sea. *Geophysical Journal International* 106: 433–490
- Teng FZ, McDonough WF, Rudnick RL, Walker RJ (2006) Diffusion-driven extreme lithium isotopic fractionation in country rocks of the Tin Mountain pegmatite. *Earth and Planetary Science Letters* 243: 701–710, doi:10.1016/j.epsl.2006.01.036
- Tomascak PB (2004) Developments in the understanding and application of lithium isotopes in the earth and planetary sciences. In: Johnson CM, Beard BS, Albarède F (eds.) *Geochemistry of Non-Traditional Stable Isotopes*, vol. 55 of *Reviews in Mineralogy and Geochemistry*, 153–195, Mineralogical Society of America, Geochemical Society
- Tonarini S, Agostini S, Doglioni C, Innocenti F, Manetti P (2007) Evidence for serpentinite fluid in convergent margin systems: The example of El Salvador (Central America) arc lavas. *Geochemistry Geophysics Geosystems (G3)* 8: 1–18, doi:10.1029/2006GC001508
- Tonarini S, Agostini S, Innocenti F, Manetti P (2005)  $\delta^{11}\text{B}$  as tracer of slab dehydration and mantle evolution in Western Anatolia Cenozoic Magmatism. *Terra Nova* 17: 359–264, doi:10.1111/j.1365-3121.2005.00610.x
- Tonarini S, D'Antonio M, Vito MAD, Orsi G, Carandente A (2009) Geochemical and B-Sr-Nd isotopic evidence for mingling and mixing processes in the magmatic system that fed the Astroni volcano (4.1–3.8†ka) within the Campi Flegrei caldera (southern Italy). *Lithos* 107: 135–151, doi:10.1016/j.lithos.2008.09.012
- Tonarini S, Leeman WP, Civetta L, D'Antonio M, Ferrara G, Necco A (2004a) B/Nb and  $\delta^{11}\text{B}$  systematics in the Phlegrean Volcanic District, Italy. *Journal of Volcanology and Geothermal Research* 133: 123 – 139, doi:10.1016/S0377-0273(03)00394-9

- Tonarini S, Leeman WP, Ferrara G (2001) Boron isotopic variations in lavas of the Aeolian volcanic arc, South Italy. *Journal of Volcanology and Geothermal Research* 110: 155–170, doi:10.1016/S0377-0273(01)00203-7
- Tonarini S, Leeman WP, Leat PE (2004b) Lithium isotopic compositions of South Sandwich Arc. *Geochimica et Cosmochimica Acta* 68, doi:10.1016/j.gca.2004.05.014, abstracts 15th Goldschmidt Conference, Copenhagen, Denmark
- Tonarini S, Leeman WP, Leat PT (2011) Subduction erosion of forearc mantle wedge implicated in the genesis of the South Sandwich Island (SSI) arc: Evidence from boron isotope systematics. *Earth and Planetary Science Letters* 301: 275–284, doi:10.1016/j.epsl.2010.11.008
- Tonarini S, Pennisi M, Adorni-Braccesi A, Dini A, Ferrara G, Gonfiantini R, Wiedenbeck M, Gröning M (2003) Intercomparison of boron isotope and concentration measurements. Part I: selection, preparation and homogeneity tests of the intercomparison materials. *Geostandards Newsletter: The Journal of Geostandards and Geoanalysis* 27: 21–39, doi:10.1111/j.1751-908X.2003.tb00710.x
- Turner S, Tonarini S, Bindeman I, Leeman WP, Schaefer BF (2007) Boron and oxygen isotope evidence for recycling of subducted components over the past 2.5 Gyr. *Nature* 447: 402, doi:10.1038/nature05898
- Vamoukakis C, St. Seymour K, Williams-Jones A, Rokos D (2001) The Miocene Caldera of Stipsi on Lesbos Volcano: an example of “high sulfidation” hydrothermal system explored for gold. In: *Abstract in Volume, Geological Association of Canada–Mineralogical Association of Canada (GAC-MAC), Annual Meeting May 2001, St. John’s, New Foundland, Canada*
- Vidal N, Alvarez-Marrón J, Klaeschen D (2000) The structure of the Africa-Anatolia plate boundary in the eastern Mediterranean. *Tectonics* 19: 723–739
- Vilminot J-C, Robert U (1974) A propos des relations entre le volcanisme et la tectonique en Mer Egée. *Comptes Rendus Hebdomadaires de Séances de l’Académie des Sciences, Série D, Sciences Naturelles* 278: 2099–2102
- Voulgaris N, Parcharidis I, Pirlis E (2004) Correlation of tectonics, seismicity and geothermics of Lesbos Island using remote sensing data and geographical informations systems. *Bulletin of the Geological Society of Greece* 36: 938–947
- Le Voyer M, Rose-Koga EF, Laubier M, Schiano P (2008) Petrogenesis of arc lavas from the Rucu Pichincha and Pan de Azucar volcanoes (Ecuadorian arc): Major, trace element, and boron isotope evidences from olivine-hosted melt inclusions. *Geochemistry Geophysics Geosystems (G3)* 9, doi:10.1029/2008GC002173
- Watson EB, Harrison TM (1983) Zircon saturation revisited: temperature and composition effects in a variety of crustal magma types. *Earth and Planetary Science Letters* 64: 295–304, doi:10.1016/0012-821X(83)90211-X
- Westaway R (1994) Present-day kinematics of the Middle East and eastern Mediterranean. *Journal of Geophysical Research* 99: 12 071–12 090

## Bibliography

---

- Woodland AB, Seitz H-M, Altherr R, Olker B, Marschall H, Ludwig T (2002) Li abundances in eclogite minerals: a clue to a crustal or mantle origin? *Contributions to Mineralogy and Petrology* 143: 587–601; Erratum: *Contribs. Mineral. Petrol.* 144, 128–129
- Woodside JM (1976) Regional vertical tectonics in the eastern Mediterranean. *Geophysical Journal of the Royal Astronomical Society* 47: 493–514, doi:10.1111/j.1365-246X.1976.tb07098.x
- Woodside JM (1977) Tectonic elements and crust of the eastern Mediterranean Sea. *Marine Geophysical Research* 3: 317–354
- Yılmaz Y (1989) An approach to the origin of young volcanic rocks of western Turkey. In: Şengör AMC (ed.) *Tectonic evolution of the Tethyan region*, 159–189, Kluwer Academic Publishers
- Yılmaz Y (1990) Comparison of young volcanic associations of western and eastern Anatolia formed under a compressional regime: a review. *Journal of Volcanology and Geothermal Research* 44: 69–87
- Yılmaz Y, Genç ŞC, Karacık Z, Altunkaynak Ş (2001) Two contrasting magmatic associations of NW Anatolia and their tectonic significance. *Journal of Geodynamics* 31: 243–271
- Zhang Y, Ni H, Chen Y (2010) Diffusion Data in Silicate Melts. In: Zhang Y, Cherniak DJ (eds.) *Diffusion in Minerals and Melts*, vol. 72 of *Reviews in Mineralogy and Geochemistry*, chap. 8, 311–408, Mineralogical Society of America, Geochemical Society
- Ziegler PA (1988) *Evolution of the Arctic-North Atlantic and the Western Tethys*, vol. 43 of *AAPG Memoir*. AAPG/Datapages

# Appendix



## A. Individual sample descriptions

### A.1. Vertical profiles - sample locations

Most of the samples used in this study are from two vertical profiles through the Polychnitos Ignimbrite. The first profile (Profile A) was taken at a cape at the NE side of Kalloni Gulf, close to the village Kofinas (Fig. A.1) and consists of 11 samples. The second profile through the ignimbrite (Profile B), with four samples, was taken at the N side of Tavros mountain (374 m above sea-level), W of Nees Kidonies village (Fig. A.1). Additional samples of volcanic glass were taken from fiamme at road cuts from two different roads NE of the Gulf of Kalloni.

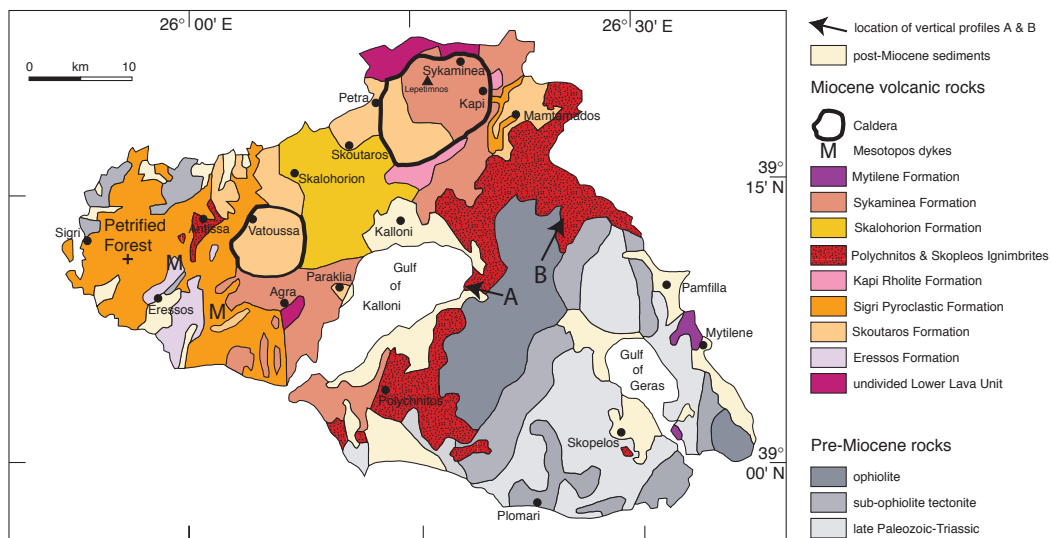


**Fig. A.1.** Map showing the location of the two vertical profiles A, a cape near Kofinas, and Profile B, at the N side of Tavros mountain.

## A.2. Sample descriptions – individual samples of profile A

Profile A was taken close to the village Kofinas at a cape at the NE side of Kalloni Gulf, between Ancient Pyra (an archaeological site) and Aghia Nikolao (a chapel). (Fig. A.1)

Samples will be described from bottom to top following the vertical profile and not according to their numbers.

**Sample LE-57** See page 177, after the description of sample LE-62, according to position in the vertical profile.

### A.2.1. Sample LE-58

The sample was taken at 0.5 m (from the bottom of the profile). The unwelded matrix consists of ash with a light grey to white colour. The sample contains  $\approx 15$  vol% of pumice up to 3 cm in size,  $\approx 5$  vol% lithoclasts usually around 1 cm in size, but up to  $2 \times 4$  cm, and  $< 1$  vol% crystals of macroscopically visible biotite and feldspar. Fiamme are absent. (Fig. A.2a)

The ash matrix consists of cusped and platy glass shards, mostly around a few to a couple of tenths of  $\mu\text{m}$ . Some of the cusped shards are substantially larger with up to  $500 \times 300 \mu\text{m}$  (Fig. A.2b). The sample contains pumice up to  $3.0 \times 2.0$  cm (Fig. A.2c), mostly with round vesicles, but some display elongated tube vesicles. However, one quite flattened out piece of pumice was found ( $4 \times 0.5$  cm, flattening ratio 1 : 8), which appears macroscopically white.

Crystals are mainly Pl (with substantial Akf overgrowth), Akf, and Bt. Of 18 phenocrysts documented (100%), 8 grains (33%) are Pl (of which 7 grains have substantial Akf overgrowth), 5 grains Bt (21%), and 4 grains (17%) Akf.

Pl phenocrysts are subhedral to rounded, up to  $600 \times 500 \mu\text{m}$  and have overgrowth of euhedral Akf up to  $30 \mu\text{m}$  wide at half to all of their rims. Additionally these phenocrysts are covered with a glass selvages up to  $50 \mu\text{m}$  wide (for example Fig. A.2d) I found only one Pl phenocryst with very little Akf overgrowth and glass seldge. This crystal (b III-1) is large ( $1.2 \times 0.6$  cm) and appears to be zoned.

Akf phenocrysts are euhedral and bear all thick selvages of glass, which frequently display cusped forms (Fig. A.2e). The crystals are up to  $400 \times 100 \mu\text{m}$ , a fragment of an euhedral Akf measures  $400 \times 400 \mu\text{m}$  and is in one piece with a large glass shard  $500 \times 400 \mu\text{m}$ .

Bt phenocrysts are up to  $1200 \times 150 \mu\text{m}$  and  $500 \times 200 \mu\text{m}$ , they are kinked, banded, have holes, and appear generally mechanically stressed. They are strongly zoned with FeO and MgO  $\approx 6\%$  and K<sub>2</sub>O  $\approx 4\%$  higher, and BaO in the core nearly

A.2. Sample descriptions – individual samples of profile A

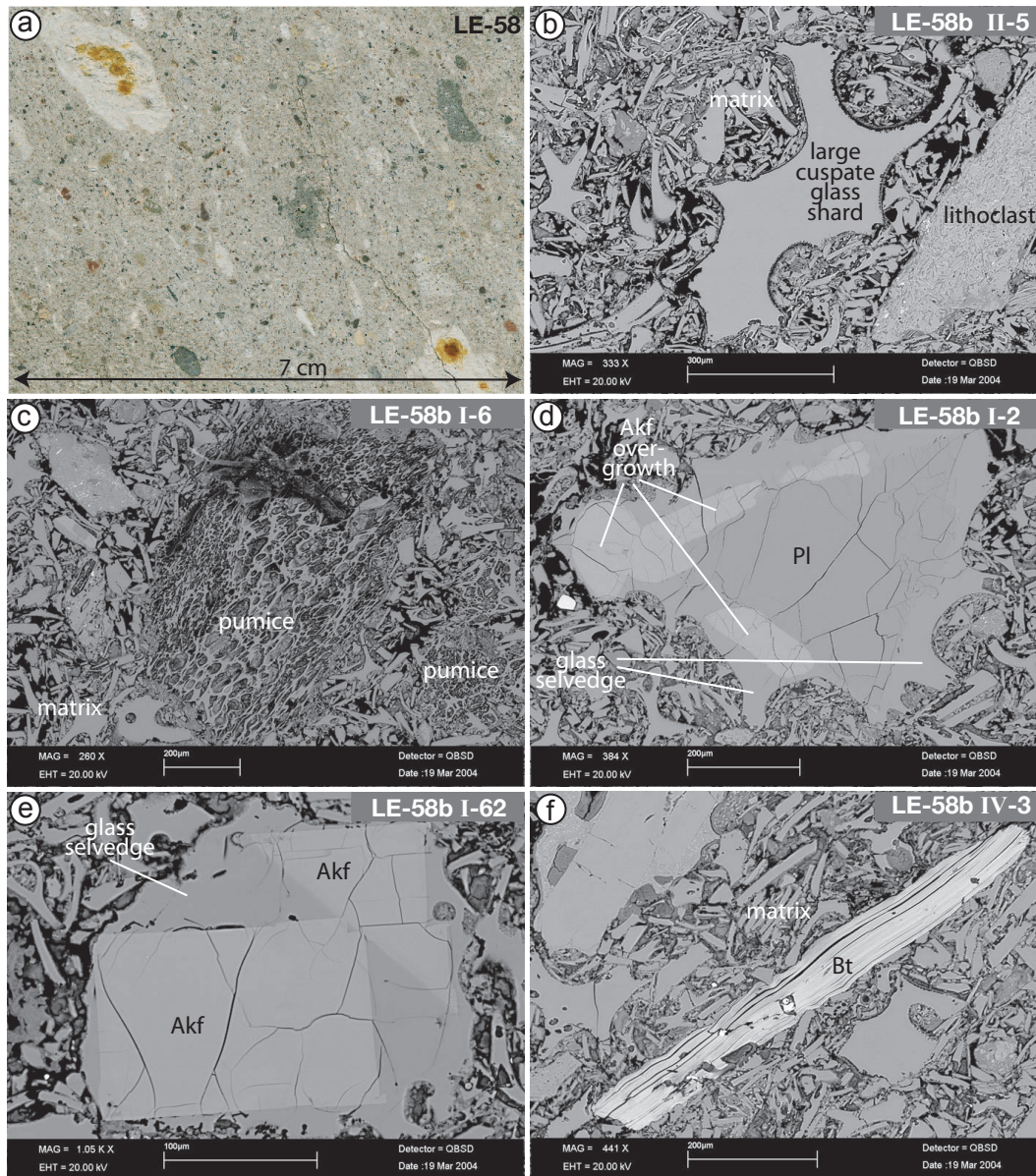


**Fig. A.2.** Characteristics of sample LE-58. (a) Photo of the hand specimen. (b) BSE image of matrix of cusped and platy glass shards, with one large cusped shard in the centre of the picture. (c) BSE image of a piece of pumice in the matrix. (d) BSE image of anhedral Pl phenocryst, with substantial Akf overgrowth and thick glass selvage. The Akf overgrowth is corroded (rounded) in places, while the Pl phenocryst seems unblemished. (e) BSE image of an euhedral Akf phenocryst in a thick glass selvage. (f) BSE image of typical Bt phenocryst, kinked, banded, with holes and a zonation.

2% (from 0% in the rim) (for example Fig. A.2f). One Bt crystal (b III-2) seems to be a xenocryst, it is neither kinked, nor stressed, nor zoned. However the crystal has an irregular, broken, in places slightly rounded rim. On one side is a broken former melt inclusion (now open), on the other side the crystal is attached to a piece of basaltic glass.

### A.2.2. Sample LE-59

The sample was taken at 3m. The matrix consists of ash with a light grey colour. The sample is composed  $\approx 15$  vol% of pumice up to 3cm in size,  $\approx 5$  vol% lithoclasts up to 0.5cm in size, and  $< 1$  vol% crystals of macroscopically visible biotite and feldspar. Fiamme are absent. (Fig. A.3a)

The ash matrix is built from cusped and platy glass shards, mostly around a few to a couple of tenths of  $\mu\text{m}$ . Some of the shards are substantially larger with up to  $500 \times 300 \mu\text{m}$  without vesicles and up to  $800 \times 500 \mu\text{m}$  with filled and un-filled vesicles of various size from  $\varnothing 25 \mu\text{m}$  to  $\varnothing 200 \mu\text{m}$  (Fig. A.3b). One shard is attached to a  $200 \mu\text{m}$  long lath of Akf (b VI-6). Pumice was found up to  $800 \times 600 \mu\text{m}$ , with some elongated tubes and signs of some flattening, and other pumice with filled vesicles (Fig. A.3c).

Crystals are mainly Pl, Bt, Akf, and Pl with Akf overgrowth. Of 22 grains documented (100%), 12 grains (55%) are Pl, 3 grains (14%) Akf, and 4 grains Bt (18%).

Pl phenocrysts are mostly subhedral, but some euhedral and some anhedral. About half of the phenocrysts are fragments, and about half of them have a glass selvage, which can be around  $30 - 50 \mu\text{m}$  thick. Crystal zonation is common, so is Akf overgrowth, which ranges from a few euhedral crystals around the rim of the Pl crystals to completely enclosing a Pl core. Pl crystals are up to  $1.2 \times 0.7 \text{ mm}$ .

I documented only three Akf grains (additionally to the Akf overgrowth) in the thin section. One is the lath at the glass shard mentioned above (b VI-6), the other (b VI-1) is a fragment  $500 \times 400 \mu\text{m}$  with a strong and step-wise Ba-zonation which ranges from  $10000 \mu\text{g/g}$  at the possible former core to  $20000 \mu\text{g/g}$  at the possible former rim (Fig. A.3d). The third (b/VII-1) is a subhedral phenocryst with an old Pl core, irregular, corroded rims and a glass selvage.

Bt phenocrysts are banded and bend, one even kinked, another one contains a hole. Bt phenocrysts are up to  $800 \times 200 \mu\text{m}$ , in BSE pictures they seem irregularly zoned.

A.2. Sample descriptions – individual samples of profile A

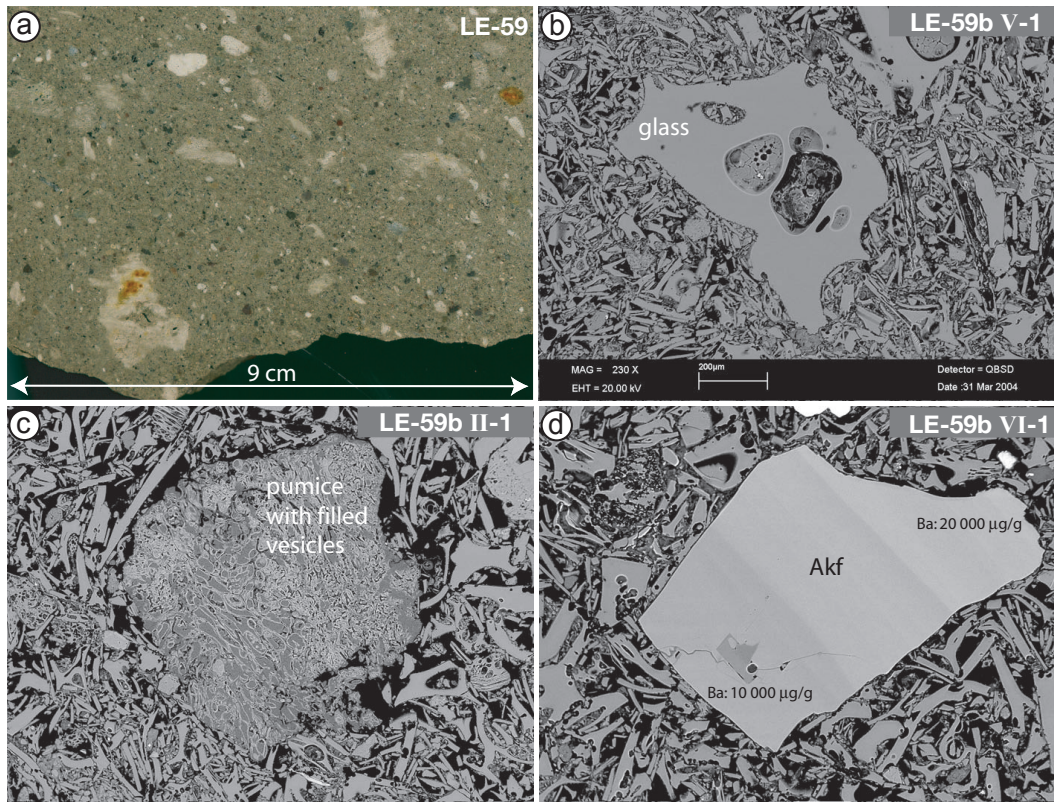


**Fig. A.3.** Characteristics of sample LE-59. (a) Photo of the hand specimen. (b) BSE image of a piece of pumice with filled vesicles in the matrix. (c) BSE image of a piece of glass with large filled and unfilled vesicles in the matrix. (d) BSE image of a fragment of an Akf with a strong stepwise Ba-zonation. Ba ranges from 10 000 µg/g at the former core to 20 000 µg/g at the former rim.

### A.2.3. Sample LE-60

The sample was taken at 15 m. The matrix is composed of grey coloured ash. The sample consists of  $\approx 5$  vol% pumice up to 0.5 cm in size,  $\approx 5$  vol% lithoclasts up to 0.5 cm in size, and  $< 1$  vol% crystals of macroscopically visible biotite and feldspar. Fiamme are absent. (Fig. A.4a)

The matrix consists of cusped and platy glass shards with small vesicles  $\approx 5 - 10 \mu\text{m}$  (Fig. A.4b). Only one larger shard (b I-4) was found in this sample. The cusped shard measures  $400 \times 300 \mu\text{m}$  and contains a subhedral, partly rounded Pl crystal  $200 \times 150 \mu\text{m}$  with very many cracks, suggesting mechanical or thermal stress. (Fig. A.4c)

Two pieces of pumice were found, one (b II) only slightly flattened and with some elongated tubes, while the other (b IV) appears macroscopically white, is quite large ( $5 \times 1$  mm) and shows a lot more flattening (flattening ratio 5 : 1) showing beginning transition into fiamme (Fig. A.4d). Both pieces have small vesicles  $\approx 5 - 10 \mu\text{m}$  within the glass walls.

The contained phenocrysts are mainly Pl (some few with Akf overgrowth), and some Akf and Bt. Of 22 grains documented (100%), 15 grains (68%) are Pl (including two with substantial Akf overgrowth, 9%), 4 grains (18%) Akf of which 3 have an old Pl core or inclusion, and 3 grains Bt (14%).

Pl phenocrysts are up to  $1 \times 0.6$  mm, they range from subhedral to anhedral, one is partly rounded. About a fifth are fragments of larger crystals, while more than a third has glass selvages. Some Pl phenocrysts have inclusions, some appear zoned in the BSE image (Fig. A.4b).

In the thin section (LE-60 b) two of the Pl phenocrysts show Akf overgrowth. One of them (b V-4) is a fragment of Pl with Akf overgrowth at the preserved crystal rim. The other (b VI-1) has a subhedral Pl core, which is largely overgrown by Akf laths.

Of the Akf phenocrysts two are euhedral, up to  $400 \times 300 \mu\text{m}$ , and display a glass selvedge, which is partly cusped. The third crystal is clearly rounded,  $250 \times 180 \mu\text{m}$ , and also displays a glass selvedge. The fourth crystal (b IV-4) has an anhedral Pl core enclosed in a subhedral Akf phenocryst (Fig. A.4e).

---

**Fig. A.4.** (*next page*) Characteristics of sample LE-60. (a) Photo of the hand specimen. (b) BSE image of matrix of cusped and platy glass shards, with numerous small vesicles ( $5 - 10 \mu\text{m}$ ). The Pl phenocryst is a fragment with an old core with inclusions and a glass selvedge. (c) BSE image of a large glass shard with Pl phenocrysts. The glass shard is free from vesicles in contrast to the matrix. However the shard shows embayments at the rim. (*continued next page*)

A.2. Sample descriptions – individual samples of profile A

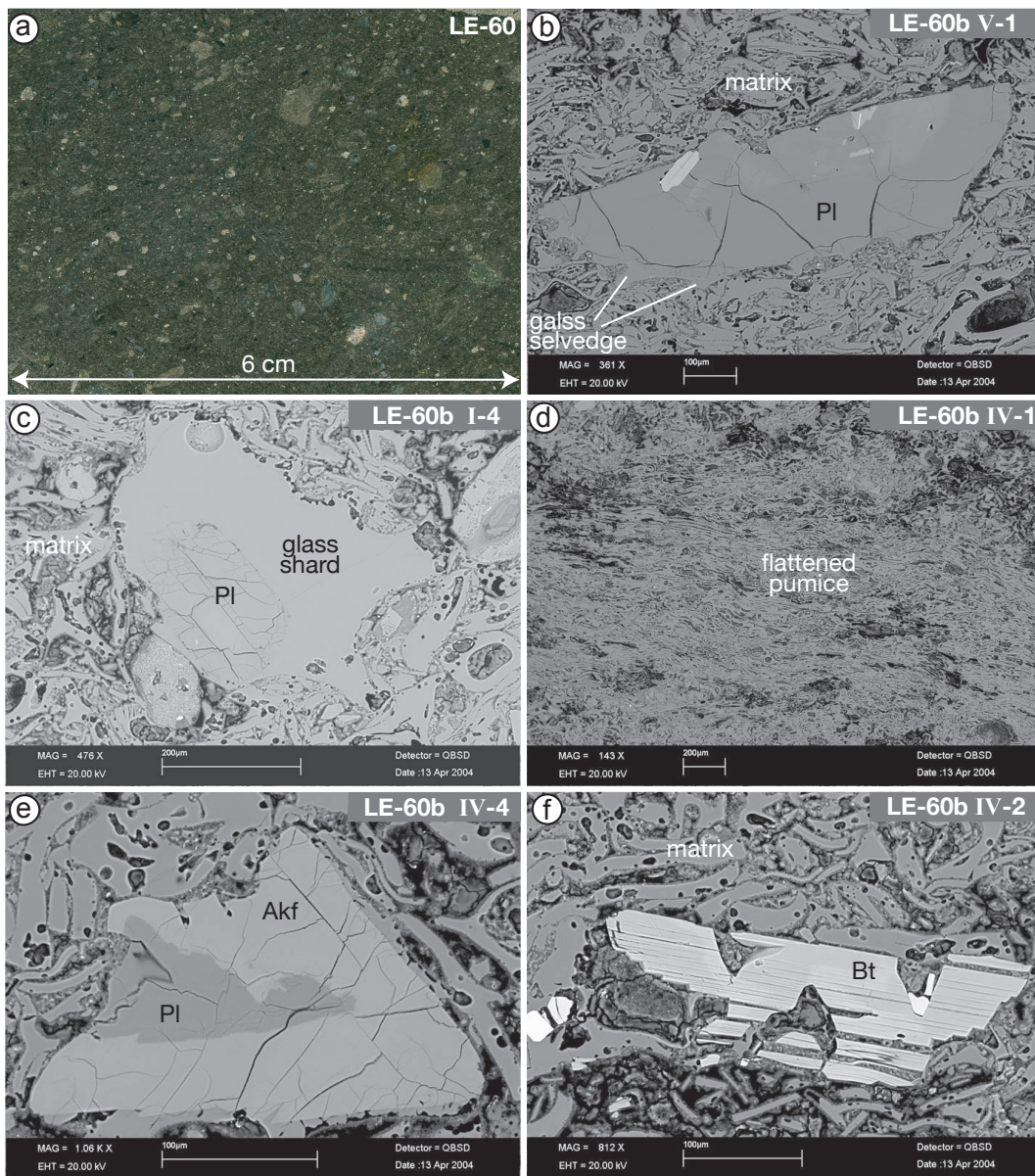


**Fig. A.4. (continued)** Characteristics of sample LE-60. (d) The fiamme appears macroscopically white. In the BSE image the individual glass components are still visible, showing the same vesicles as the matrix. This fiamme has a flattening ration of 1 : 5. (e) BSE image of an Akf phenocryst fragment with Pl core in a narrow glass selvage. (e) BSE image of typical Bt phenocryst, dissolved and slightly fractured, with inclusions.

Of the Bt phenocrysts two formerly euhedral crystals are strongly dissolved and slightly fractured to make an irregularly and dented form, which is up to  $400 \times 100 \mu\text{m}$  (Fig. A.4f). A third Bt is euhedral,  $300 \times 50 \mu\text{m}$ , and contains several inclusions.

#### A.2.4. Sample LE-61

The sample was taken at 18 m. The matrix comprises ash of grey colour. The sample contains  $\approx 2 \text{ vol}\%$  of pumice up to 0.5 cm in size. The pumice is elongate, beginning the transition into fiamme. Fiamme are present as fine strands up to 0.5 cm long.  $\approx 10 \text{ vol}\%$  are made up of lithoclasts, up to 1 cm in size.  $< 1 \text{ vol}\%$  are crystals of macroscopically visible biotite and feldspar. (Fig. A.5a)

The matrix consists of platy, bend and cusped partly vesicular glass. The glass shards are less discrete and more round as in sample LE-60 and lower (Fig. A.5b). The sample contains some larger glass shards. Of the larger shards only one documented (b I-35) shows a well defined form with a clear rim (cusped,  $800 \times 300 \mu\text{m}$  with a large central vesicle  $70 \times 40 \mu\text{m}$ ), the other ones (e.g. a II-2, b I-35) have frizzy rims and holes, additionally to vesicles (Fig. A.5b). These glass shards appear like amalgamations of smaller portions of melt, the holes marking spaces, where two portions did not completely fuse together.

Fiamme, in the thin section up to  $5 \times 1.3 \text{ mm}$  (b IX, flattening ratio 3.8 : 1) and  $2 \times 0.3 \text{ mm}$  (b III-1, flattening ratio 6.7 : 1) appear to be made out of platy and bend glass shards moderately fused together. Basically it looks like the matrix, only denser and more fused. (Fig. A.5c & d)

Lithoclasts in the thin section are of various kind, they are up to  $900 \times 500$ . Eight lithoclasts have been documented in thin sections (LE-61 a and LE-61 b) of the sample.

The contained grains are mainly Pl, some Akf, Bt and a few Fe-Ti oxides. Of 44 grains documented (100%), 23 grains (50%) are Pl, 10 grains (22%) Akf, 8 grains Bt (17%), and 3 grains are Fe-Ti oxides (7%).

Pl is by far the most common phenocryst in the sample. About half of the phenocrysts are fragments, they are mostly anhedral, with some subhedral, rarely euhedral, and also rarely rounded. A bit less than half of the Pl phenocrysts have a

---

**Fig. A.5.** (next page) Characteristics of sample LE-61. (a) Photo of the hand specimen. (b) BSE image of matrix which consists of platy, bend and cusped partly vesicular glass. Shown here is also a larger shard, which is clearly bend and squashed. (continued next page)

A.2. Sample descriptions – individual samples of profile A

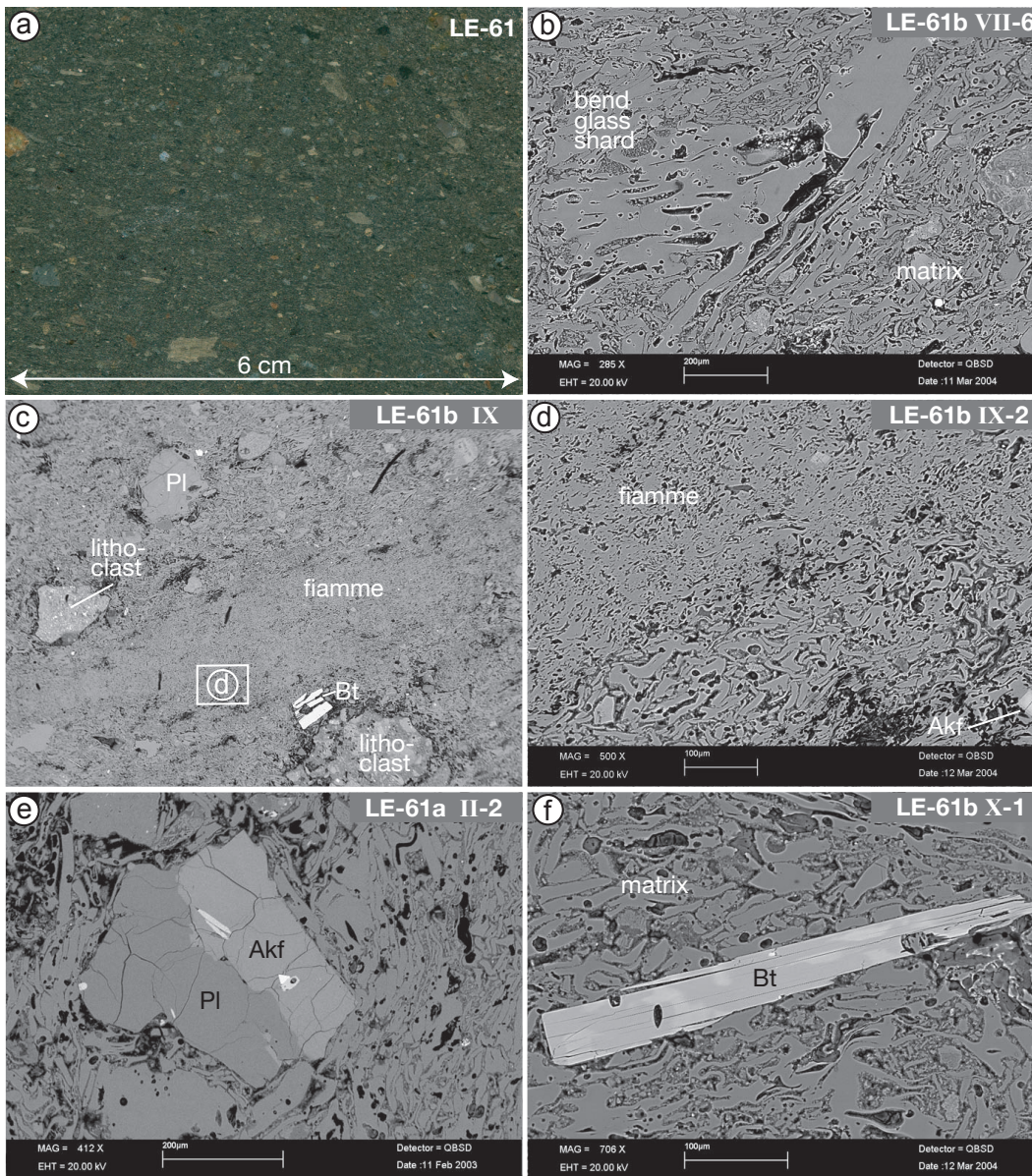


**Fig. A.5. (continued)** Characteristics of sample LE-61. © BSE image of the matrix, showing a fiamme, amongst the matrix, phenocrysts (PI and Bt), and lithoclasts. The rectangle marked d shows the location of the close-up view in the following picture. © Close-up of the fiamme in the previous picture. The texture of the fiamme is clearly shown, which appears like the matrix, only denser and more compacted. © BSE image of an aggregate of Akf and PI with inclusions. The relationship is not clear, but it appears that the PI is the older phase, overgrown by Akf. © BSE image of a Bt phenocryst with irregular patches of zonations.

## A. Individual sample descriptions

---

glass selvage, a third is zoned (Ba, An/Ab, Ba/Sr), while few have inclusions of Akf, Ap and Zrn, and another few have overgrowth of tiny Akf crystals (few  $\mu\text{m}$ ) around their rims. Pl is usually around  $400 \times 200 \mu\text{m}$ , but larger crystals of up to  $1.2 \times 0.8 \text{mm}$  occur. (Fig. A.5b)

One Pl grain,  $500 \times 300 \mu\text{m}$ , occurs as aggregate with a Bt grain,  $900 \times 200 \mu\text{m}$  (a IV-7). The Bt has several holes, is fragmented and parts are rounded, while the Pl seems to have grown into the gaps of the Bt. There is some glass selvage, and some glass filling in a hole between Pl and Bt. Both crystals contain inclusions of probably Ap, one of the inclusions extends into both crystals.

The Akf phenocrysts in the sample are fewer and smaller than Pl, with up to  $300 \times 170 \mu\text{m}$ . All of them have a glass selvage, which can be substantially thick, especially around the euhedral crystals (a third of the Akf). Half of the Akf crystals are fractured, and a third were substantially rounded prior to fracturing.

One phenocrysts (a V-1),  $180 \times 100 \mu\text{m}$  has a small Pl core ( $\varnothing 30 \mu\text{m}$ ) which is completely enclosed by a euhedral Akf and a wide glass selvage. The other (a II-2) comprises an anhedral Pl and a subhedral Akf of similar size; both contain various inclusions (Fig. A.5e). The contact is anhedral, the Pl is anhedral, while the Akf is subhedral. Therefore I think, Pl must be the older phase, which is overgrown by Akf.

Bt phenocrysts vary in size from  $70 \times 50 \mu\text{m}$  to  $600 \times 50 \mu\text{m}$  and  $320 \times 220 \mu\text{m}$ . Most crystals are kinked and broken, half of them display large holes and dented rims. Bt with irregular patches of zonation occur (Fig. A.5f).

In the sample three Fe-Ti oxides were documented. They vary substantially in size from  $150 \times 100 \mu\text{m}$  to  $1.2 \times 0.6 \text{mm}$ , are aggregates of one, two or more round grains, all have faint exsolution lamellae, and contain inclusions of at least two kinds.

### A.2.5. Sample LE-62

The sample was taken at 19.5 m. The matrix is composed of grey coloured ash. The sample contains  $\approx 2 \text{vol}\%$  of pumice up to 0.5 cm in size. The pumice is elongate, beginning the transition into fiamme. Fiamme are present as fine strands up to 2 cm

---

**Fig. A.6.** Characteristics of sample LE-62. (a) Photo of the hand specimen. (b) BSE image of matrix which consists of platy and cusped glass shards, partly with vesicles and frizzy rims, which seem bend and compacted (see left hand upper corner). The glass shards are less discrete and more round as in sample LE-60 and lower. (c) BSE image of an euhedral Akf phenocryst with a Ba-zonation and glass inclusion enclosed in a glass selvage. (*continued next page*)

A.2. Sample descriptions – individual samples of profile A

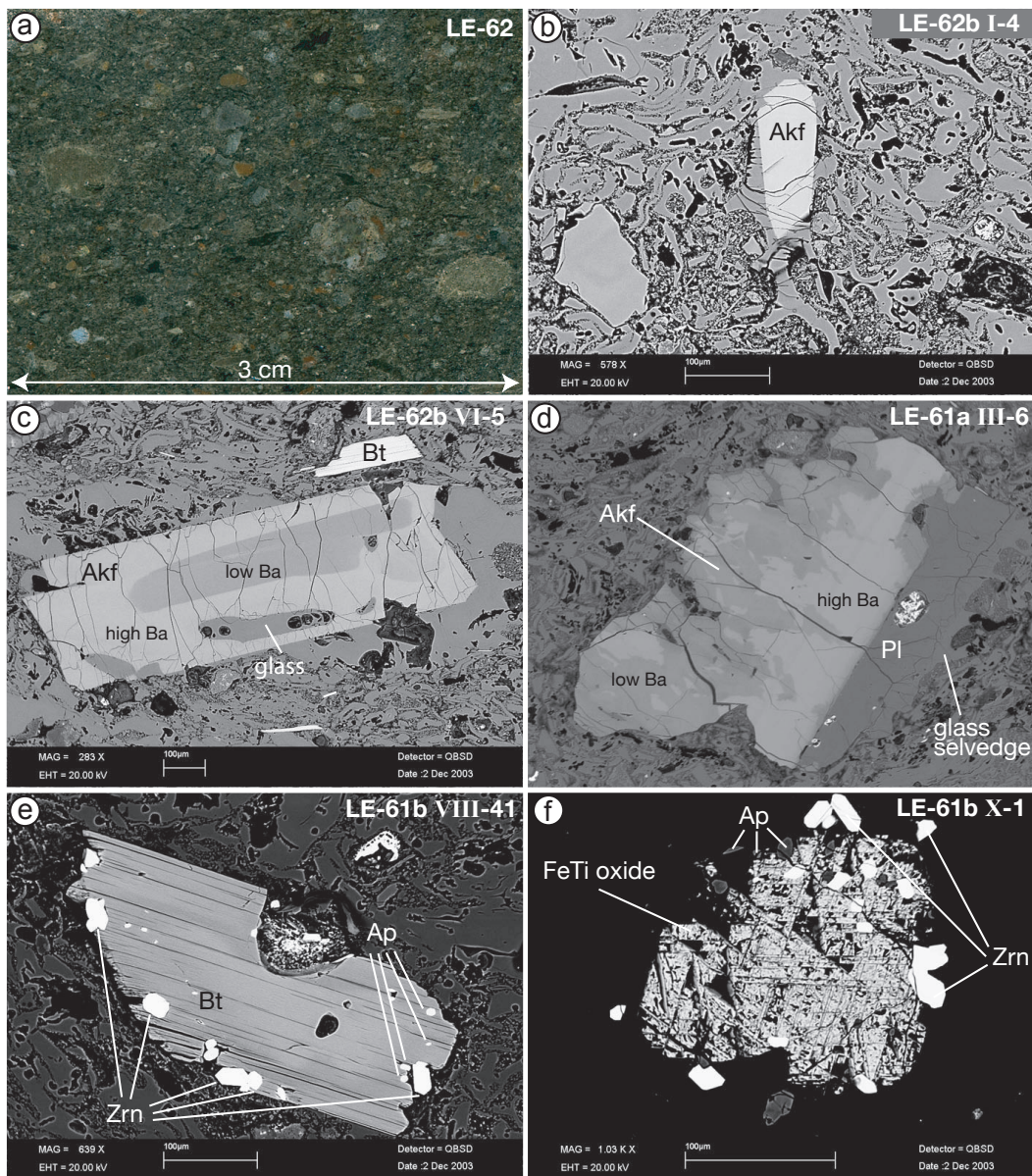


**Fig. A.6. (continued)** Characteristics of sample LE-62. (d) BSE image of an aggregate consisting of Akf with a patchy zonation and PI. The contact is mostly straight, while both minerals are corroded and have a glass selvage. The relationship is not clear. (e) BSE image of a Bt phenocryst, fragmented and with holes. The phenocryst contains numerous inclusions of Ap and Zrn, especially at the rim. (c) BSE image of a Fe-Ti oxide. The phenocryst has a typical rounded form, with exsolution lamellae and inclusions of Ap and Zrn.

## A. Individual sample descriptions

---

long. The sample consists of  $\approx 10$  vol% lithoclasts up to 1 cm in diameter.  $< 1$  vol% are crystals of macroscopically visible biotite and feldspar. (Fig. A.6a)

The matrix of this sample consists of platy and cusped glass shards, partly with vesicles and frizzy rims, which seem bent and slightly compacted. The glass shards are less discrete and more round as in sample LE-60 and lower and only very few larger ones up to  $500 \times 150 \mu\text{m}$  occur. (Fig. A.6b)

The sample contains fiamme, lithoclasts and crystals of mainly Pl (some Pl with Akf) and Akf, subordinately of Bt and Fe-Ti oxides with inclusions of Zrn and Ap.

Fiamme, like in sample LE-61, in the profile just below, appear to be made out of platy and bent glass shards fused together. Basically it looks like the matrix, only denser and more fused.

The contained phenocrysts are mainly Pl and Akf, also Bt and Fe-Ti oxides. Of 58 grains documented (100%), 25 grains (43%) are Pl, 18 grains (31%) Akf, 7 grains Bt (14%), and 4 grains Fe-Ti oxides (7%).

Pl is usually between  $220 \times 100 \mu\text{m}$  and  $600 \times 600 \mu\text{m}$ , but phenocrysts up to  $1.5 \times 1.0 \text{mm}$  occur. Pl is mostly subhedral to euhedral, also anhedral and sometimes the phenocrysts are only fragments of larger ones. More than half of the Pl have selvages and more than a third are zoned. Three phenocrysts found have inclusions of Ap and one also of Bt, a quarter have Akf overgrowth, about half of them substantially.

Akf phenocrysts are between  $300 \times 200 \mu\text{m}$  and  $1200 \times 500 \mu\text{m}$ . Half of them are euhedral to subordinately subhedral, few are fragments or rounded. More than two thirds of the phenocryst display selvages and about a third are zoned. Some of them have small old cores or inclusions of Pl. (Fig. A.6c)

One Fs aggregate ( $180 \times 120 \mu\text{m}$ , a III-6) consists of a Pl and an Akf joined together along a straight line. The Pl is corroded and has some larger holes ( $\varnothing 100 \mu\text{m}$ ). The Akf also has a very irregular rim and is covered in a selvedge. The grain has large patches of more Ba-rich areas. The relationship of two components could not be established. (Fig. A.6d)

Bt phenocrysts are from  $200 \times 100 \mu\text{m}$  to  $400 \times 200 \mu\text{m}$  and  $700 \times 80 \mu\text{m}$ , they are euhedral to subhedral, a few are slightly rounded and usually zoned. Only one Bt displays a glass selvedge and has an inclusion of Ap. Another Bt phenocryst is clearly a fragment, it shows holes and dents, and has numerous inclusions of Ap and Zrn up to  $25 \times 20 \mu\text{m}$ . (Fig. A.6e)

Fe-Ti oxides are all round and usually about  $200 \times 150 \mu\text{m}$ , all have faint exsolution lamellae, and all have inclusions of Ap and Zrn, especially close to the rim. (Fig. A.6f)

### A.2.6. Sample LE-57

The sample was taken at 21 m. The matrix consists of grey ash. The sample contains  $\approx 5$  vol% fiamme up to 2 cm long,  $\approx 10$  vol% lithoclasts up to 2 cm in size, and  $< 1$  vol% crystals of macroscopically visible biotite and feldspar. Pumice is absent. (Fig. A.7a)

The matrix of sample LE-57 consists of platy and cusped glass shards (some with craggy rims) with selvages of microcrystals, of areas of dense glass with perlitic rings, and of areas made out of strings of microcrystals (Fig. A.7b&c). The matrix shows beginning devitrification. However, the portion of pristine glass is still high.

The sample contains fiamme and lithoclasts. The fiamme are more dense than in sample LE-62 and lower in the vertical profile. The glass contains no more holes, only streaks where the different glass pieces welded together. Some fiamme contain perlitic rings. However two fiamme exist (b II-2, b V-3), which display the new texture and areas which resemble the glass texture of sample LE-61 and lower. Fiamme in the thin section are  $\approx 2 \times 0.5$  mm, resulting in a flattening ratio of 4 : 1. One fiamma (a III-1) contains an inclusion of four small crystals of Fe-Ti oxide with Ap and Zrn.

The contained minerals are mainly Pl and Akf, also Bt and Fe-Ti oxides. Of 30 grains documented (100%), 14 grains (47%) are Pl, 10 grains (33%) Akf, 4 grains Bt (13%), and 2 Fe-Ti oxide (7%).

Of the Pl phenocrysts half are subhedral and half anhedral, they are often fractured, and sometimes zoned. Crystals are up to  $800 \times 600 \mu\text{m}$ , but when Pl has Akf overgrowth, like about a third of the phenocrysts, crystals are smaller than that (up to  $500 \times 500 \mu\text{m}$ ). Akf overgrowth can be as “satellite” (b I-5), as small crystallites around the Pl rim (b IV-1), or completely surrounding the core and reaching an area much larger than the core (a IV-2), then counting as Akf with small old core. About half of the Pl phenocrysts have a glass selvedge.

The Akf phenocrysts are up to  $1.0 \times 0.8$  mm, euhedral to subhedral, sometimes fractured, all have glass selvages, and are mostly zoned (e.g. Ba-zonation). A third of the Akf phenocryst have small old Pl cores.

Bt phenocrysts are mostly euhedral, around  $200 \times 100 \mu\text{m}$  but nevertheless have holes and dents in their rims. Glass selvages occur, but are not common, while only one crystal (a II-2) is mechanically stressed, appearing bend.

The two documented Fe-Ti oxides are quite different: one is a aggregate of four round grains with definite exsolution lamellae and inclusions of unknown size in the centre of a fiamme, while the other is a single round Fe-Ti oxide,  $120 \times 80 \mu\text{m}$ , with only faint exsolution lamellae and inclusions as aggregate with Pl (Fig. A.7c).

## A. Individual sample descriptions

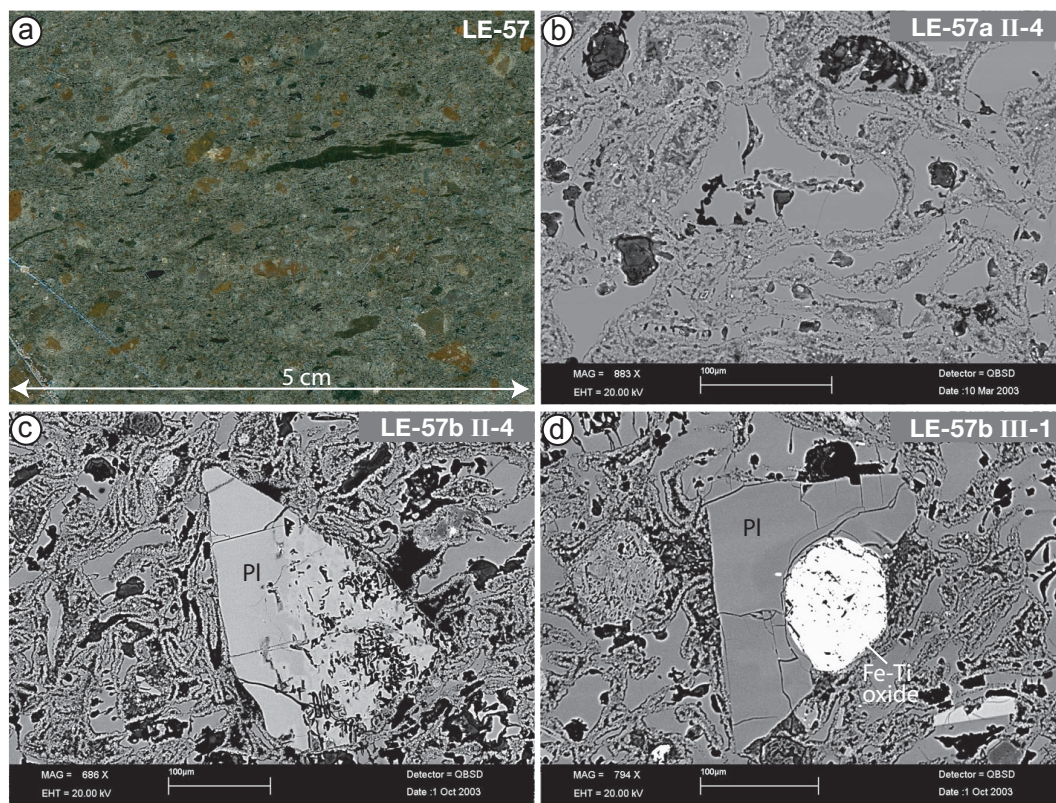


**Fig. A.7.** Characteristics of sample LE-57. (a) Photo of the hand specimen. (b) BSE image of matrix which consists of platy and cusped glass shards with craggy rims and areas made from strings of micro-crystals. (c) BSE image of the matrix with a smaller amount of glass shards and more micro-crystals. In the centre of the picture is a An-rich, highly corroded PI, which is considered a xenocryst. (d) BSE image of an aggregate consisting of PI and Fe-Ti oxide. It is possible, that before fragmentation the Fe-Ti oxide was a large central inclusion in the PI.

### A.2.7. Sample LE-63

The sample was taken at 24 m. The matrix is welded and grey to light pink in colour. The sample consists of  $\approx 5$  vol% mostly weathered fiamme up to 2 cm long, and  $\approx 10$  vol% lithoclasts up to 1 cm in size.  $< 1$  vol% are crystals of macroscopically visible biotite and feldspar. Pumice is absent. (Fig. A.8a)

The glass contained in the matrix of sample LE-63 is not suitable for analysis. While the outlines of individual platy and cusped shards are still visible the shards have a fuzzy texture, mostly vertical to the rims, which includes cavities (Fig. A.8b). Analyses sums are on average 99.6 vol% for the matrix of this sample, while the

A.2. Sample descriptions – individual samples of profile A

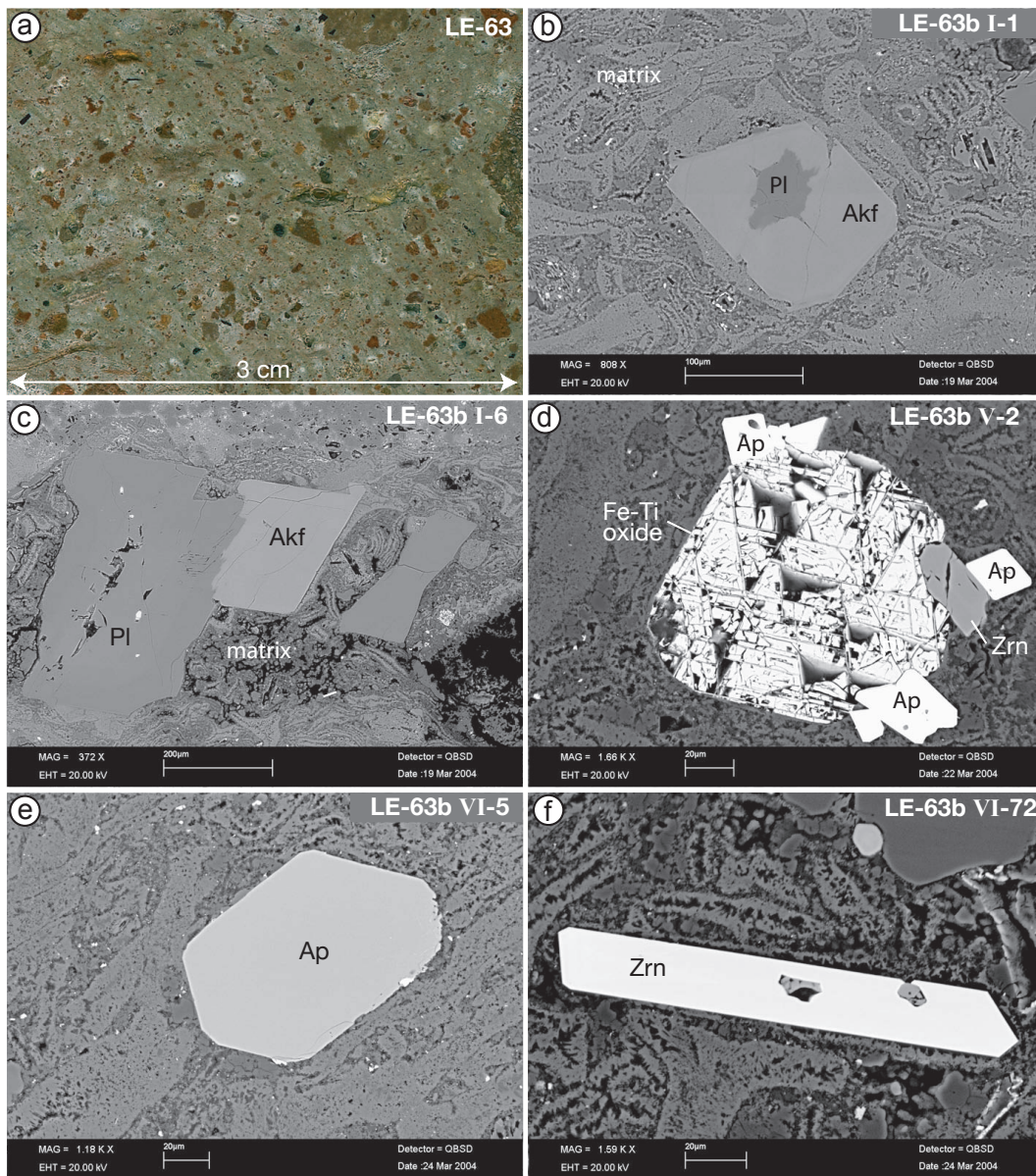


**Fig. A.8.** Characteristics of sample LE-63. (a) Photo of the hand specimen. (b) BSE image of matrix, outlines of individual platy and cusped shreds are still visible the shreds have a fuzzy texture, mostly vertical to the rims, which includes cavities. In the centre of the image is a typical subhedral Akf phenocrysts with an old Pl core. (c) BSE image of a Pl phenocryst with satellitic Akf overgrowth. (d) BSE image of a round Fe-Ti oxide with exsolution lamellae and inclusions of Ap and Zrn. (e) BSE image of Ap phenocryst. (f) BSE image of Zrn phenocryst. (For CL image see Fig. 3.8 d on page 43)

analyses sums in samples with pristine glass are on average 96.1 vol%. The glass is dehydrated and devitrified.

The sample contains grains of mainly Pl with and without Akf overgrowth, Akf with and without old Pl cores, subordinately grains of Bt and Fe-Ti oxides, and each a single grains of Ap and of Zrn. Of 26 grains documented (100%), 9 grains (32%) each are Pl and Akf, 6 grains Bt (21%), 2 Fe-Ti oxide (7%), and each 1 grain (4%) Ap and Zrn. Crystals contain inclusions of Ap and Zrn (in Fe-Ti oxides), and Fe-Ti oxides and Bt (in Pl).

The Pl phenocrysts are usually between  $280 \times 220 \mu\text{m}$  and  $700 \times 400 \mu\text{m}$  and up to  $1000 \times 600 \mu\text{m}$ . They are mostly subhedral to euhedral, one is anhedral, half of them are zoned and have a selvedge of former glass. A third of the Pl have Akf overgrowth, as satellites (Fig. A.8c) or as a selvedge of microcrystals. One anhedral Pl (b VIII-1) has a selvedge of small euhedral Akf crystals. Two of the Pl crystals have inclusions of Fe-Ti oxides and one has an inclusion of Bt.

The Akf phenocrysts in the sample are usually around  $200 \times 180$ , but up to  $800 \times 900 \mu\text{m}$ . They are euhedral to subhedral, two thirds of the phenocryst contain small old cores of Pl. The Pl cores are all anhedral and mostly very irregularly shaped, while the Akf overgrowth is euhedral to subhedral and most of them have additionally a selvedge of devitrified glass. (Fig. A.8b)

All Bt phenocrysts in sample LE-63 are subhedral, however they show signs of mechanic stress and are at least a little fractured. The Bt phenocrysts are between  $600 \times 350 \mu\text{m}$  and  $260 \times 30 \mu\text{m}$ . Few contains inclusions of Zrn and Ap.

The Fe-Ti oxides are  $300 \times 250 \mu\text{m}$  and  $120 \times 100 \mu\text{m}$ , they are round, have large inclusions of Zrn and Ap (up to  $20 \times 30 \mu\text{m}$ ) and faint exsolution lamellae; one Fe-Ti oxide has a selvedge of devitrified glass. (Fig. A.8d)

The sample contains also one quite large ( $100 \times 70 \mu\text{m}$ ), euhedral phenocryst of Ap and one big ( $150 \times 25 \mu\text{m}$ ), euhedral phenocryst of Zrn, which are not inclusions, but individual phenocrysts. (Fig. A.8e&f)

#### **A.2.8. Sample LE-64**

The sample was taken at 27 m. The matrix is welded and is of pink colour. The sample contains  $\approx 10 \text{ vol}\%$  of mostly weathered fiamme, up to 1 cm long. Lithoclasts of up to 2 cm make up  $\approx 15 \text{ vol}\%$ .  $< 1 \text{ vol}\%$  are crystals of macroscopically visible biotite and feldspar. Pumice is absent. (Fig. A.9a)

The glass contained in the matrix of sample LE-64 is not suitable for analysis. While the outlines of individual platy and cusped shards are still visible, the shards have a fuzzy texture, mostly vertical to the rims, which includes cavities (Fig. A.9b). The amount of fuzziness seems larger than in sample LE-63. The glass therefore

## A.2. Sample descriptions – individual samples of profile A

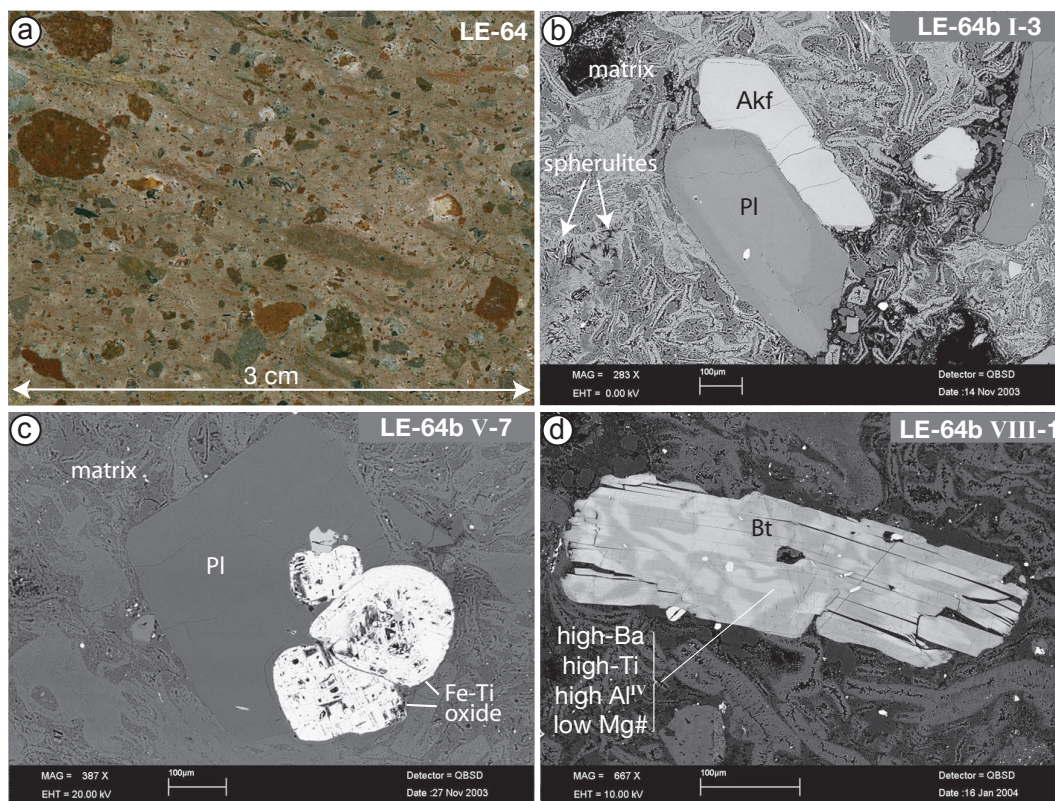


**Fig. A.9.** Characteristics of sample LE-64. (a) Photo of the hand specimen. (b) BSE image of matrix with outlines of individual platy and cusped shards still visible. The shards have a fuzzy texture, mostly vertical to the rims, which includes cavities. The amount of fuzziness seems larger than in sample LE-63. The matrix also contains spherulites. In the centre of the image is a zoned PI phenocryst with satellitic Akf overgrowth. (c) BSE image of an PI phenocryst with large Fe-Ti oxide inclusions. (d) BSE image of a Bt phenocryst with patchy zonation. The light coloured patches are high-Ba, high-Ti, high-Al<sup>IV</sup>, low Mg#.

seems devitrified to a larger extent, which is also supported by the fact that some very few spherulites can be found (b I-3, b II-4), which are a characteristic product of high-temperature devitrification in natural glass (MCPHIE *et al.*, 1993). Analyses sums are on average 99.8 vol% for the matrix in this sample, while the analyses sums in samples with pristine glass are on average 96.1 vol%.

Sample LE-64 contains mainly PI, also Akf and Bt. Inclusions of Fe-Ti oxides, Zrn and Bt exist in PI. Of 30 grains documented (100%), 17 grains (57%) are PI, 5 grains each are Bt and Akf (17%), and 3 grains (10%) are Fe-Ti oxides.

PI is subhedral to anhedral, nearly half of the PI phenocrysts are fragments of

larger ones, few have a selvage and are zoned, while only one each is rounded and dissolved. About a third of the phenocrysts have inclusions of large Fe-Ti oxides (Fig. A.9c), Ap and Zrn, as well as Bt. Pl is between  $800 \times 400 \mu\text{m}$  and  $250 \times 200 \mu\text{m}$ . Two phenocrysts of Pl recorded have Akf overgrowth. The first one (b I-3) is only partly. An euhedral Akf ( $500 \times 200 \mu\text{m}$ ) is attached as satellite to an euhedral, zoned Pl ( $600 \times 250 \mu\text{m}$ ) (Fig. A.9b). In the second case (b VIII-2) the Pl ( $700 \times 200 \mu\text{m}$ ) is subhedral to anhedral with cracks and zoned, the Akf overgrowth is subhedral as a selvage at about half the rim.

The Akf phenocrysts are anhedral to subhedral, fragmented and usually around  $300 \times 150 \mu\text{m}$  or rounded, zoned and smaller,  $140 \times 50 \mu\text{m}$ . Only one Akf phenocryst has an older, small Pl core. The small ( $\varnothing 25 \mu\text{m}$ ), very irregular Pl cores are encased in a subhedral Akf ( $300 \times 100 \mu\text{m}$ ). The Akf is zoned and partly Ba-rich.

The Bt phenocrysts are between  $600 \times 400 \mu\text{m}$  and  $200 \times 50 \mu\text{m}$ . They are subhedral and rounded mostly and all have inclusions of probably Ap and Zrn. One Bt (b VIII-1) is subhedral, not rounded, but slightly fractured. The crystal shows irregular patches of light colour and irregular zonation. The light patches are high-Ba, high-Ti, high-Al<sup>IV</sup>, and low Mg# in comparison to the rest of the crystal. (Fig. A.9c)

Fe-Ti oxides have three documented occurrences in this sample. The first two are an individual round grain (b III-1)  $\varnothing 400 \mu\text{m}$  and a cluster of several grains (b V-7),  $350 \times 300 \mu\text{m}$ , with all grains round, inclusions of Ap and Zrn, and exsolution lamellae. The third smaller ( $100 \times 40 \mu\text{m}$ ), irregular shaped, with faint exsolution lamellae, but no inclusions.

#### A.2.9. Sample LE-65

The sample was taken at 32m. The matrix is welded and of the colour pink. The sample contains  $\approx 10 \text{ vol}\%$  of mostly weathered fiamme up to 1 cm long, and  $\approx 18 \text{ vol}\%$  of lithoclasts up to 1 cm in size.  $< 1 \text{ vol}\%$  consists of crystals of macroscopically visible biotite and feldspar. Pumice is absent. (Fig. A.10a)

The glass contained in the matrix of sample LE-64 is not suitable for analysis, it is devitrified. The shapes of platy and cusped shards are still visible, but the texture is fuzzy and includes cavities. In contrast to the next underlying sample (LE-65)

---

**Fig. A.10.** Characteristics of sample LE-65. (a) Photo of the hand specimen. (b) BSE image of matrix with outlines of individual platy and cusped shards still visible. The shards have a fuzzy texture, mostly vertical to the rims, which includes cavities. The amount of fuzziness seems increased. The matrix also contains "blobs" of SiO<sub>2</sub>. (*continued next page*)

A.2. Sample descriptions – individual samples of profile A

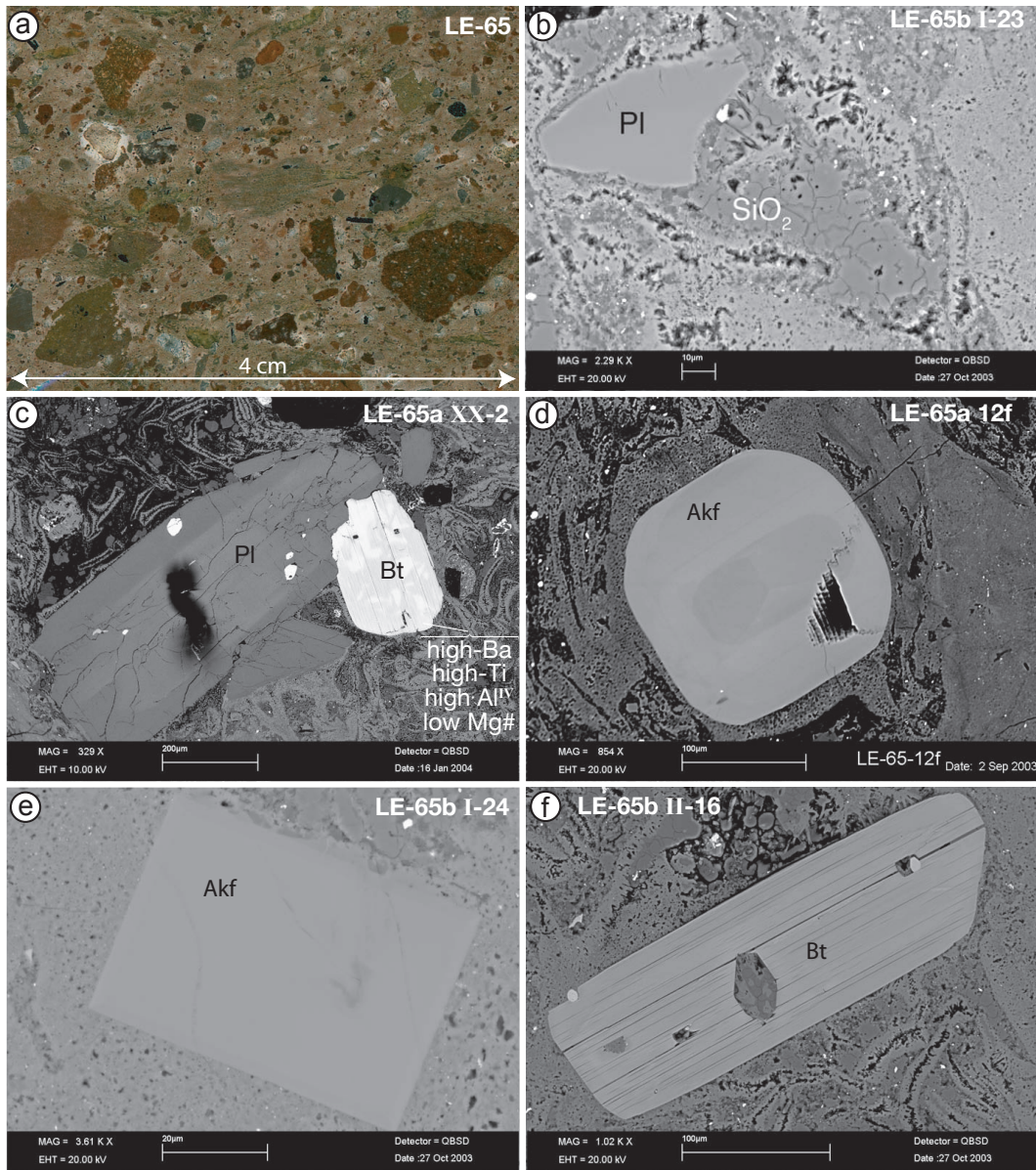


**Fig. A.10.** (*continued*) Characteristics of sample LE-65. (c) BSE image of an aggregate of PI and Bt. The PI is subhedral and zoned, while the Bt is anhedral, slightly rounded and has a patchy zonation. The light coloured patches are high-Ba, high-Ti, high-Al<sup>IV</sup>, low Mg#. (d) BSE image of a very small, rounded and zoned Akf phenocryst. (e) BSE image of an euhedral Akf phenocryst. (f) BSE image of a subhedral and slightly rounded Bt phenocryst with some holes.

no spherulites were found in the matrix. However the matrix frequently contains “blobs” of SiO<sub>2</sub> from a few μm to 100 × 30 μm (Fig. A.10b). Analyses sums are on average 99.7 vol% for the matrix of this sample, while the analyses sums in samples with pristine glass are on average 96.1 vol%.

Sample LE-65 contains mainly Pl, subordinately Akf, Bt and Fe-Ti oxides. Inclusions of Ap and Zrn, Bt, Akf were also found in Pl. Of 27 grains documented (100%), 14 grains (52%) are Pl, 5 grains Akf (19%), and 4 grains Bt and Fe-Ti oxides (15%) each.

Pl phenocrysts are mainly anhedral to subhedral and they are usually around 1000 × 500 μm, with only one very small (80 × 70 μm) euhedral crystal documented (b II-14). Nearly all of the crystals have inclusions of Ap and Zrn, Bt and even some Akf. A quarter of the phenocryst are zoned and another quarter has remains of glass selvages. (Fig. A.10c)

The Akf phenocrysts are euhedral to subhedral, with half of them fragmented and zoned in respect to Ba. Fragmented and zoned Akf are large ~ 1200 × 600 μm, while an non-fragmented and unzoned crystal is small 80 × 70 μm. (Fig. A.10d&e)

Bt phenocrysts are between 700 × 350 μm and 280 × 180 μm and just a bit less common than Akf. They used to be euhedral laths, but half are fractured, the other half are rounded or corroded at the rims. The phenocrysts contain holes and/or inclusions of Ap and Zrn. One half of the phenocrysts have a noticeable patchy colour texture. Light coloured patches are high-Ti, high-Ba, high-Al<sup>IV</sup>, and low-Mg#. The same characteristics as the patchy Bt in LE-64 (b VIII-1). (Fig. A.10f)

Fe-Ti oxides measure between 250 × 230 μm and 180 × 170 μm. They are all round, have exsolution lamellae, and have inclusions of Ap and Zrn; one grain has a selvedge of some kind (former glass or Pl?).

#### **A.2.10. Sample LE-67**

This sample is a loose block found at the slope of the vertical profile. It probably originated from in-between the site of sample LE-65 at 32m and the site of sample LE-66 at 40m.

The matrix of this sample is welded and of red colour. The sample consists of ≈ 15 vol% fiamme, which are up to 7 cm long, and ≈ 20 vol% of lithoclasts up to 1.5 cm in size. < 1 vol% consists of crystals of macroscopically visible biotite and feldspar. Pumice is absent. (Fig. A.11a)

The glass in the matrix of sample LE-67 is not suitable for analysis. The matrix has a fuzzy texture including cavities, with the outlines of platy and cusped shards barely visible. The matrix contains some few spherulites (b V-2) and some “blobs” (b I-21, b IV-3), similar to the ones in sample LE-65 consisting of SiO<sub>2</sub> (Fig. A.11b).

A.2. Sample descriptions – individual samples of profile A

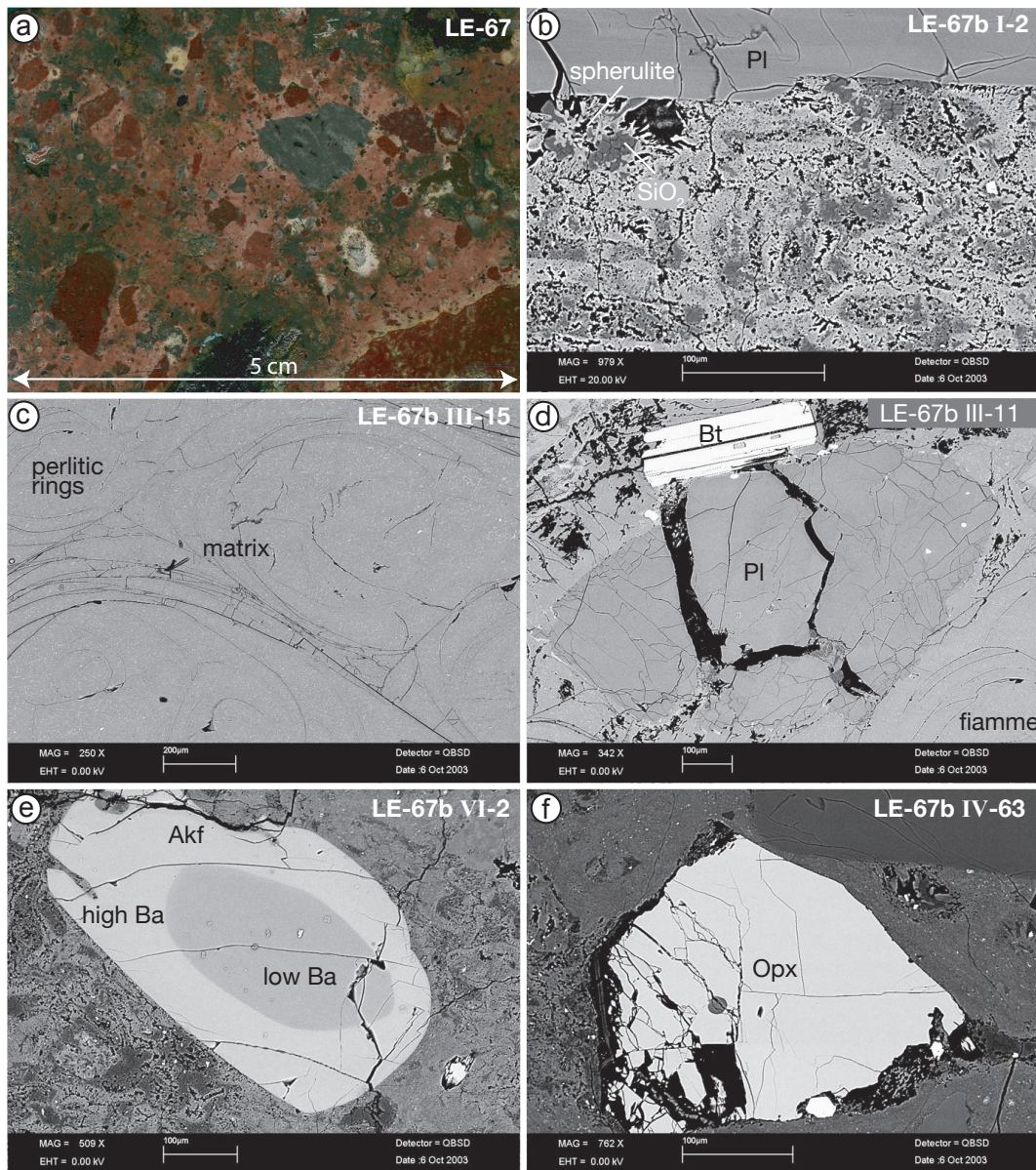


**Fig. A.11.** Characteristics of sample LE-67. (a) Photo of the hand specimen. (b) BSE image of matrix with outlines of individual platy and cusped barely visible. The matrix has spherulites and “blobs” similar to the ones found in LE-65. (c) BSE image the pristine glass in a fiamme: it has perlitic rings and contains crystallites. (d) BSE image of a large, fractured PI phenocryst with Bt. (e) BSE image of a rounded and step-wise zoned Akf phenocryst. The rim is high in Ba (25000 mg/g), the core is low (15000 mg/g Ba). (f) BSE image of a subhedral and slightly fractured Opx phenocryst.

Following this the glass of the matrix is devitrified.

However, pristine glass was found and analysed in a large fiamma contained in the sample. The glass is corroded at the rims of the fiamma (b I-6) and more and more pristine towards the centre of it (b I-61, b III-15) (Fig. A.11c).

Analyses sums are on average 96.2 vol% for the glass in the fiamma of this sample, which is within the average for analyses sums in samples with pristine glass of 96.1 vol%.

Sample LE-67 contains phenocrysts of mainly Pl, to lesser extent Bt and Akf, and subordinately Fe-Ti oxide and Cpx. Inclusions of Ap, Zrn, Fe-Ti oxide are found in Pl, while inclusions of Ap and Zrn are found in Bt. Of 36 grains documented (100%), 21 grains (55%) are Pl, 8 grains Bt (21%), and 7 grains Akf (18%), and one grain of Fe-Ti oxide and Cpx each (3%).

Nearly three quarters of the Pl phenocrysts are fragmented and anhedral, and most of them have cracks, some of them substantial ones. Overall it seems the phenocryst had been objected to a lot of stress, nearly all of the crystals are corroded at the rims. About a quarter of the phenocrysts are strongly zoned, with high-Ba and high-Ab at the rims. Phenocrysts measure between  $1800 \times 1200 \mu\text{m}$  and  $400 \times 180 \mu\text{m}$ .

Two phenocrysts have Akf overgrowth; in one case (b IV-3) the overgrowth consists of a narrow selvedge at one side of the subhedral Pl phenocryst, in the other case (b I-4) the subhedral Pl ( $175 \times 80 \mu\text{m}$ ) is completely encased in substantial and thick ( $75 - 25 \mu\text{m}$ ), but irregular (anhedral) Akf overgrowth.

Bt phenocrysts are all subhedral to euhedral, containing inclusions of Ap and Zrn, they are between  $400 \times 150 \mu\text{m}$  and  $220 \times 20 \mu\text{m}$ . Half of the crystals have light and dark coloured patches, like observed on Bt from sample LE-65 and LE-64. The analyses from the light coloured patches show more or less the same characteristic: high-Ba and low Mg#. The Bt phenocrysts show only mild traces of mechanical stress, a quarter is mildly fragmented, one tiny lath is slightly bend.

The Akf phenocrysts range hugely in size from  $180 \times 150 \mu\text{m}$  to  $1000 \times 400 \mu\text{m}$ . The phenocrysts are anhedral to subhedral, or even highly corroded and rounded, half of them are zoned, showing high-Ba concentrations in the rims. Two Akf have Pl cores; one subhedral Akf (b V-2) contains a tiny subhedral Pl, while another (b IV-5) might show either fractured remains of a crystal with an old small Pl core or incomplete encasing of the core. (Fig. A.11e)

There is one individual Fe-Ti oxide recorded. The grain is round and measures  $230 \times 150 \mu\text{m}$ , like most other recorded Fe-Ti oxides it has inclusions and very clearly developed exsolution lamellae.

There is also one separate recorded Opx, which is subhedral and fractured and has some cracks. The crystal is  $300 \times 250 \mu\text{m}$  (Fig. A.11f). It is the only Opx found in all samples from Profile A, there is one other one found in LE-68 in Profile B.

### A.2.11. Sample LE-66

The sample was taken at 40 m. The matrix is welded, and glassy black, fiamme are hard to distinguish from it. The sample consists of  $\approx 20$  vol% vesicular fiamme, up to 7 cm in size. Lithoclasts make up  $\approx 15$  vol% and are up to 1.5 cm in size.  $< 1$  vol% consists of crystals of macroscopically visible biotite and feldspar. Pumice is absent. (Fig. A.12a)

The glass contained in the matrix and the fiamme of sample LE-66 is not suitable for analysis. The matrix and fiamme have a fuzzy texture, including cavities. The outline of former glass shards are not visible any more. The sample contains some “blobs” (b IV-4 (Fig. A.12b)), b VIII-1, b VIII-52; probably  $\text{SiO}_2$ ) similar to sample LE-67, and sample LE-65. Some few small spherulites can also be found in the matrix (b II-2, b IV-3 (Fig. A.12c)). Devitrification of this glass sample seems probable. Analyses sums are on average 100.6 vol% for the matrix and fiamme of this sample, while the analyses sums in samples with pristine glass are on average 96.1 vol%.

The most common crystal by far is Pl, followed Akf and subordinately Bt, and Fe-Ti oxide. Inclusions of Fe-Ti oxides and possibly Ap and Zrn are found in Pl. Of 42 grains documented (100%), 30 grains (70%) are Pl, 9 grains Akf (21%), 2 grains Bt (5%), one grain of Fe-Ti oxide (2%), and one grain of a  $\text{SiO}_2$ -component (2%).

Some Pl phenocrysts are quite large  $2.0 \times 0.5$  mm and  $1.1 \times 1.0$  mm, the smallest phenocrysts measured are  $200 \times 250$   $\mu\text{m}$ . Two thirds of Pl is subhedral of which more than half are zoned with high-Ba, high-Ab at the crystal rims, however, one grain shows low Ba content at the rim (b VIII-1). The remaining third of the phenocrysts is anhedral. Only one of the anhedral phenocrysts shows zonation (b VIII-52). One third of the phenocrysts are fragments of larger ones, while one sixth have inclusions of Fe-Ti oxides and possibly Ap and Zrn, and another sixth have large cracks and cavities.

Overgrowth of the Pl phenocrysts with Akf is rare, only four grains show overgrowth. Half of the Akf overgrowth consists of large satellites (which are rounded, while the Pl has clear sharp edges, Fig. A.12c). The other half comprises a selvage of individual small Akf crystals (Fig. A.12d). One additional crystal shows even the opposite relationship: the euhedral, zoned Akf is partly replaced by Pl, forming anhedral borders with the older grain (Fig. A.12e).

About half of the Akf phenocrysts are subhedral, while the other half is highly corroded and rounded or anhedral. Grains are  $\approx 200 \times 100$   $\mu\text{m}$  of which half show zonation. A third of the Akf phenocrysts have small older Pl cores, however the cores are in one case off-centre and in another case the core is not fully encased.

## A. Individual sample descriptions

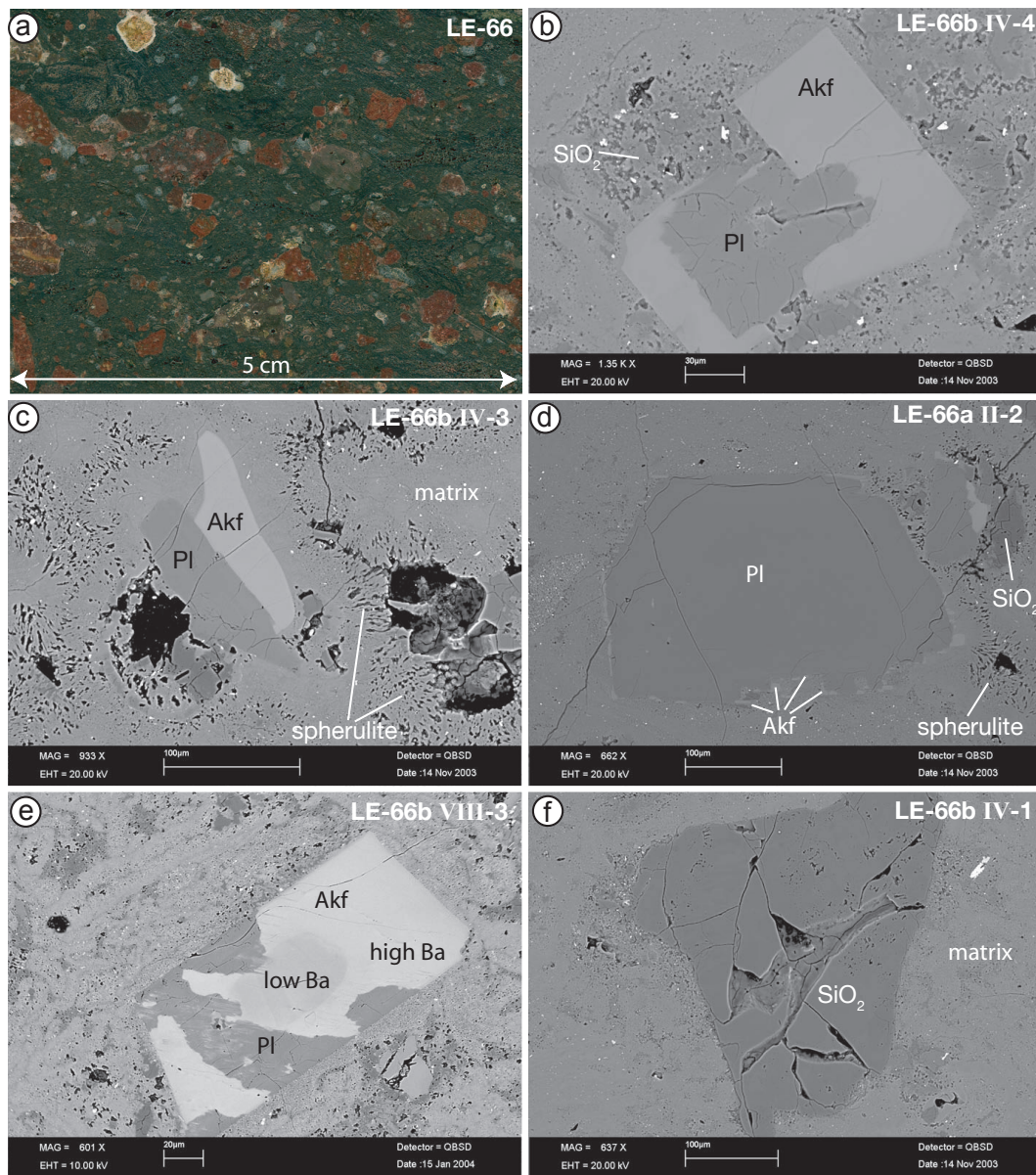


**Fig. A.12.** Characteristics of sample LE-66. (a) Photo of the hand specimen. (b) BSE image of matrix, which contains some “blobs” similar to sample LE-67 and sample LE-65. The picture also shows an anhedral Pl with substantial euhedral Akf overgrowth. (c) BSE image of matrix, showing some spherulites. The picture also shows a Pl with satellitic Akf overgrowth. The overgrowth is rounded, while the Pl retains discrete and straight rims. (d) BSE image of a large, subhedral Pl phenocryst with a selvage of small Akf crystals. The matrix is fuzzy, outlines of former shards are not visible. The matrix contains spherulites and “blobs” of  $\text{SiO}_2$ . (continued next page)

**Fig. A.12.** (*continued*) Characteristics of sample LE-66. © BSE image of an euhedral and zoned Akf, replaced in patches by Pl. The Akf is zoned: the rim is high in Ba ( $\approx 25000$  mg/g), the core is low ( $\approx 12000$  mg/g Ba). ⓘ BSE image of a subhedral and slightly fractured Opx phenocryst.

---

One phenocryst is a fragment of a larger one.

Only two Bt phenocryst were documented in the thin section of sample LE-66. They are both  $\approx 600 \times 150 \mu\text{m}$ , subhedral, show cracks, cavities and embayments, and have inclusions of probably Ap and Zrn.

One Fe-Ti oxide was documented, which is round, small ( $\varnothing 140 \mu\text{m}$ ) and has no inclusions. One large grain of a  $\text{SiO}_2$ -component was also found and documented (b IV-1, Fig. A.12f). It is  $320 \times 220 \mu\text{m}$ , anhedral, with large cracks and cavities, and a corroded rim.

### A.3. Sample descriptions – individual samples of profile B

Profile B consists of four samples and was taken at the N side of Tavros mountain (374 m above sea-level), in the valley between Tavros mountain and Mesovouni flank. The location is close to the chapel Aghia Haralambos, W of the village Nees Kidonies and NNW of the villages Komi and Pigi. (Fig. A.1, page 165)

#### A.3.1. Sample LE-68

The sample was taken  $\approx 22$  m above the bottom of the outcrop. The matrix consists of welded ash with a pink colour. The sample contains  $\approx 20$  vol% of extremely elongated fiamme (low thickness : length ratio) up to 7 cm long.  $\approx 15$  vol% are made up by lithoclasts, up to 1 cm in size.  $< 1$  vol% consists of crystals of macroscopically visible biotite and feldspar. Pumice is absent. (Fig. A.13a)

The glass in the matrix of sample LE-68 is only partly suitable for analysis. The matrix has a fuzzy texture including cavities, with the outlines former shards barely visible. The matrix contains some some “blobs”, similar to the ones in sample LE-65 and LE-67 consisting of  $\text{SiO}_2$ . However pieces of pristine glass are frequently found as “islands” within the matrix (Fig. A.13b). The pristine shards are surrounded by the fuzzy texture and often have very irregular rims. Analyses show to be as good as analyses of the pristine glass additionally found and analysed in a large fiamme contained in the sample. The glass in the fiamme shows schlieren and inclusions of crystallites (Fig. A.13b). Analyses sums are on average 96.3 vol% for

## A. Individual sample descriptions

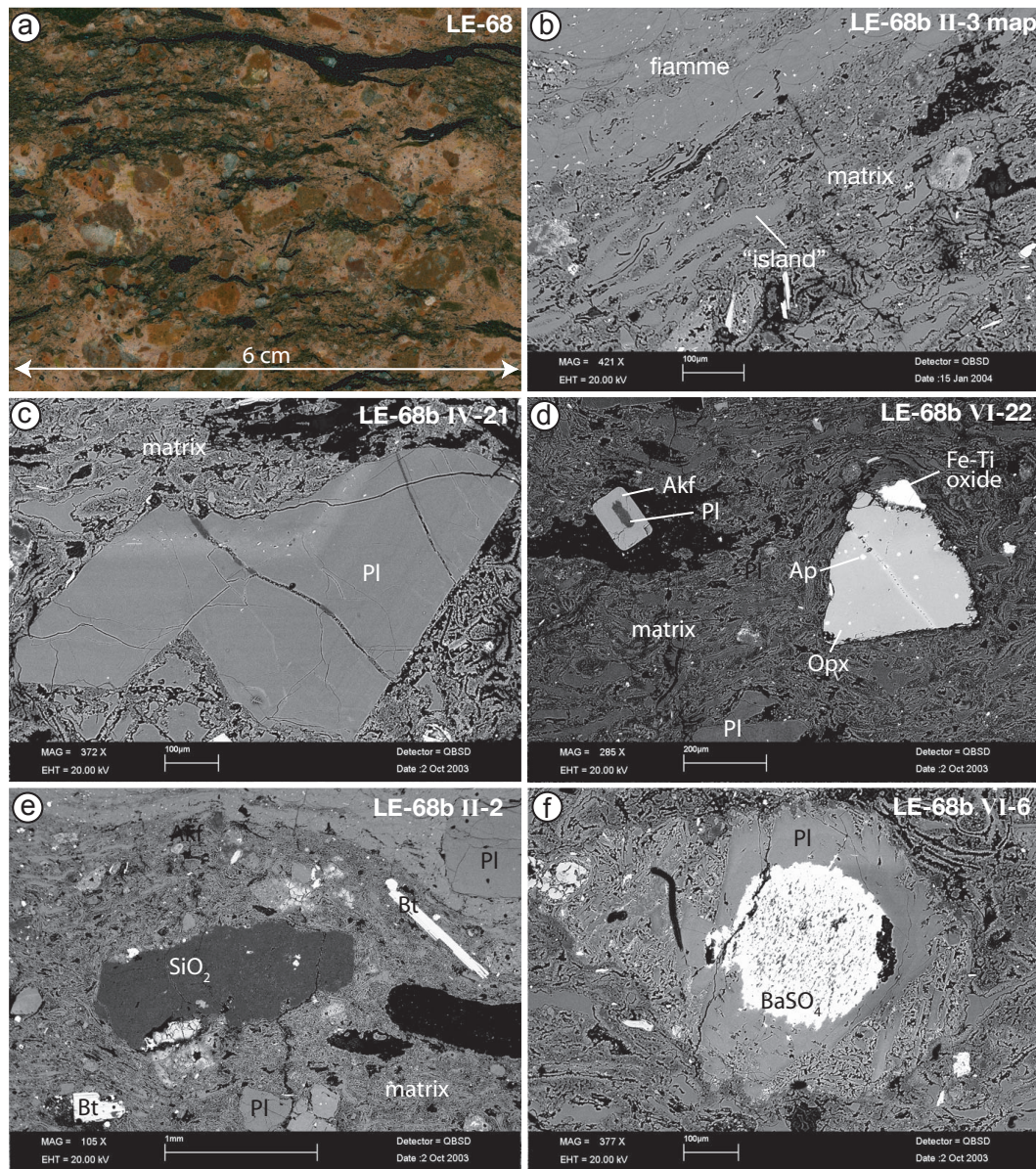


**Fig. A.13.** Characteristics of sample LE-68. (a) Photo of the hand specimen. (b) BSE image of matrix and fiamme, pristine glass is found in “islands” within the matrix and in fiamme, while the rest of the matrix with a fuzzy and irregular texture is devitrified. (c) BSE image of a large, zoned Pl phenocryst, which is a fragment of a formerly much larger crystal. (d) BSE image of an anhedral Opx phenocryst with Ap inclusions. The phenocryst shows beginning dissolution at the rim. Also shown in the picture is a very untypical Fe-Ti oxide (anhedral, without inclusions and exsolution lamellae) and an euhedral Akf phenocryst with a small Pl core. (*continued next page*)

**Fig. A.13.** (continued) © BSE image of a large anhedral SiO<sub>2</sub>-phase, probably a xenocryst, showing signs of corrosion and dissolution. ⓘ BSE image of a BaSO<sub>4</sub>-phase as large inclusion in a Pl crystal. The Pl is anhedral and zoned, while the BaSO<sub>4</sub> is round. Probably a xenocryst, the encasing Pl shows all signs of corrosion and dissolution.

---

the pristine glass in this sample, which is within the average for analyses sums in samples with pristine glass of 96.8 vol%. So the main part of glass in the matrix is devitrified. However pristine glass was found and analysed in the matrix and in a large fiamma.

The phenocrysts in sample LE-68 consist mainly of coarse grained Pl. Of 62 grains documented (100%), 44 grains (71%) are Pl, 12 grains (19%) are Bt, 2 grains (3%) are Fe-Ti oxides and 1 grain each (2%) is Akf, Opx, SiO<sub>2</sub>, and BaSO<sub>4</sub>.

The Pl phenocrysts are on average around 600 × 350 μm and up to 2.2 × 2.0 mm. Most of the phenocrysts are subhedral, about a third are anhedral. More than half of the phenocrysts contain inclusions (usually Ap and Zrn, but also frequently Bt, as well as sometimes Fe-Ti oxides, and Cpx, all of the latter three contain also inclusions of Ap and Zrn), about a third of the phenocrysts show zonation. Some few Pl show embayments, while only one documented phenocrysts (b VII-5) has a small pristine glass selvage around a small part of it's rim. (Fig. A.13c)

Bt phenocrysts are mostly subhedral, few are euhedral. Most Bt have inclusions, while zonation, signs of stress, fracturing, and corrosion are rarely seen. Bt phenocrysts are usually 300 × 100 μm, but one crystal up to 900 × 70 μm is found.

Two single Fe-Ti oxides have been documented in this sample. One is an anhedral, irregularly shaped phenocrysts with lots of embayments (b VI-22), measuring 300 × 300 μm, which possibly formerly was an inclusion in a corroding Cpx crystal (see below, Fig. A.13d). The other phenocryst (b VII-1) is subhedral, 500 × 350 μm, with embayments and many holes showing beautiful exsolution lamellae.

The Opx crystal (Fig. A.13d) is anhedral, 300 × 300 μm, has many inclusions of Ap and has a fringe of tiny embayments showing beginning corrosion and dissolution. The crystal is thought to be a xenocryst picked up possibly from the Skoutaros Formation.

The Akf phenocryst documented in this sample is euhedral, 170 × 90 μm, encasing a small, anhedral Pl core. The crystal shows round corners, indication of a late onset of dissolution. (Fig. A.13b)

Additionally to the “blobs” of SiO<sub>2</sub> in the matrix, there is one large anhedral

phenocryst of a  $\text{SiO}_2$ -phase, measuring  $1750 \times 500 \mu\text{m}$ . It is probably a xenocryst, as it shows all signs of corrosion and dissolution. (Fig. A.13e)

There is also a  $\text{BaSO}_4$ -phase as large inclusion in a Pl crystal. The Pl is anhedral and zoned,  $500 \times 400 \mu\text{m}$ , while the  $\text{BaSO}_4$  is round ( $\varnothing 300 \mu\text{m}$ ) with a sieve structure and an irregular rim. Probably a xenocryst, the encasing Pl shows all signs of corrosion and dissolution. (Fig. A.13f)

### A.3.2. Sample LE-69

The sample was taken at 23.8 m. The matrix is welded and shows a quick transition from the colour red to black (bottom to top) which can be seen within 15 cm in the hand specimen. The sample contains  $\approx 20 \text{ vol}\%$  vesicular fiamme up to 7 cm long and hard to distinguish from the matrix.  $\approx 15 \text{ vol}\%$  consist of lithoclasts, which are up to 1 cm in size, and  $< 1 \text{ vol}\%$  of crystals of macroscopically visible biotite and feldspar. Pumice is absent. (Fig. A.14a)

The matrix of sample LE-69 is unsuitable for analysis. The matrix has a fuzzy texture, which contains cavities, and the outline of former glass shards are barely visible. The matrix contains faint spherulites in fan and bow tie shaped and darker irregular “blobs” which probably consist of a  $\text{SiO}_2$ -phase, like observed in samples LE-65, LE-67 and LE-66 (Fig. A.14b). The glass in the matrix of this sample is devitrified and not suitable for analysis. However the sample also contains areas of pristine glass within two large fiamme. The glass of the fiamme shows schlieren, perlitic rings and inclusions of crystallites arranged along the schlieren (Fig. A.14c). The analyses sums are  $96.2 \text{ vol}\%$  on average, which is within the average for analyses sums in samples with pristine glass of  $96.6 \text{ vol}\%$ .

The most common phenocryst in the sample is Pl, subordinately there are Bt phenocrysts, one cluster of Cpx crystals and a specimen of Akf. Of 31 grains documented (100%), 17 grains (65%) are Pl, 7 grains (27%) are Bt, and 1 grain each (4%) is Akf and Cpx.

There are as many subhedral Pl phenocrysts as anhedral ones. Phenocrysts are on average  $600 \times 350 \mu\text{m}$ , but can be up to  $2.2 \times 2.0 \text{ mm}$  (Fig. A.14d). The subhedral phenocrysts show zonations (more or less high-Ba and high-Ab rims), some of them have cracks that are healed over by some fuzzy growth. About half of all Pl phenocrysts have small inclusions of Zrn and Ap, like in the samples described before. Pl also occurs in clots with one or more Bt crystals (between  $500 \times 150 \mu\text{m}$  and  $1200 \times 300 \mu\text{m}$ , Fig. A.14e), which also contain inclusions of probably Ap and Zrn.

Additionally to be set in clots with Pl, Bt also exists as separate, single crystals. They are subhedral to euhedral,  $\approx 650 \times 130 \mu\text{m}$ . One in three documented crystals

### A.3. Sample descriptions – individual samples of profile B

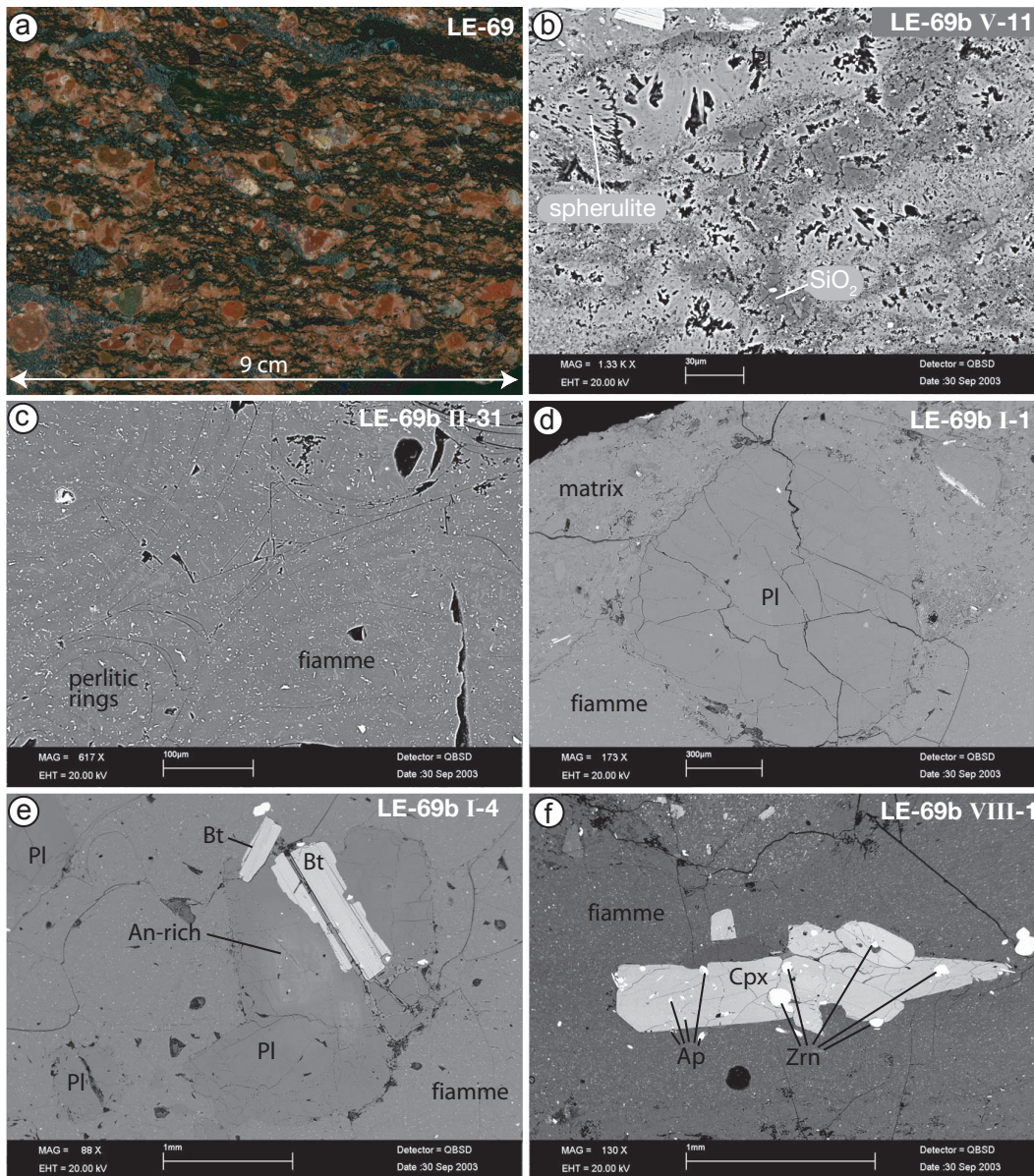


**Fig. A.14.** Characteristics of sample LE-69. (a) Photo of the hand specimen. (b) BSE image of the matrix with a fuzzy and irregular texture, spherulites and “blobs” of SiO<sub>2</sub>. (c) BSE image the pristine glass in a fiamme, which shows perlitic rings and microcrystals. (d) BSE image of an phenocryst, consisting of a cluster of PI (with a An-rich core) and Bt crystals within a fiamme. (e) BSE image of an anhedral PI phenocryst, without zonation and consisting only of a single crystal. The PI is surrounded by glass of the matrix and of fiamme. (f) BSE image of a Cpx phenocrysts, consisting of several Cpx crystals, all with inclusions of Ap and Zrn.

has inclusions.

One cluster of several Cpx grains was found in this sample. The cluster contains subhedral crystals as well as anhedral and dissolved (i.e. rounded) ones, which all contains numerous inclusions of Ap and Zrn. According to the chemical composition all crystals are of the same diopsidic composition. (Fig. A.14f)

In the sample is one documented phenocryst of Akf ( $1000 \times 400 \mu\text{m}$ ), which is anhedral, zoned and somewhat rounded, i.e. dissolved around the rim.

### A.3.3. Sample LE-70

The sample was taken at 24.5 m. The matrix is welded and black. The sample consists of  $\approx 20 \text{ vol}\%$  vesicular fiamme, up to 7 cm length, and hard to distinguish from the matrix. Lithoclasts, up to 1 cm make up of  $\approx 15 \text{ vol}\%$ , while crystals of macroscopically visible biotite and feldspar contribute  $< 1 \text{ vol}\%$ . Pumice is absent. (Fig. A.15a)

The glass in the sample shows schlieren, perlitic rings and inclusions of crystallites arranged along the schlieren (Fig. A.15b). It is not possible to distinguish a difference between matrix and fiamme in the thin section. However, a few patches of fuzzy textured glass can be observed (a 12 (Fig. A.15c), a 12 e, b I-11) and also small confined areas in the glass, where through abundance of crystallites a sieve texture is created (a 11 c). These areas are thought to show beginning devitrification. The analyses sums in the glass are 96.9 vol% on average, which is within the average for analyses sums in samples with pristine glass of 96.6 vol%.

By far the most common phenocryst in this sample is Pl, followed by Bt and subordinately Cpx and Akf. Fe-Ti oxides, Ap, and Zrn exist as inclusions. Some grains exist in clots of two or more, comprising different phases. Of 74 grains documented (100%), 56 grains (73%) are Pl, 16 grains (21%) are Bt, 3 grains (4%) are Cpx, and 2 grains (3%) are Akf.

The Pl phenocrysts are subhedral ( $\approx 60\%$ ) to anhedral ( $\approx 35\%$ ), few are euhedral. The size of Pl is between  $140 \times 100 \mu\text{m}$  and  $3.3 \times 1.5 \text{ mm}$ , but on average  $850 \times 450 \mu\text{m}$ . Of the subhedral phenocrysts about half are zoned. Zonations vary greatly. More than 10% of the Pl phenocrysts are set in clots with Bt (up to  $450 \times 130 \mu\text{m}$ ) or Fe-Ti oxides.  $< 10\%$  show additional attributes, like corrosion, fragmentation, or embayments. (Fig. A.15b&c)

Bt phenocrysts are usually between  $600 \times 250 \mu\text{m}$  and  $100 \times 50 \mu\text{m}$  (on average  $500 \times 150 \mu\text{m}$ , but can be up to  $1500 \times 100 \mu\text{m}$ ). Two thirds of the Bt phenocrysts are subhedral, the remaining third is euhedral (Fig. A.15d). Half of the phenocrysts have inclusion (Ap, Zrn, Fe-Ti oxides), about a quarter is embayed, and another quarter is fragmented.

### A.3. Sample descriptions – individual samples of profile B

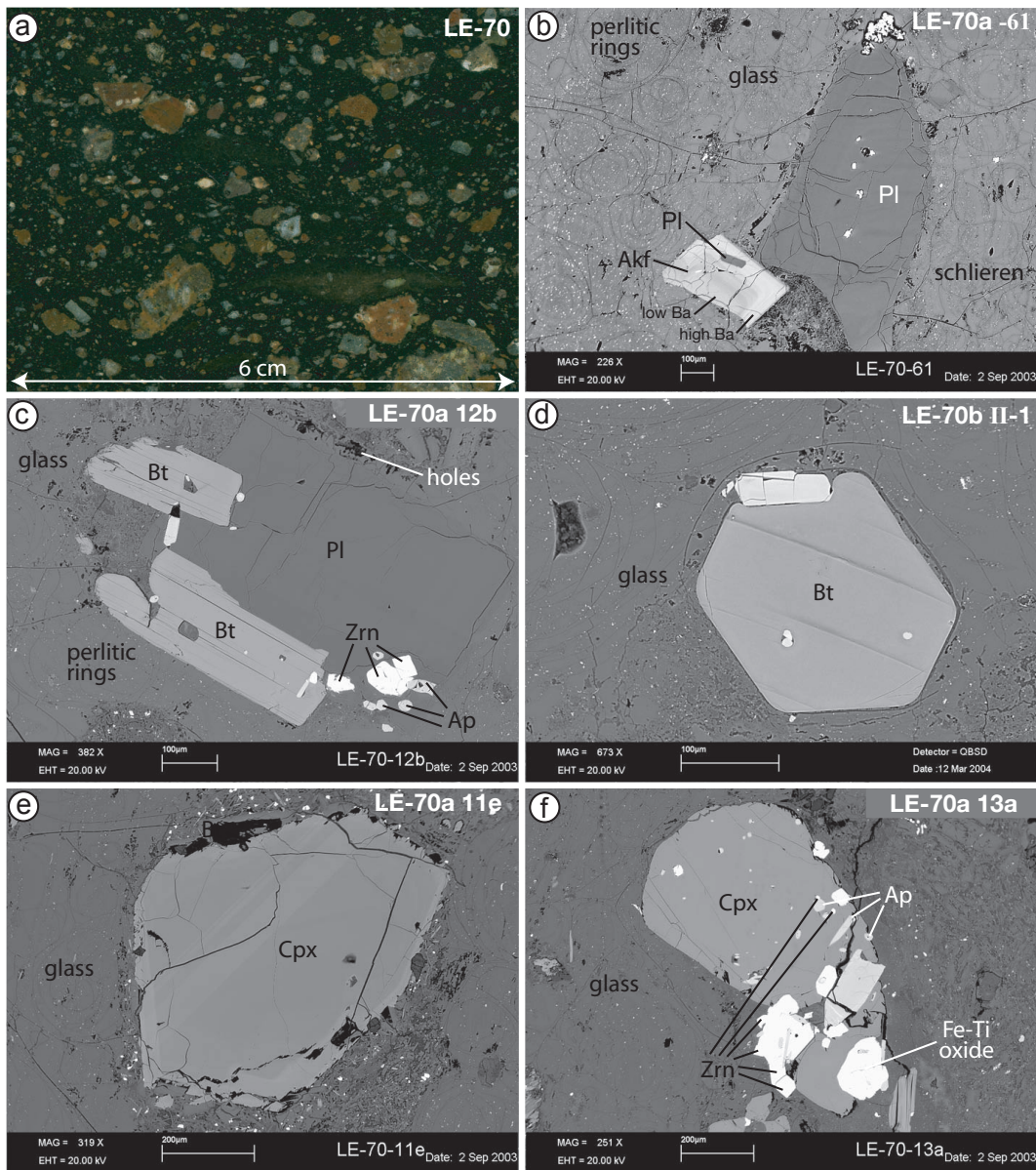


**Fig. A.15.** Characteristics of sample LE-70. (a) Photo of the hand specimen. (b) BSE image of the glass (matrix or fiamme), showing perlitic rings, crystallites and schlieren. In the centre of the image are two phenocrysts: an Akf phenocryst, which is a fragment, showing a Ba-zonation and a PI inclusion, and an anhedral PI phenocryst. (c) BSE image of the glass with holes, thought to show beginning devitrification. The picture also shows a PI phenocryst in a cluster with Bt and inclusions of Ap and Zrn. (d) BSE image of a Bt phenocryst, cut perpendicular to the c-axis. (e) BSE image of a subhedral Cpx phenocryst with oscillating zonation and without any inclusions. (f) BSE image of an anhedral Cpx phenocryst, with numerous inclusions of Fe-Ti oxide, Ap and Zrn.

There are three documented Cpx phenocrysts in sample LE-70, which are all of diopsidic composition and  $\approx 650 \times 500 \mu\text{m}$ . Apart from composition and size, they vary greatly: one (a-94) is subhedral, unzoned and has numerous small inclusions (Ap, Zrn, Fe-Ti oxides), another (a-11 e) is subhedral, zoned and has no inclusions (Fig. A.15e), the third (a-13 a) is anhedral with large inclusions (Ap, Zrn, Fe-Ti oxides, Fig. A.15a).

The sample contains two documented Akf phenocrysts, they are  $\approx 350 \times 200 \mu\text{m}$ . One is a subhedral fragment, heavily zoned with a Pl inclusion (a-61, Fig. A.15a), the other (b IV-1) is subhedral, unzoned, without inclusions.

#### A.3.4. Sample LE-71

The sample was taken at 26.8m. The matrix is welded and black. The sample consists of  $\approx 20 \text{ vol}\%$  vesicular, highly weathered fiamme, up to 7cm length. Lithoclasts, up to 1cm make up of  $\approx 15 \text{ vol}\%$ , and crystals of macroscopically visible biotite and feldspar  $< 1 \text{ vol}\%$ . Pumice is absent. (Fig. A.16a)

The glass contained in the matrix and highly vesicular fiamme of sample LE-71 is not suitable for analysis. The texture is fuzzy, outlines of former shards can not be observed, however spherulites or  $\text{SiO}_2$  “blobs” are also missing (Fig. A.16b). Analyses sums are on average 100.4 vol% for the matrix of this sample, while the analyses sums in samples with pristine glass are on average 96.6 vol%. The glass in the matrix of this sample is devitrified.

The most common crystal is Pl, with subordinately Bt, Fe-Ti oxide, Akf and Cpx. Of 72 grains documented (100%), 44 grains (72%) are Pl, 10 grains (16%) are Bt, 4 grains (7%) are Fe-Ti oxides, 2 grains (3%) are Akf, and 1 grain (2%) is Cpx.

Pl phenocrysts in this sample are between  $200 \times 200 \mu\text{m}$  and  $3.1 \times 0.5 \text{ mm}$ , on average  $1000 \times 560 \mu\text{m}$ . Three quarters are subhedral, one quarter is anhedral, and only one Pl documented is euhedral. A quarter of the crystals is zoned, while some few occur in clots of a few Pl crystals or Pl with Bt. One phenocryst has a small selvedge of Akf around a little part of its rim, another has a corroded zone at the core. (Fig. A.16c&d)

Bt phenocrysts are all subhedral, mostly have inclusions and are on average  $400 \times 200 \mu\text{m}$ .

The Fe-Ti oxides vary in their appearance: one (a II-13) is euhedral,  $\varnothing 120 \mu\text{m}$ , with no inclusions, while the other three are subhedral, rounded,  $\varnothing 125 - 250 \mu\text{m}$ , and have inclusions of Ap and Zrn. All four show exsolution lamellae.

Only two phenocrysts of Akf are documented in sample LE-71, they are euhedral and relatively small ( $\approx 190 \times 180 \mu\text{m}$ ). They are free from any inclusions and from zonations. (Fig. A.16d)

### A.3. Sample descriptions – individual samples of profile B

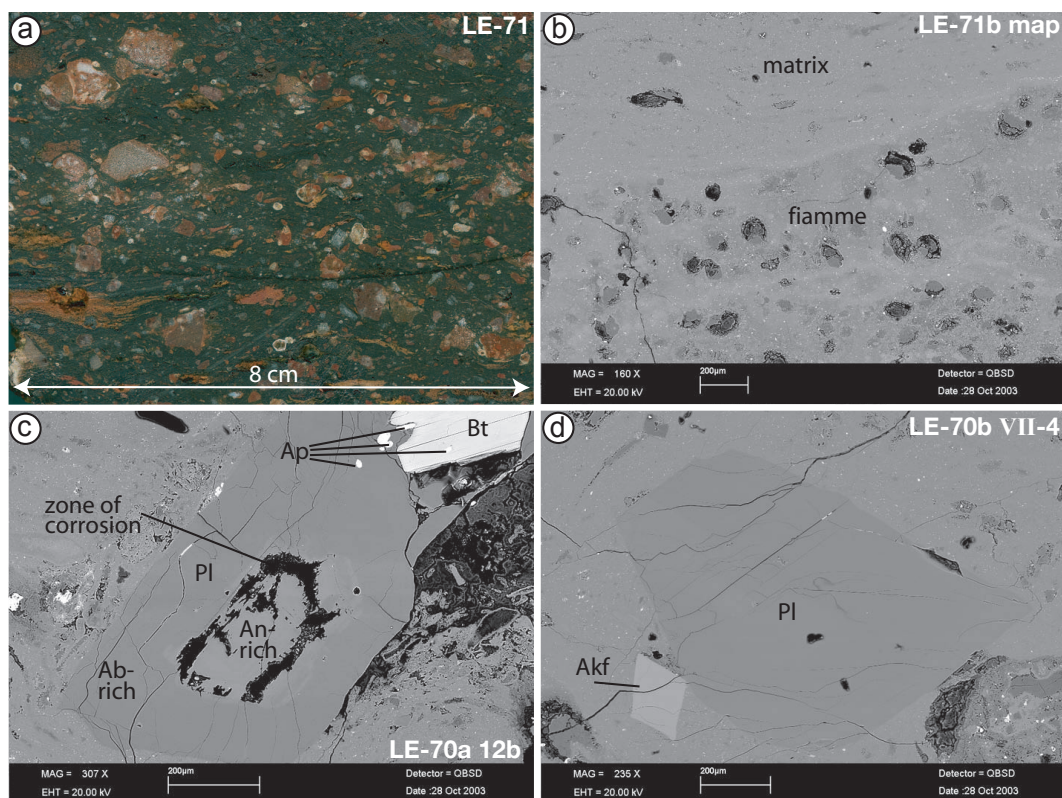


**Fig. A.16.** Characteristics of sample LE-71. (a) Photo of the hand specimen. (b) BSE image of the matrix and the vesicular fiamme. The glass is fuzzy, outlines of former shards are not visible. (c) BSE image of a Pl phenocryst, showing a zone of corrosion around an An-rich core. The phenocryst is in a cluster with Bt, Bt and Pl both have inclusions of Ap. (d) BSE image of a Pl phenocryst and an Akf phenocryst. The Pl is subhedral, slightly rounded, while the Akf is euhedral and small.

The only documented Cpx is subhedral, contains numerous inclusions of Ap, Zrn and Fe-Ti oxide. The rim is corroded, the crystal measures  $1.0 \times 0.8$  mm

## A. Individual sample descriptions

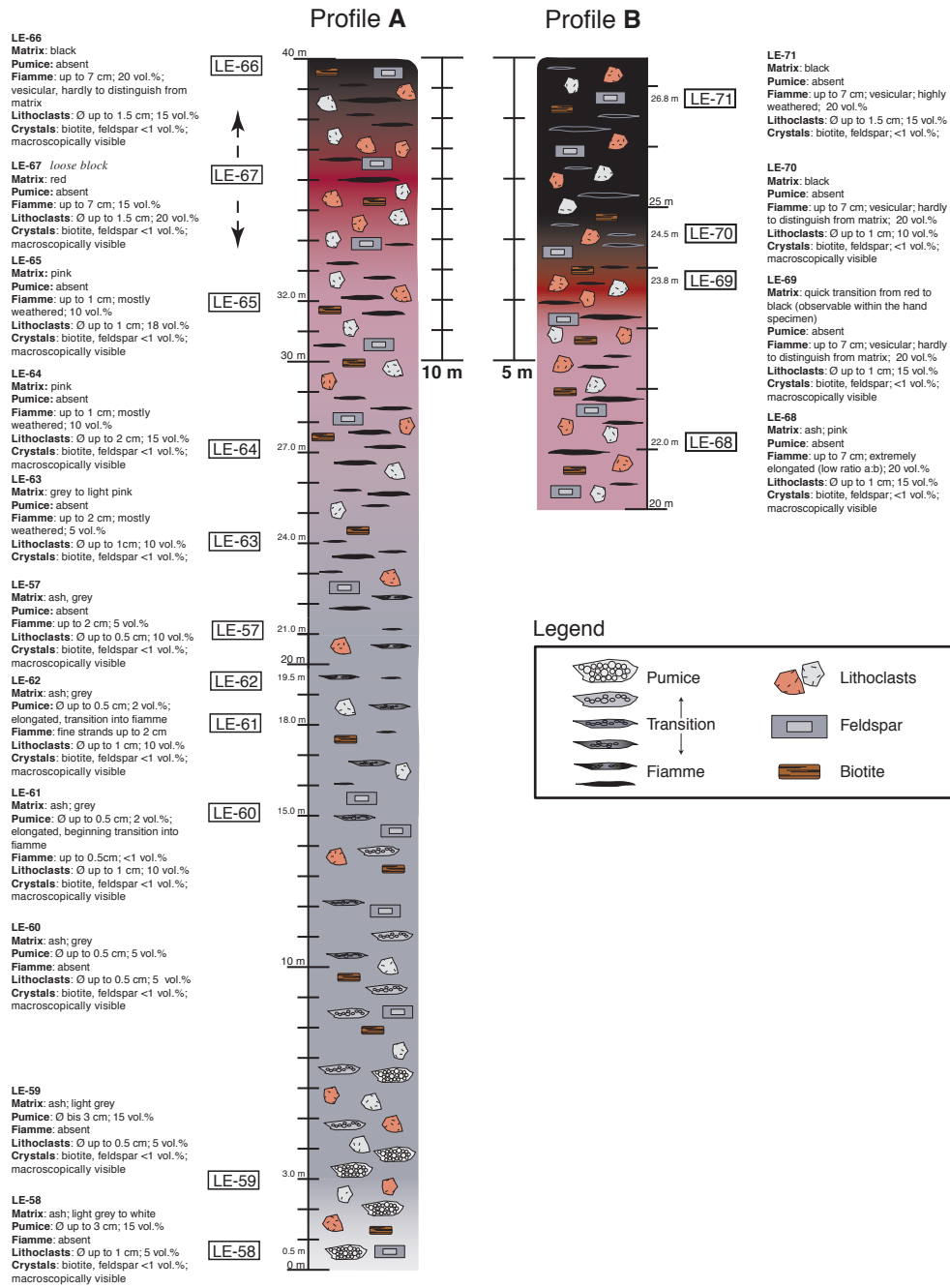


**Fig. A.17.** Schematic sketch of the two vertical profiles A (cape near Kofinas) and B (N side of Tavros mountain).

## A.4. Additional samples from other locations

Additional samples of volcanic glass were taken from fiamme at road cuts from two different roads NE of the Gulf of Kalloni.

**Sample LE-2** This sample was taken at the road from Mandamados to Aghia Paraskevi, 1.1 km NE of Napi. The section of the ignimbrite consists of pink and grey coloured parts of dense, fine-grained, unweathered rocks with numerous fiamme up to 7 cm long and 0.7 cm thick. Other parts of the ignimbrite are white and kaolinised.

The sample consists mainly of glass (modal percentage 95 %) taken from several larger fiamme.

### A.4.1. Sample LE-3

The sample was taken at the road which runs from the E coast of Kalloni Gulf towards the E to Lambou Mili, some 2.1 km to the E from the coast. It was collected from several large fiamme exposed in the road cut.

The sample consists mainly of glass (modal percentage 95 %, Fig. A.18a). The glass has schlieren and perlitic rings ( Fig. A.18b). Crystals of mainly Pl, Akf and subordinately Bt, Fe-Ti oxide, and Cpx are present.

Pl is up to  $2.0 \times 1.5$  mm with inclusions of Fe-Ti oxides ( $\varnothing 60 \mu\text{m}$ ), Zrn ( $\varnothing 15 \mu\text{m}$ ), and Ap ( $\varnothing 15 \mu\text{m}$ ). There are also inclusions of Akf in Pl, with dimensions of  $150 \times 100 \mu\text{m}$  and clots together with Bt (Fig. A.18b).

Akf crystals are up to  $600 \times 400 \mu\text{m}$ , some featuring subhedral shapes, while others are substantially corroded and rounded. Inclusions of Pl in Akf up to  $100 \times 80 \mu\text{m}$ . In this sample Pl and Akf often occur together as clots.

There is also a small Fe-Ti oxide documented (Fig. A.18d), a clot of two rounded Fe-Ti oxides with exsolution lamellae, and numerous Ap and Zrn.

In the sample also a crystal of Cpx, a diopside ( $2.5 \times 0.6$  mm, Fig. A.18d), and a crystal of Bt ( $600 \times 150 \mu\text{m}$ ) can be found. They both contain a large number of inclusions, probably Zrn and/or Ap which have diameters up to  $25 \mu\text{m}$  in Cpx and up to  $10 \mu\text{m}$  in Bt.

### A.4.2. Sample LE-5

The sample was taken at the road which runs from the E coast of Kalloni Gulf towards the E to Lambou Mili, like sample LE-3, but only some 1.3 km from the gulf to the E. It was collected from several large fiamme exposed in the road cut.

A. Individual sample descriptions

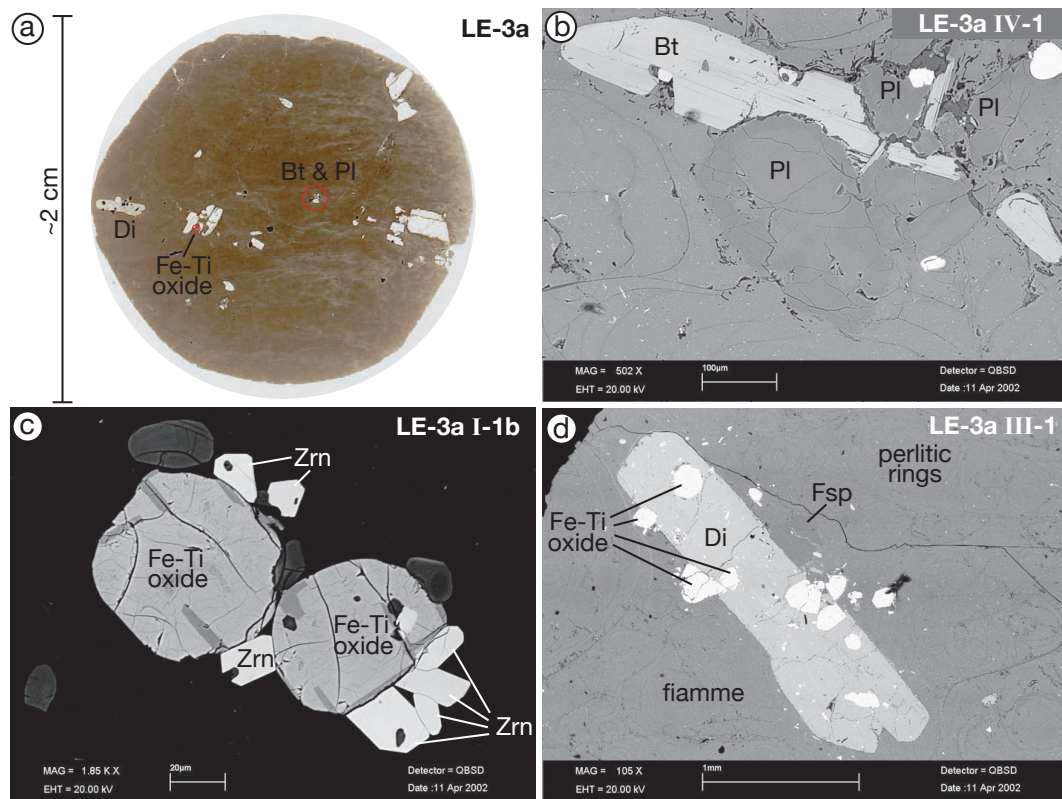


**Fig. A.18.** Characteristics of sample LE-3. (a) Thin section (LE-3 a) in transmitted light. (b) BSE image of a phenocryst, a cluster of Pl and Bt, in the glass fiamme. The glass has schlieren, perlitic rings, and some microcrystals. (c) BSE image of a small Fe-Ti oxide cluster, showing exsolution lamellae, and inclusions of Ap and Zrn. (d) BSE image of a Cpx (Di) phenocryst with numerous inclusions of Ap and/or Zrn.

#### A.4. Additional samples from other locations

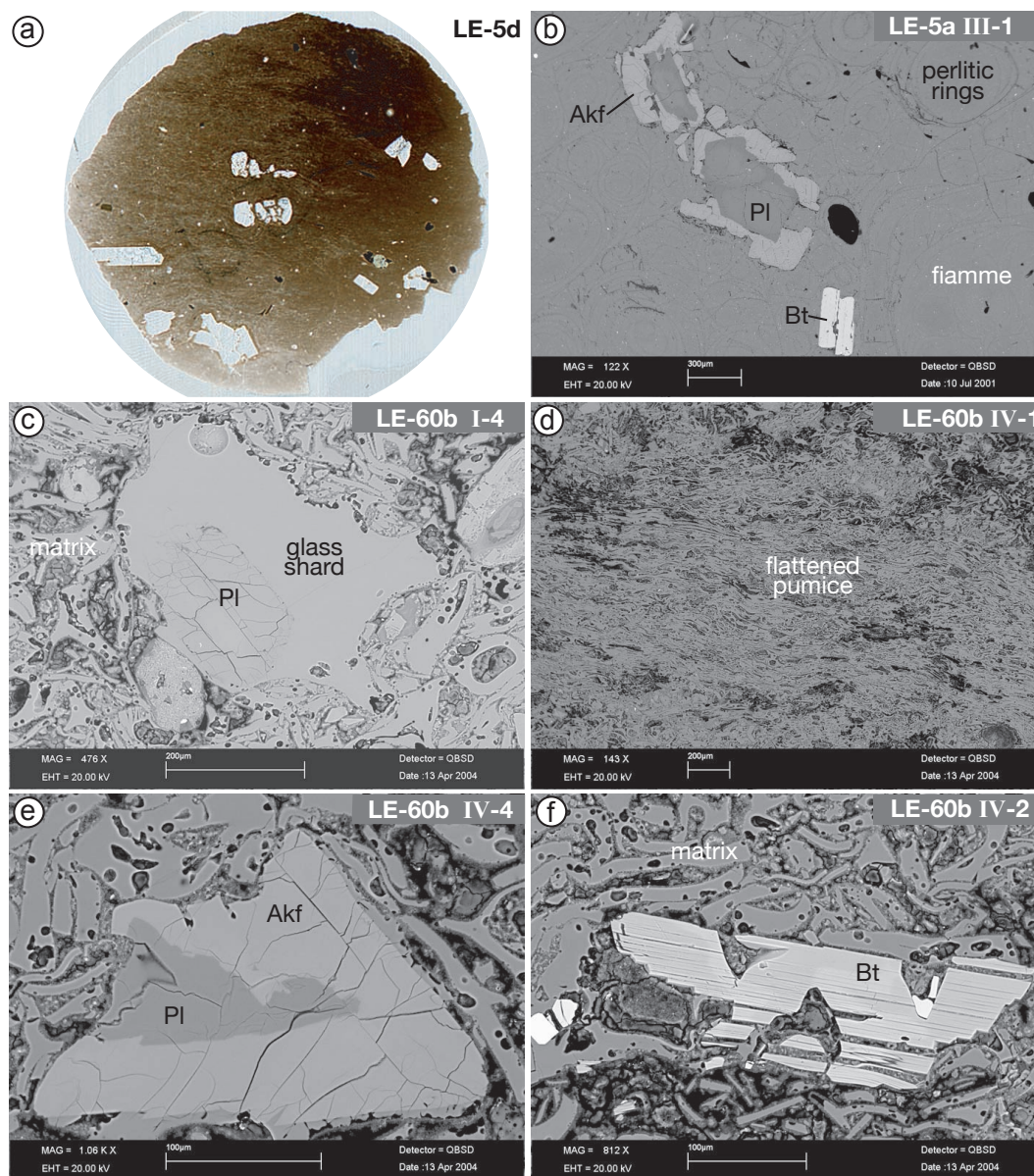


**Fig. A.19.** Characteristics of sample LE-5. (a) Thin section (LE-5 d) in transmitted light. (b) BSE image of the fiamme. The glass is dense, has schlieren and perlitic rings. Central in the picture is a subhedral, zoned PI phenocryst with nearly complete Akf overgrowth. (c) BSE image of an anhedral, cracked PI phenocryst with an anhedral Akf core. Also shown is a small, rounded Akf phenocryst in the right hand lower corner. (d) BSE image of a Bt phenocryst. The subhedral, slightly corroded mineral has a patchy core and numerous inclusions and holes. (e) BSE image of a subhedral Cpx phenocryst with numerous inclusions. (f) BSE image of an euhedral Am phenocryst with a selvage.

## A. Individual sample descriptions

---

The sample consists mainly of glass (modal percentage 95%), crystals of Akf, Pl, Bt, Cpx, Am, Fe-Ti oxide, and Zrn are present in the matrix. (Fig. A.19a)

Akf exists as large crystals up to  $3.0 \times 0.8$  mm or  $2.5 \times 100$   $\mu$ m, but a number of smaller Akf crystals ( $50 \times 50$   $\mu$ m) with dissolved rims and therefore round shapes exist as well.

Pl crystals up to  $2.5 \times 2.0$  mm occur, one (I-1, Fig. A.19b)  $1.5 \times 2.2$  mm with a large Akf core, two others (III-1, Fig. A.19c) -in contrast- are euhedral zoned Pl with nearly complete Akf overgrowth. Bt inclusions up to  $300 \times 100$   $\mu$ m, Ap inclusions as crystal needles 150  $\mu$ m long, and Fe-Ti oxides  $220 \times 220$   $\mu$ m are found in Pl.

Bt crystals exist  $400 \times 200$   $\mu$ m and  $400 \times 100$ , some of them with many inclusions (Ap and Zrn with a diameter of 10  $\mu$ m) and holes (Fig. A.19d).

The Fe-Ti oxides in the glass matrix are up to  $450 \times 400$   $\mu$ m with many inclusions of Ap only a few  $\mu$ m. Zrn also occurs as solitary crystals up to  $80 \times 50$   $\mu$ m.

In this sample also two phenocrysts of cpx and one of Am were found. The Cpx crystals are diopsides,  $900 \times 300$   $\mu$ m with numerous inclusions of Ap, Zrn and Fe-Ti oxide up to  $150 \times 100$   $\mu$ m, which also has inclusions of Ap and Zrn (Fig. A.19e). The Am is euhedral  $150 \times 200$   $\mu$ m and completely free from inclusions (Fig. A.19f).

### A.4.3. Sample LE-8

The sample was taken at the road along the E coast of Kalloni Gulf, about 2 km N of Cape Kofinas (Profile A). Sample LE-8 was collected as coherent piece from an large fiamma (exposed length  $\approx 70$  cm, thickness  $\approx 15$  cm).

The sample consists mainly of glass (modal percentage 95%) with perlitic rings, with fine schlieren and some microcrystals. Only few crystals, mainly Pl, and subordinately Akf and Bt are present. Pl is up to  $3 \times 1.5$  mm and contains inclusions of Ap ( $100 \times 25$   $\mu$ m) and Zrn ( $\approx 10$   $\mu$ m) and Bt ( $80 \times 50$   $\mu$ m).

The Pl crystals are strongly zoned and some parts sometimes display corroded forms. Akf crystals are  $1.5 \times 0.4$  mm and Bt crystals, which are often corroded are  $400 \times 250$   $\mu$ m.

Ap and Zrn inclusions also occur in Bt and as small crystals (the size of the inclusions) in the glass matrix.

### A.4.4. Sample LE-9

The sample was taken from smaller fiamme at the same location as sample LE-8, see page 202.

The sample consists mainly of glass modal percentage 97% with perlitic rings and fine schlieren, and some microcrystals (Fig. A.20 a & b). The few crystals

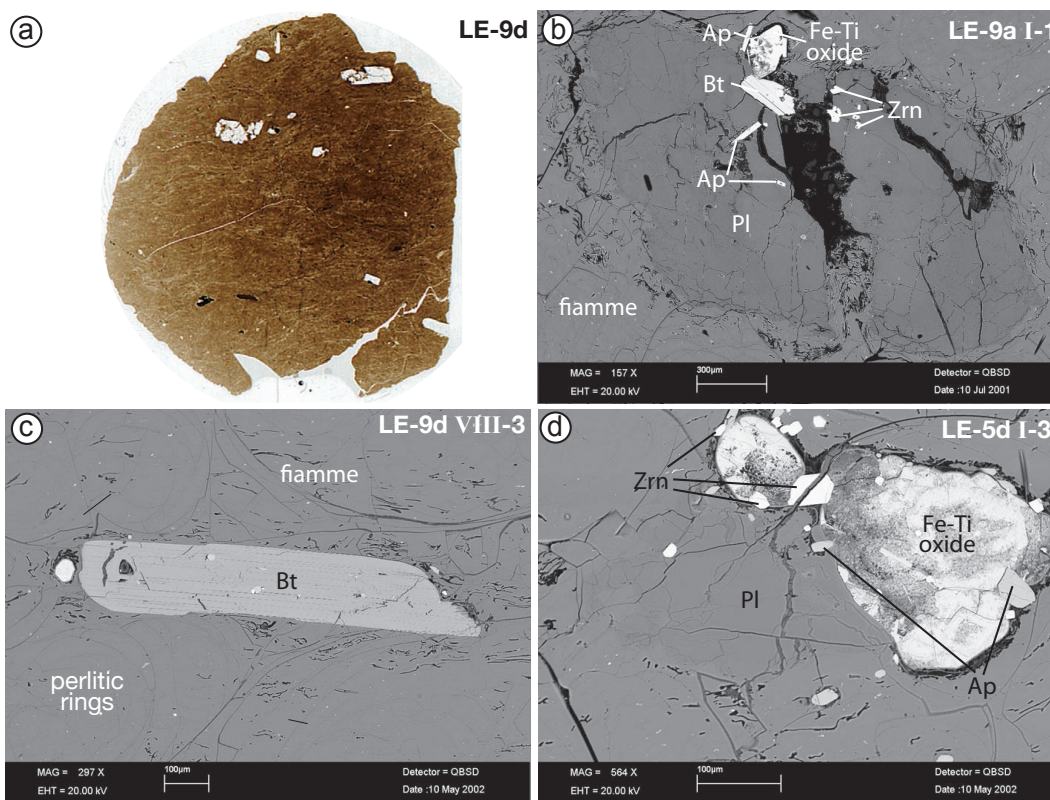


**Fig. A.20.** Characteristics of sample LE-9. (a) Thin section (LE-9 d) in transmitted light. (b) BSE image of the glass in the flamme, showing dense texture, perlitic rings and some microcrystals. In the centre of the picture is a subhedral Bt phenocryst with some few inclusions. (c) BSE image of a subhedral, cracked Pl phenocryst with inclusions of Bt, Fe-Ti oxide, Ap and Zrn. Some melt has pushed into the crack, leaving a glass “finger” stuck. (d) BSE image of a phenocryst, consisting of Pl and two (one large) Fe-Ti oxides with inclusions of Ap and Zrn.

(3%) contained are mainly Pl and subordinately Bt and Fe-Ti oxide. Pl is up to  $2.5 \times 2.0$  mm and often contains inclusions of Ap, Zrn, Bt, and of very corroded Akf (few tens  $\mu$ m) (Fig. A.20 b).

Bt is often corroded and up to  $800 \times 200$   $\mu$ m and contains inclusions of Ap and Zrn, both usually a few  $\mu$ m (Fig. A.20 a), however one Zrn measures  $25 \times 25$   $\mu$ m.

Fe-Ti oxide is up to  $200 \times 200$   $\mu$ m. The phenocryst is round, may consists of a few crystals, and has inclusions of Ap and Zrn.



## B. Element concentration profiles

The following pages document element concentration profiles across plagioclase, alkali feldspar, biotite, and glass fragments for main elements determined by electron probe micro-analysis (EPMA) and for light elements Li, Be, and B determined by secondary ion mass spectrometry (SIMS). Element concentration profiles are accompanied by back-scattered electron images and optical images of gold coated samples under reflected light after SIMS analysis, where analytical spots appear black on gold coating.

EPMA analytical spot size is 10  $\mu\text{g/g}$  for profile in plagioclase, alkali feldspar, biotite and glass, usually spots are spaced every 10  $\mu\text{g/g}$ . The profiles were analysed using an automatic setting of the EMPA.

Samples will be listed according to their position in the vertical profiles from bottom to top and not according to their numbers, i.e. for LE-57 see p. 227 after LE-62, and LE-66 after LE-67, according to position in vertical profile. Combination of roman with arabic numbers identify minerals in the thin sections (roman numbers: area in thin-section, arabic numbers: specific mineral); numbers sometimes have an additional letter for further specification of a certain element profile.

Element profiles determined by SIMS use the same number. SIMS profiles have all been determined in manual setting, the distance of analytical spots was calculated from their xy-coordinates.

## B. Element concentration profiles

LE-59b Profile I-1

Plagioclase

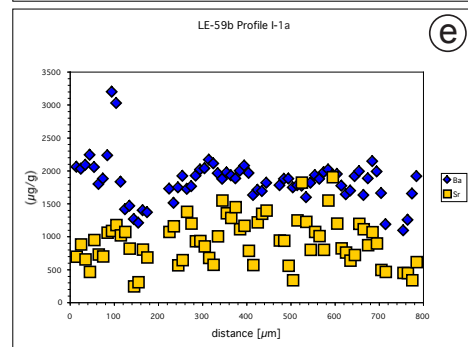
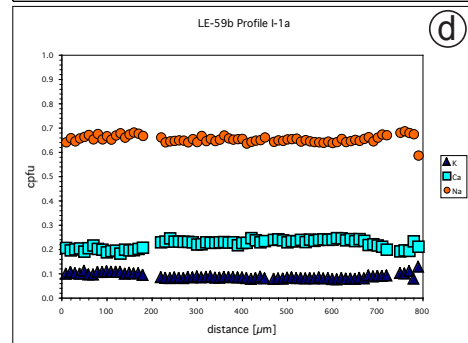
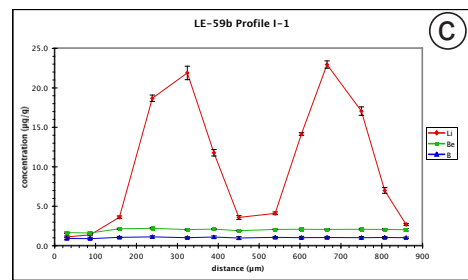
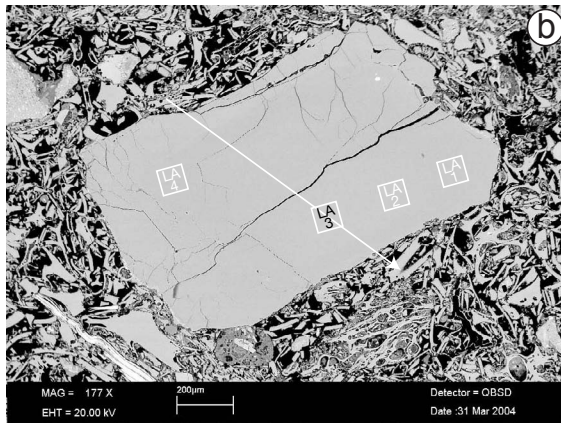
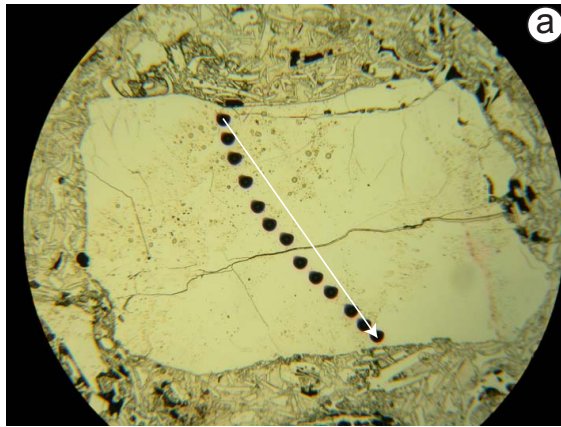


**Fig. B.1.** Sample LE-59b, plagioclase I-1, (a) reflected light image of gold coated sample after SIMS analysis, analytical spots appear black on gold coating, (b) BSE image, arrow indicates location of EPMA profile, squares mark locations of laser-ablation ICP-MS analyses (Sr isotopes), (c) SIMS profile for elements Li, Be, B, (d) EPMA profile for K, Ca, Na, (e) EPMA profile for Ba, Sr.

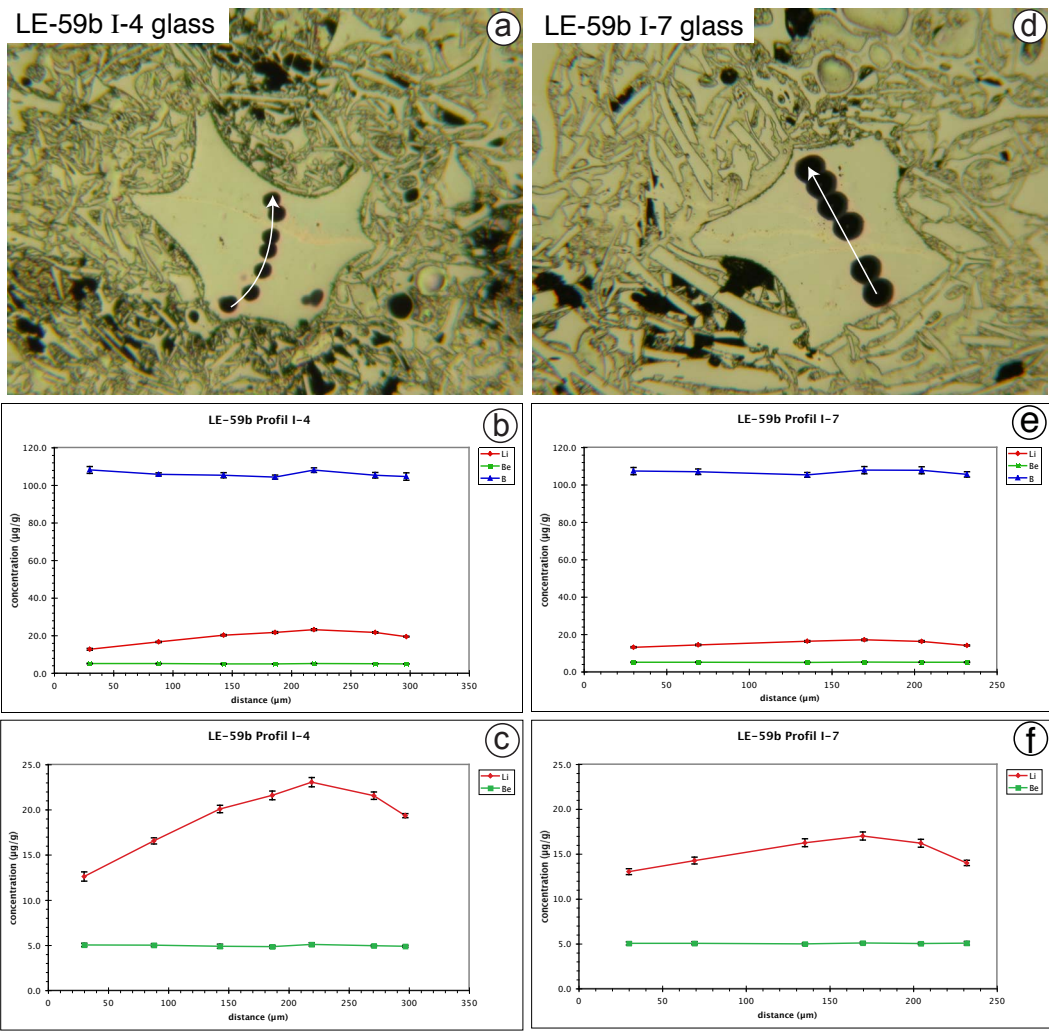


**Fig. B.2.** Sample LE-59b (a) glass fragment I-4, reflected light image of gold coated sample, SIMS analytical spots appear black on gold coating, (b) & (c) glass fragment I-4, SIMS profile for elements Li, Be, B, (d) glass fragment I-7, reflected light image of gold coated sample, SIMS analytical spots appear black on gold coating, (e) & (f) glass fragment I-7, SIMS profile for elements Li, Be, B.

## B. Element concentration profiles

LE-59b I-8, biotite

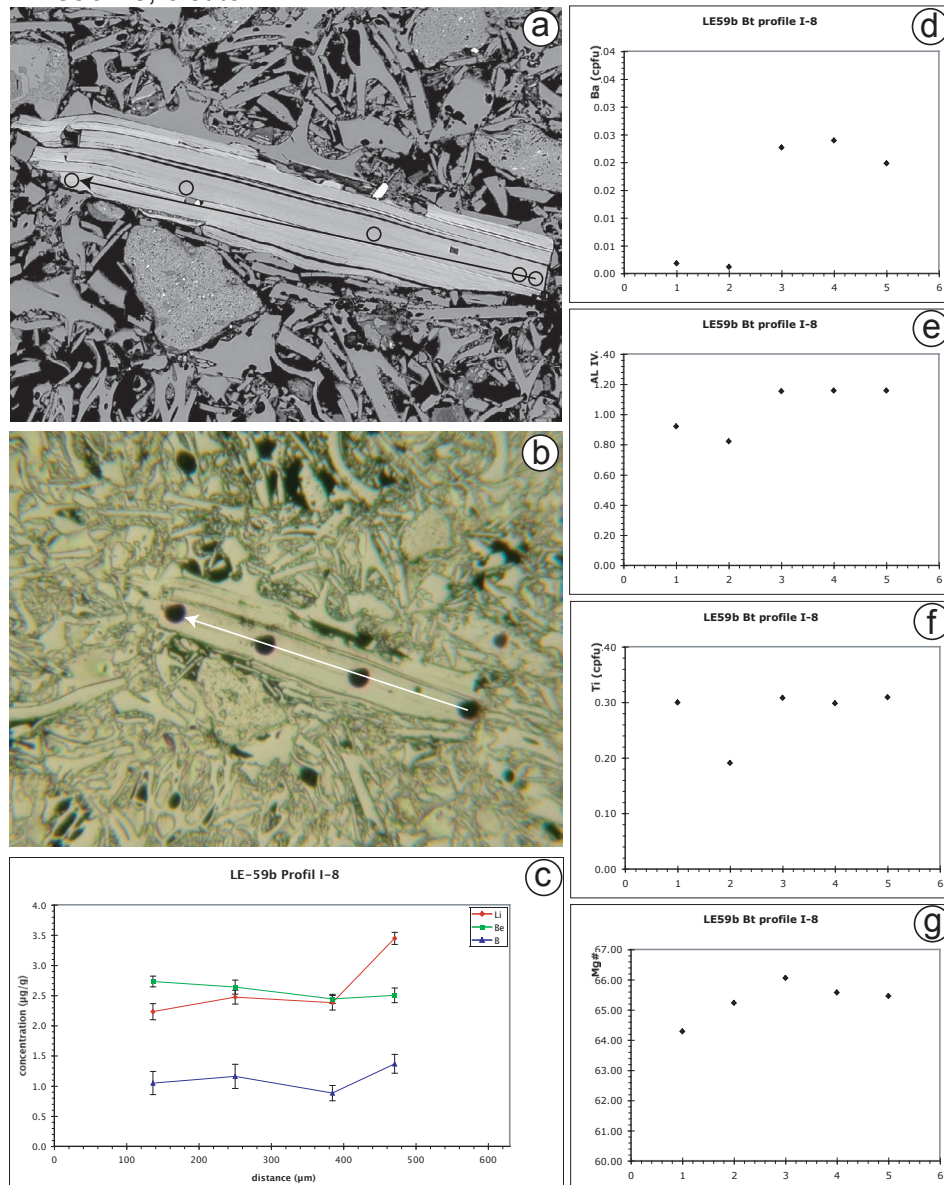


**Fig. B.3.** Sample LE-59b biotite I-8, (a) BSE image, EPMA analytical spots, arrow indicates profile direction, (b) reflected light image of gold coated sample, SIMS analytical spots appear black on gold coating, (c) SIMS profile for elements Li, Be, B ( $\mu\text{g/g}$ ) (d) EPMA profile for Ba (cpfu), (e) EPMA profile for Al<sup>IV</sup>, (f) EPMA profile for Ti (cpfu), (g) EPMA profile for Mg#.

LE-59b profile III-1

plagioclase

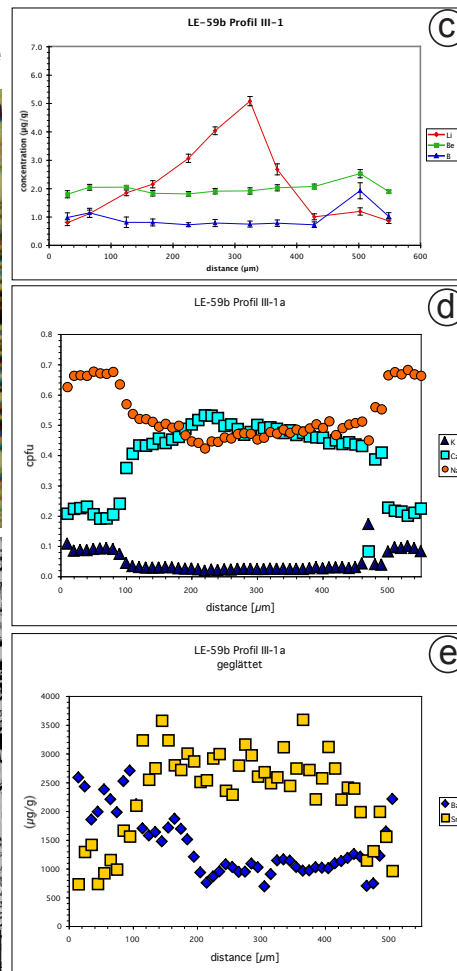
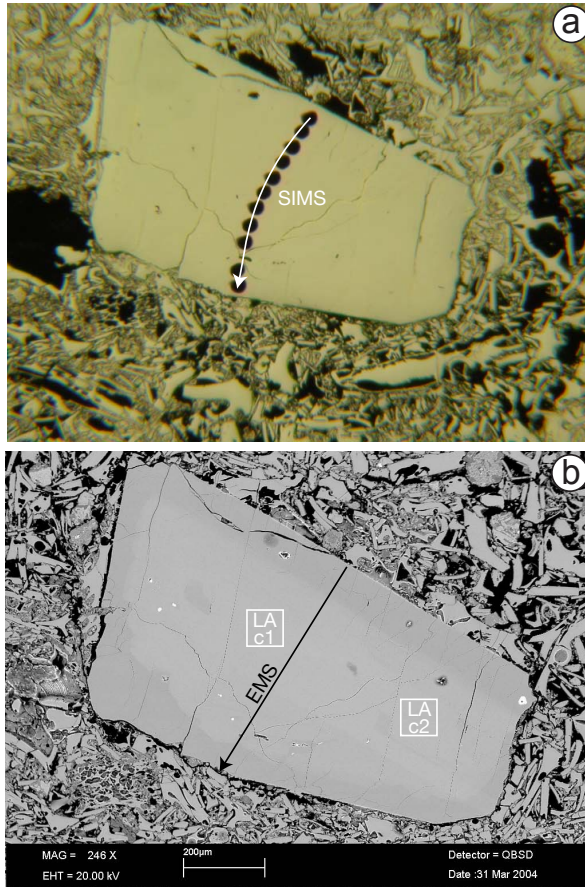


**Fig. B.4.** Sample LE-59b III-1, plagioclase (a) reflected light image of gold coated sample after SIMS analysis, analytical spots appear black on gold coating, (b) BSE image, squares mark locations of laser-ablation ICP-MS analyses (Sr isotopes), (c) SIMS profile for elements Li, Be, and B, (d) EPMA profile for elements K, Ca, and Na (cpfu), (e) EPMA profile for elements Ba and Sr ( $\mu\text{g/g}$ ).

## B. Element concentration profiles

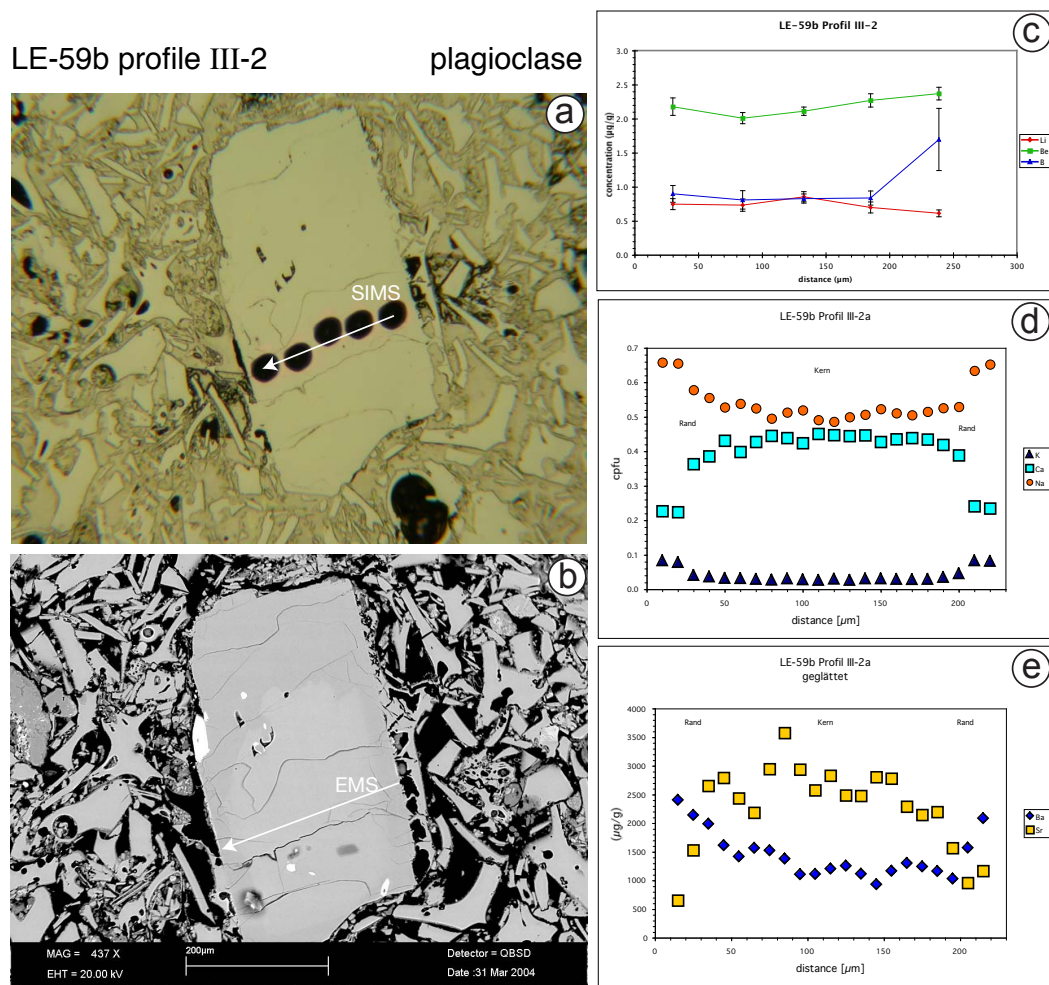


**Fig. B.5.** Sample LE-59b III-2, plagioclase (a) reflected light image of gold coated sample after SIMS analysis, analytical spots appear black on gold coating, (b) BSE image, arrow indicates location of EPMA profile (c) SIMS profile for elements Li, Be, and B, (d) EPMA profile for elements K, Ca, and Na (cpfu), (e) EPMA profile for elements Ba and Sr ( $\mu\text{g/g}$ ).

LE-59b profile V-5

glass

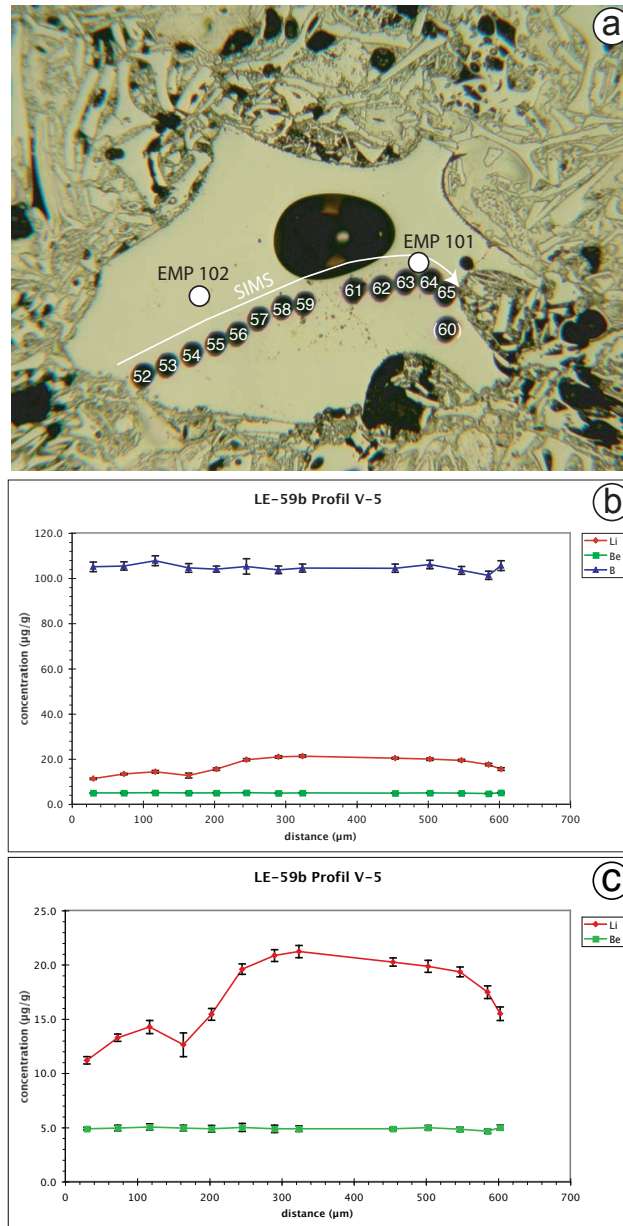


**Fig. B.6.** Sample LE-59b V-5, glass fragment, (a) reflected light image of gold coated sample after SIMS analysis, analytical spots appear black on gold coating, EPMA analytical spots are marked with white circles. (b) & (c) SIMS profile for elements Li, Be, and B.

## B. Element concentration profiles

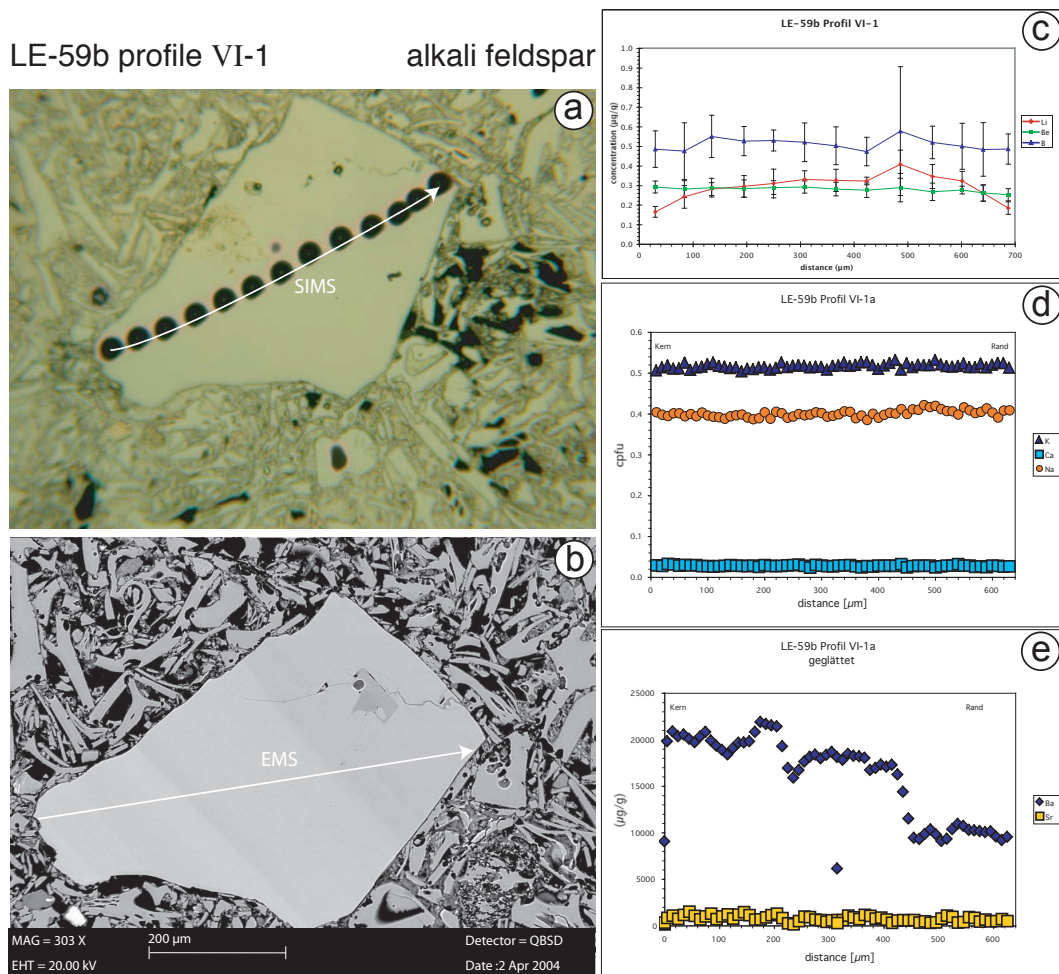


**Fig. B.7.** Sample LE-59b VI-1, alkali feldspar (a) reflected light image of gold coated sample after SIMS analysis, analytical spots appear black on gold coating, (b) BSE image, arrow indicates location of EPMA profile (c) SIMS profile for elements Li, Be, and B, (d) EPMA profile for elements K, Ca, and Na (cpfu), (e) EPMA profile for elements Ba and Sr (µg/g).

LE-60b profile I-4 glass selvage (at PI)

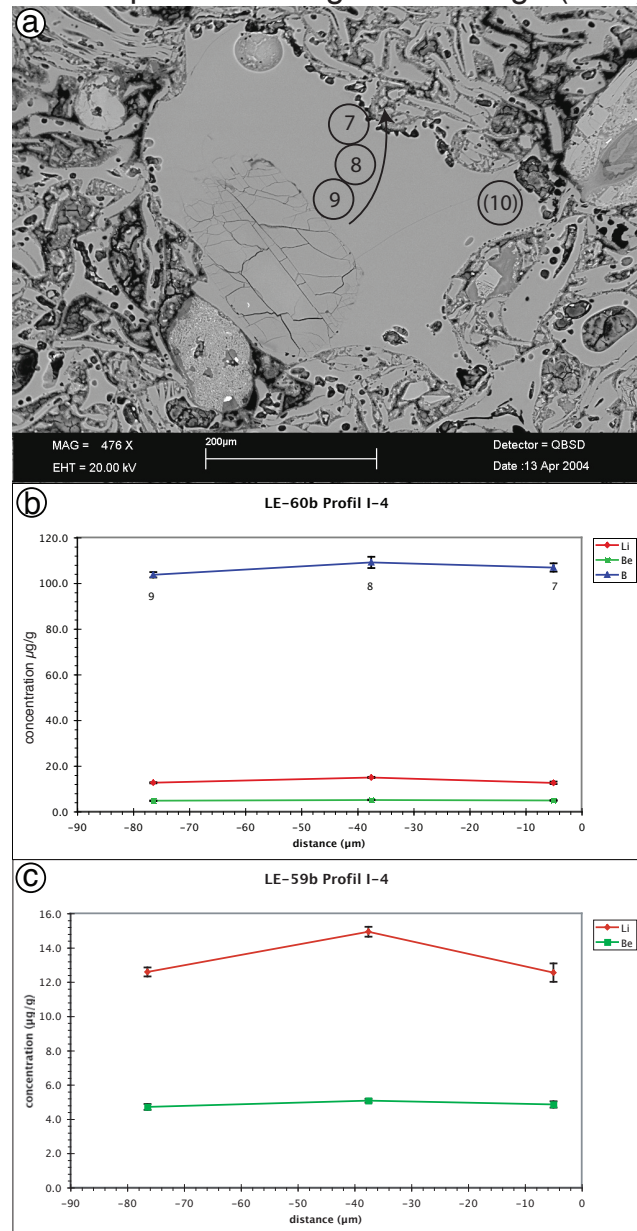


**Fig. B.8.** Sample LE-60b I-4, thick glass selvage and plagioclase (a) BSE image, arrow indicates location of SIMS profile, (b) & (c) SIMS profile for elements Li, Be, B (µg/g).

## B. Element concentration profiles

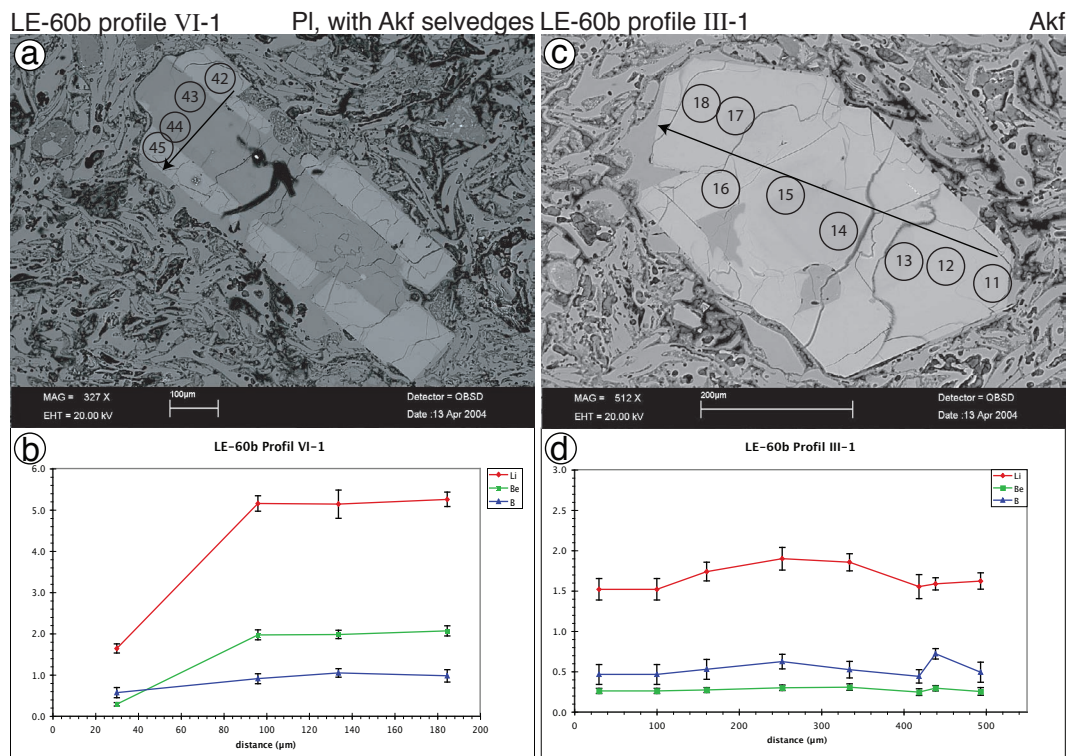


**Fig. B.9.** Sample LE-60b (a) VI-1, PI with Akf selvedges, BSE image, arrow indicates location of SIMS profile, circles denote locations of analytical spots (b) VI-1 SIMS profile for elements Li, Be, and B ( $\mu\text{g/g}$ ), (c) III-1, Akf with PI inclusions and glass selvage, BSE image, arrow indicates location of SIMS profile, circles denote locations of analytical spots (d) III-1 SIMS profile for elements Li, Be, and B ( $\mu\text{g/g}$ ),

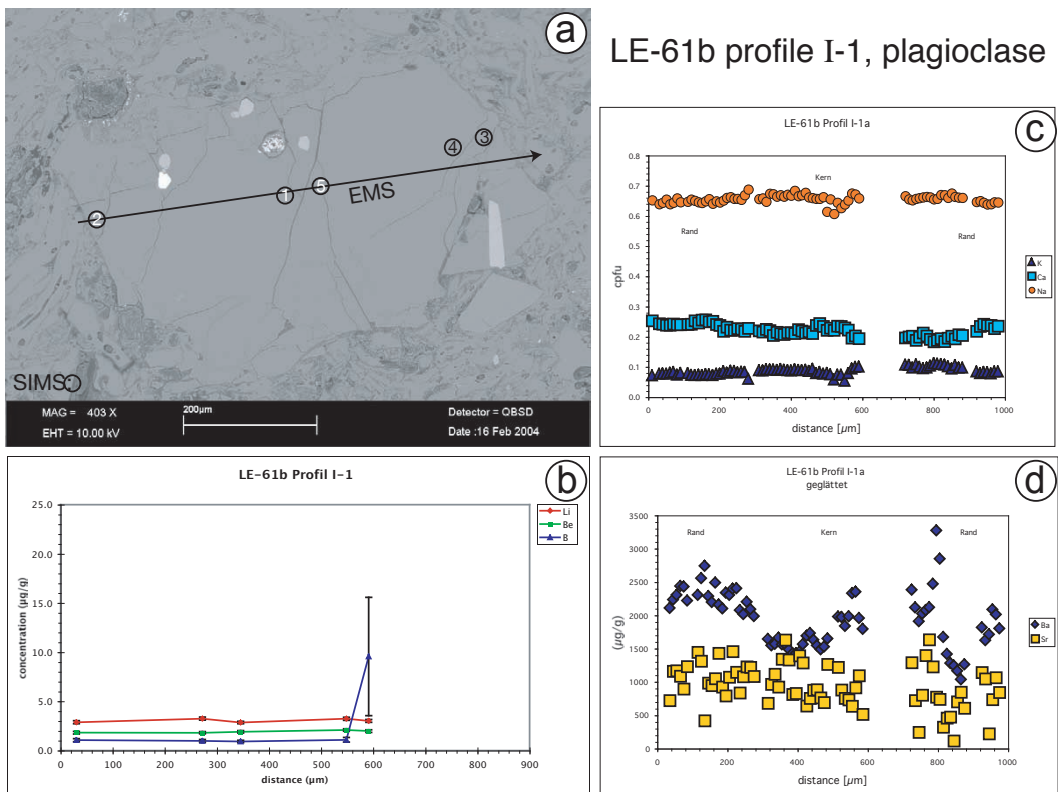


**Fig. B.10.** Sample LE-61b I-1, plagioclase (a) BSE image, arrow indicates location of EPMA profile, circles mark SIMS analytic spots (b) SIMS profile for elements Li, Be, B ( $\mu\text{g/g}$ ), data points have been ordered according to profile direction, (c) EPMA profile for elements K, Ca, and Na (cpfu) (d) EPMA profile for elements Ba and Sr ( $\mu\text{g/g}$ )

## B. Element concentration profiles

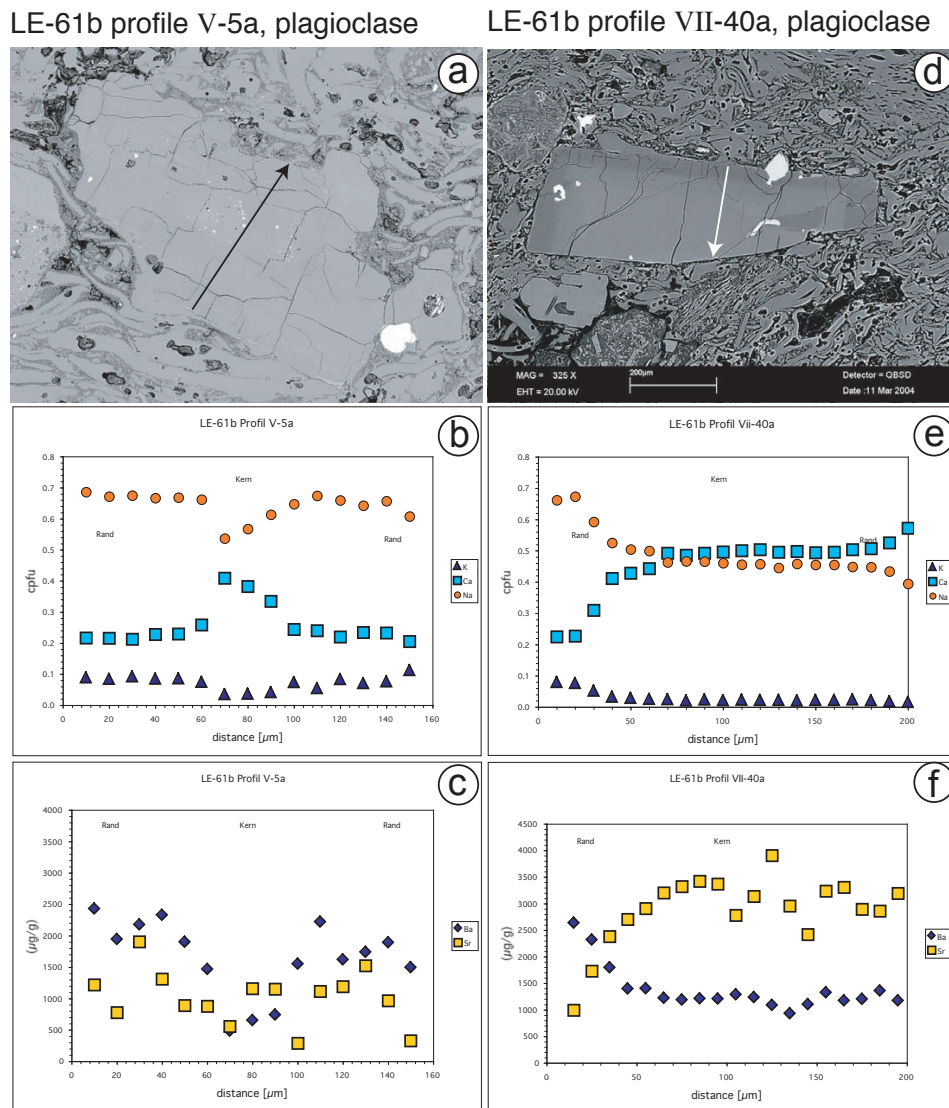


**Fig. B.11.** Sample LE-61b (a) profile V-5a, plagioclase, BSE image, arrow indicates location of EPMA profile, (b) V-5a EPMA profile for elements K, Ca, and Na (cpfu), (c) V-5a EPMA profile for elements Ba and Sr ( $\mu\text{g/g}$ ) (d) profile VII-40a, plagioclase, BSE image, arrow indicates location of EPMA profile, (e) VII-40a EPMA profile for elements K, Ca, and Na (cpfu), (f) VII-40a EPMA profile for elements Ba and Sr ( $\mu\text{g/g}$ )

LE-61b VII-1, alkali feldspar

LE-61b VIII-11, plagioclase

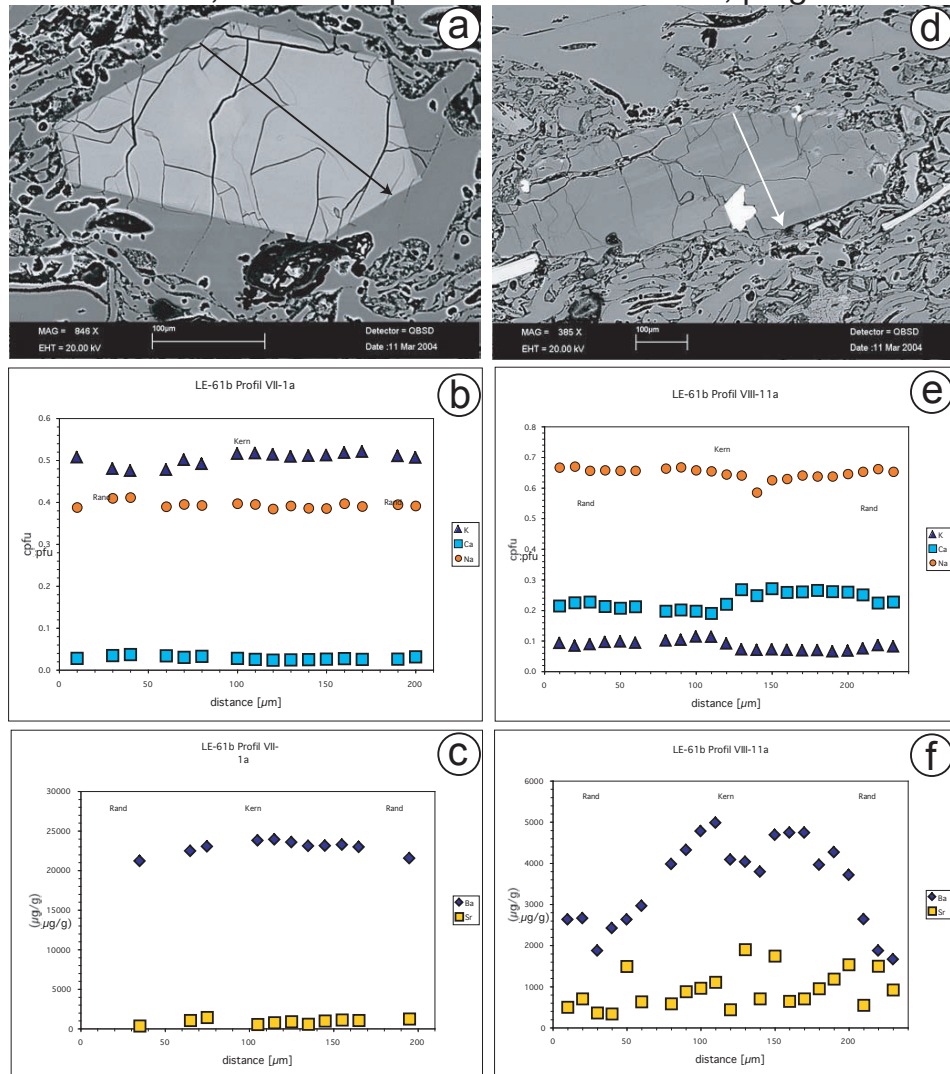


**Fig. B.12.** Sample LE-61b (a) VII-1, alkali feldspar, BSE image, arrow indicates location of EPMA profile, (b) VII-1 EPMA profile for elements K, Ca, and Na (cpfu) (c) VII-1 EPMA profile for elements Ba and Sr ( $\mu\text{g/g}$ ) (for profile location see reflected light image, in a) (d) profile VIII-11, plagioclase, BSE image, arrow indicates location of EPMA profile, (e) VIII-11, EPMA profile for elements K, Ca, and Na (cpfu) (f) VIII-11, EPMA profile for elements Ba and Sr ( $\mu\text{g/g}$ ).

B. Element concentration profiles

LE-62b IV-1,  
PI & Akf selvedges

LE-62b XX-3,  
PI & Akf selvedges

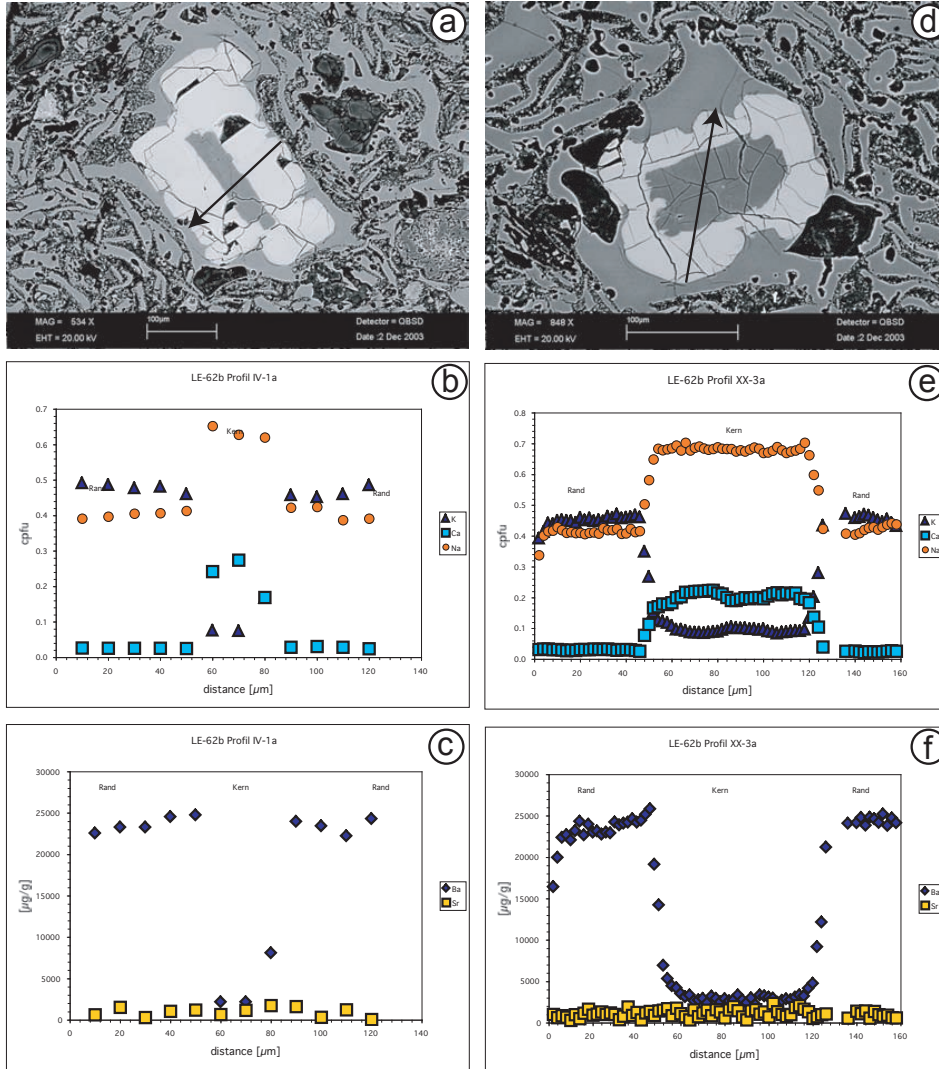


**Fig. B.13.** Sample LE-61b (a) IV-1 plagioclase core with alkali feldspar selvedge, BSE image, arrow indicates location of EPMA profile, (b) VII-1 EPMA profile for elements K, Ca, and Na (cpfu) (c) VII-1 EPMA profile for elements Ba and Sr ( $\mu\text{g/g}$ ) (d) XX-3, plagioclase core with alkali feldspar selvedge, BSE image, arrow indicates location of EPMA profile, this profile has an analytical spot every  $2\mu\text{g/g}$ , with a spot size of  $10\mu\text{g/g}$ , therefore producing overlap and a number of mixed analyses at the boundary between PI and Akf, (e) XX-3, EPMA profile for elements K, Ca, and Na (cpfu) (f) XX-3, EPMA profile for elements Ba and Sr ( $\mu\text{g/g}$ ).

LE-62b profile IV-2      alkali feldspar

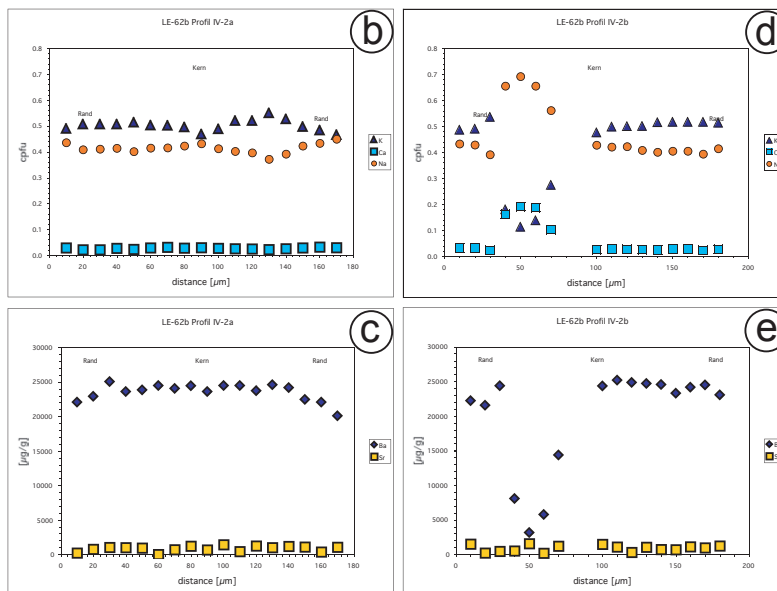
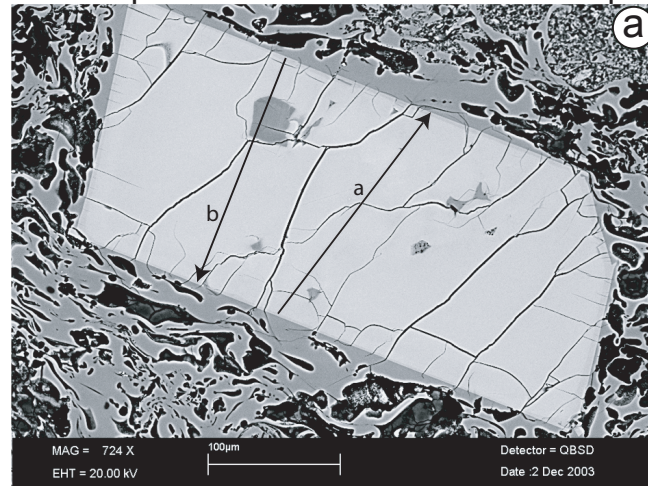
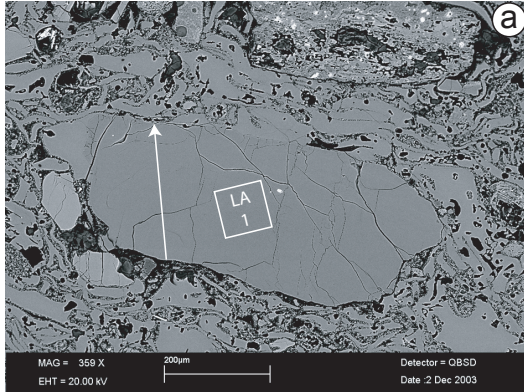


**Fig. B.14.** Sample LE-61b IV-2, alkali feldspar with plagioclase inclusions, (a) BSE image, arrow indicates location of EPMA profiles, IV-2a & IV-2b (b) EPMA profile a for elements K, Ca, and Na (cpfu) (c) EPMA profile a for elements Ba and Sr ( $\mu\text{g/g}$ ) (d) EPMA profile b for elements K, Ca, and Na (cpfu) (e) EPMA profile b for elements Ba and Sr ( $\mu\text{g/g}$ ).

## B. Element concentration profiles

LE-62b V-2, plagioclase



LE-62b V-9, plagioclase

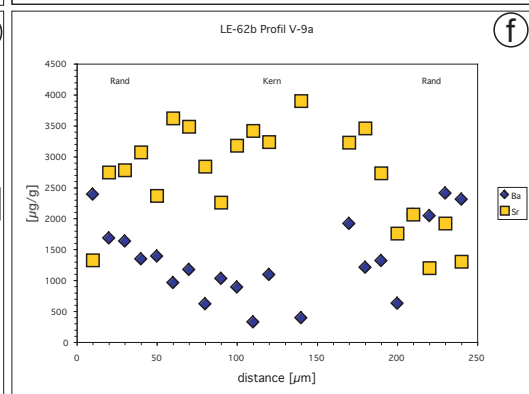
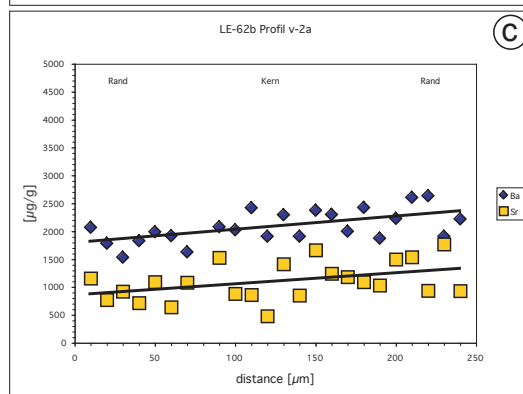
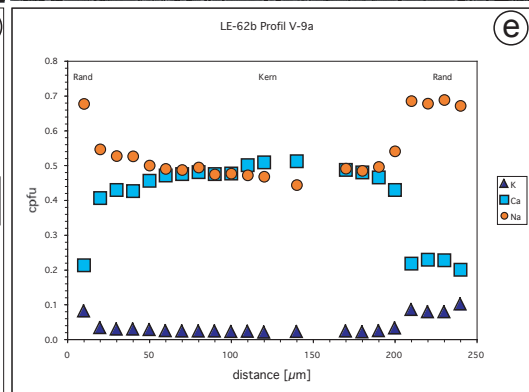
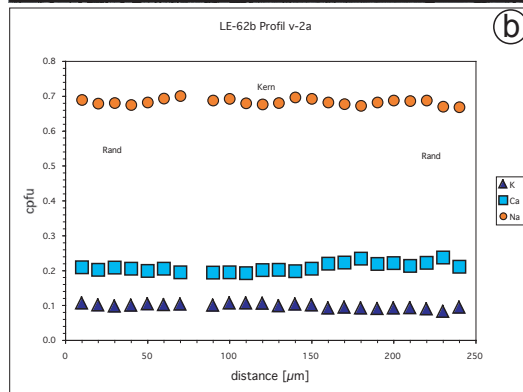
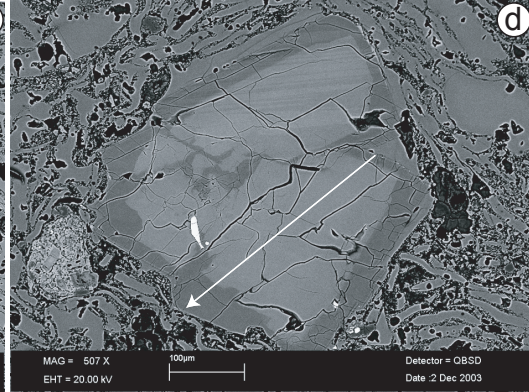


**Fig. B.15.** Sample LE-62b (a) V-2 plagioclase, BSE image, arrow indicates location of EPMA profile, square marks location of laser-ablation analysis (Sr isotopes) (b) V-2 EPMA profile for elements K, Ca, and Na (cpfu) (c) V-2 EPMA profile for elements Ba and Sr ( $\mu\text{g/g}$ ) (d) V-9 plagioclase, BSE image, arrow indicates location of EPMA profile, (e) V-9 EPMA profile for elements K, Ca, and Na (cpfu) (f) V-9 EPMA profile for elements Ba and Sr ( $\mu\text{g/g}$ ).

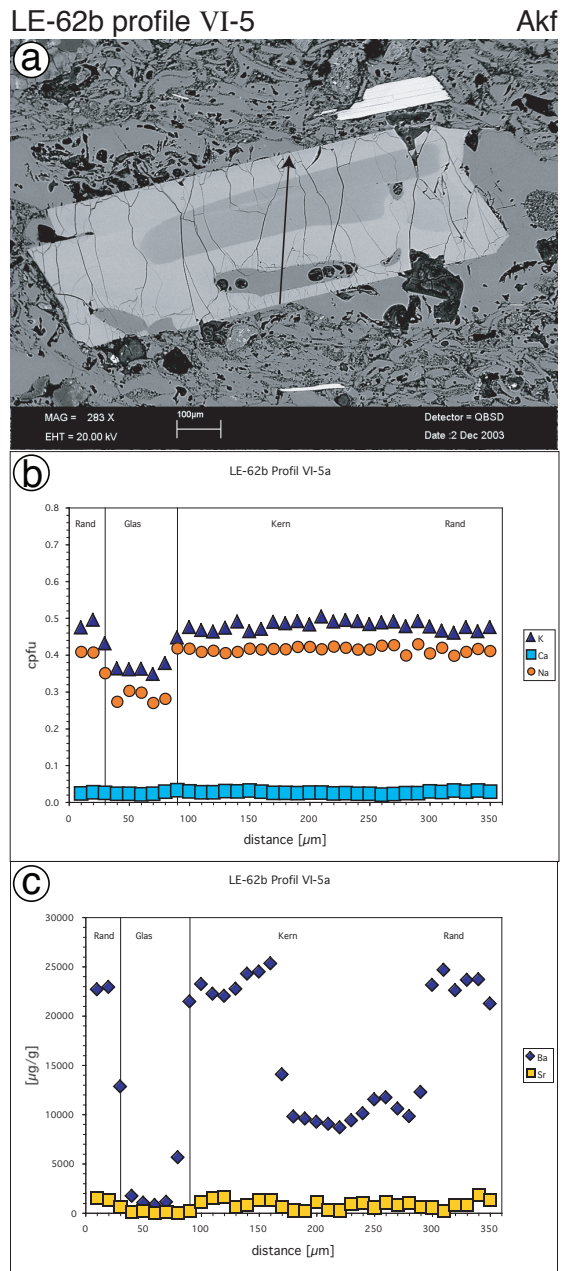


**Fig. B.16.** Sample LE-61b VI-5, alkali feldspar with Ba zonation and glass inclusion (a) BSE image, arrow indicates location of EPMA profile, (b) EPMA profile for elements K, Ca, and Na (cpfu) (c) EPMA profile for elements Ba and Sr (μg/g)

## B. Element concentration profiles

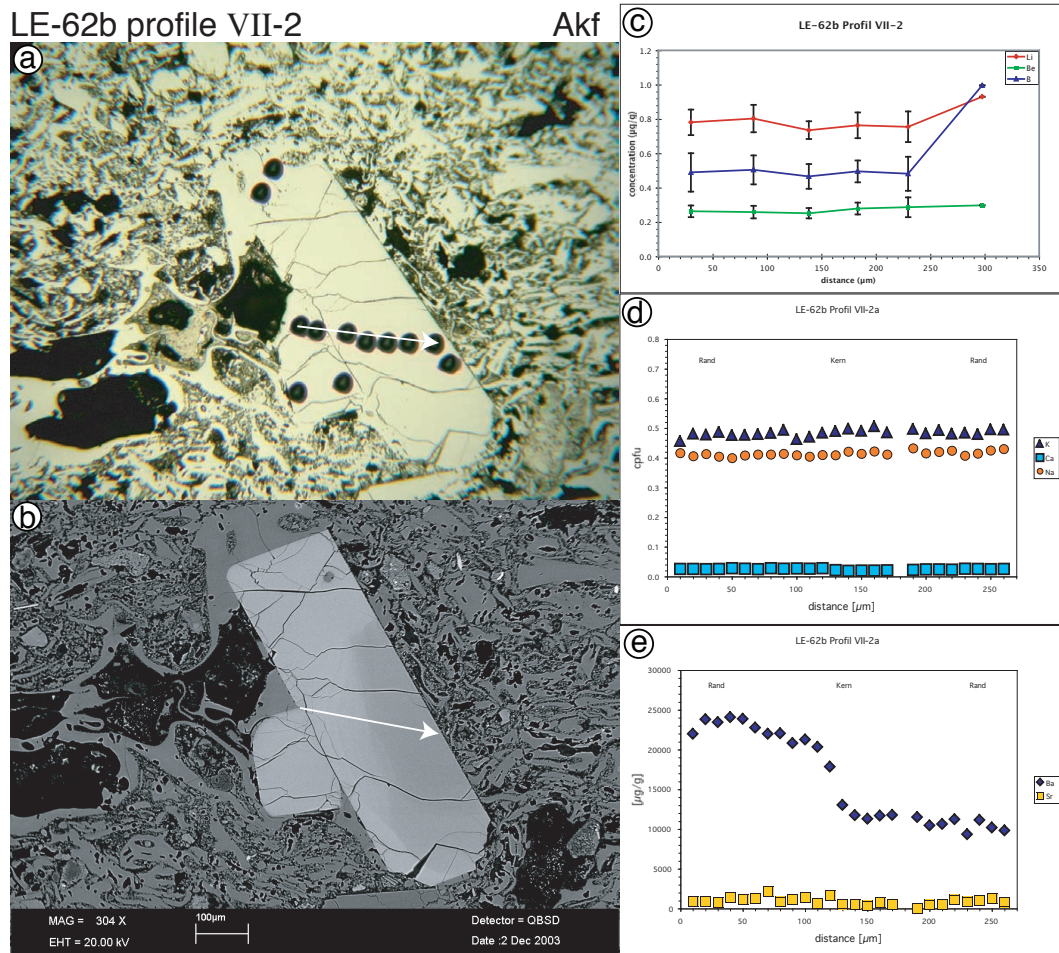


**Fig. B.17.** Sample LE-62b VII-2, alkali feldspar (a) reflected light image of gold coated sample after SIMS analysis, analytical spots appear black on gold coating, (b) BSE image, arrow indicates location of EPMA profile, (c) SIMS profile for elements Li, Be, B ( $\mu\text{g/g}$ ), (d) EPMA profile for elements K, Ca, and Na (cpfu), (e) EPMA profile for elements Ba and Sr ( $\mu\text{g/g}$ ).

LE-62b profile VII-3

plagioclase

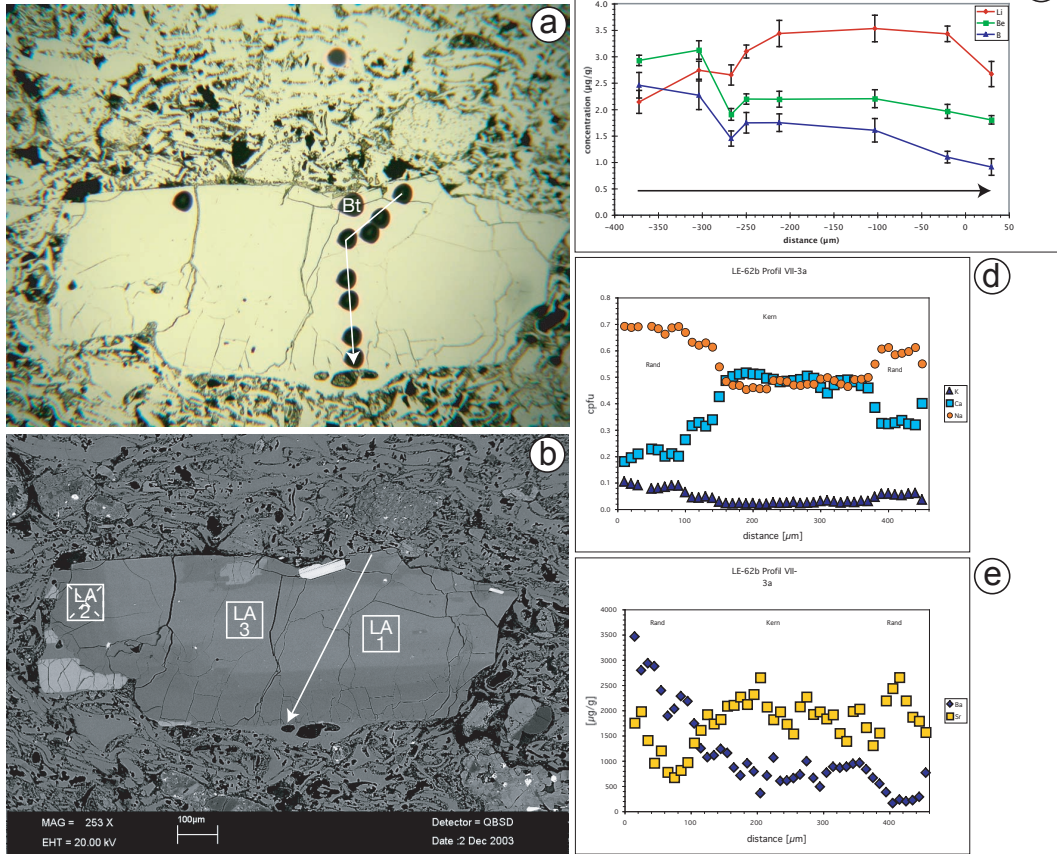


**Fig. B.18.** Sample LE-62b VII-3, plagioclase (a) reflected light image of gold coated sample after SIMS analysis, analytical spots appear black on gold coating, (b) BSE image, arrow indicates location of EPMA profile, squares indicate locations for Sr isotopic analysis (LA-ICP-MS), (c) SIMS profile for elements Li, Be, B ( $\mu\text{g/g}$ ), (d) EPMA profile for elements K, Ca, and Na (cpfu), (e) EPMA profile for elements Ba and Sr ( $\mu\text{g/g}$ ).

## B. Element concentration profiles

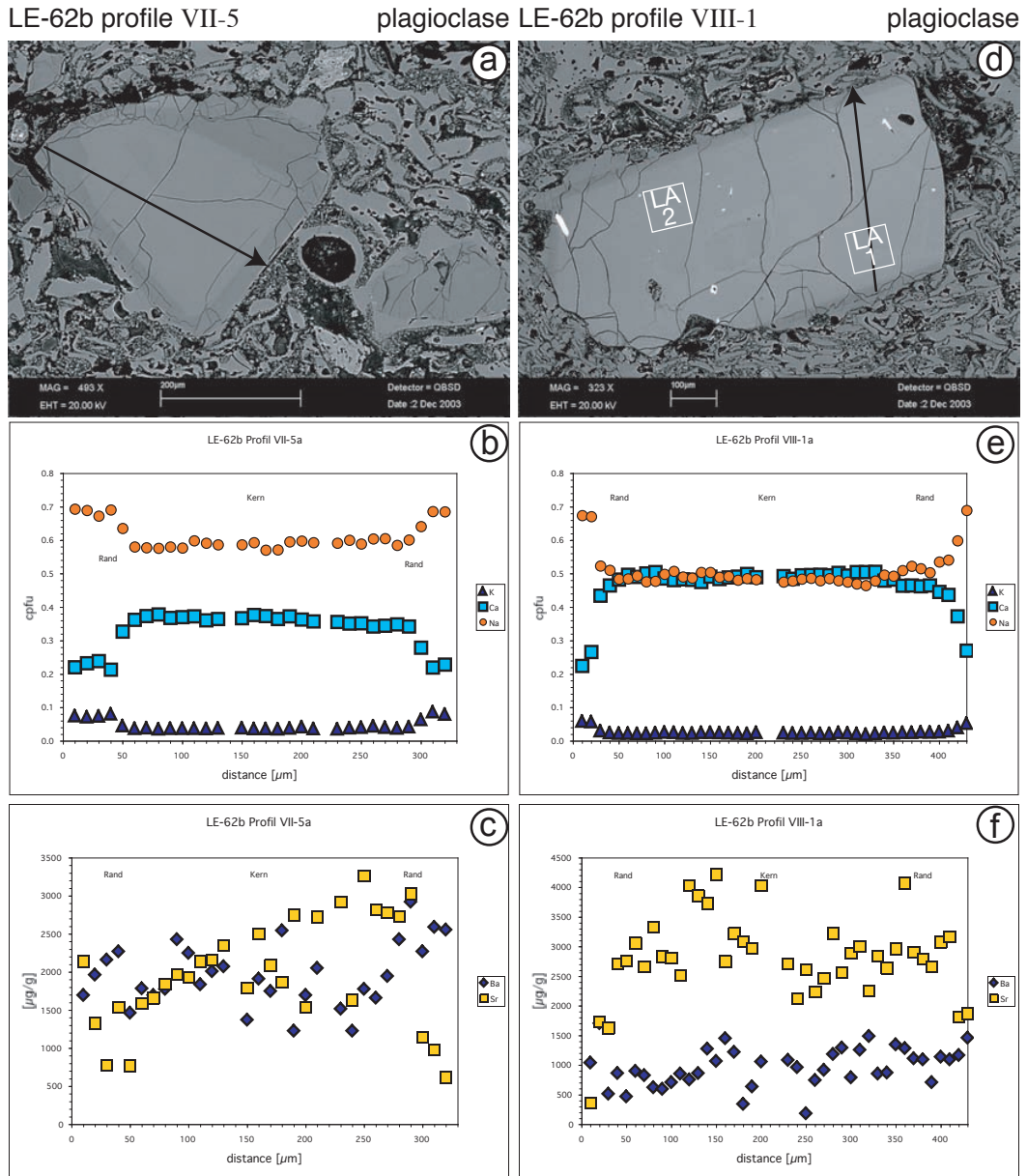


**Fig. B.19.** Sample LE-61b (a) VII-5, plagioclase, BSE image, arrow indicates location of EPMA profile, (b) EPMA profile for elements K, Ca, and Na (cpfu), (c) EPMA profile for elements Ba and Sr ( $\mu\text{g/g}$ ), (d) VIII-1, plagioclase, BSE image, arrow indicates location of EPMA profile, squares mark locations of laser-ablation analyses (Sr isotopes) (e) EPMA profile for elements K, Ca, and Na (cpfu), (f) EPMA profile for elements Ba and Sr ( $\mu\text{g/g}$ ).

LE-62b VIII-3, biotite

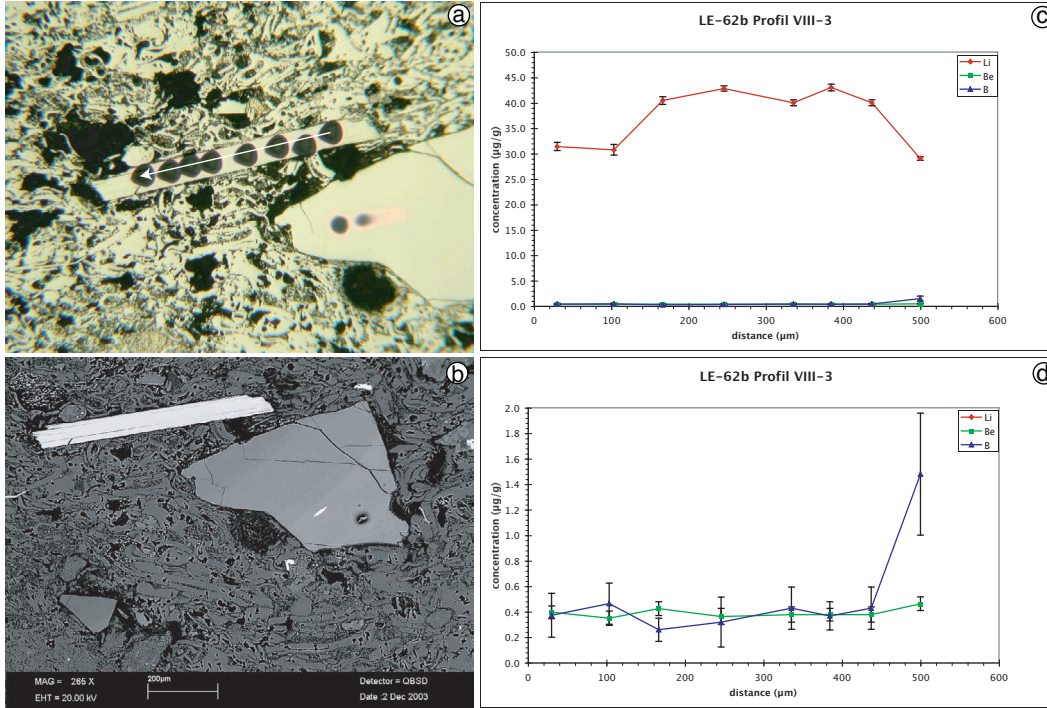


**Fig. B.20.** Sample LE-62b VIII-3, biotite, (a) reflected light image of gold coated sample after SIMS analysis, analytical spots appear black on gold coating, (b) BSE image, (c) SIMS profile for elements Li, Be, B ( $\mu\text{g/g}$ ), (d) SIMS profile for elements Be, B ( $\mu\text{g/g}$ ).

B. Element concentration profiles

LE-62b VIII-4, biotite

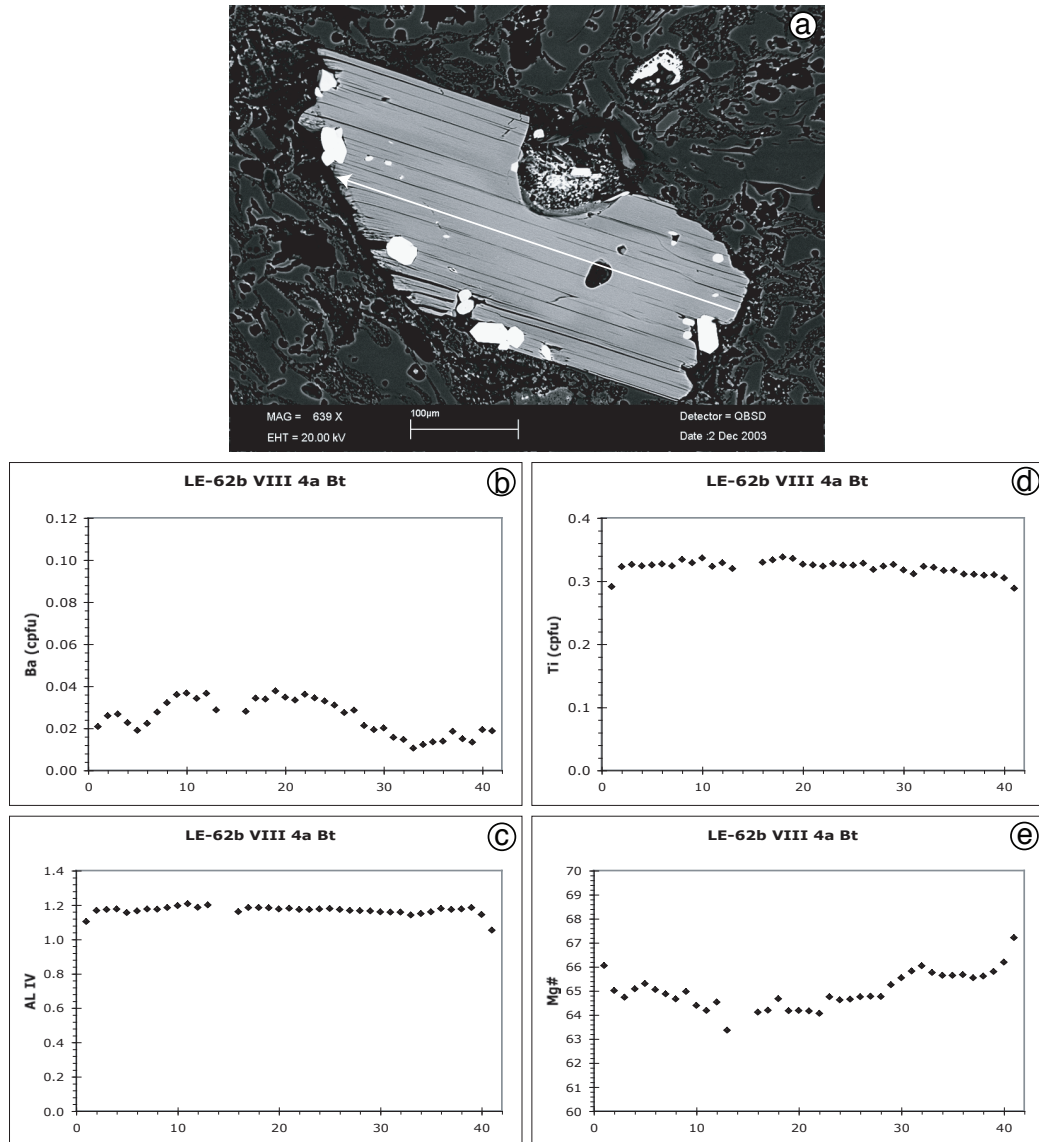


**Fig. B.21.** Sample LE-62b VIII-4, biotite, (a) BSE image, arrow indicates location of EPMA (b) EPMA profile for Ba (cpfu), (c) EPMA profile for Al<sup>IV</sup>, (d) EPMA profile for Ti (cpfu), (e) EPMA profile for Mg#.

LE-57b profile I-5, alkali feldspar

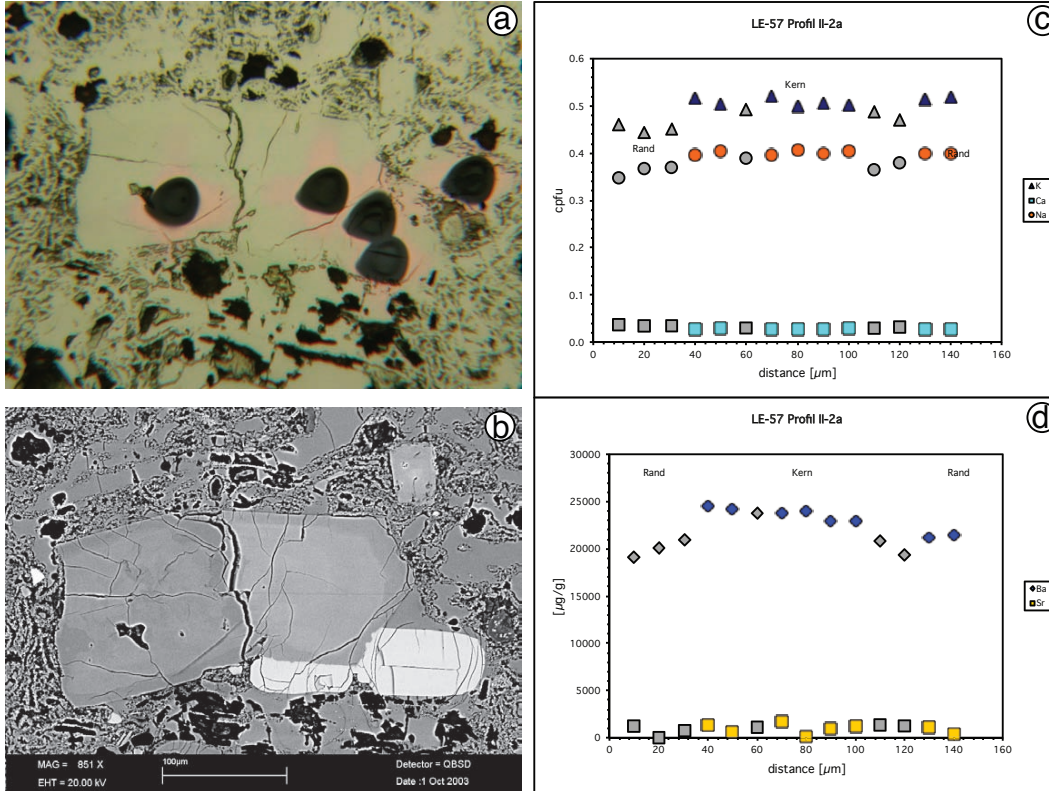


**Fig. B.22.** Sample LE-57b I-5, alkali feldspar, (a) reflected light image of gold coated sample after SIMS analysis, analytical spots appear black on gold coating, (b) BSE image, (c) SIMS profile for elements Li, Be, B ( $\mu\text{g/g}$ ), (d) EPMA profile for elements K, Ca, and Na (cpfu), (e) EPMA profile for elements Ba and Sr ( $\mu\text{g/g}$ ).

B. Element concentration profiles

LE-57b profile II-2, alkali feldspar

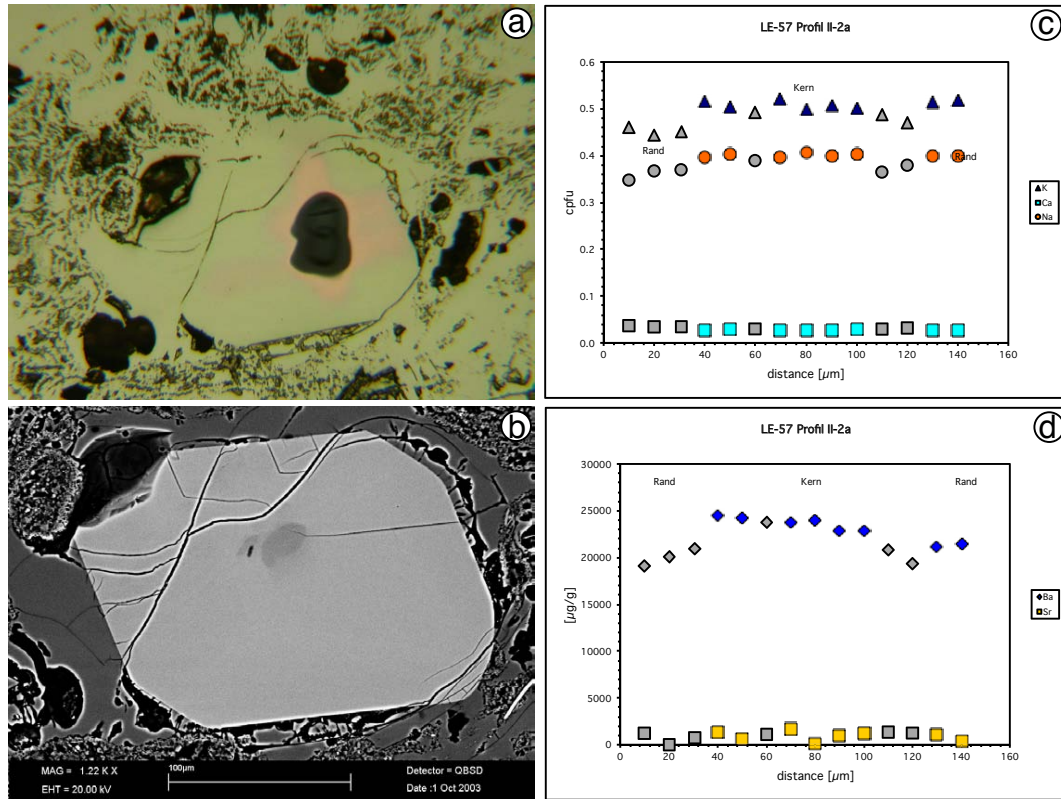


**Fig. B.23.** Sample LE-57b II-2 (a) reflected light image of gold coated sample after SIMS analysis, analytical spots appear black on gold coating, (b) BSE image, (c) EPMA profile for elements K, Ca, and Na (cpfu), (d) EPMA profile for elements Ba and Sr ( $\mu\text{g/g}$ ).

LE-57b profile II-3, plagioclase

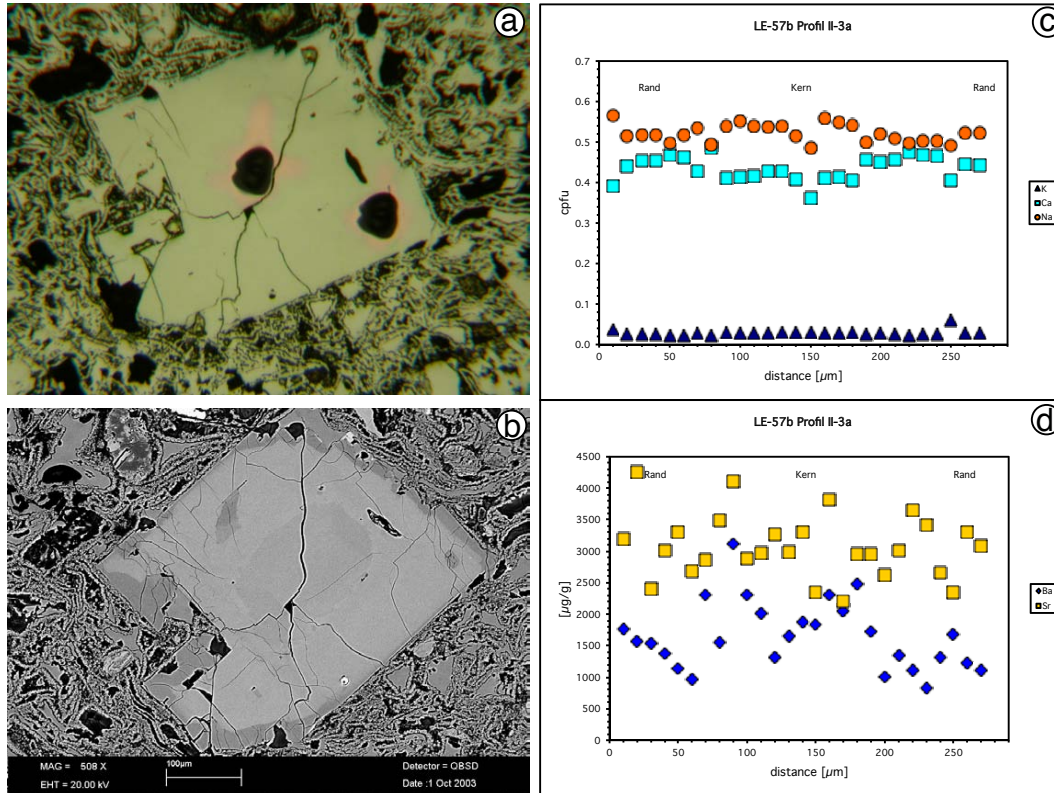


**Fig. B.24.** Sample LE-57b II-3 (a) reflected light image of gold coated sample after SIMS analysis, analytical spots appear black on gold coating, (b) BSE image, (c) EPMA profile for elements K, Ca, and Na (cpfu), (d) EPMA profile for elements Ba and Sr ( $\mu\text{g/g}$ ).

## B. Element concentration profiles

LE-63b I-5, Pl core and thick Akf selvedge LE-63b I-6, plagioclase and alkali feldspar

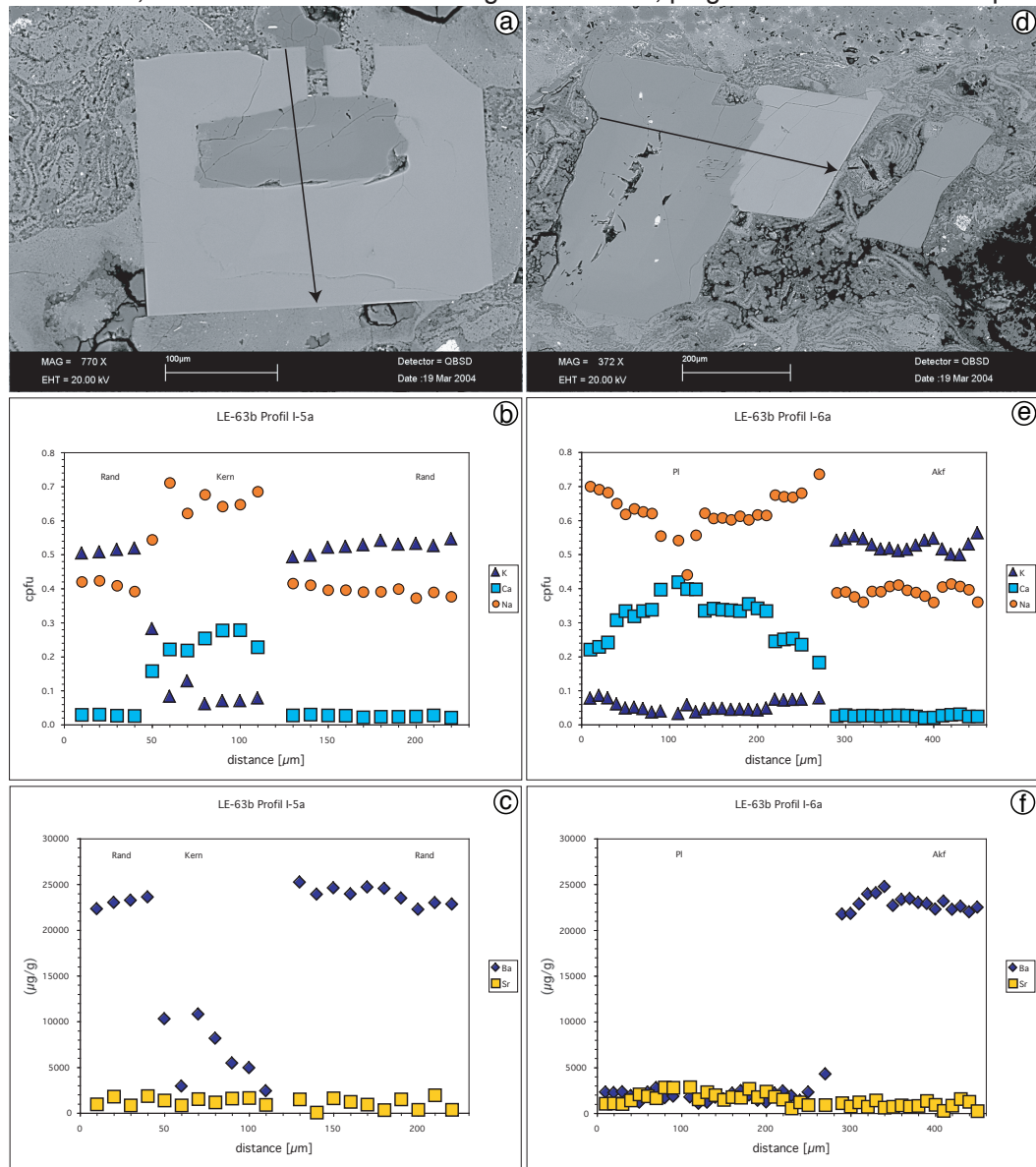


**Fig. B.25.** Sample LE-63b (a) I-5, plagioclase core with alkali feldspar selvage, BSE image, arrow indicates location of EPMA profile, (b) I-5, EPMA profile for elements K, Ca, and Na (cpfu), (c) I-5, EPMA profile for elements Ba and Sr ( $\mu\text{g/g}$ ), (d) I-6, plagioclase and alkali feldspar, BSE image, arrow indicates location of EPMA profile, (e) I-6, EPMA profile for elements K, Ca, and Na (cpfu), (f) I-6, EPMA profile for elements Ba and Sr ( $\mu\text{g/g}$ ).

LE-63b II-2, alkali feldspar

LE-63b II-3, alkali feldspar

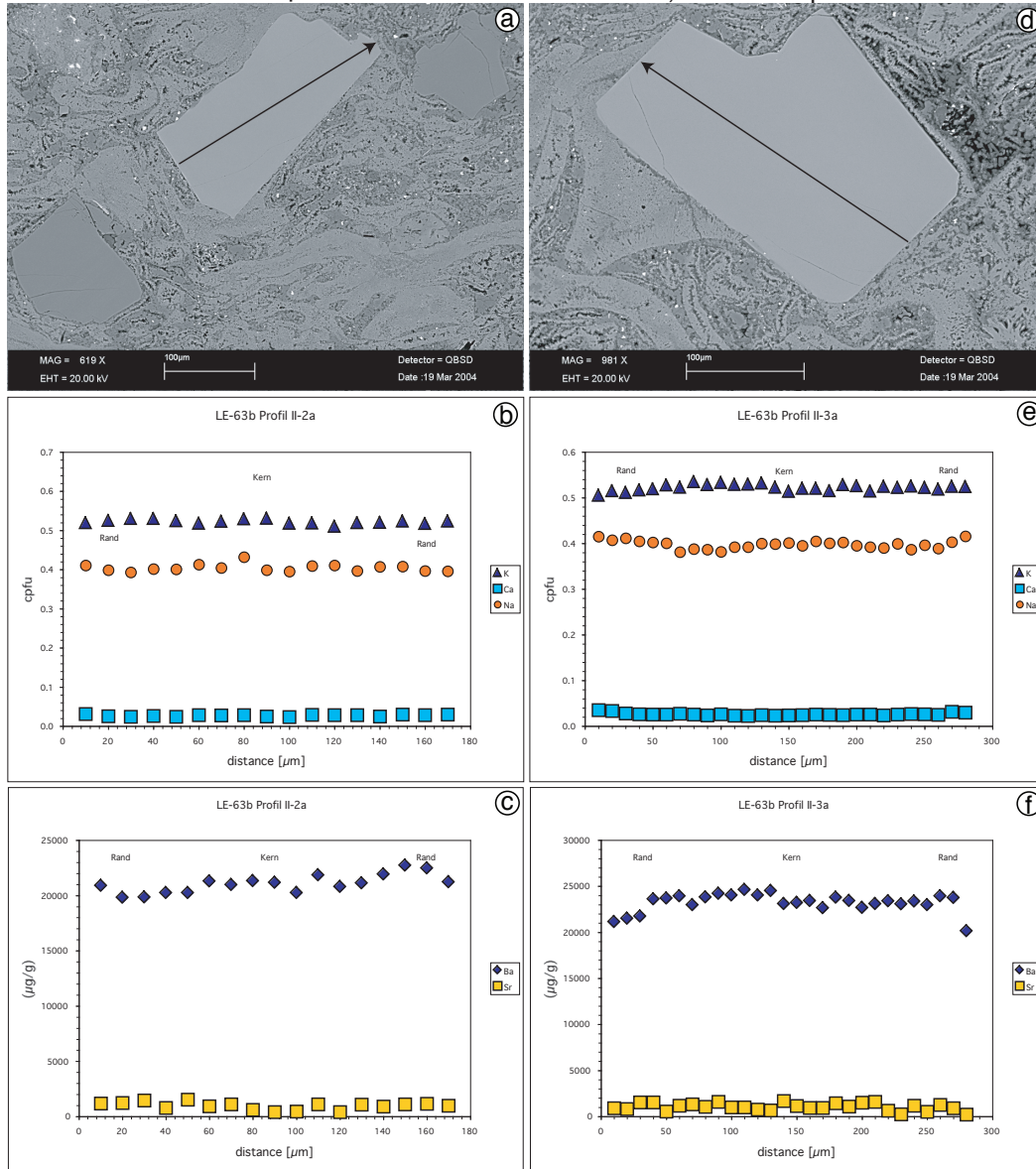


**Fig. B.26.** Sample LE-63b (a) II-2, alkali feldspar, BSE image, arrow indicates location of EPMA profile, (b) II-2, alkali feldspar, EPMA profile for elements K, Ca, and Na (cpfu), (c) II-2, alkali feldspar, EPMA profile for elements Ba and Sr ( $\mu\text{g/g}$ ), (d) II-3, alkali feldspar, BSE image, arrow indicates location of EPMA profile, (e) II-3, alkali feldspar, EPMA profile for elements K, Ca, and Na (cpfu), (f) II-3, alkali feldspar, EPMA profile for elements Ba and Sr ( $\mu\text{g/g}$ ).

B. Element concentration profiles

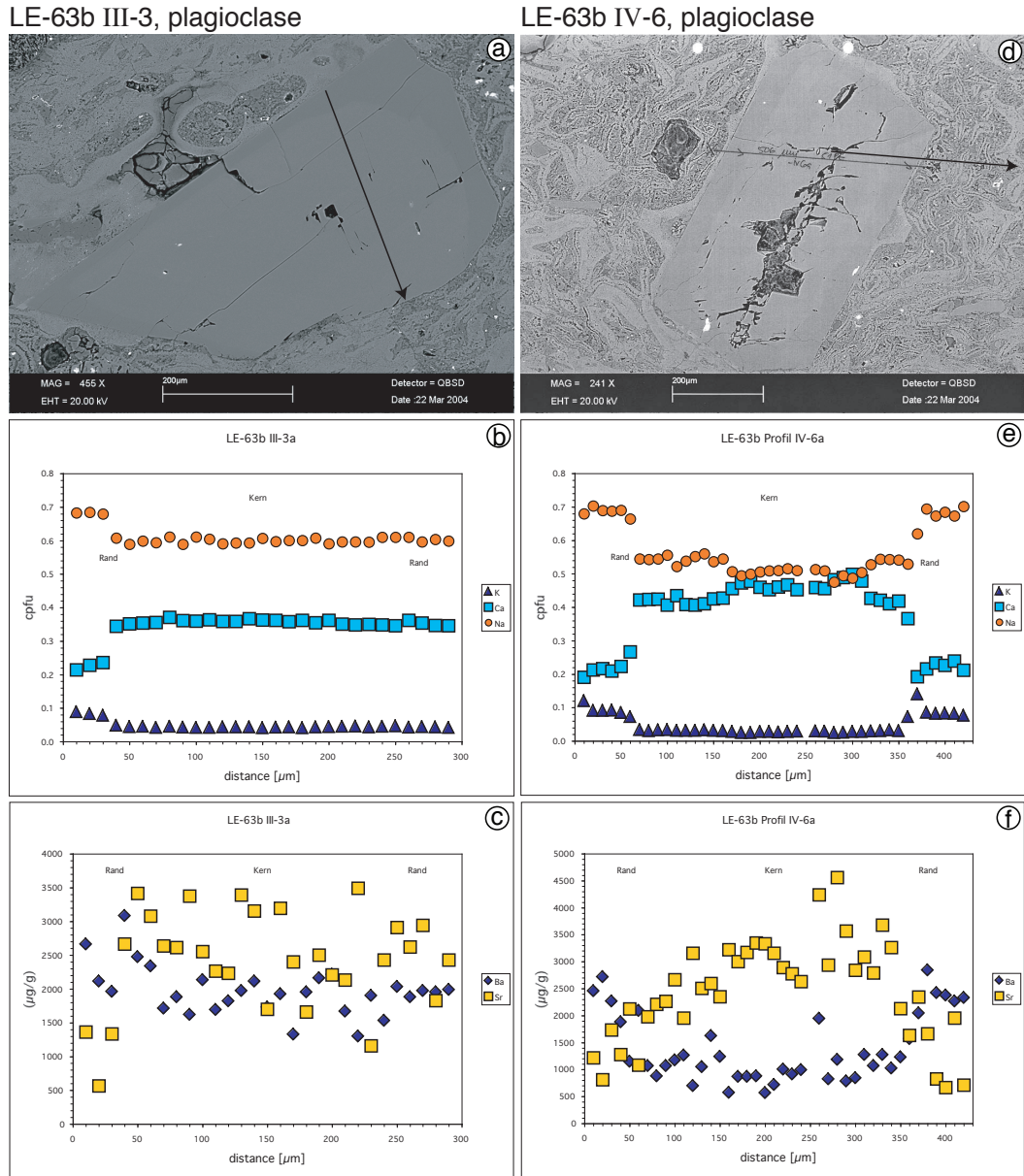
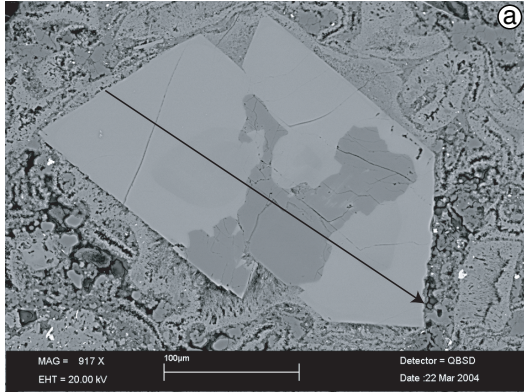


**Fig. B.27.** Sample LE-63b (a) III-3, plagioclase, BSE image, arrow indicates location of EPMA profile, (b) III-3, plagioclase, EPMA profile for elements K, Ca, and Na (cpfu), (c) III-3, plagioclase, EPMA profile for elements Ba and Sr ( $\mu\text{g/g}$ ), (d) IV-6, plagioclase, BSE image, arrow indicates location of EPMA profile, (e) IV-6, plagioclase, EPMA profile for elements K, Ca, and Na (cpfu), (f) IV-6, plagioclase, EPMA profile for elements Ba and Sr ( $\mu\text{g/g}$ ).

LE-63b IV-1, alkali feldspar



LE-63b IV-5, alkali feldspar

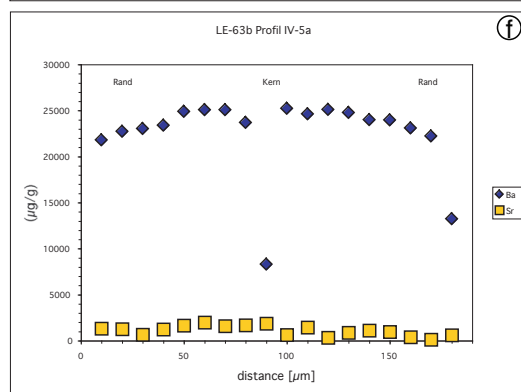
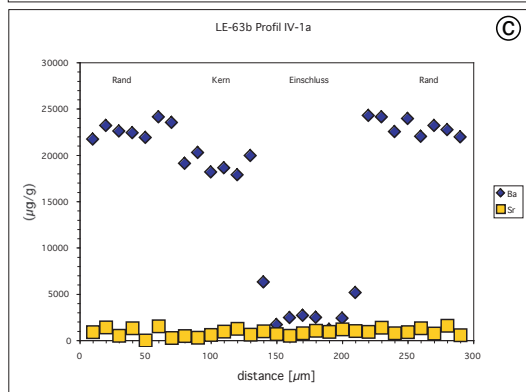
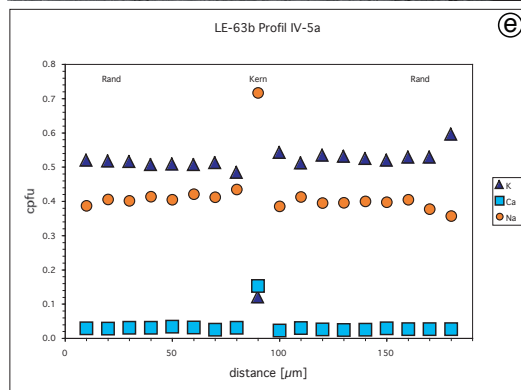
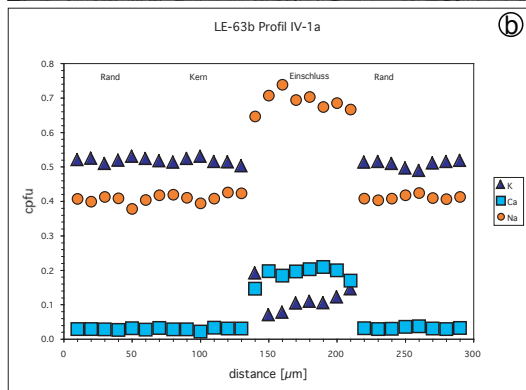
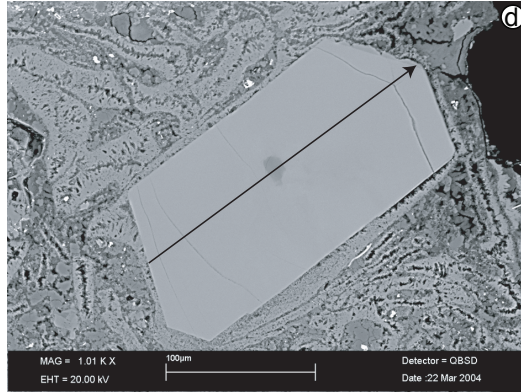


**Fig. B.28.** Sample LE-63b (a) IV-1, alkali feldspar, BSE image, arrow indicates location of EPMA profile, (b) IV-1, alkali feldspar, EPMA profile for elements K, Ca, and Na (cpfu), (c) IIV-1, alkali feldspar, EPMA profile for elements Ba and Sr ( $\mu\text{g/g}$ ), (d) IV-5, alkali feldspar, BSE image, arrow indicates location of EPMA profile, (e) IV-5, alkali feldspar, EPMA profile for elements K, Ca, and Na (cpfu), (f) IV-5, alkali feldspar, EPMA profile for elements Ba and Sr ( $\mu\text{g/g}$ ).

## B. Element concentration profiles

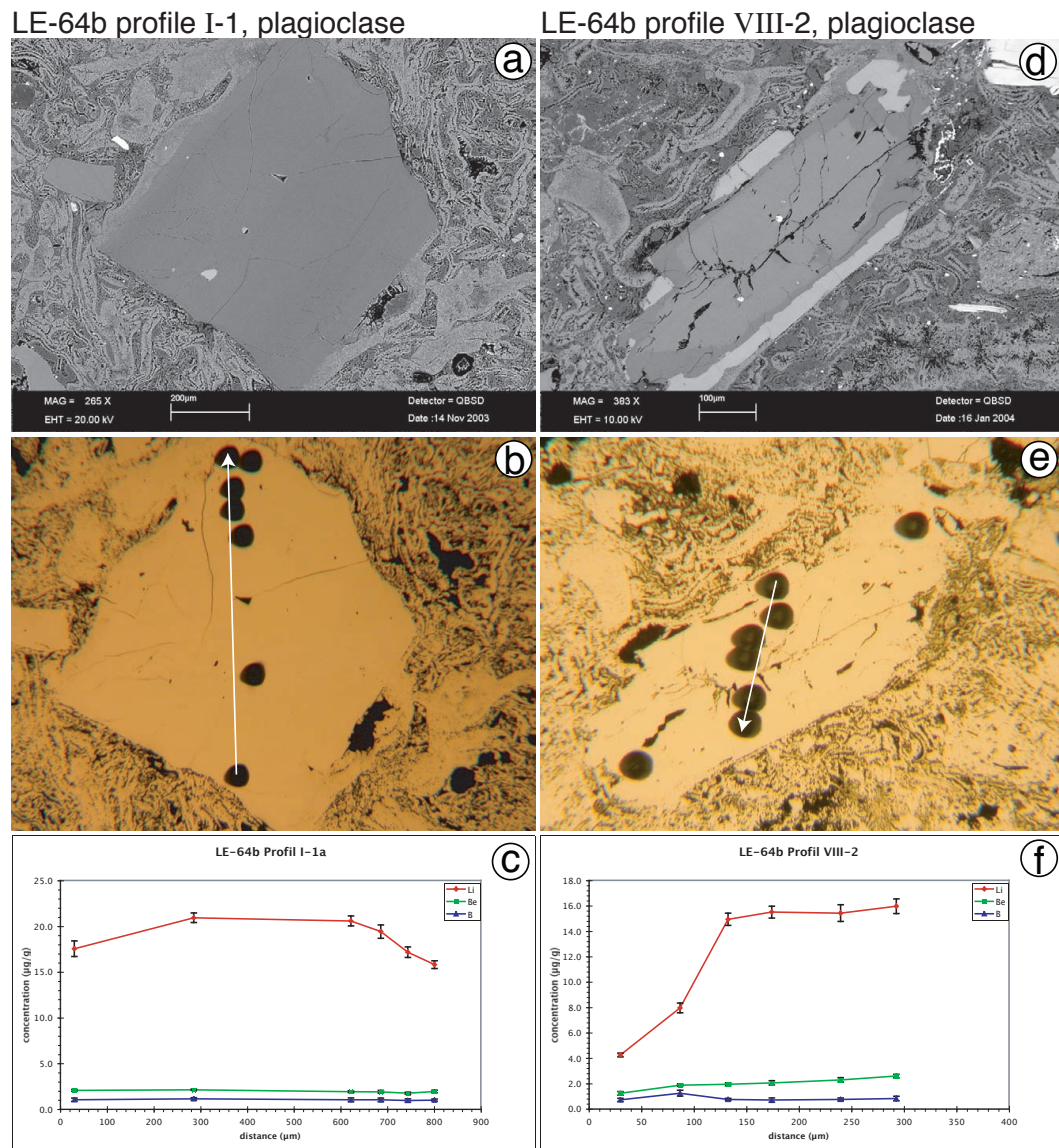


**Fig. B.29.** Sample LE-64b (a) BSE image, I-1, plagioclase, (b) I-1, reflected light image of gold coated sample after SIMS analysis, analytical spots appear black on gold coating, arrow indicates direction of SIMS profile, (c) I-1, SIMS profile for elements Li, Be, B ( $\mu\text{g/g}$ ), (d) BSE image, VIII-2, plagioclase, (e) VIII-2, reflected light image of gold coated sample after SIMS analysis, analytical spots appear black on gold coating, arrow indicates direction of SIMS profile, (f) VIII-2, SIMS profile for elements Li, Be, B ( $\mu\text{g/g}$ ).

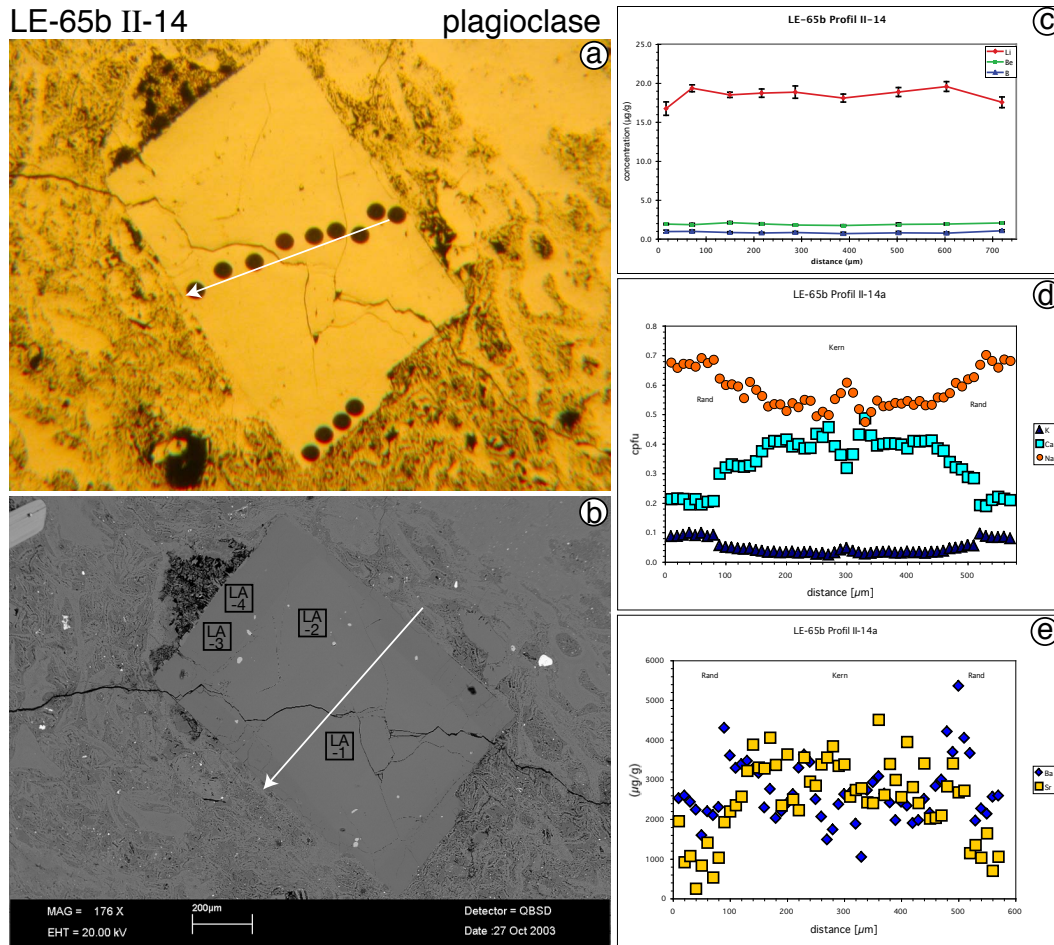


**Fig. B.30.** Sample LE-65b II-14, plagioclase, (a) reflected light image of gold coated sample after SIMS analysis, analytical spots appear black on gold coating, arrow indicate direction of SIMS profile, (b) BSE image, arrow indicates location of EPMA profile, squares indicate locations for Sr isotopic analysis (LA-ICP-MS), (c) SIMS profile for elements Li, Be, B ( $\mu\text{g/g}$ ), (d) EPMA profile for elements K, Ca, and Na (cpfu), (e) EPMA profile for elements Ba and Sr ( $\mu\text{g/g}$ ).

## B. Element concentration profiles

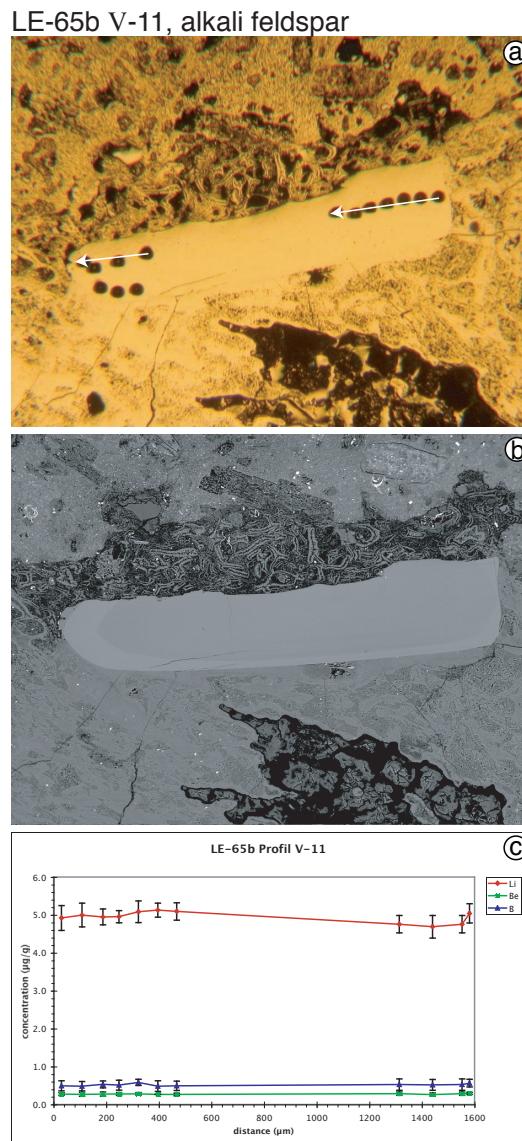


**Fig. B.31.** Sample LE-65b V-11, alkali feldspar, (a) reflected light image of gold coated sample after SIMS analysis, analytical spots appear black on gold coating, arrows indicate direction of SIMS profile, (b) BSE image, (c) SIMS profile for elements Li, Be, B ( $\mu\text{g/g}$ ).

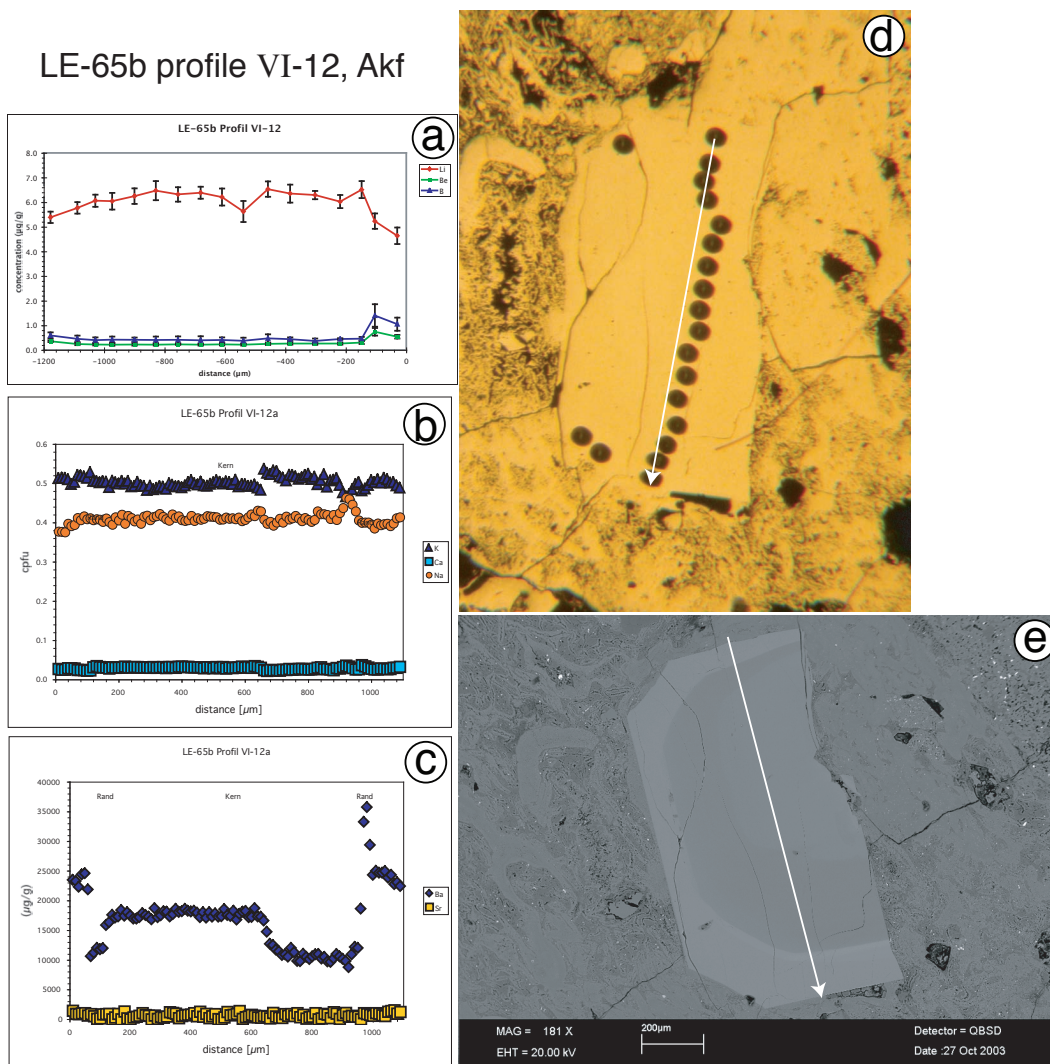


**Fig. B.32.** Sample LE-65b VI-12, alkali feldspar, (a) SIMS profile for elements Li, Be, B ( $\mu\text{g/g}$ ), (b) EPMA profile for elements K, Ca, and Na (cpfu), (c) EPMA profile for elements Ba and Sr ( $\mu\text{g/g}$ ), (d) reflected light image of gold coated sample after SIMS analysis, analytical spots appear black on gold coating, arrow indicates direction of SIMS profile, (e) BSE image, arrow indicates location of EPMA profile.

## B. Element concentration profiles

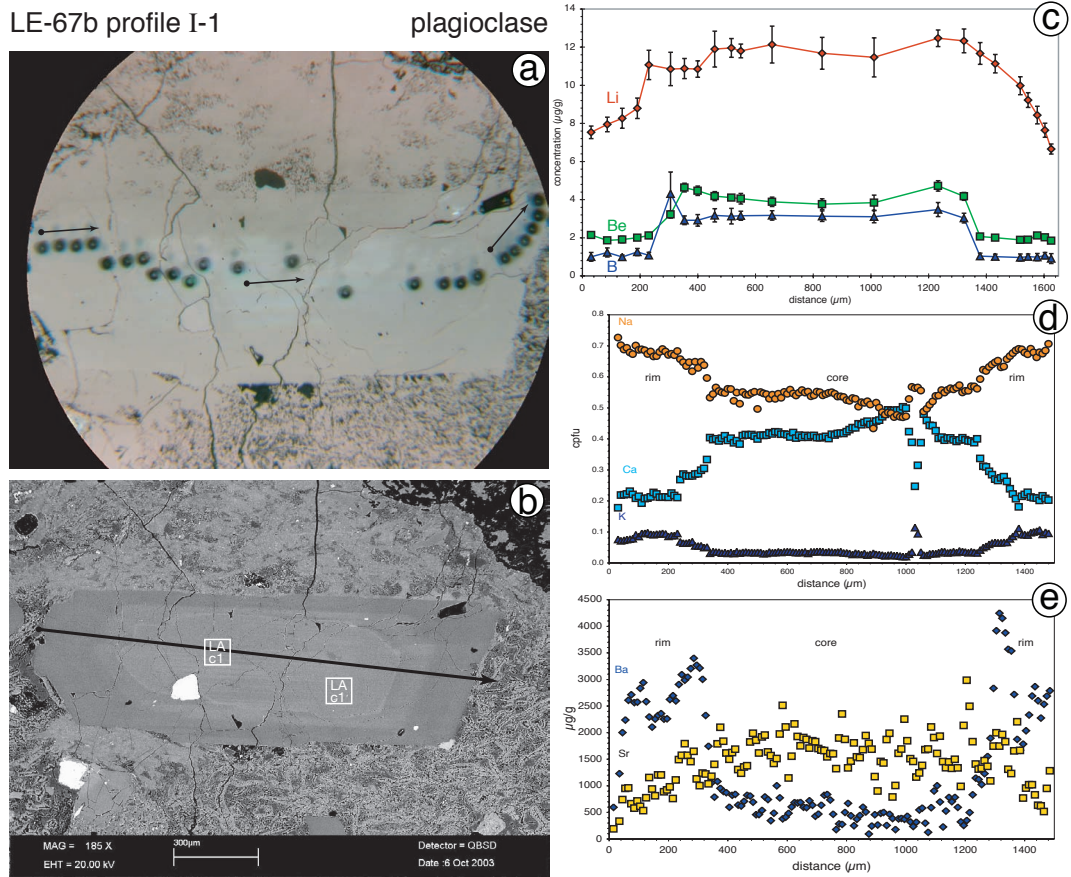


**Fig. B.33.** Sample LE-67b I-1, plagioclase, (a) reflected light image of gold coated sample after SIMS analysis, analytical spots appear black on gold coating, arrow indicates direction of SIMS profile, (b) BSE image, arrow indicates location of EPMA profile, squares indicate locations for Sr isotopic analysis (LA-ICP-MS), (c) SIMS profile for elements Li, Be, B ( $\mu\text{g/g}$ ), (d) EPMA profile for elements K, Ca, and Na (cpfu), (e) EPMA profile for elements Ba and Sr ( $\mu\text{g/g}$ ).

LE-67b I-5, plagioclase

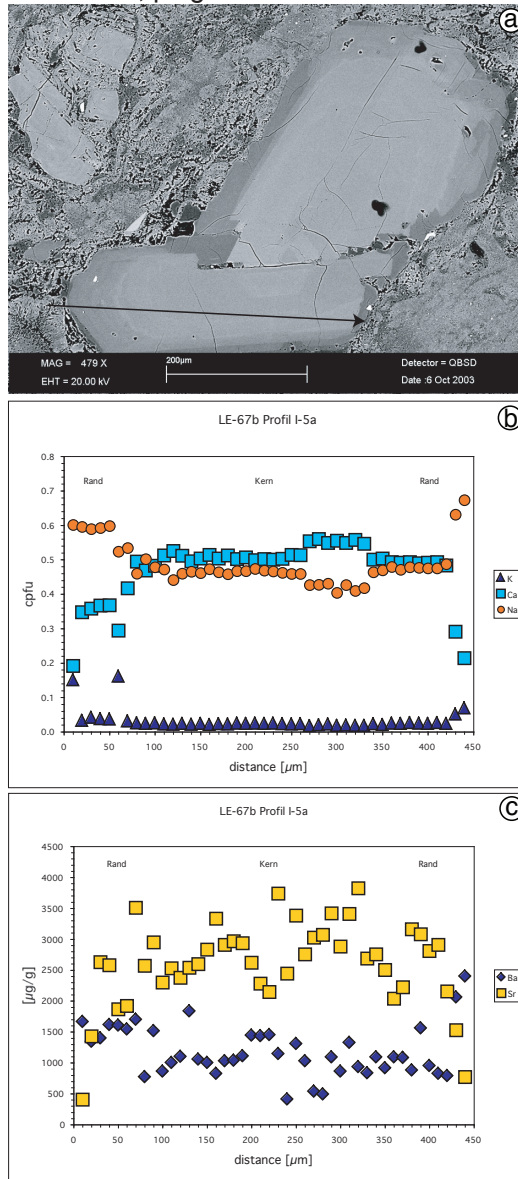


**Fig. B.34.** Sample LE-67b I-5, plagioclase, (a) BSE image, arrow indicates location of EPMA profile, (b) EPMA profile for elements K, Ca, and Na (cpfu), (c) EPMA profile for elements Ba and Sr ( $\mu\text{g/g}$ ).

B. Element concentration profiles

LE-67b III-14a&b, plagioclase

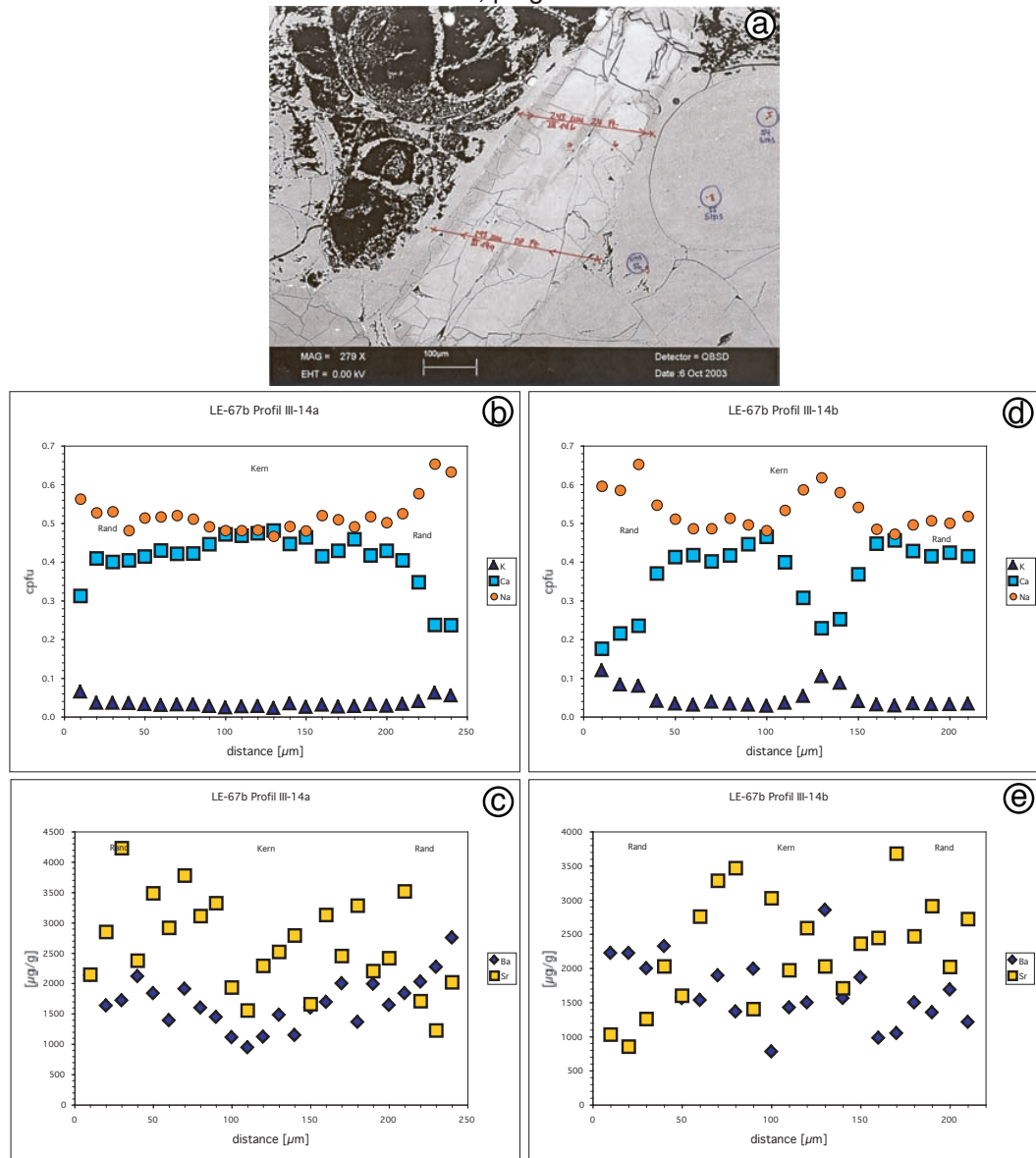


**Fig. B.35.** Sample LE-67b III-14, plagioclase, (a) BSE image, arrow indicate location of EPMA profiles a & b, (b) EPMA profile a for elements K, Ca, and Na (cpfu), (c) EPMA profile a for elements Ba and Sr ( $\mu\text{g/g}$ ), (d) EPMA profile b for elements K, Ca, and Na (cpfu), (e) EPMA profile b for elements Ba and Sr ( $\mu\text{g/g}$ ).

LE-67b V-3, plagioclase

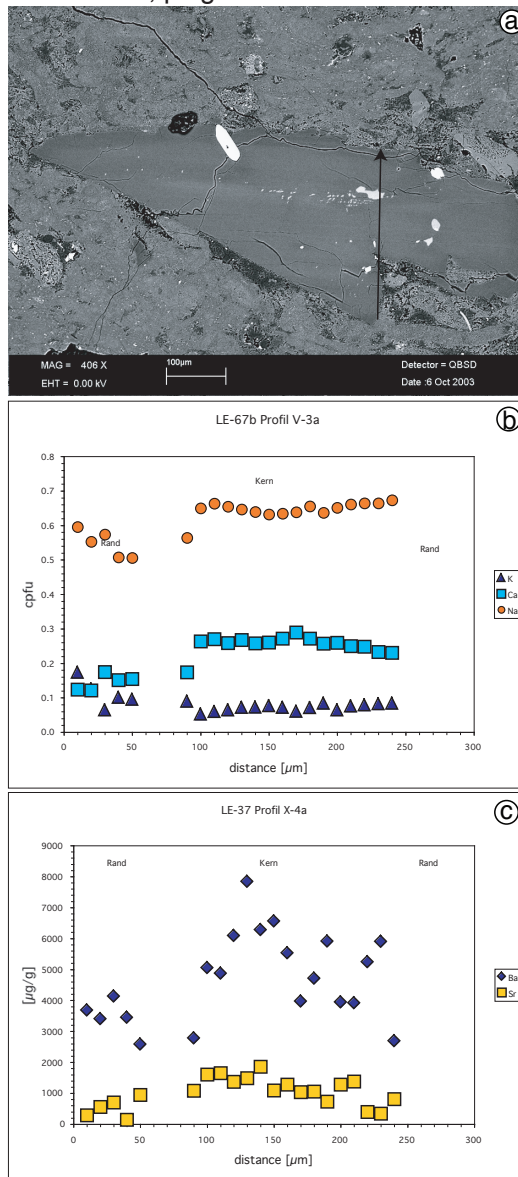


**Fig. B.36.** Sample LE-67b V-3, plagioclase, (a) BSE image, arrow indicates location of EPMA profile, (b) EPMA profile for elements K, Ca, and Na (cpfu), (c) EPMA profile for elements Ba and Sr ( $\mu\text{g/g}$ ).

For LE-67 IV-2 see page 242.

## B. Element concentration profiles

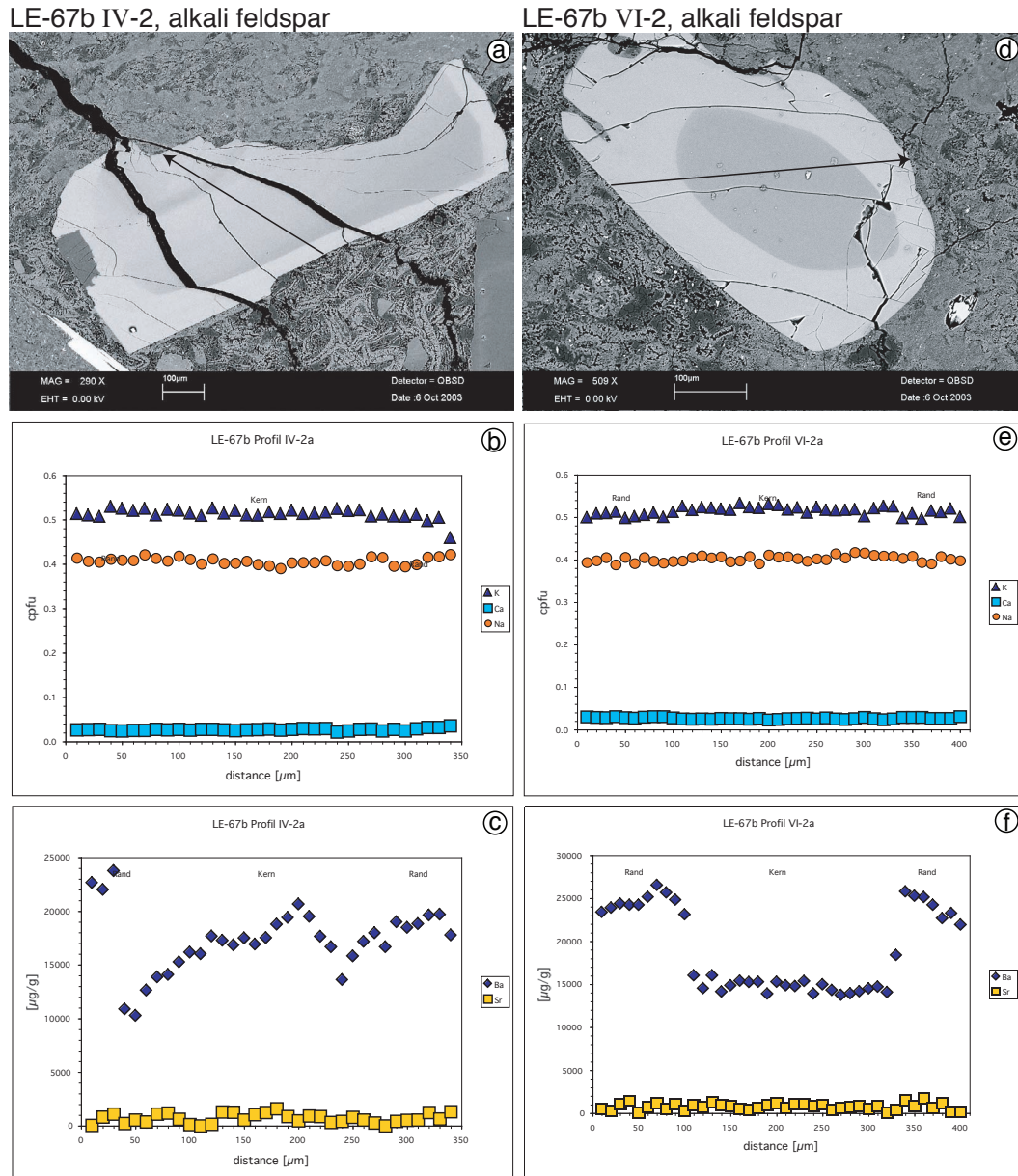


**Fig. B.37.** Sample LE-67b (a) IV-2, alkali feldspar, BSE image, arrow indicates location of EPMA profile, (b) IV-2, alkali feldspar, EPMA profile for elements K, Ca, and Na (cpfu), (c) IV-2, alkali feldspar, EPMA profile for elements Ba and Sr ( $\mu\text{g/g}$ ), (d) VI-2, alkali feldspar, BSE image, arrow indicates location of EPMA profile, (e) VI-2, alkali feldspar, EPMA profile for elements K, Ca, and Na (cpfu), (f) VI-2, alkali feldspar, EPMA profile for elements Ba and Sr ( $\mu\text{g/g}$ ).

LE-67b VI-3, plagioclase

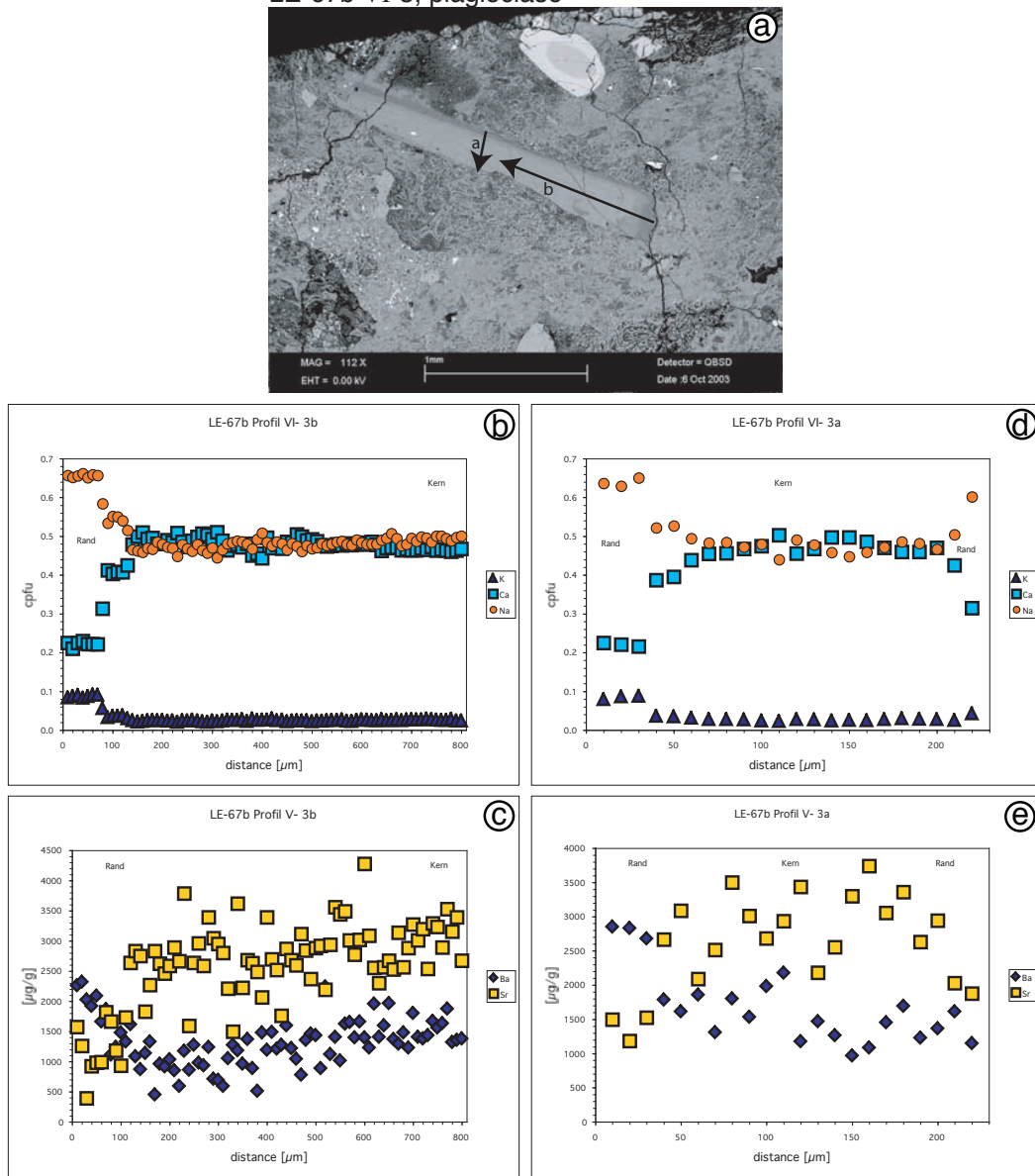


**Fig. B.38.** Sample LE-67b VI-3, plagioclase, (a) BSE image, arrow indicates location of EPMA profiles a and b, (b) EPMA profile b for elements K, Ca, and Na (cpfu), (c) EPMA profile b for elements Ba and Sr ( $\mu\text{g/g}$ ), (d) EPMA profile a for elements K, Ca, and Na (cpfu), (e) EPMA profile a for elements Ba and Sr ( $\mu\text{g/g}$ ).

## B. Element concentration profiles

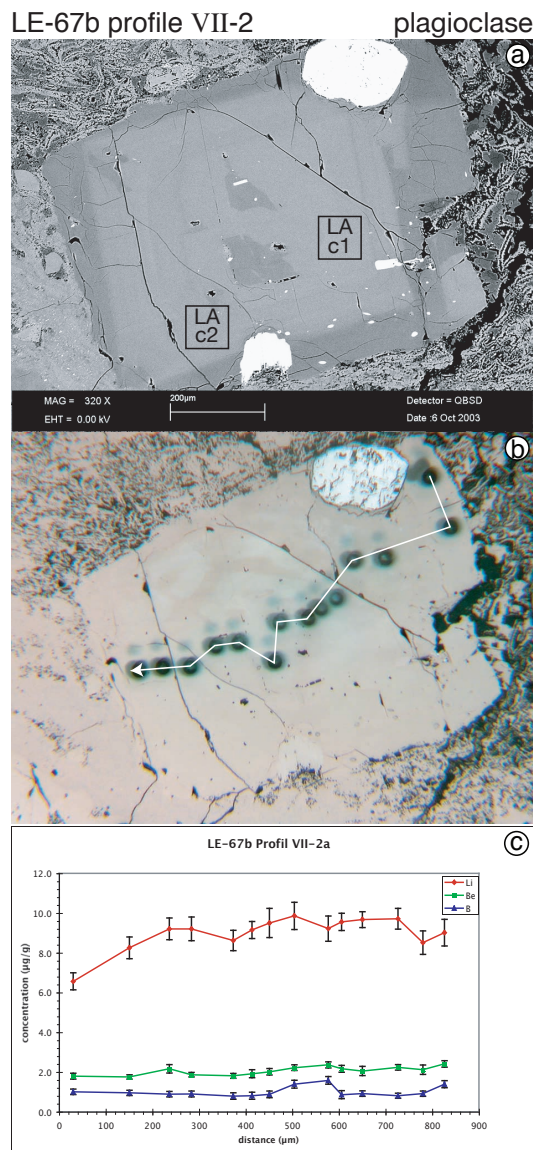
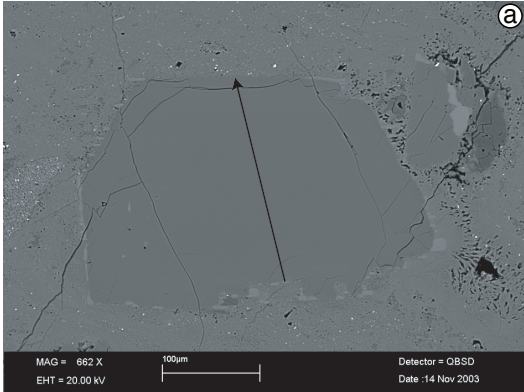


**Fig. B.39.** Sample LE-67b VII-2, plagioclase, (a) BSE image, square indicate LA-ICP-MS analytical spot (Sr isotopic analysis), (b) reflected light image of gold coated sample after SIMS analysis, analytical spots appear black on gold coating, arrow indicates direction of SIMS profile, (c) SIMS profile for elements Li, Be, B ( $\mu\text{g/g}$ ).

LE-66b II-2, plagioclase



LE-66b III-1, plagioclase

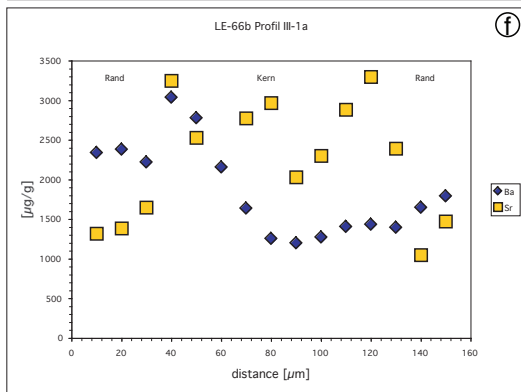
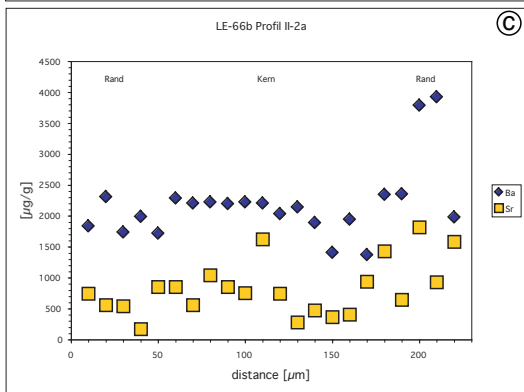
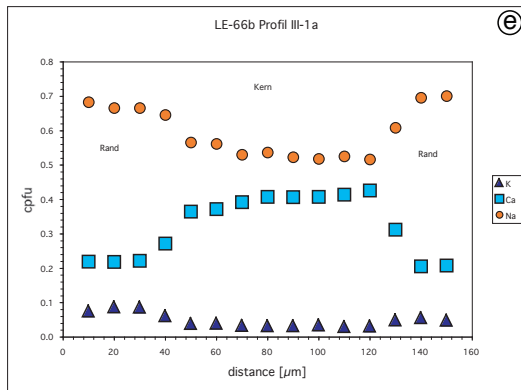
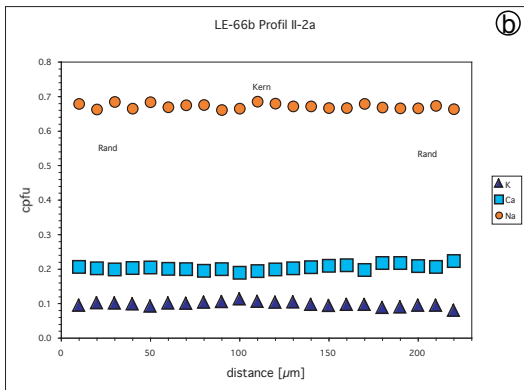
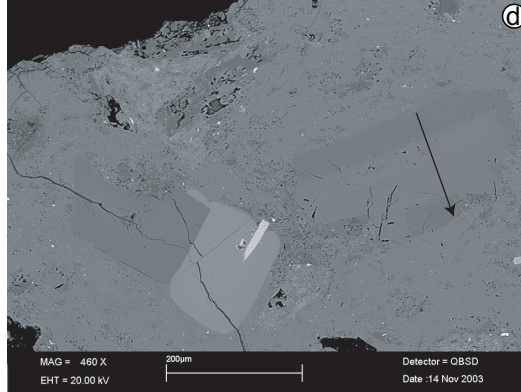


**Fig. B.40.** Sample LE-66b (a) II-2, plagioclase, BSE image, arrow indicates location of EPMA profile, (b) II-2, plagioclase, EPMA profile for elements K, Ca, and Na (cpfu), (c) II-2, plagioclase, EPMA profile for elements Ba and Sr ( $\mu\text{g/g}$ ), (d) III-1, plagioclase, BSE image, arrow indicates location of EPMA profile, (e) III-1, plagioclase, EPMA profile for elements K, Ca, and Na (cpfu), (f) III-1, plagioclase, EPMA profile for elements Ba and Sr ( $\mu\text{g/g}$ ).

## B. Element concentration profiles

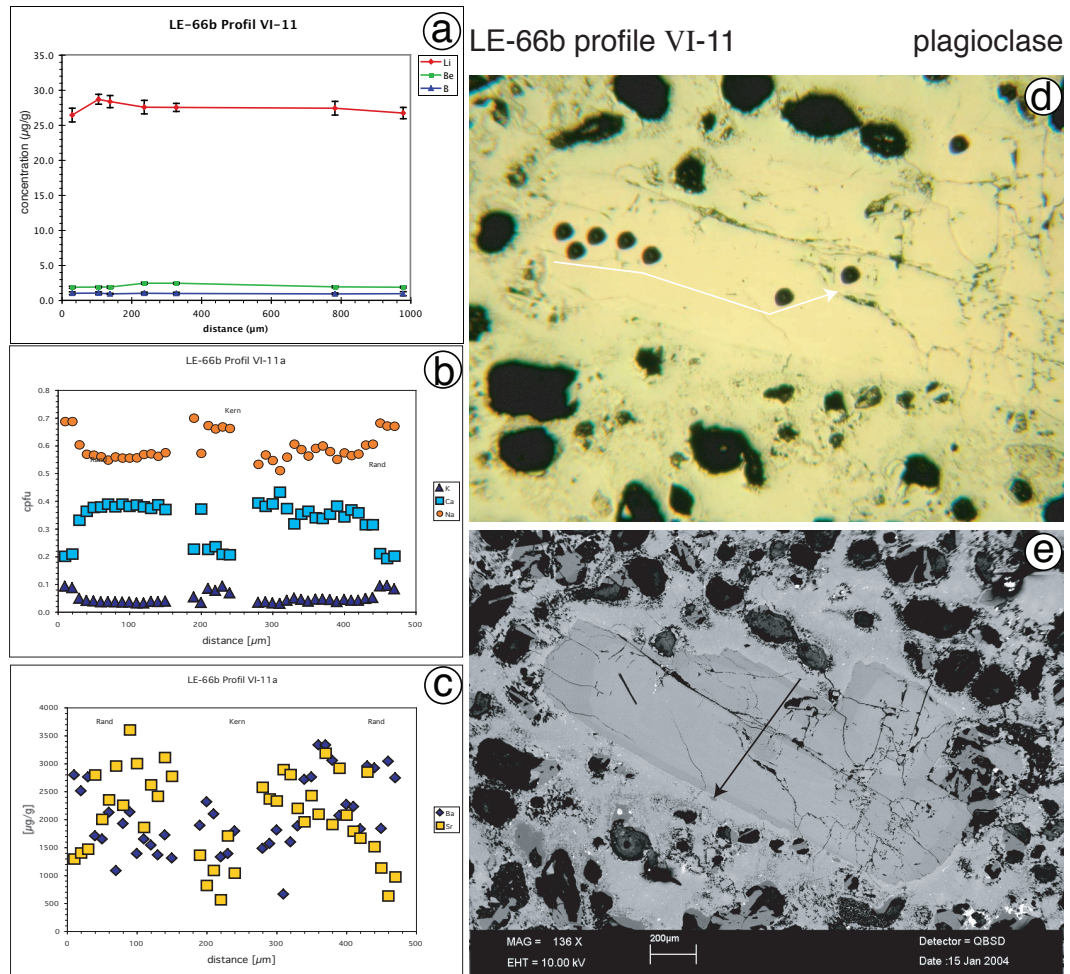


**Fig. B.41.** Sample LE-66b VI-11, plagioclase, (a) SIMS profile for elements Li, Be, B ( $\mu\text{g/g}$ ), (b) EPMA profile for elements K, Ca, and Na (cpfu), (c) EPMA profile for elements Ba and Sr ( $\mu\text{g/g}$ ), (d) reflected light image of gold coated sample after SIMS analysis, analytical spots appear black on gold coating, arrow indicates direction of SIMS profile, (e) BSE image, arrow indicates location of EPMA profile.

LE-66b VI-32, plagioclase

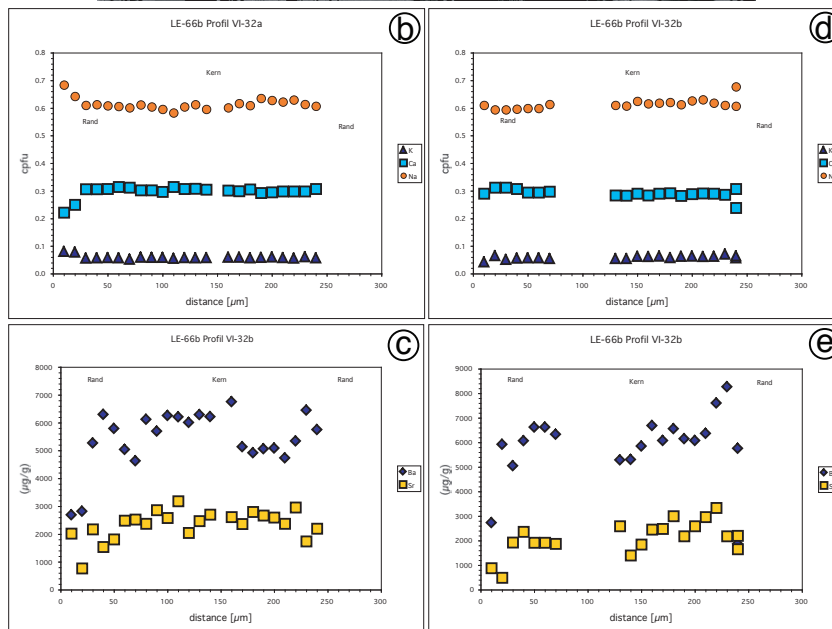
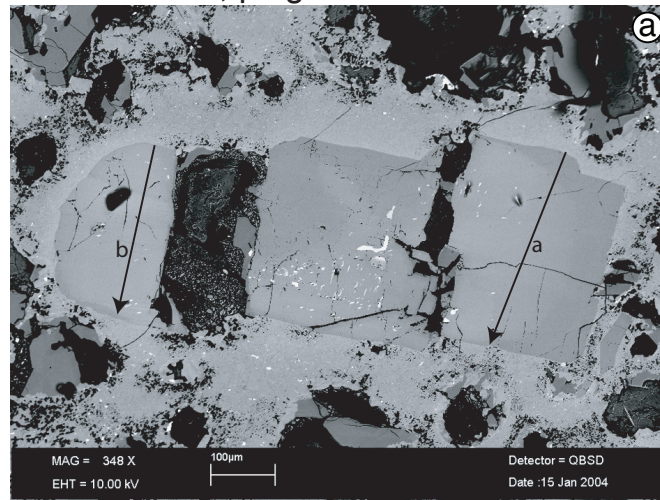


**Fig. B.42.** Sample LE-66b VI-32, plagioclase, (a) BSE image, arrows indicate location of EPMA profiles a and b, (b) EPMA profile a for elements K, Ca, and Na (cpfu), (c) EPMA profile a for elements Ba and Sr ( $\mu\text{g/g}$ ), (d) EPMA profile b for elements K, Ca, and Na (cpfu), (e) EPMA profile b for elements Ba and Sr ( $\mu\text{g/g}$ ).

## B. Element concentration profiles

LE-66b VII-22, plagioclase

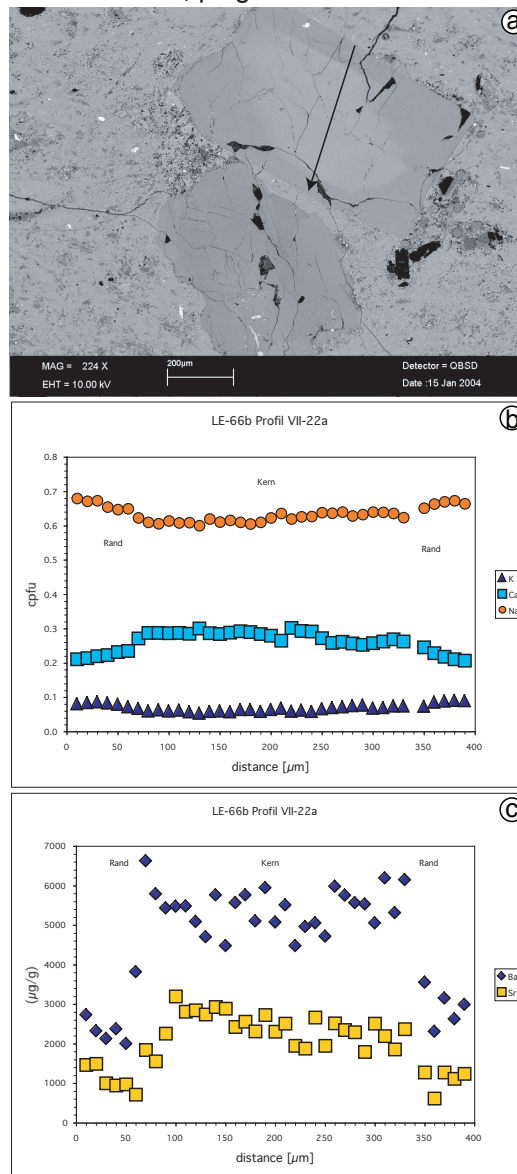
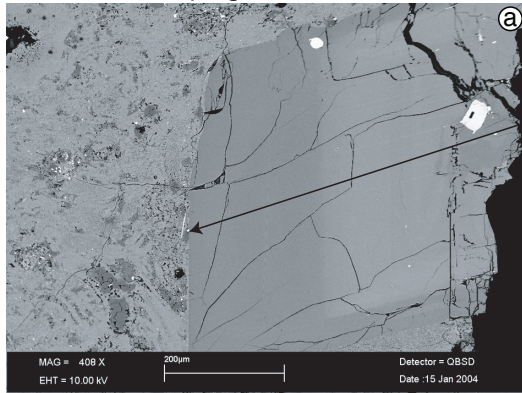


**Fig. B.43.** Sample LE-66b VII-22, plagioclase, (a) BSE image, arrow indicates location of EPMA profile, (b) EPMA profile for elements K, Ca, and Na (cpfu), (c) EPMA profile for elements Ba and Sr ( $\mu\text{g/g}$ ).

LE-66b VIII-1, plagioclase



LE-66b VIII-3, alkali feldspar, plagioclase

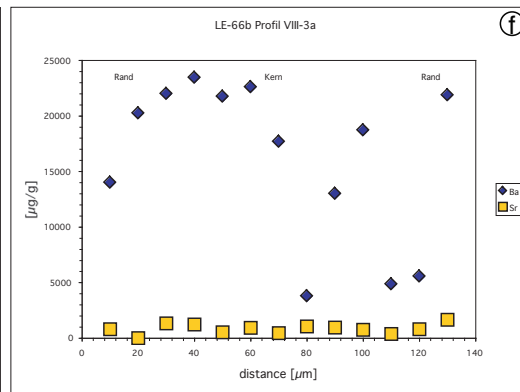
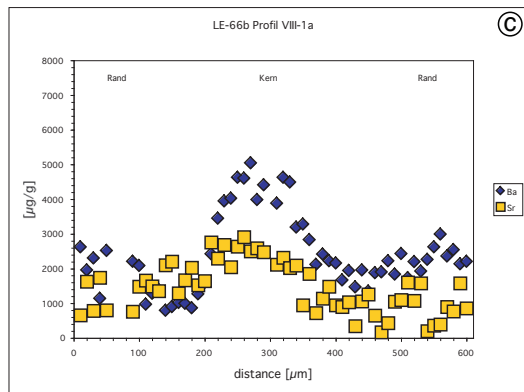
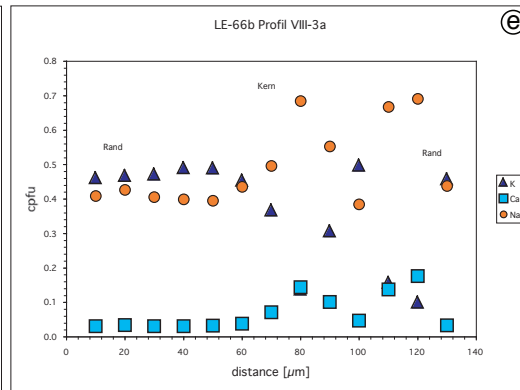
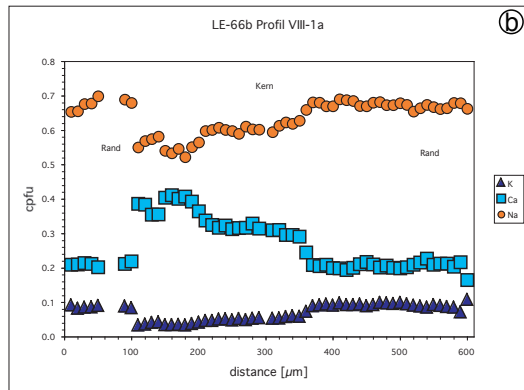
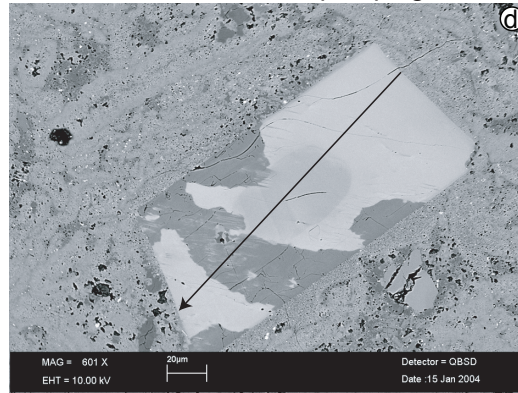


**Fig. B.44.** Sample LE-66b (a) VIII-1, plagioclase, BSE image, arrow indicates location of EPMA profile, (b) VIII-1, plagioclase, EPMA profile for elements K, Ca, and Na (cpfu), (c) VIII-1, plagioclase, EPMA profile for elements Ba and Sr ( $\mu\text{g/g}$ ), (d) VIII-3, alkali feldspar and plagioclase, BSE image, arrow indicates location of EPMA profile, (e) VIII-3, alkali feldspar and plagioclase, EPMA profile for elements K, Ca, and Na (cpfu), (f) VIII-3, alkali feldspar and plagioclase, EPMA profile for elements Ba and Sr ( $\mu\text{g/g}$ ).

B. Element concentration profiles

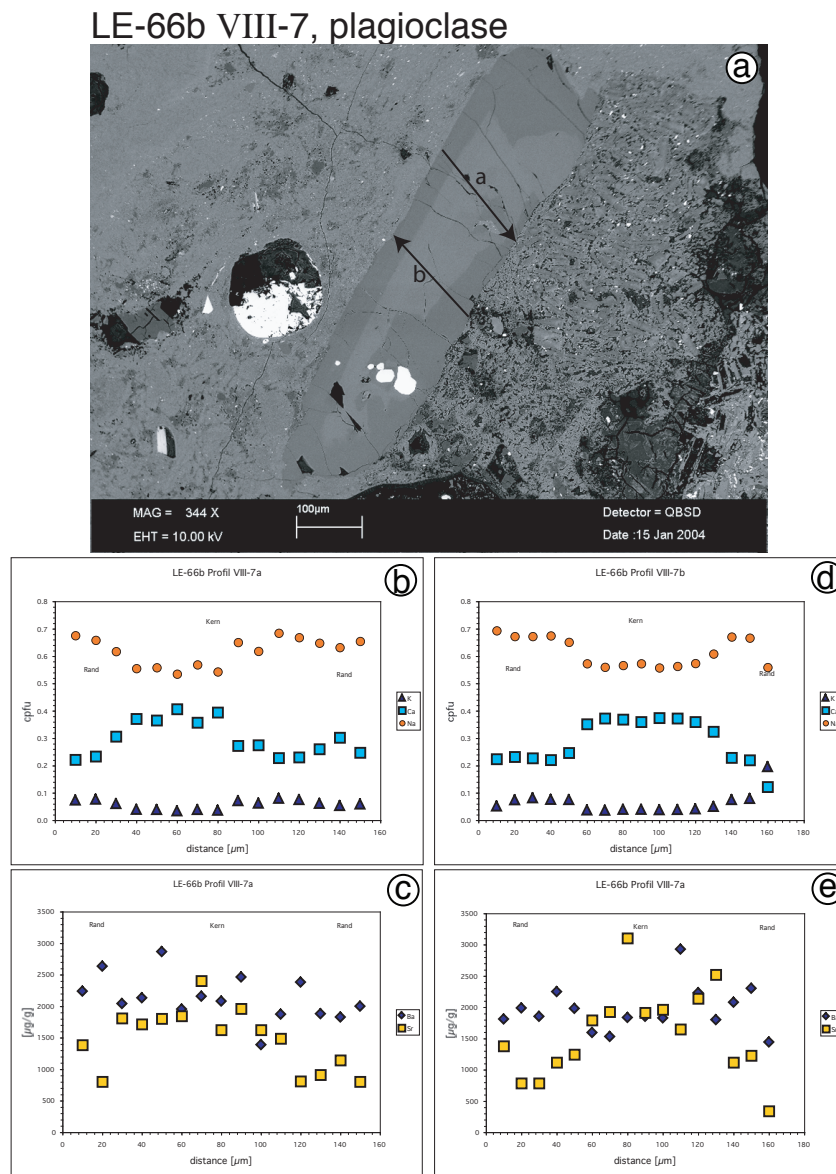


**Fig. B.45.** Sample LE-66b VIII-7, plagioclase, (a) BSE image, arrow indicates location of EPMA profiles a and b, (b) EPMA profile a for elements K, Ca, and Na (cpfu), (c) EPMA profile a for elements Ba and Sr ( $\mu\text{g/g}$ ), (d) EPMA profile b for elements K, Ca, and Na (cpfu), (e) EPMA profile b for elements Ba and Sr ( $\mu\text{g/g}$ ).

LE-68b profile II-1, plagioclase

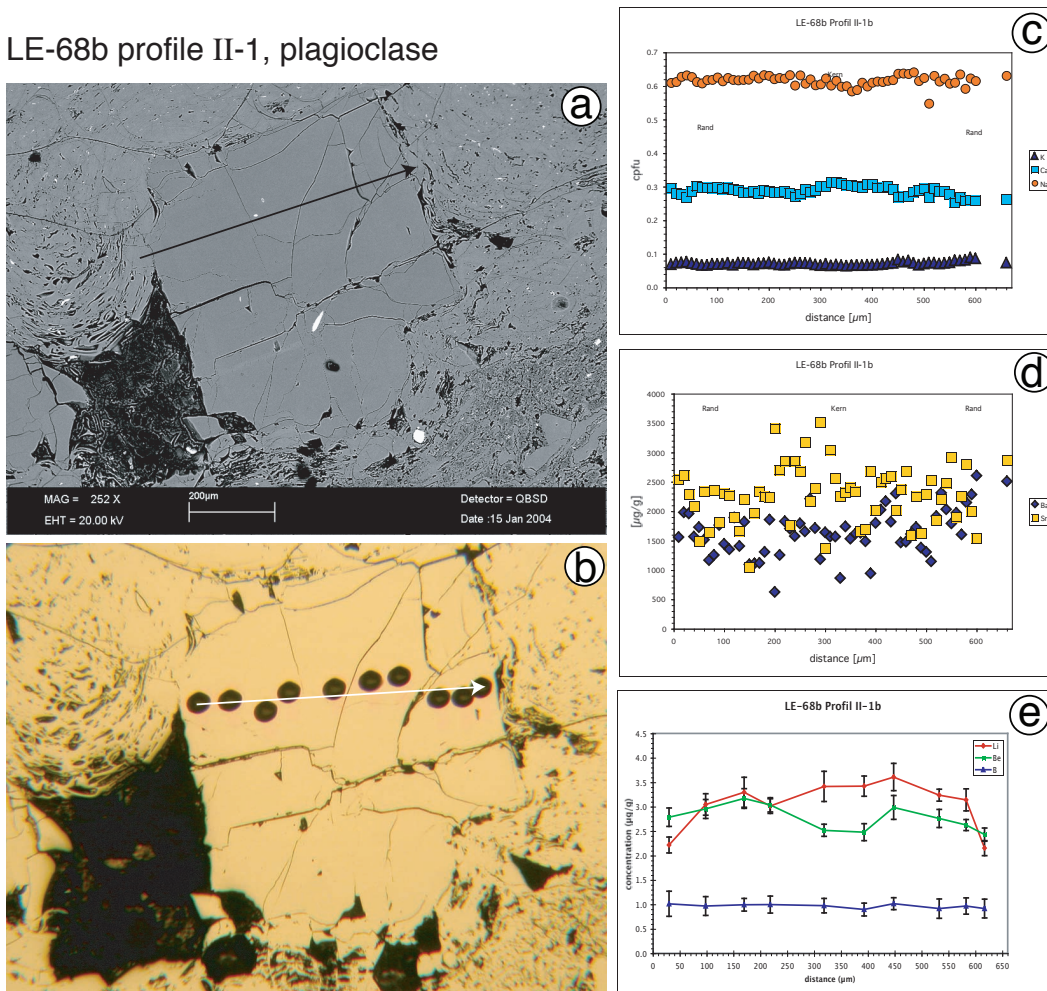


**Fig. B.46.** Sample LE-68b II-1, plagioclase, (a) BSE image, arrow indicates location of EPMA profile, (b) reflected light image of gold coated sample after SIMS analysis, analytical spots appear black on gold coating, arrow indicates direction of SIMS profile, (c) EPMA profile for elements K, Ca, and Na (cpfu), (d) EPMA profile for elements Ba and Sr ( $\mu\text{g/g}$ ), (e) SIMS profile for elements Li, Be, B ( $\mu\text{g/g}$ ).

## B. Element concentration profiles

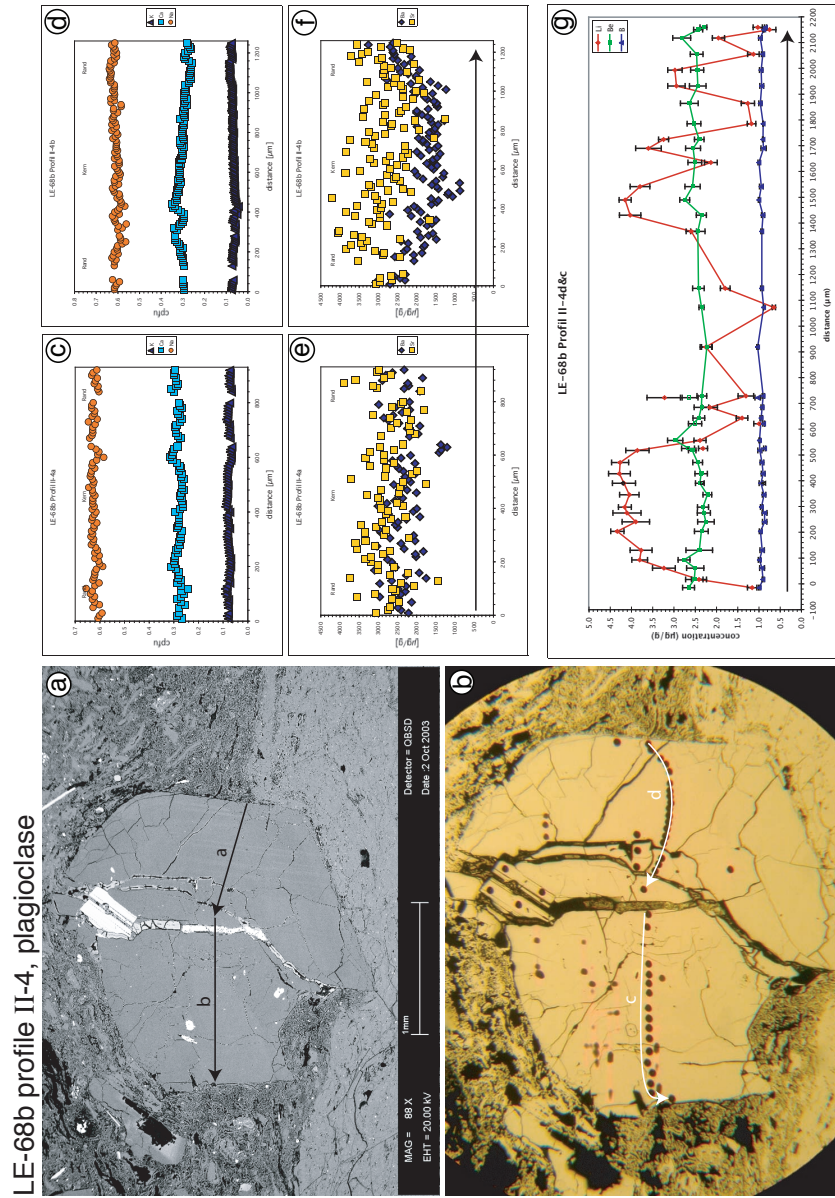


**Fig. B.47.** Sample LE-68b II-4, plagioclase. (a) BSE image, arrow indicates location of EPMA profiles a and b, (b) reflected light image of gold coated sample after SIMS analysis, analytical spots appear black on gold coating, arrow indicates direction of SIMS profile, (c) EPMA profile a for elements K, Ca, and Na (cpfu), (d) EPMA profile b for elements Ba and Sr ( $\mu\text{g/g}$ ), (e) EPMA profile a for elements Ba and Sr ( $\mu\text{g/g}$ ), (f) EPMA profile b for elements Ba and Sr ( $\mu\text{g/g}$ ), (g) SIMS profile for elements Li, Be, B ( $\mu\text{g/g}$ ).

LE-69b profile I-3, plagioclase

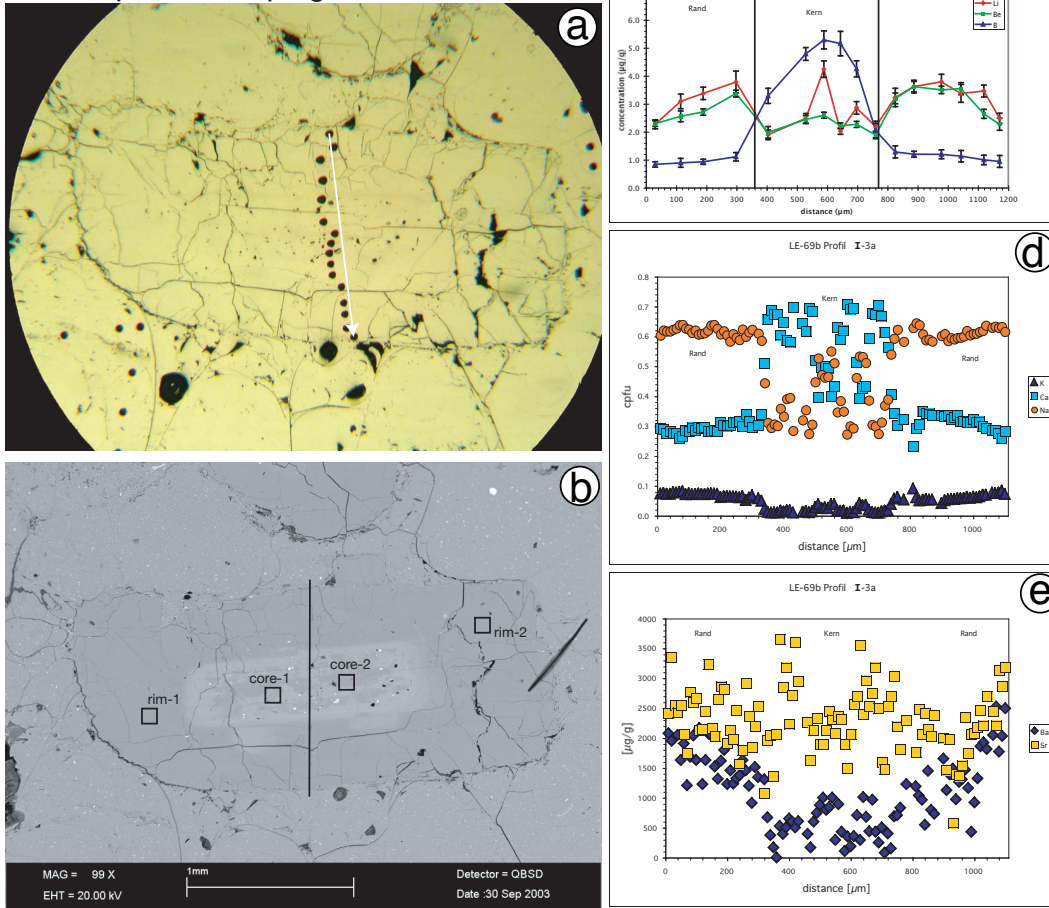


**Fig. B.48.** Sample LE-69b I-3, plagioclase, (a) reflected light image of gold coated sample after SIMS analysis, analytical spots appear black on gold coating, arrow indicates direction of SIMS profile, (b) BSE image, arrow indicates location of EPMA profile, squares indicate locations of LA-ICM-PS analysis (Sr isotopes), (c) SIMS profile for elements Li, Be, B ( $\mu\text{g/g}$ ), (d) EPMA profile for elements K, Ca, and Na (cpfu), (e) EPMA profile for elements Ba and Sr ( $\mu\text{g/g}$ ).

B. Element concentration profiles

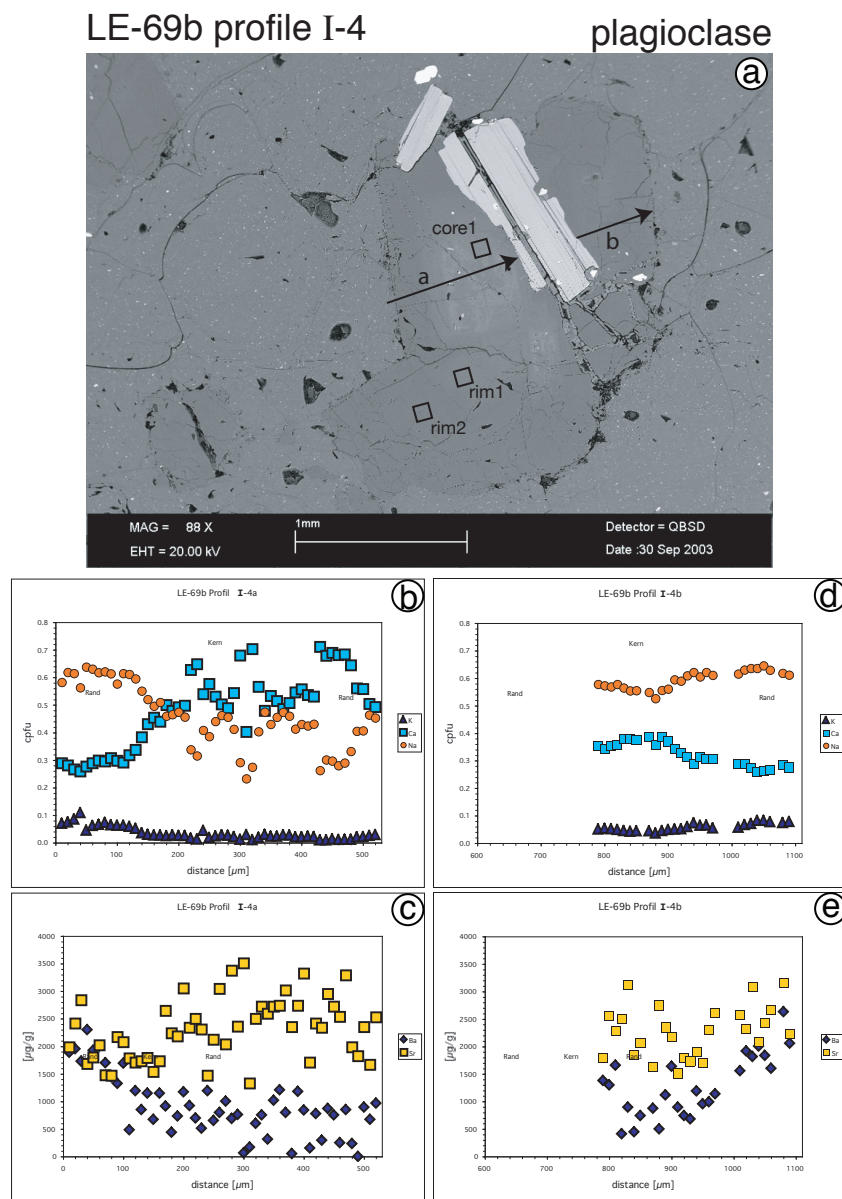


**Fig. B.49.** Sample LE-69b I-4, plagioclase, (a) BSE image, arrow indicates location of EPMA profiles a and b, squares indicate locations of LA-ICM-PS analysis for Sr isotopes, (b) EPMA profile a for elements K, Ca, and Na (cpfu), (c) EPMA profile a for elements Ba and Sr ( $\mu\text{g/g}$ ), (d) EPMA profile b for elements K, Ca, and Na (cpfu), (e) EPMA profile b for elements Ba and Sr ( $\mu\text{g/g}$ ).

LE-69b III-2a&b, plagioclase

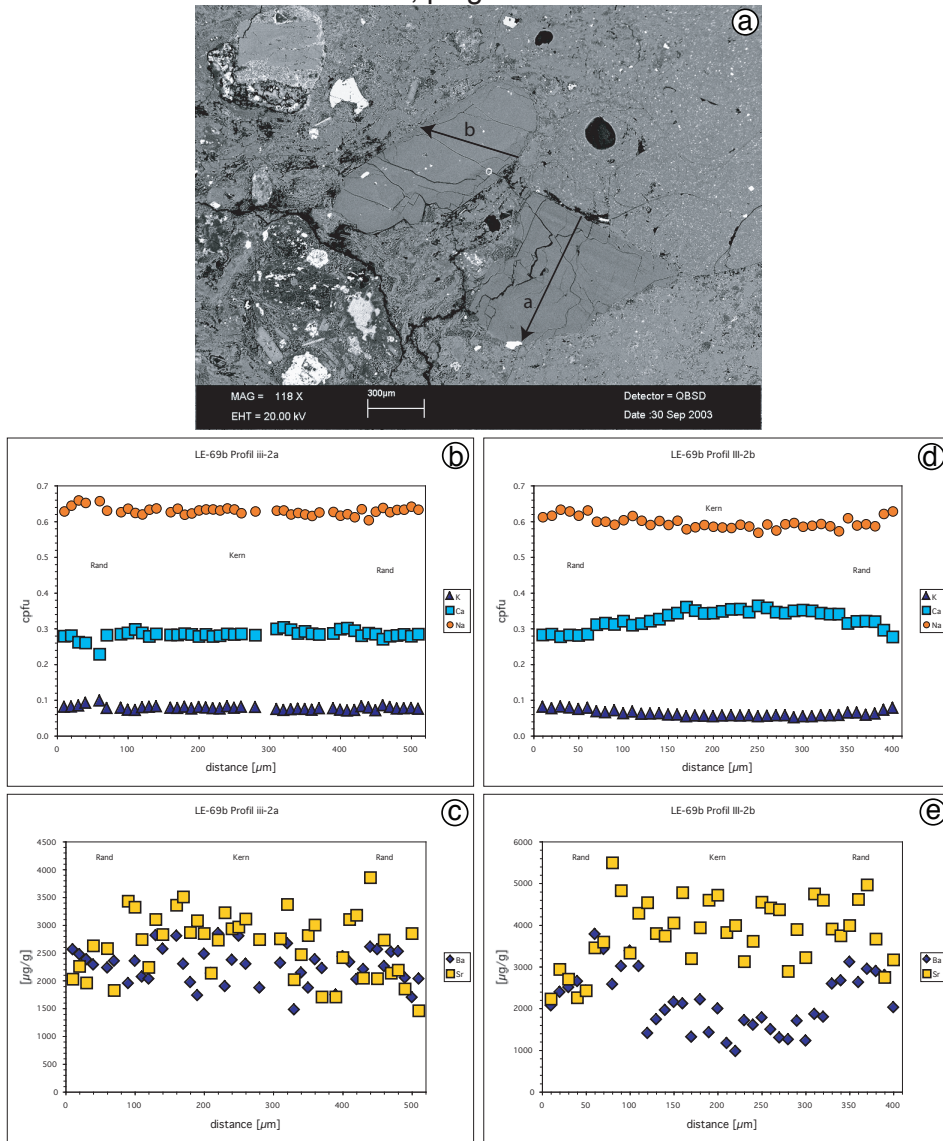


**Fig. B.50.** Sample LE-69b III-2, plagioclase, (a) BSE image, arrow indicates location of EPMA profiles a and b, (b) EPMA profile a for elements K, Ca, and Na (cpfu), (c) EPMA profile a for elements Ba and Sr ( $\mu\text{g/g}$ ), (d) EPMA profile b for elements K, Ca, and Na (cpfu), (e) EPMA profile b for elements Ba and Sr ( $\mu\text{g/g}$ ).

## B. Element concentration profiles

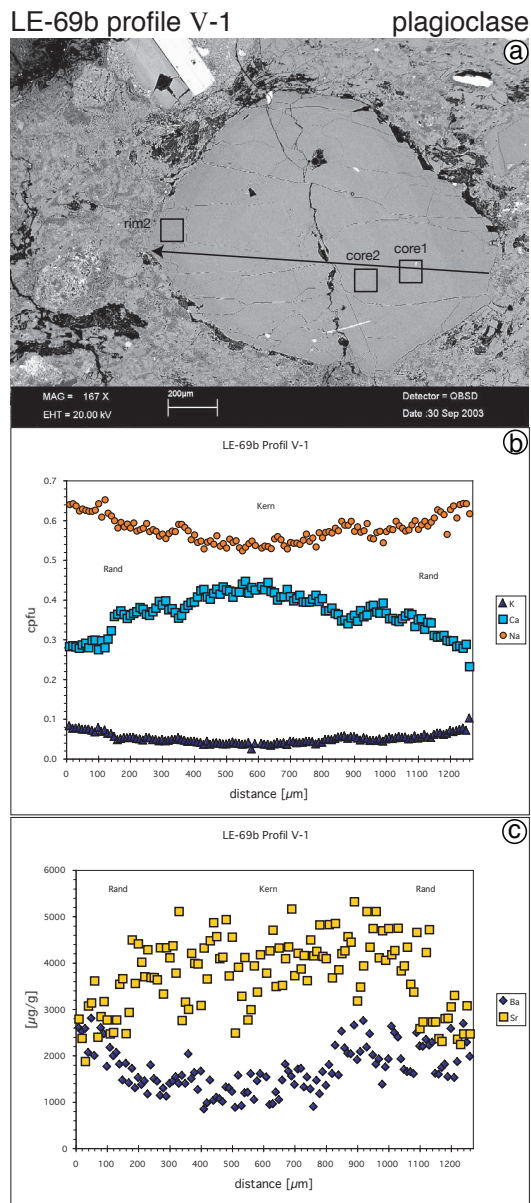
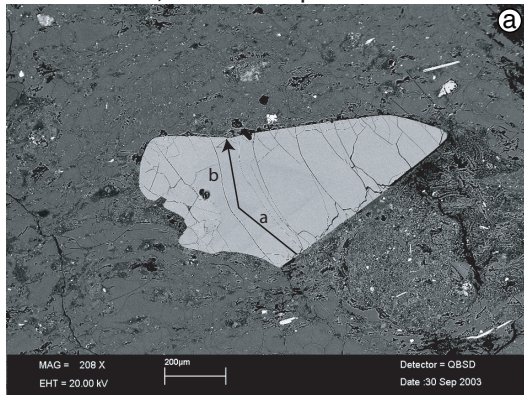


**Fig. B.51.** Sample LE-69b V-1, plagioclase, (a) BSE image, arrow indicates location of EPMA profile, squares indicate locations of Sr isotope analysis (LA-ICP-MS), (b) EPMA profile for elements K, Ca, and Na (cpfu), (c) EPMA profile for elements Ba and Sr ( $\mu\text{g/g}$ ).

LE-69b VI-1, alkali feldspar



LE-69b VII-2, plagioclase

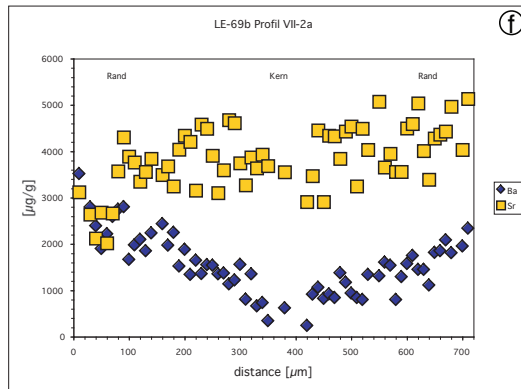
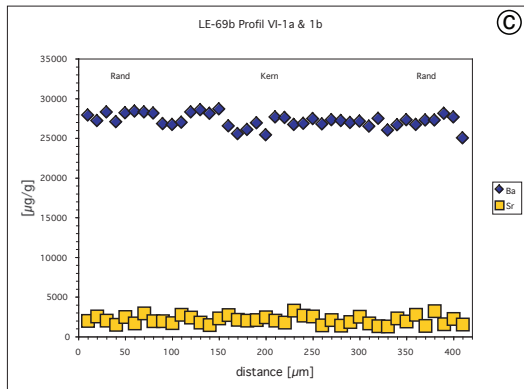
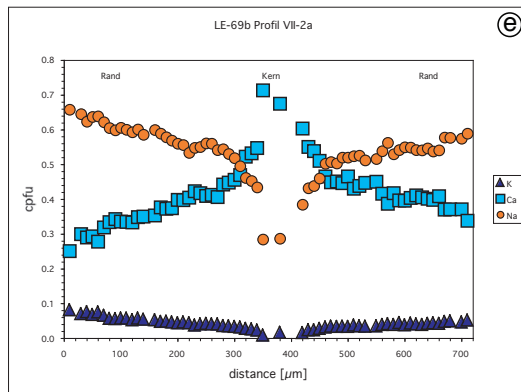
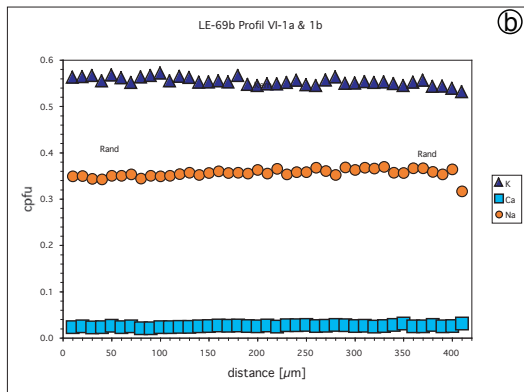
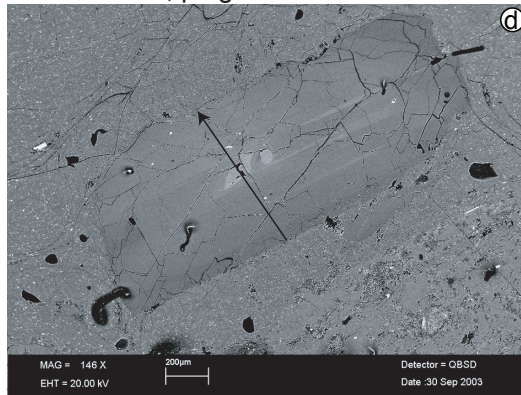


**Fig. B.52.** Sample LE-69b (a) VI-1, alkali feldspar, BSE image, arrow indicates location of EPMA profile, (b) VI-1, alkali feldspar, EPMA profile for elements K, Ca, and Na (cpfu), (c) VI-1, alkali feldspar, EPMA profile for elements Ba and Sr ( $\mu\text{g/g}$ ), (d) VII-2, plagioclase, BSE image, arrow indicates location of EPMA profile, (e) VII-2, plagioclase, EPMA profile for elements K, Ca, and Na (cpfu), (f) VII-2, plagioclase, EPMA profile for elements Ba and Sr ( $\mu\text{g/g}$ ).

## B. Element concentration profiles

LE-70b II-2, plagioclase

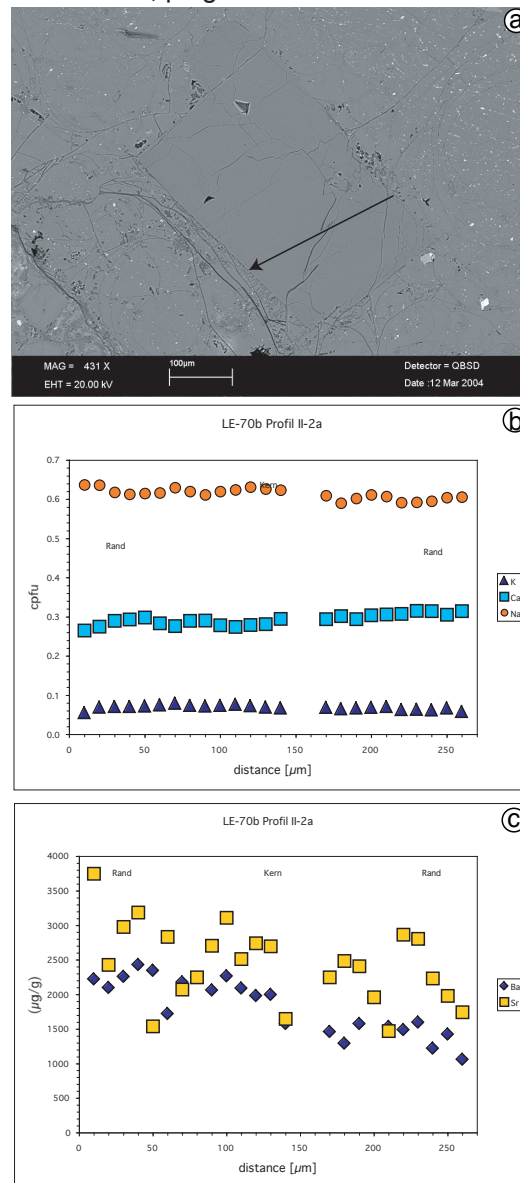


**Fig. B.53.** Sample LE-70b II-2, plagioclase, (a) BSE image, arrow indicates location of EPMA profile, (b) EPMA profile for elements K, Ca, and Na (cpfu), (c) EPMA profile for elements Ba and Sr ( $\mu\text{g/g}$ ).

LE-70b profile II-7, plagioclase

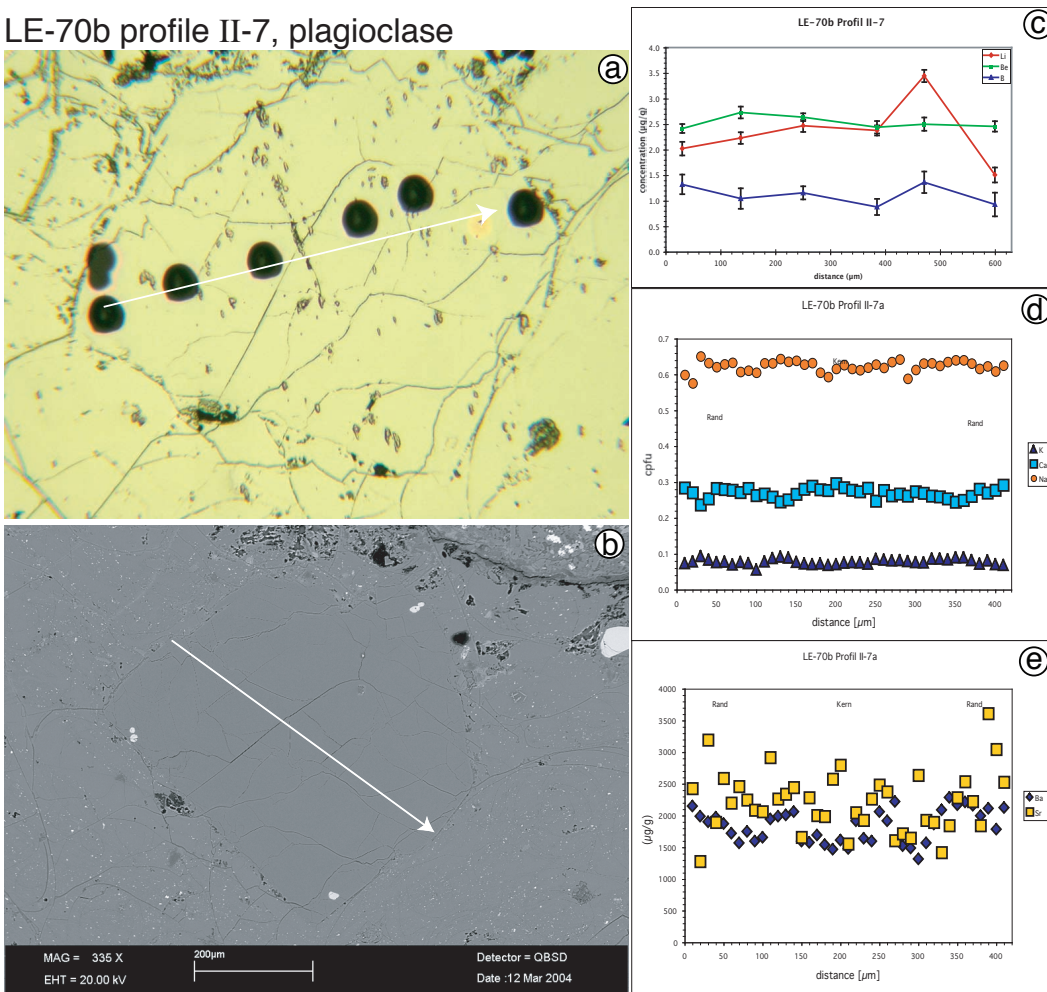


**Fig. B.54.** Sample LE-70b II-7, plagioclase, (a) reflected light image of gold coated sample after SIMS analysis, analytical spots appear black on gold coating, arrow indicates direction of SIMS profile, (b) BSE image, arrow indicated location of EMPA profile, (c) SIMS profile for elements Li, Be, B ( $\mu\text{g/g}$ ), (d) EPMA profile for elements K, Ca, and Na (cpfu), (e) EPMA profile for elements Ba and Sr ( $\mu\text{g/g}$ ).

## B. Element concentration profiles

LE-70b profile III-1, biotite

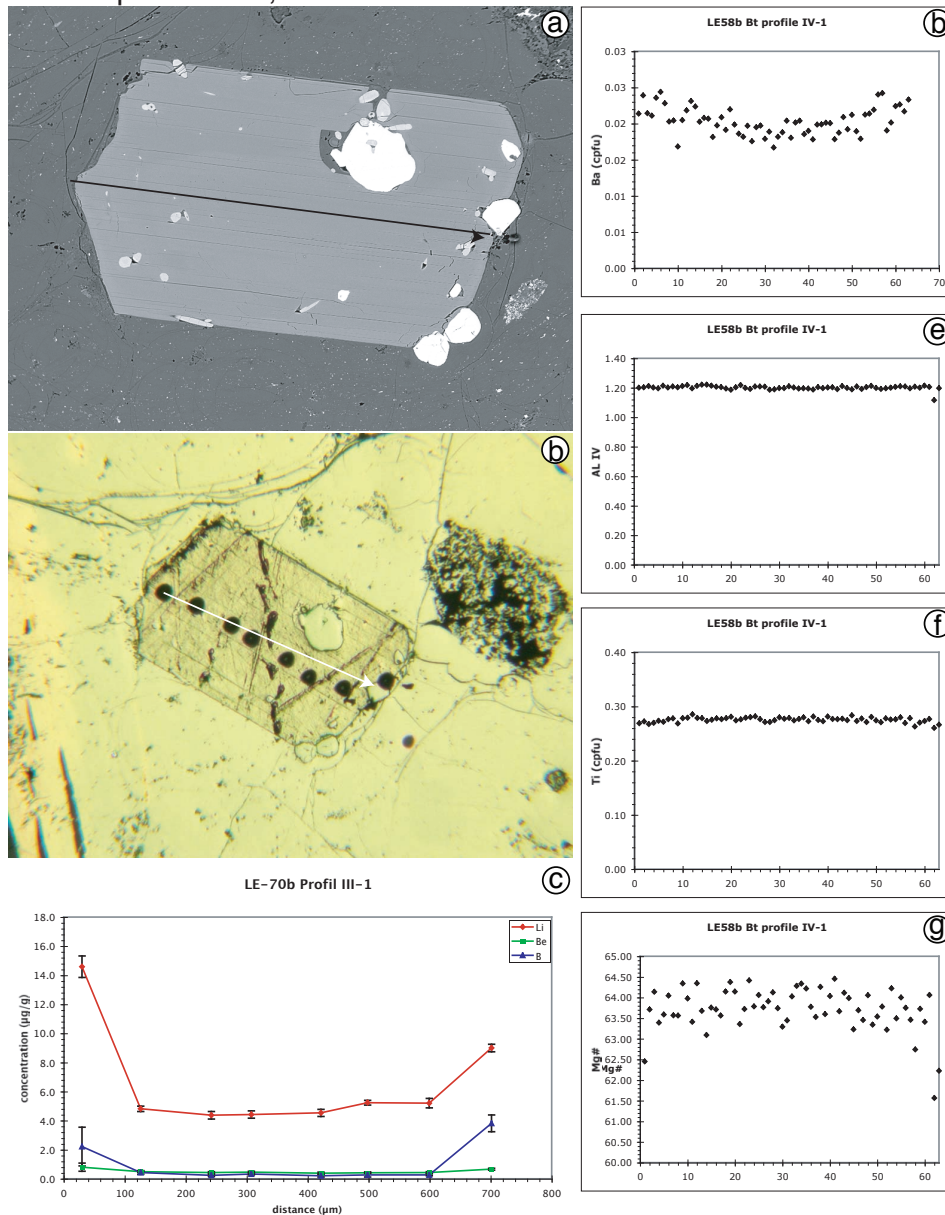


**Fig. B.55.** Sample LE-70b III-1, biotite, (a) BSE image, EPMA profile (black arrow), (b) reflected light image of gold coated sample, SIMS analytical spots appear black on gold coating, (c) SIMS profile for elements Li, Be, and B, (d) EPMA profile for Ba (cpfu), (e) EPMA profile for Al<sup>IV</sup>, (f) EPMA profile for Ti (cpfu), (g) EPMA profile for Mg#.

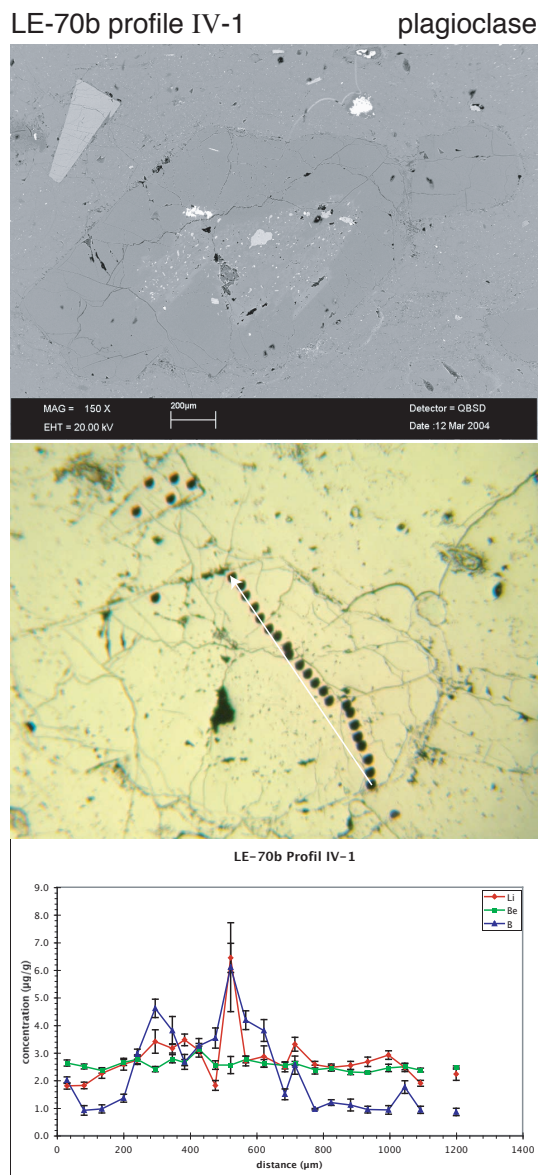


**Fig. B.56.** Sample LE-70b IV-1, plagioclase, (a) BSE image, (b) reflected light image of gold coated sample, SIMS analytical spots appear black on gold coating, (c) SIMS profile for elements Li, Be, B ( $\mu\text{g/g}$ ).

## B. Element concentration profiles

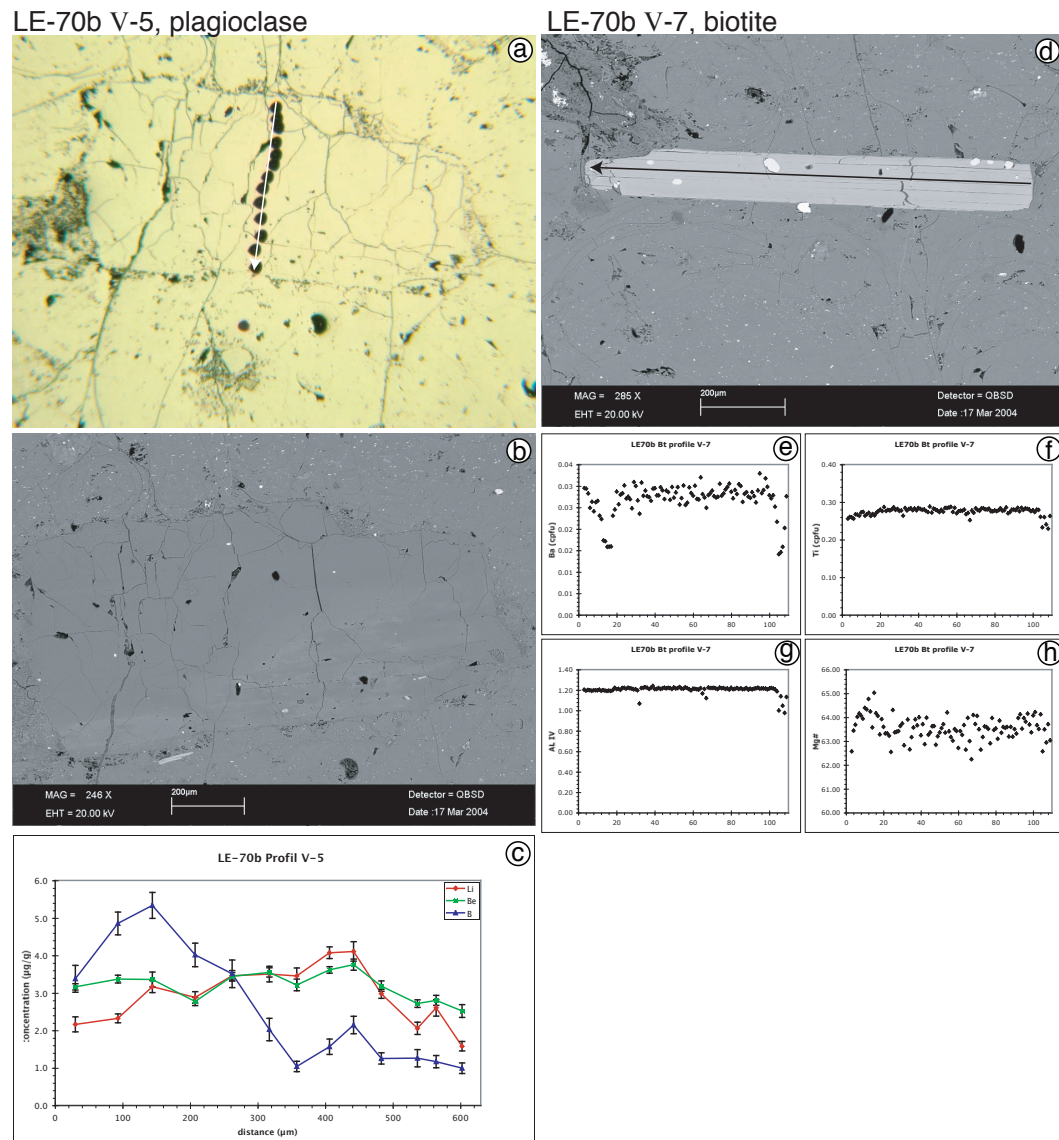


**Fig. B.57.** Sample LE-70b (a) V-5, plagioclase, reflected light image of gold coated sample after SIMS analysis, analytical spots appear black on gold coating, arrow indicates direction of SIMS profile, (b) V-5, plagioclase, BSE image, (c) V-5, plagioclase, SIMS profile for elements Li, Be, B ( $\mu\text{g/g}$ ) (d) V-7, biotite, BSE image, arrow indicated location of EMP profile, (e) V-7, biotite, EMP profile Ba(cpfu), (f) V-7, biotite, EMP profile Ti (cpfu), (g) V-7, biotite, EMP profile  $\text{Al}^{\text{IV}}$ (cpfu), (h) V-7, biotite, EMP profile Mg# .

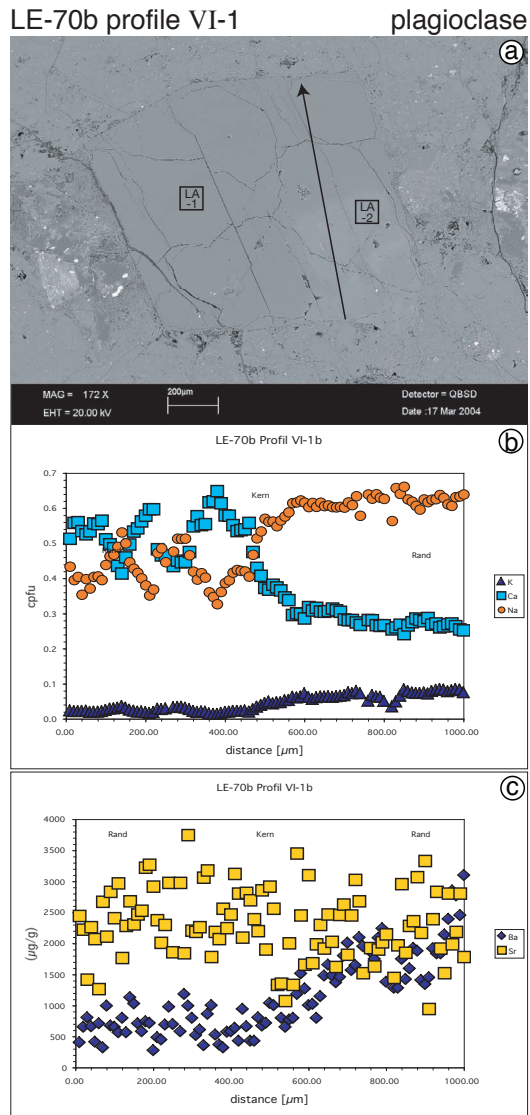


**Fig. B.58.** Sample LE-70b VI-1, plagioclase, (a) BSE image, EPMA profile (black arrow), squares mark locations of laser-ablation analyses (Sr isotopes) (b) EPMA profile a for elements K, Ca, and Na (cpfu), (c) EPMA profile a for elements Ba and Sr ( $\mu\text{g/g}$ ).

B. Element concentration profiles

LE-70b VI-8, plagioclase

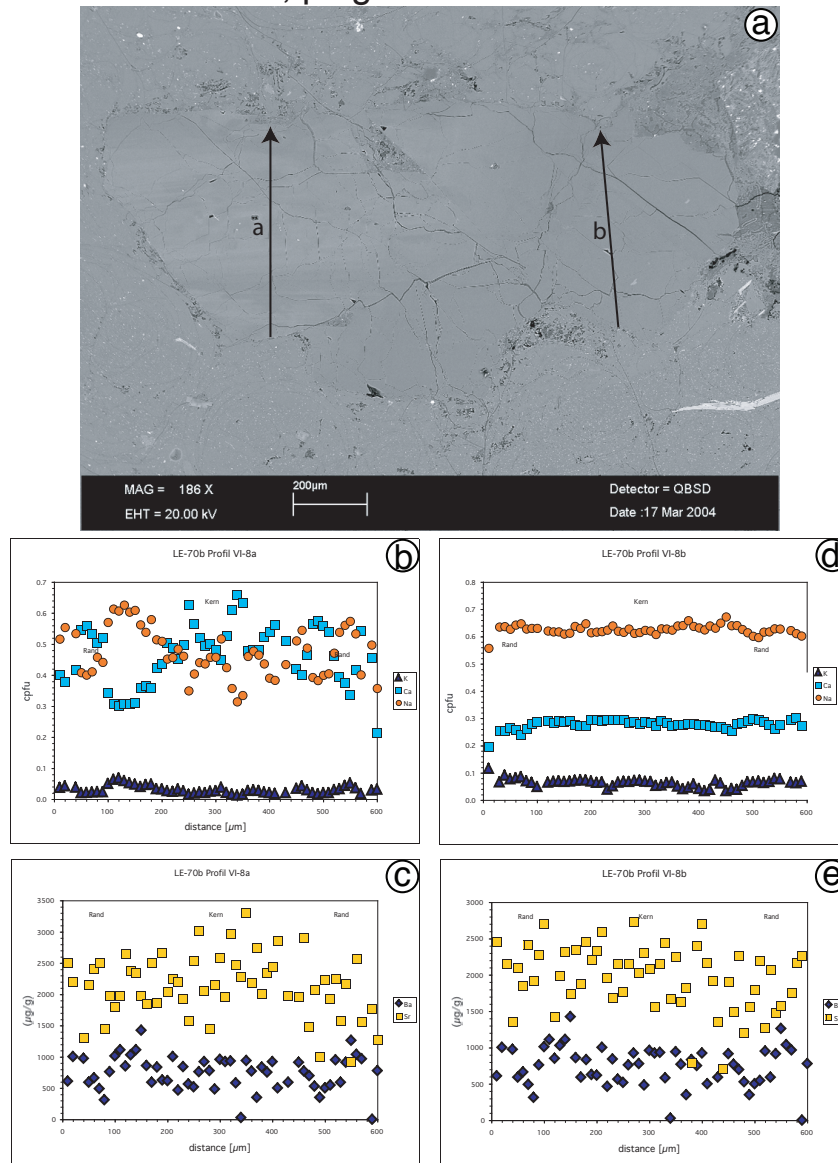


**Fig. B.59.** Sample LE-70b VI-8, plagioclase, (a) BSE image, arrows indicate locations of EPMA profiles a and b, (b) EPMA profile a for elements K, Ca, and Na (cpfu), (c) EPMA profile a for elements Ba and Sr ( $\mu\text{g/g}$ ), (d) EPMA profile b for elements K, Ca, and Na (cpfu), (e) EPMA profile b for elements Ba and Sr ( $\mu\text{g/g}$ ).

LE-71b VI-22, plagioclase

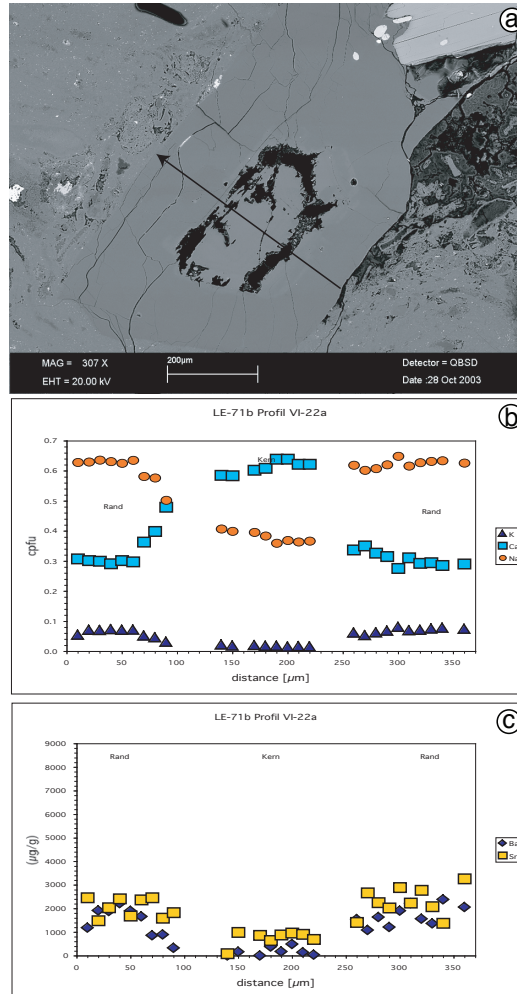


**Fig. B.60.** Sample LE-71b VI-22, plagioclase, (a) BSE image, arrows indicate location of EPMA profile, (b) EPMA profile a for elements K, Ca, and Na (cpfu), (c) EPMA profile a for elements Ba and Sr ( $\mu\text{g/g}$ ).

B. Element concentration profiles

LE-71b profile VI-24, plagioclase

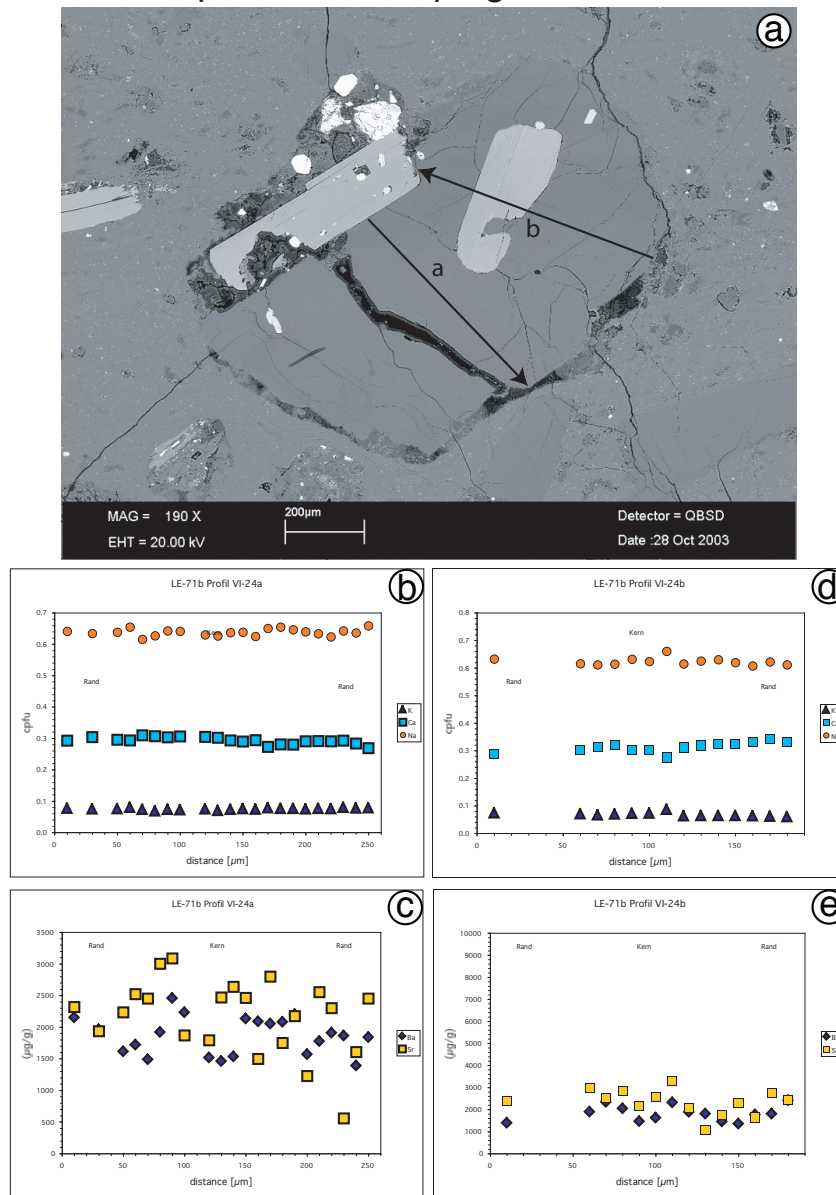


**Fig. B.61.** Sample LE-71b VI-24, plagioclase, (a) BSE image, arrows indicate location of EPMA profiles a and b, (b) EPMA profile a for elements K, Ca, and Na (cpfu), (c) EPMA profile a for elements Ba and Sr ( $\mu\text{g/g}$ ), (d) EPMA profile b for elements K, Ca, and Na (cpfu), (e) EPMA profile b for elements Ba and Sr ( $\mu\text{g/g}$ ).

LE-71b profile VII-13, plagioclase

LE-71b profile VII-21, plagioclase

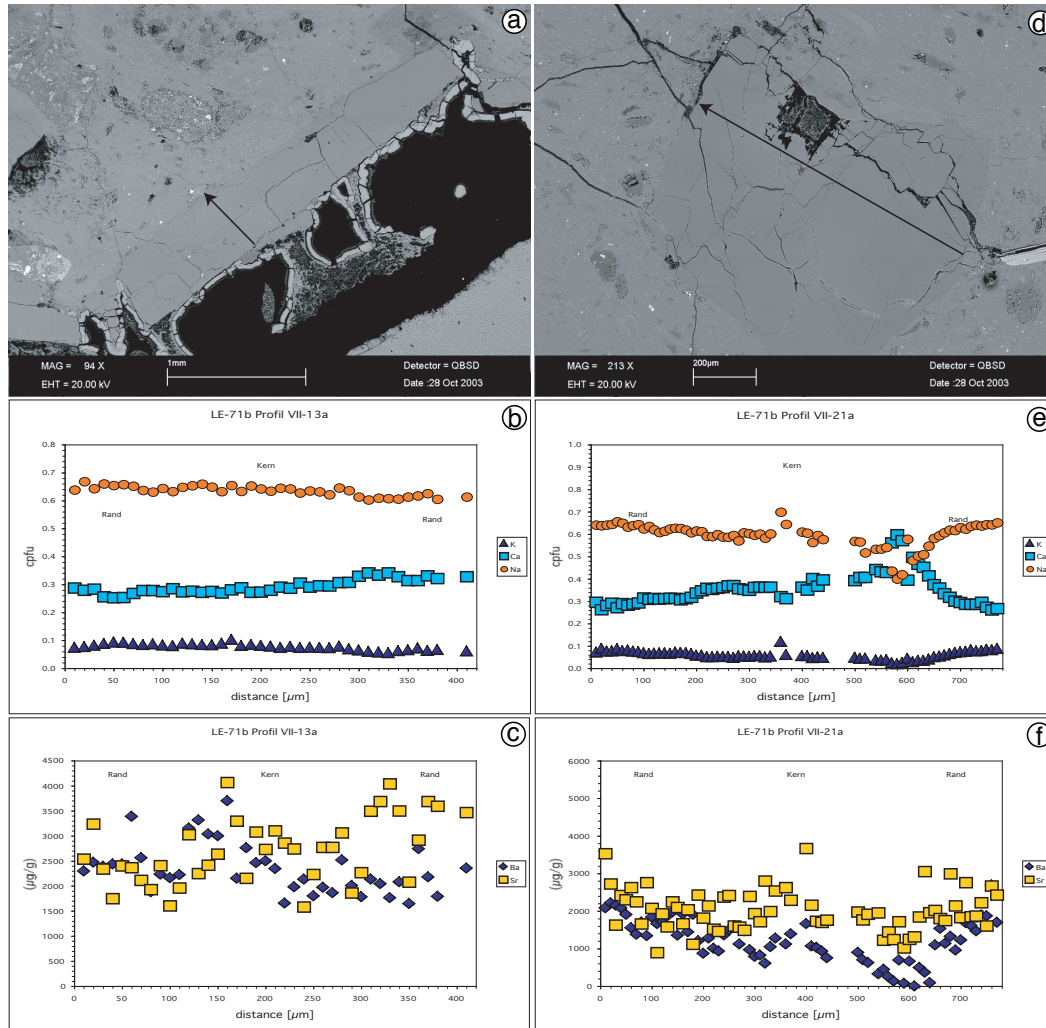


**Fig. B.62.** Sample LE-71b (a) VII-13, plagioclase, BSE image, arrow indicates location of EPMA profile, (b) EPMA profile for elements K, Ca, and Na (cpfu), (c) EPMA profile for elements Ba and Sr ( $\mu\text{g/g}$ ), (d) VII-21, plagioclase, BSE image, arrow indicates location of EPMA profile, squares mark locations of laser-ablation analyses (Sr isotopes), (e) EPMA profile for elements K, Ca, and Na (cpfu), (f) EPMA profile for elements Ba and Sr ( $\mu\text{g/g}$ ).



## **C. Analytical methods**

### **C.1. Sample documentation**

For this study nearly 100 samples were collected on Lesbos Island. Of these, 20 samples were chosen for analyses. Fifteen of the samples stem from two vertical profiles; another five samples from additional locations were chosen for their high proportion of well-preserved glass.

In-situ analyses were performed on all 20 samples, using EPMA (electron probe micro analysis), SIMS (secondary ion mass spectrometry), and LA-ICP-MS (laser-ablation inductively coupled plasma mass spectrometry). Separated quantities of volcanic glass from two samples were analysed by TIMS (thermal ionisation mass spectrometry).

All samples were documented in detail before and sometimes after analyses: optical images were taken from the thin sections using the polarisation microscope in combination with a digital camera. Reflected light images were taken in the same manner of gold coated samples after laser-ablation analysis and after SIMS analysis, with holes in the gold cover marking location of analytic points. Back-scattered electron (BSE) images and element-mappings were taken using a Leo 440 scanning electron microscope (SEM; Institut für Geowissenschaften, Universität Heidelberg).

### **C.2. Electron probe micro-analysis – EPMA**

Chemical compositions of minerals and glass (16 chemical elements) were determined using a Cameca<sup>®</sup> SX 51 electron microprobe with five wave-length-dispersive spectrometers (Institut für Geowissenschaften, Universität Heidelberg). Operating conditions were 20 nA beam current and 15 kV acceleration voltage. For analyses of feldspar, biotite and volcanic glass the beam was defocused to 10 µm spot size in order to avoid loss of alkalis and halogens. PAP correction was applied to the raw data (POUCHOU & PICOIR, 1984, 1985). For elements analysed, counting times, crystals, standards and detection limits see Table C.1.

The analysis of volcanic glass by EPMA is challenging. It is likely for certain elements (e.g. alkalis) to evaporate, due to heat generation from the electron beam,

Table C.1. Analytical setups and parameters used for electron microprobe analyses

Atomic number	Element	Spectral line	Crystal	Analysed phases	Standard	Concentration in standard (wt%)	Integration time (s)	Detection limit* at 15kV/20nA
9	F	K $\alpha$	PC0	glass	Topaz	20.65 % F	40	0.05 % F
		K $\alpha$	PC0	glass	Topaz	20.65 % F	80	0.04 % F
11	Na	K $\alpha$	TAP	all	Albite	8.71 % Na	10	0.04 % Na <sub>2</sub> O
12	Mg	K $\alpha$	TAP	all	MgO	60.31 % Mg	10	0.07 % MgO
		K $\alpha$	TAP	glass	MgO	60.31 % Mg	20	0.06 % MgO
		K $\alpha$	TAP	glass	MgO	60.31 % Mg	30	0.04 % MgO
13	Al	K $\alpha$	TAP	all but Fsp, glass	Al <sub>2</sub> O <sub>3</sub>	52.93 % Al	10	0.06 % Al <sub>2</sub> O <sub>3</sub>
		K $\alpha$	TAP	Fsp, glass	Anorthite	19.07 % Al	20	0.03 % Al <sub>2</sub> O <sub>3</sub>
		K $\alpha$	TAP	Fsp, glass	Anorthite	19.07 % Al	40	0.02 % Al <sub>2</sub> O <sub>3</sub>
14	Si	K $\alpha$	TAP	all	Wollastonite	24.08 % Si	20	0.02 % SiO <sub>2</sub>
15	P	K $\alpha$	PET	glass	Apatite	18.43 % P	20	0.13 % P <sub>2</sub> O <sub>5</sub>
17	Cl	K $\alpha$	PET	glass	Scapolite	1.43 % Cl	30	0.01 % Cl
19	K	K $\alpha$	PET	all	Orthoclase	12.18 % K	10	0.03 % K <sub>2</sub> O
20	Ca	K $\alpha$	PET	all but Fsp	Wollastonite	34.12 % Ca	10	0.04 % CaO
		K $\alpha$	PET	Fsp, glass	Anorthite	13.64 % Ca	10	0.03 % CaO
		K $\alpha$	PET	Ap	Apatite	39.74 % Ca	10	0.05 % CaO
22	Ti	K $\alpha$	PET	all but glass	TiO <sub>2</sub>	59.95 % Ti	10	0.06 % TiO <sub>2</sub>
		K $\alpha$	PET	glass	TiO <sub>2</sub>	59.95 % Ti	20	0.04 % TiO <sub>2</sub>
24	Cr	K $\alpha$	PET	all	Cr <sub>2</sub> O <sub>3</sub>	68.42 % Cr	10	0.07 % Cr <sub>2</sub> O <sub>3</sub>
25	Mn	K $\alpha$	LiF	all	Rhodonite	33.68 % Mn	30	0.05 % MnO
26	Fe	K $\alpha$	LiF	all	Fe <sub>2</sub> O <sub>3</sub>	69.94 % Fe	20	0.08 % Fe <sub>2</sub> O <sub>3</sub>
		K $\alpha$	LiF	glass	Fe <sub>2</sub> O <sub>3</sub>	69.94 % Fe	30	0.07 % Fe <sub>2</sub> O <sub>3</sub>
		K $\alpha$	LiF	glass	Fe <sub>2</sub> O <sub>3</sub>	69.94 % Fe	80	0.04 % Fe <sub>2</sub> O <sub>3</sub>
28	Ni	K $\alpha$	LiF	mica	NiO	78.58 % Ni	30	0.08 % NiO
38	Sr	L $\alpha$	PET	all but Fsp	Celestine	47.70 % Sr	20	0.14 % SrO
		L $\alpha$	PET	Fsp, glass	Celestine	47.70 % Sr	30	0.12 % SrO
56	Ba	L $\alpha$	PET	glass, all but Fsp	Baryte	58.84 % Ba	20	0.09 % BaO
		L $\alpha$	PET	Fsp	Baryte	58.84 % Ba	30	0.07 % BaO
		L $\alpha$	PET	glass	Baryte	58.84 % Ba	40	0.06 % BaO

\* 3 SD (standard deviation) of background

before they can be analysed. This effect depends on the chemical compositions of the glass and is especially pronounced in glasses with high contents of alkalis and H<sub>2</sub>O.

Different analytical setups (i.e. spot sizes) for analyses of glass were tested, in order to assure data quality. Test measurements were performed in large areas of glass, of both matrix and fiamme, in sample LE-70. The test ran for 150 s with a data integration time of only 1 s. The tests were performed several times for different spot sizes: 1 µm diameter, 10 µm diameter, and a square scanned area of 10 × 12 µm.

The test shows that using a spot with a diameter of 1 µm produces rapidly decreasing element counts and would lead to faulty data. Using a round spot with a diameter of 10 µm or a square scanning area of 10 × 12 µm makes no significant difference within the integration time of the usual setup for analyses. The tests demonstrate, that the integration times and element order chosen for the setup with a spot size of 10 µm, produces reliable data with sufficient accuracy. A summary of the test results is given in Fig. C.1.

During the chosen analytical setup, among the first elements to be analysed are Na and K, as they evaporate easily, while more refractory elements such as Si can be analysed subsequently. However, count rates for refractory elements are influenced by evaporation of the more volatile ones. Count rates for Si increase during the test due to loss of Na and K (Fig. C.1).

### C. Analytical methods

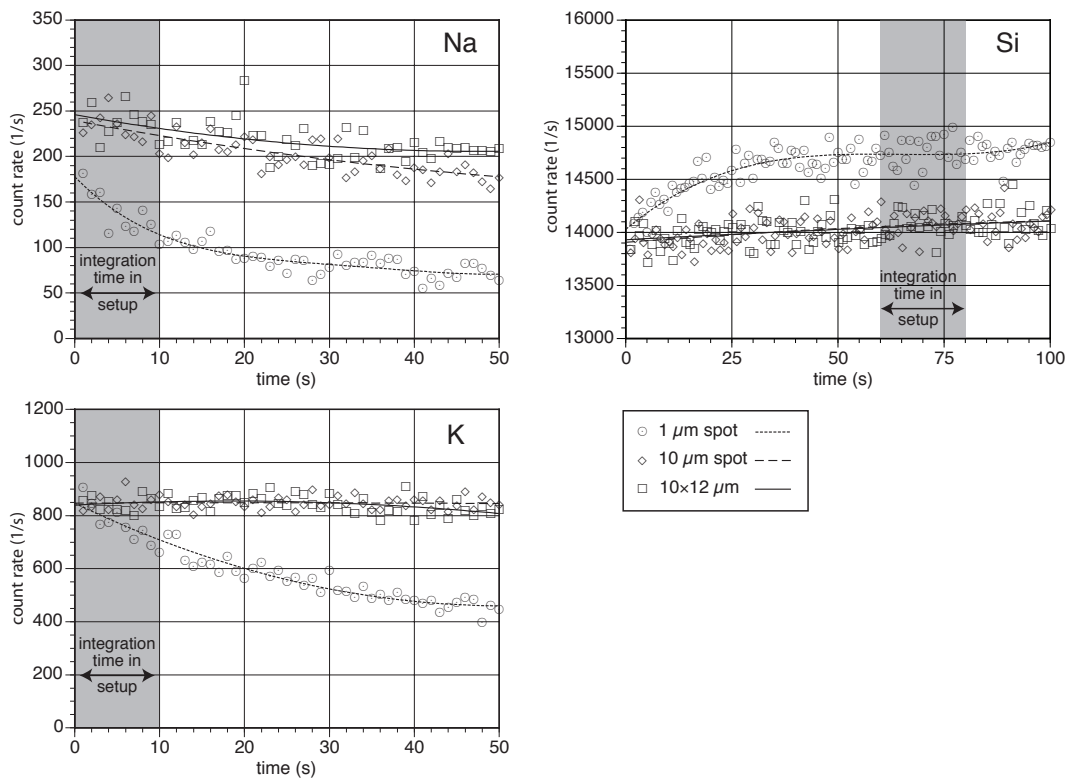


**Fig. C.1.** Selected results (three elements and three spot sizes each) for the test of EPMA setups for volcanic glass. Data was integrated every second for the duration of 150 s, however only the first 50 s (Na and K), and 100 s (Si) are displayed. The grey areas marked "integration time in setup" refer to the exact moment and duration the respective elements are analysed during the chosen analytical setup.

### C.3. Secondary ion mass spectrometry – SIMS

#### C.3.1. In-situ analysis of Lithium, Beryllium, and Boron

Concentrations of Li, Be, and B were measured in volcanic glass and plagioclase (Pl), alkali feldspar (Akf), biotite (Bt), clinopyroxene (Cpx), and amphibole (Am) using a modified Cameca<sup>®</sup> IMS 3f ion microprobe, equipped with a primary beam mass filter, at the Institut für Geowissenschaften, Universität Heidelberg (Fig. C.2).

A primary ion beam of  $^{16}\text{O}^-$  with 10kV acceleration voltage and 20nA beam current was used. Positive secondary ions were accelerated through a nominal 4.5kV and the energy window was set to 40eV. In order to suppress interfering molecules and to minimise matrix effects, the energy filtering technique (OTTOLINI *et al.*, 1993) was applied with an offset of 75eV at a mass resolution  $m/\Delta m$  (10%) of  $\approx 1000$ .

For all silicates, secondary ion intensities of  $^7\text{Li}$ ,  $^9\text{Be}$  and  $^{11}\text{B}$  were normalised to the count rate of  $^{30}\text{Si}$  and calibrated against the NIST SRM 610 glass reference material using the concentrations of PEARCE *et al.* (1997). Background near mass 11 was  $\leq 10^{-2}$  cps ( $\leq 1$  ng/g). Therefore, results are not corrected for background. Each spot was pre-sputtered for 5 minutes. One analysis comprised 10 cycles with an integration time of 8s/cycle for Li in minerals, and 16s/cycle each for Be and B. The volcanic glass contains higher levels of Li, Be and B than the minerals and, therefore, an integration time of 4s/cycle for Li, and 8s/cycle for Be and B each was sufficient.

Contamination on the surface of thin sections is a serious problem for analyses of trace elements and especially B at low concentration levels ( $< 5 \mu\text{g/g}$ ). Samples, e.g. polished thin sections, are generally contaminated with boron on the surface, in cracks and at grain boundaries (SHAW *et al.*, 1988). Using the procedure described in MARSCHALL & LUDWIG (2004), the following measures were taken to avoid contamination:

1. Customary lubricants and cooling liquids for rock saws and polishing machines usually contain several percent boric acid. They were banned from the thin section preparation lab at the Institut für Geowissenschaften, Universität Heidelberg and replaced by pure glycol.
2. Carbon coating on the samples, which had been applied for previous SEM and EMP analysis, was removed with  $\gamma$ -alumina powder and where conductive silver had been used, it had to be cleaned off with acetone. Afterwards the samples were cleaned with distilled water.

3. The samples then were cleaned twice for 15 minutes in an ultrasonic bath using ultrapure water from a Milli-Q water purification system (Millipore).
4. In the SIMS the influence of the remaining contamination was suppressed by choosing an imaged area smaller than the spot size. This measure is explained further below.

During SIMS analysis material is removed from the sample's surface (typical erosion rates: 30 nm/h to 10  $\mu\text{m}/\text{h}$ ). Theoretically the surface contamination would not contribute to the analytical result once the contamination layer was removed. This would require a perfectly homogeneous and well-defined primary beam at an incidence angle of  $0^\circ$ . In reality however, the beam current density distribution is not homogeneous, the beam is not perfectly spatially confined, it carries a halo of poorly focused neutrals and the incidence angle is  $>0^\circ$ . So the bottom of the sputtered crater is not flat, its edge is not perfectly vertical and therefore the surface contamination at the crater's edge continues to contribute to the result of the analysis.

The IMS 3f has three field apertures to limit the field imaged by the secondary beam. The influence of contamination was reduced by using the intermediate field aperture FA2 (750  $\mu\text{m}$ ), which reduces the imaged field to 12  $\mu\text{m}$  in the 25  $\mu\text{m}$  imaged field mode. This is common practice in order to overcome the effect of the crater's edge (BENNINGHOVEN *et al.*, 1987).

#### C.3.2. In-situ analysis of Boron isotopes

Boron isotope ratios were determined in volcanic glass using the modified ion microprobe Cameca<sup>®</sup> IMS 3f at the Institut für Geowissenschaften, Universität Heidelberg (Fig. C.2). Glass portions of the samples were prepared by separating large pieces of glass from selected samples, mounted in epoxy, and polished.

In order to improve the precision of the analysis of isotope ratios, significant alterations to both, software and hardware of the machine were necessary, which were designed and assembled by Thomas Ludwig (Heidelberg). The most important modification concerned the electronic control device of the magnet. As a means to switch faster between different masses and to ensure a better stability of the magnetic field, the control device has been newly constructed to a large extent. More detailed information on software and hardware modifications can be found in MARSCHALL (2005).

The  $^{16}\text{O}^-$  primary ion beam was accelerated to 10 keV with a beam current of 20 nA. The energy window was set to 100 eV and no offset was applied. 200 cycles

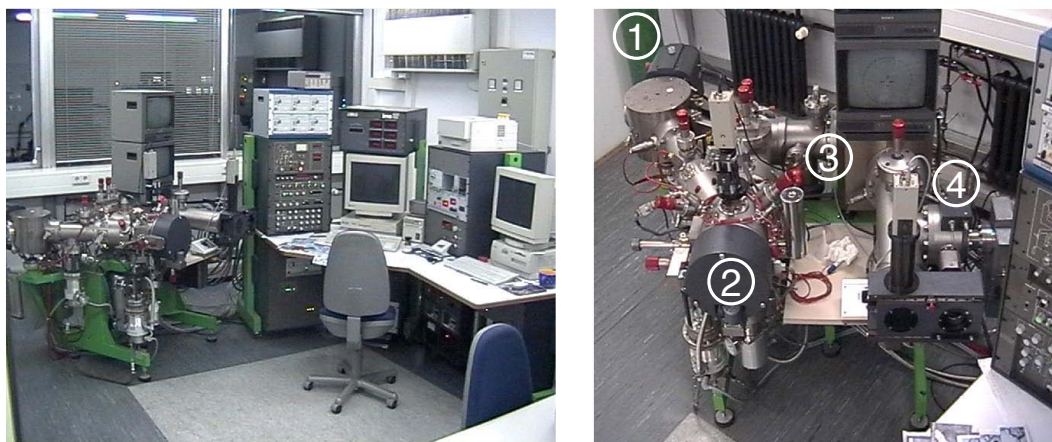


**Fig. C.2.** Photographs of secondary ion mass spectrometer Cameca® IMS 3f installed at the Institut für Geowissenschaften, Universität Heidelberg. Left image shows spectrometer and attached electronic equipment. Right image shows close-up of spectrometer with oxygen ion source and primary magnet ① on the left, sample chamber ② in the front, electrostatic sector, magnetic sector ③ and ion detection device ④.

were measured on each analysis spot with integration times of 1.66 s on  $^{11}\text{B}$  and 3.32 s on  $^{10}\text{B}$ , respectively. The integration time for  $^{10}\text{B}$  was split into two periods of 1.66 s, taking place before and after integration of  $^{11}\text{B}$ , respectively, during each acquisition cycle.

Mass resolution was set to  $m/\Delta m$  (10%)  $\approx 1200$ . Pre-sputtering and peak calibration lasted for 230 s and settling time between two different masses was 200 ms, resulting in total analysis time for one spot of approximately 23 minutes. Internal precision of any single analysis was  $\leq 1.6\text{‰}$  ( $2\sigma$ ).

For boron isotope determination the imaged field was not reduced by field aperture 2 (FA 2), since contamination is not considered a problem in a well-cleaned glass with high boron contents ( $\approx 100\ \mu\text{g/g}$ ).

Boron isotopic compositions of samples are reported in delta notation ( $\delta^{11}\text{B}$  in ‰) relative to the B isotope standard material NBS SRM 951 (CATANZARO *et al.*, 1970). Instrumental mass fractionation was  $1.0472 \pm 0.78\text{‰}$  ( $2\sigma$ ) determined using obsidian glass B 6 (TONARINI *et al.*, 2003). B 6 is a natural rhyolitic glass from Lipari Island, Italy, which is widely available through the geochemical community. For this study a value of  $-1.8\text{‰}$  (ROSNER *et al.*, 2008) was used. This value is a simple average from three P-TIMS results (GONFIANTINI *et al.*, 2003), which is nearly identical to the mean of repeated analyses conducted during preliminary evaluation prior to the distribution of the material (TONARINI *et al.*, 2003).

### C.3.3. In-situ analysis of Hydrogen

Concentrations of H in volcanic glass were determined using a modified ion microprobe Cameca<sup>®</sup> IMS 3f at the Institut für Geowissenschaften, Universität Heidelberg (Fig. C.2), equipped with a primary beam mass filter, a cryopump and a liquid nitrogen trap for the sample chamber. The setup, which partly follows LUDWIG & STALDER (2007), will be summarised below.

The  $^{16}\text{O}^-$  primary ion beam with 10kV acceleration voltage and a beam current of 20nA was used. The primary beam was mass filtered to remove  $^{16}\text{OH}^-$ , slightly defocused to a constant spot size of  $\approx 30\ \mu\text{m}$ . Positive secondary ions were energy filtered with an offset of 75 eV and an energy window of 40 eV, mass resolution was set to the lowest value possible for  $m/\Delta m$  (10%) of  $\approx 400$ . The nominal imaged field was chosen at  $25\ \mu\text{m}$  and reduced to  $12\ \mu\text{m}$  using the intermediate field aperture FA2 ( $750\ \mu\text{m}$ ). The beam was centered using the channel plate image with the largest field aperture and  $^{28}\text{Si}^+$ . (Please, note that  $^{28}\text{Si}^+$  was chosen over  $^{30}\text{Si}^+$  for the image, because of higher intensity.) However, a weak ambient magnetic field will effect ions according to their masses and shift the ion image with respect to the field aperture. This would cause the  $\text{H}^+$  image to be off-centre in respect to the  $^{28}\text{Si}^+$  image, but is overcome by two magnetic field coils installed perpendicular to each other close to the sample (LUDWIG & STALDER, 2007).

Each spot was pre-sputtered for 400s. One analysis comprised 10 cycles with an integration time of 4s/cycle for H. Secondary ion intensities of H were normalised to the count rate of  $^{30}\text{Si}$  and calibrated against three reference tourmalines (DYAR *et al.*, 2001): elbaite (#98144), dravite (#108796) and schorl (#112566). The relative ion yield (RIY) of the three tourmaline standards deviate substantially from each other ( $\pm 25\%$ ), which leads to a reduced accuracy of  $\pm 25\%$  accordingly. We used a value of 0.1 for RIY.

## C.4. Laser-ablation inductively-coupled-plasma mass spectrometry – LA-ICP-MS

Work on the LA-ICP-MS was carried out in cooperation with Yann Lahaye at the Institut für Geowissenschaften at the Universität Frankfurt am Main.

### C.4.1. Trace-element analysis in volcanic glass

Laser-ablation technique was used for in-situ analysis of 35 trace elements in the volcanic glass of 10 samples. Glass portions of the samples were prepared by separating large pieces of glass from selected samples, mounted in epoxy, and polished. Analysed elements included Ca, REE, LILE, HSFE, transition metals, U, Th and Pb.

The Thermo-Finnigan<sup>®</sup> Element 2 high-resolution single-collector ICP-MS at the Institut für Geowissenschaften, Universität Frankfurt is equipped with a double-focusing magnetic sector field, a discrete dynode detector system, and a fast-scanning option. The New Wave<sup>®</sup> ablation system UP-213 consists of a Q-switched Nd:YAG (neodymium-doped yttrium aluminium garnet) ultraviolet laser (213 nm wavelength) and was operated at 10 Hz. Ablation occurred in a He atmosphere. The He carrier gas (0.31/min) was mixed with the Ar nebulizer gas (11/min) flow prior to the plasma torch. Spot analyses were done using a typical spot diameter of 45 – 55  $\mu\text{m}$  at a fluence of about 2 – 4 J/cm<sup>2</sup>.

The NIST SRM 612 standard glass was used for external calibration of the trace elements using the values published by PEARCE *et al.* (1997). Calcium was used for internal standardisation. A gas blank was measured before each measurement. The raw data was processed externally using GLITTER 4.0 (ACHTERBERGH *et al.*, 2001).

### C.4.2. In-situ Strontium isotope analysis in plagioclase

Strontium isotopes in plagioclase were analysed in-situ using a Thermo-Finnigan<sup>®</sup> Neptune multi-collector ICP-MS at the Institut für Geowissenschaften, Universität Frankfurt. Strontium isotopes were obtained for 33 analysis spots in 13 different plagioclase phenocrysts in six different samples.

The Neptune multi-collector ICP-MS was coupled with the laser described above. Ablation occurred in a He atmosphere, the He carrier gas (0.31/min) was mixed with the Ar nebuliser gas flow (11/min) prior to the plasma torch. The target ion beam intensity for <sup>88</sup>Sr was around 4 V (Faraday cup signal) on the samples. The

laser spot sizes (a square of  $90\ \mu\text{m} \times 90\ \mu\text{m}$ ) and repetition rates (typically 10Hz) were adjusted for optimum Sr intensity measured in the sample.

For data collection, 6 of the 9 Faraday cups of the MC-ICP-MS were used, with  $^{86}\text{Sr}$  at the axial position. Samples were ablated and measured in 5 cycles for 100s after a 30s baseline measurement. Measured isotope ratios were corrected for instrument fractionation using an exponential law and a  $^{86}\text{Sr}/^{88}\text{Sr}$  value of 0.1194. The isobaric interference on  $^{87}\text{Rb}$  and  $^{86}\text{Sr}$  was monitored and corrected using the  $^{85}\text{Rb}$  and  $^{83}\text{Kr}$  ion signal respectively. The accuracy of the laser-ablation protocol was verified throughout the day of measurement by repeated analysis ( $n = 5$  measurements) of an in-house plagioclase standard from a megacryst of the Cameroon volcanic chain (sample Mir a, RANKENBURG *et al.*, 2004). The laser ablation parameters were similar on the samples and the standards. During the course of this study, the average  $^{87}\text{Sr}/^{86}\text{Sr}$  value obtained was  $0.70308 \pm 0.00011 (2\sigma)$ , similar to the TIMS value of  $0.70310 \pm 0.00006 (2\sigma)$  (RANKENBURG *et al.*, 2004).

### **C.5. Data comparison between laser-ablation ICP-MS data and secondary ion mass spectrometer**

Lithium, Beryllium, and Boron analyses used in this study are usually determined by secondary ion mass spectrometer (SIMS), however in some cases data obtained by LA-ICP-MS has been used. The LA-ICP-MS had not been specifically adjusted for analysis of Li, Be, and B, therefore the data is expected to be less reliable than data determined by SIMS. The average data for samples analysed by both methods is compared in the following (Fig. C.3).

Lithium data scatters widely for both analytical methods, indicating the Lithium inhomogeneity in the volcanic glass studied. A useful comparison of the data is not possible.

Beryllium data for LE-57, LE-68, and LE-69 contains data, that was not obtained as absolute values. They were given as relative values, being below a specific minimum detection limit (confidence 99%) for this data point. For LE-57 one of four data points was below detection limit, for LE-68 seven out of 10 and for LE-69 five out of 10. However, these data points have been included in the calculation of the average value. Had they been left out, resulting averages would have been even higher, than the average values presented here. Yet, the averages for these points should be even lower than here.

Beryllium data obtained by LA-ICP-MS has a much larger  $2\sigma$  than data determined by SIMS. Data from most samples are in good agreement, while data for LE-68 and LE-69 is higher for LA-ICP-MS than for SIMS. These sample averages

contain high proportions of data points which are below detection limit, and therefore are too high, as described in the paragraph above.

This will not play any role with LA-ICP-MS data for Be used later, since none of the additional samples only determined by LA-ICP-MS and not displayed here, have values below detection limit.

Boron values obtained by LA-ICP-MS seem systematically lower, than B data from SIMS. LA-ICP-MS data is between 6% and 17% lower in comparison to SIMS data. Data also have a larger  $2\sigma$  than data from SIMS.

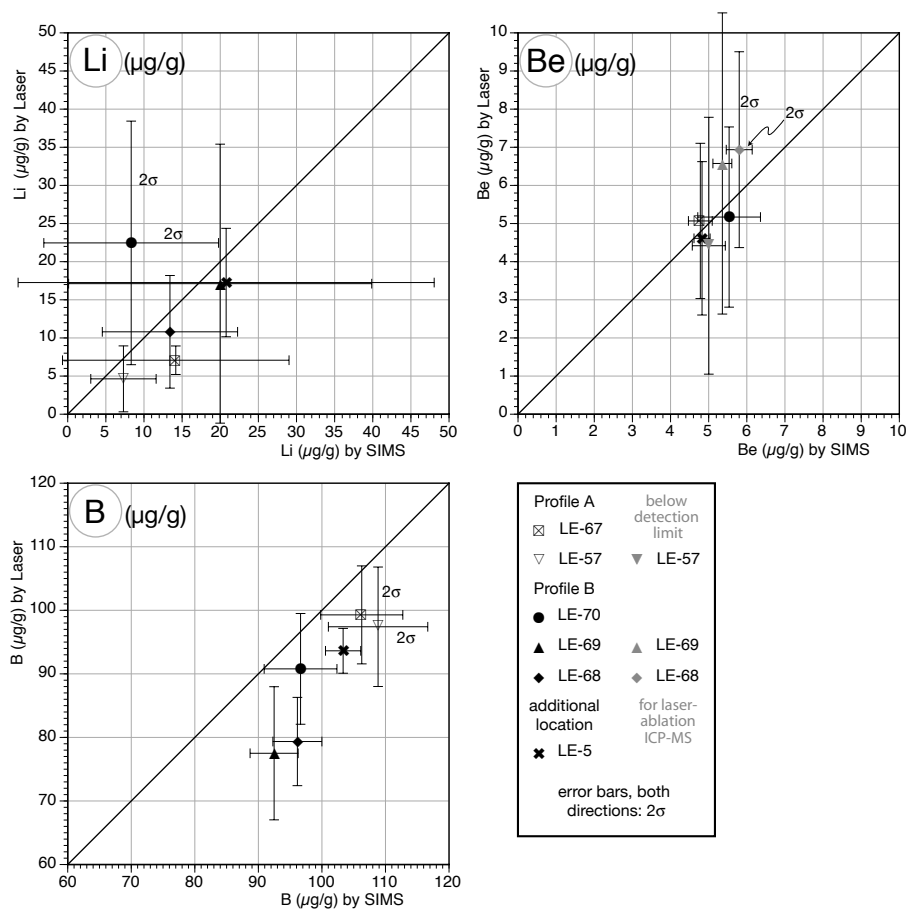


**Fig. C.3.** Comparison of average data for Li, Be, and B for each sample between LA-ICP-MS (“Laser”) and secondary ion mass spectrometer (“SIMS”). Laser-ablation ICP-MS data for Be includes values, which were not absolute values, but were relative values, below the individual detection limit (confidence 99%). These values are included in the average calculation, however, average for these points could be lower than displayed.

## C.6. Thermal ionisation mass spectrometry – TIMS

Strontium, neodymium, and lead isotopes were obtained by TIMS from separated and homogenised fractions of volcanic glass. Samples were crushed, cleaned in distilled water, and hand-picked under a binocular, in order to ensure inclusions and phenocrysts were isolated from the glass. Sample preparation was carried out at the Universität Heidelberg by myself, while all further work was performed at the Universität Tübingen by Wolfgang Siebel.

The radiogenic isotope lab at the Institut für Geowissenschaften, Universität Tübingen runs a Finnigan<sup>®</sup> MAT 262 solid source mass spectrometer (Fig. C.4). The MAT 262 is equipped with seven adjustable Faraday cup multi-collectors. The centre channel slit is fixed, and the beam can be deflected either into a Faraday cup or the secondary electron multiplier (SEM).

Standard NBS 987 was used for Sr and determined at  $0.710244 \pm 0.000010$  (Reference value: 0.710248). Standard La Jolla was used for Nd and determined at  $0.511843 \pm 0.000010$  (Reference-value 0.511850). Due to the good agreements with the reference values, Sr and Nd were not corrected. Standard NBS 981 was used for Pb isotopes. Pb-ratios were corrected 0.8‰ per mass unit for mass fractionation, uncertainty of reported Pb isotope ratios was better than 0.1%. Blank values were 86 pg Sr, 18 pg Nd, and 40 pg Pb.



**Fig. C.4.** Finnigan MAT 262 solid source mass spectrometer at the Institut für Geowissenschaften, Universität Tübingen, image taken from the following website: <http://homepages.uni-tuebingen.de/wolfgang.siebel/lab/lab.html>

Isotope measurements were made on unspiked powders of cleaned and hand-picked volcanic glass. Strontium and neodymium were separated using standard cation exchange techniques. (Exchange resin for Sr: Bio Rad AW 50 W-X, 100–200 mesh, exchange resin for Nd: HDEHP-coated Teflon powder). Samples for Sr and Nd were loaded with phosphoric acid (1 mol and 0.1 mol, respectively) on Ta filaments, and the measurements were performed in static mode using the single filament mode for Sr and double filament mode for Nd. The sample for Pb was loaded with a Si-gel onto a Re filament and measured in single-filament mode at temperatures between 1170 – 1220°C.



## D. Analytical data

### D.1. Geochemistry of the glass

**Table D.1.** Average EMP data for glass from Profile A and Profile B. Only samples with unaltered glass have been included. Please note: all concentration have been recalculated to a water-free basis prior to averaging. Oxide concentrations are in wt% $\pm 2\sigma$ . Oxides marked n.a. were not analyzed.

	Profile A									
	LE-58 (0.5 m)		LE-59 (3.0 m)		LE-60 (15.0 m)		LE-61 (18.0 m)		LE-62 (19.5 m)	
SiO <sub>2</sub>	72.61	$\pm 0.91$	71.64	$\pm 0.51$	72.90	$\pm 0.67$	72.63	$\pm 0.62$	72.24	$\pm 0.70$
TiO <sub>2</sub>	0.31	$\pm 0.04$	0.32	$\pm 0.02$	0.31	$\pm 0.05$	0.31	$\pm 0.05$	0.31	$\pm 0.05$
Al <sub>2</sub> O <sub>3</sub>	14.93	$\pm 0.39$	15.21	$\pm 0.29$	15.09	$\pm 0.25$	15.12	$\pm 0.19$	15.24	$\pm 0.18$
FeO	1.33	$\pm 0.07$	1.36	$\pm 0.08$	1.19	$\pm 0.31$	1.10	$\pm 0.45$	1.18	$\pm 0.34$
MnO	n.a.		n.a.		n.a.		n.a.		0.06	$\pm 0.04$
MgO	0.19	$\pm 0.02$	0.18	$\pm 0.02$	0.13	$\pm 0.10$	0.11	$\pm 0.05$	0.14	$\pm 0.08$
CaO	0.72	$\pm 0.07$	0.74	$\pm 0.07$	0.69	$\pm 0.08$	0.60	$\pm 0.05$	0.58	$\pm 0.10$
BaO	0.10	$\pm 0.05$	0.10	$\pm 0.07$	0.10	$\pm 0.06$	0.11	$\pm 0.05$	0.11	$\pm 0.09$
SrO	n.a.		n.a.		n.a.		n.a.		0.01	$\pm 0.05$
Na <sub>2</sub> O	3.47	$\pm 0.92$	3.86	$\pm 0.48$	3.00	$\pm 0.83$	3.31	$\pm 0.43$	3.34	$\pm 0.48$
K <sub>2</sub> O	6.26	$\pm 0.38$	6.41	$\pm 0.43$	6.50	$\pm 0.52$	6.55	$\pm 0.22$	6.63	$\pm 0.16$
F corr	0.11	$\pm 0.02$	0.06	$\pm 0.05$	0.02	$\pm 0.09$	0.07	$\pm 0.05$	0.05	$\pm 0.04$
Cl	0.02	$\pm 0.03$	0.13	$\pm 0.01$	0.11	$\pm 0.03$	0.13	$\pm 0.03$	0.13	$\pm 0.01$

	Profile A					Profile B				
	LE-57 (21.0 m)		LE-67 (40.0 m)		LE-68 (22.0 m)	LE-69 (23.8 m)		LE-70 (24.5 m)		
SiO <sub>2</sub>	72.44	$\pm 0.77$	72.18	$\pm 0.55$	71.27	$\pm 0.60$	70.82	$\pm 0.55$	71.30	$\pm 1.53$
TiO <sub>2</sub>	0.30	$\pm 0.04$	0.30	$\pm 0.05$	0.23	$\pm 0.05$	0.23	$\pm 0.06$	0.23	$\pm 0.04$
Al <sub>2</sub> O <sub>3</sub>	15.25	$\pm 0.19$	15.30	$\pm 0.06$	15.66	$\pm 0.24$	15.64	$\pm 0.12$	15.60	$\pm 0.28$
FeO	1.17	$\pm 0.33$	0.86	$\pm 0.27$	1.10	$\pm 0.51$	1.13	$\pm 0.44$	0.88	$\pm 1.25$
MnO	0.04	$\pm 0.04$	0.06	$\pm 0.03$	0.06	$\pm 0.06$	0.07	$\pm 0.04$	n.a.	
MgO	0.13	$\pm 0.13$	0.08	$\pm 0.05$	0.20	$\pm 0.08$	0.22	$\pm 0.05$	0.15	$\pm 0.23$
CaO	0.37	$\pm 0.17$	0.53	$\pm 0.12$	0.64	$\pm 0.34$	0.87	$\pm 0.13$	0.72	$\pm 0.42$
BaO	0.08	$\pm 0.08$	0.12	$\pm 0.09$	0.09	$\pm 0.12$	0.14	$\pm 0.07$	0.14	$\pm 0.07$
SrO	0.01	$\pm 0.04$	0.01	$\pm 0.03$	0.02	$\pm 0.06$	0.02	$\pm 0.06$	n.a.	
Na <sub>2</sub> O	3.24	$\pm 0.60$	3.66	$\pm 0.35$	2.88	$\pm 0.38$	3.11	$\pm 0.54$	3.08	$\pm 0.56$
K <sub>2</sub> O	6.86	$\pm 0.20$	6.66	$\pm 0.21$	7.85	$\pm 0.30$	7.72	$\pm 0.67$	7.66	$\pm 0.66$
F corr	0.08	$\pm 0.05$	0.20	$\pm 0.05$	n.a.		n.a.		0.05	$\pm 0.04$
Cl	0.06	$\pm 0.11$	0.13	$\pm 0.01$	n.a.		n.a.		0.14	$\pm 0.03$

note: all concentration have been recalculated for water-free samples prior to averaging

**Table D.2.** In-situ H<sub>2</sub>O concentrations of glass samples from Profile A and Profile B. In-situ concentrations of Hydrogen were determined by ion microprobe and <sup>1</sup>H/<sup>30</sup>Si count ratios were converted into H<sub>2</sub>O concentrations. Element concentration were analysed by secondary ion mass-spectrometry (SIMS) at the Universität Heidelberg. Details about the analytical setup can be found in section C.3.1 on page 273 in the appendix.

Profile A														
LE-588b±st.dev.	LE-590b±st.dev.	LE-600b±st.dev.	LE-610b±st.dev.	LE-620b±st.dev.	E-570b±st.dev.v	LE-670b±st.dev.	LE-588b±st.dev.	LE-590b±st.dev.	LE-600b±st.dev.	LE-610b±st.dev.	LE-620b±st.dev.			
4.41	0.53	3.86	0.29	5.18	0.33	4.38	0.31	4.23	0.34	4.58	0.34	4.11	0.26	
4.19	0.28	3.82	0.27	5.24	0.45	4.31	0.24	4.29	0.25	4.83	0.27	4.09	0.30	
4.36	0.21	3.89	0.31	5.42	0.32	4.43	0.48	4.27	0.45	4.48	0.50	3.97	0.25	
3.94	0.29	3.82	0.37	5.39	0.29	4.23	0.32					3.97	0.36	
3.90	0.27	3.94	0.28	5.33	0.32	4.23	0.25					4.03	0.49	
3.96	0.40	3.86	0.36	4.64	0.31	4.18	0.27					4.03	0.22	
		4.18	0.41			4.21	0.32					4.01	0.42	
		3.98	0.32			4.21	0.32					4.02	0.48	
		3.94	0.25			4.22	0.42					4.51	0.41	
		3.97	0.36			4.47	0.27					3.98	0.28	
		3.70	0.30			4.12	0.44					4.08	0.33	
		3.99	0.25			4.13	0.17					3.92	0.36	
		4.09	0.43			4.13	0.20					3.79	0.26	
		3.93	0.31			4.18	0.28					4.09	0.38	
average±s.e.	4.13	0.18	3.93	0.06	5.20	0.24	4.24	0.06	4.26	0.04	4.63	0.21	4.04	0.08

Profile B			
LE-680b±st.dev.	LE-690b±st.dev.	LE-700b±st.dev.	add. location
3.62	0.24	3.90	0.34
3.89	0.54	3.68	0.29
3.52	0.50	3.96	0.27
3.77	0.35	3.73	0.26
3.66	0.42		
3.83	0.70		
3.66	0.27		
3.82	0.32		
3.84	0.56		
3.38	0.49		
average±s.e.	3.70	0.10	3.82
		0.14	3.96
			0.38
			3.59
			0.08

**Table D.3.** LA-ICP-MS analyses of glass from Profile A (LE-57, LE-67) and Profile B (LE-68, LE-69, LE-70), element concentrations in  $\mu\text{g/g} \pm 2\sigma$ .

	LE-57 (n=5)		LE-67 (n=5)		LE-68 (n=10)		LE-69 (n=10)		LE-70 (n=5)	
Li	4.64	$\pm 4.32$	7.08	$\pm 1.87$	10.80	$\pm 7.38$	17.12	$\pm 18.29$	22.46	$\pm 15.97$
Be	4.42	$\pm 3.37$	5.07	$\pm 2.04$	6.94	$\pm 2.57$	6.58	$\pm 3.95$	5.17	$\pm 2.36$
B	97.41	$\pm 9.40$	99.28	$\pm 7.71$	79.35	$\pm 6.95$	77.50	$\pm 10.47$	90.78	$\pm 8.71$
Ca	4910.88	$\pm 1276.11$	5067.00	$\pm 568.14$	5804.83	$\pm 3035.36$	6509.41	$\pm 3098.26$	5854.53	$\pm 719.19$
Sc	7.84	$\pm 1.28$	7.54	$\pm 1.11$	10.16	$\pm 2.41$	9.00	$\pm 2.02$	8.25	$\pm 1.24$
V	5.79	$\pm 1.18$	4.97	$\pm 0.49$	4.70	$\pm 1.65$	5.28	$\pm 2.95$	4.57	$\pm 0.28$
Mn	442.41	$\pm 130.26$	509.87	$\pm 71.03$	535.98	$\pm 198.47$	931.05	$\pm 262.24$	540.18	$\pm 25.06$
Rb	273.32	$\pm 39.22$	399.71	$\pm 20.55$	299.49	$\pm 45.87$	299.17	$\pm 32.22$	266.06	$\pm 14.80$
Sr	72.81	$\pm 23.01$	51.56	$\pm 10.58$	166.74	$\pm 32.33$	157.88	$\pm 16.58$	121.27	$\pm 18.50$
Y	21.38	$\pm 0.80$	20.88	$\pm 1.40$	20.45	$\pm 1.59$	18.93	$\pm 1.50$	18.49	$\pm 0.67$
Zr	275.36	$\pm 7.43$	267.51	$\pm 11.80$	322.34	$\pm 17.20$	306.69	$\pm 21.58$	303.61	$\pm 12.90$
Nb	25.22	$\pm 1.16$	24.37	$\pm 0.68$	28.18	$\pm 1.12$	26.49	$\pm 2.03$	26.54	$\pm 0.78$
Sn	2.88	$\pm 0.73$	1.77	$\pm 0.31$	2.20	$\pm 1.07$	2.94	$\pm 1.22$	2.85	$\pm 0.25$
Cs	11.48	$\pm 0.98$	11.21	$\pm 0.26$	11.40	$\pm 0.93$	11.33	$\pm 1.16$	11.83	$\pm 0.72$
Ba	1206.67	$\pm 585.78$	968.40	$\pm 140.37$	1105.01	$\pm 207.69$	1042.92	$\pm 47.68$	997.20	$\pm 142.89$
La	74.33	$\pm 3.96$	73.08	$\pm 5.55$	67.06	$\pm 5.82$	64.46	$\pm 5.00$	60.73	$\pm 3.17$
Ce	143.84	$\pm 4.21$	141.85	$\pm 8.40$	127.78	$\pm 10.25$	130.55	$\pm 3.01$	125.28	$\pm 5.97$
Pr	13.72	$\pm 0.46$	13.56	$\pm 0.67$	12.54	$\pm 1.36$	12.11	$\pm 0.74$	11.83	$\pm 0.89$
Nd	47.81	$\pm 3.15$	45.73	$\pm 2.76$	45.57	$\pm 4.28$	42.90	$\pm 3.90$	41.46	$\pm 1.82$
Sm	6.87	$\pm 1.18$	6.70	$\pm 0.51$	6.93	$\pm 1.92$	6.97	$\pm 1.27$	6.44	$\pm 0.45$
Eu	1.01	$\pm 0.18$	1.12	$\pm 0.24$	1.23	$\pm 0.50$	1.18	$\pm 0.33$	1.11	$\pm 0.11$
Gd	5.50	$\pm 0.64$	5.27	$\pm 0.62$	6.66	$\pm 1.59$	5.39	$\pm 0.87$	5.16	$\pm 0.49$
Tb	0.69	$\pm 0.04$	0.64	$\pm 0.12$	0.70	$\pm 0.42$	0.62	$\pm 0.32$	0.60	$\pm 0.13$
Dy	4.01	$\pm 0.39$	3.81	$\pm 0.37$	3.97	$\pm 1.28$	3.63	$\pm 0.71$	3.49	$\pm 0.43$
Ho	0.74	$\pm 0.07$	0.75	$\pm 0.07$	0.76	$\pm 0.21$	0.67	$\pm 0.19$	0.67	$\pm 0.04$
Er	2.17	$\pm 0.27$	2.17	$\pm 0.32$	2.15	$\pm 0.60$	1.85	$\pm 0.85$	1.91	$\pm 0.26$
Tm	0.33	$\pm 0.06$	0.33	$\pm 0.07$	0.34	$\pm 0.13$	0.35	$\pm 0.19$	0.30	$\pm 0.06$
Yb	2.26	$\pm 0.41$	2.34	$\pm 0.44$	2.53	$\pm 1.12$	2.10	$\pm 0.51$	2.09	$\pm 0.23$
Lu	0.34	$\pm 0.06$	0.35	$\pm 0.04$	0.36	$\pm 0.15$	0.34	$\pm 0.16$	0.32	$\pm 0.04$
Hf	7.63	$\pm 0.31$	7.41	$\pm 0.58$	8.68	$\pm 1.34$	8.27	$\pm 0.83$	7.77	$\pm 0.68$
Ta	2.01	$\pm 0.25$	1.83	$\pm 0.34$	2.20	$\pm 0.43$	2.03	$\pm 0.20$	1.95	$\pm 0.16$
Pb	66.01	$\pm 2.31$	56.88	$\pm 10.57$	36.42	$\pm 5.09$	44.06	$\pm 3.09$	53.71	$\pm 8.32$
Th	44.83	$\pm 1.49$	44.49	$\pm 3.40$	45.43	$\pm 3.50$	42.53	$\pm 2.58$	41.18	$\pm 2.12$
U	9.45	$\pm 0.41$	9.76	$\pm 0.62$	9.88	$\pm 0.45$	9.78	$\pm 0.64$	10.66	$\pm 0.30$

Table D.3. (continued) LA-ICP-MS analyses of glass from additional locations, element concentrations in  $\mu\text{g/g} \pm 2\sigma$ .

	LE-2 (n=5)	LE-3 (n=5)	LE-5 (n=5)	LE-8 (n=5)	LE-9 (n=5)
Li	11.41 $\pm$ 9.85	17.87 $\pm$ 20.23	17.26 $\pm$ 7.11	6.63 $\pm$ 0.99	6.37 $\pm$ 3.19
Be	4.55 $\pm$ 1.99	5.13 $\pm$ 2.55	4.61 $\pm$ 2.01	4.37 $\pm$ 2.39	4.98 $\pm$ 3.03
B	86.79 $\pm$ 4.05	93.00 $\pm$ 5.64	93.63 $\pm$ 3.53	90.85 $\pm$ 4.68	95.30 $\pm$
Ca	5161.21 $\pm$ 229.26	5023.99 $\pm$ 645.09	5013.54 $\pm$ 599.42	4991.99 $\pm$ 178.50	5005.81 $\pm$ 388.90
Sc	6.95 $\pm$ 0.32	7.58 $\pm$ 0.25	7.51 $\pm$ 0.53	7.32 $\pm$ 0.69	7.94 $\pm$ 0.72
V	5.14 $\pm$ 0.29	5.38 $\pm$ 0.52	5.40 $\pm$ 0.57	5.48 $\pm$ 0.40	5.26 $\pm$ 0.21
Mn	504.20 $\pm$ 38.69	536.80 $\pm$ 26.52	573.87 $\pm$ 31.43	567.26 $\pm$ 41.68	555.14 $\pm$ 28.84
Rb	221.44 $\pm$ 19.61	262.87 $\pm$ 24.10	279.77 $\pm$ 13.42	233.31 $\pm$ 8.03	246.99 $\pm$ 45.54
Sr	65.99 $\pm$ 20.31	61.18 $\pm$ 3.56	60.17 $\pm$ 3.90	60.74 $\pm$ 1.62	60.94 $\pm$ 4.65
Y	22.30 $\pm$ 0.73	22.09 $\pm$ 1.37	20.96 $\pm$ 1.97	20.90 $\pm$ 0.72	20.51 $\pm$ 0.59
Zr	271.80 $\pm$ 16.05	273.58 $\pm$ 19.18	264.02 $\pm$ 23.01	259.34 $\pm$ 9.38	257.85 $\pm$ 15.13
Nb	24.80 $\pm$ 0.88	24.92 $\pm$ 0.66	24.72 $\pm$ 0.63	24.36 $\pm$ 0.92	24.45 $\pm$ 1.58
Sn	2.74 $\pm$ 0.63	2.79 $\pm$ 0.43	2.84 $\pm$ 0.54	2.77 $\pm$ 0.43	2.88 $\pm$ 0.43
Cs	10.48 $\pm$ 0.28	10.56 $\pm$ 0.32	10.76 $\pm$ 0.78	10.57 $\pm$ 0.42	11.14 $\pm$ 0.90
Ba	1085.75 $\pm$ 232.03	1033.04 $\pm$ 38.36	994.49 $\pm$ 55.33	992.33 $\pm$ 17.33	965.62 $\pm$ 45.55
La	78.48 $\pm$ 4.25	76.65 $\pm$ 5.83	73.31 $\pm$ 6.09	71.95 $\pm$ 2.56	72.19 $\pm$ 4.70
Ce	152.54 $\pm$ 7.46	149.16 $\pm$ 9.98	148.92 $\pm$ 7.64	147.95 $\pm$ 5.44	145.78 $\pm$ 10.10
Pr	14.28 $\pm$ 0.89	14.04 $\pm$ 0.92	13.70 $\pm$ 1.21	13.65 $\pm$ 0.63	13.42 $\pm$ 0.68
Nd	49.72 $\pm$ 3.28	48.73 $\pm$ 1.71	47.12 $\pm$ 3.55	46.08 $\pm$ 1.76	45.36 $\pm$ 1.71
Sm	7.30 $\pm$ 0.39	7.12 $\pm$ 0.52	7.01 $\pm$ 0.54	6.85 $\pm$ 0.29	6.71 $\pm$ 0.50
Eu	1.09 $\pm$ 0.18	1.08 $\pm$ 0.09	1.09 $\pm$ 0.10	1.01 $\pm$ 0.10	1.01 $\pm$ 0.14
Gd	5.45 $\pm$ 0.48	5.33 $\pm$ 0.27	5.05 $\pm$ 0.34	5.05 $\pm$ 0.30	4.93 $\pm$ 0.13
Tb	0.69 $\pm$ 0.11	0.65 $\pm$ 0.04	0.64 $\pm$ 0.09	0.64 $\pm$ 0.08	0.62 $\pm$ 0.08
Dy	3.98 $\pm$ 0.60	4.06 $\pm$ 0.43	3.79 $\pm$ 0.50	3.76 $\pm$ 0.24	3.74 $\pm$ 0.26
Ho	0.77 $\pm$ 0.07	0.76 $\pm$ 0.06	0.74 $\pm$ 0.08	0.74 $\pm$ 0.02	0.74 $\pm$ 0.11
Er	2.33 $\pm$ 0.11	2.27 $\pm$ 0.20	2.17 $\pm$ 0.19	2.08 $\pm$ 0.38	2.08 $\pm$ 0.23
Tm	0.34 $\pm$ 0.06	0.35 $\pm$ 0.06	0.33 $\pm$ 0.04	0.34 $\pm$ 0.05	0.31 $\pm$ 0.02
Yb	2.34 $\pm$ 0.11	2.40 $\pm$ 0.25	2.33 $\pm$ 0.25	2.27 $\pm$ 0.28	2.23 $\pm$ 0.14
Lu	0.35 $\pm$ 0.05	0.38 $\pm$ 0.03	0.33 $\pm$ 0.03	0.34 $\pm$ 0.05	0.33 $\pm$ 0.04
Hf	7.47 $\pm$ 0.38	7.68 $\pm$ 0.27	7.25 $\pm$ 0.69	7.04 $\pm$ 0.40	7.26 $\pm$ 0.30
Ta	1.74 $\pm$ 0.21	1.80 $\pm$ 0.10	1.76 $\pm$ 0.12	1.67 $\pm$ 0.06	1.77 $\pm$ 0.11
Pb	66.43 $\pm$ 3.83	62.43 $\pm$ 4.10	52.84 $\pm$ 3.88	64.97 $\pm$ 2.13	69.01 $\pm$ 2.64
Th	44.18 $\pm$ 3.38	46.11 $\pm$ 1.00	43.35 $\pm$ 2.61	41.60 $\pm$ 0.80	42.93 $\pm$ 1.58
U	9.23 $\pm$ 1.65	9.80 $\pm$ 1.73	9.78 $\pm$ 1.71	9.44 $\pm$ 1.61	9.66 $\pm$ 0.41

D.1. Geochemistry of the glass

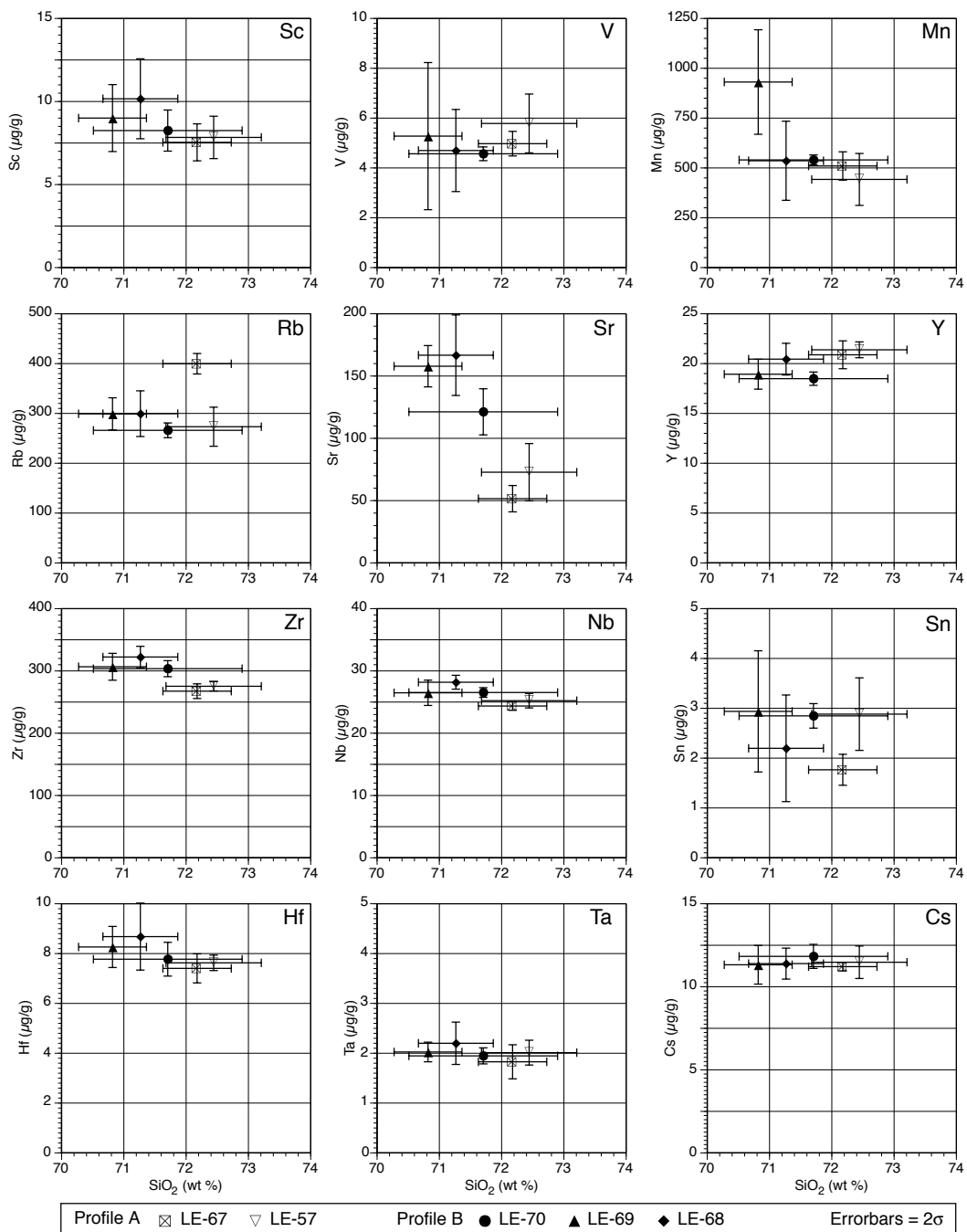


**Fig. D.1.** Various trace element contents determined by LA-ICP-MS plotted versus SiO<sub>2</sub>. SiO<sub>2</sub> contents have been recalculated to 100% without H<sub>2</sub>O. (continued next page)

## D. Analytical data

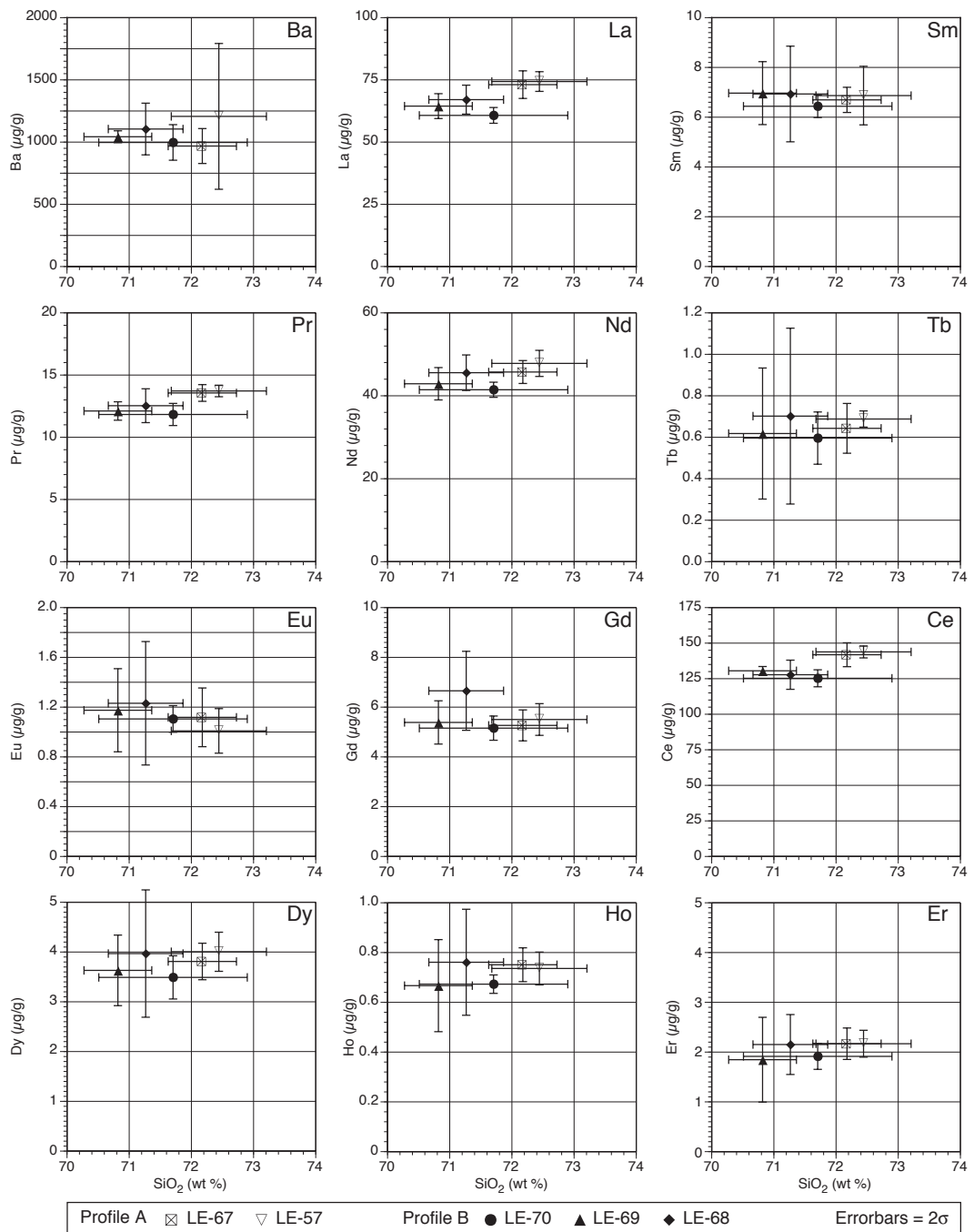


**Fig. D.1.** (continued) Various trace element contents determined by LA-ICP-MS plotted versus  $\text{SiO}_2$ .  $\text{SiO}_2$  contents have been recalculated to 100% without  $\text{H}_2\text{O}$ . (continued next page)

D.1. Geochemistry of the glass

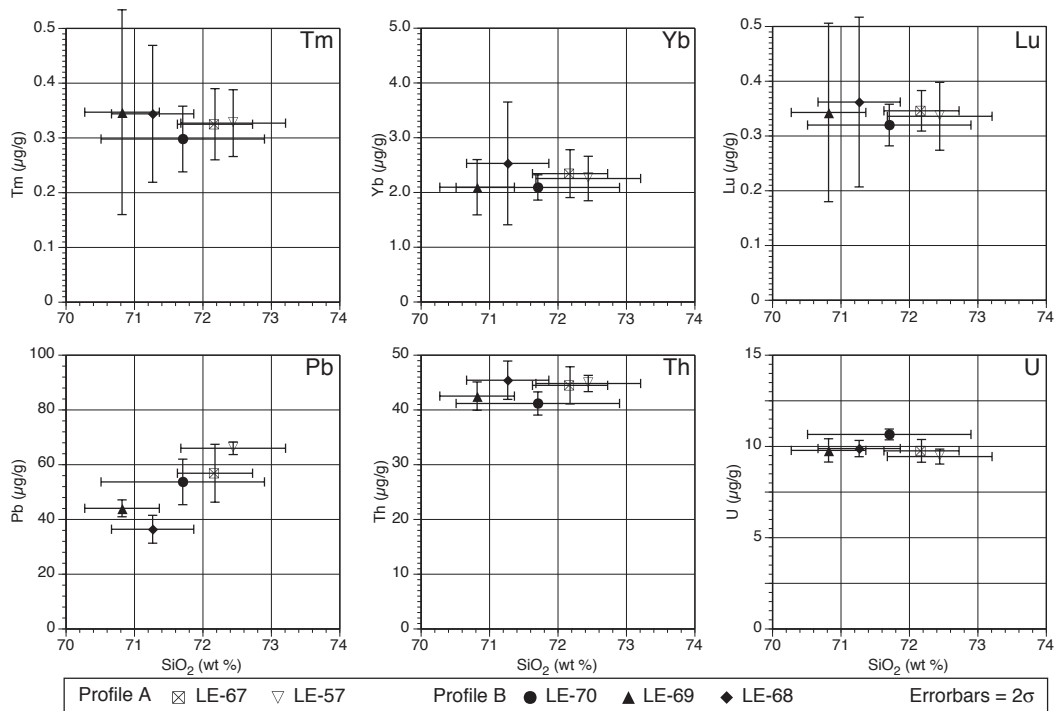


**Fig. D.1.** (continued) Various trace element contents determined by LA-ICP-MS plotted versus SiO<sub>2</sub>. SiO<sub>2</sub> contents have been recalculated to 100% without H<sub>2</sub>O.

#### D. Analytical data

---

**Table D.4.** Sr, Nd, and Pb isotopic composition of glass from samples LE-3 and LE-9 from an additional location. Separates of volcanic glass, hand-picked from two samples, which were chosen for their high glass content, were analysed using TIMS. Detailed information on sample preparation and analytical setup can be found on page 280 in section C.6 in the appendix.

Sample Type	LE-3 glass	LE-9 glass
Age (Ma)	17	17
Sr	61	61
Rb	263	247
Sm	7.1	6.7
Nd	49	45
Pb	62	69
U	9.8	9.7
Th	42.2	44
$^{87}\text{Rb}/^{86}\text{Sr}$	12.48	11.72
$^{87}\text{Sr}/^{86}\text{Sr}$	0.710597	0.710783
$^{87}\text{Sr}/^{86}\text{Sr}_i$	0.70758	0.70795
$^{147}\text{Sm}/^{144}\text{Nd}$	0.0880	0.0904
$^{143}\text{Nd}/^{144}\text{Nd}$	0.512313	0.512313
$^{143}\text{Nd}/^{144}\text{Nd}_i$	0.512303	0.512303
$\epsilon\text{Nd}_{(T)}$	-6.1	-6.1
$\epsilon\text{Nd}_{(0)}$	-6.3	-6.3
TDM*	0.97	0.99
$^{206}\text{Pb}/^{204}\text{Pb}$	18.629	18.672
$^{206}\text{Pb}/^{204}\text{Pb}_i$	18.60	18.65
$^{207}\text{Pb}/^{204}\text{Pb}$	15.709	15.763
$^{207}\text{Pb}/^{204}\text{Pb}_i$	15.71	15.76
$^{208}\text{Pb}/^{204}\text{Pb}$	39.060	39.236
$^{208}\text{Pb}/^{204}\text{Pb}_i$	39.02	39.20

\* Nd-stage model age, calculated with depleted mantle present-day parameters  $^{143}\text{Nd}/^{144}\text{Nd} = 0.513151$  and  $^{147}\text{Sm}/^{144}\text{Nd} = 0.219$

## D.2. Geochemistry of the phenocrysts

### D.2.1. Geochemistry of plagioclase and alkali feldspar

**Table D.5.** Average composition (weight %  $\pm 2\sigma$  standard error) of plagioclase rims in samples from Profile A and Profile B as determined by electron probe microanalysis. Formulas calculated to 8 oxygens. Additionally to orthoclase (Or), anorthoclase (An), and albite (Ab), celsian (Cls, Ba feldspar) and slawsonite (Slw, Sr feldspar) contents are calculated. n.a. = not analysed. Table continued next page.

	Profile A									
	LE-58 $\pm 2\sigma$ s.e.		LE-59 $\pm 2\sigma$ s.e.		LE-60 $\pm 2\sigma$ s.e.		LE-61 $\pm 2\sigma$ s.e.		LE-62 $\pm 2\sigma$ s.e.	
SiO <sub>2</sub>	62.39	0.31	62.94	0.18	62.20	0.29	62.46	0.15	62.08	0.83
Al <sub>2</sub> O <sub>3</sub>	23.23	0.11	23.16	0.12	23.21	0.23	23.62	0.10	23.33	1.00
FeO	0.42	0.05	0.35	0.01	0.37	0.04	0.38	0.02	0.42	0.05
CaO	4.17	0.32	4.44	0.13	4.61	0.22	4.60	0.08	4.71	0.49
BaO	0.43	0.12	0.30	0.04	0.24	0.03	0.26	0.02	0.20	0.05
SrO	0.10	0.10	0.12	0.03	0.14	0.05	0.12	0.02	0.14	0.05
Na <sub>2</sub> O	8.06	0.13	7.63	0.05	7.94	0.09	7.81	0.05	7.89	0.31
K <sub>2</sub> O	1.93	0.12	1.73	0.07	1.57	0.11	1.61	0.04	1.39	0.31
Total	100.72	0.37	100.67	0.17	100.28	0.42	100.86	0.17	100.19	0.57
Si	2.771		2.786		2.769		2.763		2.764	
Al	1.216		1.209		1.218		1.231		1.224	
Fe <sup>3+</sup>	0.015		0.013		0.014		0.014		0.016	
Ca	0.198		0.210		0.220		0.218		0.225	
Ba	0.008		0.005		0.004		0.005		0.004	
Sr	0.003		0.003		0.004		0.003		0.004	
Na	0.694		0.655		0.685		0.670		0.681	
K	0.109		0.098		0.089		0.091		0.079	
Total	5.015		4.979		5.002		4.995		4.997	
Or	10.8		10.1		8.9		9.2		8.0	
Ab	68.6		67.4		68.4		67.9		68.6	
An	19.6		21.6		21.9		22.1		22.7	
Cls	0.7		0.5		0.4		0.5		0.4	
Slw	0.3		0.3		0.4		0.3		0.4	

## D. Analytical data

Profile A										
	LE-57 ± 2σ s.e.		LE-63 ± 2σ s.e.		LE-64 ± 2σ s.e.		LE-65 ± 2σ s.e.		LE-67 ± 2σ s.e.	
SiO <sub>2</sub>	61.21	0.90	62.22	0.18	62.66	0.16	62.40	0.10	62.18	0.78
Al <sub>2</sub> O <sub>3</sub>	24.09	0.62	23.76	0.09	23.39	0.12	23.68	0.07	23.84	0.51
FeO	0.37	0.01	0.39	0.03	0.36	0.02	0.35	0.02	0.39	0.03
CaO	5.32	0.67	4.68	0.09	4.56	0.11	4.50	0.13	5.04	0.61
BaO	0.20	0.03	0.26	0.02	0.24	0.02	0.25	0.04	0.24	0.03
SrO	0.16	0.04	0.14	0.03	0.13	0.02	0.10	0.04	0.13	0.02
Na <sub>2</sub> O	7.82	0.32	8.09	0.08	7.92	0.05	8.05	0.10	7.86	0.30
K <sub>2</sub> O	1.31	0.14	1.41	0.08	1.47	0.09	1.36	0.11	1.22	0.09
Total	100.46	0.25	100.95	0.14	100.73	0.12	100.69	0.17	100.90	0.09
Si	2.724		2.752		2.773		2.762		2.749	
Al	1.263		1.238		1.220		1.235		1.242	
Fe <sup>3+</sup>	0.014		0.014		0.013		0.013		0.014	
Ca	0.253		0.222		0.216		0.214		0.239	
Ba	0.004		0.005		0.004		0.004		0.004	
Sr	0.004		0.004		0.003		0.003		0.003	
Na	0.675		0.693		0.679		0.690		0.674	
K	0.074		0.080		0.083		0.077		0.069	
Total	5.012		5.008		4.992		4.998		4.994	
Or	7.4		7.9		8.4		7.8		6.9	
Ab	66.8		69.2		68.9		69.9		68.2	
An	25.1		22.1		21.9		21.6		24.1	
Cls	0.3		0.5		0.4		0.4		0.4	
Slw	0.4		0.4		0.3		0.3		0.3	

Profile A			Profile B							
	LE-66 ± 2σ s.e.		LE-68 ± 2σ s.e.		LE-69 ± 2σ s.e.		LE-70 ± 2σ s.e.		LE-71 ± 2σ s.e.	
SiO <sub>2</sub>	62.20	0.19	60.62	0.14	60.57	0.30	60.49	0.21	60.26	0.20
Al <sub>2</sub> O <sub>3</sub>	23.61	0.14	24.45	0.12	24.74	0.15	24.31	0.28	24.72	0.17
FeO	0.35	0.03	0.36	0.02	0.35	0.02	0.39	0.03	0.40	0.04
CaO	4.57	0.15	5.81	0.12	5.92	0.16	5.63	0.32	6.05	0.12
BaO	0.28	0.02	0.26	0.02	0.25	0.02	0.32	0.16	0.22	0.02
SrO	0.14	0.05	0.29	0.03	0.28	0.03	0.30	0.02	0.31	0.04
Na <sub>2</sub> O	8.17	0.15	7.28	0.09	7.29	0.09	7.26	0.20	7.33	0.09
K <sub>2</sub> O	1.23	0.10	1.27	0.06	1.33	0.06	1.48	0.47	1.17	0.08
Total	100.55	0.22	100.34	0.19	100.73	0.20	100.18	0.10	100.44	0.20
Si	2.759		2.705		2.694		2.707		2.689	
Al	1.234		1.286		1.297		1.282		1.300	
Fe <sup>3+</sup>	0.013		0.013		0.013		0.015		0.015	
Ca	0.217		0.278		0.282		0.270		0.289	
Ba	0.005		0.005		0.004		0.006		0.004	
Sr	0.004		0.008		0.007		0.008		0.008	
Na	0.702		0.630		0.629		0.630		0.634	
K	0.069		0.072		0.075		0.085		0.066	
Total	5.004		4.996		5.003		5.002		5.004	
Or	7.0		7.3		7.6		8.5		6.6	
Ab	70.4		63.5		63.0		63.1		63.3	
An	21.8		28.0		28.3		27.1		28.9	
Cls	0.5		0.5		0.4		0.6		0.4	
Slw	0.4		0.8		0.7		0.8		0.8	

## D.2. Geochemistry of the phenocrysts

**Table D.6.** Average composition (weight %  $\pm 2\sigma$  standard error) of alkali feldspar rims in samples from Profile A and Profile B as determined by electron probe microanalysis. Formulas calculated to 8 oxygens. Additionally to orthoclase (Or), anorthoclase (An), and albite (Ab), celsian (Cls, Ba feldspar) and slawsonite (Slw, Sr feldspar) contents are calculated. n.a. = not analysed. Table *continued next page.*

	Profile A									
	LE-58 $\pm 2\sigma$ s.e.		LE-59 $\pm 2\sigma$ s.e.		LE-60 $\pm 2\sigma$ s.e.		LE-61 $\pm 2\sigma$ s.e.		LE-62 $\pm 2\sigma$ s.e.	
SiO <sub>2</sub>	63.46	0.14	63.89	0.10	63.71	0.30	63.90	0.23	63.76	0.19
Al <sub>2</sub> O <sub>3</sub>	19.94	0.12	19.92	0.05	19.78	0.10	20.08	0.09	19.91	0.07
FeO	0.26	0.02	0.27	0.02	0.27	0.02	0.28	0.02	0.24	0.02
CaO	0.58	0.03	0.54	0.02	0.54	0.03	0.57	0.02	0.55	0.02
BaO	2.51	0.08	2.51	0.08	2.33	0.16	2.51	0.05	2.29	0.19
SrO	0.12	0.03	0.11	0.02	0.10	0.02	0.13	0.03	0.12	0.03
Na <sub>2</sub> O	4.49	0.09	4.40	0.08	4.66	0.10	4.59	0.08	4.76	0.07
K <sub>2</sub> O	8.84	0.12	8.84	0.09	8.71	0.14	8.57	0.14	8.36	0.16
Total	100.20	0.20	100.50	0.11	100.11	0.33	100.63	0.21	99.99	0.15
Si	2.915		2.923		2.923		2.917		2.923	
Al	1.080		1.074		1.070		1.080		1.076	
Fe <sup>3+</sup>	0.010		0.010		0.010		0.011		0.009	
Ca	0.028		0.027		0.027		0.028		0.027	
Ba	0.045		0.045		0.042		0.045		0.041	
Sr	0.003		0.003		0.003		0.004		0.003	
Na	0.400		0.390		0.415		0.406		0.423	
K	0.518		0.516		0.510		0.499		0.489	
Total	4.999		4.988		4.999		4.990		4.990	
Or	52.1		52.6		51.2		50.8		49.7	
Ab	40.2		39.8		41.7		41.4		43.0	
An	2.9		2.7		2.7		2.8		2.8	
Cls	4.5		4.6		4.2		4.6		4.2	
Slw	0.3		0.3		0.3		0.4		0.3	

## D. Analytical data

Profile A										
	LE-57 ± 2σ s.e.		LE-63 ± 2σ s.e.		LE-64 ± 2σ s.e.		LE-65 ± 2σ s.e.		LE-67 ± 2σ s.e.	
SiO <sub>2</sub>	63.41	0.25	63.32	0.14	64.16	0.35	63.67	0.43	64.25	0.18
Al <sub>2</sub> O <sub>3</sub>	19.87	0.18	20.20	0.07	19.84	0.15	20.14	0.17	20.00	0.10
FeO	0.29	0.06	0.28	0.04	0.33	0.10	0.21	0.07	0.24	0.03
CaO	0.59	0.08	0.59	0.03	0.53	0.05	0.60	0.05	0.57	0.03
BaO	2.31	0.16	2.64	0.08	2.06	0.34	2.48	0.28	2.25	0.19
SrO	0.14	0.05	0.11	0.03	0.11	0.03	0.10	0.04	0.12	0.02
Na <sub>2</sub> O	4.76	0.18	4.48	0.07	4.45	0.12	4.51	0.09	4.58	0.12
K <sub>2</sub> O	8.47	0.25	8.81	0.12	9.06	0.25	8.71	0.13	8.77	0.18
Total	99.84	0.21	100.44	0.17	100.55	0.13	100.44	0.42	100.78	0.13
Si	2.916		2.905		2.927		2.914		2.924	
Al	1.077		1.092		1.067		1.086		1.073	
Fe <sup>3+</sup>	0.011		0.011		0.012		0.008		0.009	
Ca	0.029		0.029		0.026		0.030		0.028	
Ba	0.042		0.047		0.037		0.044		0.040	
Sr	0.004		0.003		0.003		0.003		0.003	
Na	0.425		0.398		0.394		0.400		0.405	
K	0.497		0.516		0.527		0.508		0.509	
Total	5.001		5.001		4.994		4.994		4.991	
Or	49.9		51.9		53.4		51.6		51.7	
Ab	42.7		40.1		39.9		40.6		41.1	
An	2.9		2.9		2.6		3.0		2.8	
Cls	4.2		4.8		3.7		4.5		4.1	
Slw	0.4		0.3		0.3		0.3		0.3	

Profile A			Profile B							
	LE-66 ± 2σ s.e.		LE-68 ± 2σ s.e.		LE-69 ± 2σ s.e.		LE-70 ± 2σ s.e.		LE-71 ± 2σ s.e.	
SiO <sub>2</sub>	63.99	0.64	n.a.		n.a.		62.58	0.00	63.95	0.96
Al <sub>2</sub> O <sub>3</sub>	20.09	0.05	n.a.		n.a.		20.11	0.03	19.56	0.48
FeO	0.24	0.03	n.a.		n.a.		0.28	0.05	0.44	0.16
CaO	0.63	0.04	n.a.		n.a.		0.56	0.03	0.86	0.25
BaO	2.09	0.44	n.a.		n.a.		3.90	0.19	2.23	0.15
SrO	0.09	0.06	n.a.		n.a.		9.23	0.15	0.24	0.06
Na <sub>2</sub> O	4.82	0.25	n.a.		n.a.		3.08	0.02	4.08	0.42
K <sub>2</sub> O	8.31	0.37	n.a.		n.a.		0.31	0.01	8.54	0.78
Total	100.26	0.22					100.04	0.01	99.89	0.82
Si	2.920						2.915		2.934	
Al	1.080						1.104		1.058	
Fe <sup>3+</sup>	0.009						0.011		0.017	
Ca	0.031						0.028		0.042	
Ba	0.037						0.071		0.040	
Sr	0.002						0.249		0.006	
Na	0.426						0.278		0.363	
K	0.484						0.018		0.500	
Total	4.990						4.675		4.960	
Or	49.3						2.8		52.6	
Ab	43.5						43.1		38.1	
An	3.1						4.3		4.4	
Cls	3.8						11.1		4.2	
Slw	0.2						38.7		0.7	

**Table D.7.** Orthoclase (Or), anorthoclase (An), and albite (Ab) contents of alkali feldspar rims and plagioclase rims from samples from Profile A and Profile B. Table shows minimum values (min), maximum values (max), arithmetic mean (mean), and  $2\sigma$  standard deviation ( $2\sigma$ ) for each sample.

		Akf rim values (r)				Pl rim values (r)				
		min	max	mean	$2\sigma$	min	max	mean	$2\sigma$	
Profile A	LE-58	Or	54.80	60.90	56.52	3.08	10.80	12.30	11.53	1.50
		An	2.60	3.90	3.16	0.76	19.00	21.30	19.83	2.55
		Ab	36.40	42.00	40.33	2.88	67.90	69.40	68.60	1.51
	LE-59	Or	54.60	58.80	57.11	2.68	9.00	12.40	10.61	1.71
		An	2.50	3.40	3.01	0.53	20.00	23.70	21.96	2.42
		Ab	37.90	42.60	39.89	2.79	66.60	68.40	67.41	1.21
	LE-60	Or	53.00	57.30	55.03	3.43	8.10	10.80	9.32	1.64
		An	2.50	3.20	2.83	0.49	19.40	24.80	22.26	2.89
		Ab	39.90	44.30	42.14	3.52	67.10	69.80	68.42	1.54
	LE-61	Or	50.17	57.20	54.59	3.69	8.71	10.40	9.58	0.92
		An	2.87	3.50	3.14	0.46	21.00	23.69	22.47	1.69
		Ab	39.60	46.44	42.26	3.71	67.10	68.80	67.92	1.04
	LE-62	Or	47.08	56.60	53.28	4.49	5.22	8.79	7.53	2.78
		An	2.50	3.63	3.07	0.61	21.93	26.60	23.99	3.35
		Ab	40.40	46.99	42.97	3.48	64.42	69.61	68.05	3.34
	LE-57	Or	48.44	54.02	52.26	3.86	6.62	8.77	7.73	1.40
		An	2.69	4.66	3.07	1.30	21.71	26.07	23.34	3.07
		Ab	43.05	48.87	44.68	4.14	67.31	70.63	68.93	2.20
	LE-63	Or	55.20	59.59	56.67	2.58	6.03	9.78	8.37	1.98
		An	2.59	3.78	3.23	0.61	20.63	24.51	22.44	2.05
		Ab	37.82	41.29	40.10	2.15	66.86	72.58	69.19	2.75
	LE-64	Or	55.23	58.62	56.65	2.07	5.40	11.62	8.82	2.92
		An	2.02	3.80	3.03	0.86	19.14	25.67	22.25	2.84
		Ab	38.77	41.51	40.31	1.76	66.73	70.86	68.93	1.79
LE-65	Or	54.00	57.17	55.70	2.75	5.11	9.55	7.46	4.46	
	An	3.03	3.66	3.25	0.55	20.32	21.75	21.24	1.59	
	Ab	39.80	42.60	41.05	2.28	69.14	72.73	70.52	3.87	
LE-67	Or	54.30	56.90	55.22	1.84	6.00	9.10	7.51	1.80	
	An	2.70	3.50	3.13	0.55	20.10	24.70	22.45	2.43	
	Ab	39.90	42.30	41.63	1.73	68.60	72.70	70.06	2.52	
LE-66	Or	50.31	57.05	53.15	5.51	5.88	8.82	7.44	1.73	
	An	3.19	3.51	3.36	0.27	20.08	23.54	22.16	2.37	
	Ab	39.63	46.40	43.49	5.39	67.81	73.02	70.40	3.31	
LE-68	Or	n.a.	n.a.	n.a.	n.a.	7.12	9.61	8.21	1.78	
	An	n.a.	n.a.	n.a.	n.a.	26.55	30.90	28.51	2.87	
	Ab	n.a.	n.a.	n.a.	n.a.	61.45	64.22	63.28	1.97	
LE-69	Or	n.a.	n.a.	n.a.	n.a.	6.32	8.15	7.34	1.58	
	An	n.a.	n.a.	n.a.	n.a.	27.82	29.55	28.56	1.16	
	Ab	n.a.	n.a.	n.a.	n.a.	62.68	65.52	64.10	2.04	
LE-70	Or	60.21	62.43	61.19	1.98	5.79	9.63	7.69	2.22	
	An	2.50	3.72	3.32	1.11	24.78	32.32	28.05	3.43	
	Ab	34.75	36.24	35.49	1.38	61.21	66.19	64.26	2.44	
LE-71	Or	51.93	59.26	56.77	8.38	5.71	8.19	7.51	1.87	
	An	3.74	6.22	5.10	2.52	27.22	29.94	28.71	2.02	
	Ab	35.42	41.84	38.13	6.66	61.87	65.48	63.78	2.97	

n.a. not analysed

## D. Analytical data

**Table D.8.** Or, An, and Ab contents of alkali feldspar and plagioclase internal data (middles, m); all data except rim data from samples from Profile A and Profile B. Tabel shows minimum values (min), maximum values (max), arithmetic mean, and  $2\sigma$  standard deviation for each sample.

		Akf internal values (m)				Pl internal values (m)				
		min	max	mean	$2\sigma$	min	max	mean	$2\sigma$	
Profile A	LE-58	Or	53.72	57.00	55.89	2.58	9.17	12.29	10.37	2.24
		An	2.68	3.17	2.98	0.34	19.05	22.27	21.16	2.57
		Ab	39.93	43.35	41.12	2.51	67.80	69.40	68.47	1.13
	LE-59	Or	54.39	58.83	56.55	3.10	1.93	13.03	9.12	5.26
		An	2.58	3.79	2.96	0.81	19.15	54.95	25.72	18.11
		Ab	38.58	42.60	40.49	2.90	43.11	69.73	65.16	13.24
	LE-60	Or	53.60	61.28	56.66	3.38	4.27	10.06	8.21	4.07
		An	2.11	3.39	2.86	0.68	20.81	37.73	25.54	11.75
		Ab	36.62	43.56	40.48	2.94	58.00	69.32	66.25	7.81
	LE-61	Or	46.17	59.74	53.26	8.21	2.52	12.35	7.00	6.15
		An	2.55	5.01	3.22	1.20	17.42	54.71	30.36	23.01
		Ab	37.60	48.81	41.86	5.25	41.35	71.55	62.09	17.46
	LE-62	Or	51.01	60.14	54.39	3.76	1.98	11.78	6.47	6.68
		An	1.69	4.36	2.93	1.10	18.81	58.40	33.38	26.93
		Ab	37.31	45.36	42.68	3.33	38.53	70.66	60.15	20.61
	LE-57	Or	48.76	56.58	53.50	3.22	2.23	10.01	6.14	5.78
		An	2.14	3.79	2.87	0.72	19.83	58.56	34.26	26.43
		Ab	41.28	47.45	43.63	2.74	39.02	70.23	59.60	21.06
	LE-63	Or	54.20	61.73	57.14	4.59	2.46	13.43	7.62	5.81
		An	2.20	3.77	2.86	0.85	15.64	49.69	28.29	21.53
		Ab	35.43	43.12	40.00	4.23	47.57	73.41	64.09	16.43
LE-64	Or	50.51	57.61	55.63	3.87	2.55	11.54	7.87	5.08	
	An	2.09	4.20	3.05	1.09	19.27	51.99	26.87	17.23	
	Ab	39.23	45.29	41.32	3.39	45.46	69.92	65.26	12.65	
LE-65	Or	49.09	58.05	54.64	4.11	2.67	12.43	7.32	5.24	
	An	2.28	4.54	3.02	1.12	18.07	49.66	28.26	18.34	
	Ab	39.04	47.12	42.35	4.05	47.32	71.11	64.42	13.46	
LE-67	Or	51.70	59.19	55.93	3.73	1.80	11.59	6.81	5.93	
	An	1.80	4.20	3.01	1.18	18.24	59.28	31.09	24.61	
	Ab	38.99	44.10	41.06	2.91	38.18	73.69	62.10	19.25	
LE-66	Or	46.71	59.51	54.68	6.49	2.76	12.80	7.46	4.44	
	An	1.48	4.14	3.07	1.55	17.70	46.73	26.24	14.73	
	Ab	38.83	49.29	42.25	5.45	50.47	73.81	66.30	11.43	
LE-68	Or	n.a.	n.a.	n.a.	n.a.	1.89	9.55	6.39	3.94	
	An	n.a.	n.a.	n.a.	n.a.	25.10	53.28	34.60	14.74	
	Ab	n.a.	n.a.	n.a.	n.a.	42.03	65.40	59.00	12.05	
LE-69	Or	57.96	60.70	59.62	2.68	0.82	11.69	6.24	5.53	
	An	2.22	3.35	2.65	0.88	23.20	72.31	36.14	28.46	
	Ab	36.86	39.26	37.73	2.06	26.73	66.80	57.62	23.59	
LE-70	Or	60.75	60.79	60.77	0.07	1.04	9.91	6.14	4.76	
	An	2.89	3.24	3.06	0.48	24.19	72.02	36.01	23.00	
	Ab	35.97	36.36	36.17	0.55	26.93	68.81	57.86	18.78	
LE-71	Or	59.37	61.66	60.10	2.10	1.57	10.54	7.12	3.73	
	An	2.68	3.45	3.05	0.65	25.62	62.96	31.88	15.33	
	Ab	35.21	37.96	36.86	2.36	35.29	65.70	61.00	12.17	

n.a. not analysed

**Table D.9.** Strontium isotope data for plagioclase from Profile A (LE-59, LE-62, LE-65, LE-67) and Profile B (LE-69, LE-70), determined by LA-ICP-MS.

Work on the LA-ICP-MS was carried out in cooperation with Yann Lahaye at the Institut für Geowissenschaften at the Universität Frankfurt am Main. For details on the analytical setup see section C.4 on page 277.

sample	crystal no.	data point	$^{87}\text{Sr}/^{86}\text{Sr}$			core/rim		
			high	low	average			
LE-59	III-1	1	0.70849	0.70824	0.70836	c	Profile A	
		2	0.70849	0.70821	0.70835	c		
	I-1	4	0.70815	0.70783	0.70799	c		
		2	0.70837	0.70814	0.70825	r		
		3	0.70857	0.70801	0.70829	r		
		1	0.70833	0.70792	0.70813	r		
	V-2	1	0.70826	0.70788	0.70807	c		
	LE-62	VII-3	1	0.70831	0.70818	0.70824		c
			3	0.70839	0.70814	0.70826		c
		VIII-1	1	0.70846	0.7083	0.70838		c
2			0.7085	0.70822	0.70836	c		
LE-65	II-14	1	0.70832	0.7081	0.70821	c		
		2	0.70843	0.70823	0.70833	c		
		3	0.70855	0.70781	0.70818	r		
		4	0.70840	0.70804	0.70822	r		
LE-67	I-1	1	0.70855	0.70829	0.70842	c		
		2	0.70851	0.70827	0.70839	c		
	VII-2	1	0.70841	0.70824	0.70833	c		
		2	0.70845	0.70829	0.70837	c		
LE-69	I-3	c1	0.70808	0.70758	0.70783	c	Profile B	
		c2	0.70796	0.70785	0.7079	c		
		r1	0.70802	0.70734	0.70768	r		
		r2	0.70809	0.70783	0.70796	r		
	I-4	c1	0.70808	0.70786	0.70797	c		
		r1	0.7081	0.70764	0.70787	r		
	I-5	r2	0.70812	0.70767	0.70789	r		
		c1	0.70812	0.70784	0.70798	c		
	LE-70	II-7	c2	0.70818	0.70804	0.70811		c
			r2	0.7082	0.70801	0.7081		r
VI-1		c1	0.70818	0.70789	0.70803	c		
		c2	0.70828	0.70793	0.7081	c		
		r1	0.70836	0.70801	0.70818	c		
		r2	0.70831	0.70784	0.70807	c		

### D.2.2. Geochemistry of biotite

See next page

D. Analytical data

**Table D.10.** Typical biotite compositions in samples from Profile A and Profile B. Formulas calculated to 10 oxygens + 2 OH; all Fe is calculated as Fe<sup>2+</sup>. *Table continued next page.*

Sample	Profile A																
	LE-58		LE-59		LE-60		LE-61		b-VIII4 a-39		LE-62		LE-57		LE-63		
Analysis no.	b-74	b-89	b-58	b-61	b-80	b-87	b-109	b-115	b-119	b-VIII4 a-39	b-68	b-70	b-123	b-127	b-37	b-40	b-44
SiO <sub>2</sub>	36.60	36.21	37.55	36.82	36.76	38.14	36.66	37.10	35.62	37.23	35.63	35.62	36.93	37.44	38.83	36.41	35.74
TiO <sub>2</sub>	6.38	5.75	5.52	5.76	5.91	5.56	4.46	5.69	5.92	5.63	4.86	5.82	5.85	5.61	5.52	4.55	6.15
Al <sub>2</sub> O <sub>3</sub>	13.90	14.27	13.20	13.51	14.49	13.00	14.93	13.37	14.04	13.04	14.06	13.76	13.39	13.21	12.73	13.79	13.61
Cr <sub>2</sub> O <sub>3</sub>	.00	.00	.03	.00	.00	.02	.02	.00	.00	.00	.00	.00	.00	.00	.03	.00	.00
FeO	14.11	14.98	14.18	14.49	13.34	13.80	13.53	14.08	14.94	14.12	14.78	14.59	14.29	13.94	14.35	14.54	14.83
MnO	.20	.34	.34	.32	.22	.33	.19	.30	.36	.32	.35	.32	.31	.36	.35	.32	.34
MgO	14.50	13.97	15.07	14.82	15.17	15.60	15.10	15.13	14.02	15.13	14.79	14.45	15.00	15.34	15.16	15.42	14.44
BaO	1.73	1.97	.68	1.15	1.82	.42	1.69	.75	2.28	.48	1.67	1.64	1.21	.65	.34	1.48	1.84
CaO	.01	.06	.02	.00	.02	.00	.07	.00	.00	.02	.00	.00	.00	.00	.05	.00	.01
Ni <sub>2</sub> O	.70	.67	.71	.70	.87	.73	.80	.62	.68	.68	.72	.71	.70	.77	.78	.77	.75
K <sub>2</sub> O	8.31	8.23	8.61	8.66	8.24	8.87	7.91	8.43	8.05	8.73	8.51	8.53	8.52	8.80	8.72	8.43	8.30
H <sub>2</sub> O	4.02	4.00	4.03	4.02	4.06	4.07	4.01	4.01	3.96	4.01	3.95	3.95	4.02	4.04	4.09	3.98	3.97
Total	100.46	100.44	99.93	100.23	100.89	100.53	99.37	99.47	99.86	99.39	99.32	99.38	100.22	100.15	100.94	99.70	99.97
Si	2.727	2.716	2.794	2.749	2.717	2.811	2.743	2.771	2.696	2.785	2.705	2.700	2.754	2.781	2.849	2.740	2.698
Ti	0.357	0.324	0.309	0.323	0.328	0.308	0.251	0.320	0.337	0.317	0.277	0.332	0.328	0.313	0.305	0.258	0.349
Al	1.221	1.261	1.157	1.189	1.262	1.129	1.317	1.177	1.252	1.149	1.258	1.229	1.177	1.156	1.101	1.223	1.210
Cr	0.000	0.000	0.002	0.000	0.000	0.001	0.001	0.000	0.000	0.000	0.000	0.000	0.000	0.000	0.002	0.000	0.000
Fe <sup>2+</sup>	0.880	0.940	0.882	0.905	0.825	0.851	0.847	0.880	0.945	0.884	0.938	0.925	0.891	0.866	0.881	0.915	0.936
Mn	0.013	0.021	0.021	0.020	0.014	0.021	0.012	0.019	0.023	0.020	0.023	0.020	0.019	0.023	0.022	0.020	0.022
Ni	0.000	0.000	0.000	0.000	0.000	0.000	0.000	0.000	0.000	0.000	0.000	0.000	0.000	0.000	0.000	0.000	0.000
Mg	1.611	1.562	1.672	1.649	1.672	1.714	1.685	1.685	1.582	1.688	1.673	1.633	1.668	1.698	1.658	1.730	1.624
Ba	0.050	0.058	0.020	0.034	0.053	0.012	0.050	0.022	0.068	0.014	0.050	0.049	0.035	0.019	0.010	0.044	0.054
Ca	0.001	0.005	0.001	0.000	0.002	0.000	0.006	0.000	0.000	0.002	0.000	0.000	0.000	0.000	0.004	0.000	0.000
Na	0.101	0.097	0.102	0.102	0.125	0.105	0.116	0.090	0.099	0.099	0.107	0.105	0.101	0.110	0.111	0.113	0.109
K	0.790	0.787	0.817	0.825	0.777	0.834	0.755	0.803	0.778	0.833	0.824	0.825	0.811	0.834	0.816	0.809	0.799
OH	2.000	2.000	2.000	2.000	2.000	2.000	2.000	2.000	2.000	2.000	2.000	2.000	2.000	2.000	2.000	2.000	2.000
Total/750	7.771	7.777	7.796	7.775	7.785	7.782	7.767	7.780	7.790	7.854	7.818	7.785	7.800	7.758	7.851	7.802	7.839
Mg#	64.7	62.4	65.5	64.6	67.0	66.8	66.6	65.7	62.6	65.6	64.1	63.8	65.2	66.2	65.3	65.4	63.4
K+Na+Ba+Ca	0.942	0.947	0.940	0.961	0.957	0.951	0.926	0.915	0.945	0.948	0.980	0.978	0.947	0.963	0.941	0.965	0.963
Al <sup>IV</sup>	1.221	1.261	1.157	1.189	1.262	1.129	1.257	1.177	1.252	1.149	1.258	1.229	1.177	1.156	1.101	1.223	1.210
Ti <sup>IV</sup>	0.052	0.023	0.049	0.062	0.021	0.060	0.000	0.051	0.052	0.066	0.037	0.071	0.069	0.063	0.049	0.037	0.092
Octahedral	2.809	2.825	2.837	2.836	2.818	2.834	2.856	2.852	2.835	2.842	2.874	2.840	2.838	2.837	2.817	2.886	2.839

**Table D.10.** *Table continued from previous page.* Typical biotite compositions in samples from Profile A and Profile B. Formulas calculated to 10 oxygens + 2 OH; all Fe is calculated as Fe<sup>2+</sup>.

Sample	Profile A										Profile B									
	LE-64		LE-65		LE-67		LE-66		LE-68		LE-69		LE-70		b-V7a					
Analysis no.	b-200	a-91	a-90	a-91	a-94	b-177	b-87	b-72	b-74	b-88	b-2	b-3	b-29	a-15p1	b-107	b-V7a				
SiO <sub>2</sub>	37.79	35.09	36.98	36.79	37.58	36.93	36.30	36.15	35.80	37.04	36.52	36.32	36.40	36.72	36.87	38.00				
TiO <sub>2</sub>	5.52	6.12	5.58	5.71	5.46	5.52	6.12	5.76	4.70	5.53	5.02	4.90	5.03	3.94	4.80	4.73				
Al <sub>2</sub> O <sub>3</sub>	12.91	13.82	13.37	13.24	12.72	12.71	13.37	12.23	12.79	11.57	13.44	13.42	13.59	14.26	13.94	13.71				
Cr <sub>2</sub> O <sub>3</sub>	.01	.00	.00	.00	.02	.00	.00	.00	.00	.00	.00	.00	.00	.00	.00	.01				
FeO	14.19	15.40	14.18	15.24	15.19	15.31	13.91	14.45	14.55	13.23	15.17	15.54	14.65	14.76	15.00	14.56				
MnO	.27	.33	.33	.33	.27	.24	.16	.29	.33	.25	.30	.27	.16	.28	.20	.25				
NiO	.00	.00	.00	.00	.00	.00	.00	.00	.00	.00	.00	.00	.00	.00	.00	.00				
MgO	15.39	13.99	14.93	15.01	14.54	14.20	14.60	14.31	15.41	15.90	14.65	14.76	14.80	15.22	14.54	15.18				
BaO	.38	2.90	1.35	1.19	.65	.94	1.68	1.72	1.66	.91	.94	1.14	1.20	1.04	1.37	.55				
CaO	.01	.00	.03	.01	.03	.02	.00	.03	.00	.02	.00	.00	.00	.00	.00	.01				
Nb <sub>2</sub> O <sub>5</sub>	.72	.73	.71	.65	.74	.83	.64	.82	.78	.68	.60	.63	.68	.60	.62	.58				
K <sub>2</sub> O	9.09	8.06	8.42	8.17	8.57	8.70	8.25	8.36	8.46	8.57	8.55	8.44	8.57	8.42	8.66	8.84				
H <sub>2</sub> O	4.05	3.95	4.01	4.02	4.01	3.96	3.97	3.90	3.91	3.94	3.97	3.96	3.96	3.98	4.00	4.06				
Total	100.31	100.38	99.89	100.37	99.78	99.25	99.20	97.83	98.43	97.72	99.15	99.38	99.05	99.22	100.00	100.47				
Si	2.801	2.665	2.767	2.748	2.813	2.793	2.740	2.782	2.743	2.821	2.760	2.748	2.753	2.763	2.766	2.809				
Ti	0.307	0.350	0.314	0.321	0.308	0.314	0.347	0.333	0.271	0.317	0.285	0.279	0.286	0.223	0.271	0.263				
Al	1.128	1.237	1.179	1.165	1.122	1.133	1.190	1.110	1.155	1.038	1.198	1.196	1.211	1.265	1.233	1.194				
Cr	0.001	0.000	0.000	0.000	0.001	0.000	0.000	0.000	0.000	0.000	0.000	0.000	0.000	0.000	0.000	0.001				
Fe <sup>2+</sup>	0.880	0.978	0.888	0.952	0.951	0.968	0.878	0.930	0.932	0.843	0.959	0.983	0.927	0.929	0.941	0.900				
Mn	0.017	0.021	0.021	0.021	0.017	0.015	0.010	0.019	0.021	0.016	0.019	0.018	0.010	0.018	0.013	0.016				
Ni	0.000	0.000	0.000	0.000	0.000	0.000	0.000	0.000	0.000	0.000	0.000	0.000	0.000	0.000	0.000	0.000				
Mg	1.701	1.585	1.666	1.671	1.623	1.601	1.643	1.642	1.761	1.805	1.651	1.665	1.669	1.707	1.625	1.673				
Ba	0.011	0.086	0.040	0.035	0.019	0.028	0.050	0.052	0.050	0.027	0.028	0.034	0.036	0.031	0.040	0.016				
Ca	0.000	0.000	0.002	0.001	0.002	0.001	0.000	0.002	0.000	0.002	0.000	0.000	0.000	0.000	0.000	0.001				
Na	0.103	0.107	0.102	0.094	0.107	0.107	0.122	0.096	0.122	0.115	0.088	0.092	0.099	0.088	0.090	0.083				
K	0.859	0.781	0.804	0.778	0.818	0.839	0.795	0.821	0.827	0.833	0.825	0.815	0.827	0.808	0.828	0.834				
OH	2.000	2.000	2.000	2.000	2.000	2.000	2.000	2.000	2.000	2.000	2.000	2.000	2.000	2.000	2.000	2.000				
Total	7.808	7.811	7.782	7.785	7.780	7.799	7.776	7.787	7.883	7.817	7.812	7.829	7.818	7.830	7.806	7.789				
Mg#	65.9	61.8	65.2	63.7	63.1	62.3	65.2	63.8	65.4	68.2	63.3	62.9	64.3	64.8	63.3	65.0				
K+Na+Ba+Ca	0.974	0.974	0.948	0.908	0.947	0.975	0.967	0.970	0.999	0.976	0.940	0.940	0.962	0.926	0.958	0.933				
Al <sup>IV</sup>	1.128	1.237	1.179	1.165	1.122	1.133	1.110	1.110	1.155	1.038	1.198	1.196	1.211	1.237	1.233	1.191				
Ti <sup>IV</sup>	0.071	0.098	0.054	0.087	0.065	0.074	0.070	0.108	0.101	0.140	0.042	0.056	0.036	0.000	0.002	0.000				
Octahedral	2.835	2.836	2.834	2.877	2.834	2.824	2.809	2.817	2.884	2.840	2.872	2.888	2.856	2.904	2.848	2.855				

D. Analytical data

**D.2.3. Geochemistry of amphibole and orthopyroxene**

**Table D.11.** Typical amphibole and orthopyroxene compositions in samples from Profile A (LE-67) and from an additional location (LE-5). Am calculated to 22 oxygens + 2 OH and 13 cations without Ca, Na, and K. Opx calculated to 6 oxygens and a fixed number of 4 cations.

Sample Mineral Analysis no.	additional location		Profile A		
	LE-5		LE-67		
	Am		Opx		
	a-86	a-87	b-143	b-144	b-146
SiO <sub>2</sub>	41.95	41.50	53.14	53.28	52.95
TiO <sub>2</sub>	2.59	2.72	.39	.41	.39
Al <sub>2</sub> O <sub>3</sub>	11.45	11.67	1.15	1.23	1.15
Cr <sub>2</sub> O <sub>3</sub>	.00	.00	.06	.02	.02
Fe <sub>2</sub> O <sub>3</sub>	8.76	7.18	20.95	20.42	20.66
FeO	4.42	5.54	.00	.00	.00
MnO	.21	.24	.43	.42	.44
MgO	14.21	13.99	22.52	22.42	22.81
BaO	.01	.04	.05	.00	.02
CaO	10.94	11.26	1.88	1.92	1.92
Na <sub>2</sub> O	2.30	2.29	.06	.04	.07
K <sub>2</sub> O	.94	.94	.00	.02	.04
H <sub>2</sub> O	2.05	2.04	.00	.00	.00
Total	99.83	99.38	100.62	100.18	100.46
Si	6.125	6.103	1.983	1.990	1.978
Ti	0.284	0.301	0.011	0.011	0.011
Al	1.970	2.022	0.050	0.054	0.051
Cr	0.000	0.000	0.002	0.001	0.000
Fe <sup>3+</sup>	0.963	0.795	0.000	0.000	0.000
Fe <sup>2+</sup>	0.540	0.681	0.588	0.574	0.581
Mn	0.026	0.029	0.013	0.013	0.014
Mg	3.092	3.066	1.253	1.248	1.270
Ba	0.001	0.002	0.001	0.000	0.000
Ca	1.712	1.774	0.075	0.077	0.077
Na	0.651	0.652	0.005	0.003	0.005
K	0.176	0.176	0.000	0.001	0.002
OH	2.000	2.000	0.000	0.000	0.000
Total	15.538	15.602	3.982	3.973	3.989
Mg-Value	67.3	67.5	68.1	68.5	68.6
Mg#	85.1	81.8	68.1	68.5	68.6

## D.2.4. Geochemistry of clinopyroxene

**Table D.12.** Typical clinopyroxene compositions in samples from Profile A (LE-67) and from an additional location (LE-5). Cpx calculated to 6 oxygens fixed number of 4 cations.

Sample Mineral	additional location					Profile B					
	LE-5 Cpx					LE-69 Cpx			LE-70 Cpx		
	dVI4					b-4	b-6	b-9	a #11e		a#13a
a-91	a-103	a-10	a-27	a-44	-101 rim				-105 core	-107	
Grain no.											
Analysis no.											
SiO <sub>2</sub>	52.67	50.80	52.18	52.84	52.24	53.17	51.98	51.80	48.72	52.54	53.14
TiO <sub>2</sub>	.35	.61	.28	.24	.30	.15	.20	.31	1.20	.44	.23
Al <sub>2</sub> O <sub>3</sub>	1.13	2.08	1.12	.82	1.13	.69	1.12	1.46	6.13	3.18	1.13
Cr <sub>2</sub> O <sub>3</sub>	.00	.01	.00	.06	.00	.00	.02	.01	.05	.23	.03
Fe <sub>2</sub> O <sub>3</sub>	2.44	3.45	2.43	1.10	2.16	.80	2.19	1.47	2.29	1.03	.39
FeO	5.85	6.63	6.18	7.32	6.47	7.42	7.11	9.54	5.37	4.26	8.79
MnO	.96	.93	.94	.71	.83	.88	.88	.90	.13	.19	.91
NiO	.00	.00	.00	.00	.00	.00	.00	.00	.00	.00	.00
MgO	14.28	12.82	13.67	13.88	13.78	14.68	13.38	12.39	13.56	16.39	13.71
BaO	n.a.	n.a.	n.a.	n.a.	n.a.	n.a.	n.a.	n.a.	.00	.00	.03
CaO	22.22	21.52	22.41	22.46	22.20	21.38	22.09	21.50	21.91	22.07	21.31
Na <sub>2</sub> O	.55	.72	.52	.39	.52	.38	.47	.46	.33	.28	.49
K <sub>2</sub> O	.00	.00	.01	.01	.00	.04	.00	.00	.01	.00	.01
H <sub>2</sub> O	.00	.00	.00	.00	.00	.00	.00	.00	.00	.00	.00
Total	100.44	99.56	99.74	99.83	99.62	99.57	99.44	99.85	99.70	100.61	100.16
Si	1.951	1.914	1.952	1.973	1.955	1.984	1.955	1.954	1.812	1.912	1.981
Ti	0.010	0.017	0.008	0.007	0.008	0.004	0.006	0.009	0.034	0.012	0.006
Al	0.049	0.092	0.049	0.036	0.050	0.030	0.050	0.065	0.268	0.136	0.050
Cr	0.000	0.000	0.000	0.002	0.000	0.000	0.001	0.000	0.001	0.007	0.001
Fe <sup>3+</sup>	0.068	0.098	0.069	0.031	0.061	0.022	0.062	0.042	0.064	0.028	0.011
Fe <sup>2+</sup>	0.181	0.209	0.193	0.229	0.202	0.231	0.224	0.301	0.167	0.130	0.274
Mn	0.030	0.030	0.030	0.022	0.026	0.028	0.028	0.029	0.004	0.006	0.029
Ni	0.000	0.000	0.000	0.000	0.000	0.000	0.000	0.000	0.000	0.000	0.000
Mg	0.789	0.720	0.762	0.773	0.769	0.817	0.750	0.697	0.752	0.889	0.762
Ba	n.a.	n.a.	n.a.	n.a.	n.a.	n.a.	n.a.	n.a.	0.000	0.000	0.000
Ca	0.882	0.868	0.898	0.899	0.890	0.855	0.891	0.869	0.873	0.860	0.851
Na	0.039	0.052	0.038	0.028	0.038	0.027	0.034	0.034	0.024	0.020	0.035
K	0.000	0.000	0.001	0.000	0.000	0.002	0.000	0.000	0.001	0.000	0.001
OH	0.000	0.000	0.000	0.000	0.000	0.000	0.000	0.000	0.000	0.000	0.000
Total	4.000	4.000	4.000	4.000	4.000	4.000	4.000	4.000	4.000	4.000	4.000
Mg-Value	76.0	70.1	74.4	74.9	74.5	76.3	72.4	67.0	76.5	84.9	72.8
Mg#	81.3	77.5	79.8	77.2	79.2	77.9	77.0	69.8	81.8	87.3	73.6

n.a. not analysed

### D.3. Lithium, Beryllium, and Boron in glass and phenocrysts

#### D.3.1. Lithium, Beryllium, and Boron concentrations

**Table D.13.** Partition coefficients  $D$  for Be and B between Pl and glass and Akf and glass, respectively. For samples with devitrified glass (LE-63, LE-64, LE-65, LE-66, LE-67 in Profile A and LE-71 in Profile B) partition coefficients were not calculated, since the devitrification process altered element concentration in glass and minerals. Other partition coefficient were not calculated due to the lack of satisfactory mineral analyses. Average An contents for Pl rims and average Or contents for Akf rims for each sample are shown in the last two columns.

Element concentration were analysed by secondary ion mass-spectrometry (SIMS) at the Universität Heidelberg. Details about the analytical setup can be found in section C.3.1 on page 273 in the appendix.

sample	$D_{\text{Be}}$ mineral/glass				$D_{\text{B}}$ mineral/glass				An	Or	
	$\text{Pl} \pm 2\sigma$ s.e.		$\text{Akf} \pm 2\sigma$ s.e.		$\text{Pl} \pm 2\sigma$ s.e.		$\text{Akf} \pm 2\sigma$ s.e.		Pl rims	Akf rims	
Profile A	LE-58			0.0567	0.0022			0.00521	0.00073	19.8	56.5
	LE-59	0.364	0.038	0.0565	0.0029	0.00887	0.00047	0.00516	0.00040	22.0	57.1
	LE-60	0.378	0.027	0.0561	0.0042	0.00899	0.00048	0.00517	0.00055	22.3	55.0
	LE-61	0.358	0.009			0.00925	0.00084			22.5	54.6
	LE-62	0.382	0.025	0.0580	0.0016	0.00917	0.00017	0.00505	0.00009	24.0	53.3
	LE-57	0.389	0.064			0.00900	0.00137			23.3	52.3
average A	0.363	0.013	0.0573	0.0011	0.00912	0.00014	0.00506	0.00009			
Profile B	LE-68	0.438	0.169			0.00976	0.00328			28.5	
	LE-69	0.426	0.009			0.00962	0.00230			28.6	
	LE-70	0.484	0.086	0.0532	0.0020	0.0129	0.0019	0.00511	0.00047	28.1	61.2
average B	0.427	0.009			0.0113	0.0050					
average A+B	0.389	0.029	0.0563	0.0026	0.00915	0.00028	0.00506	0.00008			

Averages for  $D$  are weighted means, errors are  $2\sigma$  standard errors; averages for An and Or are arithmetic means.

**Table D.14.** Lithium, Beryllium, an Boron contents in glass, plagioclase and alkali feldspar in samples from Profile A and Profile B. For each phase the first column shows element contents, the second column shows errors. Averages are arithmetic means, errors are  $2\sigma$  standard errors. Element concentration were analysed by secondary ion mass-spectrometry (SIMS) at the Universität Heidelberg. Details of the analytical setup can be found in section C.3.1 on page 273 in the appendix.

sample	Li $\mu\text{g/g} \pm 2\sigma$ s.e.			Be $\mu\text{g/g} \pm 2\sigma$ s.e.			B $\mu\text{g/g} \pm 2\sigma$ s.e.			number of analyses		
	glass	Pl rims	Akf rims	glass	Pl rims	Akf rims	glass	Pl rims	Akf rims	gl	Pl	Akf
Profile A												
LE-58	11.3	0.9	0.151	5.05	0.10	0.286	107.8	2.4	0.562	7		3
LE-59	16.5	1.4	0.626	4.93	0.04	0.279	105.4	0.7	0.544	29	5	18
LE-60	11.7	3.0	1.59	4.96	0.19	0.279	106.6	2.9	0.551	4	6	11
LE-61	12.6	1.9	2.90	5.07	0.06	0.280	106.6	1.9	0.536	3	4	4
LE-62	8.39	2.2	2.59	4.82	0.08	0.280	106.2	1.9	0.536	22	5	12
LE-57	7.31	2.5	5.98	5.00	0.25	0.280	108.8	4.5	0.536	3	5	5
LE-63*												
LE-64*												
LE-65*												
LE-67**	14.2	2.7	7.52	4.78	0.06	0.319	106.3	1.2	0.557	31	19	19
LE-66*												
average A				4.94	0.08	0.296	106.8	0.9	0.556			
Profile B												
LE-68b	13.4	3.4	1.64	5.80	0.13	0.294	96.14	1.46	0.494	7	5	5
LE-69b	20.0	4.8	2.38	5.36	0.06	0.294	92.48	0.92	0.494	17	2	2
LE-70b	8.32	2.86	2.14	5.54	0.21	0.294	96.64	1.43	0.494	16	6	3
LE-71*												
average B	13.9	6.8	2.05	5.57	0.26	0.25	95.08	2.62	1.03			

\* samples with devitrified glass matrix, the analysed phenocrysts in petrographic equilibrium with the devitrified matrix.

\*\* sample with devitrified glass matrix, pristine glass was found and analysed, however, the analysed phenocrysts are in petrographic equilibrium with the devitrified matrix.



## E. Miscellaneous

**Table E.1.** Alphabetic list of alternative place names, used for towns and villages, islands and regions in the study area.

Ayvalik	Kidoniae			
Bergama	Pergamos			
Eressos	Eresos			
Chios	Khios	Hios	Khóra	Scio
Chios	Sakız	Castro	Kastron	
İzmir	Smyrna			
Kaloyeri	Koca Ada	Koca Adası		
Lepetemos	Lepetimnos	Lepetymnos		
Lisbori	Lisvorio			
Lesbos	Lesvos	Mytilini	Mytilene	
Mamtamos	Mandamos			
Mithimna	Molivos			
Mytilene	Mytilini	Midilli		
Nea Kidonia	Nees Kidonies			
Oinousai	Oinoussai	Oinousses	Aignoussa	
Skalohorion	Skalochori			
Sykaminea	Sikaminia			
Thasos	Thassos			



## **Eidesstattliche Erklärung**

Hiermit erkläre ich, Angela Herta Helbling-Marschall, geboren am 31.05.1972 in Darmstadt, an Eides statt, dass ich die vorliegende Dissertation selbst verfasst und mich dabei keiner anderen als der von mir ausdrücklich bezeichneten Quellen und Hilfen bedient habe.

Ich, Angela Herta Helbling-Marschall, geboren am 31.05.1972 in Darmstadt, erkläre zudem an Eides statt, dass ich an keiner anderen Stelle ein Prüfungsverfahren beantragt habe, dass ich die Dissertation nicht in dieser oder anderer Form bereits anderweitig als Prüfungsarbeit verwendet habe und dass ich sie an keiner anderen Fakultät als Dissertation vorgelegt habe.

Heidelberg, am 8. August 2011